Development of selective fluorescent imaging agents for neurofibrillary tangles in Alzheimer's diagnosis

TECHNISCHE UNIVERSITÄT DARMSTADT

Vom Fachbereich Chemie
der Technischen Universität Darmstadt

zur Erlangung des akademischen Grades eines
Doctor rerum naturalium (Dr. rer. nat.)

genehmigte

kumulative Dissertation

vorgelegt von

Upendra Rao Anumala, M.Sc.
aus Nelakondapally (Indien)

Referent: Prof. Dr. Boris Schmidt

Korreferenten: Prof. Dr. Harald Kolmar

Tag der Einreichung: 25. Juli 2013

Tag der mündlichen Prüfung: 07. Oktober 2013

Darmstadt (2013)

D17

The present work was performed under the supervision of Prof. Dr. Boris Schmidt at the Clemens Schöpf-Institute of Organic Chemistry and Biochemistry of the Technische Universität Darmstadt from February 2010 to June 2013.

To my mother

Acknowledgements

The work embodied in this thesis was carried out from February 2010 to June 2013 at the Clemens Schöpf-Institute of Organic Chemistry and Biochemistry of the Technische Universität Darmstadt. These three years that I had been through was truly once in a life time experience. I realize there are many people who deserve to be thanked for what I have become now.

First and foremost, I would like to express my sincere gratitude to my supervisor and guide, Prof. Dr. Boris Schmidt, for his continuous support and helpful guidance. I indeed consider it an honor to have worked under such a renowned scientist in the field of Alzheimer's research. His simplicity, enthusiasm and passion towards research has inspired and motivated me in my work at each and every step of my tenure at Technische Universität Darmstadt (TUD). Discussions with him have always given me invaluable insights into my work.

Secondly, I owe my thanks to several people at our Institute of Organic Chemistry at the TUD for contributing towards my successful research and eventful life in Darmstadt. Our group secretary Birgit, fellow lab-mates, namely Daniel, Andrea, Constantin, Christoph, Stefan, Binia, and Eva helped me during my days at the institute to get myself quickly accustomed to the life at TUD. My co-researchers, namely Jiamin, Fabio, Thomas, Marlyse, Stephanie and Azadeh played a significant role in terms of chemistry and non-chemistry discussions, help with German language, and not-to-forget a great friendship. Big thanks to all of you. Several bachelor students at the institute, namely Alex, Kai, and Dennis, too made valuable contributions towards my research through their thesis works. I would like to thank all these people for their help and positive influence in my work.

Thirdly, my work would not have been accomplished if not for the kind cooperation from various collaborating institutes, research groups, and companies. I would like to thank Prof. Dr. Adrian Palacios, Dr. Christian Czech, Prof. Dr. Eckhard Mandelkow, Prof. Dr. Ingrid Hilger, Prof. Dr. Jochen Herms, Dr. Martin Fuhrmann, Prof. Dr. Robert Berger, Dr. Roland Heyny von Hauβen, Christian Schön, Jana Hoelzer and Valeria Goetschy for their

collaborations with respect to analysis and testing of my compounds. Thanks go to research groups of Prof. Dencher and Prof. Schmitz for their kind cooperation during ultra-violet and fluorescence emission experiments.

I also would like to thank to Prof. Dr. Harald Kolmar, Prof. Dr. Barbara Albert and PD. Dr. Stefan Immel for being in my Ph.D. committee.

Besides work life, Darmstadt gave me several moments and friendships to cherish about. I have made a lot of friends through cricket matches and the Darmstadt Indian Association. I take this opportunity to thank all these friends, for example Pritam, Mani, Titu, Murthy, Uday, Jagan, Prashant, Rajesh, Subramanyam, Timir, Parul and Shamsiyah for making Darmstadt my new home away from my home in India.

I am deepely grateful to colleagues at my previous workplaces, Dr. Steven Ball, Dr. Praveen Cherukupally, Mr. Sahadev Katam, Dr. Ramulu Akula, Dr. Raj Narlawar and all my masters' classmates for their encouragement.

I wish to acknowledge the financial support for this work from the Federal German government and Bundesministerium für Bildung und Forschung (BMBF).

Last but not least, I owe my heartfelt gratitude to my family members, Mrs. Janaki Anumala, Mr. Ravindranath Anumala, Mrs. Rajani Anumala and Mr. Umashankar Vangaveti and Mrs. Anitha Vangaveti, for their love and continuous encouragement.

Partial results of this thesis have been accepted or submitted for publication:

1. Fabio Lo Monte, Thomas Kramer, Jiamin Gu, Upendra Rao Anumala, Luciana Marinelli, Valeria La Pietra, Ettore Novellino, Bénédicte Franco, David Demedts, Fred Van Leuven, Ana Fuertes, Juan Manuel Dominguez, Batya Plotkin, Hagit Eldar-Finkelman, Boris Schmidt. Identification of Glycogen Synthase Kinase-3 Inhibitors with a Selective Sting for Glycogen Synthase Kinase-3α, *Journal of Medicinal Chemistry,* **2012**, *55*, 4407-4424*.*

2. Jiamin Gu, Upendra Rao Anumala, Fabio Lo Monte, Thomas Kramer, Roland Heyny von Haußen, Jana Hölzer, Valérie Goetschy-Meyer, Gerhard Mall, Ingrid Hilger, Christian Czech, Boris Schmidt. 2-Styrylindolium based fluorescent probes visualize neurofibrillary tangles in Alzheimer's disease. *Bioorganic & Medicinal Chemistry Letters* **2012***, 22, 7667-7671.*

3. Jiamin Gu, Upendra Rao Anumala, Roland Heyny von Haußen, Jana Hölzer, Valérie Goetschy-Meyer, Gerhard Mall, Ingrid Hilger, Christian Czech, Boris Schmidt. Design, synthesis and biological evaluation of trimethine cyanine dyes as fluorescent probes for the detection of tau fibrils in Alzheimer's disease brain and olfactory epithelium. *ChemMedChem* **2013**, *8, 891-897*.

4. Upendra Rao Anumala, Jiamin Gu, Fabio Lo Monte, Thomas Kramer, Roland Heyny von Haußen, Jana Hölzer, Valérie Goetschy-Meyer, Christian Schön, Gerhard Mall, Ingrid Hilger, Christian Czech, Jochen Herms, Boris Schmidt. Fluorescent rhodanine-3-acetic acids visualize neurofibrillary tangles in Alzheimer's disease brains. (Accepted in *Bioorganic & Medicinal Chemistry*. doi: 10.1016/j.bmc.2013.06.039)

Zusammenfassung

Die Alzheimer-Krankheit ist eine langsam fortschreitende neurodegenerative Form der Demenz. Die Anzahl an Neuerkrankungen steigt Jahr für Jahr. Derzeit sind mehr als 25 Millionen Menschen betroffen. Schätzungen zufolge wird die Anzahl an betroffenen Patienten bis 2030 auf 63 Millionen ansteigen. Gedächtnisstörungen, Gemütsschwankungen sowie Probleme mit dem Sprechen und Schreiben charakterisieren den Verlauf dieser Krankheit. Derzeitige diagnostische Methoden sind oft ungenau und können nicht hinreichend zwischen der Alzheimer-Krankheit und anderen Formen der Demenz unterscheiden. Die Alzheimer-Krankheit ist auf zwei verschiedene Proteinablagerungen zurückzuführen: Senile Plaques (SPs) und neurofibrilläre Bündel (NFTs). Die Bildung der Senilen Plaques ist auf die Aggregation des unlöslichen amyloid Vorläuferproteins (APP) zurückzuführen, wohingegen die NFTs durch die Aggregation von hyperphophorylierten Tau entstehen.

Es ist möglich SPs und NFTs bildlich darzustellen. Angewandte Techniken sind hierbei die Positronen-Emissions-Tomographie oder die Fluoreszenz Spektroskopie, welche auch eine frühe Diagnose der Alzheimer-Krankheit ermöglicht. Obwohl die Visualisierung der SPs bereits bekannt ist, korrelieren diese nicht mit der Krankheit, da SPs ebenfalls in Gehirnen gesunder Patienten gefunden werden. Deswegen ist eine Diagnose der Alzheimer-Krankheit, welche ausschließlich auf SPs Visualisierung beruht, sehr ungenau. Im Gegensatz dazu stehen die NFTs mit der Entstehung der Alzheimer-Krankheit in Beziehung und deshalb kann die Fluoreszenz-Bildgebung als Methode den fortschreitenden Verlauf aufzeigen.

Die vorliegende Arbeit zeigt eine Reihe von Verbindungen, welche SPs und NFTs auf Gehirnschnitten visualisiert. Unterschiedliche Klassen von Verbindungen wurden hierbei synthetisiert und auf ihre Fähigkeit als Marker für die NFTs untersucht. Hierbei waren vor allem die Derivate von Rhodanin-3-essigsäure sowie Bis(arylvinyl)pyrazin- und 5H-Imidazo[4,5-c]pyridin Derivate aussichtsvolle Verbindungen für die Tau-Bildgebung. Unsere Untersuchungen mit diesen Verbindungen zeigte uns, dass diese Verbindungen an NFTs in Gehirnen binden, was durch Fluoreszenz-Mikroskopie deutlich gemacht wurde. Zusätzlich dazu wurden ausgewählte Verbindungen auf ihre Zytotoxizität in einem hepatozellulären Karzinom-Assay und in einem Zebrafisch-Toxizitäts-Assay getestet. Diese Experimente zeigten, dass die untersuchten Verbindungen keine oder nur geringfügige Zytotoxizität aufwiesen. Des Weiteren zeigten in vitro Studien der Derivate von Rhodanin-3-essigsäure in P301S Mäuse-Retina und in vitro Experimente in menschlicher Alzheimer-Retina das

Ausbleiben des Färbens des Retinagewebes. Das Anfärben mit dem Antikörper AT8 zeigte hingegen positive Ergebnisse. Dieses machte deutlich, dass Tau-Aggregate der Retina P301S Maus unterschiedlich zu der menschlichen Form des Tau-Aggregats sind. Weiterhin wurden in vitro Experimente mit Verbindungen von 5H-Imidazo[4,5-c]pyridin an olfaktorischen Epithelgewebe durchgeführt. Die Ergebnisse zeigten, dass diese Verbindungsklasse Tau-Ablagerungen anfärbte.

Abbreviations

Å	Angstrom
Aβ	β-amyloid
AD	Alzheimer's disease
ADDLs	amyloid beta diffusible ligands
ADME	absorption, distribution, metabolism and elimination
AICD	APP intracellular domain
Ala	alanine
Arg	arginine
Asp	asparagine
ApoE	apolipoprotein E
APP	amyloid precursor protein
aq.	aqueous
Ar	aryl
A2M	alpha 2-macroglobulin
BACE	β-site APP cleavage enzyme
BBB	blood brain barrier
BINAP	2,2'-bis(diphenylphosphino) -1,1'-binaphthyl
Bn	benzyl
BP	benzophenone
Boc	*tert*-butoxy carbonyl
cat.	catalytic
CDK5	cyclin-dependent kinase 5
CNS	central nervous system
Conc	concentration
CR	congo red
CSF	cerebrospinal fluid
CT	computerized tomography
DCM	dichloromethane
DAST	diethylaminosulfur trifluoride
DLB	dementia with lewis bodies
DMF	*N*,*N*'-dimethyl formamide
DMSO	dimethyl sulfoxide
DOI	diffuse optical imaging
EC_{50}	concentration required for obtaining 50% of the maximum response
EGFP	enhanced green fluorescent protein
EI	electron impact
eq.	equivalents
EROS	event-related optical signal
ESI-MS	electron spray ionization mass spectrometry
Et	ethyl
Et_3N	triethylamine
EtOAc	ethyl acetate
FAD	familial Alzheimer's disease
FEOAD	familial early-onset Alzheimer's disease
fMRI	functional magnetic resonance imaging
FTD	fronto temporal dementia
GSK-3	glycogen synthase kinase-3
h	hour
HepG2	hepatocellular carcinoma cell lines
HMGR	hydroxmethylglutaryl-CoA reductase
HPLC	high performance liquid chromatography
HTS	high throughput screening
Hz	hertz
IC_{50}	the half maximal inhibitory concentration
ICD	intracellular domain
IDE	insulin degrading enzyme
IR	infra-red
K_i	binding affinity
K_2CO_3	potassium carbonate
*t*BuONa	sodium tertiary butoxide
*t*BuOK	potassium tertiary butoxide
LRP	LDL receptor related protein
M^+	molecular ion (molecular mass)
MCI	mild cognitive impairment
MD	mixed dementia
Me	methyl
MEG	magneto encephalography
$MgSO_4$	magnesium sulphate
MHz	mega Hertz
mp	melting point
MRI	magnetic resonance imaging
MS	mass spectroscopy
NaCl	sodium chloride
NaH	sodium hydride
NaN_3	sodium azide
Na_2SO_4	sodium sulfate
NFT	neurofibrillary tangle
NGF	nerve growth factor
NH_4Cl	ammonium chloride
NMR	nuclear magnetic resonance
NPH	normal pressure hydrocephalus
NSAIDs	non-steroidal anti-inflammatory drugs
NTF	*N*-terminal fragment

PALM	Photo Activated Localization Microscopy
PD	Parkinson's disease
Pd	palladium
Pd_2dba_3	Tris(dibenzylideneacetone) dipalladium(0)
Pen-2	presenilin enhancer-2
PET	positron emission tomography
Ph	phenyl
Phg	phenylglycine
PHF	paired helical filament
PPh_3	triphenyl phosphine
$Pd(PPh_3)_4$	tetrakis triphenyl phosphine palladium
PS1	presenilin-1
PS2	presenilin-2
PSP	progressive supranuclear palsy
ROS	reactive oxygen species
RT	room temperature
SAR	structure activity relationship
s-APP	secreted form of APP
SIFT	scanning for intensely fluorescent target
SP	senile plaque
SPECT	single photon emission computed tomography
STORM	stochastic optical reconstruction microscopy
SUV	standardized uptake value
THF	tetrahydrofuran
TLC	thin-layer chromatography
*t*Bu	tertiary butyl
tPSA	topological polar surface area
Tyr	tyrosine
UV	ultra violet
VD	vascular dementia

Table of Content

1. INTRODUCTION

1.1 Dementia

Dementia is the common term for diseases and conditions that include nerve cell death or loss of their function in a healthy brain. In a dementia patient, loss of cognitive ability is observed beyond, what might be expected from normal aging. Due to conflict of symptoms associated with normal aging, diagnosis of dementia is always difficult especially in the early stages.[1] Protein misfoldings are common causes of dementia.

In the year 2000, the number of patients worldwide with dementia reached nearly 25 million. It is expected that this number will go closer to 63 and 114 million by 2030 and 2050 respectively. This indicates that for every 20 years the number of patients will almost double.[2] After cancer and cardiac vascular disorders, dementia is the 3rd major cause of death. Several forms of dementia are known, for example Alzheimer Disease (AD),[3] Mild Cognitive Impairment (MCI),[4] Fronto Temporal Dementia (FTD),[5] Vascular Dementia (VD),[6] Mixed Dementia (MD),[7] Parkinson's Disease (PD),[8] Normal Pressure Hydrocephalus (NPH),[9] and Dementia with Lewy Bodies (DLB).[10]

1.2 Alzheimer's disease (AD)

Alzheimer's disease is a progressive, irreversible neurodegenerative disorder, which is often characterized by memory loss, unusual behavior and decline in cognitive abilities.[11] Although, Dr. Alois Alzheimer first described it almost 106 years ago, research into its symptoms, causes, risk factors and treatment has gained significant momentum over the past 30 years.[12] The impaired ability to perform tasks associated with mental activity, includes: the planning of familiar tasks, challenges in problem solving, trouble understanding visual images or spatial relationships, misplacing things, problems speaking or writing and changes in the mood or personality. The number of patients facing this devastating neurodegenerative disease is increasing, especially in the United States of America (USA). The number of patients increases with the number of people over 65 years of age. AD is the sixth leading cause of death in the USA. As the baby boomer generation has already met the age of 65, this number is expected to rise year by year.[13] Recent calculations revealed that one in eight older Americans has this disease, at least 13% of people age 65 or older and 45% of people age 85 and older are already suffering from AD. Every 68 seconds, a new patient will develop AD. These appalling numbers indicate the need of diagnosis and treatment for this disease.

1.2.1 Neuropathology

The actual cause of AD is still a mystery, although many pathological and neuropsychological characteristics had been studied. One way to characterize AD is by atrophy of certain brain areas such as limbic and association cortices leading to loss of brain mass up to 30%. The other way to characterize the disease is the reduction of synaptic density, loss of neurons in hippocampus formation and reduction in hippocampal volume by 40%.[14] A clear diagnosis of AD is possible only at autopsy.

The two primary cardinal lesions found in autopsy of AD patients are flame shaped intraneuronal neurofibrillary tangles (NFTs) and extracellular spherical senile plaques (SPs) **(Fig 1.2.1).**[15] SPs consist of a central core of aggregated beta amyloid protein and NFTs consist of hyperphosphorylated forms of microtubule associated tau protein. Ultra structure analysis of filaments using electron microscopy confirmed that the fibril of NFTs is a twisted tubule with periodical constrictions made of eight helically wound protofilaments. In the mid 1980's the amyloid fibrils and paired helical filaments (PHFs) were isolated from the human brain[17] and their partial sequence analysis was also reported. The Aβ peptide was identified as a key component in vascular and parenchyma amyloid and it was also shown that $A\beta_{42}$ is essential in the parenchymal and vascular amyloid deposition in mice. It was also learned that formation of SPs and NFTs begins long before actual cognitive symptoms arise.[18] These changes start in the medial temporal lobe including the entorhinal cortex and the hippocampus and later progress to the paralimbic, the basal temporal cortex and then to other neocortical association areas.[19]

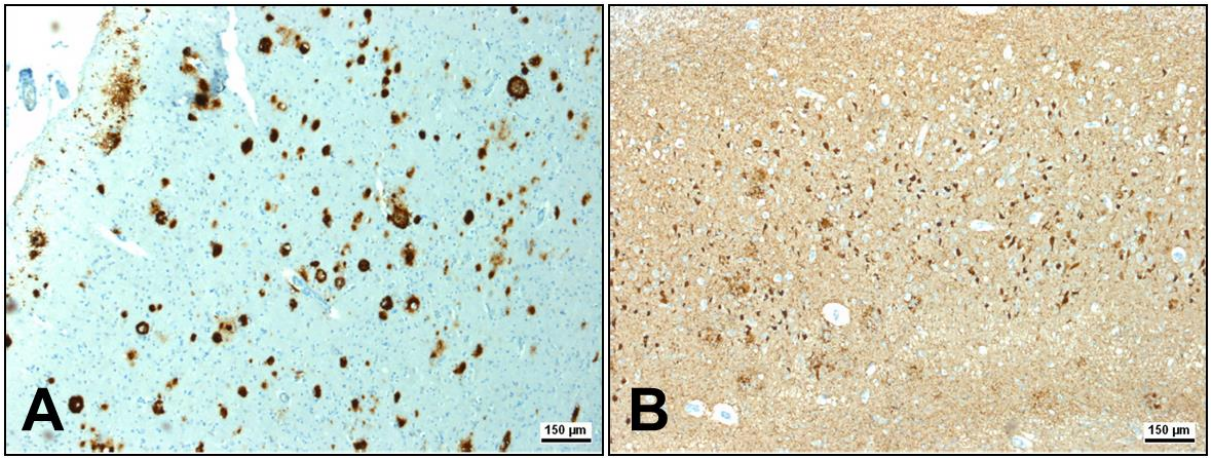

Fig 1.2.1: Immunohistochemical staining of hippocampal sections: Aβ plaques with antibody amyloid A4 (A) and NFTs with antibody AT8 mAb (B) (Tissues: hippocampus, patient: male, 71 years old, CERAD Score: 3, NFTs-level: [V])

1.2.2 Genetics

AD is a complex disease, and a number of genes have been discovered that may increase the risk of developing the disease. Although AD is genetically heterogeneous, it is divided into familial and sporadic forms. If more than one person in a family is affected, it is considered as familial AD. The sporadic form refers to cases when there is no other case of AD in the family. The sporadic form accounts for 75% of all AD cases and the remaining are all familial AD.[20] The relationship between AD and familial early-onset AD (FEOAD) is well established. The genes, which are known to be responsible for FEOAD, are *app* and *psen* genes. Gene *app* is located on chromosome 21 that is one of the 23 pair chromosomes in humans.[21] This gene was identified to contribute to amyloid formation and also plays a role in Down's syndrome.[22] It is well-known that all six mutations of this gene are penetrant. These mutations in *app* result in incorrect cleavage of APP and form Aβ that is commonly found in plaques. The two *psen* (presenilin) genes that are responsible for FEOAD are psen1 and psen2. The psen1 gene is located on chromosome 14 and the psen2 gene is located on chromosome 1. The presenilin genes encode the protein, which is involved in the cleavage of APP and mutations in the presenilin genes result in incorrect cleavages of APP. This leads to the formation of SPs which are responsible for AD,[23] and 30% - 70% of the cases associated with FEOAD resulted from psen1 whereas less than 5% of the cases result from mutations of psen2.[24]

Sporadic AD is likely to be caused by a number of mutations, combined with either aging and/or environmental agents. The most well established protein that is responsible for late onset of sporadic AD and encodes the cholesterol transport protein, is apolipoprotein E (ApoE).[25] The gene for ApoE is located on chromosome 19 and generates a 35-kDa-plasma protein with functions of cholesterol transport, metabolism and storage. ApoE is isolated from cerebrospinal fluid (CSF) using synthetic Aβ protein as immobilized ligand.[26] It was found that polymorphism of the ApoE protein represents one of the major genetic risk factors for AD development.[27] AD patients with one or two e4 alleles of apoE4 have plaques and vascular Aβ deposits with higher density of Aβ protein.[28] Amyloid-β deposits are richer in e4-positive than in e4-negative cases.[29] The following table **(Table 1.2.2)** shows the gene modifications result in that enhanced Aβ production.

Serial Number	Gene responsible	Chromosome
1	Beta app mutation	21
2	Presenilin 1 mutation	14
3	Presenilin 2 mutation	1
4	ApoE4 polymorphism	19

Table 1.2.2: Genes responsible for excess Aβ production.

Cholesterol **(Fig 1.2.2.1)** is directly linked with Aβ production. It was reported that excess formation and deposition of Aβ protein from amyloid precursor protein is a result of excess cholesterol in the brain.[30] The risk of developing AD and other types of dementia may be reduced by low consumption of hydrogenated fats and regular intake of unsaturated and omega-3 fatty acids from fish or vegetable sources.[31]

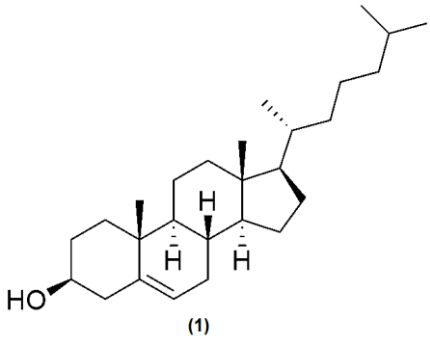

Fig 1.2.2.1: Chemical structure of cholesterol

Ageing, genetic and other environmental risk factors in sporadic AD, mutations in app and presenilin genes in familial AD, increase $A\beta_{42}$ levels. This increase followed by increased aggregation and decreased clearance of Aβ results in Aβ oligomer and deposition in the brain. Formation of hyperphosphorylated tau and NFTs by Aβ deposits, cause inflammation microglia and astrocyte activation. In addition to this altered ionic homeostasis that resulted from Aβ deposits, cause neuronal dysfunction and ultimately neuronal death which leads to dementia. The progress of sporadic and familial AD to dementia is explained by below figure **(Fig 1.2.2.2)**. Genes found in the sporadic and familial forms of AD are responsible for excess Aβ production and lead to dementia.

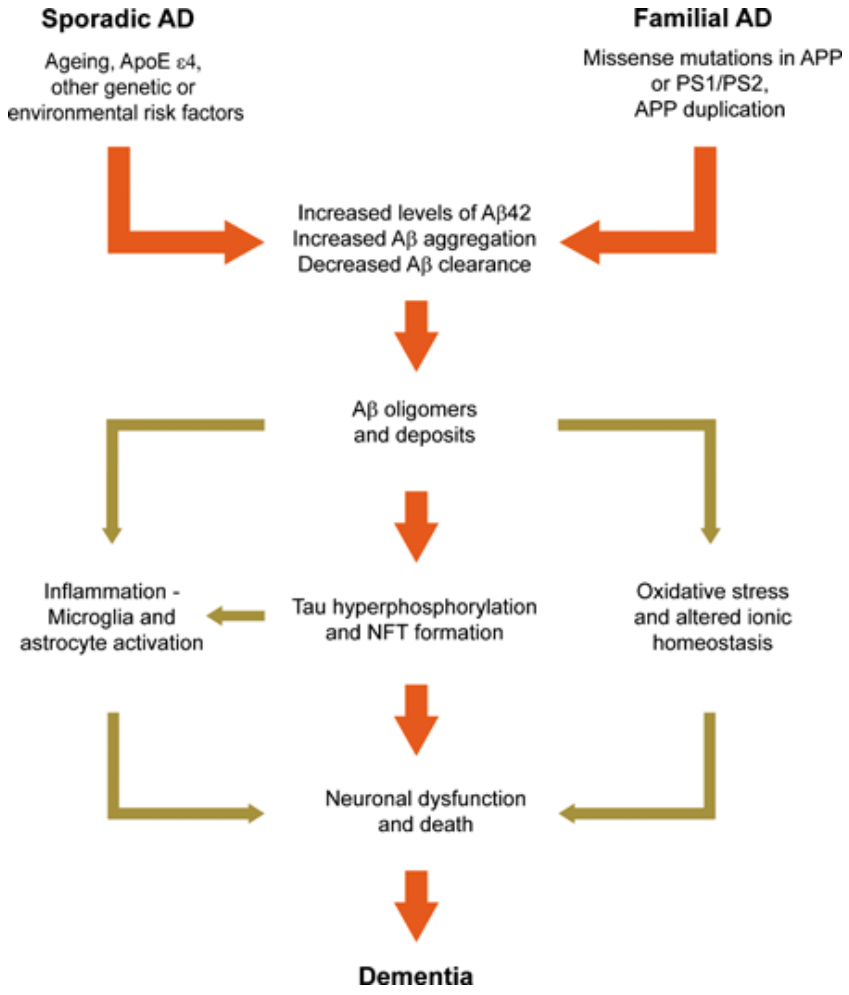

Fig: 1.2.2.2: AD pathogenesis according to the amyloid cascade hypothesis. This theory suggests that altered metabolism of Aβ, in particular aggregation-prone Aβ species like $A\beta_{42}$, initiates AD pathogenesis. Oligomeric assemblies of Aβ trigger aggregation of tau and the formation of NFTs, but also inflammation and oxidative stress, by unclear mechanisms. These downstream processes give rise to progressive neurodegeneration, which ultimately results in dementia. The main pathogenic pathway of AD is illustrated with red arrows, whereas minor contributory pathways are shown with thinner brown arrows. The experimental support for the hypothesis comes mainly from studies of families in which AD is inherited as a dominant trait due to mutations in APP, PS1 or PS2. The evidence that the theory applies to sporadic AD is less solid, although risk factors such as age and ApoE genotype both strongly impact on Aβ aggregation in transgenic models and post mortem AD brain[32]. (Modified and reprinted from FEBS journal with permission Copyright © 1999–2012 John Wiley & Sons, Inc)

1.2.3 Amyloid beta

Amyloid is a generic term that describes all fibrillar aggregates that possess β-pleated sheet structure. The aggregates of amyloid-β (Aβ) isolated from human brain at autopsy show birefringent properties in the presence of Congo red under planar polarized light.[33] Aβ protein is a fragment of APP with a size of 4kDa and is the major component in plaques of Alzheimer disease patients.[34] The carboxy terminus is crucial for seeding of amyloid and it affects the rate of amyloid formation rather than solubility.[35] This protein in SPs is hard to

dissolve and has no homology to previously known proteins. It was also observed in other diseases such as inclusion body myositis, a muscle disease, where Aβ forms an aggregate in an ordered manner. In cerebral amyloid angiopathy, amyloid aggregates coat cerebral blood vessels.[36]

Amyloid-β found in Alzheimer's patients mainly exists in three different chain lengths. $A\beta_{38}$, $A\beta_{40}$ and $A\beta_{42}$. The amino acid sequence of $A\beta_{42}$ is as shown below.

Asp - Ala - Glu - Phe - Arg - His - Asp - Ser - Gly - Tyr - Glu - Val - His - His - Gln - Lys - Leu - Val - Phe - Phe - Ala - Glu - Asp - Val - Gly - Ser - Asn - Lys - Gly - Ala - Ile - Ile - Gly - Leu - Met - Val - Gly - Gly - Val - Val - Ile – Ala

The solubility of the protein is indirectly proportional to chain length. Appropriately $A\beta_{38}$ is more soluble than $A\beta_{40}$, which is more soluble than $A\beta_{42}$. Alkyl chains in isoleucine and alanine increase the hydrophobicity of the protein.

1.2.4 Amyloid cascade hypothesis

AD is the result of disruption of many cellular processes, initiated by different events. John Hardy and David Allsop proposed the amyloid cascade hypothesis.[37] According to this hypothesis, mis-metabolism is the initiating agent of AD pathogenesis, which further leads to aggregation of Aβ protein, specifically $A\beta_{42}$.[38] Formation of these neuritic plaques results in several changes in the brain, including formation of NFTs, disruption of synaptic connections that leads to reduction of neurotransmitters, death of tangle-bearing neurons and finally dementia.[39]

In 1984, it was observed that Aβ is the main component present in plaques and it was suggested that this protein is primarily responsible for AD.[33] The majority of the mutations causing FEOAD have supported this hypothesis. Aβ can express its neurotoxicity in several pathways. Some of them include disruption of mitochondrial function,[40] initiating imbalance in calcium homeostasis as well as ion channel formation.[41] It was also identified that Aβ can activate microglia cells which leads to the expression of pro-inflammatory genes, which in turn resulted in increased reactive oxygen species production and ultimately leads to neuronal toxicity and death.[42]

Aβ formation and clearance in neurons is usually well balanced. Neprilysin cleaves both Aβ monomers and the pathological oligomeric form.[43] Insulin degrading enzyme (IDE) can cleave the monomeric forms of Aβ protein,[44] whereas other proteases cleave oligomeric and fibrillogenic Aβ. Extracellular Aβ is cleared by binding to Alpha 2-macroglobulin (A2M)[45] and ApoE to LDL receptor related protein (LRP), and subsequent degradation via the lysomal pathway.

Early reports indicate a strong correlation between SPs and dementia[46] while others observed that the correlation between these two are weak.[47]. However, the strong correlation between tangle formation and dementia[48] and the relationship between tangles and plaques formation suggests that tangles appear first.[49] Recent attention has turned to plaque independent cognitive impairment, which suggests that soluble Aβ correlate stronger with dementia than Aβ plaques.[50] In demented people, monomers of soluble Aβ were observed in the cortical extracellular space and in the CSF.[50b, 51] Amyloid plaques were observed in the brains of non-demented people; however, in CSF of non-demented people amyloid-β diffusible ligands (ADDLs) were absent.[52] The disconnection between fibrils and synaptotoxicity in human amyloid precursor protein (APP) was observed using transgenic mice that express high levels of $A\beta_{1-42}$.[53]

1.2.5 Amyloid Precursor Protein

The gene encoding amyloid precursor protein was assigned to human chromosome 21.[54] APP is a large, type-1 trans membrane glycoprotein expressed on the cell surface and has an uncertain function. Proteolytic cleavage of APP mainly occurs in the amylodogenic and non-amyloidgenic pathways **(Fig 1.2.5)**. This proteolytic processing is mediated by three different proteases namely α-secretase, β-secretase and γ secretase.[55] There are three isoforms of APP, which include the number of amino acids with the length of 695, 751 and 770.[56] The 695 amino acids containing APP is mainly produced in neurons[57] and proteolytic cleavage of 695 amino acid protein by α-secretase and β-secretase results in 83 and 99 peptide fragments in the cell respectively.[58] α-secretase cleaves APP at the position 16-17 position of Aβ protein. The 99-chain length protein is further cleaved by γ-secretase resulting in the p3 fragment. This process is called the non-amylodogenic pathway,[59] as it does not produce amyloid. APP cleavage by β-secretase results in 83 amino acid protein and subsequent site-specific cleavage by γ-secretase results in 40 or 42 fragments of Aβ protein. This series of cleavages is called the amyloidogenic pathway.[60]

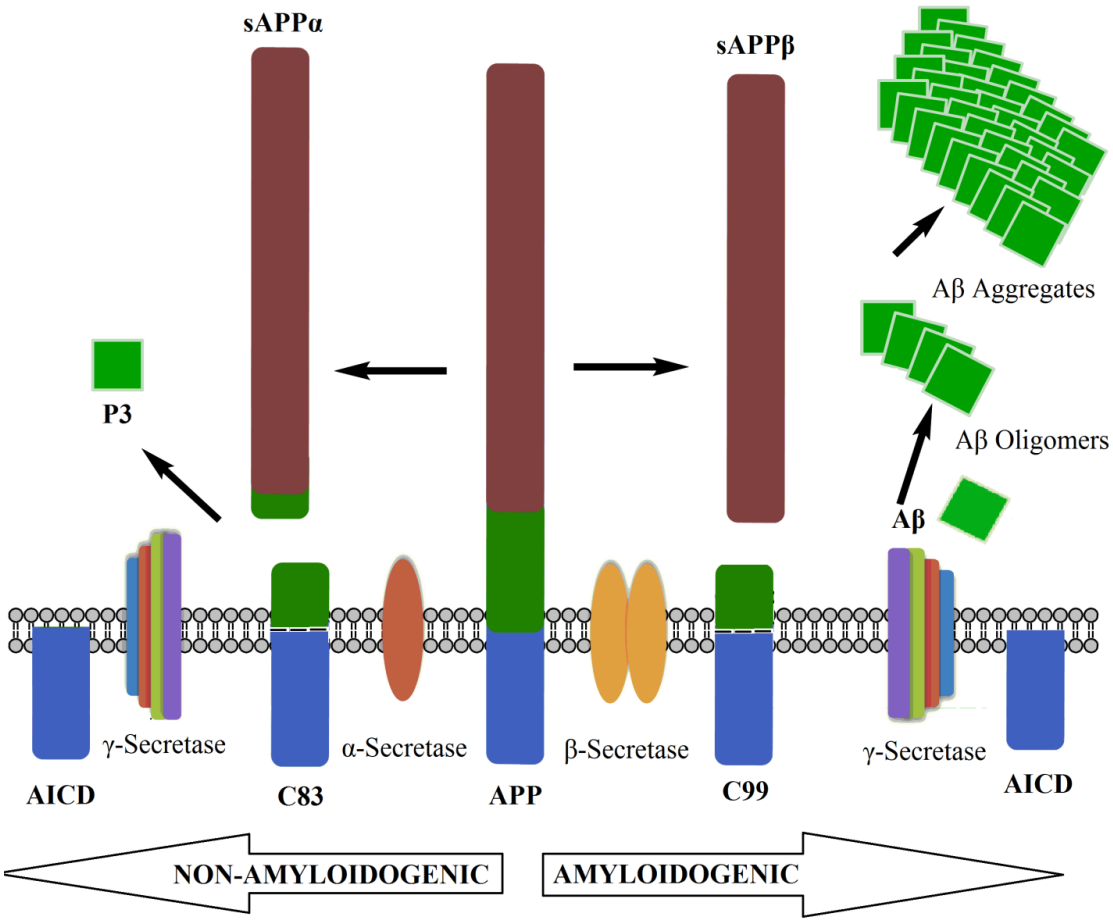

Fig 1.2.5: Schematic illustration of APP processing by the amyloidogenic and the non-amyloidogenic pathways. Cleavage of amyloid precursor protein (APP) by α-secretase and γ-secretase produces the non-plaque forming p3 fragment, while APP cleavage by β-secretase and γ-secretase produces plaque forming Aβ.

$A\beta_{1\text{-}42}$ is the major component of the fibrils found in plaques associated with AD, Down's syndrome and normal aging. Senile plaques consist of $A\beta_{40}$ and $A\beta_{42}$ whereas diffuse plaques consist predominantly of $A\beta_{42}$. The formed Aβ peptides initially form oligomers and further convert into aggregated form.[61] Oligomers of different molecular weight are formed from Aβ monomers. This oligomer adopts a well-ordered intermolecular β-sheet structure. These oligomers further transform into aggregates and ultimately SPs. SPs accumulate between neurons. These plaques are closely surrounded by reactive astrocytes, dystrophic axons and activated microglia.

1.2.6 Structure of amyloid beta protein aggregates

Amyloid fibrils are considered end products of the nucleation polymerization. This proteinaceous self-aggregates form filamentous structures which exhibit a diameter in the range of 70-120 Å. These fibrils are straight and with lengths up to micrometers.[62] These fibrils are formed by a number of peptides with different sequences and molecular weights.[63] This fibrilization process is driven by hydrophobic interactions and is also dependent on pH and concentration of the protein. Aβ peptide adopts a mixture of β-sheet, α-helix and random coil structures, but in aqueous solution the β-sheet is the preferred conformation.[64] The rate of aggregation *in vitro* depends on pH and concentration of the peptide. The maximum β-sheet formation occurred at pH 5.4 and at concentration of 666 μM.[65] The hydrophobic nature of the carboxylic acid terminal is responsible for formation of plaques.[35] This peptide aggregated into highly ordered β-pleated sheet structures forming fibrillar aggregates of different dimensions. Pairs of β-sheets readily associate to form protofilaments, which are tubular cylinders with a diameter of approximately 28 Å. Three to five protofilaments aggregate to form amyloid fibrils with a diameter of approximately 70 Å.

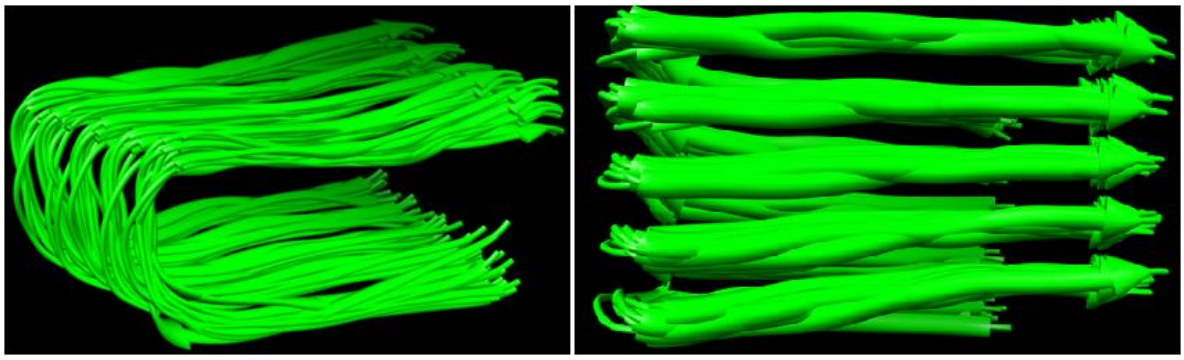

Fig 1.2.6.1: 3D structure of Alzheimer's amyloid beta fibrils ($A\beta_{42}$). Image created using UCSF Chimera molecular modeling system[66] (PDB: 2BEG).[67]

The Aβ fibrils are non-crystalline and insoluble; therefore, solid state NMR was used to understand the structure of Aβ oligomer, and the structure of amyloid fibrils ($A\beta_{40}$). From this investigation, it was observed that the first 10 amino acid residues of $A\beta_{40}$ are disordered; amino acids from 12-24 and 30-40 adopt β-strand conformations. These two β-sheets are in parallel to each other by an inter-molecular hydrogen bonding **(Fig 1.2.6.2)**. Amino acids from 25-29 of $A\beta_{40}$ are irregular in conformation. The bend between these two β-sheets are formed via sidechain – sidechain interactions from amino acids from 25^{th} to 29^{th} of $A\beta_{40}$. A salt bridge between aspartic acid residue at 23^{rd} position and lysine at 28^{th} position was also observed.[68]

More recent studies on the 3D structure of $A\beta_{42}$ also revealed that, two β-sheets are formed in 1-42 amino acid chain. From this study, amino acid residues 1-17 are disordered and amino acid residues from 18-26 and 31-42 form two independent β-sheets named β1 and β2 respectively.[69] NMR studies also revealed that L17, F19 and A21 amino acid residues of $A\beta_{42}$ are in hydrophobic contact with the even numbered residues of the β2 sheet. Amino acids 27-30 are in the loop region which is located between two sheets and connected to sheet β1 by inter molecular salt bridges and also form contact to I32 and L34 residues of sheet β2. The salt bridges between aspartic acid and lysine are shown below in **Figure 1.2.6.2 B** (with box).

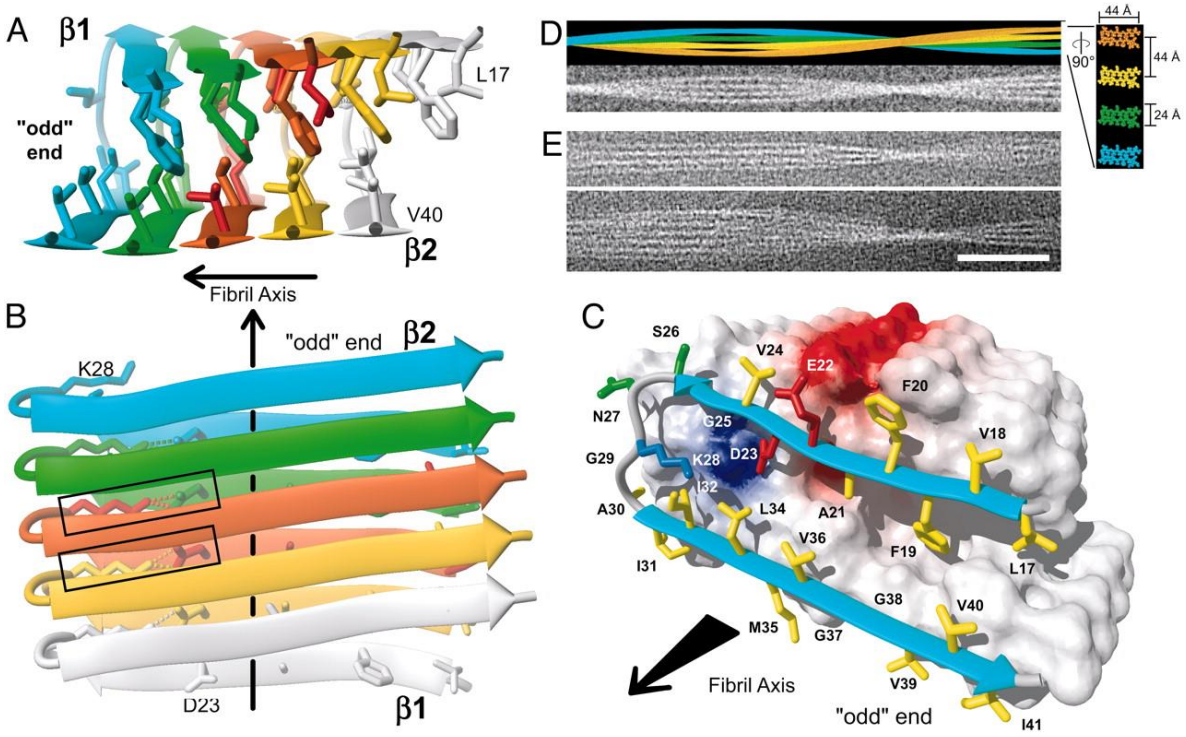

Fig 1.2.6.2: The 3D structure of a 35MoxA$\beta_{(1–42)}$ fibril. (A and B) Ribbon diagrams of the core structure of residues 17–42 illustrating the inter molecular nature of the inter-β-strand interactions. Individual molecules are colored. For example, the monomer at the odd end is shown in cyan. The β-strands are indicated by arrows, non-regular secondary structure is indicated by spline curves through the Cα atom coordinates of the corresponding residues, and the bonds of side chains that constitute the core of the protofilament are shown. In B, the intermolecular salt bridge between residues D23 and K28 is indicated by dotted lines, and the two salt bridges formed by the central Aβ(1–42) molecule are highlighted by rectangles. (C) Van der Waals contact surface polarity and ribbon diagram at the odd end of the 35MoxAβ(1–42) protofilament comprising residues 17–42. The β-sheets are indicated by cyan arrows, and non-regular secondary structure is indicated by gray spline curves. The hydrophobic, polar, negatively charged, and positively charged amino acid side chains are shown in yellow, green, red, and blue, respectively. Positively and negatively charged surface patches are shown in blue and red, respectively, and all others are shown in white. The direction of the fibril axis is indicated by an arrow pointing from even to odd. (D) (Upper) Simulation of a 35MoxAβ(1–42) fibril that consists of four protofilaments colored individually. (Lower) shows the same fibril in a noisy gray-scale image, which has been blurred corresponding to a resolution of 2 nm. In Right, a×5-magnified cross section perpendicular to the fibril axis is shown, using the same color code. Dimensions are indicated. To match the experimental twist of the protofilament of the fibril shown in E, a twist

angle of 0.45° per molecule was used. (E) Two examples of cryoelectron micrographs of single 35MoxAβ(1–42) fibrils.[67] Scale bar, 50 nm. (Modified and Reprinted from PNAS journal with permission Copyright © 2005, The National Academy of Sciences)

This structural organization of amyloid fibrils explains uni directed growth and sequence selectivity that leads to insoluble neurotoxic fibrils. Using NMR studies, inter atomic distances between F19 side chain and I32 and V36 have been predicted and are approximately 6 Å. The cross peak between F19/I32 and F19/V36 supports internal quaternary contacts.[70] From polymorphic studies of these aggregates, it is clear that several interaction sites are present at multiple peptide residues between $A\beta_{11}$ to $A\beta_{25}$ and $A\beta_{27}$ to $A\beta_{42}$, which were responsible for self-aggregation and the formation of different fibril morphologies with varied physicochemical properties that link to different levels of cellular toxicity.[71] These amyloid fibrils gum up the parenchymal space in between neurons in the brain.

1.2.7 Tau protein

Tau proteins, discovered in 1975, are random coil proteins, which are microtubule associated proteins abundant in neurons in the CNS.[72] The tau protein stabilizes microtubules by interacting with tubulin and promoting tubulin assembly into microtubules. A detectable amount of tau is secreted into the CSF under normal conditions.[73] Tau exists in six isoforms in the adult brain and only one isoform (Tau-352) in the fetal brain, Tau-352 is the shortest isoform.[74] All six tau isoforms in the adult brain are derived from a single gene by alternative mRNA splicing. The size of these isoforms varies from 352 to 441 amino acids (36.8 to 45.9 kDa). These isoforms differ by the number of microtubule binding repeats (R) of 31-32 amino acids each or the number (0,1 or 2) of amino terminal inserts (N) of 29 amino acids each or both as shown in below **(Fig 1.2.7)**.[75]

A Tau protein consists of four domains; N-terminal domain, proline-rich domain, microtubule-binding domain and carboxy-terminal domain.[76]

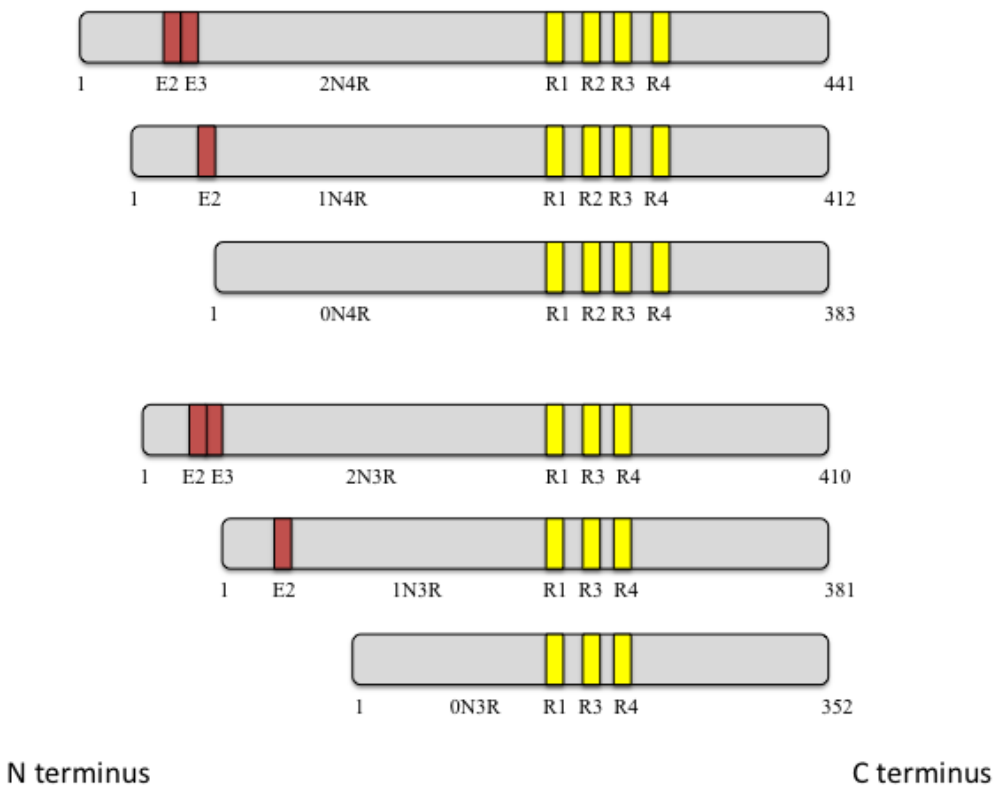

Fig 1.2.7: Domain structure of six different isoforms of adult human brain. These isoforms can be differed by two ways. The first difference is the presence or absence of one or two 29 amino acid chain (shown in red) or they may differ by number of tubulin binding units (shown in yellow)

The tau binding site overlaps with the motor protein-binding site, thus it can effectively modulate axonal transport. Tau was observed in amyloid plaque; in AD, SPs in cerebral cortices contain 5.1% to 27.5% of tau protein.[77]

1.2.8 Neurofibrillary Tangles

More than 100 years ago, Dr. Alois Alzheimer first described NFTs in neocortical neurons of his former patient Auguste Deter, who died of dementia. The flame shaped protein aggregates that are commonly found in the brains of AD patients are hyperphosphorylated tau protein aggregates also known as NFTs. These aggregates are formed by aggregation of microtubule associated protein (MAP) tau. Tau promotes microtubule formation and stability. Three repetitions (3R) or four repetitions (4R) of microtubule binding units are formed by alternative mRNA splicing of exon 10. Although the function of these two isoforms is microtubule stabilization, some qualitative and quantitative differences exist between these isoforms. One difference, 4R tau binds to microtubules with greater avidity than the 3R tau isoform.[78] Another difference between these two isoforms is that the 4R tau is a potent

inhibitor of microtubule shortening, whereas 3R tau has a threefold minimal effect on this parameter of microtubule dynamics in EGFP-tubulin expressing cultured MCF7 cells.[79] In a healthy brain 3R tau and 4R tau units are almost equal in ratio, but disruption of this ratio may have serious consequences.[80] This ratio is unequal during embryogenesis where the 3R form of tau is expressed exclusively.[75]

AD patients express both the 3R and 4R tau isoforms. Whereas, in comparison, patients with Pick's disease predominately have the 3R isoform,[81] and patients with progressive supranuclear palsy (PSP) and corticobasal degeneration express the 4R isoform.[82]

Post-translational modifications of tau include phosphorylation, nitration, glycation, truncation, glycosylation, ubiquitination and polyaminations.[83] Phosphorylated tau contains 2 to 3 moles of phosphate group per mole of tau in the normal adult brain. In the case of AD patients, hyperphosphorylated tau contains 5 to 9 moles of phosphate group per mole of tau.[84] Hyper phosphorylation of tau is a major cause of tauopathy. Different kinases are responsible for phosphorylation: glycogen synthase kinase 3β (GSK 3β),[85] cyclin-dependent kinase 5 (CDK5)[86], mitogen activated protein kinase 1 (MAPK1, ERK 1), microtubule affinity regulating kinase 1 (MARK1)[87] and casein kinase 1α.[88] Approximately 45 phosphorylation sites have been observed on the proline rich C-terminal area of the tau protein.[89] The largest isoform has 79 phosphorylation sites. In addition to phosphorylation of tau protein, co-operation between two kinases has been also observed. For example, cdk5-mediated phosphorylation of tau promotes further phosphorylation by GSK3 beta *in vitro*.[90] Together, these results reveal that more than one kinase is responsible for tau phosphorylation.

The process of tau aggregation is explained below **(Figure 1.2.8.1)**. Monomers of hyperphosphorylated tau initially detach from the microtubules. These monomers start to form oligomers. The formed oligomers bind to each other and form paired helical filaments. The aggregation of paired helical filaments results in NFTs in a AD brain.

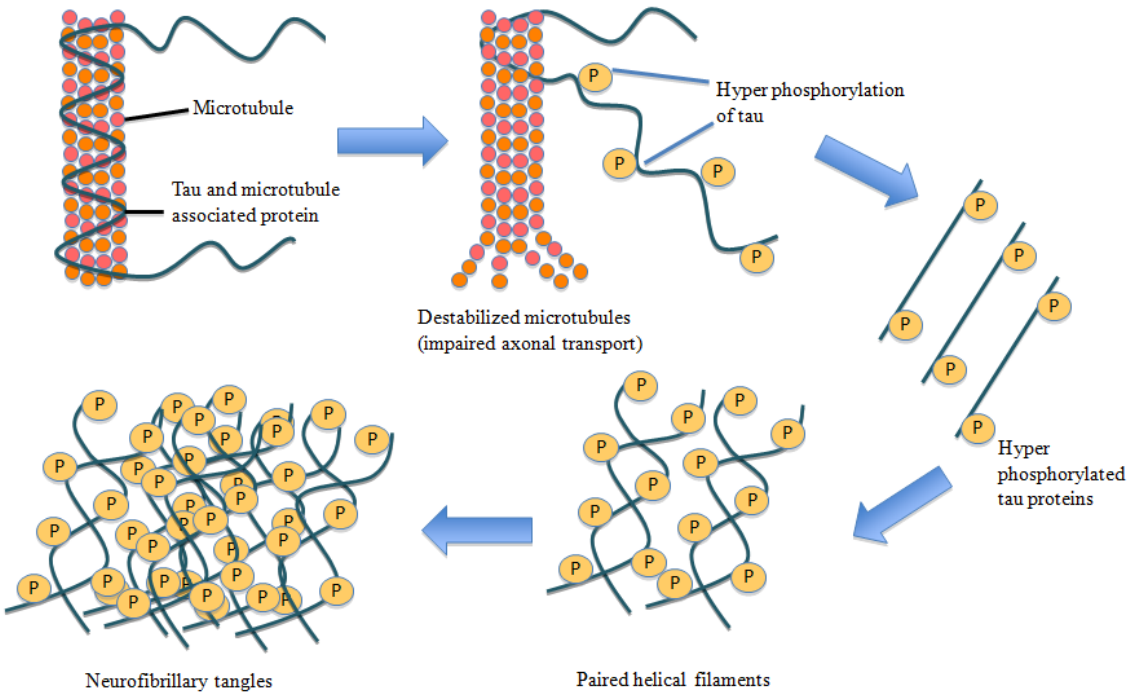

Fig 1.2.8.1: Diagram of tau from microtubule-associated protein is destabilized by hyper phosphorylation forms paired helical filaments, which aggregate to form NFTs.

The fibrillization pathway of tau proceeds in three steps **(Fig 1.2.8.2)**. In the initial step, phosphorylated and non-phosphorylated tau epitopes induce the aggregation of tau protein into non-fibrillar deposits, which can be detected by immunohistochemistry using antibodies against different phosphorylated and non-phosphorylated tau epitopes.[91] These pre-tangles are non-fibrillar, not reactive with β-sheet sensitive dyes such as thioflavin S (ThS) or thiazine red. The second step involves conversion into a β-sheet structure. This can be detected using fluorescent dyes binding to tau aggregates. In the third step, nucleation of tau filaments forms NFTs.[92] Further, NFTs may turn into “ghost tangles”, which are extracellular fibrillar aggregates of tau, formed by the death of the host neuron.[93] *In vitro*, recombinant full-length tau doesn’t form fibrils spontaneously under physiological pH, temperature, ionic strength and concentration.[94] But tau fibrillation is spontaneous at >200 μM concentration, which is required to overcome charge repulsions.[95] Under oxidizing conditions, the 3R tau forms inter molecular disulfide bonds since it has one cysteine group whereas the 4R tau predominantly forms an intramolecular disulfide bond since it has two cysteine groups.[96]

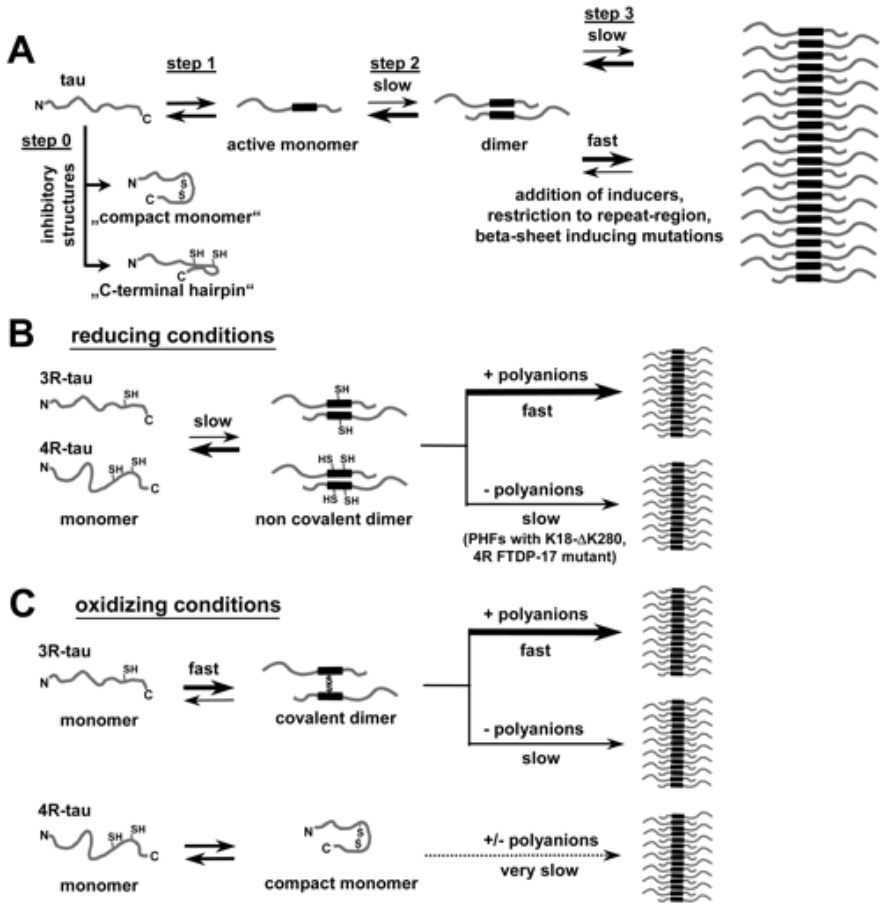

Fig 1.2.8.2: Pathways of tau aggregation. (A) Generalized mechanism: step 1, soluble tau normally adopts a mostly random-coil structure, but can undergo a conformational change where part of the repeat domain adopts an extended conformation (here shown as black bar), ready to enter β-sheet interactions with other molecules. Step 2: Two tau molecules align to form a dimer (presumably by β -sheet formation around the hexapeptide motifs in R2 or R3). Step 3: Further tau monomers or dimers associate, form a nucleus and grow into a filament. Step 0: If a tau molecule is locked in the “wrong” conformation (e.g., compact monomer of a four-repeat tau, or tau isoforms without inserts in the presence of arachidonic acid (C-terminal hairpin structure cannot promote aggregation, and possibly even inhibits aggregation. For normal soluble tau, k_1 and k_2 are large so that the equilibrium is shifted to the left; dimers do not form at all or only transiently, and aggregation is negligible. The equilibrium can be shifted to the right toward aggregation by increasing available tau concentrations (e.g., by detachment from microtubules), removal of N- or C-terminal tau domains (because the repeats form the cores for aggregation) or FTDP-17 mutations (facilitating the transition to β -structure), oxidation (when it leads to stabilized dimers), and polyanions or fatty acid micelles (which improve “stickiness” of tau by charge compensation). (B), (C) Aggregation of 3R tau and 4R tau in reducing and oxidizing conditions: In reducing conditions (B), 3R tau or 4R tau can undergo the required conformational change and form non-covalent dimers, but polyanions must be present to drive the reaction toward aggregation. An exception to the rule is 4R tau with the ΔK280 mutation, which shows appreciable PHF aggregation even without polyanions because of its high propensity for beta-structure and interactions. In oxidizing conditions (C) in the case of 3R tau, covalent dimerization at C322 pushes the equilibrium toward aggregation; the reaction is further accelerated by polyanions. In the case of 4R tau, the intramolecular disulfide bridge locks tau in an inactive conformation, which does not aggregate readily, even if polyanions are present. In the case of AA-induced aggregation, the state of oxidation is of secondary importance, but instead an inhibitory state prevails when tau lacks the N-terminal inserts.[96] (Modified and reprinted from *Biochemistry* Copyright © 2002 with permission from American Chemical Society).

The filaments observed in the paired helical form and the individual filaments of the pair are L-shaped in the transverse section. These filaments which appear straight consist of two strands, but under an electron microscope they appear as single filament due to a dissimilar arrangement.[97] Inhibition of tau aggregation by small molecules is one approach to treat AD. Tau aggregation inhibitors reduce the aggregation of tau or stabilize tau in an unaggregated form. Several classes of small molecules were identified as tau aggregation inhibitors. These small molecule inhibitors include rhodanine derivatives, phenylthiazolylhydrazides, *N*-phenylamines, benzothiazoles, aminothienopyridazines, polyphenols, phenothiazines and anthraquinones.[98] Amyloid fibrils induce phosphorylation of tau and further lead to microtubule instability.[99] Activation of both GSK3β and CDK5 are observed when young neurons are incubated with fibrillar Aβ.[100]

1.2.9 Tau aggregates in retina.

Tau aggregates are one of the two hallmarks of AD. The observations of retinal abnormalities in some AD patients such as visual function impairment and loss of retinal ganglion cells were previously reported.[101] This might be due to the formation of Aβ and tau deposits in retinal cells which was suggested by studies from transgenic Drosophila.[102] Fluorescent probes that stain tau aggregates may offer a possibility to diagnose AD and facilitate non-invasive imaging of AD. Several transgenic mouse models were developed that express human mutant APP. It was observed with transgenic mice that Aβ in the retina can be detected.[103] Tau mediated mechanisms were also reported relating to the decrease of tau levels in the retina and the increase of hyperphosphorylated tau in the optical nerve of glaucoma patients.[104] The observation of tau aggregates in retinae of tau transgenic P301S mice may allow to study of tau pathology. Tau-mediated degeneration and long term *in vivo* imaging of hyperphosphorylated tau in retinae may create a platform for non-invasive imaging of AD.[105]

1.2.10 Tau aggregates in Bowmann glands and olfactory epithelium.

A key obstacle in the development of *in vivo* imaging agent is blood brain barrier (BBB) permeation. The non-existance of a BBB between the brain and the nasal mucosa provides a delivery point of diagnostic probes for nasal application. The existence of tau aggregates in the olfactory epithelium and olfactory bulb provide a link between AD in the nose and brain.[106] The presence of tau aggregates in nasal mucous membranes, especially in the nasal bowman's glands and olfactory epithelium was reported.[107] Tau aggregates that were stained by fluorescent probes may be observed by using an illuminating endoscope. Hence,

the imaging of tau aggregates in the olfactory epithelium and Bowman's glands of the nasal mucous membranes may provide an early stage detection of AD associated pathology.

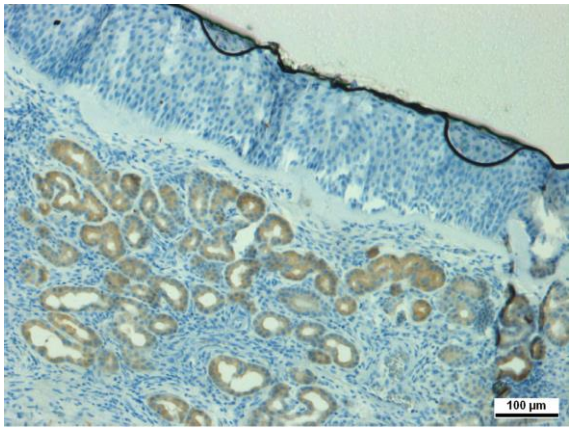

Fig 1.2.10: Immunohistological staining of Bowman's glands of the olfactory epithelium containing tau aggregates (Tissues: olfactory epithelium; patient: male, 78 years old, CERAD-Score 3, Braak: V) with antibody Tau Ab-3.

1.3 Neuroimaging

The mini mental state examination is often inaccurate and cannot distinguish between different cognitive impairments. Neuroimaging is a technique, which either directly or indirectly images the structure and functional details of the brain. The available imaging techniques developed include: Computed Tomography (CT), Diffuse Optical Imaging (DOI), Event Related Optical Signal (EROS), Magnetic Resonance Imaging (MRI), Functional Magnetic Resonance Imaging (fMRI), Magneto Encephalography (MEG), Positron Emission Tomography (PET), and Single Photon Emission Computed Tomography (SPECT). In post mortem AD patients, it is possible to diagnose the disease by imaging SPs and/or NFTs in the brain. For *in vivo* imaging of SPs and NFTs in AD patients, PET, SPECT and fluorescence imaging probes are currently under development.

1.3.1 Imaging senile plaques by Positron Emission Tomography (PET) and Single Photon Emission Computed Tomography (SPECT).

PET uses short-lived positron emitting isotopes such as ^{15}O (half-life 2 min), ^{11}C (20 min) and ^{18}F (110 min).[108] This technique requires very small sample quantity for imaging. With the help of advanced positron emission scanners and sensitivity of probes, it is possible to measure the probe concentration *in vivo.* When a radioactive probe is administered into the object, it will be distributed by the blood stream into the body and accumulate in the target tissue.[109] Detection of this accumulation is based on nuclear physical process "annihilation". Briefly, in a positron emitter the nuclear origin is a proton. Under the influence of other

nucleons the proton is converted into a neutron, a positron and a neutrino. The immediate result of the breakdown is that the positron and the neutrino are ejected from the nucleus while the neutron remains. The released positron carries kinetic energy depending on the binding energy in the nucleus and loses it while traveling in the surrounding media. The annihilation reaction is a result of a collision between the positron and an electron. In annihilation, the masses of the two particles completely turn into energy. The energy is divided equally between the two photons (each of 511 keV), traveling to the opposite directions (180 +/- 0.25^{o}) of each other. These photons appear either in the form of x-ray or in the form of gamma ray.[110] A ^{18}F labeled probe has advantage over ^{15}O and ^{13}C due to very short half-life periods of ^{15}O labeled and ^{11}C labeled probes. ^{15}O labeled and ^{11}C labeled require a fully equipped PET center with cyclotron and radio pharmacy. In contrast, ^{18}F has a sufficient life time to be transferred from the production site to the PET scan center.

The various criteria for an AD diagnostic probe are:

- It must be safe
- It should display sufficient fluorescence or has to be tagged by a radioactive tracer
- Maximum signal to noise ratio
- Good binding affinity to amyloid or tau aggregates
- Fast elimination of unspecific binding
- Able to cross BBB
- Good biodistribution properties (uptake and rapid clearance from brain) to warrant fast appearance and low unspecific binding

Molecular properties of the drug to be considered are good physiochemical properties, ADME (absorption, distribution, metabolism and elimination) attributes, *in vitro* binding efficiencies and safety.[111] In addition to all the above properties, the drug should have a molecular weight of less than 500 Daltons and a good distribution ratio between lipid and aqueous phases i.e., a low partition coefficient (log P).

1.3.2 Imaging agents for senile plaques

Several fluorescent, PET and SPECT tracers designed for the imaging of SPs in the human AD brain are currently in clinical trials. Congo red and Thioflavin T are the best known compounds used for the diagnosis of AD at autopsy. Congo red and Thioflavin T are unable to cross the BBB but modification of these probes has resulted in improved derivatives which permeate the BBB.

1.3.2.1 Congo red derivatives

Congo red (CR) **(2)** is a histological dye known to bind to Aβ aggregates and NFTs.[112] The absorption spectrum of CR shifts from orange red to rose after it binds to fibrillar $A\beta_{1-40}$. Interactions between CR and amyloid aggregates have been reported previously.[113] CR binds to amyloid fibrils with a β-sheet conformation only. Several PET and SPECT agents have been developed based on the modification of the CR core structure **(Fig 1.3.2.1.1).** CR is toxic in nature; it can reduce the serum protein concentration to cause platelet aggregation and is unable to cross the BBB, due to low lipophilicity. This low lipophilicity is derived from its negative charge (-2) at physiological pH.[114] Chrysamine G (CG) **(4)** is a modified derivative of CR that was identified as an amyloid binding agent with an improved distribution coefficient (Log D).[115] The log D of CG is 1.8, whereas the Log D of CR is -0.2. The lipophilic properties of CG are improved by introducing an intra-molecular hydrogen bond between the hydroxyl and carboxylic acid groups that shield the negative charge of the carboxylic acid at pH 7.4. Radio labeled CG derivatives with higher log D values failed to show higher brain uptake when compared with CR.[116] Modification of the biphenyl group and the azo system of CG resulted in X compounds, such as X-34 **(3)**, FSB **(5)**, BSB **(6)**, K-114 **(7)** and ISB **(8)**. FSB, BSB and MeX04 **(10)** have been shown to cross the BBB and bind to SPs of APP/PSI mice.[117] The iodinated derivative ISB has shown to bind to SPs and is able to cross the BBB.[118] PET imaging results with the probe X-34 visualized the SPs and NFTs in the brain which are not observed with ThS. The sulphonic acid group in CR and carboxylic acid group in CG are not necessary for amyloid imaging as MeX04 binds to amyloid plaques.[119] Tetrafluorostyryl benzene derivatives were also investigated as amyloid imaging agents in mice.[120] In addition to AD, multidentate fluorine polypegylated styryl pyridines were also reported to stain amyloid deposits in cerebral amyloid angiopathy.[121]

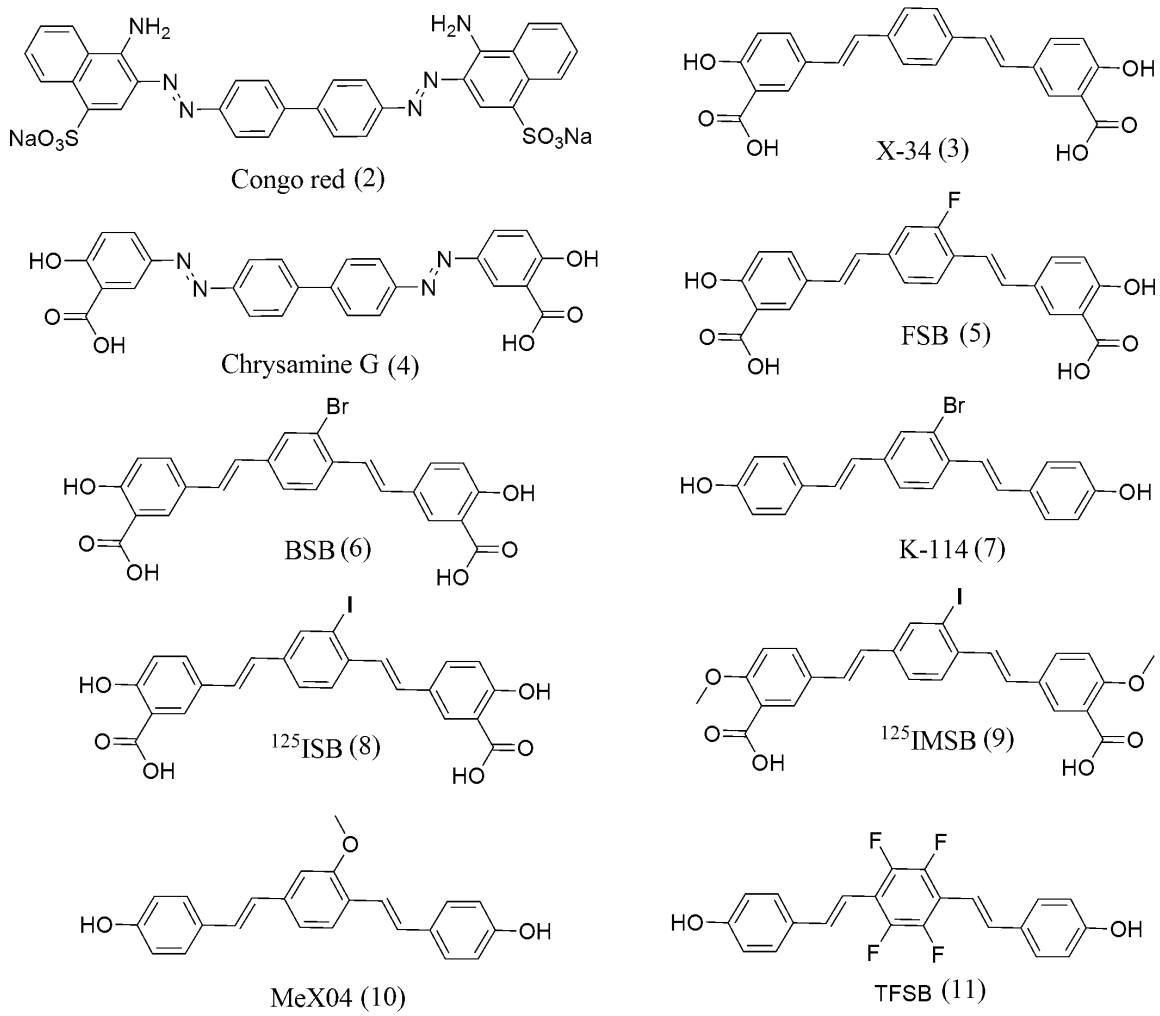

Fig 1.3.2.1.1: Chemical structure of PET, SPECT and fluorescent probes derived from Congo red for the detection of senile plaques.

1.3.2.2 Thioflavin Derivatives

Thioflavin T (ThT) **(14)** is a positively charged benzothiazole derivative which is widely used for the visualization and quantification of amyloid aggregates *in vitro*. The positive charge on ThT prevents it from crossing the BBB. When ThT binds to highly ordered Aβ structures, it exhibits a red shift in its fluorescence emission and enhanced fluorescence. Upon binding to amyloid fibrils, ThT displays a dramatic shift in its excitation maximum (from 385 nm to 450 nm) and emission maximum (from 445 to 482 nm). This enhancement in fluorescence originates from the dye bound to amyloid fibrils only.[122] The twist in the ThT molecule is responsible for enhanced fluorescence. In the unbound state the energy barrier between the excited and ground states of ThT is affected by C-C bond rotation between the benzyl amine and benzothiazole ring. When bound to amyloid fibrils this rotation is blocked and rotational immobilization of ThT preserves the excited state that results in a high quantum yield of

fluorescence. The chirality and twisted conformation of ThT was confirmed with circular dichroism experiments. ThT shows a Cotton effect peak at 450 nm in circular dichroism experiments.[123] It was observed that neutral derivatives of ThT have better brain permeability than ThT.[124] Hence, the structure activity relationship of these derivatives was performed to identify a lead compound with optimal *in vivo* and *in vitro* properties. Many amyloid imaging agents have been developed based on Thioflavin T **(Fig 1.3.2.2.1).**[125]

Modification of ThT resulted in several PET imaging agents. PIB **(19)** and AZD2184 **(20)** are ^{11}C labeled PET imaging probes. Whereas, FEM-IMPY **(16)**, FPM-IMPY **(17)** and GE-067 **(18)** are ^{18}F labeled PET imaging probes. TZDM **(12)**, IBOX **(13)** and I-IMPY **(15)** are iodine labeled PET probes. Iodine labeled PET probes have longer half-life period than ^{11}C labeled and ^{18}F labeled probes.

[^{11}C]TZDM **(12)** is a modified ThT derivative that exhibits high binding affinity to $A\beta_{1-40}$ and $A\beta_{1-42}$ aggregates.[115] [^{11}C]TZDM displayed good brain uptake, but was unable to distinguish between white matter and plaques, hence it is not suitable for *in vivo* imaging. [^{125}I]IBOX **(13)** is devised by replacing sulfur with oxygen, this modification reduced the molecular weight and improved cerebral uptake and retention.[126] [^{125}I]IBOX bound to amyloid fibrils with good binding affinity; both [^{125}I]IBOX and [^{11}C]TZDM are have slow brain wash in normal mice and also have high background-to-noise ratio and may not be suitable as *in vivo* imaging agents. Another SPECT derivative of ThT is [^{125}I]IMPY **(15)**, which showed *in vivo* localization of amyloid plaques in living brain.[127] [^{18}F]FEM-IMPY **(16)** and [^{18}F]FPM-IMPY **(17)** are two other ^{18}F labeled probes that have been shown to bind SPs. [^{18}F]FEM-IMPY and [^{18}F]FPM–IMPY displayed high radioactivity in bones resulting from ^{18}F uptake.[128] [^{18}F]GE-067 **(18)** is another ligand that binds to SPs in the brain and has been studied in healthy humans for adverse effects; it satisfied estimated effective dose for a PET ligand that is defined by World Health Organization (WHO) but a relatively low variability was observed between the studied subjects.[129]

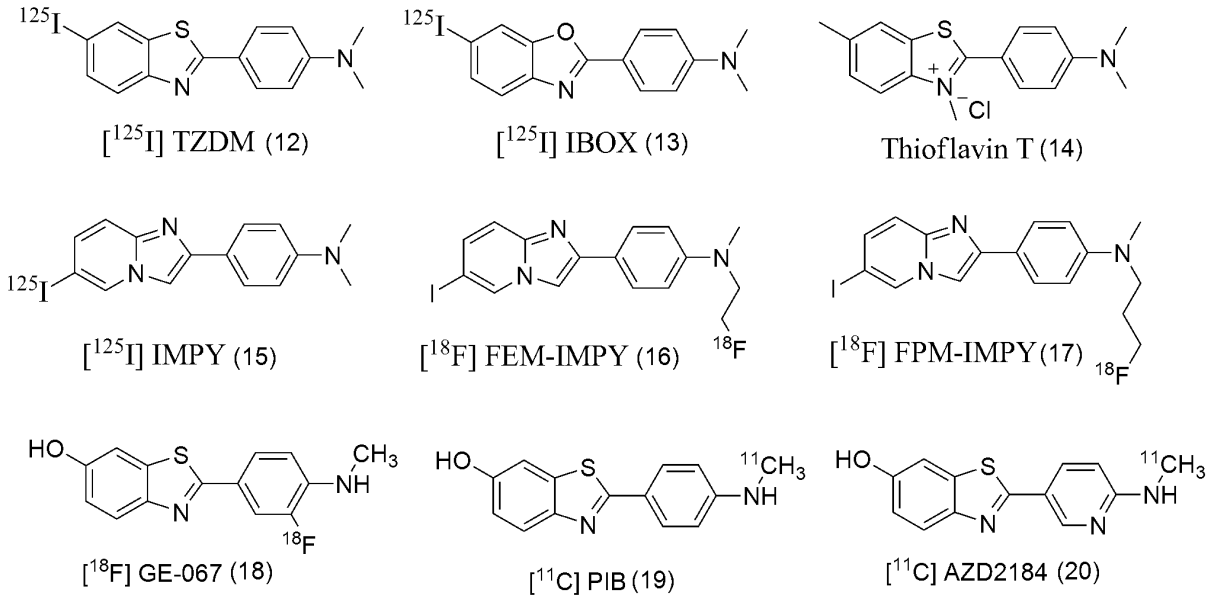

Fig 1.3.2.2.1: Chemical structure of PET/SPECT probes derived from Thioflavin T (ThT) for detection of senile plaques.

[^{11}C]PIB **(19)** is one of the most studied compounds for amyloid imaging. PIB is a benzothiazole derivative. [^{11}C]PIB binds to SPs with higher affinity than to NFTs.[130] [^{11}C]PIB binds to SPs in human brain and this probe presently in clinical trials.[131] [^{11}C]PIB has shown a high affinity binding site and a low affinity binding site on postmortem human brain tissue.[132]

[^{11}C]PIB standardized uptake value (SUV) images are shown below **(Fig 1.3.2.2.2)**. The SUV images display the [^{11}C]PIB retention differences between an AD patient brain and a healthy brain. In the healthy control, non-specific [^{11}C]PIB retention is seen in the white matter (top left). The right column shows high retention of PIB in the frontal and temporoparietal cortices of the AD patient (top right) and a typical pattern of [^{18}F]FDG hypometabolism present in the temporoparietal cortex (arrows; bottom right) along with preserved metabolic rate in the frontal cortex.

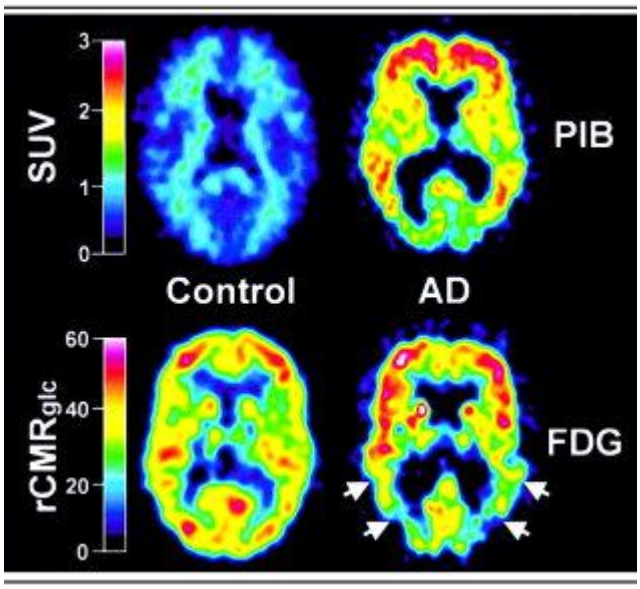

Fig 1.3.2.2.2: PIB standardized uptake value (SUV) images demonstrate a marked difference between PIB retention in Alzheimer's disease (AD) patients and healthy control (HC) subjects. PET images of a 67-year-old HC subject (left) and a 79-year-old AD patient (AD6; MMSE = 21; right). (top) SUV PIB images summed over 40 to 60 minutes; (bottom) 18FDG rCMRglc images (µmol/min/100ml). The left column shows lack of PIB retention in the entire gray matter of the HC subject (top left) and normal 18FDG uptake (bottom left). Non-specific PIB retention is seen in the white matter (top left). The right column shows high PIB retention in the frontal and temporoparietal cortices of the AD patient (top right) and a typical pattern of 18FDG hypometabolism present in the temporoparietal cortex (arrows; bottom right) along with preserved metabolic rate in the frontal cortex. PIB and 18FDG scans were obtained within 3 days of each other.[131] (Reprinted from Ann. Neurol. Copyright © 2003 with permission from American Neurological Association. Published by Wiley-Liss, Inc., through Wiley Subscription Services)

[^{11}C]AZD2184 **(20)** was shown to bind to SPs with high affinity (Kd – 8.4 + 10 nm) but with lesser affinity than [^{11}C]PIB (Kd – 3.3 + 0.8 nm). This probe also displayed amyloid aggregates in APP/PS1 mice.[133]

1.3.2.3 Other Positron Emission Tomography (PET) imaging probes:

In addition to several Congo red and Thioflavin derivatives, a few other probes are also known for their ability to bind to postmortem Aβ plaques. The chemical structures of these probes are shown below **(Fig 1.3.2.3.1)**

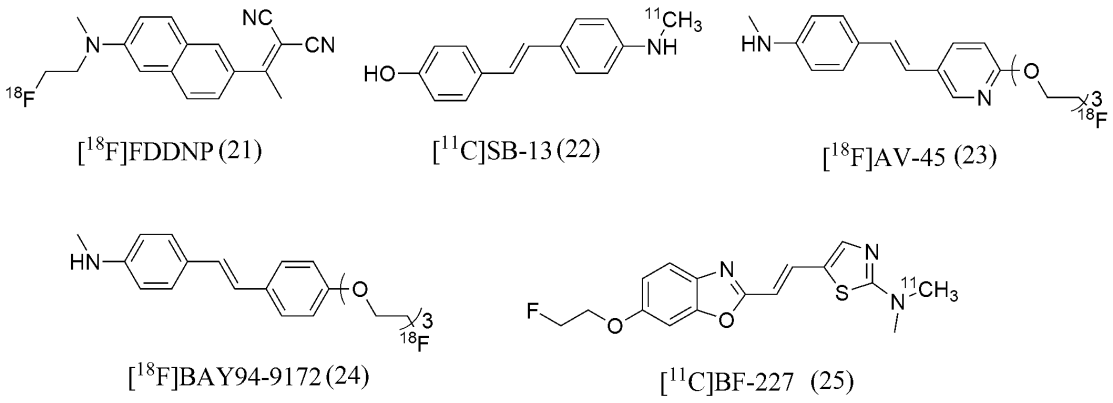

Fig 1.3.2.3.1: Chemical structures of PET probe for detection of amyloid plaques.

[^{11}C]SB-13 **(22)** is a stilbene derivative that has been shown to cross the BBB and image SPs in the AD brain. It has also showed increased retention in the frontal and posterior temporal-inferior parietal association cortices in Alzheimer's patients in comparison with controls.[134] [^{18}F]BAY 94-9172 **(24)** is a ^{18}F labeled PET tracer that binds to SPs in brain *in vivo*.[135]

[^{11}C]BF-227 **(25)** contains thiazole and benzoxazole groups in its structure and visualized SPs *in vivo*.[136] In familial transthyretin-related systemic amyloidosis, this probe was found to stain transthyretin, another kind of amyloid that found in the submucosal space of the small intestine in patients.[137]

[^{18}F]FDDNP **(21)** is a non-specific cellular membrane dye that is a lipophillic ^{18}F labeled tracer. It binds to SPs, NFTs and diffuse plaques in patients of AD. It was recently reported that PET imaging of FDDNP correlates with Aβ burden in transgenic rats.[138]

The United States Food and Drug Administration (USFDA) recently approved Amyvid (**23**). "Amyvid is indicated for Positron Emission Tomography (PET) imaging of the brain to estimate β-amyloid neuritic plaque density in adult patients with cognitive impairment who are being evaluated for AD and other causes of cognitive decline." A negative scan with Amyvid indicates the lower risk of patient cognitive impairment with AD and a positive scan indicates moderate to frequentness of amyloid neuritic plaques (USFDA approved indication).

In addition to these probes, peptide based compounds have also been developed for imaging amyloid brains. One example is 10H3 (structure not shown), which is a monoclonal antibody known to bind SPs. Labeling 10H3 with Tc99m resulted in a SPECT tracer

probe,[139] which was shown to bind to plaques with high affinity and specificity. Unfortunately, this probe is unable to cross the BBB. Serum amyloid protein, a non fibrillary glycol protein also known to bind to amyloid fibrils *in vitro*,[140] has the potential to cross the BBB, but when labeled with ^{123}I, the resultant probe was unable to differentiate between AD patients and controls. Radio labeled β-amyloid peptide was also used as an amyloid binding agent but this also demonstrated very low uptake by the brain in rats. To improve the brain permeability, it is conjugated with the monoclonal antibody OX26 to the rat transferrin receptor. The resulting complex has improved brain uptake and high affinity for cerebral SPs.[141]

1.3.3 PET and SPECT tracers for imaging neurofibrillary tangles:

Although imaging Aβ plaques may provide information about plaque density, it is unable to correlate with the severity of disease progression. Recent research findings suggest that the tau pathology might be a more reliable biomarker for AD. Also, in AD patients, the load of NFTs in the brain tissue correlates better to the severity of dementia. Imaging such NFTs is an alternative way to diagnose AD. Chemical compounds that known to bind to NFTs are shown below (**Fig 1.3.3.1**)

BF – 158 **(27)** is a quinoline derived ^{11}C labeled radio tracer for imaging of NFTs in post mortem AD patients. [^{11}C]BF-158 binds to the β-structure of NFTs rather than the monomeric tau protein and coincides with immunostaining. It has also been confirmed that [^{11}C]BF-158 can selectively stain the NFTs of AD, but was unable to stain the brain sections from other tauopathies such as pick bodies, globose tangles and glial pathology in a progressive supranuclear palsy (PSP) brain.[142]

Another probe for tau imaging is THK523 **(26),** an ^{18}F labeled, quinolone derivative. *In vitro* saturation assay results showed that [^{18}F]THK523 binds at two different sites on tau fibrils in contrast to only one site on Aβ fibrils. [^{18}F]THK523 has a 10-fold higher affinity to tau aggregates than to amyloid aggregates. From *in vivo* experiments, it was observed that 30 mins after intravenous injection, tau transgenic mice (rTg4510) have higher retention of the probe in the brain than their wild-type littermates (CamKII).[143]

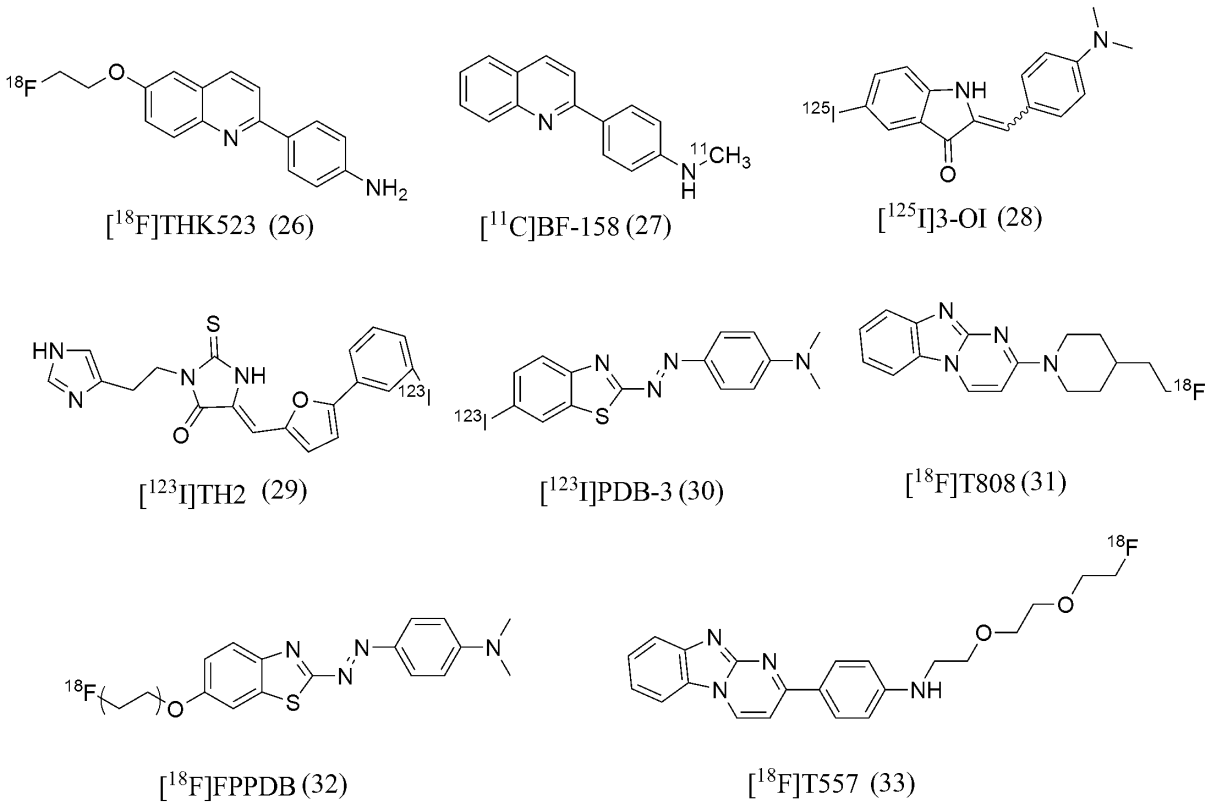

Fig 1.3.3.1: Chemical structures of PET/SPECT probe for detection of NFTs.

PDB-3 **(30)** is a ^{123}I based SPECT tracer. In the ThT displacement assay, this probe displayed K_i values of 0.48 nm and 8.24 nm to tau and amyloid aggregates, respectively. The K_i ratio of tau aggregates to that of amyloid fibrils are 17.2.[144]

FPPDB **(32)** is derived from [^{123}I]PDB-3 by replacing the iodine with a fluoropolyethylene glycol side chain. Although this compound displayed poorer affinity to tau aggregates than PDB-3, it has sufficient affinity to stain NFTs. It has K_i values of 13.0 nm and 20.0 nm to tau and Aβ aggregates respectively. The ratio between K_i of tau to amyloid aggregates is 1.52, whereas [^{123}I]PDB-3 showed higher ratio (17.2). Saturation assay results revealed that [^{18}F]FPPDB has almost similar affinity to tau and Aβ aggregates.[145]

Rhodanine and thiohydantoin derivatives have been reported for the imaging of NFTs. TH2 **(29)** possesses a good binding affinity to tau aggregates and Aβ ($Aβ_{42}$) aggregates (K_i values of 64 nm and 469 nm respectively).[146] Very recently, iodinated, 3-oxoindoles ([^{125}I]3-OI) **(28)** have been reported as novel tau imaging agents. This probe has an inhibitory constant of 17 nM to tau aggregates and 31 nM to $Aβ_{42}$ aggregates. The ratio between K_i is 1.77 which is far lower than PDB-3.[147]

Other probes, such as [^{18}F]T808 **(31)** and [^{18}F]T557 **(33)** are ^{18}F labeled PET tracers that selectively detect NFTs in an AD brain. The observed dissociation constant (K_d) for T808 ligand is 22 nM, but due to weak binding of T808 to SPs this compound is unable to distinguish between plaques and tissue background.[148]

Recently, the *N*-methyl (^{11}C) derivative of lansaprazole was reported for imaging of NFTs in rodents.[149] This compound has shown poor brain uptake in rodents, but in rhesus monkeys it showed maximum brain uptake of 1600 nCi/cc at 3 min and rapid clearance of 500 nCi/cc after 30 min.

Several of these probes have good affinity to SPs and NFTs, but imaging with radio labeled probes is an expensive method and also require trained scientists with handling knowledge of radiolabeled probes and instruments. In the case of ^{11}C labeled probes, a cyclotron must be on the site of production along with radiochemistry experts as a result of very short half-life time.

Imaging with fluorescent compounds may provide an alternative and cheaper method for the detection of NFTs.

1.4 Fluorescence Imaging

Fluorescence is a physical property of a molecule with the capability of emitting light by singlet-excited states of molecules following absorption of light from an external source (UV or blue/green spectral range). This can be explained by the below Jablonski diagram **(Fig 1.4.1)**. Fluorophores are excited from the ground state to the first electronic excited state. Single-photon excitation occurs through the absorption of one photon, the fluorophore relaxes to the lowest energy level of the first electronic excited state via vibrational relaxation.[150] In contrast to the linear process, two-photon excitation occurs through a non-linear process by light simultaneous absorption of two protons from light and matter. Two photons of lower energy (normally infrared spectral range) are absorbed by short-lived intermediate processes. Three and higher photon excitation is also possible with intense excitation. Although, two-photon microscopy is limited to lower resolution, it allows deeper penetration of light and absorbs lower energy near infrared radiation. In two photon microscopy scattering of light is also low.[150] Two-photon microscopy is useful for *in vivo* imaging of neuronal function in living animals.

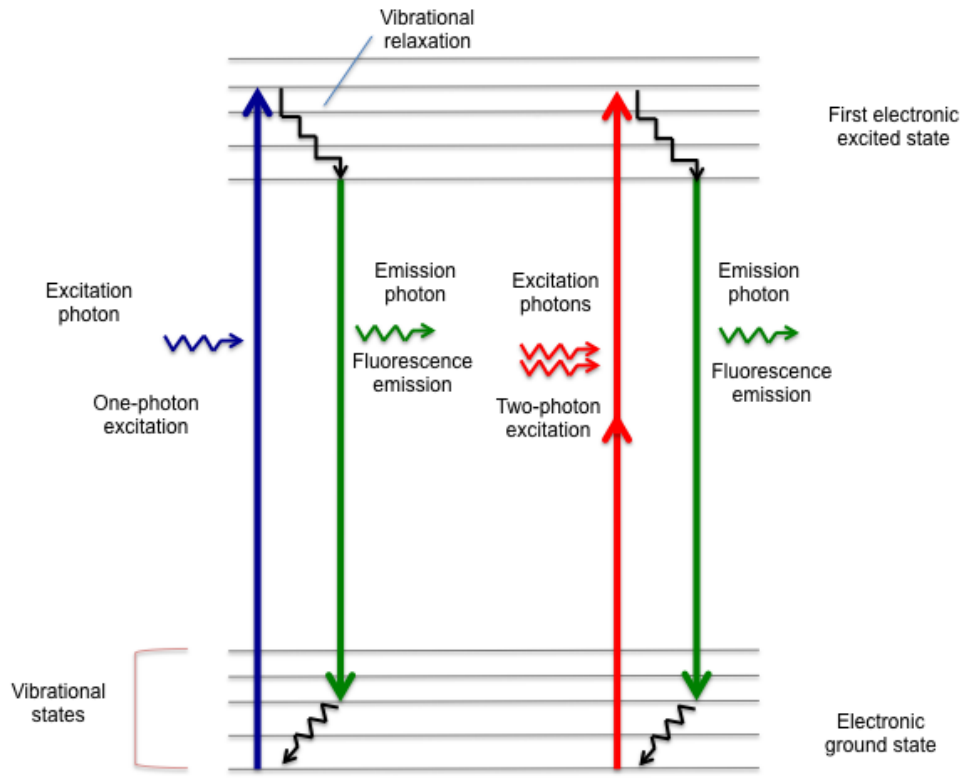

Fig 1.4.1: Jablonski diagram of one-photon (left) and two-photon (right) excitation.

Fluorescence imaging is a quantitative and sensitive method that is rapidly expanding in molecular biology and biochemistry. Molecules that are used by benefit of their ability to be fluorescent are called fluorophores. Fluorophores allow sensitive detection of countless biological molecules. These are much more sensitive than colorimetric methods. Some advantages of fluorescent probes, are that they may chelate to metal ions and thus allow to track the transport of ions in cells,[151] and can be employed in new techniques such as Photo Activated Localization Microscopy[152] (PALM) and STochastic Optical Reconstruction Microscopy[153] (STORM). The advantages of fluorescent probes over radio labeled probes in imaging are safety, speed and cost effectiveness; so the need of fluorescent probes for biomedical research is increasing. These optical probes have the ability to reveal the mechanistic function of different cellular processes.[154]

There are a few common characteristics that need to be considered when designing an *in vivo* fluorescent imaging probe such as wavelength, brightness, stability and pharmacokinetics. The wavelength is an important factor because ultra violet radiation can damage the tissue and infrared radiation can heat the tissue. An ideal fluorophore should have low or no auto fluorescence in the unbound state. To attain sufficient brightness of the

fluorophore, the use of higher conjugation may be employed. The fluorophore stability is an important factor, particularly for *in vivo* applications, as it was observed that after intravenous injection, many fluorophores decayed in a few days.[155] Another important factor is pharmacokinetic properties; fluorescent probes may display altered pharmacokinetics after binding to larger proteins.[156]

In addition to CR, there are other fluorescent probes that are in the development for imaging of SPs and NFTs in AD **(Fig 1.4.2)**.

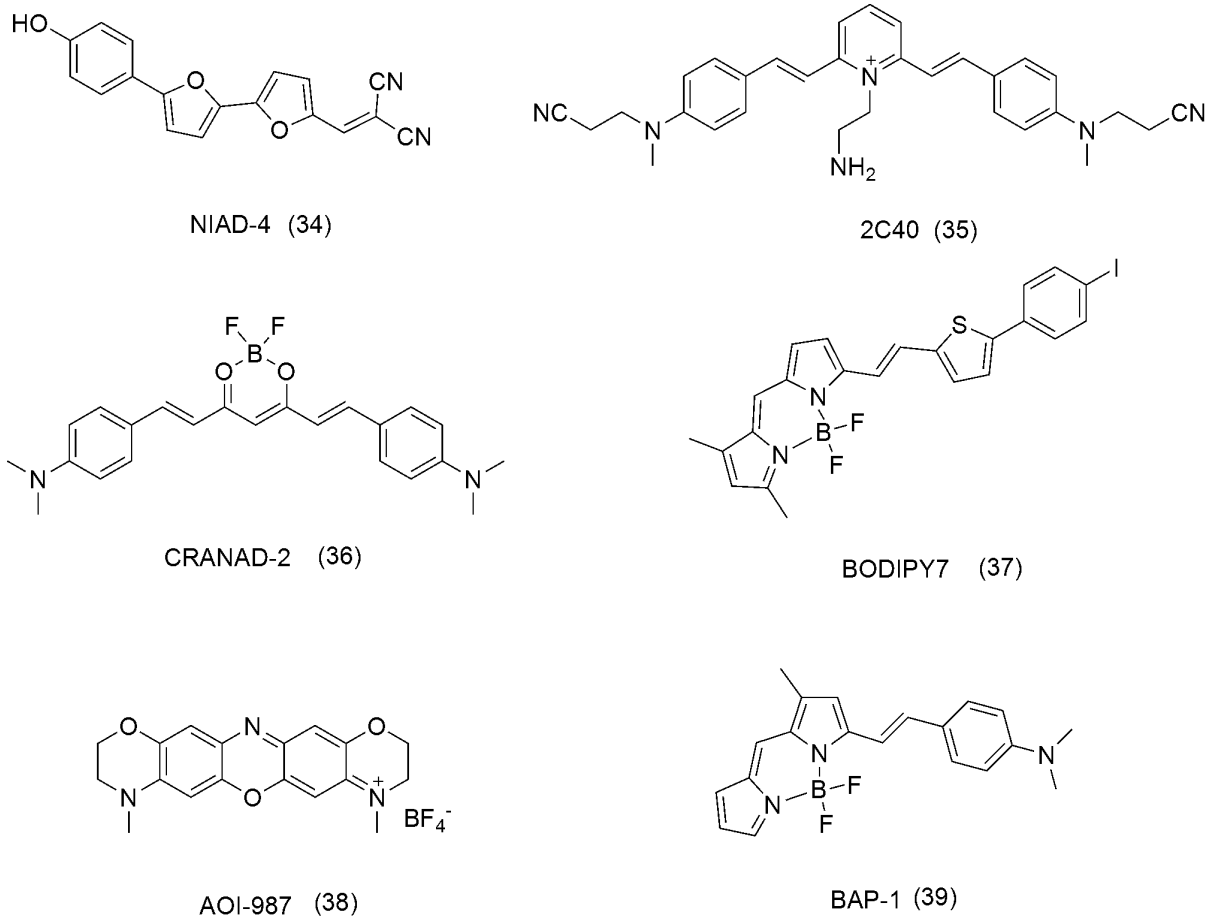

Fig 1.4.2: Fluorescent probes for detection of SPs in brain tissue by optical imaging.

NIAD-4 **(34)** is an optical imaging agent shown to cross the BBB which images SPs *in vivo*. It was shown to bind to SPs with higher affinity than to NFTs and it was also observed that this probe binds to the same binding site as BTA-1.[157] BODIPY 7 **(37)** is a boron dipyrro - methane derivative, which was shown to bind to SPs. The binding affinity (K_i) of this compound to $A\beta_{1-42}$ aggregates is 108 nM, but this compound failed to show brain uptake

and thus it is not suitable for *in vivo* imaging.[158] Styryl based compounds with a positive charge such as 2C40 have been found to stain SPs *in vitro.* Nevertheless these compounds are not able to cross the BBB and therefore are useless for in vivo applications.[159] Modification of these compounds resulted in a new class of amyloid imaging agents found to bind to plaques *in vivo*.[160] A difluoroboran derivate of curcumin was shown to cross the BBB and detect SPs *in vivo*.[161] A new class of oxazine derivative was shown to act as amyloid binding agents *in vivo*.[162] Recently, the BODIPY- based molecular probe BAP-1 **(39)** has been reported for imaging of cerebral SPs in *ex vivo*.[163] *In vivo* experiments with this probe showed that the fluorescence of BAP-1 accumulated non-specifically in the scalp in both groups. To improve non-specific accumulation in the scalp, further modification of the BODIPY scaffold will be needed. There are many ligands for amyloid plaque detection *in vivo*, but NFTs correlate stronger with the disease progression than SPs. Thus the development of fluorescent ligands for imaging of NFTs in AD is crucial. In the current hypothesis, we explored a different set of fluorescent compounds for highly selective NFT imaging with novel *Thiazine Red R* displacement assay.

Fluorescence microscopy has two additional capabilities in addition to the capabilities of conventional light microscope. Conventional microscopy uses 400-700 nm light for imaging, whereas fluorescence microscopy uses a broader range of light that extends from far UV to short IR with higher intensity light source that excite fluorescent species in the sample of interest. It also enhances 3D image details of specimen at small scales. In vivo imaging in the retina of APP(SWE)/PS1(Δ)(E9) transgenic mice for Aβ retinal plaques has been reported recently.[164] In addition to this, the recent development of fluorescent probes for the detection of tau aggregates in the olfactory epithelium provides a chance for early diagnosis of AD.[107c] Taken together, the development of fluorescent probes for the imaging of tau aggregates in mice may enable steps for early detection of AD.

1.5 Animal models

In the 1980's several reports from pharmaceutical industries showed that a lack of pharmacokinetics and poor efficacy resulted in the termination of many drugs from clinical trials.[165] Immediate developments in molecular biology helped to study pharmacokinetic properties such as chemical stability in the gastrointestinal tract, metabolic stability, ADME, solubility and toxicity. Molecular biology and genetic engineering made it possible to express human proteins in models such as mice, worms, squirrels, hamsters and fish which resulted in considerable improvement in the drug development process for the filtration of new

libraries. Animal models are necessary for the understanding of the pathogenesis of diseases at cellular and molecular levels and for the evaluation of previously untestable potential therapeutic interventions. Cell culture models allow to transfect genes of interest into these cells; however, cells cannot accurately reflect the activities of the whole organism. By introduction of a human gene sequence into the model animal's genome, human proteins can be expressed in animal models. When selecting an animal model, a range of factors from evolutionary proximity to anatomical similarity needs to be considered.[166] Larger animals such as rats, baboons and sheep have organ sizes that are considerably similar to humans and will be advantageous for understanding therapeutic effects. It is also possible to mimic these cellular level changes in small animals such as mice, flies, worms and fishes. Using these smaller models will be cost-effective and easier to handle. When considering large-scale screenings, fish models have an advantage for studies such as toxicity in embryos since embryos are needed on a large scale.

In AD, the two hallmarks responsible for the disease are SPs and NFTs. Several transgenic and non-transgenic models for SPs and tau aggregates were developed to understand the mechanisms of phosphorylation of tau and formation of Aβ deposits.

The challenge in mousemodel development is that in humans the diseases develop over a very long span, which has to be reduced to the shorter life span of mice. Several models have been developed for the expression of SPs (APP) and the expression of tau protein. Different APP mice models are (APPki, BRI- Aβ42, arc Aβ, TgAPParc, APP695, APP695/PSEN1, APPdutch, APPARcSwe, APPS1, APPSWE, Apbb1, Human BACE, APPSw, APPSw-NSE, APP-C99, A-R1.40, Aplp2, APP, APP23, hBACE).[167] Tau research models include ΔTau74, Tau K369I, TTBK1, Thy-Tau22, Tau4R-P301L, Tau-4R-KOKI, Tau R406W, Human wt Tau, Tau α1-3RT, human Tau, Tau P301L, Tau R406W and Tau V336M, T44 (3 repeats), Tau 4-Repeats-Alz17, Tau 4R/2N.[168]

Squirrels and hamsters are also used as tau models for the study of hyperphosphorylation during torpor, which is reversible upon arousal.[169] P301S tau transgenic mice that express tau inclusions in retinal ganglion cells were used in this study.[170] Human tau expression was observed by histochemical and biochemical analysis with tau antibody Tau-14.

In a search to overcome the limitations of mammalian models, such as cost and slow development, the zebrafish has been found to be an alternative model organism **(Fig 1.5.1)** and is a common aquarium fish. The Latin name for zebrafish is *Danio* (formerly

Brachydanio) *rerio*, which originates from the river *Ganges* in India. The zebrafish has become a popular and simpler model in the past decade for the study of vertebrate development. Zebrafish are small freshwater teleost that promises to contribute to several aspects in the drug development process.[171] A few advantages of zebrafish over the other animal models are: its larvae are small in size, they are optically transparent and they undergo rapid development *ex utero*, which makes handling extremely easy. Zebrafish are small in size (typically 3-5 cm), making them easy to use in large numbers for breeding. The females are very reproductive and can generate three hundreds eggs per time.

The Zebrafish became a widely used model in the drug development process, including target identification, disease modeling, lead identification, lead validation and evaluation of toxicity. Numerous genetic studies have been carried out in zebrafish and several mutations have been identified. Several phenotypes, which resemble human diseases, have been identified.[172] It has also been used in several disease-related screens such as heart disease, cholesterol processing, tissue regeneration, cancer, anemia and AD.[173] Zebrafish allows recapitulation of pathologies associated with AD.

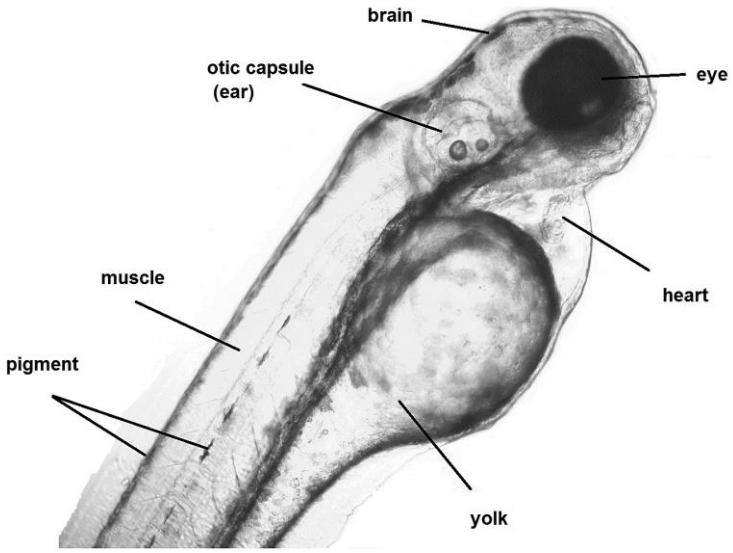

Fig 1.5.1: Zebrafish larva at 2-day post fertilization (tail not shown). Organs can be visualized under the microscope. Brain, heart, eye and other organs can be observed.

Toxicity is one of the most important factors to consider during drug development. Initial toxicity screenings help to avoid toxic compounds and may save time and cost. Animal models such as mice and baboons exist, but a quick toxicity study with these models is not possible and requires high manpower. Zebrafish have been shown to be a useful alternative model and is gaining rapid acceptance for toxicity studies. As mentioned before, transparent embryos and larvae made it possible to observe organ development closely. Pre-screening

studies of toxicity for a large number of compounds aimed for High Throughput Screening (HTS) can be performed quickly with this model.[174] In the current study, for the development of new imaging agents for NFTs, toxicity experiments were performed using zebrafish embryos.

2. AIM OF THE STUDY

NFTs and SPs are known as hallmarks for AD. By imaging these proteins, it is possible to diagnose the disease at early stages of disease progression. The load in SPs does not correlate with the disease progression, whereas NFT deposition does. Therefore, imaging such NFTs could result in an early diagnosis of AD and may provide an early opportunity to quantify the level of the disease. Although, there are several other techniques such as PET or SPECT imaging, due to disadvantages such as cost, requirement of skilled people, radioactivity exposure and short half-life time of the probes, an alternative technique is in demand.

The present study is a part of the "*Molecular Diagnosis of Neurodegenerative Diseases in the Eye"* (MINDE) project. In this context, the aim of this thesis is to develop a fluorescence imaging agent able to visualize NFTs with high selectivity. This fluorescence imaging agent may allow detection of tau aggregates in retinal tissues of P301S mice and in Bowman glands of olfactory epithelium tissue via nasal application.

The fluorescent probes for tau aggregates in the retina and the olfactory epithelium were designed according to the general criteria described for imaging NFTs in the brain.

1. Partition coefficient ratio between octanol and water in the range of 1-2.8 and topological polar surface area <70 $Å^2$, to cross the BBB and to bind to target protein.
2. Molar mass of the probe should be <500 Daltons.
3. Absorption wavelength in the range of 400 - 450 nm or 520 - 600 nm for 1-photon absorption and 400 - 450 nm or 520 - 750 nm for 2-photon absorption.
4. Emission wavelength in the range of 420-450 nm or 520 - 1000 nm.
5. Stokes shift >20 nm.
6. Excitation coefficient ε >10.000 M^{-1} cm^{-1}.
7. Higher intensity of fluorescence emission upon binding to target protein, to improve the signal to noise ratio with respect to unbound compound.
8. *In vivo* half-life >60 min.
9. Rapid clearance from the target.

Following, these criteria, several probes were designed and synthesized. Absorption and fluorescence emission properties were determined. The affinity of these probes was measured in the *Thiazine red R* displacement assay. Cytotoxicity of these probes was

determined by zebrafish embryo development and in a hepatocellular carcinoma cell line. Further analysis of these probes was performed in mouse retina and human olfactory epithelium tissues. In addition, inhibitors of GSK3 selective to GSK3α were studied.

3. GENERAL AND CUMULATIVE PART

The results obtained in this study are presented below. Several probes were designed and synthesized for the diagnosis of Alzheimer's disease. The histology of these probes on post mortem brain sections was examined by a fluorescence microscopy. Affinity of these fluorescent probes was determined using 4R tau and $A\beta_{40}$ aggregates. Selected compounds were measured for their cytotoxicity in human liver carcinoma (HepG2) cells and zebrafish embryos. Furthermore, for certain compounds in these compound classes, *in vivo* evaluation has been performed in mice models of AD.

3.1 Fluorescent probes in Alzheimer's disease imaging

3.1.1. Strategies for the design of selective fluorophores

These probes were designed by two different strategies. In the first strategy, a structural modification of existing probes was performed. Modification of known amyloid binding probes to tau selective probes was carried out to improve pharmacokinetic properties. In addition, structure activity relationships were also examined to find a probe with higher affinity to tau aggregates. In the second strategy, a structural modification of tau aggregate inhibitors was performed. As tau aggregate inhibitors bind to tau and prevent aggregation, introduction of a fluorophore moiety to the inhibitors resulted in NFT selective fluorescent probes. Both of these strategies resulted in different NFT selective probes, which are shown below.

3.1.2 Fluorescent rhodanine-3-acetic acids visualize neurofibrillary tangles in Alzheimer's disease brains

The content of this chapter has been published

Upendra Rao Anumala, Jiamin Gu, Fabio Lo Monte, Thomas Kramer, Roland Heyny-von Haußen, Jana Hölzer, Valerie Goetschy-Meyer, Christian Schön, Gerhard Mall, Ingrid Hilger, Christian Czech, Jochen Herms, and Boris Schmidt.

Fluorescent rhodanine-3-acetic acids visualize neurofibrillary tangles in Alzheimer's disease brains, *Bioorganic & Medicinal Chemistry* (DOI: 10.1016/j.bmc.2013.06.039)

Summary

Alzheimer's disease (AD) is a neurodegenerative disorder which is often characterized by memory loss and cognitive failure. Senile plaques (SPs) and neurofibrillary tangles (NFTs) are known as hallmarks of the disease. Imaging these NFTs and SPs in the AD brain may provide early stage diagnosis of the disease. In this chapter, synthesis and evaluation of rhodanine-3-acetic acids (RA), known tau aggregation inhibitors, was performed. In the present study, a group of seven fluorescent RA derivatives was synthesized. Substitution of variety of a variety of fluorophores on RA resulted in probes with different absorption and emission properties. Histological examination of postmortem AD brain sections with these probes displayed NFTs. *In vitro* evaluation of these probes in *Thiazine red R* assay confirmed the higher affinity of these probes to NFTs over SPs. The cytotoxicity of these probes on Heptocellular carcinoma cell lines (HepG2) and zebrafish embryos were examined. All probes displayed no or negligible cytotoxicity. Further evaluation of these probes in retinal tissues of P301S mice resulted in no staining. These results indicate that RA derivatives only stain to fibrillary tau aggregates and are unable to visualize non-fibrillary tau aggregates.

Contribution of Upendra Rao Anumala: Synthesis and purification of probes **1-7**, histological examination on postmortem AD brain sections, UV absorption and emission measurements, cytotoxicity evaluation in zebrafish embryo assay, and manuscript preparation.

Bioorganic & Medicinal Chemistry
journal homepage: www.elsevier.com

Fluorescent rhodanine-3-acetic acids visualize neurofibrillary tangles in Alzheimer's disease brains

Upendra Rao Anumala[a], Jiamin Gu[a,†], Fabio Lo Monte[a,‡], Thomas Kramer[a], Roland Heyny-von Haußen[b], Jana Hölzer[c], Valerie Goetschy-Meyer[d], Christian Schön[e], Gerhard Mall[b], Ingrid Hilger[c], Christian Czech[d], Jochen Herms[e], Boris Schmidt[a,*]

[a]Clemens Schöpf-Institute of Chemistry and Biochemistry, Technische Universität Darmstadt, Petersenstrasse 22, 64287, Darmstadt, Germany
[b]Institute of Pathology, Klinikum Darmstadt, Grafenstrasse 9, Darmstadt 64283, Germany
[c]Institute of Diagnostic and Interventional Radiologygy I, Jena University Hospital – Friedrich Schiller University Jena, Erlanger Allee 101, 07747 Jena, Germany
[d]F. Hoffmann-La Roche AG, Grenzacherstrasse 124, Gebäude 93/3.44, Basel 4070, Switzerland
[e]Department of Translational Brain Research, DZNE, German Center for Neurodegenerative Diseases, Munich, Germany
*Corresponding author. Tel.: +49 6151 164531; fax: +49 6151 163278.
E-mail address: schmidt_boris@t-online.de (B. Schmidt).
†Present address: Alberta Glycomics Centre, Department of Chemistry, University of Calgary, 2500 University Drive NW, Calgary Alberta T2N 1N4, Canada
‡ Present address: Institute of Organic Chemistry, University of Zurich, Winterthurerstrasse 190, CH-8057, Zurich, Switzerland

ARTICLE INFO

Article history:
Received
Received in revised form
Accepted
Available online

Keywords:
Alzheimer's disease
Neurofibrillary tangles
Zebrafish
Cytotoxicity
Fluorescence imaging

ABSTRACT

There is a high demand for the development of an imaging agent for neurofibrillary tangles (NFTs) detection in Alzheimer's diagnosis. In the present study, a series of rhodanine-3-acetic acids was synthesized and evaluated for fluorescence imaging of NFTs in brain tissues of AD patients. Five out of seven probes have shown excellent binding affinity to NFTs over amyloid plaques in the *Thiazine red R* displacement assay. However, the selectivity in this *in vitro* assay is not confirmed by the histopathological evaluation, which indicates significant differences in the binding sites in the assays. Probe 6 showed binding affinity (IC_{50} = 19 nM) to tau aggregates which is the highest among this series. Probes 2, 3, 4 and 5 display IC_{50} values of lower than 100 nM to tau aggregates to displace *Thiazine red R*. Evaluation of the cytotoxicity of these five probes with human liver carcinoma cells revealed that these compounds excert negligible cytotoxicity. The *in vivo* studies with zebrafish embryos confirmed negligible cytotoxicity at 24 and 72 hours post fertilization.

1. Introduction

Alzheimer's disease (AD) is one of the most common forms of dementia. This disease is a progressive neurodegenerative disorder associated with cognitive decline, disorientation and language impairment. Incidence of new AD cases worldwide is growing with the age of the baby boomer generation.[1, 2] The major cause is still unknown for the disease but it is usually accepted that the formation of two abnormal proteins; extra cellular senile plaques (SPs) and neurofibrillary tangles (NFTs) are the two key pathological findings in postmortem histology. They are observed in hippocampus and cerebral cortex but also in other areas of the brain. SPs are composed of aggregated β-amyloid (Aβ) peptides and NFTs are formed by the aggregated microtubule associated tau protein.[3]

Non-invasive imaging is vital for early diagnosis of AD. Currently there are few positron emission tomography (PET) imaging agents available for the early diagnosis. PET imaging is a very well-known technique which provides good sensitivity deep in tissue.[4] Nevertheless it is limited by a time-consuming

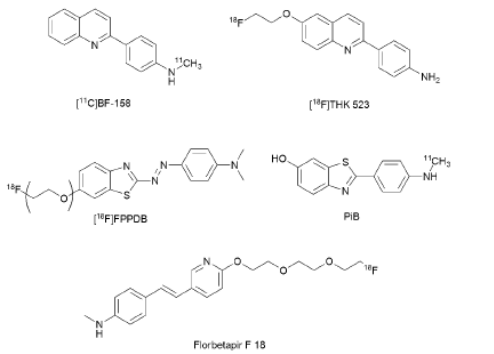

Figure 1. Structure of PET imaging probes for the detection of NFTs and Aβ plaques in AD brain tissues

Table 1

General properties, optical properties, competitive *Thiazine Red R* displacement from tau-/$A\beta_{40}$-aggregates for probes **1-7** and cytotoxicity.

Compound	Yield[a]	M.Wt[b]	*c*Log*P*[c]	λ_{max}^{abs} (nm)[d]	λ_{max}^{em} (nm)[d]	Aggr.Tau-IC_{50}/nM	Aggr. $A\beta_{40}$-IC_{50}/nM	Cytotox. EC_{50} (μM)[e]
1	79	345.39	2.70	445	511	662	5002	>100*
2	61	348.44	2.19	497	645	32	55	>100*
3	53	367.49	3.03	444	525	43	292	>100*
4	83	391.48	3.11	391	533	28	91	>100*
5	85	348.44	1.70	468	555	63	218	>100*
6	71	512.71	7.12	466	651	19	91	18
7	69	414.52	3.41	455	645	238	1156	>100*

[a] Isolated yields [b,c] Determined by CS Chemoffice 10.0. [d] Measured in ethanol. [e] EC_{50} declares the dye concentration in which 50% of the cells died after incubation with the probe after 24 h of exposure. * a decrease of cell viability ≥ 50% was not observed at the tested concentrations. The IC_{50} data were obtained from the average of technical replicates and are thus presented without standard deviation

data acquisition process and exposure to radioactivity, insufficient spatial resolution along with expensive equipment and need of highly skilled personnel. Pittsburgh compound B (PiB) and Florbetapir F18 are well studied PET ligands targeting SPs.[5, 6] Florbetapir F18 is a PET probe for the imaging of Aβ plaque density in AD patients and other causes of cognitive decline.[7] Florbetapir is the most widely used amyloid marker for Aβ PET-imaging. PET ligands for imaging of NFTs were also reported. These include [^{11}C]-BF-158, [^{18}F]-THK 523 and [^{18}F]-FPPDB (Figure 1).[8-10] Moreover, Aβ imaging cannot differentiate between different forms of frontotemporal lobe degeneration and Aβ plaque load plateaus as disease progresses. Additionally, PIB imaging is negative in up to 25% of the patients diagnosed with AD.[11] Furthermore, the formation of neurofibrillary tangles brain correlates better with disease progression in AD.[12] Fluorescence imaging is a relatively new modality that offers real time, non-radioactive, inexpensive *in vivo* imaging.[13] It is frequently rejected to be a non-viable modality in humans, however the recent reports on pathological changes in the retina and the human olfactory system suggest to investigate a non-invasive access to amyloid and tau deposits by either scanning of the retina or endoscopic nasal examination.[14, 15]

Fluorescence imaging of a boron dipyrromethane derivative (BAP-1) and curcumin has been reported for Aβ deposits.[16] The presence of hyperphosphorylated non-fibrillar tau was reported for both the retina of P301S transgenic mice and the human retina.[17] Thus, there is an immediate need for fluorescent NFT-imaging agents, which may complement the established amyloid PET imaging tools.

Rhodanine based compounds are known for their ability to inhibit tau aggregation *in vitro and in vivo*.[18-20] Rhodanine and thiohydantoin derivatives were reported as single photon emission computed tomography (SPECT) imaging agents for NFTs.[21] Rhodanine-3-acetic acids are known as amyloid imaging agents, dye sensitized solar cells and anthrax lethal factor protease inhibitors.[22-25] In the present study we synthesized and studied the fluorescence imaging properties of rhodanine-3-acetic acid (RA) derivatives as fluorescent probes for NFTs and evaluated their affinities in the *Thiazine red R* assay. We evaluated the effects of these probes on cell metabolism on human hepato-cellular carcinoma cells (HepG2) and zebrafish embryo development. These compounds were evaluated in human and transgenic P301 mice retinae for their ability as imaging agents. However, the absence of fibrillar tau deposits in the retina of both species excluded a proof of concept.[17]

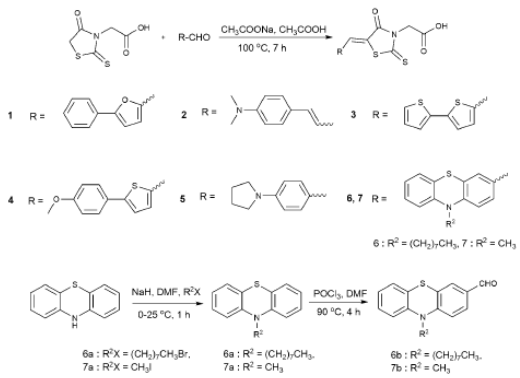

Scheme 1. Synthesis of rhodanine-3-acetic acids and 10-alkyl-10H-phenothiazine-3-carbaldehyde.

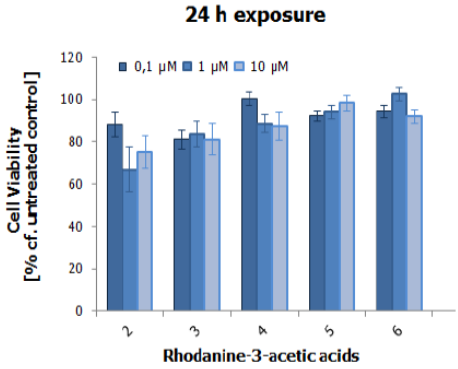

Figure 2. Cell viabilities of HepG2 cells after 24 hours of exposure with the probes **2** to **6** at 0.1, 1 and 10 μM concentrations after 24 hours of exposure. +/- SD

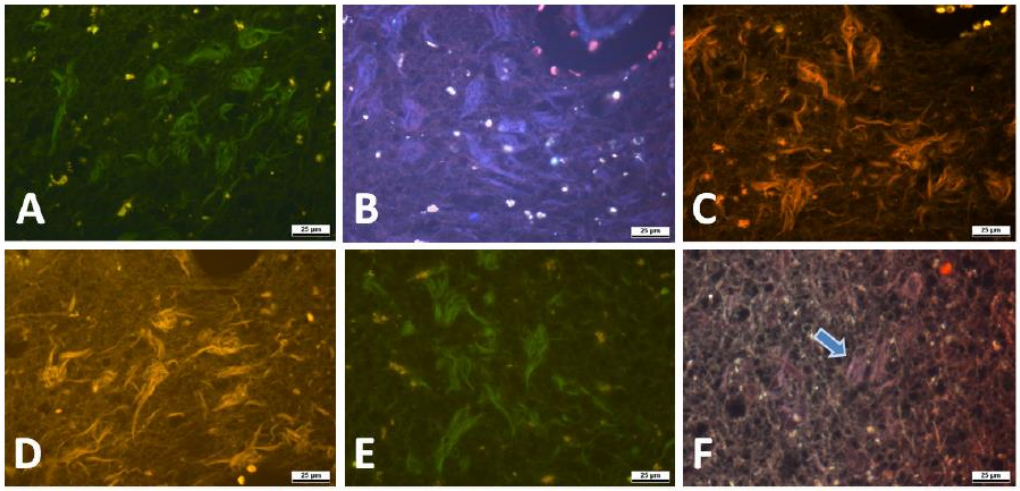

Figure 3. Neuropathological staining of brain sections from the hippocampus of an AD patient (A-F). Probe **1** (A), **2** (B), **3** (C), **4** (D), **5** (E) clearly stained flame shaped neurofibrillary tangles and Probe **6** (F) showed photo bleaching and high background tissue staining to NFTs. (NFTs are shown with arrow). Tissues: hippocampus; patient: female, 80 years old, CERAD Score: 3; NFTs-level: V.

2. Results and discussion

RA derivatives were synthesized by known methods using a Knoevenagel condensation between RA and corresponding aldehydes using sodium acetate in acetic acid.[26] Most of the aldehydes used in the present study were commercial but a few aldehydes had to be synthesized by known methods. Probes **6** and **7** were synthesized in a three step procedure. In the first step, alkylation of phenathiazine in the presence of sodium hydride and dimethyl formamide was performed. The *N*-alkyl phenathiazine was formylated in the second step employing the Vilsmeier-Haack reaction of phosphorous oxychloride and dimethylformamide. In the final step a Knoevenagel condensation was carried out between the RA derivatives and *N*-alkyl phenathiazine aldehyde to obtain the probes **6** and **7**. The yields of the Knoevenagel condensation for probes **1-7** varied from 61-85% depending on the aldehydes. The presence of electron donating groups increased the reactivity whereas electron withdrawing groups decreased the reactivity and yield of derivative formation.

All of these compounds were further evaluated for their ability to visualize NFTs in *post mortem* human AD brain sections. Initial immune histochemical staining confirmed that these tissues contain both NFTs and SPs (supporting info). The RA derivatives were used to stain these protein aggregates on brain sections of the same patient. All of these compounds showed selective binding to NFTs of *post mortem* AD brain tissues. Our observations with RA derivatives showed selective staining to NFTs rather than that of Aβ plaques, which stands in contrast with the selectivity observed in the *Thiazine red R* displacement assay. This striking difference indicates a significant difference between the binding sites in the protein aggregation assay and the human brain. A related discrepancy was reported for amyloid binding agents in filtration assays and upon binding to human tissue.[27] Thus the affinity data obtained from the displacement assays must be analyzed with care. The introduction of a bis-thiophene moiety on RA leads to probe **3**, which displayed good fluorescence. Under the fluorescence microscope, this compound displayed excellent staining of NFTs in brain tissues. Most of these compounds showed reduced background staining in comparison to the staining of NFTs. Probe **1** stained NFTs in good contrast to the background, whereas photo bleaching was observed with probe **6**. (Figure 3).

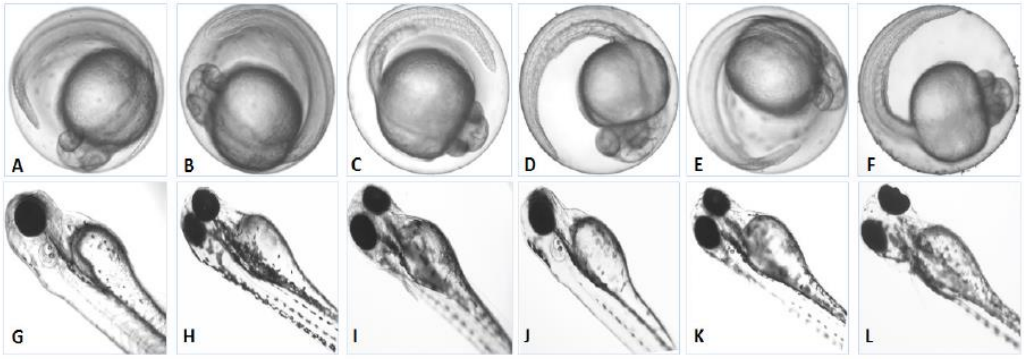

Figure 4. *In vivo* cytotoxicity studies with embryos of zebrafish after 24 (A-F) and 72 (G-L) hpf. Controls (A and G), Probe **2** (B and H), **3** (C and I), **4** (D and J), **5** (E and K) at 10 μM concentration and Probe **6** (F and L) at 5 μM concentration.

The *in vitro* affinity studies of these compounds were performed by the *Thiazine red R* displacement assay.[15, 28, 29] *Thiazine red R* is known for its binding to tau aggregates *in vitro* and for its superiority over *Thioflavin T*.[30] Aggregates of recombinant human-microtubule associated tau protein, which was purified from Escherichia coli, and synthetic Aβ peptides were used in this study. The in vitro aggregates of $A\beta_{40}$ and $A\beta_{42}$ display differences in the binding sites for amyloid ligands, which depend on the aggregation conditions and differ from the binding situation observed in human tissue. Thus we selected $A\beta_{40}$ for the aggregation assay as it is the predominant component in amyloid plaques and thus likely to be engaged in binding of the probes.

IC_{50} values of *Thiazine red R* are depicted in Table 1. All of these probes have higher affinity to aggregated tau than aggregated $A\beta_{40}$ in the *Thiazine red R* assay. However, the apparent selectivity in the histology was even higher than indicated by the affinity assays. This suggests fundamental differences between the protein aggregates. Caveat: chemically induced synthetic tau fibrils are not a reliable surrogate for native NFTs, they differ in size, morphology and binding properties.[31] Five compounds out of seven showed IC_{50} values of less than 100 nM. Probe **6** showed almost five fold higher affinity to tau aggregates (19 nM) than to amyloid-β aggregates (91 nM), the highest selectivity to tau aggregates in this series. Probe **3** showed around 7-fold higher affinity to aggregated tau but weaker binding in comparison to probe **6**.

Probes **2**, **3**, **4** and **5** displayed IC_{50} values of 32 nM, 43 nM, 28 nM and 63 nM, respectively. Probes **1** and **7** display poor affinity compared to the other probes in this series. Apparently, the binding affinities of RA derivatives are higher to tau aggregates than to $A\beta_{40}$ aggregates. It is generally known that compounds with a *c*Log*P* lesser than 3 and a molecular weight less than 500 Daltons are most favourable for blood brain barrier (BBB) penetration.[32] RA derivatives were designed according to these *c*Log*P* values. According to the *c*Log*P* value, Probe **5** (*c*Log*P* value of 1.7) has the lowest *c*Log*P* value in this series and other probes except probe **6** are in the range of 2.0 to 3.5. Probe **6** is characterized by a *c*Log*P* of 7.12. Despite the high affinity of probe **6** to tau aggregates the lipophilicity, poor solubility and photo bleaching make it unsuitable for *in vivo* studies.

As safety is one of the most important factors during the development of an imaging agent, the effects of these compounds on HepG2 cell proliferation and zebrafish embryo development were evaluated. Except for probes **1** and **7**, all other probes were tested for their cytotoxicity in zebrafish embryos. The cytotoxicity evaluation of probes **2-5** clearly showed that most of these probes have no or negligible cytotoxicity at concentrations up to 10 µM. Probe **6** showed cytotoxicity at 10 µM concentration. Yet, no lesions in embryos of zebrafish were observed at 5 µM concentration at 24 and 72 hours post fertilization (hpf), which indicates that all of these compounds display negligible cytotoxicity up to a concentration of 5 µM. It was observed that zebrafish embryos developed normally in comparison with control for all RA derivatives at 5 µM. Further experiments with liver HepG2 cells were performed and the effective doses (EC_{50}) were calculated via the best-fitted trend line of cell viability as a function of dye concentration. Probes within the range of 1-100 nM affinity to tau aggregates were considered for the cytotoxicity studies. Probes **2**, **3**, **4**, **5** and **6** were studied *in vitro* for their cytotoxicity in HepG2 cells. Apart from compound 6, the EC_{50} values of all compounds are > 100 µM and loss of cell viability ≥ 50 % was not observed at the tested concentrations (100 µM was the highest concentration tested). The EC_{50} of probe **6** after 24 h of incubation is about 18 µM. Figure 2 shows the cell viability of these compounds in HepG2 cells at 24 h after incubation.

It was recently reported that fibrillar tau inclusions can be observed in retinal ganglion cells of P301S mice *in* and *ex vivo*.[17, 33] However, we could not visualize fibrillar tau aggregates with these compounds (Probe **1**, **2**, **3** and **4**) in the retina of P301S mice. These results suggest that the tau aggregates in the retina of P301S mice may be distinctly different from human tau aggregates that can be stained with compounds **1-4**. This may be due to the fact that the human brain produces a mixture of 3R and 4R isoforms of tau, whereas the P301S mice do produce one isoform only.

3. Conclusion

In summary, RA derivatives provide selective visualization of NFTs over Aβ plaques in brain sections of *post mortem* AD patient. Excellent affinity to fibrillar tau aggregates was observed in the *Thiazine red R* displacement assay and no or negligible cytotoxicity of these compounds in HepG2 cells or in zebrafish embryo development. Hyperphosporylated, non-fibrillar Tau aggregates as present in aggresomes or mouse retina are not stained by these dyes, this observation indicates selective binding to fibrillar tau. Further evaluation of these compounds is needed in mammals that produce a similar isoform mixture of tau aggregates as humans.

4. Experimental

4.1. General

All commercial chemicals, reagents, solvents were purchased from Sigma-Aldrich. All reactions were performed under argon atmosphere using dry solvents unless otherwise specified. ^{1}H-NMR spectra were recorded on a Bruker AC300, ARX300 and DRX 500 spectrometer at 300 MHz and 500 MHz respectively. The ^{13}C-NMR spectra were recorded on a Bruker AC300, ARX300 and DRX 500 spectrometer at 75 MHz and 125 MHz respectively. Chemical shifts values were reported as % values (ppm) downfield from Me_4Si. UV-Vis spectra were carried out by Shimadzu UV-2401PC. Fluorescence emission experiments were carried out by TECAN Infinite® M1000 PRO. Mass spectrometry was performed on a MAT 95 double focusing sector field MS. Flash column chromatography was carried out with Merck silica gel 60 (15-40 mm). Acid protons are not visible in ^{1}H-NMR for some compounds measured in DMSO-d_6.

4.2. General procedure for the synthesis of RA derivatives

4.2.1. (Z)-2-(4-Oxo-5-((5-phenylfuran-2-yl)methylene)-2-thioxothiazolidin-3-yl)acetic acid (1)

To a solution of 5-phenylfuran-2-carbaldehyde (1.0 mmol, 1 equiv.) and rhodanine-3-acetic acid (1.0 mmol, 1 equiv) in glacial acetic acid (5 ml) was added of sodium acetate (3.0 mmol, 3 equiv) and the reaction mixture was stirred for 7 hours at 100°C, forming a precipitate after cooled to room temperature. The resulted crude product was recovered by filtration and recrystallized from acetone/water mixture to give 272 mg of the titled compound as an orange solid; ^{1}H-NMR (500 MHz, DMSO-d6) δ = 13.42 (s, 1H), 7.91 – 7.85 (m, 2H), 7.77 (s, 1H), 7.61 – 7.55 (m, 2H), 7.49 – 7.44 (m, 1H), 7.42 (d, *J* = 3.8 Hz, 1H), 7.36 (d, *J* = 3.8 Hz, 1H), 4.75 (s, 2H); ^{13}C-NMR (125 MHz, DMSO-d6) δ = 194.24, 167.78, 166.48, 158.78, 149.61, 129.91, 129.85, 128.97, 124.96, 124.18, 119.62, 118.28, 110.84, 45.46;

MS (EI, 70 eV) m/z = 345 [M^+]; UV/Vis (Ethanol) λ_{max} = 445 nm.

4.2.2. 2-((Z)-5-((E)-3-(4-(dimethylamino)phenyl)allylidene)-4-oxo-2-thioxothiazolidin-3-yl)acetic acid (2)

Further purification of this compound was carried out using column chromatography. A red solid; ^{1}H-NMR (500 MHz, DMSO-d6): δ = 7.58 (dd, *J* = 7.2, 4.8 Hz, 3H), 7.35 (d, *J* = 14.8 Hz, 1H), 6.87 – 6.78 (m, 1H), 6.74 (d, *J* = 9.0 Hz, 2H), 4.69 (s, 2H), 3.02 (s, 6H); ^{13}C-NMR (125 MHz, DMSO-d6): δ = 192.84, 167.89, 166.03, 152.34, 148.57, 136.69, 130.91, 123.49, 118.62, 118.53, 112.35, 45.37. 39.65 (NMe_2 peak un resolved from DMSO); HRMS *m/z* [M^+] calcd for $C_{16}H_{16}N_2O_3S_2^+$: 348.0602, found 348.0603; UV/Vis (Ethanol) λ_{max} = 497 nm.

4.2.3. (Z)-2-(5-(2,2'-Bithiophen-5-ylmethylene)-4-oxo-2-thioxothiazolidin-3-yl)acetic acid (3)

A brick red solid; ^{1}H-NMR (500 MHz, DMSO-d_6) δ = 8.14 (s, 1H), 7.78 (dd, *J* = 4.0 , 0.5 Hz, 1H), 7.70 (dd, *J* = 5.0 , 1.0 Hz, 1H), 7.59 (dd, *J* = 3.7,1.0 Hz, 1H), 7.54 (d, *J* = 4.0 Hz, 1H), 7.18 (dd, *J* = 3.6, 1.4 Hz, 1H), 4.73 (s, 2H); ^{13}C-NMR (125 MHz, DMSO-d_6) δ = 192.18, 167.72, 166.41, 145.64, 138.39, 136.11, 135.66, 129.40, 128.52, 127.12, 126.91, 126.32, 118.98, 45.63; MS (EI, 70 eV) *m/z* = 367 [M^+]; UV/Vis (Ethanol) λ_{max} = 444 nm.

4.2.4. (Z)-2-(5-((5-(4-Methoxyphenyl)thiophen-2-yl)methylene)-4-oxo-2-thioxothiazolidin -3-yl)acetic acid (4)

A maroon solid; ^{1}H-NMR (500 MHz, DMSO-d_6) δ = 8.08 (s, 1H), 7.77 (d, *J* = 4.5 Hz, 1H), 7.75 (d, *J* = 8.7 Hz, 2H), 7.64 (d, *J* = 4.0 Hz, 1H), 7.03 (d, *J* = 8.7 Hz, 2H), 4.56 (s, 2H), 3.82 (s, 3H); ^{13}C-NMR (125 MHz, DMSO-d_6) δ = 192.33, 167.35, 166.70, 160.67, 152.66, 138.38, 135.88, 127.88, 126.74, 125.62, 125.11, 118.96, 115.26, 55.86, 46.98; MS (EI, 70 eV): *m/z* = 391 [M^+]; UV/Vis (Ethanol): λ_{max} = 451 nm.

4.2.5. (Z)-2-(4-Oxo-5-(4-(pyrrolidin-1-yl)benzylidene)-2-thioxothiazolidin-3-yl)acetic acid (5)

A maroon solid; ^{1}H-NMR (500 MHz, DMSO-d_6): δ = 7.69 (s, 1H), 7.49 (t, *J* = 5.8 Hz, 2H), 6.71 (t, *J* = 5.9 Hz, 2H), 4.54 (s, 2H), 3.36 (t, *J* = 6.6 Hz, 4H), 1.99 (t, 4H); ^{13}C-NMR (125 MHz, DMSO-d_6): δ = 192.94, 167.39, 167.13, 149.93, 135.24, 133.84, 120.04, 113.81, 112.97, 47.86, 46.82, 25.37; MS (EI, 70 eV): *m/z* = 348 [M^+]; UV/Vis (Ethanol): λ_{max} = 468 nm.

4.2.6. (Z)-2-(5-((10-Octyl-10H-phenothiazin-3-yl)methylene)-4-oxo-2-thioxothiazolidin-3-yl)acetic acid (6)

A maroon solid; ^{1}H-NMR (500 MHz, DMSO-d_6) δ = 7.77 (s, 1H), 7.48 (dd, *J* = 8.8, 2.2 Hz, 1H), 7.40 (d, *J* = 2.1 Hz, 1H), 7.25 – 7.20 (m, 1H), 7.18 – 7.14 (m, 2H), 7.09 – 7.05 (m, 1H), 7.00 (td, *J* = 7.5, 1.0 Hz, 1H), 4.73 (s, 2H), 3.93 (t, *J* = 7.0 Hz, 2H), 1.73 – 1.64 (m, 2H), 1.43 – 1.34 (m, 2H), 1.30 – 1.17 (m, 8H), 0.82 (t, *J* = 6.9 Hz, 3H); ^{13}C-NMR (125 MHz, DMSO-d_6) δ = 193.17, 167.75, 166.78, 147.71, 143.43, 133.58, 131.30, 129.95, 128.42, 127.71, 127.37, 124.38, 123.94, 122.68, 119.04, 116.86, 116.62, 47.30, 45.49, 31.53, 29.03, 28.89, 26.51, 26.39, 22.47, 14.39; MS (EI, 70 eV): *m/z* = 512.0 [M^+]; UV/Vis (Ethanol) λ_{max} = 466 nm.

4.2.7. (Z)-2-(5-((10-Methyl-10H-phenothiazin-3-yl)methylene)-4-oxo-2-thioxothiazolidin-3-yl)acetic acid (7)

A dark red solid; ^{1}H-NMR (500 MHz, DMSO-d_6) δ = 7.79 (s, 1H), 7.51 (dd, *J* = 2.20, 8.59 Hz, 1H), 7.43 (d, *J* = 2.17 Hz, 1H), 7.26 (td, *J* = 1.60, 7.70 Hz, 1H), 7.19 (dd, *J* = 1.56, 7.82 Hz, 1H), 7.11 (d, *J* = 8.62 Hz, 1H), 7.03 (dd, *J* = 5.68, 8.03 Hz, 2H), 4.73 (s, 2H), 3.39 (s, 3H); ^{13}C-NMR (125 MHz, DMSO-d_6): δ = 192.70, 167.25, 166.28, 147.68, 143.72, 133.13, 130.98, 129.11, 128.08, 126.99, 126.92, 123.45, 122.86, 120.99, 118.69, 115.32, 115.20, 45.02, 35.50; MS (EI, 70 eV) *m/z* = 414 [M^+]; UV/Vis (Ethanol) λ_{max} = 455 nm.

4.3. Methods

4.3.1. Immunohistochemical staining

Immunohistochemical staining was carried out on four micrometers thick sections of the AD patient tissues by a Ventana Benchmark automated stainer (Ventana, Tuscon, AZ). The antibodies are anti-PHF-Tau 75 clone AT8 mAb (Thermo Scientific Pierce Protein Research Products, Rockford, IL), TAU Ab-3 (Neomarkers, Freemont, CA), and amyloid A4 (BAM10, Sigma, St. Louis, MO) and the Ultraview Universal DAB Detection Kit (Ventana, Tuscon, AZ) were used in staining experiments.

4.3.2. Neuropathological staining of AD brain sections

Post mortem brain tissues from an AD patient (80-year old female) were obtained at autopsy. Four micrometer thick paraffin embedded serial sections of the hippocampus area were deparaffinized with xylene and ethanol. These sections were then hydrated in distilled water. Ethanol solution (500 µL) of probes **1** to **7** with concentration of 1 mM was poured on tissue slide and waited for 10 min. These sections were washed with methanol and differentiated in 1% acetic acid solution for 20 min and washed with water. These tissue sections were finally treated with Roti – Mount Fluor Care (from Sigma-Aldrich) and covered with coverslip. Fluorescence microscopic examination was performed using a Axioskop microscope with a HBO100 fluorescence illuminator (Carl Zeiss, Oberkochen, Germany) with band pass filter set 09 BP450-490, FT510, LP515, the filter set 02 G365, FT395, LP420 and the filter set 15 BP546, FT580, LP590.

4.3.3. *In vitro* cell proliferation assay

The cytotoxicity data were determined via CellTiter 96®AQueous non-radioactive cell proliferation assay (Promega, Madison, USA), which is based on the reduction of a tetrazolium salt [3-(4,5-dimethylthiazol-2-yl)-5-(3-carboxymethoxy phenyl)-2-(4sulfophenyl)-2H-tetrazolium, inner salt; MTS] into a formazan product by intrinsic dehydrogenases of living cells.

In short, human liver hepatocellular carcinoma cells HepG2, maintained in DMEM/F12 1+1 and supplemented with 10 % fetal bovine serum, were seeded in 96-well plates and incubated with 0.1 µM, 1 µM, 10 µM and 100 µM of probe **2**, **3**, **4**, **5** and **6** for 24 hours. After washing, CellTiter 96®AQueous non-radioactive cell proliferation assay reagent was added to the cells and the number of metabolically active cells was calculated by measuring the amount of formazan product via photometric analysis at λ = 492 nm. The absorbance of treated samples was normalized to untreated controls (percent of non-treated controls), which resulted in cell viability. Finally effective doses (EC_{50}) that induced a loss in cell viability of 50 % were calculated via the best-fitted trend line of cell viability as a function of dye concentration.

4.3.4. *Thiazine Red R* displacement assay

Recombinant human-microtubule associated 4R tau protein purified from Escherichia coli and Synthetic $A\beta_{40}$ was used in this assay. Tau protein was aggregated at 5 uM concentration with arachidonic acid (100 uM) in Tris 10 mM pH = 8, 24h at 37°C, whereas $A\beta_{40}$ was aggregated at a concentration of 50 µM with arachidonic acid (100 µM) in Tris 10 mM pH = 8, for three

days at 37°C. For the displacement assay, *Thiazine red R* was added at same concentration of the *Kd* to the respective aggregated binding sites (K_d for aggregated Tau = 18 nM, K_d for aggregated Aß = 49 nM). To determine the affinity of the required probe, the probe was added at different concentrations in the assay ranging from 0.1 nM to 10000 nM. Auto fluorescence of the probe was measured together with aggregated proteins. Negative controls were obtained from *Thiazine red R* and aggregated proteins. Assay was performed in Perkin Elmer OptiPlate 384, black, 45 ul assay volume, assay buffer was DPBS no $CaCl_2$ no $MgCl_2$ (GIBCO N. 14020). Tested compounds were diluted in DMSO and 2.25 µl was added to the assay (5% DMSO final). Assay experiment was initiated by the addition of the aggregated protein (competitive condition). Plates were shortly shacked (1 min with Sterico variomag teleshake) and incubated for 30 min at room temperature. Measurements were performed with En:Vision (Perkin Elmer), at excitation 531 nm/emission 595 nm. Corresponding IC_{50} were calculated by excel fit.

4.3.5. *In vivo* zebrafish embryo development assay

Zebra fish were bred in 2L spawning tank and maintained according to the methods described by Christiane Nuesslein-Volhard and Ralf Dahm. Briefly, zebrafish were raised on 14 h light 10 h dark cycle at 26.0 ± 0.5°C. The embryos were obtained via natural mating and cultured in the water. The embryos were collected and placed into 24-well plates, every ten embryos per well. When the embryos older than 6 hpf, more than 50% epiboly, they were treated with 1, 5, 10 µM of RA derivatives in E2 solution. The phenotypes were observed and images were captured using the Axio Scope A1 microscope system from Carl Zeiss at 24 and 72 hpf. All experiments in this study were carried out according to the ethical and welfare principles in legislation on animal research in Germany.

4.3.6. *In vivo* scanning of the mouse retina

Mixed genders of homozygous mice expressing human mutant P301S tau, those were backcrossed for at least 7 generations to obtain animals on a pure C57Bl/6 background were used in this study. The ophthalmological examinations of the mouse retinas were performed using a modified Spectralis HRA + OCT system (Heidelberg Engineering, Dossenheim, Germany) like described elsewhere.[17] In short, mice received 24 h before the imaging sessions i.p. injections of the fluorescent probes (28-31 mM in DMSO). Imaging was performed using two different lasers wavelengths for the excitation of the fluorophores (450 and 488 nm). Emission filters used in this study were LP 458 nm, BP 512/25, BP 550/49 nm and BP 617/73 nm. To exclude false positive signals from retinal autofluorescence, pre-examinations of the retinas before the application of the fluorophores were performed.

5. Acknowledgement

This work was supported by grants from the German Federal Ministry of Education and Research (Bundesministerium für Bildung und Forschung, Germany, 13N10636) and the Hans and Ilse Breuer-foundation.

6. References and Notes

1. Jakob-Roetne, R.; Jacobsen, H. *Angew. Chem. Int. Ed.* **2009,** *48*, 3030.
2. Alzheimer's Association, *J. Alz. Assoc.*, 2012; Vol. March 2012, 131.
3. Selkoe, D. *Physiol. Rev.* **2001,** *81*, 741.
4. Clark, C.; Pontecorvo, M.; Beach, T.; Bedell, B.; Coleman, R.; Doraiswamy, P.; Fleisher, A.; Reiman, E.; Sabbagh, M.; Sadowsky, C.; Schneider, J.; Arora, A.; Carpenter, A.; Flitter, M.; Joshi, A.; Krautkramer, M.; Lu, M.; Mintun, M.; Skovronsky, D.; Group, A.-A. S. *Lancet neurol.* **2012,** *11*, 669.
5. Klunk, W. E. *Neurobiol. Aging* **2011,** *32, Supplement 1*, S20.
6. Clark Cm, S. J. A. B. B. J.; et al. *J. Am. Med. Assoc.* **2011,** *305*, 275.
7. Camus, V.; Payoux, P.; Barré, L.; Desgranges, B.; Voisin, T.; Tauber, C.; La Joie, R.; Tafani, M.; Hommet, C.; Chételat, G.; Mondon, K.; de La Sayette, V.; Cottier, J.; Beaufils, E.; Ribeiro, M.; Gissot, V.; Vierron, E.; Vercouillie, J.; Vellas, B.; Eustache, F.; Guilloteau, D. *Eur. J. Nucl. Med. Mol. Imaging* **2012,** *39*, 621.
8. Okamura, N.; Suemoto, T.; Furumoto, S.; Suzuki, M.; Shimadzu, H.; Akatsu, H.; Yamamoto, T.; Fujiwara, H.; Nemoto, M.; Maruyama, M.; Arai, H.; Yanai, K.; Sawada, T.; Kudo, Y. *J. Neurosci.* **2005,** *25*, 10857.
9. Fodero-Tavoletti, M. T.; Okamura, N.; Furumoto, S.; Mulligan, R. S.; Connor, A. R.; McLean, C. A.; Cao, D.; Rigopoulos, A.; Cartwright, G. A.; O'Keefe, G.; Gong, S.; Adlard, P. A.; Barnham, K. J.; Rowe, C. C.; Masters, C. L.; Kudo, Y.; Cappai, R.; Yanai, K.; Villemagne, V. L. *Brain* **2011,** *134*, 1089.
10. Matsumura, K.; Ono, M.; Kimura, H.; Ueda, M.; Nakamoto, Y.; Togashi, K.; Okamoto, Y.; Ihara, M.; Takahashi, R.; Saji, H. *ACS Med. Chem. Lett.* **2011,** *3*, 58.
11. Takeuchi, J.; Shimada, H.; Ataka, S.; Kawabe, J.; Mori, H.; Mizuno, K.; Wada, Y.; Shiomi, S.; Watanabe, Y.; Miki, T. *Dement. Geriatr. Cogn. Disord.* **2012,** *34*, 112.
12. Arriagada, P. V.; Growdon, J. H.; Hedley-Whyte, E. T.; Hyman, B. T. *Neurology* **1992,** *42*, 631.
13. Rao, J.; Dragulescu-Andrasi, A.; Yao, H. *Curr. Opin. Biotechnol.* **2007,** *18*, 17.
14. Koronyo, Y.; Salumbides, B. C.; Black, K. L.; Koronyo-Hamaoui, M. *Neurodegener. Dis.* **2012,** *10*, 285.
15. Bolander, A.; Kieser, D.; Voss, C.; Bauer, S.; Schon, C.; Burgold, S.; Bittner, T.; Holzer, J.; Heyny-von Haussen, R.; Mall, G.; Goetschy, V.; Czech, C.; Knust, H.; Berger, R.; Herms, J.; Hilger, I.; Schmidt, B. *J. Med. Chem.* **2012,** *55*, 9170.
16. Ono, M.; Watanabe, H.; Kimura, H.; Saji, H. *ACS Chem. Neurosci.* **2012,** *3*, 319.
17. Schon, C.; Hoffmann, N. A.; Ochs, S. M.; Burgold, S.; Filser, S.; Steinbach, S.; Seeliger, M. W.; Arzberger, T.; Goedert, M.; Kretzschmar, H. A.; Schmidt, B.; Herms, J. *PloS one* **2012,** *7*, e53547.
18. Bulic, B.; Pickhardt, M.; Schmidt, B.; Mandelkow, E.-M.; Waldmann, H.; Mandelkow, E. *Angew. Chem. Int. Ed.* **2009,** *48*, 1740.
19. Bulic, B.; Pickhardt, M.; Khlistunova, I.; Biernat, J.; Mandelkow, E.-M.; Mandelkow, E.; Waldmann, H. *Angew. Chem. Int. Ed.* **2007,** *46*, 9215.
20. Messing, L.; Decker, J. M.; Joseph, M.; Mandelkow, E.; Mandelkow, E.-M. *Neurobiol. Aging* **2013,** *34*, 1343.
21. Ono, M.; Hayashi, S.; Matsumura, K.; Kimura, H.; Okamoto, Y.; Ihara, M.; Takahashi, R.; Mori, H.; Saji, H. *ACS Chem. Neurosci.* **2011,** *2*, 269.
22. La Pietra, V.; Marinelli, L.; Cosconati, S.; Di Leva, F. S.; Nuti, E.; Santamaria, S.; Pugliesi, I.; Morelli, M.; Casalini, F.; Rossello, A.; La Motta, C.; Taliani, S.; Visse, R.; Nagase, H.; da Settimo, F.; Novellino, E. *Eur. J. Med. Chem.*, **2012,** *47*, 143.
23. Augelli-Szafran, C., Elizabeth; Glase, S., Ann; Walker, L., Craswell; Yasunaga, T. Patent WO2000/76987, 2000.
24. Chen, Y.; Li, C.; Zeng, Z.; Wang, W.; Wang, X.; Zhang, B. *Chem. Lett.*, **2005,** *34*, 762.
25. Johnson, S. L.; Jung, D.; Forino, M.; Chen, Y.; Satterthwait, A.; Rozanov, D. V.; Strongin, A. Y.; Pellecchia, M. *J Med. Chem.*, **2006,** *49*, 27.
26. Ohishi, Y.; Mukai, T.; Nagahara, M.; Yajima, M.; Kajikawa, N.; Miyahara, K.; Takano, T. *Chem. Pharm. Bull.* **1990,** *38*, 1911.

27. Narlawar, R.; Pickhardt, M.; Leuchtenberger, S.; Baumann, K.; Krause, S.; Dyrks, T.; Weggen, S.; Mandelkow, E.; Schmidt, B. *ChemMedChem*, **2008**, *3*, 165.
28. Gu, J.; Anumala, U. R.; Lo Monte, F.; Kramer, T.; Heyny von Haussen, R.; Holzer, J.; Goetschy-Meyer, V.; Mall, G.; Hilger, I.; Czech, C.; Schmidt, B. *Bioorg. Med. Chem. Lett.*, **2012**, *22*, 7667.
29. Gu, J.; Anumala, U. R.; Heyny-von Haussen, R.; Holzer, J.; Goetschy-Meyer, V.; Mall, G.; Hilger, I.; Czech, C.; Schmidt, B. *ChemMedChem*, **2013**, *8, 891-897*.
30. Uchihara, T.; Nakamura, A.; Yamazaki, M.; Mori, O. *Acta Neuropathol.* **2000**, *100*, 385.
31. Xia, C. F.; Arteaga, J.; Chen, G.; Gangadharmath, U.; Gomez, L. F.; Kasi, D.; Lam, C.; Liang, Q.; Liu, C.; Mocharla, V. P.; Mu, F.; Sinha, A.; Su, H.; Szardenings, A. K.; Walsh, J. C.; Wang, E.; Yu, C.; Zhang, W.; Zhao, T.; Kolb, H. C. *Alzheimers Dement.* **2013**.
32. Wager, T.; Chandrasekaran, R.; Hou, X.; Troutman, M.; Verhoest, P.; Villalobos, A.; Will, Y. *ACS Chem. Neurosci.* **2010**, *1*, 420.
33. Gasparini, L.; Crowther, R.; Martin, K.; Berg, N.; Coleman, M.; Goedert, M.; Spillantini, M. *Neurobiol. Aging* **2011**, *32*, 419.

Supporting Information

Contents:

Probe 1

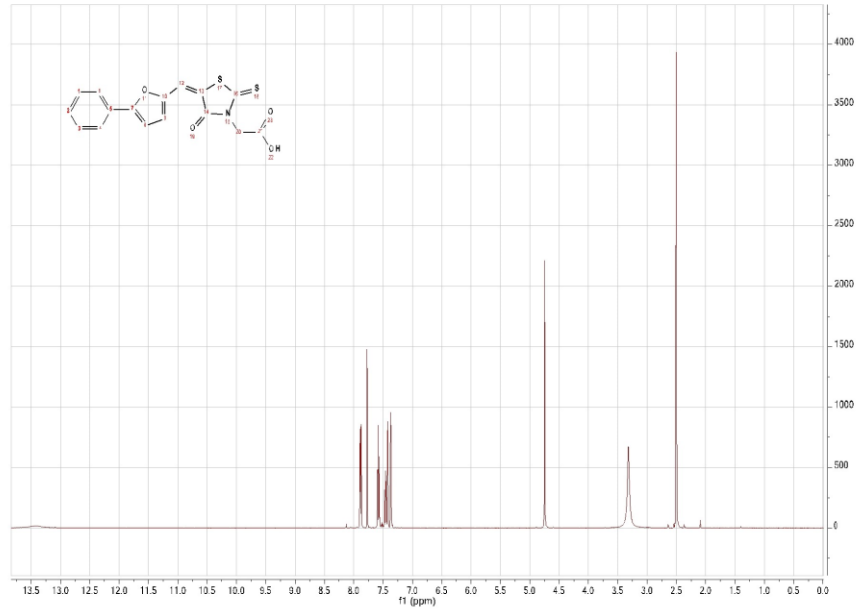

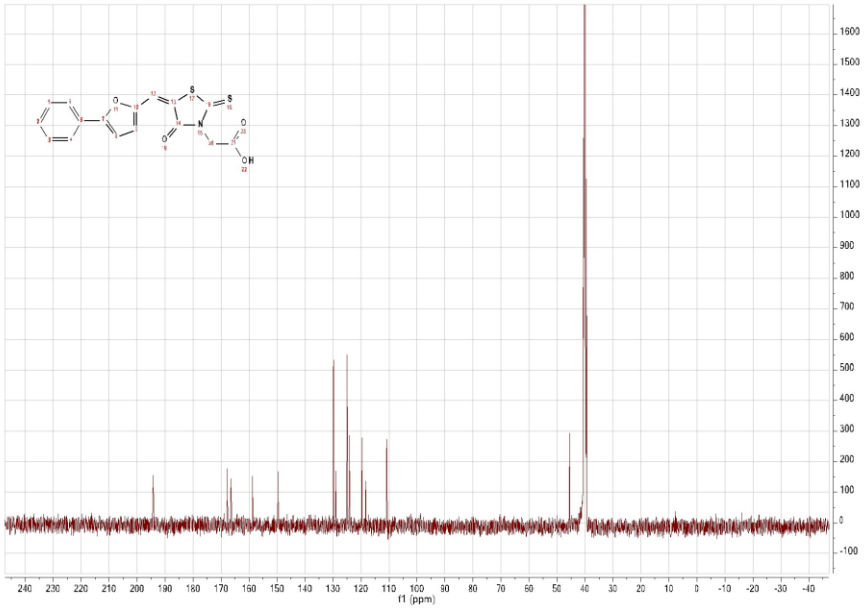

2

Probe 2

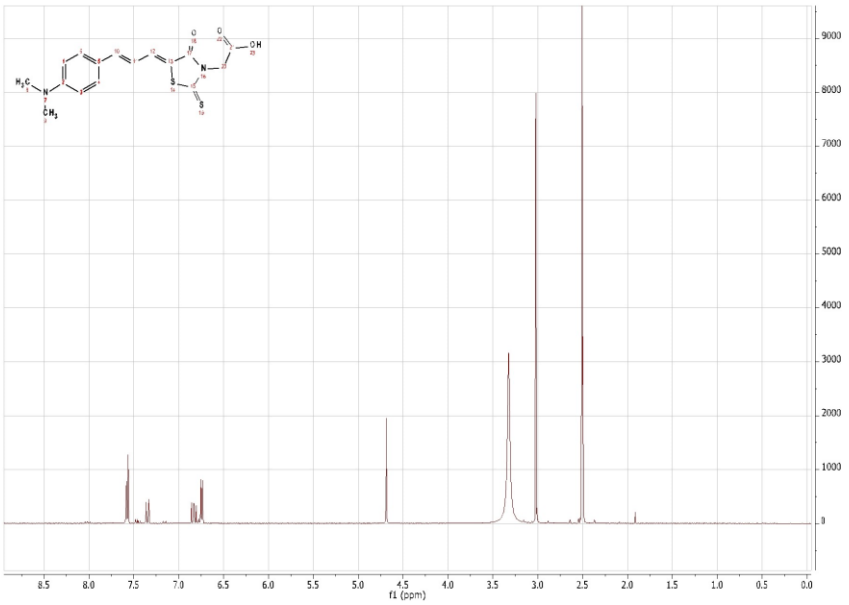

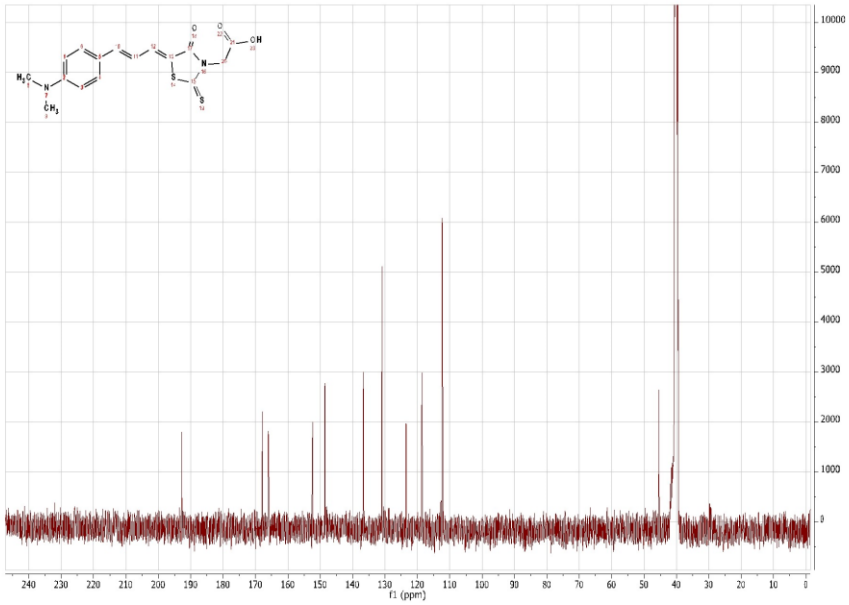

3

Probe 3

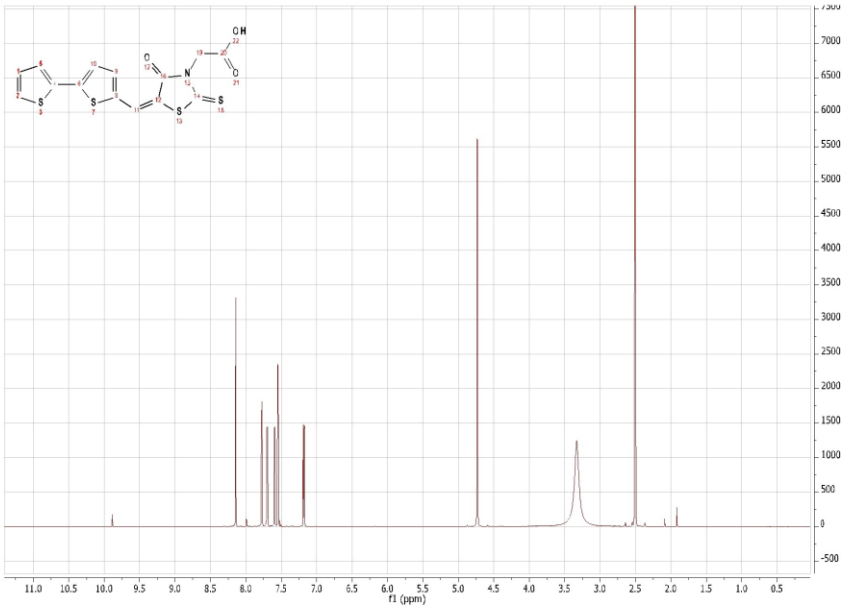

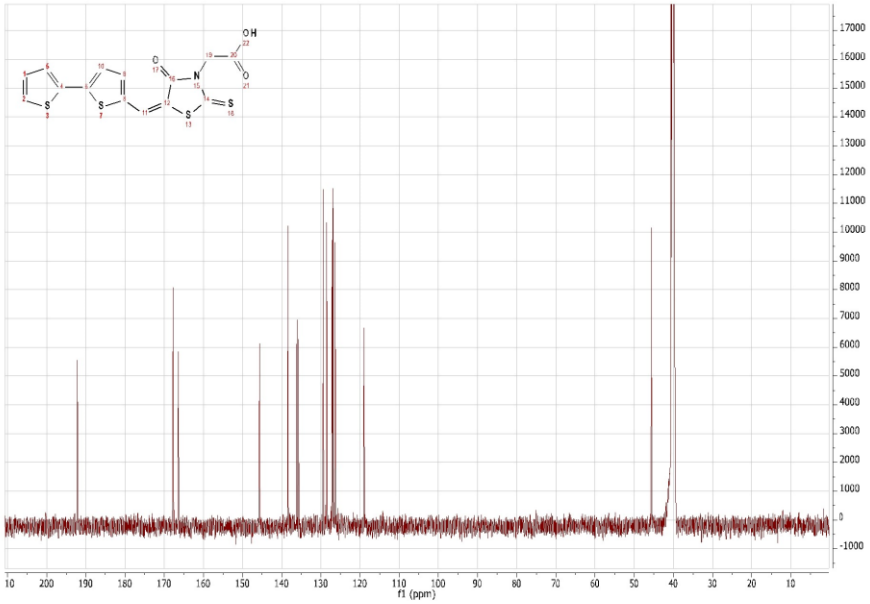

4

Probe 4

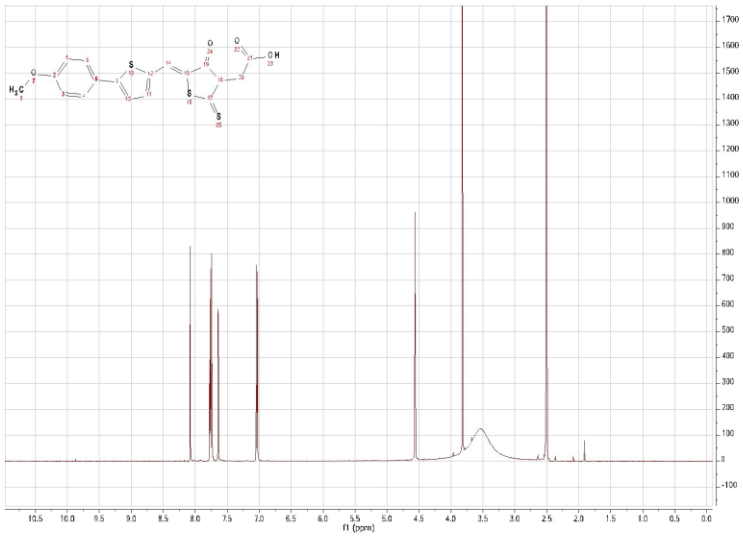

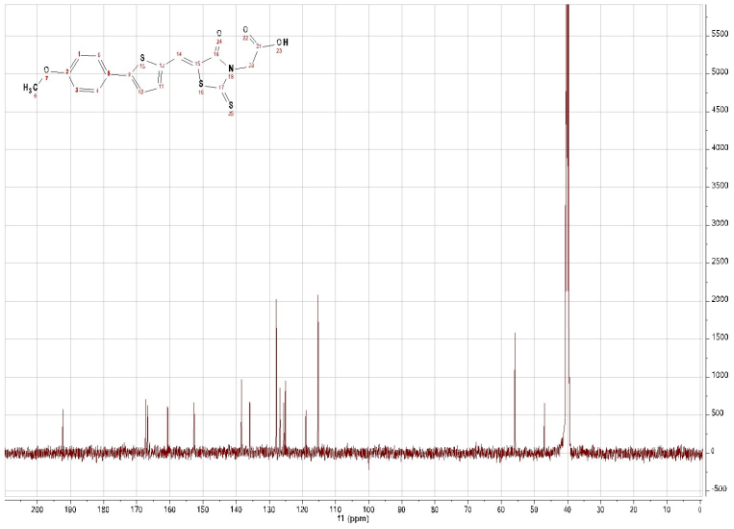

5

Probe 5

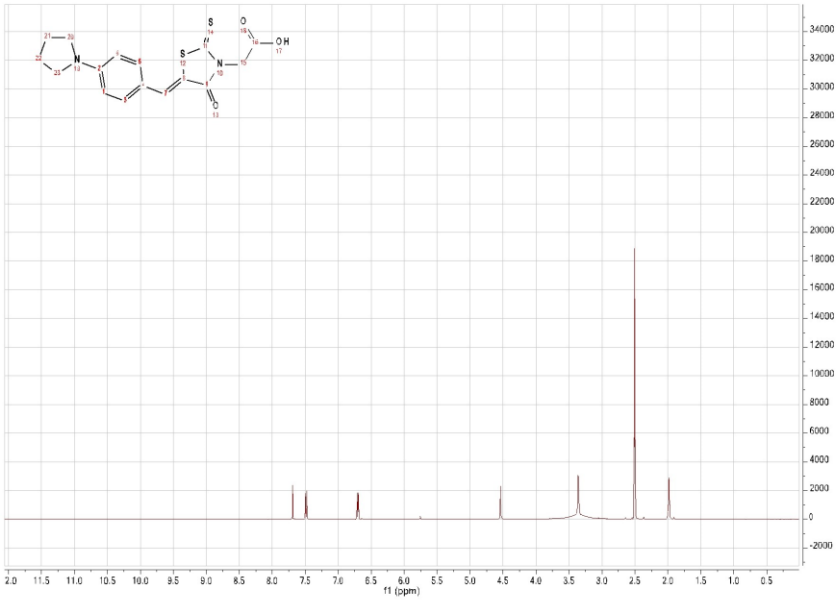

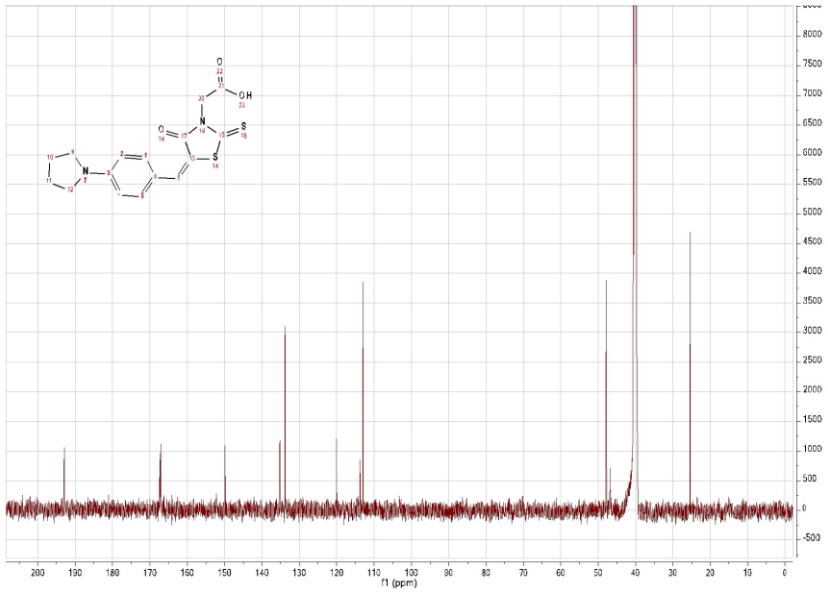

6

Probe 6

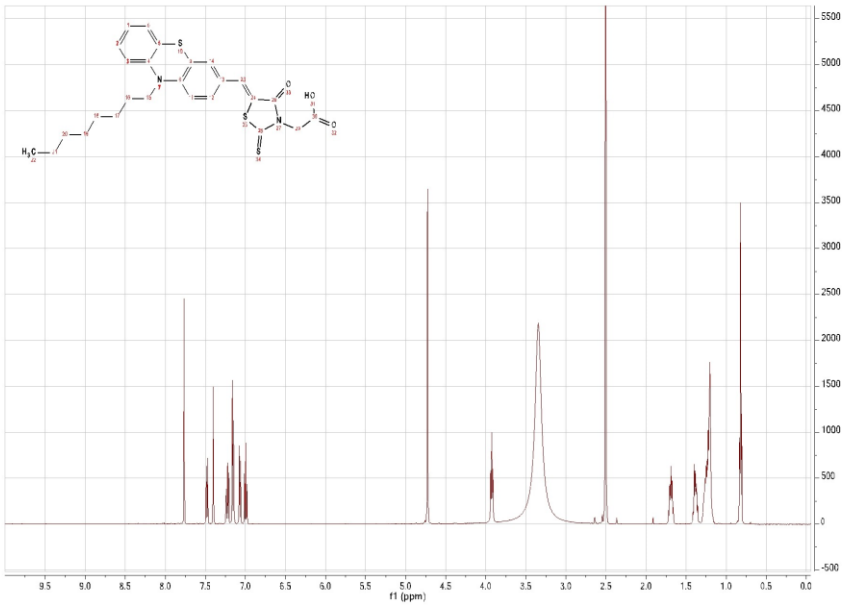

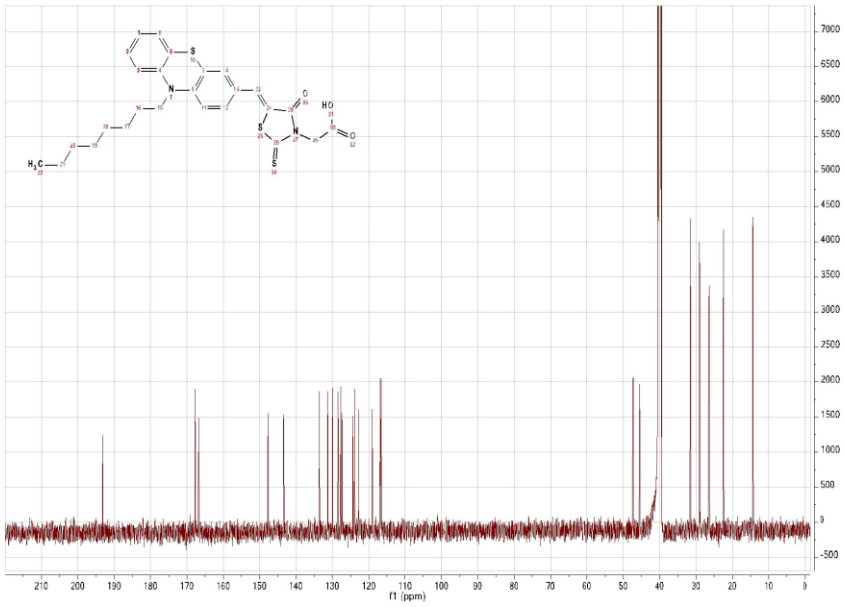

7

Probe 7

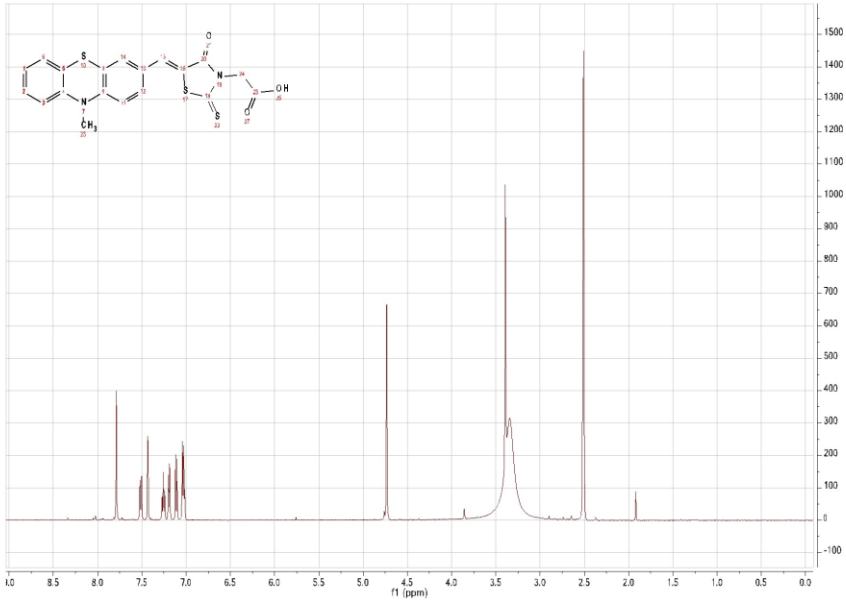

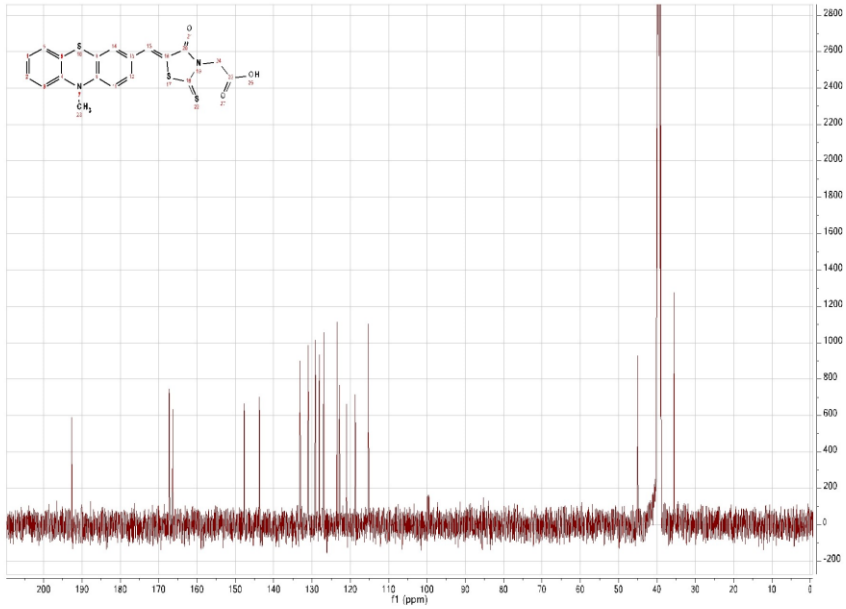

8

Immunohistochemical staining of AD brain sections

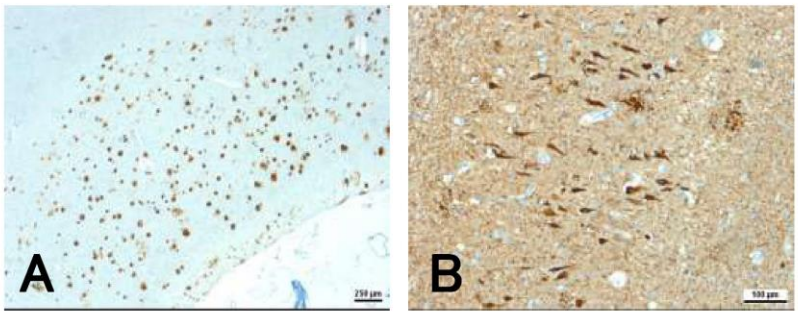

Figure 1 Immunohistochemical staining of hippocampal sections: Aβ plaques with antibody amyloid A4 (A) and NFTs with antibody AT8 mAb (B)

Cell Toxicity of Dyes (2-6) on HepG2 cells[1]

- HepG2: human liver carcinoma
- Incubation time: 24 hours
- MTS-Assay after incubation times
- explanation: MW ... mean (cell vitality, n=6); STABW ... standard deviation

Probe 2:

24 h

	0.1 µM	1 µM	10 µM	100 µM
MW	88,13	66,92	75,00	87.92
STABW	5,98	10,65	7,73	5,91

Probe 3:

24 h

	0.1 µM	1 µM	10 µM	100 µM
MW	81,09	83,71	81,03	84,10
STABW	4,40	5,91	7,41	7,49

Probe 4:

24 h

	0.1 µM	1 µM	10 µM	100 µM
MW	100,16	88,58	87,33	85,76
STABW	3,27	4,38	6,84	5,15

Probe 5:

24 h

	0.1 µM	1 µM	10 µM	100 µM
MW	92,14	94,05	98,30	99,53
STABW	2,24	3,06	3,63	4,15

Probe 6:

24 h

	0.1 µM	1 µM	10 µM	100 µM
MW	94,37	102,45	91,89	0.00
STABW	2,84	3,29	3,36	1,21

***Thiazine red R* assay data for known probes[1, 2]**

Probe	**Aggr. tau - IC_{50} (nM)**	**Aggr. Aß$_{40}$ - IC_{50} (nM)**

10

Evans Blue	1.0	89
Congo Red	5.4	14
BSB	18	78
MeXO4	246	140
Crystal Violet	1545	1280
FDDNP	1635	1467
IMPY	2707	5671
PIB	3255	5190
AZD2184	9802	>10000
FENE	>10000	>10000
BF-158	>10000	>10000

Retina imaging of P301S mice

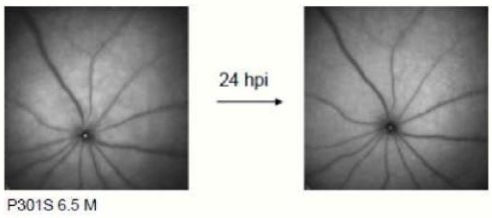

Figure 2: In vivo imaging in retina of P301S mice of 6.5 months of age. No signal was observed after 24 hours of post injection.

Probe concentrations for in vivo study in P301S mice.

Probe	MW (g/mol)	Injected amount	Concentration
1	345.39	40 µl (28 mM in DMSO)	13.3 mg/kg
2	348.44	40 µl (28 mM in DMSO)	14.2 mg/kg
3	367.49	40 µl (27 mM in DMSO)	13.8 mg/kg
4	391.48	40 µl (31 mM in DMSO)	13.8 mg/kg
FSB	420	300 µl (2.4 mM in 10%DMSO, 90% PBS/MA)	10 mg/kg

1. Gu, J.; Anumala, U. R.; Lo Monte, F.; Kramer, T.; Heyny von Haussen, R.; Holzer, J.; Goetschy-Meyer, V.; Mall, G.; Hilger, I.; Czech, C.; Schmidt, B. *Bioorg. Med. Chem. Lett.* 2012, *22*, 7667.
2. Bolander, A.; Kieser, D.; Voss, C.; Bauer, S.; Schon, C.; Burgold, S.; Bittner, T.; Holzer, J.; Heyny-von Haussen, R.; Mall, G.; Goetschy, V.; Czech, C.; Knust, H.; Berger, R.; Herms, J.; Hilger, I.; Schmidt, B. *J. Med. Chem.* 2012, *55*, 9170.

3.1.3 2-Styrylindolium based fluorescent probes visualize neurofibrillary tangles in Alzheimer's disease

The content of this chapter has been published

Jiamin Gu, Upendra Rao Anumala, Fabio Lo Monte, Thomas Kramer, Roland Heyny-von Haußen, Jana Hölzer, Valerie Goetschy-Meyer, Gerhard Mall, Ingrid Hilger, Christian Czech, and Boris Schmidt.

2-Styrylindolium based fluorescent probes visualize neurofibrillary tangles in Alzheimer's disease, *Bioorganic & Medicinal Chemistry Letters* **2012**, 22, 7667-7671.

Summary

Imaging senile plaques (SPs) and neurofibrillary tangles (NFTs) is crucial in Alzheimer's disease (AD) diagnosis. In this chapter, synthesis and evaluation of 2-styryl indolium derivatives was performed. A group of six fluorescent 2-styrylindolium derivatives was synthesized. Condensation of a variety of aldehydes with 2, 3, 3-trimethylindolenine resulted in probes with different absorption and emission properties. Histological examination of postmortem AD brain sections with these probes visualized NFTs in the presence of SPs. *In vitro* evaluation of selected probes in *Thiazine red R* assay confirmed the almost equal affinity to tau aggregates and amyloid aggregates. The cytotoxicity of these probes on hepatocellular carcinoma cell lines (HepG2) and zebrafish embryos was examined. All probes displayed no or negligible cytotoxicity. These results indicate that 2-styryl indolium derivatives selectively visualize NFTs in AD brain sections obtained at autopsy.

Contribution of Upendra Rao Anumala: Purification of probes 9, 10, support in histological examination on postmortem AD brain sections, cytotoxicity evaluation in zebrafish embryo assay, and manuscript preparation.

Bioorganic & Medicinal Chemistry Letters 22 (2012) 7667–7671

Contents lists available at SciVerse ScienceDirect

Bioorganic & Medicinal Chemistry Letters

journal homepage: www.elsevier.com/locate/bmcl

2-Styrylindolium based fluorescent probes visualize neurofibrillary tangles in Alzheimer's disease

Jiamin Gu [a], Upendra Rao Anumala [a], Fabio Lo Monte [a], Thomas Kramer [a], Roland Heyny von Haußen [b], Jana Hölzer [c], Valérie Goetschy-Meyer [d], Gerhard Mall [b], Ingrid Hilger [c], Christian Czech [d], Boris Schmidt [a,*]

[a] Clemens Schöpf Institute of Chemistry and Biochemistry, Technische Universität Darmstadt, Petersenstrasse 22, Darmstadt 64287, Germany
[b] Institute of Pathology, Klinikum Darmstadt, Grafenstrasse 9, Darmstadt 64283, Germany
[c] Institute of Diagnostic and Interventional Radiology I, Jena University Hospital—Friedrich Schiller Universität Jena, Erlanger Allee 10, Jena 07747, Germany
[d] F. Hoffmann-La Roche AG, Grenzacherstrasse 124, Gebäude 93/3.44, Basel 4070, Switzerland

ARTICLE INFO

Article history:
Received 21 June 2012
Revised 27 September 2012
Accepted 29 September 2012
Available online 6 October 2012

Keywords:
Alzheimer's disease
Neurofibrillary tangles
Zebrafish
Cytotoxicity
Imaging

ABSTRACT

We evaluated 2-styrylindolium derivatives (**6**–**11**) as novel and selective probes for neurofibrillary tangles (NFTs) on brain sections of AD patients. The staining experiments indicated that these compounds may bind selectively to NFTs in the presence of ß-amyloid (Aß) plaques. Cell free binding assays confirmed that 2-[2-[4-(1-pyrrolidinyl)phenyl]ethenyl]-1,3,3-trimethyl-3*H*-indolium iodide (**9**) and 2-[2-[4-(diethylamino)phenyl]ethenyl]-1-butyl-3,3-dimethyl-3*H*-indolium iodide (**11**) display excellent affinities to Tau-aggregates (IC_{50} values of 5.1 and 1.4 nM, respectively) in the displacement of Thiazin Red R. These probes have good solubility in distilled water and low or no cytotoxicity in zebrafish embryo and liver hepatocellular carcinoma cell assays.

Alzheimer's disease (AD) is the most common form of dementia, which is a progressive neurodegenerative disorder associated with memory loss, spatial disorientation, and gradual deterioration of intellectual capacity.[1–3] Age is the major risk factor for disease progression, and most individuals with the disease are age 65 or older. After age 65, the possibility of developing dementia roughly doubles every five years. It was estimated that 36 million people live with Alzheimer's disease and other dementias worldwide in 2011. This number is expected to rise to 66 million by 2030 and 115 million by 2050.[4]

The presence of two abnormal proteins in patients' brains: senile plaques (SPs) and neurofibrillary tangles (NFTs) are the characteristic hallmarks of AD.[5,6] SPs are composed of ß-amyloid peptide (Aß), a fragment of the amyloid peptide precursor protein (APP), whereas the intracellular NFTs are comprised of hyperphosphorylated aggregates of the twisted strands of Tau protein.[7–9] Diagnostic probes which specifically bind to Aß plaques and NFTs are considered to be a significant advance not only to diagnosis but as an enabling tool for drug development. Several probes have been developed in order to detect Aß plaques pathology in the brains of patients with AD by either single-photon emission computed tomography (SPECT) or positron emission tomography (PET),[10–15] whereas few probes for NFTs have been reported yet.[16–19,41] Non-invasive in vivo imaging of Aß plaques in the brain is well established, yet limited by the late onset of detectable amyloid deposition and a plateau phase in plaque load in late stage AD. The presence of ß-amyloid in the human retina was demonstrated by several groups and monitored in the mouse retina by fluorescence microscopy after high dosage of curcumin.[20,21] Systemic application of curcumin to humans at the necessary concentration is likely to cause adverse events as curcumin is photo labile and toxic to most human cell lines >50 μmol/L. Recent reports suggest Tau pathology to be a more reliable biomarker for AD.[8,22] These results showed that the number of NFTs in the brain correlates better with the progress of dementia in AD patients and does not reach a plateau as reported for amyloid pathology. Thus, in vivo imaging of NFTs or Aß plaques in the human retina may provide an efficient diagnosis of AD in the early, presymptomatic stages. Current data suggest [^{18}F]FDDNP,[16] Methoxy-X04,[17] [^{11}C]PIB,[18] benzimidazole and quinoline derivatives[19] as candidates for in vivo imaging of Tau pathology. However, these probes display equipotent affinity for both Aß plaques and NFTs. Moreover, these probes do not display the appropriate fluorescence to be applied to human tissue or they display undesirable pharmacokinetic properties, for example the very low clearance of Methoxy-XO4 in rodents. This lack of suitable NFTs-specific fluorescent probes imposes a limit on the in vivo quantification of neurofibrillary pathology. Therefore, the

* Corresponding author.
E-mail address: schmidt_boris@t-online.de (B. Schmidt).

0960-894X/$ - see front matter © 2012 Elsevier Ltd. All rights reserved.
http://dx.doi.org/10.1016/j.bmcl.2012.09.109

challenge remains to develop fluorescent probes with improved affinity and selectivity to NFTs. In this study, we present a series of highly water-soluble 2-styrylindolium probes with excellent affinities to NFTs and moderate toxicity. The probes may be applied to the imaging of retinal NFTs in AD animal models.(see Fig. 1)

In order to eliminate potentially unsafe compounds in the early development process and to prioritize compounds for further studies, we profiled the fluorescent probes in the in vitro liver hepatocellular carcinoma cell assay (HepG2) and in the zebrafish embryo development assay, which has become a major model in neurobiology and toxicology.[23,24] The incubation with liver cells provides information on the detoxification of the fluorophores in vivo in human tissue. The transparent body of the zebrafish embryo constitutes an important advantage of this model as it enables to observe and analyze several parameters by microscopy. The morphological and molecular basis tissues are identical or similar to other vertebrates including human beings. However, this model does not include pathological Tau-aggregates.[25–27]

The lead structure was selected from a set of established highly fluorescent dyes and evaluated for the silk dying properties versus wool reserve, which indicates ß-sheet binding of the dye. The cyanines were advanced due to their structural analogy to known Tau ligands and evaluated against 5 other lead structures, such as bis-stilbenes[41] and squaric acid derivatives. The bis-stilbenes displayed limited solubility and the squaric acid derivatives did not display sufficient binding affinity.[28] The synthesis of the 2-styrylindolium derivatives employed known methods or slight modifications [29–33] thereof, which are depicted in Scheme 1. The phenylhydrazine hydrochloride and 3-methyl-2-butanone were condensed to form the intermediate hydrazone and converted by Fischer indole synthesis to obtain the 2,3,3-trimethylindolenine **3**. Methylation of the indolenine in acetonitrile under reflux formed the indolium **4** in quantitative yield. The indolenine and 1-iodobutane were refluxed in ethylmethylketone to obtain the indolium **5**. The key transformation to the target 2-styrylindolium derivatives (**6**–**11**) compounds was achieved by the Knoevenagel condensation of the *N*-alkylated indolium backbone with the corresponding aldehyde in ethanol under reflux. The products were isolated in good yields ranging from 77 to 96% (Table 1) by standard chromatographic purification on silica gel. The ^{1}H NMR spectrum revealed that the two doublets at 8.40–8.26 and 7.54–7.19 ppm correspond to trans configured olefinic protons with a large coupling constant (15.5–16.5 Hz).

To ensure that the tissues contain both tau and Aß aggregates, we conducted a immunohistochemical staining of the tissues. Figure 2 shows that the tissues contain a rich amount of both tau and Aß aggregates. The qualitative selective binding of the fluorescent probes to NFTs was evaluated in the primary screen on hippocampal sections of human AD brain tissue and analyzed by fluorescence microscopy. This low throughput screen secured binding of the probes to Tau-aggregates in human AD pathology, as different Tau isoforms may result in different binding site on in vitro aggregates or Tau transgenic mouse models.[34] The 2-styryl-indolium probes stain NFTs in human tissue (Fig. 3) and provide a good contrast versus Aß plaques and background, especially probes **9** and **11**. These probes displayed excellent staining of NFTs (Fig. 3, D and F) in comparison to Aß plaques (Fig. 3, G and H). The results suggested a good affinity to the NFTs, which required quantification in a ligand binding assay to both aggregated amyloid and Tau. Remarkably, the probes **6**–**11** stained NFTs in human tissue strongly as observed by fluorescent microscopy, whereas plaques in the same brain preparations were stained just weakly. This observation stands in contrast to the activity in the *Thiazine Red R* displacement assay, where compound **11** displayed almost equipotent affinity to Aß$_{40}$-aggregates and Tau-aggregates (4R). The lack of potent plaque staining in the human tissue preparations may be due to interference with the fluorescence properties upon plaque binding, e.g. a fluorescence reduction or changes in the Stokes shift, which limit the detection by the DAPI- or FITC-filter employed in fluorescence microscopy. However, these results indicated that 2-styrylindolium probes **6**–**11** may be useful for the post mortem detection of NFTs in the brain of AD patients.

Probes with appropriate lipophilicity and low molecular weight may display sufficient permeability to cross the blood–brain barrier (BBB) and rapid clearance from the body when used as an *in vivo* probes.[12,35] The calculated log*P* values of all these compounds were found to be in the range of 0.81 and 3.58. Besides, the molecular weight of that 2-styrylindolium iodide salts are below 505 Daltons (Table 1).[36] These properties are in the range of accepted lipophilicity criteria for BBB permeation after intravenous injection. The solubilities of the *N*-methylated probes **6**–**10** are higher than 0.5 g/L in distilled water. The *N*-butylated probe **11** displays a solubility of >0.1 g/L at 25 °C. The solubility of established imaging agents: FDDNP, Methoxy-X04 and BF-158, is in the same range or inferior to the solubility of these 2-styrylindolium derivatives.

The affinity of the probes to aggregated tau protein was determined by displaced of the reference dye Thiazine Red R, hence IC$_{50}$ data obtained in the competition assay are reported rather than Ki values. *Thiazine Red R* was selected as reference ligand for the displacement assay, because it was previously shown to be superior to thioflavin S or immune histochemical detection of aggregated Tau and Aß$_{40}$.[37,41] It was shown to be an accurate maker for ß-pleated sheet structures and to reliably stain Aß plaques and diffuse NFTs (K_d for aggregated Aß$_{40}$ = 49 nM and K_d for aggregated tau = 18 nM). It was reported that the in vitro binding

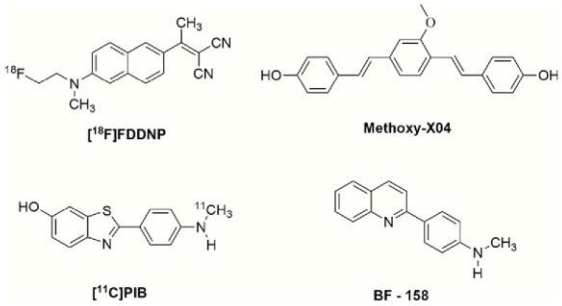

Figure 1. Chemical structures of [^{18}F]FDDNP, Methoxy-X04, [^{11}C]PIB and BF-170.

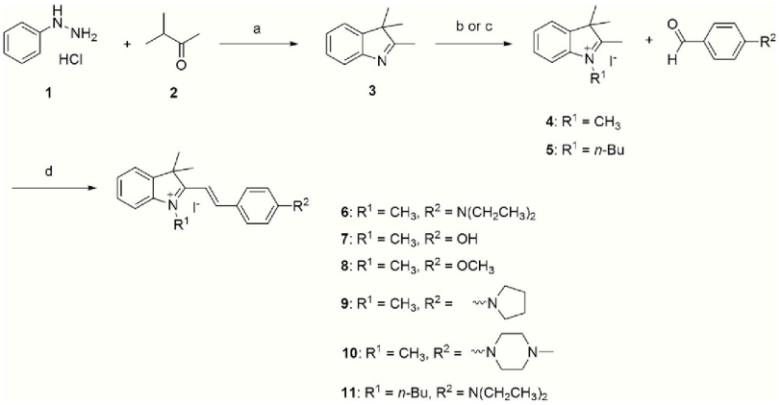

Scheme 1. Synthesis of 2-styrylindolium derivatives (**6**–**11**). Reagents and conditions: (a) 1.0 equiv **1**, 1.25 equiv **2**, CH_3COOH, 120 °C, 16 h; (b) 1.0 equiv **3**, 2.0 equiv methyl iodide, CH_3CN, reflux, 12 h; (c) 1.0 equiv **3**, 1.5 equiv 1-iodobutane, 2-butanone, reflux, 12 h; (d) 1.0 equiv **4** or **5**, 1.1 equiv corresponding aldehyde, EtOH, reflux, 12 h.

Table 1
Yields, properties and toxicity (EC_{50}) of probes **6**–**11**

Compound	Yield[a]	MW[b]	*c*Log*P*[c]	EC_{50} μM[d]
6	92%	460.39	2.14	8.57
7	83%	405.27	0.81	ND
8	77%	419.30	1.34	10.93
9	96%	458.38	1.79	8.31
10	91%	487.42	1.28	ND
11	96%	502.47	3.58	0.93

ND, not determined.
[a] Isolated yields.
[b] Determined by CS ChemOffice 10.0.
[c] Log*P* values were calculated using the Molinspiration Cheminformatics software (V2011. 04).
[d] EC_{50} declares the dye concentration in which 50% of the cells died after incubation with the probe.

affinity (K_i) of Methoxy-X04 is 26.8 nM.[17] The same compound was measured in *Thiazine Red R* assay and IC_{50} values are shown in Table. 2. Unfortunately, the affinity of most probes to Tau-aggregates could not be quantified due to spectral overlap with the reference ligand *Thiazine Red R*. Moreover it interfered with the acquisition of dose dependent fluorescence increase of the bound probe, which was employed to exclude potent protein disaggregating dyes. The affinity of the probes **9** and **11** to Tau-aggregates was determined indirectly (IC_{50} values of 5.1 and 1.4 nM) in the displacement assay for Tau affinity versus the reference ligand *Thiazine Red R* using aggregated recombinant human microtubule associated tau protein purified from *Escherichia coli* and aggregated synthetic Aß$_{40}$ as reported previously.[41] *Thiazine Red R* was added at the concentration corresponding to the K_d of the respective aggregated protein binding site to induce a fluorescent signal that can be inhibited by the addition of a displacer compound. (K_d for aggregated tau = 18 nM, and K_d for aggregated Aβ = 49 nM.) To determine the affinity of a displacer compound to the thiazine red binding sites of the aggregated proteins, the compound was added at different concentrations to the assay mixture ranging from 0.1 to 10 000 nM. Compounds were also measured together with the aggregated proteins, but in the absence of *Thiazine Red R*. Net fluorescence was calculated by subtracting the fluorescence of the wells without *Thiazine Red R* from the fluorescence of wells containing *Thiazine Red R*.

Remarkably, the pyrrolidyl substituent results in higher affinity than the *N*,*N*-diethyl derivative. This may be due to the locked conformation of the *N*-alkyl chain. The displacement ability of these 2-styrylindolium derivatives was compared against the known probes: Methoxy-X04, FDDNP, PIB and BF-158 under the same assay conditions (Table. 2). Significantly, the 2-styrylindolium derivatives **9** and **11** displayed ~50–7000 fold higher affinity to Tau-aggregates. It indicates sufficient affinity of the probes for imaging of Tau-aggregates in vivo. Furthermore, the series may be radiolabeled with $^{11}CH_3$, ^{18}F and ^{123}I at either the O or N position and evaluated as positron emission tomography (PET) and single photon emission tomography (SPECT) radioligands for NFT-imaging in vivo.

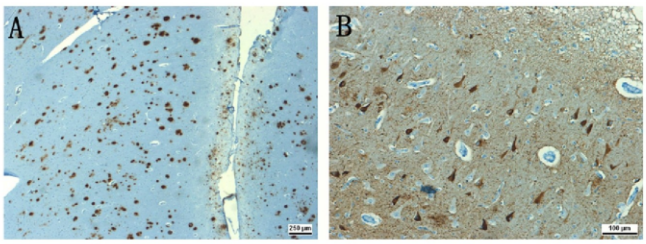

Figure 2. Immunohistochemical staining of hippocampal sections: τ antibody AT8 (B) Aβ-plaques with antibody amyloid A4 (A). See Fig. 3.

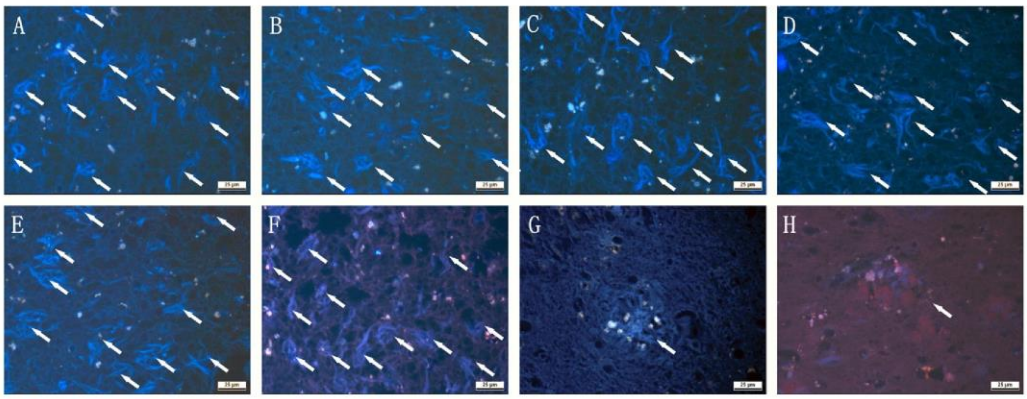

Figure 3. Neuropathological staining of brain sections from the hippocampus of an AD patient (A–H). Probes **6** (A), **7** (B), **8** (C), **9** (D), **10** (E) and **11** (F) are clearly stained neurofibrillary tangles. In contrast, the probes **9** (G) and **11** (H) faintly stained with Aß plaques. (tissues: hippocampus; patient: male, 71 years old, CERAD-score: 3; NFTs-level: V).

Table 2
Competitive *Thiazine Red R* displacement from tau-/Aβ40-aggregates for probes **9**, **11**, Methoxy-X04, FDDNP, PIB and BF158

Compound	Aggr.Tau-IC_{50}/nM	Aggr. $Aß_{40}$-IC_{50}/nM
9	5.10	ND
11	1.41	1.37
Methoxy-X04	246	140
FDDNP	1635	1467
PIB	3255	5190
BF-158	>10000	>10000

ND, not determined due to spectral overlap with the reference compound in the displacement assay.

Four of the 2-styrylindolium compounds (**6**, **8**, **9** and **11**) have been further evaluated at different concentrations in the zebrafish embryo development assay. The embryos developed well and no lesions were found at the different concentrations up to 10 μM at 24 hours post-fertilization (hpf). After 72 hpf, only the juvenile fish incubated with compound **11** showed small lesions in the yolk sac (Fig. 4, J). The HepG2 cell proliferation assay of these four compounds was used to evaluate the cytotoxicity in human cells. The effective doses (EC_{50}) were calculated via the best-fitted trendline of cell vitality as a function of dye concentration. Compounds **6**, **8**, **9** and **11** showed EC_{50} values of 8.57, 10.93, 8.31 and 0.93 μM, respectively, after 24 h incubation (Table. 1). Compound **11** displayed higher cytotoxicity in both assays than other compounds in this series. Both cytotoxicity studies suggested that 2-styrylindolium probes have no or negligible cytotoxicity against zebrafish embryos and HepG2 at the concentration employed for the histology experiments on human AD brain tissue (1 μM).

Taken together these results suggest that 2-styrylindolium compounds should be advanced to in vivo mice experiments in transgenic mice. However, the 4R Tau transgenic mice available to the project are all based on the 4R Tau repeat and deposit very little amounts of Tau. Moreover, these 4R Tau mouse models seem to be void of the Tau-aggregate binding site present in humans.[38,39] The presence of at least two different binding sites on Tau-aggregates was demonstrated for the Tau probe THK523 recently.[40]

In conclusion, we have developed a series of water soluble 2-styrylindolium probes for fluorescent imaging of NFTs in human Alzheimer's disease brain. The results of the in vitro fluorescent staining protocol using brain sections of AD patient indicated potent NFT imaging and low nonspecific binding. The cytotoxicity experiments with zebrafish embryos and HepG2 cells suggest that these probes may be suitable for further in vivo applications. This indicates sufficient safety for in vivo evaluation in mouse models.

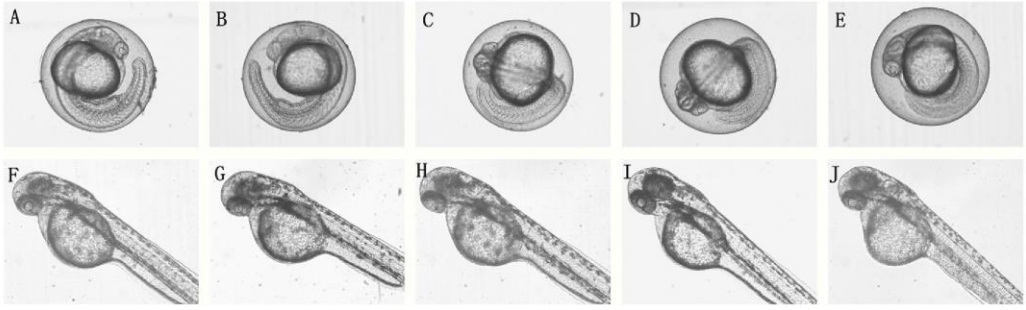

Fig. 4. In vivo cytotoxicity studies with embryos of zebrafish after 24 (A–E) and 72 (F–G) hpf at 10 μM resp.. Controls (A and F), Probe **6** (B and G), **8** (C and H), **9** (D and I) and **11** (E and J).

Acknowledgments

This work was supported by grants from German Federal Ministry of Education and Research (Bundesministerium für Bildung und Forschung, Germany, 13N10636).

Supplementary data

Supplementary data associated with this article can be found, in the online version, at http://dx.doi.org/10.1016/j.bmcl.2012.09.109. These data include MOL files and InChiKeys of the most important compounds described in this article.

References and notes

1. Citron, M. *Nat. Rev. Drug Disc.* **2010**, *9*, 387.
2. Monacelli, A. M.; Cushman, L. A.; Kavcic, V.; Duffy, C. J. *Neurology* **2003**, *61*, 1491.
3. Jakob-Roetne, R.; Jacobsen, H. *Angew. Chem., Int. Ed. Engl.* **2009**, *48*, 3030.
4. Prince, M.; Bryce, R.; Ferri, C. World Alzheimer Report 2011, 2011.
5. Selkoe, D. J. *Physiol. Rev.* **2001**, *81*, 741.
6. Ittner, L. M.; Gotz, J. *Nat. Rev. Neurosci.* **2011**, *12*, 67.
7. LaFerla, F. M. *Biochem. Soc. Trans.* **2010**, *38*, 993.
8. Bruno, B.; Pickhardt, M.; Schmidt, B.; Mandelkow, E.-M.; Waldmann, H.; Mandelkow, E. *Angew. Chem., Int. Ed.* **2008**, *48*, 1740.
9. Binder, L. I.; Guillozet-Bongaarts, A. L.; Garcia-Sierra, F.; Berry, R. W. *Biochim. Biophys. Acta* **2005**, *1739*, 216.
10. Flaherty, D. P.; Walsh, S. M.; Kiyota, T.; Dong, Y.; Ikezu, T.; Vennerstrom, J. L. *J. Med. Chem.* **2007**, *50*, 4986.
11. Mathis, C. A.; Wang, Y. M.; Holt, D. P.; Huang, G. F.; Debnath, M. L.; Klunk, W. E. *J. Med. Chem.* **2003**, *46*, 2740.
12. Sutharsan, J.; Dakanali, M.; Capule, C. C.; Haidekker, M. A.; Yang, J.; Theodorakis, E. A. *ChemMedChem* **2010**, *5*, 56.
13. Cui, M.; Ono, M.; Kimura, H.; Liu, B.; Saji, H. *Bioorg. Med. Chem. Lett.* **2011**, *21*, 4193.
14. Zhuang, Z. P.; Kung, M. P.; Kung, H. F. *J. Med. Chem.* **2006**, *49*, 2841.
15. Zha, Z.; Choi, S. R.; Ploessl, K.; Lieberman, B. P.; Qu, W.; Hefti, F.; Mintun, M.; Skovronsky, D.; Kung, H. F. *J. Med. Chem.* **2011**, *54*, 8085.
16. Braskie, M. N.; Klunder, A. D.; Hayashi, K. M.; Protas, H.; Kepe, V.; Miller, K. J.; Huang, S. C.; Barrio, J. R.; Ercoli, L. M.; Siddarth, P.; Satyamurthy, N.; Liu, J.; Toga, A. W.; Bookheimer, S. Y.; Small, G. W.; Thompson, P. M. *Neurobiol. Aging* **2010**, *31*, 1669.
17. Klunk, W. E.; Bacskai, B. J.; Mathis, C. A.; Kajdasz, S. T.; McLellan, M. E.; Frosch, M. P.; Debnath, M. L.; Holt, D. P.; Wang, Y.; Hyman, B. T. *J. Neuropathol. Exp. Neurol.* **2002**, *61*, 797.
18. Mathis, C. A.; Bacskai, B. J.; Kajdasz, S. T.; McLellan, M. E.; Frosch, M. P.; Hyman, B. T.; Holt, D. P.; Wang, Y.; Huang, G. F.; Debnath, M. L.; Klunk, W. E. *Bioorg. Med. Chem. Lett.* **2002**, *12*, 295.
19. Okamura, N.; Suemoto, T.; Furumoto, S.; Suzuki, M.; Shimadzu, H.; Akatsu, H.; Yamamoto, T.; Fujiwara, H.; Nemoto, M.; Maruyama, M.; Arai, H.; Yanai, K.; Sawada, T.; Kudo, Y. *J. Neurosci.* **2005**, *25*, 10857.
20. Koronyo, Y.; Salumbides, B. C.; Black, K. L.; Koronyo-Hamaoui, M. *Neurodegener. Dis.* **2012**, *10*, 285.
21. Koronyo-Hamaoui, M.; Koronyo, Y.; Ljubimov, A. V.; Miller, C. A.; Ko, M. K.; Black, K. L.; Schwartz, M.; Farkas, D. L. *Neuroimage* **2011**, *54*, S204.
22. Taghavi, A.; Nasir, S.; Pickhardt, M.; Heyny-von Haußen, R.; Mall, G.; Mandelkow, E.; Mandelkow, E.-M.; Schmidt, B. *J. Alzheimers Dis.* **2011**, *27*, 835.
23. Zon, L. I.; Peterson, R. T. *Nat. Rev. Drug. Disc.* **2005**, *4*, 35.
24. Ko, S. K.; Chen, X.; Yoon, J.; Shin, I. *Chem. Soc. Rev.* **2011**, *40*, 2120.
25. Kimmel, C. B.; Ballard, W. W.; Kimmel, S. R.; Ullmann, B.; Schilling, T. F. *Dev. Dyn.* **1995**, *203*, 253.
26. Paquet, D.; Bhat, R.; Sydow, A.; Mandelkow, E. M.; Berg, S.; Hellberg, S.; Falting, J.; Distel, M.; Koster, R. W.; Schmid, B.; Haass, C. *J. Clin. Invest.* **2009**, *119*, 1382.
27. Lamason, R. L.; Mohideen, M. A.; Mest, J. R.; Wong, A. C.; Norton, H. L.; Aros, M. C.; Jurynec, M. J.; Mao, X.; Humphreville, V. R.; Humbert, J. E.; Sinha, S.; Moore, J. L.; Jagadeeswaran, P.; Zhao, W.; Ning, G.; Makalowska, I.; McKeigue, P. M.; O'Donnell, D.; Kittles, R.; Parra, E. J.; Mangini, N. J.; Grunwald, D. J.; Shriver, M. D.; Canfield, V. A.; Cheng, K. C. *Science* **2005**, *310*, 1782.
28. Kieser, D. Ph.D. Dissertation, Technische Universität Darmstadt, **2011**.
29. Lindsey, J. S.; Brown, P. A.; Siesel, D. A. *Tetrahedron* **1989**, *45*, 4845.
30. Wang, J.; Cao, W. F.; Su, J. H.; Tian, H.; Huang, Y. H.; Sun, Z. R. *Dyes Pigm.* **2003**, *57*, 171.
31. Mancois, F.; Pozzo, J. L.; Pan, J.; Adamietz, F.; Rodriguez, V.; Ducasse, L.; Castet, F.; Plaquet, A.; Champagne, B. *Chem. Eur. J.* **2009**, *15*, 2560.
32. Berezin, M. Y.; Guo, K.; Teng, B.; Edwards, W. B.; Anderson, C. J.; Vasalatiy, O.; Gandjbakhche, A.; Griffiths, G. L.; Achilefu, S. *J. Am. Chem. Soc.* **2009**, *131*, 9198.
33. Boto, R. E. F.; El-Shishtawy, R. M.; Santos, P. F.; Reis, L. V.; Almeida, P. *Dyes Pigm.* **2007**, *73*, 195.
34. Zhang, W.; Arteaga, J.; Cashion, D. K.; Chen, G.; Gangadharmath, U.; Gomez, L. F.; Kasi, D.; Lam, C.; Liang, Q.; Liu, C.; Mocharla, V. P.; Mu, F.; Sinha, A.; Szardenings, A. K.; Wang, E.; Walsh, J. C.; Xia, C.; Yu, C.; Zhao, T.; Kolb, H. C. *J. Alzheimers Dis.* **2012**. http://dx.doi.org/10.3233/JAD-2012-120712.
35. Ryu, E. K.; Chen, X. *Front. Biosci.* **2008**, *13*, 777.
36. Log*P* values were calculated by the Molinspiration Cheminformatics software; http://www.molinspiration.com/ (V2011. 04).
37. Uchihara, T.; Nakamura, A.; Yamazaki, M.; Mori, O. *Acta. Neuropathol.* **2000**, *100*, 385.
38. Cashion, D. K.; Chen, G.; Kasi, D.; Kolb, H. C.; Liu, C.; Sinha, A.; Szardenings, A. K.; Wang, E.; Yu, C.; Zhang, W.; Gangadharmath, U. B.; Walsh, J. C. WO 2011119565, **2011**.
39. Mohorko, N.; Repovs, G.; Popovic, M.; Kovacs, G. G.; Bresjanac, M. *J. Neuropathol. Exp. Neurol* **2010**, *69*, 405.
40. Fodero-Tavoletti, M. T.; Okamura, N.; Furumoto, S.; Mulligan, R. S.; Connor, A. R.; McLean, C. A.; Cao, D.; Rigopoulos, A.; Cartwright, G. A.; O'Keefe, G.; Gong, S.; Adlard, P. A.; Barnham, K. J.; Rowe, C. C.; Masters, C. L.; Kudo, Y.; Cappai, R.; Yanai, K.; Villemagne, V. L. *Brain* **2011**, *134*, 1089.
41. Boländer, A.; Kieser, D.; Voss, C.; Bauer, S.; Schön, C.; Burgold, S.; Bittner, T.; Hölzer, J.; Heyny-von Haußen, R.; Mall, G.; Goetschy, V.; Czech, C.; Knust, H.; Berger, R.; Herms, J.; Hilger, I.; Schmidt, B. *J. Med. Chem.* **2012**. http://dx.doi.org/10.1021/jm300653b.

Supporting Information

Contents:

Experimental Section

General

Melting points were measured by Mettler FP5/51. The ^{1}H-NMR spectra were recorded on a Bruker DRX 500 spectrometer at 500 MHz. The ^{13}C-NMR spectra were recorded on a Bruker DRX 500 spectrometer at 125 MHz. Chemical shifts were reported downfield from Me_4Si. IR was performed by PerkinElmer FT-IR spectrometer PARAGON 1000PC. UV-Vis spectra were carried out by Shimadzu UV-2401PC. Mass spectrometry was performed on a MAT 95 double focussing sector field MS. Elemental analyses were performed by Elementar Vario EL. Flash column chromatography was carried out with Merck silica gel 60 (15-40 mm). Thin-layer chromatography (TLC) was carried out with aluminum sheets precoated with silica gel 60 F254 (0.2 mm, Merck). Chromatographic spots were visualized by UV light. All commercial chemicals were used without further purification.

Chemistry

2,3,3-trimethyl-3H-indole (3): A mixture of phenylhydrazine hydrochloride (1.45 g, 10 mmol, 1.0 eq), 3-methyl-2-butanone (1.03 g, 12 mmol, 1.2 eq) was dissolved in glacial acetic acid (25 mL) and then heated under reflux for 12 h under nitrogen. After been cooled to room temperature, the solvent was evaporated in vacuum and the residue was diluted with dichloromethane (30 mL). The organic layer was extracted with brine, was washed with saturated aqueous Na_2CO_3 (2 × 30 mL), brine, and was dried over Na_2SO_4. The solvent was evaporated in vacuo and the residue was purified by flash column chromatography eluting with Cyclohexane/EtOAc (2:1) to afford product as yellow liquid (1.28 g, 81%): R_f=0.30 (Cyclohexane/EtOAc 2:1); ^{1}H NMR

(500 MHz, [D_6]DMSO): δ=7.42 (d, J=7.5 Hz, 1H), 7.39 (d, J=7.0 Hz, 1H), 7.26 (td, J=7.5 Hz, J=1.0 Hz, 1H), 7.16 (td, J=7.5 Hz, J=1.0 Hz, 1H), 2.19 (s, 3H), 1.22 (s, 6H) ppm. ^{13}C NMR (125 MHz, [D_6]DMSO): δ=187.5, 153.5, 145.8, 127.2, 124.6, 121.4, 119.1, 53.0, 22.4, 14.9 ppm; MS (EI, 70eV): *m/z* 159.20 [*M*].

1,2,3,3-tetramethyl-3H-indolium iodide (4): 2,3,3-trimethyl-3H-indole (796 mg, 5 mmol, 1.0 eq) and methyl iodide (1.42 g, 10 mmol, 2.0 eq) were dissolved in anhydrous acetonitrile (15 mL). The reaction mixture was refluxed overnight. After the mixture cooled to room temperature, the solvent was evaporated *in vacuo* and the residue was treated with ethyl acetate (30 mL). The final product was collected by filtration and washed with ethyl acetate. The white solid was used in the next reaction without further purification. R_f=0.38 (CH_2Cl_2/MeOH 10:1); mp: 258–259°C (MeCN); ^{1}H NMR (500 MHz, [D_6]DMSO): δ=7.93-7.89 (m, 1H), 7.84-7.81 (m, 1H), 7.65-7.59 (m, 2H), 3.97 (s, 3H), 2.77 (s, 3H), 1.53 (s, 6H) ppm; ^{13}C NMR (125 MHz, [D_6]DMSO): δ=195.9, 142.0, 141.5, 129.2, 128.7, 123.1, 115.0, 53.8, 34.6, 21.6, 14.0 ppm; MS (EI, 70eV): *m/z* 173.13 [*M*-H]$^+$.

1-butyl-2,3,3-trimethyl-3H-indolium iodide (5): 2,3,3-trimethyl-3H-indole (318 mg, 2 mmol, 1.0 eq) and 1-Iodobutane (552 mg, 3 mmol, 1.5 eq) were refluxed overnight in ethylmethylketone (10 mL). After the mixture cooled to room temperature, the solvent was evaporated *in vacuo* and the residue was purified by column chromatography (SiO_2; CH_2Cl_2/MeOH 20:1) to afford product as a pale yellow solid (502 mg, 73%): R_f=4.0 ($CHCl_3$/MeOH 10:1); mp: 135-136°C; ^{1}H NMR (500 MHz, [D_6]DMSO): δ=7.99-7.94 (m, 1H), 7.96-7.82 (m, 1H), 7.66-7.60 (m, 2H), 4.45 (t, J=7.5 Hz, 2H), 2.84 (s, 3H), 1.86-1.77(m, 2H), 1.54 (s, 6H), 1.47-1.38 (m, 2H), 0.94 (t, J=7.5 Hz, 3H) ppm; ^{13}C NMR

(125 MHz, [D_6]DMSO): δ=196.3, 141.8, 141.0, 129.3, 128.9, 123.4, 115.4, 54.1, 47.3, 29.2, 21.9, 19.2, 13.9, 13.5 ppm; MS (EI, 70eV): *m/z* 215.24 [*M*-H]$^+$.

General methods for the synthesis of 2-styrylindolium derivatives: A mixture of 1-alkyl-2,3,3-trimethyl-3H-indolium iodide (0.25 mmol, 1.0 eq) and the corresponding aldehyde (0.275 mmol, 1.1 eq) was dissolved in EtOH (10 mL), and then heated with reflux for 12 h under nitrogen. The solvent was evaporated *in vacuo*. The crude product was purified by column chromatography (SiO_2; CH_2Cl_2/MeOH 10:1) to afford colourful 2-styrylindolium derivatives as solid. The derivatives were unstable in high temperature that no melting points were provided.

2-[2-[4-(dimethylamino)phenyl]ethenyl]-1,3,3-trimethyl-3H-indolium iodide (6): The title compound **6** as a dark green solid (100.8 mg, 93%): R_f=0.37 (CH_2Cl_2/MeOH 10:1); ^{1}H NMR (500 MHz, [D_6]DMSO): δ=8.30 (d, *J*=16.5 Hz, 1H), 8.07 (d, *J*=9.0 Hz, 2H), 7.77 (d, *J*=7.5 Hz, 1H), 7.70 (d, *J*=8.0 Hz, 1H), 7.55 (td, *J*=7.5 Hz, *J*=1.0 Hz, 1H), 7.48 (td, *J*=7.5 Hz, *J*=0.5 Hz, 1H), 7.25 (d, *J*=16.5 Hz, 1H), 6.88 (d, *J*=9.0 Hz, 2H), 3.96 (s, 3H), 3.16 (s, 6H), 1.75 (s, 6H); ^{13}C NMR (125 MHz, [D_6]DMSO): δ=179.5, 154.3, 154.0, 142.4, 142.0, 133.8 (brs), 128.6, 127.4, 122.5, 122.2, 113.5, 112.1, 105.1, 50.8, 33.0, 26.1 ppm; IR (KBr): $\tilde{\nu}$=3420, 2921, 1574, 1527, 1477, 1375, 1290, 1193, 1170, 1113, 832, 786, 728, 509 cm^{-1}; UV/Vis (Ethanol): λ_{max}= 547.5 nm; MS (EI, 70eV): *m/z* 304.47 [*M*-H]$^+$; Anal. calcd for $C_{21}H_{25}IN_2$: C 58.34, H 5.83, N 6.48, found: C 58.59, H 5.82, N 6.41.

2-[2-[4-(diethylamino)phenyl]ethenyl]-1,3,3-trimethyl-3H-indolium iodide (7): The title compound **7** as a dark green solid (105.3 mg, 92%): R_f=0.37 (CH_2Cl_2/MeOH 10:1); ^{1}H NMR (500 MHz, [D_6]DMSO): δ=8.26 (d, *J*=15.5 Hz, 1H), 8.02 (d, *J*=8.5 Hz, 2H), 7.74 (d, *J*=7.5 Hz, 1H), 7.67 (d, *J*=8.0 Hz, 1H),

7.53 (td, *J*=7.5 Hz, *J*=1.0 Hz, 1H), 7.46 (td, *J*=7.5 Hz, *J*=1.0 Hz, 1H), 7.19 (d, *J*=15.5 Hz, 1H), 6.86 (d, *J*=9.0 Hz, 2H), 3.93 (s, 3H), 3.57-3.51 (m, 4H), 1.73 (s, 6H), 1.17 (t, *J*=7.0 Hz, 6H); ^{13}C NMR (125 MHz, [D_6]DMSO): δ=179.4, 153.9, 152.6, 142.4, 142.1, 134.6 (brs), 128.7, 127.4, 122.6, 121.9, 113.4, 112.0, 104.6, 50.8, 44.5, 32.9, 26.3, 12.6 ppm; IR (KBr): $\tilde{\nu}$=3420, 1924, 1574, 1526, 1479, 1404, 1353, 1270, 1191, 1112, 1073, 928, 783, 714, 506 cm^{-1}; UV/Vis (Ethanol): λ_{max}=548.0 nm; MS (EI, 70eV): *m/z* 334.35 $[M+H]^+$; HRMS *m/z* $[M]^+$ calcd for $C_{23}H_{29}N_2$: 333.2331, found: 333.2336.

2-[2-(4-hydroxyphenyl)ethenyl]-1,3,3-trimethyl-3H-indolium iodide (8): The title compound **8** as a red-brown solid (83.8 mg, 83%): R_f=0.30 (CH_2Cl_2/MeOH 10:1); ^{1}H NMR (500 MHz, [D_6]DMSO): δ=8.33 (d, *J*=16.0 Hz, 1H), 8.10 (d, *J*=8.5 Hz, 2H), 7.81 (m, 2H), 7.60 (td, *J*=7.5 Hz, *J*=1.0 Hz, 1H), 7.55 (td, *J*=7.5 Hz, *J*=1.0 Hz, 1H), 7.41 (d, *J*=16.5 Hz, 1H), 6.82 (d, *J*=8.5 Hz, 2H), 4.06 (s, 3H), 1.76 (s, 6H) ppm; ^{13}C NMR (125 MHz, [D_6]DMSO): δ=180.8, 164.1, 153.3, 142.9, 141.8, 133.6, 128.7, 128.4, 125.6, 122.6, 116.7, 114.3, 108.5, 51.5, 33.7, 25.6 ppm; IR (KBr): $\tilde{\nu}$=3442, 3046, 1760, 1592, 1574, 1538, 1368, 1311, 1273, 1219, 1166, 1108, 940, 818, 766, 666, 483 cm^{-1}; UV/Vis (Ethanol): λ_{max}=546 nm; MS (EI, 70eV): *m/z* 277.42 $[M-H]^+$; Anal. calcd for $C_{19}H_{20}INO$: C 56.31, H 4.97, N 3.46, found: C 56.63, H 5.09, N 3.43.

2-[2-(4-methoxyphenyl)ethenyl]-1,3,3-trimethyl-3H-indolium iodide (9): The title compound **9** as a orange solid (80.3 mg, 77%): R_f=0.30 (CH_2Cl_2/MeOH 10:1); ^{1}H NMR (500 MHz, [D_6]DMSO): δ=8.40 (d, *J*=16.0 Hz, 1H), 8.21 (d, *J*=8.5 Hz, 2H), 7.87-7.83 (m, 2H), 7.64-7.57 (m, 2H), 7.54 (d, *J*=16.0 Hz, 1H), 7.16 (d, *J*=9.0 Hz, 2H), 4.11 (s, 3H), 3.90 (s, 3H), 1.78 (s, 6H) ppm; ^{13}C NMR (125 MHz, [D_6]DMSO): δ=181.5, 163.7, 153.1, 143.2, 141.7, 133.0, 128.9, 128.8, 127.3, 122.7, 114.9, 114.7, 110.3, 55.8, 51.8, 34.1, 25.5 ppm; IR (KBr): $\tilde{\nu}$= 3435, 2927, 1585, 1564, 1526, 1478, 1298, 1271, 1256, 1171, 1126, 1035,

828, 761, 517 cm^{-1}; UV/Vis (Ethanol): λ_{max}=424.5 nm; MS (EI, 70eV): *m/z* 291.42 [*M*-H]$^+$; Anal. calcd for $C_{20}H_{20}INO$: C 57.29, H 5.29, N 3.34, found: C 57.01, H 5.24, N 3.25.

2-[2-[4-(1-pyrrolidinyl)phenyl]ethenyl]-1,3,3-trimethyl-3H-indolium iodide(10): The title compound **10** as a purple solid (110.4 mg, 96 %): R_f=0.10 (CH_2Cl_2/MeOH 10:1); ^{1}H NMR (500 MHz, [D_6]DMSO): δ=8.30 (d, *J*=15.5 Hz, 1H), 8.07 (d, *J*=8.5 Hz, 2H), 7.76 (d, *J*=7.5 Hz, 1H), 7.68 (d, *J* = 8.0 Hz, 1H), 7.54 (td, *J*=7.5 Hz, *J*=1.0 Hz, 1H), 7.46 (td, *J*=7.5 Hz, *J*=1.0 Hz, 1H), 7.22 (d, *J*=15.5 Hz, 1H), 6.75 (d, *J*=9.0 Hz, 2H), 3.95 (s, 3H), 3.48 (t, *J*=7.5 Hz, 4H), 2.04-1.98 (m, 4H), 1.74 (s, 6H) ppm; ^{13}C NMR (125 MHz, [D_6]DMSO): δ=179.1, 154.0, 151.9, 142.3, 142.0, 134.2 (brs), 128.5, 127.2, 122.5, 122.1, 113.3, 112.6, 104.5, 50.6, 47.8, 32.8, 26.2, 24.7 ppm; IR (KBr): $\tilde{\nu}$=3429, 2925, 1614, 1576, 1529, 1477, 1396, 1293, 1188, 1114, 930, 817, 774, 706 cm^{-1}; UV/Vis (Ethanol): λ_{max}=555.5 nm; MS (EI, 70eV): *m/z* 332.37 [*M*+H]$^+$; Anal. calcd for $C_{23}H_{27}IN_2$: C 60.27, H 5.94, N 6.11, found: C 60.22, H 5.92, N 5.96.

2-[2-[4-(4-methylpiperazinyl)phenyl]ethenyl]-1,3,3-trimethyl-3H-indolium iodide(11): The title compound **11** as a red brown solid (110.9 mg, 91%): R_f=0.32 (CH_2Cl_2/MeOH 10:1); ^{1}H NMR (500 MHz, [D_6]DMSO): δ=8.30 (d, *J*=16.0 Hz, 1H), 8.07 (d, *J*=9.0 Hz, 2H), 7.79 (d, *J*=7.5 Hz, 1H), 7.74 (d, *J*=8.0 Hz, 1H), 7.56 (td, *J*=7.5 Hz, *J*=1.5 Hz, 1H), 7.51 (td, *J*=7.5 Hz, *J*=1.0 Hz, 1H), 7.32 (d, *J*=16.0 Hz, 1H), 7.10 (d, *J*=9.5 Hz, 2H), 4.00 (s, 3H), 3.53 (t, *J*=5.0 Hz, 4H), 2.46 (t, *J*=4.5 Hz, 4H), 2.25 (s, 3H), 1.75 (s, 6H) ppm; ^{13}C NMR (125 MHz, [D_6]DMSO): δ=180.1, 154.2, 153.6, 142.7, 141.9, 133.7, 128.7, 127.8, 123.5, 122.6, 113.8, 113.5, 106.5, 54.1, 51.0, 46.0, 45.4, 33.3, 26.0 ppm; IR (KBr): $\tilde{\nu}$=3434, 2919, 2802, 1568, 1520, 1479, 1439, 1375, 1291, 1242, 1190, 1172, 1114, 998, 918, 826, 786, 750, 640, 492 cm^{-1}; UV/Vis (Ethanol):

λ_{max}=526.5 nm; MS (EI, 70eV): *m/z* 361.37 $[M+H]^+$; HRMS *m/z* $[M]^+$ calcd for $C_{24}H_{30}N_3$: 360.2440, found: 360.2399.

2-[2-[4-(diethylamino)phenyl]ethenyl]-1-butyl-3,3-dimethyl-3H-indolium iodide (12): The title compound **12** as a purple solid (120.2 mg, 96%): R_f=0.40 (CH_2Cl_2/MeOH 10:1); ^{1}H NMR (500 MHz, [D$_6$]DMSO): δ=8.32 (d, *J*=16.5 Hz, 1H), 8.06 (d, *J*=8.5 Hz, 2H), 7.77 (d, *J*=7.5 Hz, 1H), 7.70 (d, *J*=8.0 Hz, 1H), 7.54 (td, *J*=7.5 Hz, *J*=1.5 Hz, 1H), 7.46 (td, *J*=7.5 Hz, *J*=0.5 Hz, 1H), 7.21 (d, *J*=16.0 Hz, 1H), 6.86 (d, *J*=8.0 Hz, 2H), 4.50 (t, *J*=7.5 Hz, 2H), 3.60-3.52 (m, 4H), 1.81-1.71 (m, 8H), 1.47-1.38 (m, 2H), 1.18 (t, *J*=7.5 Hz, 6H), 0.93 (t, *J*=7.5 Hz, 3H) ppm; ^{13}C NMR (125 MHz, [D$_6$]DMSO): δ=179.0, 154.2, 152.6, 142.5, 141.0, 134.6 (brs), 128.7, 127.3, 122.7, 121.9, 113.4, 112.0, 104.0, 50.7, 44.7, 44.4, 29.8, 26.5, 19.2, 13.6, 12.5 ppm; IR (KBr): $\tilde{\nu}$=3428, 2970, 1742, 1613, 1564, 1523, 1466, 1418, 1351, 1318, 1289, 1267, 1190, 1154, 1072, 838, 751, 715, 507 cm^{-1}; UV/Vis (Ethanol): λ_{max}=558.0 nm; MS (EI, 70eV): *m/z* 376.39 $[M+H]^+$; Anal. calcd for $C_{26}H_{35}IN_2$: C 62.15, H 7.02, N 5.58, found: C 62.28, H 7.00, N 5.66.

Compound 3

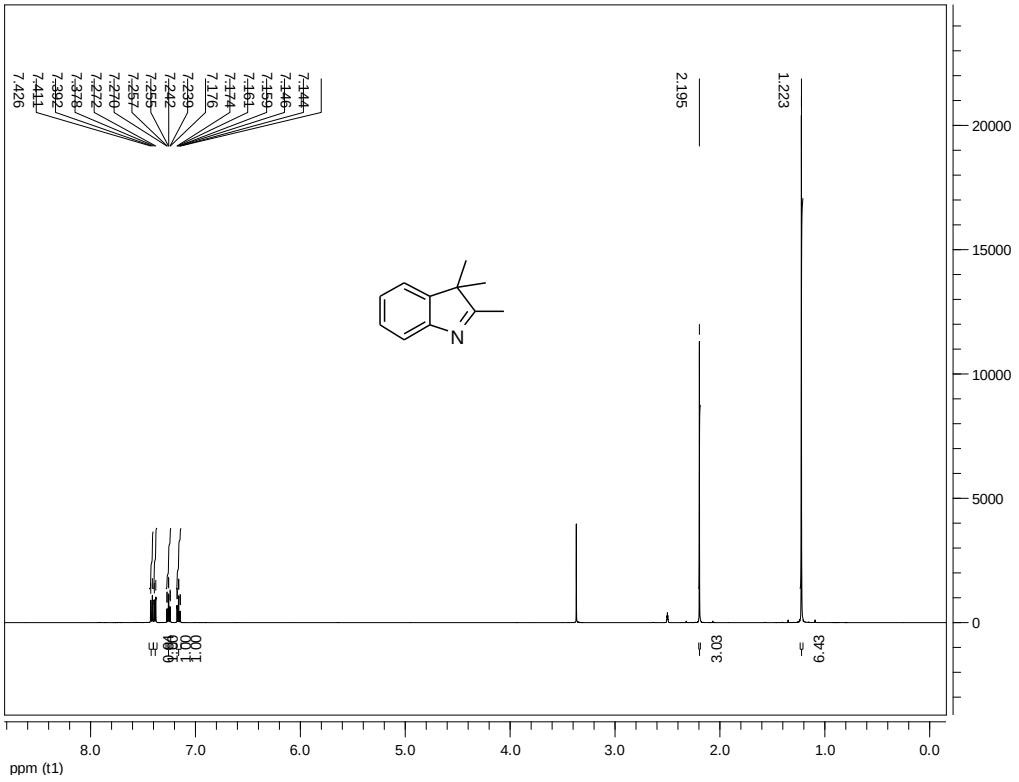
7.426
7.411
7.392
7.378
7.272
7.270
7.257
7.255
7.242
7.239
7.176
7.174
7.161
7.159
7.146
7.144
2.195
1.223
3.03
6.43
N
20000
15000
10000
5000
0
8.0
7.0
6.0
5.0
4.0
3.0
2.0
1.0
0.0
ppm (t1)

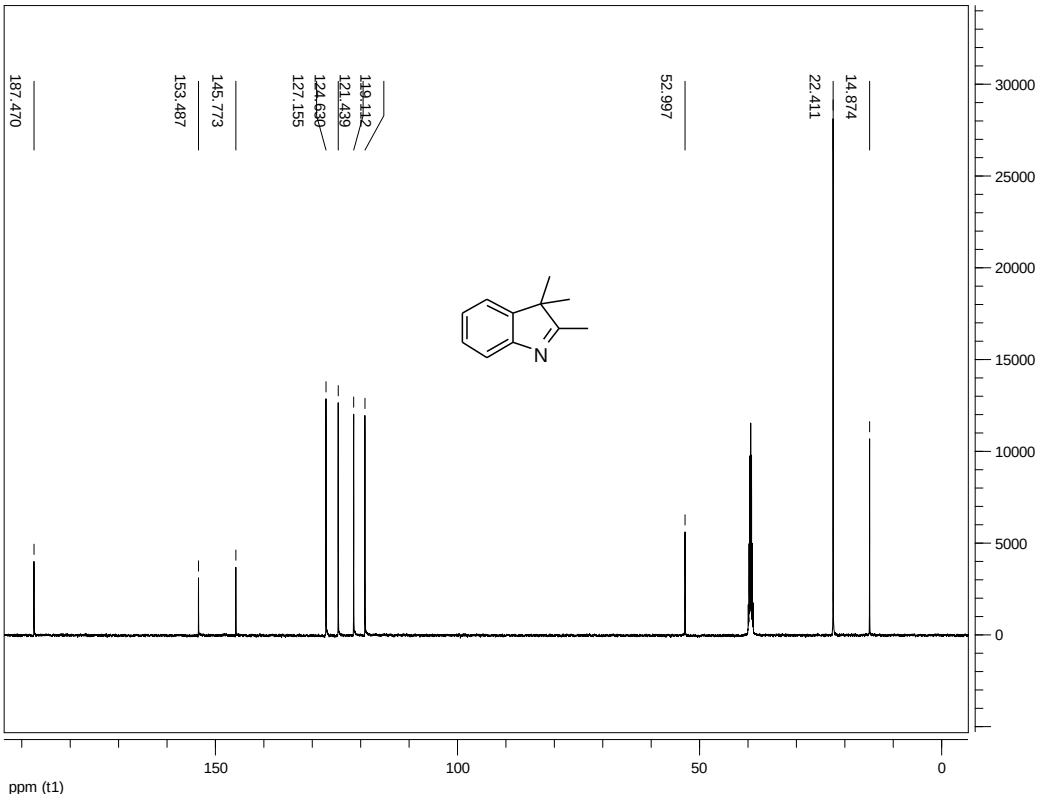
187.470
153.487
145.773
127.155
124.630
121.439
119.112
52.997
22.411
14.874
N
30000
25000
20000
15000
10000
5000
0
150
100
50
0
ppm (t1)

Compond 4

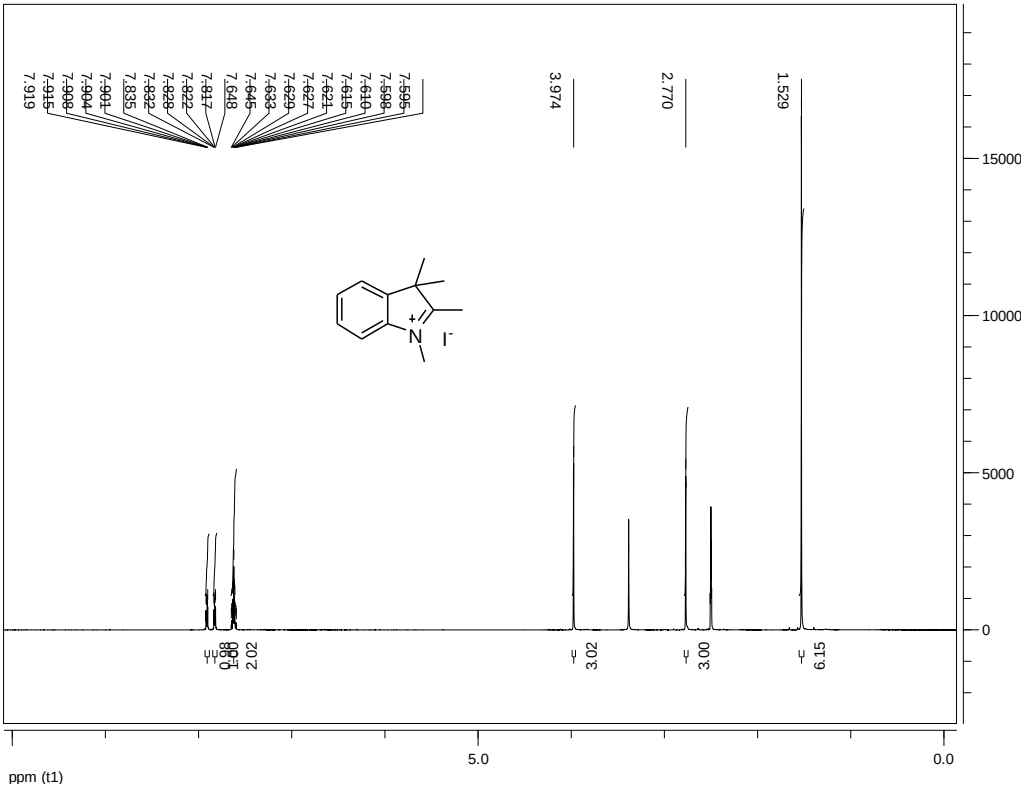
7.919
7.915
7.908
7.904
7.901
7.835
7.832
7.828
7.822
7.817
7.648
7.645
7.633
7.629
7.627
7.621
7.615
7.610
7.598
7.595
3.974
2.770
1.529
N
I-
15000
10000
5000
0
2.02
1.98
1.98
1.98
3.02
3.00
5.19
5.0
0.0
ppm (t1)

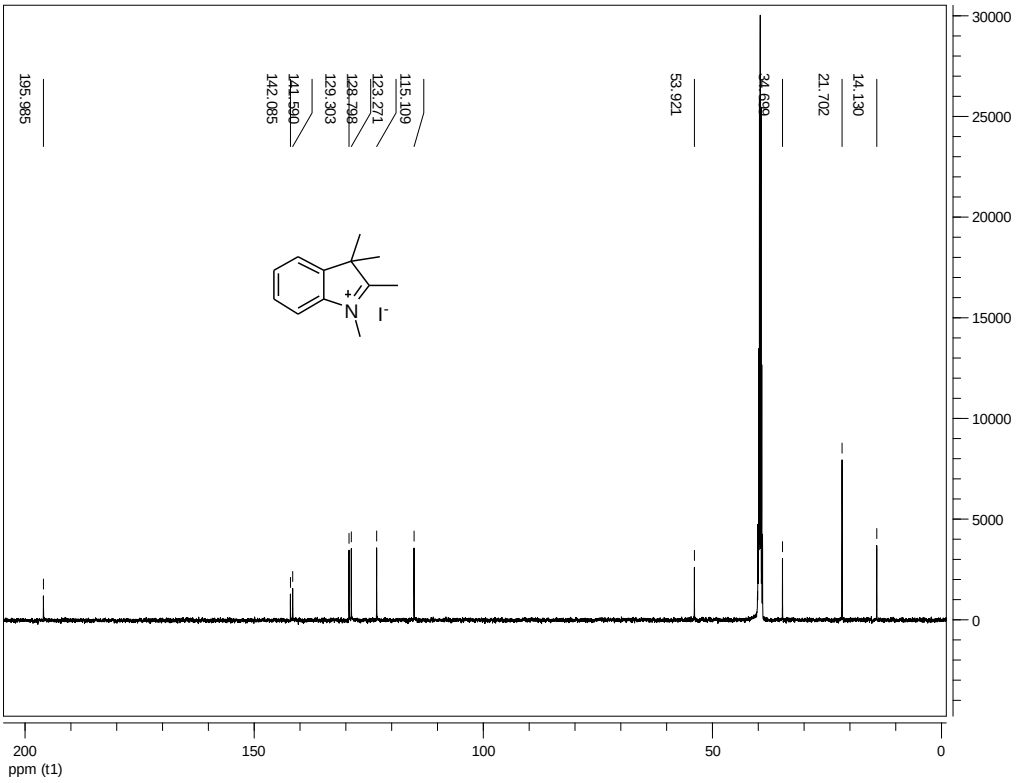
195.985
142.085
141.590
129.303
128.798
123.271
115.109
53.921
34.699
21.702
14.130
N
I-
30000
25000
20000
15000
10000
5000
0
200
150
100
50
0
ppm (t1)

Compound 5

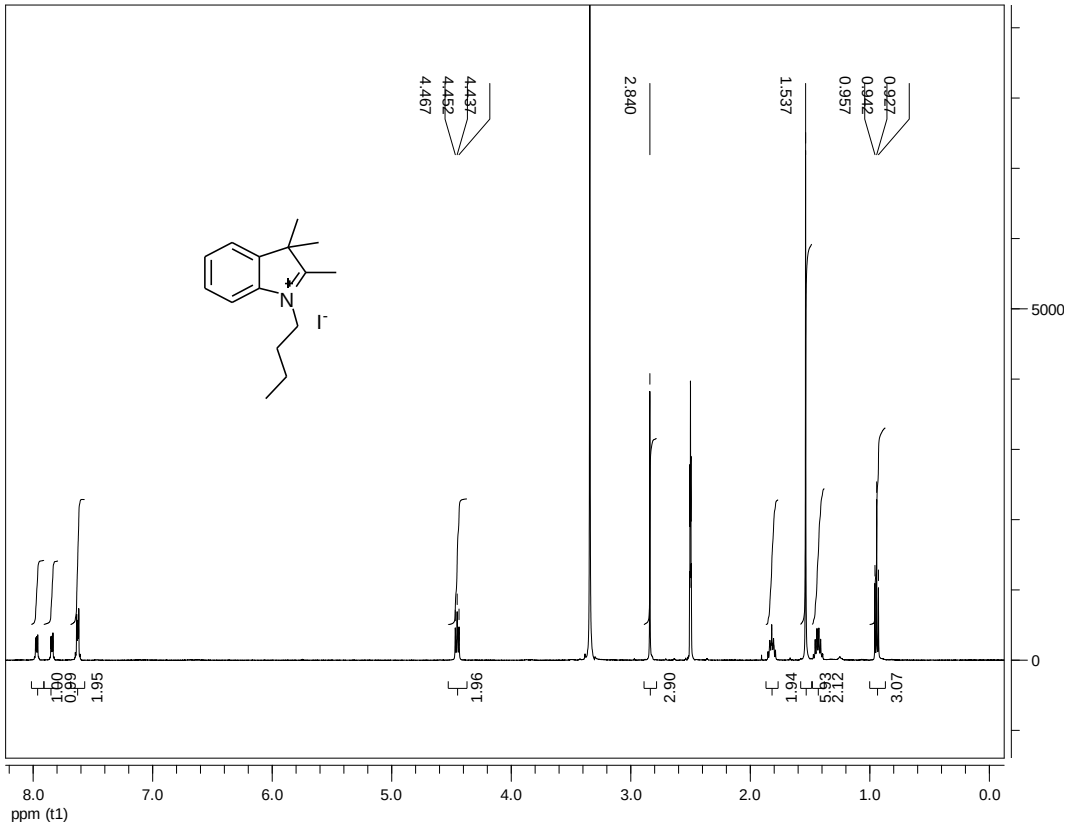
4.467
4.452
4.437
2.840
1.537
0.957
0.942
0.927
N
I-
1.00
0.98
0.95
1.96
2.96
1.96
1.64
3.12
3.07
5000
0
8.0
7.0
6.0
5.0
4.0
3.0
2.0
1.0
0.0
ppm (t1)

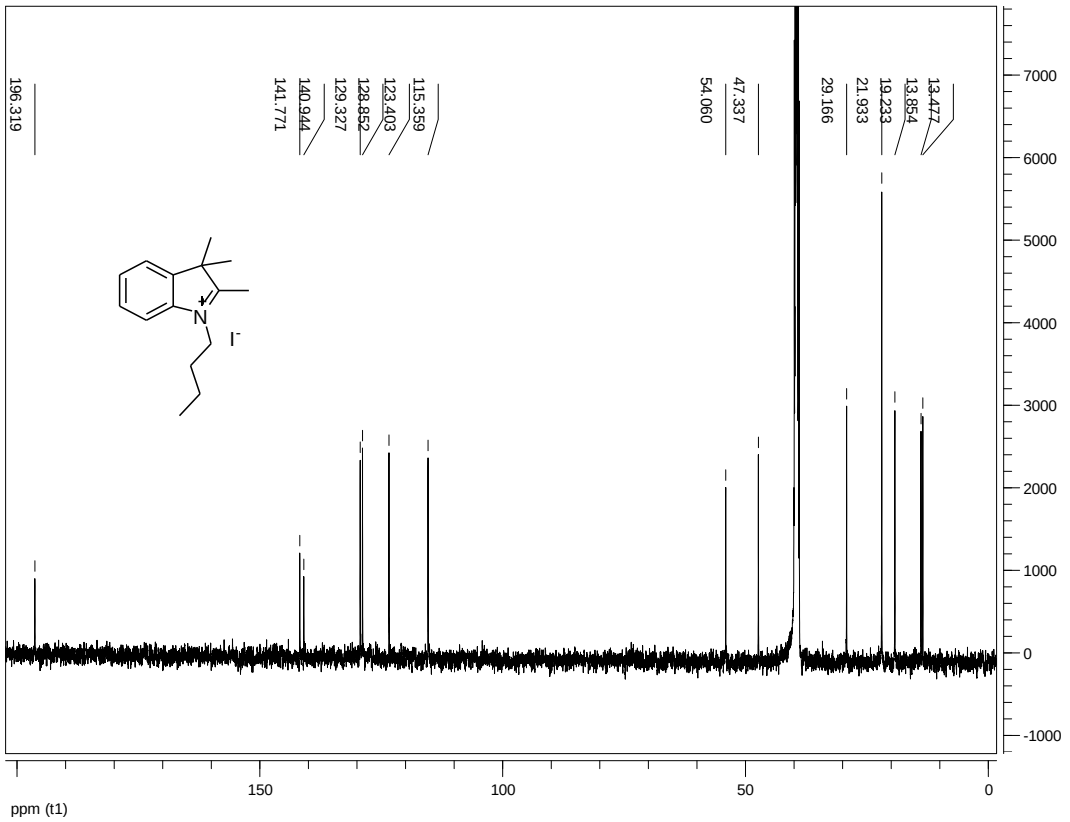
196.319
141.771
140.944
129.327
128.852
123.403
115.359
54.060
47.337
29.166
21.933
19.233
13.854
13.477
N
I-
7000
6000
5000
4000
3000
2000
1000
0
-1000
150
100
50
0
ppm (t1)

Compound 6

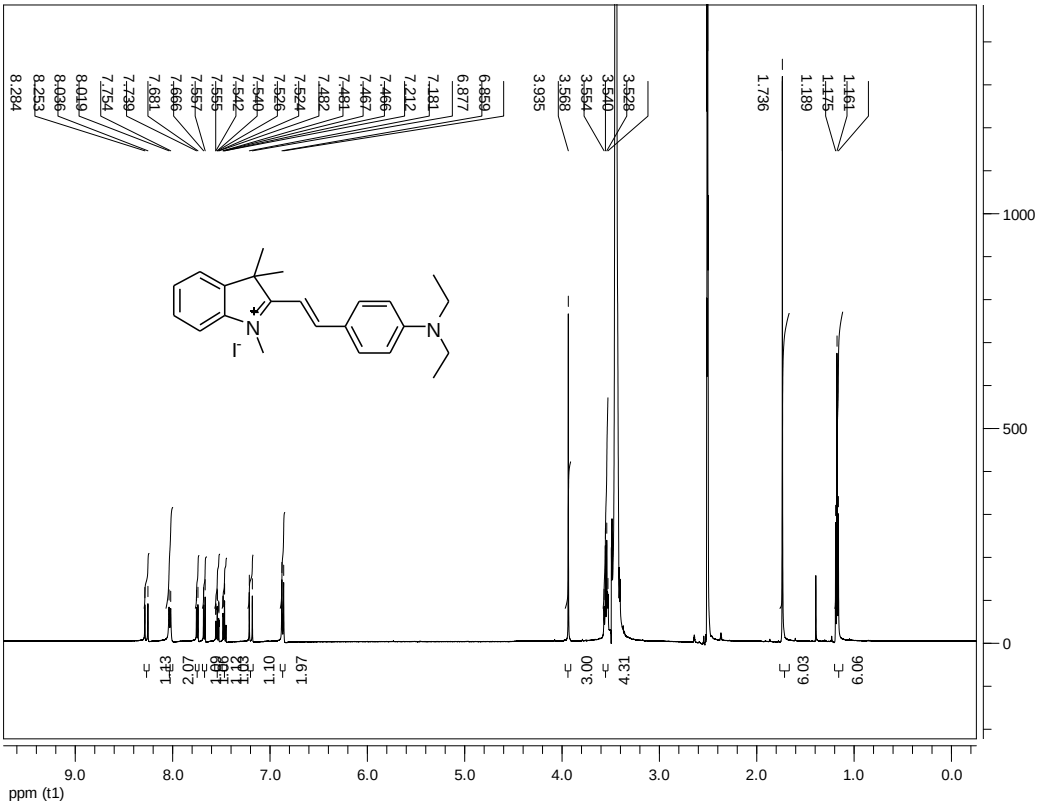
8.284
8.253
8.036
8.019
7.754
7.739
7.681
7.666
7.557
7.555
7.542
7.540
7.526
7.524
7.482
7.481
7.467
7.466
7.212
7.181
6.877
6.859
3.935
3.568
3.554
3.540
3.528
1.736
1.189
1.175
1.161
1.13
2.07
1.03
1.10
1.97
3.00
13.14
6.03
9.06
1000
500
0
9.0
8.0
7.0
6.0
5.0
4.0
3.0
2.0
1.0
0.0
ppm (t1)

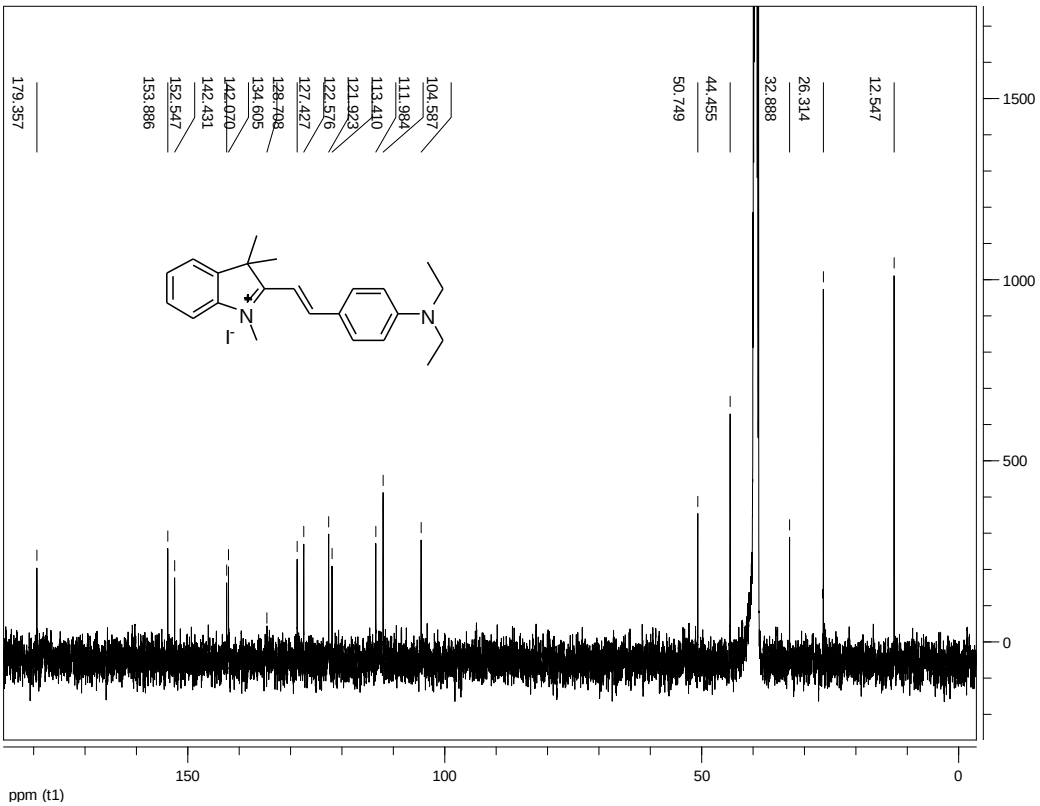
179.357
153.886
152.547
142.431
142.070
134.605
128.708
127.427
122.576
121.923
113.410
111.984
104.587
50.749
44.455
32.888
26.314
12.547
1500
1000
500
0
150
100
50
0
ppm (t1)

Compound 7

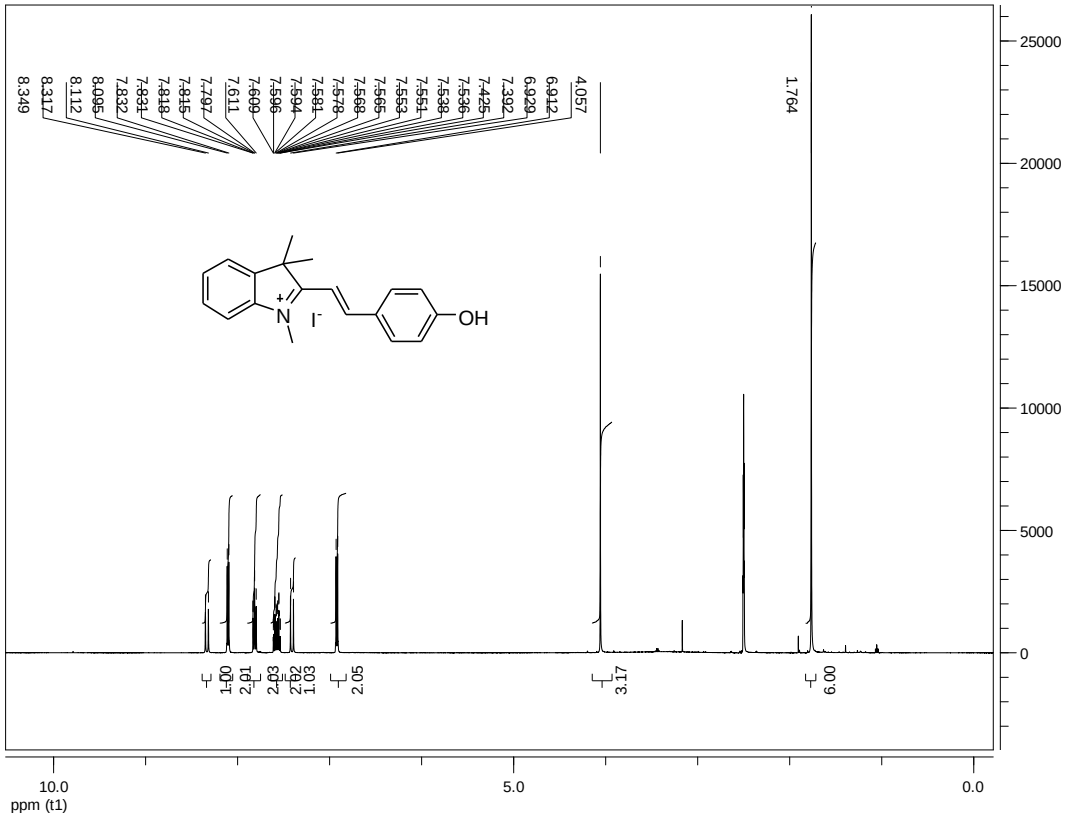
8.349
8.317
8.112
8.095
7.832
7.831
7.818
7.815
7.797
7.611
7.609
7.596
7.594
7.581
7.578
7.568
7.565
7.553
7.551
7.538
7.536
7.425
7.392
6.929
6.912
4.057
1.764
OH
I-
N
1.00
2.01
2.03
2.02
3.03
2.05
3.17
6.00
10.0
5.0
0.0
ppm (t1)

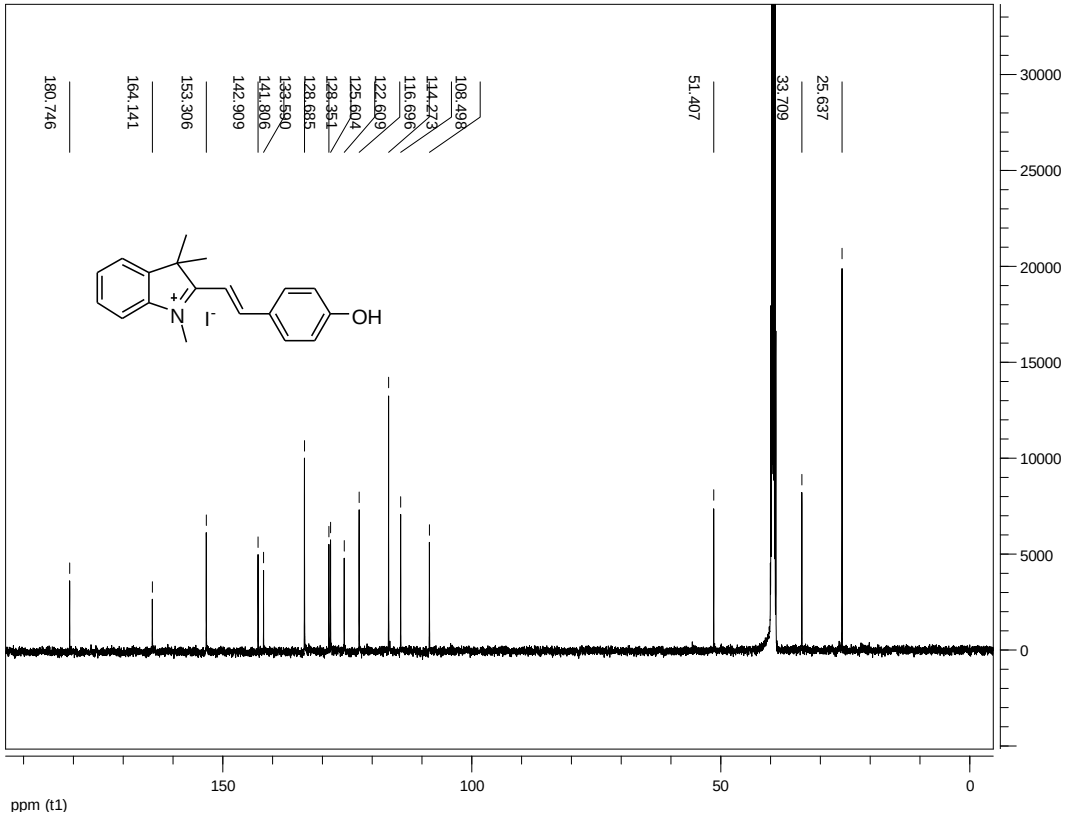
180.746
164.141
153.306
142.909
141.806
133.590
128.685
128.351
125.604
122.609
116.696
114.273
108.498
51.407
33.709
25.637
OH
I-
N
150
100
50
0
ppm (t1)

Compound 8

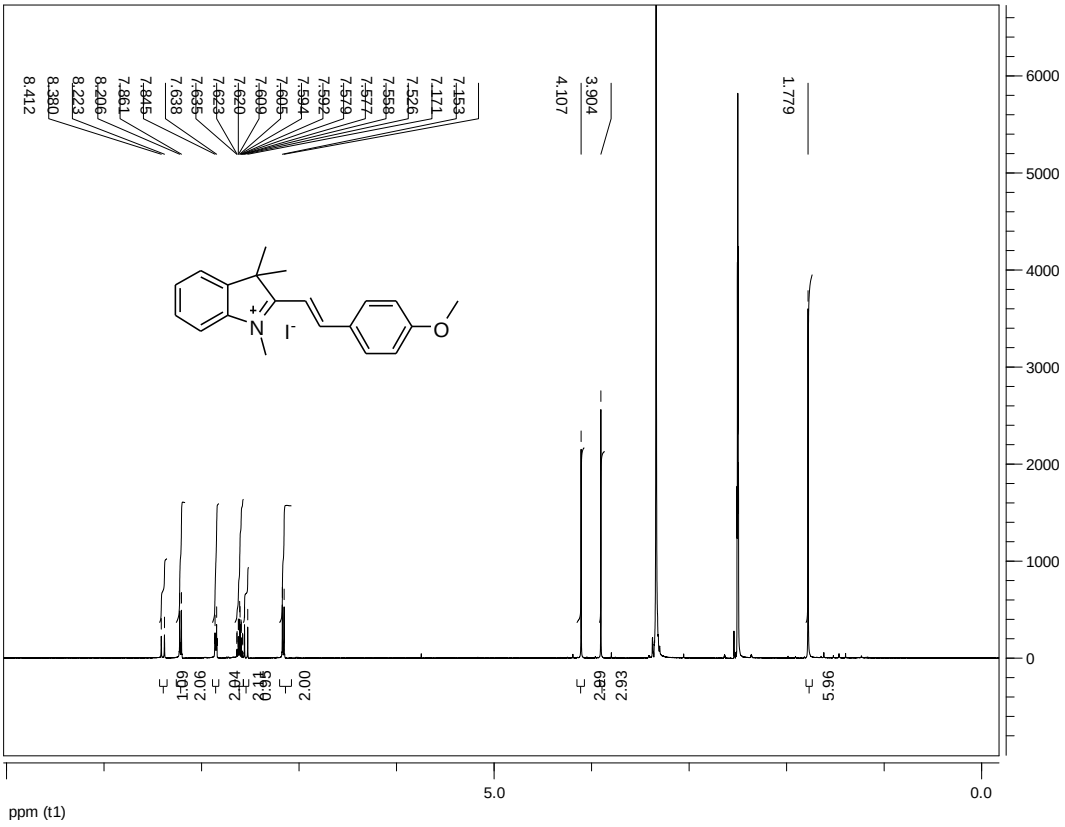
8.412
8.380
8.223
8.206
7.861
7.845
7.638
7.635
7.623
7.620
7.609
7.605
7.594
7.592
7.579
7.577
7.558
7.526
7.171
7.153
4.107
3.904
1.779
6000
5000
4000
3000
2000
1000
0
5.0
0.0
ppm (t1)

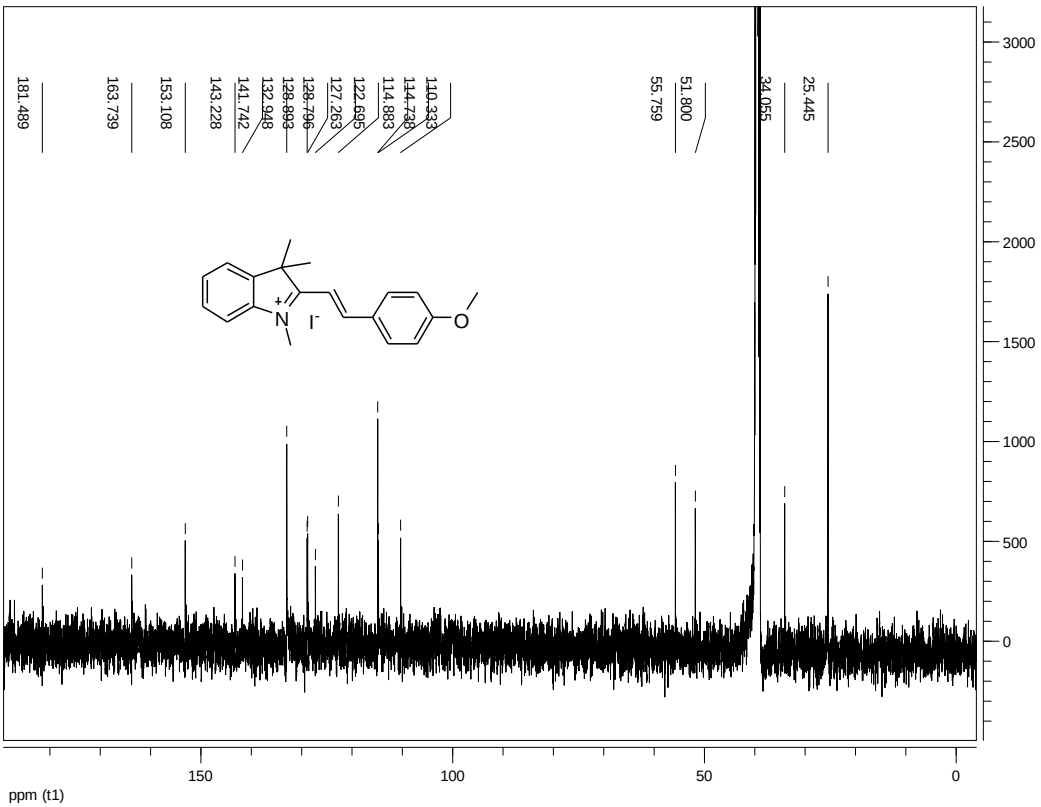
181.489
163.739
153.108
143.228
141.742
132.948
128.893
128.796
127.263
122.695
114.883
114.738
110.333
55.759
51.800
34.055
25.445
3000
2500
2000
1500
1000
500
0
150
100
50
0
ppm (t1)

Compound 9

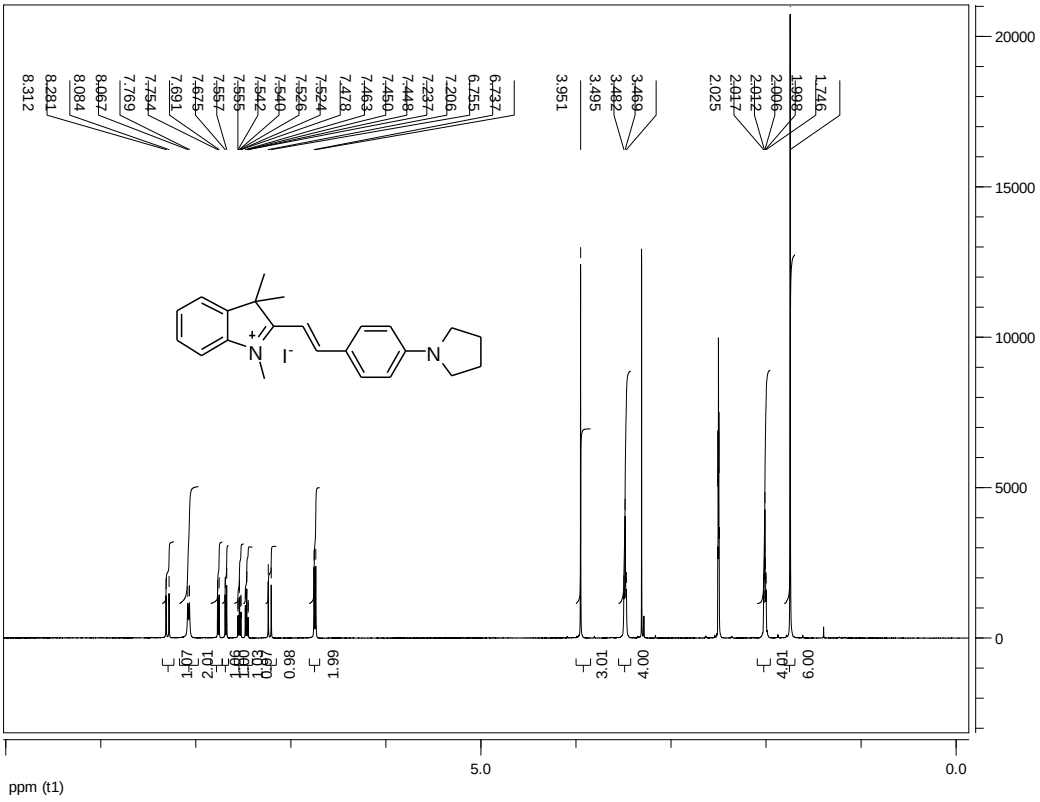
8.312
8.281
8.084
8.067
7.769
7.754
7.691
7.675
7.567
7.555
7.542
7.540
7.526
7.524
7.478
7.463
7.450
7.448
7.237
7.206
6.755
6.737
3.951
3.495
3.482
3.469
2.025
2.017
2.012
2.006
1.998
1.746
1.99
0.98
1.07
1.01
2.01
0.97
0.98
1.00
1.01
3.01
4.00
1.01
4.00
6.00
20000
15000
10000
5000
0
5.0
0.0
ppm (t1)

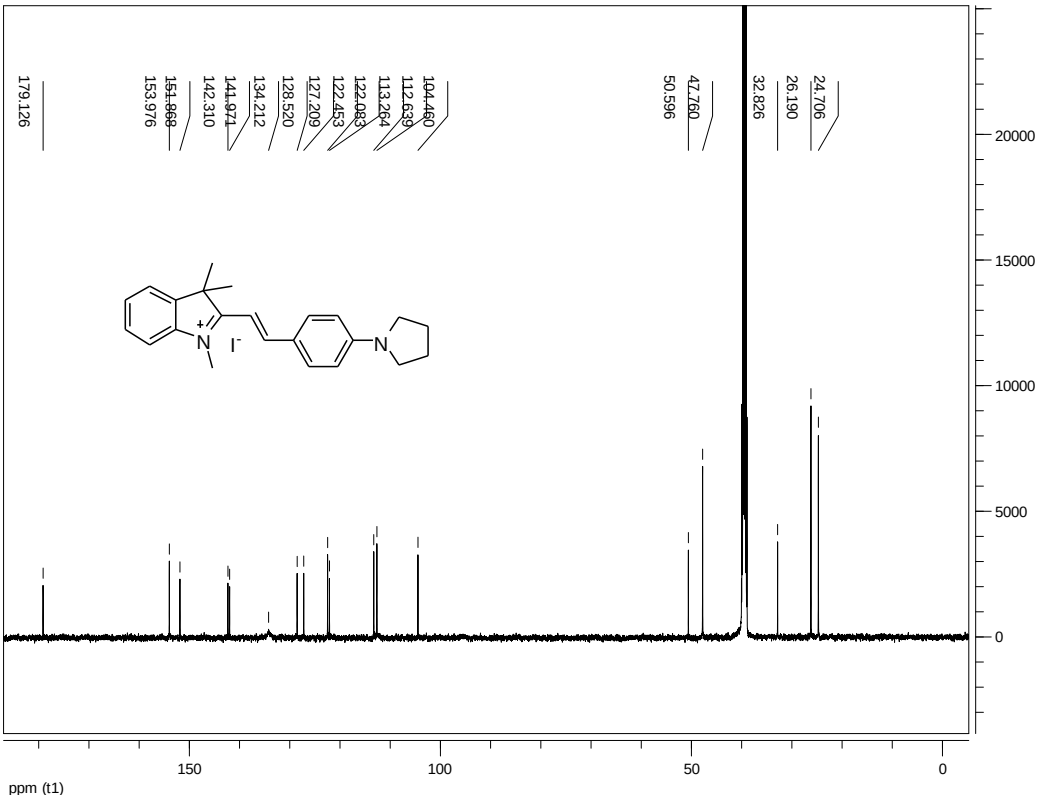
179.126
153.976
151.868
142.310
141.971
134.212
128.520
127.209
122.453
122.083
113.264
112.639
104.460
50.596
47.760
32.826
26.190
24.706
20000
15000
10000
5000
0
150
100
50
0
ppm (t1)

Compound 10

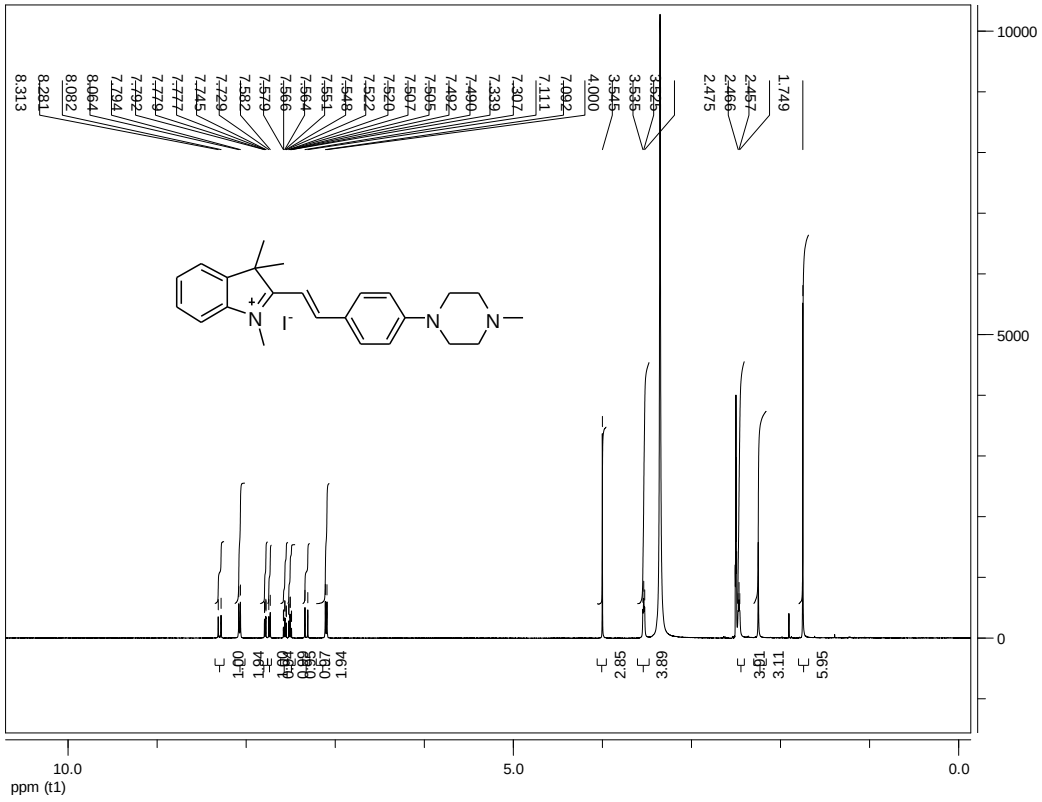
8.313
8.281
8.082
8.064
7.794
7.792
7.779
7.777
7.745
7.729
7.582
7.579
7.566
7.564
7.551
7.548
7.522
7.520
7.507
7.505
7.492
7.490
7.339
7.307
7.111
7.092
4.000
3.545
3.535
3.525
2.475
2.466
2.457
1.749
10000
5000
0
10.0
5.0
0.0
ppm (t1)

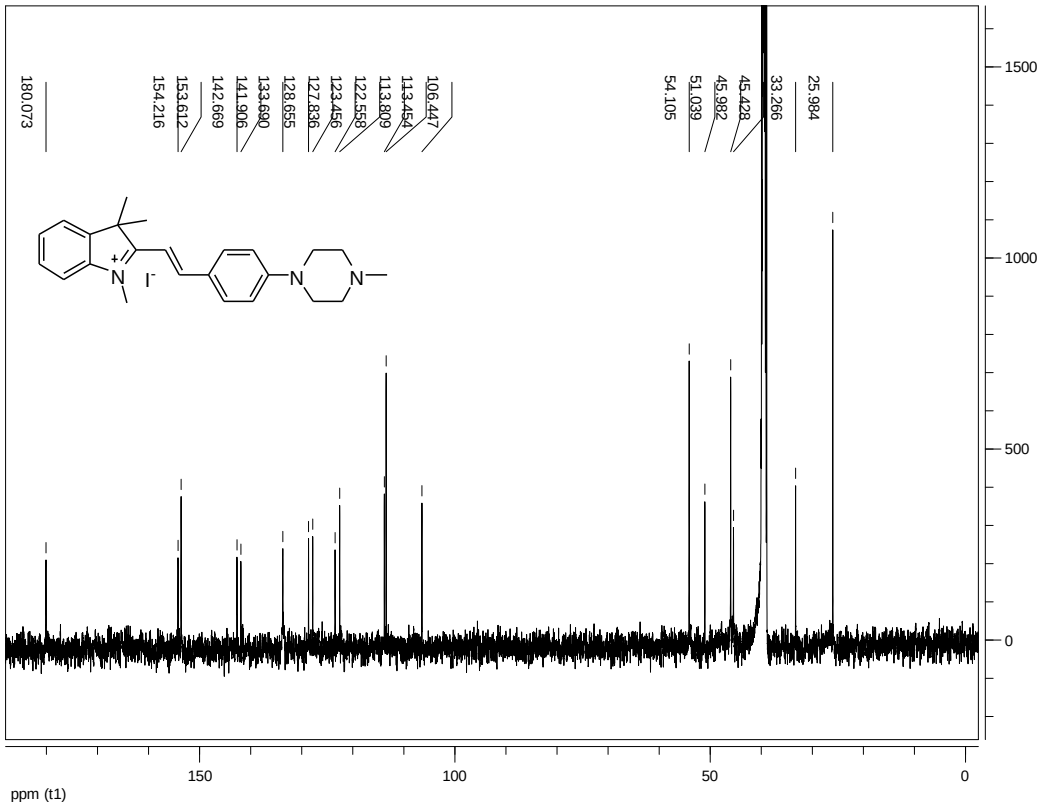
180.073
154.216
153.612
142.669
141.906
133.690
128.655
127.836
123.456
122.558
113.809
113.454
106.447
54.105
51.039
45.982
45.428
33.266
25.984
1500
1000
500
0
150
100
50
0
ppm (t1)

Compound 11

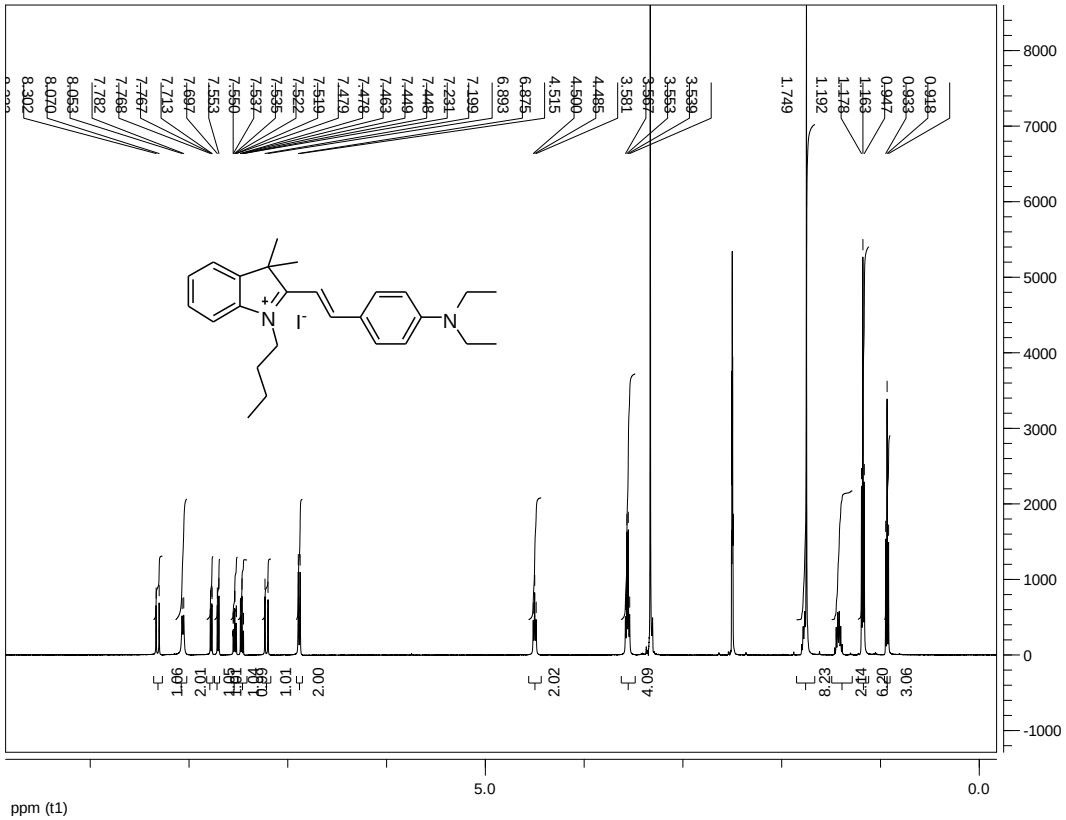
8.302
8.070
8.053
7.782
7.768
7.767
7.713
7.697
7.553
7.550
7.537
7.535
7.522
7.519
7.479
7.478
7.463
7.449
7.448
7.231
7.199
6.893
6.875
4.515
4.500
4.485
3.581
3.567
3.553
3.539
1.749
1.192
1.178
1.163
0.947
0.933
0.918
8000
7000
6000
5000
4000
3000
2000
1000
0
-1000
5.0
0.0
ppm (t1)

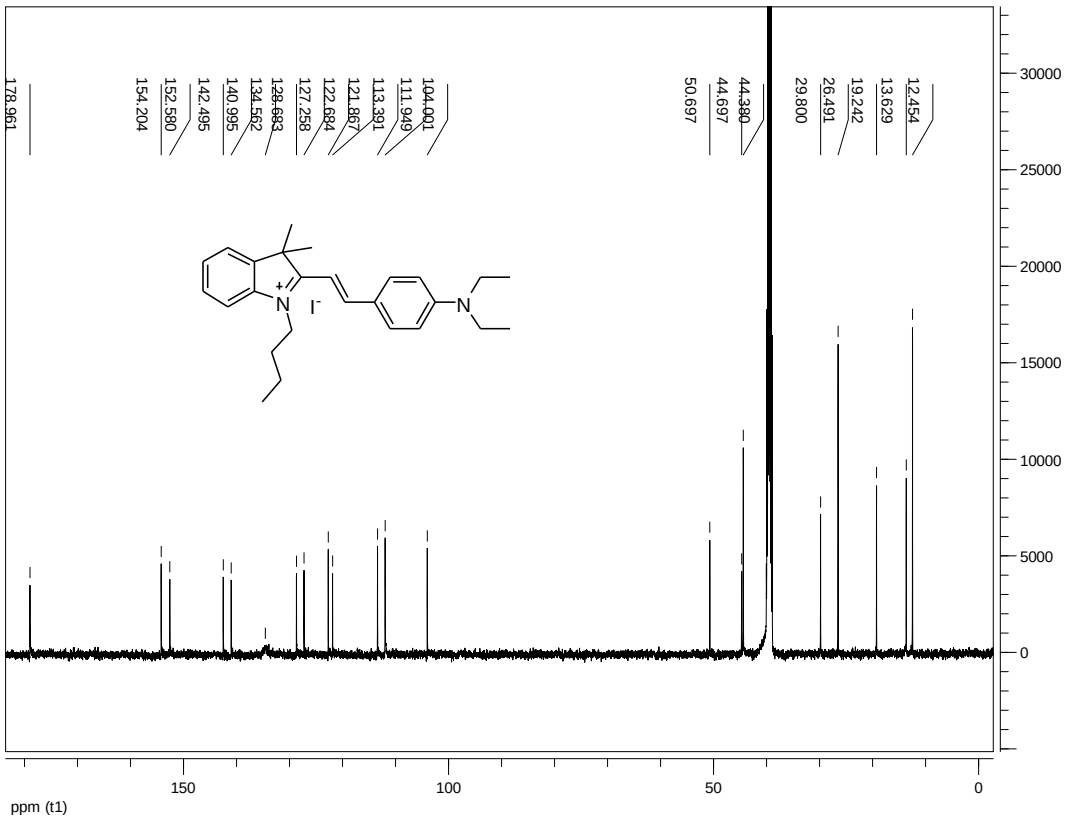
178.961
154.204
152.580
142.495
140.995
134.562
128.683
127.258
122.684
121.867
113.391
111.949
104.001
50.697
44.697
44.380
29.800
26.491
19.242
13.629
12.454
30000
25000
20000
15000
10000
5000
0
150
100
50
0
ppm (t1)

Immunohistochemical staining

Immunohistochemical staining experiments were carried out on 4 micrometers thick sections by a Ventana Benchmark automated stainer (Ventana, Tuscon, AZ). The antibodies anti-PHF-Tau clone AT8 mAb (Thermo Scientific Pierce Protein Research Products, Rockford, IL), TAU Ab-3 (Neomarkers, Freemont, CA), and amyloid A4 (BAM10, Sigma, St. Louis, MO) and the Ultraview Universal DAB Detection Kit (Ventana, Tuscon, AZ) were applied in these experiments.

In vitro neuropathological staining of AD brain sections

Four micrometers thick serial sections of paraffin-embedded brain sections of AD patient (71-years-old male) were used in this study. The brain sections were deparaffinized and hydrated in distilled water. The tissue sections were immersed in 1 mM solution of the probe in the DMSO for 10 minutes and then washed with methanol. The sections were differentiated in 1% acetic acid for 20 min, after that washed with running water for 5 min. Finally, the sections were treated with Roti®-Mount FluorCare (from Sigma-Aldrich) and covered with coverslip. The sections were analysed by fluorescence microscopy using a Axioskop microsocope with a HBO100 fluorescence illuminator (Carl Zeiss, Oberkochem, Germany) with the bandpass filter set 09 BP450-490, FT510, LP515, the filter set 02 G365, FT395, LP420 and the filter set 15 BP546, FT580, LP590 (all Carl Zeiss, Oberkochem, Germany).

In vivo zebrafish embryo assay for cytotoxicity

Zebrafish were bred and maintained according to the methods described by Christiane Nuesslein-Volhard and Ralf Dahm (Nuesslein-Volhard, C.; Dahm, R. Zebrafish: A practical approach. 2002). In brief, zebrafish were raised on 14-h

light-10-h dark cycle at 26.0 ± 0.5°C. The embryos were obtained via natural mating and cultured in the water. All experiments in this study were carried out according to the ethical and welfare principles in legislation on animal research in Germany. The embryos were collected and placed into 24-well plates, every ten embryos per well. When the embryos older than 6 hpf, more than 50% epiboly, they were treated with 1, 5, 10, 50 µM of 2-styrylindolium derivatives in E2 solution. The phenotypes were observed using the Axio Scope. A1 microscope system from Carl Zeiss at 24 and 72 hpf.

In vitro cell proliferation assay

Liver hepatocellular carcinoma cells HepG2 were maintained in DMEM/F12 1+1 supplemented with 10 % fetal bovine serum. Cells were cultivated under sterile conditions in a humidified incubator (37°C, 5% CO_2, 95 % humidity) without antibiotics. Mycoplasma contamination could be excluded via routinely examinations (PCR). To determine the number of viable cells after probes incubation, the CellTiter 96®AQueous non-radioactive cell proliferation assay (Promega, Madison, USA) was used. The HepG2 cells were seeded in 96-well plates at a density of 12000 cells per cm^2. 24 hours later, the cells were incubated with 0.1 µM, 1 µM, 10 µM and 50 µM of **6** (BSc4747), **8** (BSc4746), **9** (BSc4750) or **11** (BSc4743) for 24 hours. Afterwards, cells were washed three times with PBS and CellTiter 96®AQueous non-radioactive cell proliferation assay reagent was added to the samples. The colorimetric assay is based on the reduction of a tetrazolium salt [3-(4,5-dimethylthiazol-2-yl)-5-(3-carboxymethoxyphenyl)-2-(4sulfophenyl)-2H-tetrazolium, inner salt; [MTS] into a formazan product by intrinsic dehydrogenases of living cells. The amount of formazan product correlates directly to the number of metabolically active cells, and it was calculated after photometric analysis at λ=492 nm using a microplate reader (Tecan, Crailsheim, Germany). To quantify cell viability,

absorbances of treated samples were normalized to untreated controls (percent of nontreated controls), which resulted in cell vitality. Thereby cell vitality values between 70 % and 120 % represent neither cytotoxic nor proliferative effects on HepG2 and loss of cell vitality over 30% characterizes a substance as cytotoxic, according to the DIN ISO 10993-5:2009. Finally effective doses (EC_{50}) were calculated via the best-fitted trendline of cell vitality as a function of dye concentration. EC_{50} declares the dye concentration in which 50 % of the cells died after incubation with the probe.

Cell Toxicity of Dyes (**6**, **8**, **9** and **11**) on HepG2 cells

- HepG2: human liver carcinoma
- incubation time: 24 hours
- MTS-Assay after incubation times
- explanation: MW ... mean (cell vitality, n=6); STABW ... standard deviation

Compound **6**:

24 h

	0.1 µM	1 µM	10 µM	20 µM	50 µM
MW	87.12	64.72	54.25	32.46	1.48
STABW	4.21	9.68	2.92	6.93	2.49

Compound **8**:

24 h

	0.1 µM	1 µM	10 µM	20 µM	50 µM
MW	79.61	73.39	47.61	51.59	5.42
STABW	8.27	7.48	8.73	6.33	9.19

Compound **9**:

24 h

	0.1 µM	1 µM	10 µM	20 µM	50 µM

MW	104.63	72.73	55.31	17.62	1.90
STABW	7.44	7.14	9.24	7.42	1.06

Compound **11**:

24 h

	0.1 µM	1 µM	10 µM	20 µM	50 µM
MW	80.88	55.13	8.13	0.95	0.69
STABW	10.07	10.37	8.77	1.54	0.97

Effective doses (EC_{50}) of Dyes (**6**, **8**, **9** and **11**) on HepG2 cells

Dye	EC_{50} [µM]
6	8.573
8	10.932
9	8.313
11	0.931

***In vitro* binding assay**

Recombinant human microtubule associated tau protein purified from *E.coli* was aggregated at a concentration of 5 µM with arachidonic acid (100 µM) in Tris 10 mM pH=8, 24 h at 37°C. Synthetic $Aß_{40}$ was aggregated at a concentration of 50 µM with arachidonic acid (100 µM) in Tris 10 mM pH=8, for three days at 37°C, under shaking at 150 rpm. *Thiazine Red R* was added at the concentration corresponding to the K_d of the respective aggregated protein binding site to induce a fluorescent signal that can be inhibited by the addition of a displacer compound. (K_d for aggregated tau = 18 nM, K_d for aggregated Aβ = 49 nM). To determine the affinity of a displacer compound to the *Thiazine Red R* binding sites of the aggregated proteins, the compound was added at different

concentrations to the assay ranging from 0.1 nM to 10000 nM. For the inhibition curve, the compound was measured together with the aggregated proteins and *Thiazine Red R*. The fluorescence of some dyes overlapped with the fluorescence of *Thiazine Red R* when measured at 595 nm. Therefore, compounds were also measured together with the aggregated proteins, but without *Thiazine Red R* (autofluorescence curve). Net-fluorescence was calculated by subtracting the fluorescence of the wells without *Thiazine Red R* from the fluorescence of wells containing *Thiazine Red R* (inhibition curve). As negative control *Thiazine Red R* and aggregated protein was used. As positive control, *Thiazine Red R*, reference compound with known activity and aggregated protein was used. The assay was performed in Perkin Elmer OptiPlate 384, black, 45 mL assay volume. As assay buffer DPBS (no $CaCl_2$ no $MgCl_2$) (GIBCO N. 14020) was used. The tested compounds were diluted in DMSO and 2 µL of the solution was added to the assay (5% DMSO final). The assay was started by the addition of the aggregated protein (competitive condition). The plates were shortly shaked (1 min with Sterico variomag teleshake) and incubated at room temperature for 30 min. Measurements were performed with En:Vision (Perkin Elmer), at Excitation 531 nm / Emission 595 nm.

Corresponding IC_{50} values (inhibitory concentration for 50% decrease) were calculated using the Levenburg Marquardt algorithm:

$$y = A + ((B-A)/(1+((C/x)^D)))$$

Item	Description
A	The bottom plateau of the curve corresponds to the final minimum y value.

B	The top of the plateau of the curve corresponds to the final maximum y value.
C	The IC_{50} value represents the x value at which the half maximum y value is attained.
D	The slope factor. In this model a positive value is returned when y increases with increasing x and a negative value when y increases as x is decreasing.
x	Concentration of the tested compound (nM)
y	Net fluorescence in % of controls.

The obtained values are the average values of replicate experiments. The statistical presentation follows the guidelines laid out by G. Cumming, J. *Cell Biology*, **2007**, *177*, 7-11.

Determination of IC_{50} values for different compounds on aggregated proteins using the *Thiazine Red R* assay. Data represent average of technical replicates.

	aggr. tau - IC_{50} (nM)	aggr. Aß$_{40}$ - IC_{50} (nM)
Evans Blue	1.0	89
Congo Red	5.4	14
Hondson 1d*	8.8	13
BSB	18	78
MeXO4	246	140
Crystal Violet	1545	1280
FDDNP	1635	1467
IMPY	2707	5671
PIB	3255	5190
AZD2184	9802	>10000

FENE	>10000	>10000
BF-158	>10000	>10000

* Compound Honson 1d from Honson et al, *Neurobiol Dis.* **2007**, 28(3), 251-60.

3.1.4 Design, Synthesis and Biological Evaluation of Trimethine Cyanine Dyes as Fluorescent Probes for the Detection of Tau Fibrils in Alzheimer's disease Brain and Olfactory Epithelium

The content of this chapter has been published

Jiamin Gu, Upendra Rao Anumala, Roland Heyny-von Haußen, Jana Hölzer, Valerie Goetschy-Meyer, Gerhard Mall, Ingrid Hilger, Christian Czech, and Boris Schmidt.

Design, Synthesis and Biological Evaluation of Trimethine Cyanine Dyes as Fluorescent Probes for the Detection of Tau Fibrils in Alzheimer's disease Brain and Olfactory Epithelium, *ChemMedChem* **2013**, 8, 891-897.

Summary

Imaging of NFTs in Alzheimer's disease brains or tau aggregates in Bowman glands of olfactory epithelium tissues may provide early diagnosis of AD. In this chapter, the synthesis and evaluation of trimethine cyanine derivatives is reported. A group of six fluorescent trimethine cyanine derivatives was synthesized. The condensation reaction between substituted 2, 3, 3-trimethylindolenines and triethyl orthoformate resulted in probes with different absorption properties. Histological examination of postmortem AD brain sections with these probes visualized NFTs in the presence of SPs. *In vitro* evaluation of selected probes in the *Thiazine red R* displacement assay confirmed the slightly higher affinity to amyloid aggregates over tau aggregates. However, histological examination of the probes on human AD brain sections obtained at autopsy, visualized NFTs with good contrast. The cytotoxicity of selected probes on hepatocellular carcinoma cell lines (HepG2) and zebrafish embryos was examined. All probes examined displayed no or negligible cytotoxicity. These trimethine cyanine derivatives were further tested for their ability to visualize tau aggregates in Bowman glands of olfactory epithelium tissues. Probes 5a, 5b, 5c and 5f display tau aggregates on Bowman glands. These results suggest that trimethine cyanine derivatives should be investigated *in vivo* models.

Contribution of Upendra Rao Anumala: Support in histological examination on postmortem AD brain sections and olfactory epithelium tissues, cytotoxicity evaluation in zebrafish embryo assay and manuscript preparation.

CHEMMEDCHEM
COMMUNICATIONS

ChemPubSoc
Europe

DOI: 10.1002/cmdc.201300090

Design, Synthesis and Biological Evaluation of Trimethine Cyanine Dyes as Fluorescent Probes for the Detection of Tau Fibrils in Alzheimer's Disease Brain and Olfactory Epithelium

Jiamin Gu,[a] Upendra Rao Anumala,[a] Roland Heyny-von Haußen,[b] Jana Hölzer,[c] Valérie Goetschy-Meyer,[d] Gerhard Mall,[b] Ingrid Hilger,[c] Christian Czech,[d] and Boris Schmidt*[a]

Alzheimer's disease (AD) is the most common form of dementia. It is a slow, progressive brain disease that is characterized by impairment of memory and eventually by disturbances in reasoning, planning, language and perception.[1,2] The brains of AD patients are histopathologically characterized by two hallmark lesions: senile plaques (SPs) that are composed of extracellular deposits of amyloid β (Aβ) and neurofibrillary tangles (NFTs), which are formed by accumulation of abnormal filaments of tau.[3,4]

Recent therapeutic developments aim to prevent the accumulation of SPs and NFTs in AD patients, which requires monitoring of these biomarkers in clinical trials.[2] Furthermore, in order to facilitate the early diagnosis of AD, it is very important to visualize these AD pathological changes in the living brain. Intravenously administered radiotracers that selectively bind to SPs or NFTs for use in positron emission tomography (PET) or single-photon-emission computed tomography (SPECT) imaging offer such possibilities.

Over the past 10 years, several probes have been reported for Aβ imaging. Some agents are already in clinical trials, such as 2-(1-{6-[(2-[^{18}F]fluoroethyl)(methyl)amino]-2-naphthyl}ethylidene)malononitrile ([^{18}F]FDDNP), [*N*-methyl-^{11}C]2-(4′-methylaminophenyl)-6-hydroxybenzothiazole ([^{11}C]PIB), 2-(2-[2-dimethylaminothiazol-5-yl]ethenyl)-6-(2-[fluoro]ethoxy)benzoxazole ([^{11}C]BF-227), 4-{(1*E*)-2-(4-{2-[2-(2-[^{18}F]fluoroethoxy)ethoxy]ethoxy}phenyl)eth-1-en-1-yl}-*N*-methylaniline (^{18}F-Florbetapen/[^{18}F]BAY 94-9172) and 6-iodo-2-(4′-dimethylamino-)phenylimidazo[1,2-*a*]pyridine ([^{123}I]IMPY),[5–7] and in April 2012, (*E*)-4-(2-(6-(2-(2-(2-([^{18}F]-fluoroethoxy)ethoxy)ethoxy)pyridin-3-yl)vinyl)-*N*-methyl benzenamine (florbetapir-^{18}F, also known as Amyvid) became the first and only agent approved by the US Food and Drug Administration (FDA) as a radioactive diagnostic agent for brain imaging of Aβ plaques in patients.[8]

Despite these advances in Aβ imaging, only a few compounds, such as [^{18}F]FDDNP, (methoxy-X04), [^{11}C]PIB, benzimidazole and quinoline derivatives, have been reported to visualize NFTs.[9–12] Importantly, these probes display approximately equipotent affinity for both Aβ plaques and NFTs in vitro making it unlikely that they would be able to discriminate between the two different biomarkers in a clinical setting. Furthermore, some of these probes display undesirable pharmacokinetic and photophysical properties for application to human tissue.

Recent research suggests that tau pathology might be a more reliable biomarker for AD,[13,14] with the quantity of NFTs in the brain of AD patients correlating better with the progress of dementia. T-807, a tau-selective PET ligand with high selectivity versus human amyloid aggregates, is currently in clinical trials.[15,16]

Fluorescence imaging is a relatively new modality that offers real-time, non-radioactive in vivo imaging.[17] It is frequently rejected to be a nonviable modality in humans limited by absorption, autofluorescent tissues and insufficient penetration. However, recent reports on pathological changes in the retina and human olfactory system of AD patients suggest to investigate noninvasive access to amyloid and tau deposits by either scanning the retina or endoscopic examination of the nasal cavity.[18,19] The presence of hyperphosphorylated tau was reported in the retina of P301S transgenic mice and the human retina.[20]

Given the above considerations, there is a need for NFT imaging agents to complement the established amyloid PET imaging tools, and fluorescent probes could meet this need.

We recently reported that 2,3,3-trimethyl indolinium derivatives can visualize NFTs in AD brain sections,[21] and to continue with this, here we report trimethine cyanines of 2,3,3-trimethyl indolinium as more sensitive and benign probes to stain NFTs in human tissues. One of the major tasks was to improve solubility and decrease toxicity; these probes might be employed to visualize tau deposits in the olfactory epithelium of AD pa-

[a] *J. Gu, U. R. Anumala, Prof. Dr. B. Schmidt*
Clemens Schöpf-Institute of Chemistry and Biochemistry
Technische Universität Darmstadt
Petersenstrasse 22, 64287 Darmstadt (Germany)
E-mail: schmidt_boris@t-online.de

[b] *Dr. R. Heyny-von Haußen, Dr. G. Mall*
Institute of Pathology, Klinikum Darmstadt
Grafenstrasse 9, 64283 Darmstadt (Germany)

[c] *J. Hölzer, Prof. Dr. I. Hilger*
Institute of Diagnostic and Interventional Radiology I
Jena University Hospital-Friedrich Schiller Universität Jena
Erlanger Allee 101, 07747 Jena (Germany)

[d] *V. Goetschy-Meyer, Dr. C. Czech*
F. Hoffmann-La Roche AG
Grenzacherstrasse 124, Gebäude 93/3.44, 4070 Basel (Switzerland)

Supporting information for this article is available on the WWW under http://dx.doi.org/10.1002/cmdc.201300090.

tients for the noninvasive diagnosis of the disease in the early stages. These probes, derived from a screen of the Dyomics library of dyes, with a solubilizing sulfonic acid group in position R or R′ exhibited poor affinity for tau. Moreover, probes derived from 3-ethyl-3-methylindolines, which give rise to diastereomeric mixtures, also exhibited decreased affinity in the displacement assay. For these reasons, these derivatives were not pursued further.

We evaluated the cytotoxicity of these compounds by in vivo experiments of wild-type zebrafish (*Danio rerio*) embryo development and in vitro studies with liver hepatocellular carcinoma cells (HepG2). The zebrafish is a classic tractable vertebrate and embryological model for human diseases.[23,24] There are a number of favorable features for biomedical and behavioral genetics studies, including its small size, high fecundity, rapid external development, optical transparency during early embryogenesis, permeability to small molecules, amenability to high-throughput screening, and genetic similarity to humans.[25] In addition, the in vitro evaluation in liver cells provides information concerning the detoxification of the fluorophores in human tissue. These cytotoxic studies could help to eliminate potentially unsafe compounds early in the development process and prioritize compounds for further preclinical and clinical studies.

As more than 2000 trimethine cyanines are known, we selected a set of diverse trimethine cyanines (**5a**, **5b**, **5d** and **5f**) from the literature.[26–28] As the soluble sulfonylated cyanines dyes failed in the histopathological evaluation, we decided to include cyanine **5e** equipped with a short polyethylene glycol (PEG) substituent since this derivative was expected to display good solubility in the absence of amphiphilic properties. Surprisingly, there is no precedence in the literature for such PEGylated trimethine cyanines. We included the more lipophilic decyl derivative (**5c**) and the short ether (**5d**) in our investigations as controls.

Cyanines **5a–f** were synthesized according to known or slightly modified methods (Scheme 1).[29] Commercially available phenylhydrazine hydrochloride derivatives **1a** and **1b** and 3-methyl-2-butanone (**2**) were condensed to generate the intermediate hydrazones, which were further converted by Fischer indole synthesis to obtain 2,3,3-trimethylindolenine derivatives **3a** and **3b**. After alkylation or PEGylation in the *N*-position of the indolenines, indolium salts **4b–e** were purified by column chromatography, while **4a** and **4f** were used in the following step without further purification. In the presence of pyridine as a base and solvent, trimethine cyanine derivatives **5a–f** were formed by a condensation reaction between triethyl orthoformate and the corresponding indolium salts. This series of trimethine cyanine dyes was purified by column chromatography and characterized by NMR spectroscopy. During chromatography, the tosylate counterion of **5d** and **5e** was exchanged for chloride when the mobile phase included 2% triethylamine, as confirmed by the absence of tosylate protons in the ^{1}H NMR spectra.[30] According to the coupling constants of the olefinic protons (J = 13.0–13.5 Hz), symmetric trimethine cyanines adopt the thermodynamically favorable *trans* conformers.

Previous research suggested that probes with appropriate lipophilicity (Log$P$ = 0.1–3.5) might display sufficient permeability to cross the blood–brain barrier (BBB) and undergo rapid clearance from the brain when used as in vivo probes.[31] The calculated (c) Log$P$ values of compounds **5a–f** are shown in Table 1. cLog$P$ values increased with increasing chain length for compounds with a long hydrophobic chain as a substituent on the indolenine nitrogen atom (**5b** and **5c**); these compounds exhibited in inferior aqueous solubility (< 0.1 g mL^{-1} in distilled water at 25 °C). However, replacement of the alkyl chain substituents on the nitrogen atom by PEG chains (**5d** and **5e**) gave rise to a decrease in cLog$P$ value and an increase in aqueous solubility (> 0.5 g L^{-1} in distilled water at 25 °C). The solubility of established imaging agents, such as [^{18}F]FDDNP, methoxy-X04 and 2-[(4-methylamino)phenyl]quinoline (BF-158), is in the same range or inferior to the solubility of these

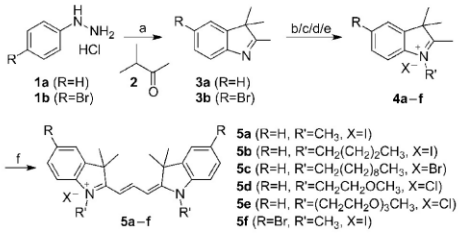

Scheme 1. Synthesis of trimethine cyanine dyes **5a–e**. *Reagents and conditions:* a) **2** (1.25 equiv), CH_3CO_2H, 120 °C, 16 h; b) **3a**/**3b** (1.0 equiv), methyl iodide (2.0 equiv), CH_3CN, reflux, 12 h; c) **3a** (1.0 equiv), 1-iodobutane (1.5 equiv), ethylmethylketone, reflux, 12 h; d) **3a** (1.0 equiv), 1-bromodecane (2.0 equiv), CH_3CN, reflux, 12 h; e) **3a** (1.0 equiv), corresponding polyethylene glycol 4-methylbenzenesulfonates (2.0 equiv), CH_3CN, reflux, 4 d; f) **4a–f** (1.0 equiv), triethyl orthoformate (2.0 equiv), pyridine, 120 °C, 12 h.

Table 1. Structures, properties and cytotoxicity (EC_{50}) of cyanine dyes.

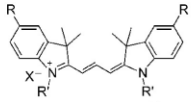

Compd	R	R′	X	MW[a]	cLog$P$[b]	EC_{50}[c] [μM]
5a[26]	H	CH_3	I	484.42	2.77	> 20
5b[27]	H	$CH_3(CH_2)_2CH_2$	I	568.58	5.64	1.1
5c	H	$CH_3(CH_2)_8CH_2$	Br	689.89	9.55	1.6
5d[28]	H	$CH_3OCH_2CH_2$	Cl	481.07	2.74	4.5
5e[28]	H	$CH_3(OCH_2CH_2)_3$	Cl	657.28	1.93	> 20
5f[26]	Br	CH_3	I	642.21	4.34	2.7

[a] Molecular weight (MW) was calculated in CambridgeSoft ChemOffice 10.0. [b] cLog$P$ values were calculated using Molinspiration Cheminformatics software (V2011. 04). [c] Half maximal effective concentration (EC_{50}): the compound concentration that gives rise to a 50% loss of cell viability compared with untreated controls. Further details are given in the Experimental Section and Supporting Information.

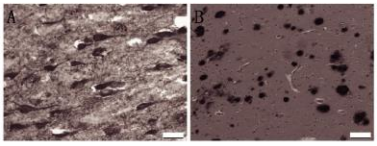

Figure 1. Immunohistochemical staining of hippocampal sections: A) NFTs with monoclonal antibody (mAb) AT8 (scale bar = 50 μm) and B) Aβ plaques with antibody amyloid A4 (scale bar = 100 μm).

trimethine cyanine derivatives.[21] Moreover, PEGylated probes **5d** and **5e** displayed decreased cytotoxicity in comparison with alkyl derivatives **5b** and **5c**.

In order to ensure that the tissues used to evaluate our probes contain both NFTs and Aβ plaques, we carried out immunohistochemical staining of human AD tissues. Figure 1 shows high levels of both NFTs and Aβ plaques in the selected brain tissue. To confirm the specific binding of **5a–f** to NFTs, hippocampus sections from pathologically confirmed postmortem AD were stained with the trimethine cyanine derivatives and visualized by fluorescence microscopy (Figure 2). It is noteworthy that all six trimethine cyanine derivatives stained NFTs strongly and provided good contrast in comparison with the background. However, Aβ plaques in the same brain tissue were not stained or were only stained just weakly, as observed by fluorescence microscopy. This observation stands in contrast to the activity of these derivatives in the thiazine red R displacement assay (Table 2).

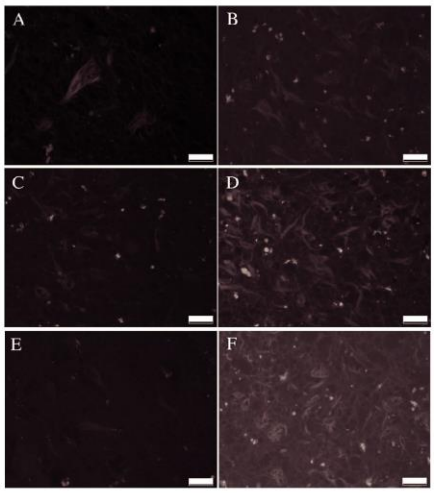

Figure 2. Neuropathological staining of brain sections from the hippocampus of an AD patient (scale bar = 25 μm). Probes **5a** (A), **5b** (B), **5c** (C), **5d** (D), **5e** (E) and **5f** (F) clearly stained neurofibrillary tangles. Tissues: hippocampus; patient: male, 71 years old, CERAD-Score = 3, NFTs level: V. Filter set 15 (A) and filter set 02 (B–F) were used for fluorescence microscopy.

The lack of Aβ plaque staining in human brain tissue was initially contributed to interference with the fluorescence properties upon binding to Aβ plaques. A decrease in fluorescence or change in the Stokes shift could limit the detection by fluorescence microscopy using filter sets 02 and 09. However, this assumed quenching was observed for several series, and this was effectively ruled out by spectral deconvolution using the Nuance FX detector. Thus, the discrepancies between the selectivity observed in the Thiazin red displacement assay and the histopathology of human brain sections must be assigned to fundamental differences in the binding sites in the vitro assay and the brain preparations. Similar discrepancies were reported for the affinity of amyloid binding agents in filtration assays and human AD tissue.[32] Thus the selectivities observed in the Thiazin red assay must be analyzed with care. Yet, these results suggest relatively good affinity of the probes for NFTs, which might be useful for the detection of NFTs in the olfactory epithelium sections or the brain of AD patients.

The affinity of these probes for tau aggregates was determined by displacement of the reference dye thiazine red R, which was previously shown to be superior to thioflavin S as an accurate marker for β-pleated sheet structures and reliably stains Aβ plaques (aggregated $A\beta_{40}$: $K_d = 49$ nM), diffuse NFTs (aggregated tau: $K_d = 18$ nM), and even ghost tangles. In previous work, IC_{50} values were determined from the results of a competition assay rather than K_i values.[19,21] The in vitro aggregates of $A\beta_{40}$ and $A\beta_{42}$ display differences in the binding sites for amyloid ligands, which depend on the aggregation conditions and differ from the binding situation observed in human tissue. Thus we selected $A\beta_{40}$ for the aggregation assay as it is the predominant component in amyloid plaques and thus likely to be engaged in binding of the probes.

The in vitro binding affinity (K_i) of the reference compound methoxy-X04 was reported in the literature as 26.8 nM.[33] However, the displacement potency of methoxy-X04 in the thiazine red R assay is far inferior ($IC_{50} = 246$ nM; Table 2). The affinity of the probes for tau aggregates was determined indirectly in a displacement assay against thiazine red R; the IC_{50} values are listed in Table 2. Unfortunately, the affinity of **5d** and **5e** could not be determined due to spectral overlap with thiazine red R.

Table 2. Results of a competitive thiazine red R displacement assay.

Compd	IC_{50}[a] [nM] agg. Tau	agg. $A\beta_{40}$
5a	2.2	0.13
5b	0.32	0.12
5f	0.33	0.12
Methoxy-X04	246	140
PIB	3255	5190
BF-158	>10000	>10000

[a] Compounds were evaluated at 0.1–10000 nM for their ability to displace thiazine red R from chemically induced synthetic tau fibrils. Data are the average values of replicate experiments. Further details are given in the Experimental Section and Supporting Information.

Moreover, the binding affinity of **5c** for $A\beta_{40}$ and tau aggregates were out of the assay range ($IC_{50} > 10000$ nM), which could be due to the high lipophilicity of **5c** (cLog $P = 9.55$). The displacement ability of trimethine cyanine derivatives **5a**, **5b** and **5f** was compared with known probes (methoxy-X04, PIB and BF-158) in the same system (Table 2). These trimethine cyanine derivatives displayed ~112–10000-fold higher affinity for tau aggregates in comparison with the reference probes. This suggests that these probes possess sufficient affinity for the detection of NFTs in vivo. Yet there is a caveat—chemically induced synthetic tau fibrils are not a reliable surrogate for native NFTs since they differ in size, morphology, and binding properties.[16]

Trimethine cyanine derivatives **5a**, **5b**, **5c**, **5e** and **5f** were further evaluated in a wild-type zebrafish embryo development assay. Embryos treated with probes **5a**, **5b**, **5c** and **5e** developed well, and no lesions were found at the different concentrations tested up to 10 μM at 24 h post-fertilization (hpf). However, probe **5f** showed cytotoxicity at 10 μM at 24 hpf, while the embryos developed well at 5 μM concentration at 24 hpf (Figure 3). Furthermore, all probes were evaluated for their cytotoxicity in a human HepG2 cell proliferation assay (Table 1). The half maximal effective concentration (EC_{50}) for each probe was calculated using the best-fitted trend line of a plot of cell vitality as a function of dye concentration (see Experimental Section). Both cytotoxicity studies suggested that these tau-selective probes have no or only negligible cytotoxicity against zebrafish embryos and HepG2 cells under the conditions employed for histological staining of human AD brain sections (24 h of incubation, 1 μM).

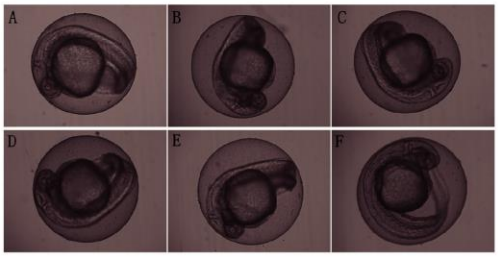

Figure 3. In vivo cytotoxicity studies with zebrafish embryos after 24 h post-fertilization at 10 μM (**5a–c** and **5e**) and 5 μM (**5f**). Control (A), probes **5a** (B), **5b** (C), **5c** (D) **5e** (E) and **5f** (F).

The absence of a BBB between the nose and brain suggests that the nasal cavity might enable drugs to access the brain and the central nervous system by pathways involving the olfactory epithelium and bulb.[34,35] As such, the efficiency of the drug might depend on cell permeability rather than brain penetration. Therefore, the human olfactory system could be conducive to the diagnosis and treatment of brain disorders such as AD. Comparing 20 confirmed AD patients and five healthy controls, our group reported that typical nasal tau protein might deposit in nasal mucous membranes, particularly in the nasal Bowman's glands and olfactory epithelium.[19,34,36] The severity of tau accumulation in the Bowman's glands and its correlation to AD is subject of ongoing investigation. However, this observation has shown potential for the noninvasive diagnosis of AD via changes in the olfactory epithelium in the early stages of disease (Figure 4).

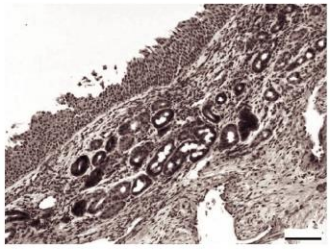

Figure 4. Immunohistological staining of Bowman's glands of the olfactory epithelium containing tau aggregates with antibody TAU Ab-3 (scale bar = 100 μm). Patient: male, 78 years old, Braak: V, CERAD-Score: 3.

Probes **5a**, **5b**, **5c** and **5g** were evaluated for their ability to detect tau deposits in olfactory epithelium tissue in vitro. Remarkably, many tau deposits were clearly stained by trimethine cyanine derivatives as seen in Figure 5. These results suggest that trimethine cyanine dyes are efficacious fluorescent probes for the detection of tau deposits on in olfactory epithelium tissue. The good aqueous solubility and negligible cytotoxicity of these probes suggest that they could be suitable for further development for in vivo applications.

In conclusion, we have successfully developed a series of non- or only weakly cytotoxic, water-soluble trimethine cyanine dyes as sensitive and biocompatible probes for fluorescent imaging of tau fibrils in human AD brain and olfactory epithelium sections. The cytotoxicity assays with zebrafish embryos and HepG2 cells suggest that these probes have sufficient safety, making them valuable for further in vivo evaluation in animal models of AD.

Experimental Section

Chemistry

General: ^1H and ^{13}C NMR spectra were recorded on a Bruker DRX 500 spectrometer at 500 MHz and 125 MHz, respectively. Chemical shifts (δ) are reported downfield from Me_4Si. UV-Vis spectra were obtained using a Shimadzu UV-2401PC spectrophotometer. Mass spectrometry (MS) was performed on a MAT 95 double focusing sector field mass spectrometer. All commercial chemicals were used without prior purification.

General synthetic procedure for trimethine cyanines: A solution of indolium (1.0 mmol, 1.0 equiv) and triethyl orthoformate (296 mg, 2.0 mmol, 4.0 equiv) in dry pyridine (1 mL) was heated at

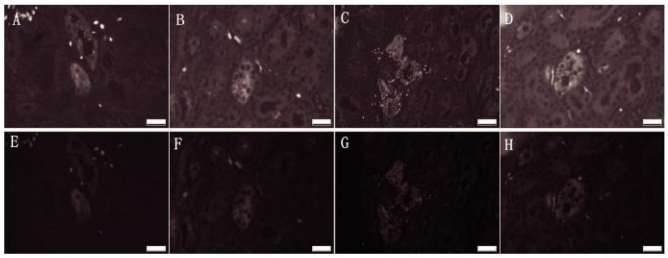

Figure 5. Neuropathological staining of Bowman's glands of the olfactory epithelium containing tau aggregates extracted from a deceased AD patient (male, 78 years old, Braak: V, CERAD-Score: 3). Probes **5a** (A and E), **5b** (B and F), **5c** (C and G) and **5f** (F and H) are clearly stained tau deposits. Scale bar = 25 μm (except C and G, where scale bar = 50 μm). Filter set 09 (A–D) and filter set 15 (E–H) were used for fluorescence microscopy. Staining protocol: All sections were immersed in 1 mM solution of compound in DMSO for 10 min and then washed with methanol. The sections were differentiated in 1% CH_3CO_2H for 20 min. After washing with running water for 5 min, the sections were treated with Roti-Mount FluorCare (Sigma–Aldrich) and covered with a coverslip.

reflux for 16 h under argon. The reaction mixture was cooled to room temperature, pyridine was removed in vacuo, and the residue was purified by column chromatography (SiO_2; CH_2Cl_2/MeOH, 10:1).

1,3,3-Trimethyl-2-((1*E*,3*E*)-3-(1,3,3-trimethylindolin-2-ylidene)-prop-1-enyl)-3*H*-indolium iodide (5a):[26] Purple solid (201 mg, 83%): ^{1}H NMR (500 MHz, [D$_6$]DMSO): δ = 8.34 (t, J = 13.5 Hz, 1H), 7.62 (d, J = 7.0 Hz, 2H), 7.46–7.42 (m, 4H), 7.32–7.27 (m, 2H), 6.44 (d, J = 13.5 Hz, 2H), 3.64 (s, 6H), 1.68 ppm (s, 12H); ^{13}C NMR (125 MHz, [D$_6$]DMSO): δ = 174.4, 149.6, 142.7, 140.6, 128.7, 125.3, 122.5, 111.5, 102.7, 48.9, 31.4, 27.4 ppm; UV/Vis (EtOH): λ_{max} = 547.0 nm; MS (EI, 70 eV): m/z 356 $[M-1]^+$; HRMS: m/z $[M]^+$ calcd for $C_{25}H_{29}N_2$: 357.2325, found: 357.2331.

1-Butyl-2-((1*E*,3*E*)-3-(1-butyl-3,3-dimethylindolin-2-ylidene)prop-1-enyl)-3,3-dimethyl-3*H*-indolium iodide (5b):[27] Purple solid (179 mg, 61%): ^{1}H NMR (500 MHz, [D$_6$]DMSO): δ = 8.36 (t, J = 13.5 Hz, 1H), 7.64 (d, J = 7.0 Hz, 2H), 7.49–7.41 (m, 4H), 7.30 (td, J = 7.5, 1.5 Hz, 2H), 6.58 (d, J = 13.5 Hz, 2H), 4.14 (t, J = 7.5 Hz, 4H), 1.77–1.71 (m, 4H), 1.70 (s, 12H), 1.48–1.40 (m, 4H), 0.94 ppm (t, J = 7.5 Hz, 6H); ^{13}C NMR (125 MHz, [D$_6$]DMSO): δ = 173.7, 149.8, 141.8, 140.5, 128.5, 125.1, 122.4, 111.5, 102.5, 48.8, 43.6, 29.1, 17.4, 19.5, 13.7 ppm; UV/Vis (EtOH): λ_{max} = 550.5 nm; MS (EI, 70 eV): m/z 442 $[M+1]^+$; HRMS: m/z $[M]^+$ calcd for $C_{31}H_{41}N_2$: 441.3264, found: 441.3270.

1-Decyl-2-((1*E*,3*E*)-3-(1-decyl-3,3-dimethylindolin-2-ylidene)prop-1-enyl)-3,3-dimethyl-3*H*-indolium bromide (5c): Purple solid (235 mg, 68%): ^{1}H NMR (500 MHz, [D$_6$]DMSO): δ = 8.35 (t, J = 13.5 Hz, 1H), 7.65 (d, J = 7.5 Hz, 2H), 7.47 (d, J = 7.5 Hz, 2H), 7.43 (td, J = 8.0, 1.0 Hz, 2H), 7.29 (td, J = 8.0, 1.0 Hz, 2H), 6.65 (d, J = 13.5 Hz, 2H), 4.15 (t, J = 7.5 Hz, 4H), 1.76–1.68 (m, 4H), 1.69 (s, 12H), 1.44–1.35 (m, 4H), 1.35–1.26 (m, 4H), 1.26–1.14 (m, 20H), 0.81 ppm (t, J = 7.0 Hz, 6H); ^{13}C NMR (125 MHz, [D$_6$]DMSO): δ = 173.6, 149.7, 141.7, 140.5, 128.5, 125.1, 122.4, 111.5, 102.7, 48.7, 43.7, 31.1, 28.8, 28.7, 28.7, 28.5, 27.3, 26.9, 25.9, 21.9, 13.8 ppm; UV/Vis (EtOH): λ_{max} = 551.0 nm; MS (EI, 70 eV): m/z 610 $[M]^+$; HRMS: m/z $[M]^+$ calcd for $C_{43}H_{65}N_2$: 609.5142, found: 609.5148.

1-(2-Methoxyethyl)-2-((1*E*,3*E*)-3-(1-(2-methoxyethyl)-3,3-dimethylindolin-2-ylidene)prop-1-enyl)-3,3-dimethyl-3*H*-indolium chloride (5d):[28] Colorless waxy solid (70 mg, 29%): ^{1}H NMR (500 MHz, [D$_6$]DMSO): δ = 8.39 (t, J = 13.0 Hz, 1H), 7.63 (d, J = 7.0 Hz, 2H), 7.48–7.40 (m, 4H), 7.29 (td, J = 8.0, 1.5 Hz, 2H), 6.53 (d, J = 13.5 Hz, 2H), 4.34 (t, J = 5.5 Hz, 4H), 3.26 (s, 6H), 1.70 ppm (s, 12H); ^{13}C NMR (125 MHz, [D$_6$]DMSO): δ = 174.5, 149.9, 142.2, 140.3, 128.4, 125.0, 122.3, 111.8, 103.0, 68.8, 58.6, 48.8, 44.1, 27.4 ppm; UV/Vis (EtOH): λ_{max} = 550.0 nm; MS (EI, 70 eV): m/z 445 $[M]^+$; HRMS: m/z $[M]^+$ calcd for $C_{29}H_{37}N_2O_2$: 445.2850, found: 445.2855.

1-(2-(2-(2-Methoxyethoxy)ethoxy)ethyl)-2-((1*E*,3*E*)-3-(1-(2-(2-(2-methoxyethoxy)ethoxy)ethyl)-3,3-dimethylindolin-2-ylidene)-prop-1-enyl)-3,3-dimethyl-3*H*-indolium chloride (5e):[28] Colorless waxy solid (125 mg, 38%): ^{1}H NMR (500 MHz, [D$_6$]DMSO): δ = 8.38 (t, J = 13.0 Hz, 1H), 7.63 (d, J = 7.0 Hz, 2H), 7.46 (d, J = 8.0 Hz, 2H), 7.42 (td, J = 8.0, 1.0 Hz, 2H), 7.29 (td, J = 8.0, 1.0 Hz, 2H), 6.55 (d, J = 13.5 Hz, 2H), 4.34 (t, J = 5.0 Hz, 4H), 3.82 (t, J = 5.0 Hz, 4H), 3.55–3.50 (m, 4H), 3.44–3.40 (m, 4H), 3.39–3.36 (m, 4H), 3.31–3.27 (m, 4H), 3.16 (s, 6H), 1.70 ppm (s, 12H); ^{13}C NMR (125 MHz, [D$_6$]DMSO): δ = 174.5, 149.7, 142.1, 140.3, 128.3, 125.0, 122.2, 111.9, 103.1, 71.1, 70.2, 69.7, 69.5, 67.1, 57.9, 48.8, 44.1, 27.4 ppm; UV/Vis (EtOH): λ_{max} = 551.5 nm; MS (EI, 70 eV): m/z 622 $[M+1]^+$.

5-Bromo-2-((1*E*,3*E*)-3-(5-bromo-1,3,3-trimethylindolin-2-ylidene)-prop-1-enyl)-1,3,3-trimethyl-3*H*-indolium iodide (5f):[26] Purple solid (186 mg, 58%): ^{1}H NMR (500 MHz, [D$_6$]DMSO): δ = 8.30 (t, J = 13.5 Hz, 1H), 7.93 (d, J = 2.0 Hz, 2H), 7.64 (dd, J = 8.5, 2.0 Hz, 2H), 7.42 (d, J = 8.5 Hz, 2H), 6.45 (d, J = 13.5 Hz, 2H), 3.63 (s, 6H), 1.68 ppm (s, 12H); ^{13}C NMR (125 MHz, [D$_6$]DMSO): δ = 174.1, 149.6, 142.7, 141.9, 131.2, 125.5, 117.4, 113.2, 103.1, 48.9, 31.5, 26.9, 26.2 ppm; UV/Vis (EtOH): λ_{max} = 556.0 nm; MS (EI, 70 eV): m/z 514 $[M-1]^+$

Biological evaluation

Immunohistochemical staining: Staining was carried out on 4 μm thick sections using a BenchMark automated stainer (Ventana, Tucson, AZ, USA). Antibodies anti-PHF-Tau clone AT8 (Thermo Scientific Pierce Protein Research Products, Rockford, USA), TAU Ab-3 (Neomarkers, Freemont, USA), and amyloid A4 (BAM10, Sigma, St. Louis, USA), and the Ultraview Universal DAB Detection Kit (Ventana) were applied in staining.

In vitro neuropathological staining of AD brain sections: Serial section (4 μm thickness) of paraffin-embedded brain sections from AD patients were used in these studies. The hippocampus (71 year old male) and olfactory epithelium (78 year old male) sections were deparaffinized and hydrated in distilled water. All sections were immersed in 1 mM solution of test compound in DMSO for 10 min and then washed with methanol. The sections were differentiated in 1% CH_3CO_2H for 20 min. After washing with running water for 5 min, the sections were treated with Roti-Mount FluorCare (Sigma–Aldrich) and covered with a coverslip. All sections were analyzed by fluorescence microscopy using a Axioskop microscope with a HBO100 fluorescence illuminator (Carl Zeiss, Oberkochem, Germany) with the bandpass filter set 09 BP450-490, FT510, LP515,

the filter set 02 G365, FT395, LP420, and the filter set 15 BP546, FT580, LP590 (all Carl Zeiss, Oberkochem, Germany). Informed signed consent for use of human tissue was obtained from either the patient or next of kin.

In vivo zebrafish embryo cytotoxicity assay: Zebrafish were raised on a 14 h/10 h light–dark cycle at 26.0±0.5 °C. Embryos were obtained by natural mating and cultured in water. The embryos were selected and placed into 24-well plates with ten embryos per well. Embryos were allowed to develop to more than 50% epiboly (around 6 hpf) and then treated with 5 μM and 10 μM test compound in E2 solution. Phenotypes were detected by using an Axio Scope A1 microscope system from Carl Zeiss at 24 hpf. All experiments in this study were carried out according to the ethical and welfare principles outlined in legislation on animal research in Germany.

In vitro cell proliferation assay: Human liver hepatocellular carcinoma cells (HepG2) were incubated with 0.1 μM, 1 μM, 10 μM and 20 μM of test compound for 24 h. Afterwards, cells were washed three times with phosphate-buffered saline (PBS), and CellTiter 96 AQueous non-radioactive cell proliferation assay reagent (Promega, Madison, USA) was added to the samples. This colorimetric assay is based on the reduction of 3-(4,5-dimethylthiazol-2-yl)-5-(3-carboxymethoxyphenyl)-2-(4sulfophenyl)-2*H*-tetrazolium (MTS) to the corresponding formazan product by intrinsic dehydrogenases by living cells, which was measured photometrically at $\lambda = 492$ nm using a microplate reader (Tecan, Crailsheim, Germany). To quantify the number of viable cells, absorbances of treated samples were normalized to untreated controls (percent of nontreated controls). EC_{50} values, the concentration required to decrease cell viability by 50% compared with untreated controls, were determined from the best-fitted trend line of a plot of cell viability as a function of compound concentration. For subcultivation and incubation procedures, HepG2 cells were maintained in Dulbecco's modified Eagle's medium (DMEM)/F12 1+1 supplemented with 10% fetal bovine serum and cultivated under sterile conditions in the humidified incubator (37 °C, 5% CO_2, 95% humidity) without antibiotics. Mycoplasma contamination could be excluded via routinely examinations (polymerase chain reaction).

In vitro thiazine red R displacement assay: Test compound was added at different concentrations to the assay ranging from 0.1–10000 nM. For the inhibition curve, the compound was measured together with the aggregated proteins and thiazine red R. The assay was performed in a PerkinElmer OptiPlate 384, black, 45 μL assay volume. Dulbecco's phosphate-buffered saline (DPBS) without $CaCl_2/MgCl_2$ (GIBCO no. 14020) was used as an assay buffer. Tested compound solutions were diluted in DMSO, and 2 μL of the solution was added to the assay (5% DMSO final concentration). The assay was started by the addition of the aggregated protein (competitive condition). The plates were shortly shaken (1 min with Sterico variomag teleshake) and incubated at room temperature for 30 min. Measurements were performed with En:Vision (PerkinElmer), at excitation 531 nm/emission 595 nm. IC_{50} values, the concentration required to inhibit binding by 50% compared with untreated controls, were calculated using the Levenburg Marquardt algorithm (see Supporting Information).[37]

Acknowledgements

This work was supported by grants from the German Federal Ministry of Education and Research (13N10636) and the Hans and Ilse Breuer Foundation (Frankfurt-am-Main, Germany).

Keywords: Alzheimer's disease · imaging agents · neurodegenerative diseases · neurofibrillary tangles · olfactory epithelium

[1] R. Jakob-Roetne, H. Jacobsen, *Angew. Chem.* **2009**, *121*, 3074–3105; *Angew. Chem. Int. Ed.* **2009**, *48*, 3030–3059.
[2] C. Ballard, S. Gauthier, A. Corbett, C. Brayne, D. Aarsland, E. Jones, *Lancet* **2011**, *377*, 1019–1031.
[3] D. J. Selkoe, *Physiol. Rev.* **2001**, *81*, 741–766.
[4] M. Citron, *Nat. Rev. Drug Discovery* **2010**, *9*, 387–398.
[5] A. B. Newberg, N. A. Wintering, K. Plössl, J. Hochold, M. G. Stabin, M. Watson, D. Skovronsky, C. M. Clark, M. P. Kung, H. F. Kung, *J. Nucl. Med.* **2006**, *47*, 748–754.
[6] A. G. Vlassenko, T. L. Benzinger, J. C. Morris, *Biochim. Biophys. Acta, Mol. Basis Dis.* **2012**, *1822*, 370–379.
[7] A. Nordberg, *Lancet Neurol.* **2004**, *3*, 519–527.
[8] H. F. Kung, *ACS Med. Chem. Lett.* **2012**, *3*, 265–267.
[9] M. N. Braskie, A. D. Klunder, K. M. Hayashi, H. Protas, V. Kepe, K. J. Miller, S. C. Huang, J. R. Barrio, L. M. Ercoli, P. Siddarth, N. Satyamurthy, J. Liu, A. W. Toga, S. Y. Bookheimer, G. W. Small, P. M. Thompson, *Neurobiol. Aging* **2010**, *31*, 1669–1678.
[10] C. A. Mathis, B. J. Bacskai, S. T. Kajdasz, M. E. McLellan, M. P. Frosch, B. T. Hyman, D. P. Holt, Y. Wang, G. F. Huang, M. L. Debnath, W. E. Klunk, *Bioorg. Med. Chem. Lett.* **2002**, *12*, 295–298.
[11] N. Okamura, T. Suemoto, S. Furumoto, M. Suzuki, H. Shimadzu, H. Akatsu, T. Yamamoto, H. Fujiwara, M. Nemoto, M. Maruyama, H. Arai, K. Yanai, T. Sawada, Y. Kudo, *J. Neurosci.* **2005**, *25*, 10857–10862.
[12] M. T. Fodero-Tavoletti, N. Okamura, S. Furumoto, R. S. Mulligan, A. R. Connor, C. A. McLean, D. Cao, A. Rigopoulos, G. A. Cartwright, G. O'Keefe, S. Gong, P. A. Adlard, K. J. Barnham, C. C. Rowe, C. L. Masters, Y. Kudo, R. Cappai, K. Yanai, V. L. Villemagne, *Brain* **2011**, *134*, 1089–1100.
[13] B. Bulic, M. Pickhardt, B. Schmidt, E.-M. Mandelkow, H. Waldmann, E. Mandelkow, *Angew. Chem.* **2009**, *121*, 1772–1785; *Angew. Chem. Int. Ed.* **2009**, *48*, 1740–1752.
[14] A. Boutajangout, E. Sigurdsson, P. Krishnamurthy, *Curr. Alzheimer Res.* **2011**, *8*, 666–677.
[15] W. Zhang, J. Arteaga, D. K. Cashion, G. Chen, U. Gangadharmath, L. F. Gomez, D. Kasi, C. Lam, Q. Liang, C. Liu, V. P. Mocharla, F. Mu, A. Sinha, A. K. Szardenings, E. Wang, J. C. Walsh, C. Xia, C. Yu, T. Zhao, H. C. Kolb, *J. Alzheimer's Dis.* **2012**, *31*, 601–612.
[16] C. F. Xia, J. Arteaga, G. Chen, U. Gangadharmath, L. F. Gomez, D. Kasi, C. Lam, Q. Liang, C. Liu, V. P. Mocharla, F. Mu, A. Sinha, H. Su, A. K. Szardenings, J. C. Walsh, E. Wang, C. Yu, W. Zhang, T. Zhao, H. C. Kolb, *Alzheimer's Dementia* **2013**, DOI: 10.1016/j.jalz.2012.11.008.
[17] J. Rao, A. Dragulescu-Andrasi, H. Yao, *Curr. Opin. Biotechnol.* **2007**, *18*, 17–25.
[18] Y. Koronyo, B. C. Salumbides, K. L. Black, M. Koronyo-Hamaoui, *Neurodegener. Dis.* **2012**, *10*, 285–293.
[19] A. Boländer, D. Kieser, C. Voss, S. Bauer, C. Schön, S. Burgold, T. Bittner, J. Holzer, R. Heyny-von Haussen, G. Mall, V. Goetschy, C. Czech, H. Knust, R. Berger, J. Herms, I. Hilger, B. Schmidt, *J. Med. Chem.* **2012**, *55*, 9170–9180.
[20] C. Schön, N. A. Hoffmann, S. M. Ochs, S. Burgold, S. Filser, S. Steinbach, M. W. Seeliger, T. Arzberger, M. Goedert, H. A. Kretzschmar, B. Schmidt, J. Herms, *PloS One* **2012**, *7*, e53547.
[21] J. Gu, U. R. Anumala, F. Lo Monte, T. Kramer, R. Heyny von Haussen, J. Holzer, V. Goetschy-Meyer, G. Mall, I. Hilger, C. Czech, B. Schmidt, *Bioorg. Med. Chem. Lett.* **2012**, *22*, 7667–7671.
[22] A. Yuan, J. Wu, X. Tang, L. Zhao, F. Xu, Y. Hu, *J. Pharm. Sci.* **2013**, *102*, 6–28.
[23] S. K. Ko, X. Chen, J. Yoon, I. Shin, *Chem. Soc. Rev.* **2011**, *40*, 2120–2130.
[24] F. Lo Monte, T. Kramer, J. Gu, U. R. Anumala, L. Marinelli, V. La Pietra, E. Novellino, B. Franco, D. Demedts, F. Van Leuven, A. Fuertes, J. M. Dominguez, B. Plotkin, H. Eldar-Finkelman, B. Schmidt, *J. Med. Chem.* **2012**, *55*, 4407–4424.
[25] N. Gonsar, A. C. Schumann, J. N. Buchard, J. O. Liang, *Zebrafish* **2012**, *9*, 50–55.
[26] A. K. Pandey, P. C. Deakin, R. D. Jansen-Van Vuuren, P. L. Burn, I. D. Samuel, *Adv. Mater.* **2010**, *22*, 3954–3958.

[27] B. Sauerwein, G. B. Schuster, *J. Phys. Chem.* **1991**, *95*, 1903 – 1906.
[28] B. Schmidt, D. Kieser, A. Boländer, J. Herms, R. Heyny-von Haussen, (Klinikum Darmstadt GmbH, Ludwig-Maximilians-Universität München, Technische Universität Darmstadt), PCT Pat. Appl. WO 2012/037928, **2012**.
[29] R. E. F. Boto, R. M. El-Shishtawy, P. F. Santos, L. V. Reis, P. Almeida, *Dyes Pigm.* **2007**, *73*, 195 – 205.
[30] H. J. Karlsson, M. H. Bergqvist, P. Lincoln, G. Westman, *Bioorg. Med. Chem.* **2004**, *12*, 2369 – 2384.
[31] J. Sutharsan, M. Dakanali, C. Capule, M. Haidekker, J. Yang, E. Theodorakis, *ChemMedChem* **2010**, *5*, 56 – 60.
[32] R. Narlawar, M. Pickhardt, S. Leuchtenberger, K. Baumann, S. Krause, T. Dyrks, S. Weggen, E. Mandelkow, B. Schmidt, *ChemMedChem* **2008**, *3*, 165 – 172.
[33] W. E. Klunk, B. J. Bacskai, C. A. Mathis, S. T. Kajdasz, M. E. McLellan, M. P. Frosch, M. L. Debnath, D. P. Holt, Y. Wang, B. T. Hyman, *J. Neuropathol. Exp. Neurol.* **2002**, *61*, 797 – 805.
[34] S. E. Arnold, E. B. Lee, P. J. Moberg, L. Stutzbach, H. Kazi, L. Y. Han, V. M. Lee, J. Q. Trojanowski, *Ann. Neurol.* **2010**, *67*, 462 – 469.
[35] W. Ying, *Future Neurol.* **2008**, *3*, 1 – 4.
[36] D. Kieser, Ph.D. Dissertation **2011**, Technische Universität Darmstadt (Germany).
[37] G. Cumming, F. Fidler, D. L. Vaux, *J. Cell Biol.* **2007**, *177*, 7 – 11.

Received: February 25, 2013
Published online on April 16, 2013

Supporting Information

Contents:

In vitro cell proliferation assay

To evaluate the impact of our compounds (**5a-f**) on cell metabolism, human liver hepatocellular carcinoma cells (HepG2) were incubated with 0.1, 1 µM, 10 µM and 20 µM of our compounds for 24 hours. Afterwards, cells were washed three times with PBS and CellTiter 96®AQueous non-radioactive cell proliferation assay reagent (Promega, Madison, USA) was added to the samples. This colorimetric assay is based on the reduction of tetrazolium salt [3-(4,5-dimethylthiazol-2-yl)-5-(3-carboxymethoxyphenyl)-2-(4sulfophenyl)-2*H*-tetrazolium, inner salt; MTS] into a formazan product by intrinsic dehydrogenases of living cells, which was measured photometrically at λ = 492 nm using a microplate reader (Tecan, Crailsheim, Germany). To quantify the number of viable cells, absorbances of treated samples were normalized to untreated controls (percent of nontreated controls). Thus cell viability values between 70 % and 120 % represent neither cytotoxic nor proliferative effects on HepG2 and loss of cell viability over 30 % characterizes a substance as cytotoxic, according to the DIN ISO 10993-5:2009. EC_{50} values, which declare the concentration at which cell viability decreases to 50 % due to dye incubation, were calculated via the best-fitted trendline of cell viability as a function of dye concentration. For subcultivation and incubation procedures, HepG2 cells were maintained in DMEM/F12 1+1 supplemented with 10 % fetal bovine serum and cultivated under sterile conditions in the humidified incubator (37 °C, 5 % CO_2, 95 % humidity) without antibiotics. Mycoplasma contamination could be excluded via routinely examinations (PCR).

Cell Toxicity of Dyes (5a-f) on HepG2 cells

- HepG2: human liver carcinoma

- Incubation time: 24 hours

- MTS-Assay after incubation times

- Explanation: MW ... mean (cell vitality, n=6); STABW ... standard deviation

Compound **5a**:

	0.1 µM	1 µM	10 µM	20 µM
MW	191.67	207.73	164.04	166.16
STABW	1.75	1.58	3.32	10.61

Compound **5b**:

	0.1 µM	1 µM	10 µM	20 µM
MW	102.79	31.94	16.46	-2.31
STABW	7.43	2.34	11.85	2.28

Compound **5c**:

	0.1 µM	1 µM	10 µM	20 µM
MW	94.20	84.68	0.00	0.00
STABW	7.09	6.96	0.00	0.00

Compound **5d**:

	0.1 µM	1 µM	10 µM	20 µM
MW	74.80	69.95	37.27	40.70
STABW	4.40	1.86	5.11	2.02

Compound **5e**:

	0.1 µM	1 µM	10 µM	20 µM
MW	224.95	206.28	217.54	191.85
STABW	7.00	6.12	2.65	2.38

Compound **5f**:

	0.1 µM	1 µM	10 µM	20 µM
MW	115.86	91.44	0.00	0.09
STABW	11.51	1.49	2.64	2.98

In vitro Thiazine Red R displacement assay

To determine the affinity of a displacer compound to the *Thiazine Red R* binding sites of the aggregated proteins, the compound was added at different concentrations to the assay ranging from 0.1 nM to 10000 nM. For the inhibition curve, the compound was measured together with the aggregated proteins and *Thiazine Red R*. The fluorescence of some dyes overlapped with the fluorescence of *Thiazine Red R* when measured at 595 nm. Therefore, compounds were also measured together with the aggregated proteins, but without *Thiazine Red R* (autofluorescence curve). Net-fluorescence was calculated by subtracting the fluorescence of the wells without *Thiazine Red R* from the fluorescence of wells containing *Thiazine Red R* (inhibition curve). As negative control *Thiazine Red R* and aggregated protein was used. As positive control, *Thiazine Red R*, reference compound with known activity and aggregated protein was used. The assay was performed in Perkin Elmer OptiPlate 384, black, 45 mL assay volume. As assay buffer DPBS (no $CaCl_2$ no $MgCl_2$) (GIBCO N. 14020) was used. The tested compounds were diluted in DMSO and 2 µL of the solution was added to the assay (5 % DMSO final). The assay was started by the addition of the aggregated protein (competitive condition). The plates were shortly shaken (1 min with Sterico variomag teleshake) and incubated at room temperature for 30 min. Measurements were performed with En:Vision (Perkin Elmer), at Excitation 531 nm / Emission 595 nm.

Corresponding IC_{50} values (inhibitory concentration for 50% decrease) were calculated using the Levenburg Marquardt algorithm:

y = A + ((B-A)/(1+((C/x)^D)))

Item	Description
A	The bottom plateau of the curve corresponds to the final minimum y value.
B	The top of the plateau of the curve corresponds to the final maximum y value.

C	The IC_{50} value represents the x value at which the half maximum y value is attained.
D	The slope factor. In this model a positive value is returned when y increases with increasing x and a negative value when y increases as x is decreasing.
x	Concentration of the tested compound (nM)
y	Net fluorescence in % of controls.

The obtained values are the average values of replicate experiments. The statistical presentation follows the guidelines laid out by G. Cumming, J. *Cell Biology*, **2007**, *177*, 7-11.

Determination of IC_{50} values for different compounds on aggregated proteins using the *Thiazine Red R* assay. Data represent average of technical replicates.

	Aggr. tau - IC_{50} (nM)	Aggr. Aß$_{40}$ - IC_{50} (nM)
Evans Blue	1.0	89
Congo Red	5.4	14
Hondson 1d*	8.8	13
BSB	18	78
MeXO4	246	140
Crystal Violet	1545	1280
FDDNP	1635	1467
IMPY	2707	5671

PIB	3255	5190
AZD2184	9802	>10000
FENE	>10000	>10000
BF-158	>10000	>10000

* Compound Honson 1d from Honson et al, *Neurobiol Dis.* **2007**, 28(3), 251-60.

Figure 1

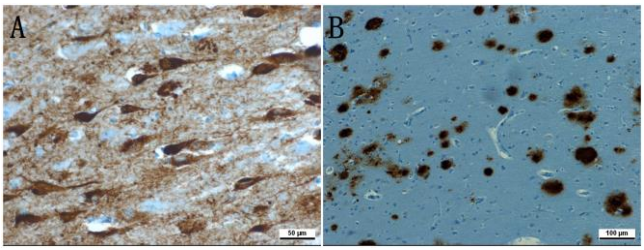

Figure 1 Immunohistochemical staining of hippocampal sections: NFTs with antibody AT8 mAb (A) and Aβ plaques with antibody amyloid A4 (B).

Figure 2

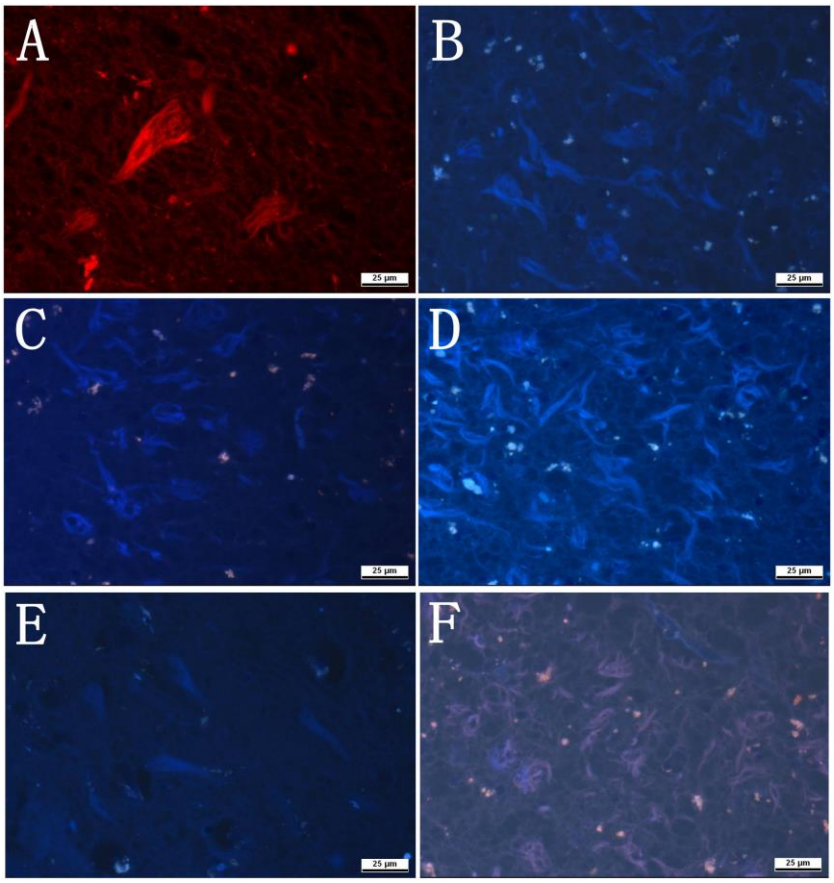

Figure 2 Neuropathological staining of brain sections from the hippocampus of an AD patient (A-F). Probes **5a** (A), **5b** (B), **5c** (C), **5d** (D), **5e** (E) and **5f** (F) are clearly stained neurofibrillary tangles (Tissues: hippocampus; Patient: male, 71 years old, CERAD-Score: 3, NFTs-level: V). Filter set 15 (A) and filter set 02 (B-F) were used for fluorescence microscopy.

Figure 4

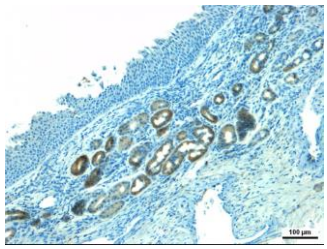

Figure 4 Immunohistological staining of Bowman's glands of the olfactory epithelium containing tau aggregates (Patient: male, 78 years old, Braak: V, CERAD-Score: 3) with antibody TAU Ab-3.

Figure 5

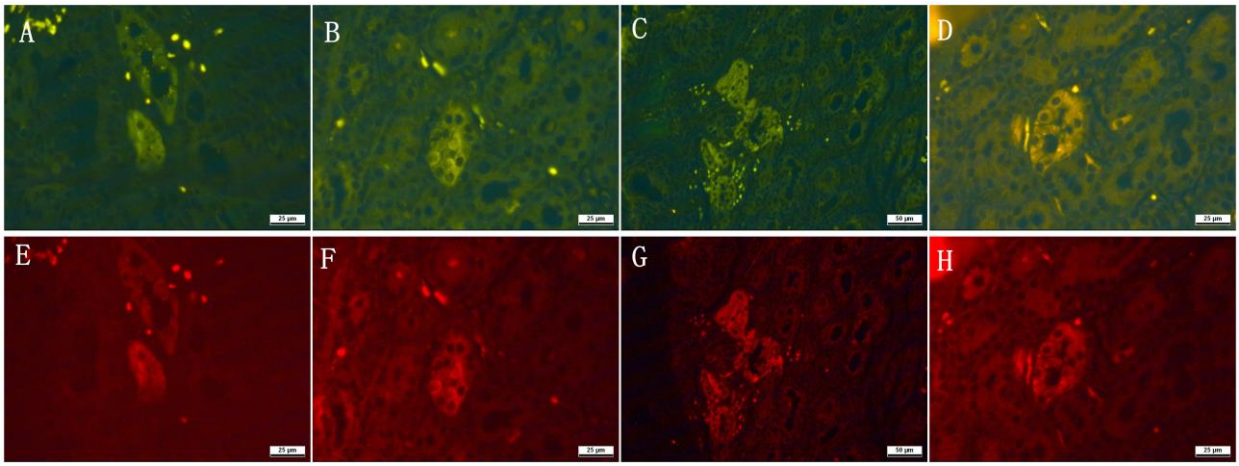

Figure 5 Neuropathological staining of Bowman's glands of the olfactory epithelium containing tau aggregates extracted from a deceased AD patient (Patient: male, 78 years old, Braak: V, CERAD-Score: 3). Probes **5a** (A and E), **5b** (B and F), **5c** (C and G) and **5f** (F and H) are clearly stained tau deposits. (Tissues: olfactory epithelium; Patient: male, 78 years old; Braak: V, CERAD-Score: 3). Filter set 09 (A-D) and filter set 15 (E-H) were used for fluorescence microscopy. Staining protocol: All sections were immersed in 1 mM solution of compound in DMSO for 10 minutes and then washed with methanol. The sections were differentiated in 1% CH_3COOH for 20 min. After washing with running water for 5 min, the sections were treated with Roti®-Mount FluorCare (from Sigma-Aldrich) and covered with coverslip.

3.1.5 Identification of Glycogen Synthase Kinase-3 Inhibitors with a Selective Sting for Glycogen Synthase Kinase-3α

The content of this chapter has been published

Fabio Lo Monte, Thomas Kramer, Jiamin Gu, Upendra Rao Anumala, Luciana Marinelli, Valeria La Pietra, Ettore Novellino, Bénédicte Franco, David Demedts, Fred Van Leuven, Ana Fuertes, Juan Manuel Dominguez, Batya Plotkin, Hagit Eldar- Finkelman, and Boris Schmidt

Identification of Glycogen Synthase Kinase-3 Inhibitors with a Selective Sting for Glycogen Synthase Kinase-3α, *Journal of Medicinal Chemistry* **2012**, 55, 4407-4424.

Summary

Alzheimer's disease is a neurodegenerative disorder defined by progressive memory loss and cognitive impairment. The presence of extracellular senile plaques (SPs), aggregates of β-amyloid and intracellular neurofibrillary tangles (NFTs), aggregates of hyperphosphorylated tau protein may cause the disease. In the late 1970s, glycogen synthase kinase-3 (GSK-3) was identified. It is a constituently active, ubiquitous serine/threonine kinase. GSK-3 has been linked to all primary abnormalities associated with AD. Two related isoforms of GSK-3 exist in mammals, GSK-3α and β, which share 98% of homology in their catalytic domain and have similar biochemical properties.

In the present study, SAR studies of three different structures which are all based on a central oxazole moiety were performed. Inhibitory activity against GSK-3α and β, and kinase selectivity experiments of several derivatives were also performed. Highly potent inhibitors were tested for their in vivo activity in a zebrafish embryo assay.

Contribution of Upendra Rao Anumala: Support in zebrafish embryo assay and manuscript preparation.

Journal of Medicinal Chemistry

Article

pubs.acs.org/jmc

Identification of Glycogen Synthase Kinase-3 Inhibitors with a Selective Sting for Glycogen Synthase Kinase-3α

Fabio Lo Monte,*[,†] Thomas Kramer,[†] Jiamin Gu,[†] Upendra Rao Anumala,[†] Luciana Marinelli,[‡] Valeria La Pietra,[‡] Ettore Novellino,[‡] Bénédicte Franco,[§] David Demedts,[§] Fred Van Leuven,[§] Ana Fuertes,[∥] Juan Manuel Dominguez,[∥] Batya Plotkin,[⊥] Hagit Eldar-Finkelman,[⊥] and Boris Schmidt*[,†]

[†]Clemens Schöpf—Institute of Organic Chemistry and Biochemistry, Technische Universität Darmstadt, 64287 Darmstadt, Germany

[‡]Dipartimento di Chimica Farmaceutica e Tossicologica, Università di Napoli "Federico II", 80131 Napoli, Italy

[§]Experimental Genetics Group, Department of Human Genetics, Katholieke Universiteit Leuven, 3000 Leuven, Belgium

[∥]Noscira SA, Drug Discovery, Tres Cantos 28760-Madrid, Spain

[⊥]Department of Human Molecular Genetics and Biochemistry, Sackler School of Medicine, Tel Aviv University, 69978 Tel Aviv, Israel

Supporting Information

ABSTRACT: The glycogen synthase kinase-3 (GSK-3) has been linked to the pathogenesis of colorectal cancer, diabetes, cardiovascular disease, acute myeloid leukemia (AML), and Alzheimer's disease (AD). The debate on the respective contributions of GSK-3α and GSK-3β to AD pathology and AML is ongoing. Thus, the identification of potent GSK-3α-selective inhibitors, endowed with favorable pharmacokinetic properties, may elucidate the effect of GSK-3α inhibition in AD and AML models. The analysis of all available crystallized GSK-3 structures provided a simplified scheme of the relevant hot spots responsible for ligand binding and potency. This resulted in the identification of novel scorpion shaped GSK-3 inhibitors. It is noteworthy, compounds **14d** and **15b** showed the highest GSK-3α selectivity reported so far. In addition, compound **14d** did not display significant inhibition of 48 out of 50 kinases in the test panel. The GSK-3 inhibitors were further profiled for efficacy and toxicity in the wild-type (wt) zebrafish embryo assay.

INTRODUCTION

Alzheimer's disease (AD), first described by Alois Alzheimer in 1906, is the most common dementia at old age. AD is characterized by the presence of two abnormal protein deposits: amyloid plaques composed of extracellular deposits of β-amyloid (Aβ) peptides and neurofibrillary tangles (NFTs) are formed by the accumulation of insoluble and hyperphosphorylated tau.[1−3] The 40−42 amino acid β-amyloid peptide is the major component of the amyloid deposits. It is produced from a larger protein, the amyloid precursor protein (APP), by proteolytic cleavage.[4] Tau is a soluble microtubule-binding protein which stabilizes the microtubules in axons.[2] Hyperphosphorylation of tau protein causes destabilization of microtubules and subsequent dissociation of tau, which in turn aggregates to form NFTs.[5] GSK-3 was identified ~30 years ago and is a serine/threonine protein kinase that participates in a plethora of cellular processes, e.g., cell proliferation, microtubule dynamics, and gene transcription.[6−8] Several studies have linked glycogen synthase kinase-3 (GSK-3) to the primary abnormalities associated with AD, particularly the phosphorylation of tau.[4,9] Two closely related isoforms GSK-3α and GSK-3β are present in mammals.[10] They share 97% sequence similarity within their catalytic kinase domains.[7] GSK-3β has been proposed as the major kinase of tau phosphorylation, suggesting it as a potential, yet risky target for the therapy of AD.[1,5] Dysregulation of GSK-3β has been associated with diseases such as diabetes, Down's syndrome, bipolar disorder, colorectal cancer, and AD.[11] The inhibition of GSK-3α was suggested for the treatment of AD and other CNS diseases.[12−14] Furthermore, GSK-3α inhibition was proposed to modulate β-adrenergic signaling.[15] Recently, it was suggested that GSK-3α is involved in acute myeloid leukemia (AML), supporting a potential role for GSK-3α directed therapy.[16] Yet, the distinct contributions of both GSK-3 isoforms are still unknown. Appropriately, a number of pan-GSK-3α/β inhibitors have been disclosed because of the structure determination of GSK-3β.[17] Lithium chloride is the most thoroughly investigated GSK-3 inhibitor in AD animal models; it results in decreased tau hyperphosphorylation and decreased Aβ levels.[6] However, it is limited by a small therapeutic window. GSK-3 inhibitors were identified from remarkably different classes: organometallic compounds, paullones, indirubins, maleimides, thiadiazolidinones, L803-mts, ureas, and other small organic molecules.[4,10,18−24]

Received: March 5, 2012
Published: April 25, 2012

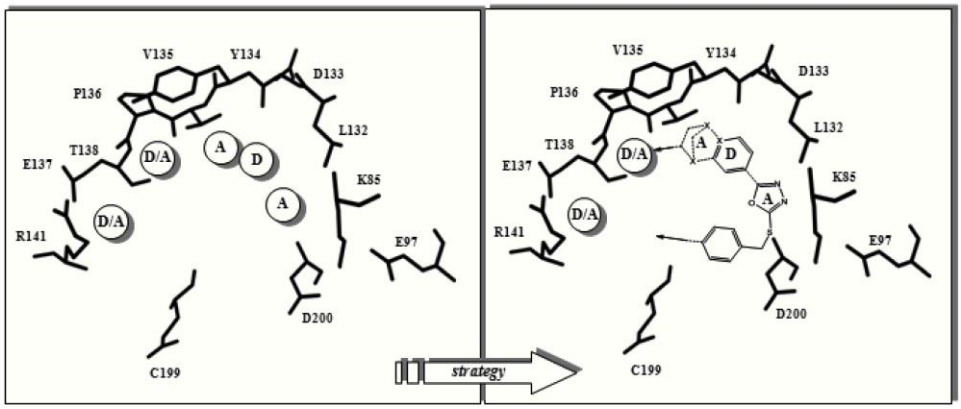

Figure 1. Synthesis strategy based on hot spot analysis of GSK-3 inhibition. The denoted acceptor (A) and donor (D) domains outline the necessary atoms respectively functional groups in the designated areas (left/right). The scaffold **I** used for the synthesis is marked on the right. X stands for heteroatoms.

Scheme 1[a]

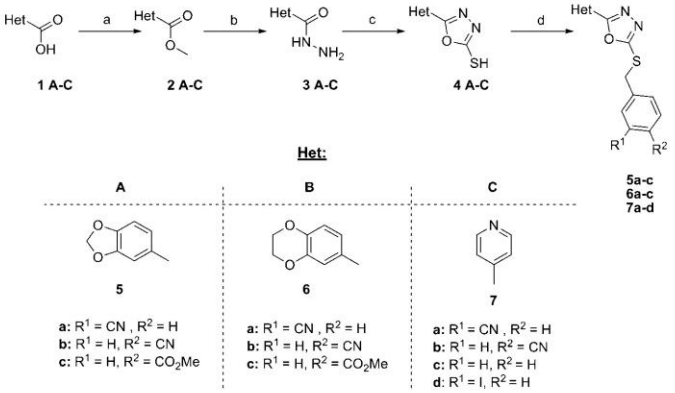

[a]Reagents and conditions: (a) MeOH, $SOCl_2$, 0−50 °C, 83−89%; (b) $NH_2NH_2{\cdot}H_2O$, EtOH, reflux, 67−75%; (c) CS_2, Et_3N, EtOH, reflux, 79−89%; (d) benzyl halides, 1N NaOH, DMF, rt, 41−84%.

All GSK-3 inhibitors, except for the thiadiazolidinones and L803-mts, are ATP competitive inhibitors and all of them inhibit the two isoforms, GSK-3α and GSK-3β, with similar potency.[6] The design of selective ligands remains a challenge despite several crystallized GSK-3 inhibitor complexes and substantial differences revealed by GSK-3α/GSK-3β sequence comparison as the major part of the ligand binding site is conserved.[17] Here we report the synthesis and optimization of novel GSK-3 inhibitors, along with their α/β selectivity and the evaluation of their in vivo efficacy in zebrafish embryos, which is an established model system for the validation of GSK-3 inhibitors. The oxadiazole moiety (scaffold **I**; Figure 1) was chosen as lead structure as it provided, if appropriately decorated, high inhibition of GSK-3β.[5,25,26]

The optimization process took advantage of the available cocrystallized GSK-3β inhibitor complexes and the analysis of the relevant hot spots (Figure 1). Most GSK-3 inhibitors occupy three or at most four acceptor/donor domains in the active site. Our main intention was the engagement with as many as possible acceptor/donor areas as depicted in Figure 1. Initially, we investigated the enlargement of **I** to reach R141. Subsequently, different substituents on the heterocyclic scaffold were explored in order to enhance the interaction with the enzyme backbone and to improve solubility at the same time. Most of the resulting compounds were tested for the selective inhibition of GSK-3α/β.

■ CHEMISTRY

The esterification of the carboxylic acids **1A−C** afforded the compounds **2A−C**,[27,28] which were converted to the hydrazides **3A−C**.[28,29] Reaction of the hydrazides **3A−C** with carbon disulfide (CS_2) resulted in the oxadiazoles **4A−C**.[30,31] The heterocyclic derivatives **5a−c**, **6a−c**, and **7a−c**[32] were prepared by benzylation of the mercaptanes **4A−C** (Scheme 1).[26]

Scheme 2[a]

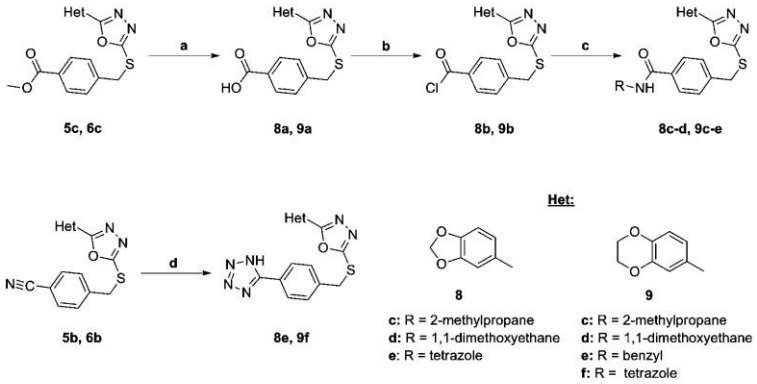

[a]Reagents and conditions: (a) 1N LiOH, THF, 60 °C, 83−91%; (b) $SOCl_2$, toluene, reflux; (c) amine, K_2CO_3, acetone, 0 °C to rt, 79−92%; (d) NaN_3, NH_4Cl, DMF, 100 °C, 67−79%.

Scheme 3[a]

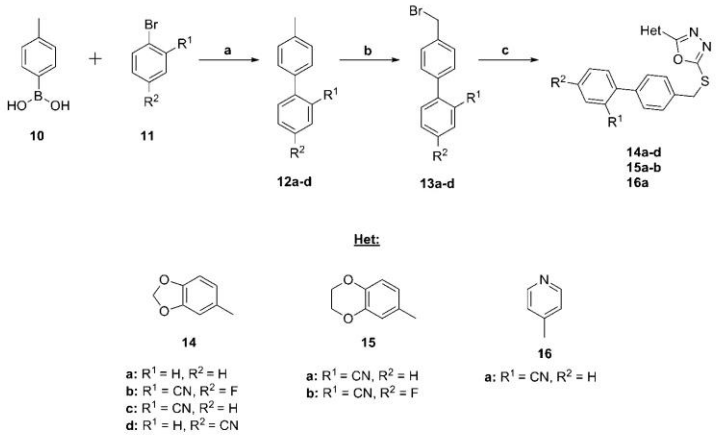

[a]Reagents and conditions: (a) aryl bromide, toluene, EtOH, $Pd(PPh_3)_4$, 2-tolylboronic acid, 2N Na_2CO_3 (aq), 80 °C; (b) NBS, AIBN, CCl_4, reflux; (c) **4**(**A**−**C**), 1N NaOH, DMF, rt, 53−75%.

Compound **7d** is commercially available. The esters **5c** and **6c** were converted to the carboxylic acids **8a** and **9a**, followed by treatment with thionyl chloride ($SOCl_2$) to form the acyl chlorides **8b** and **9b**.[33,34] Coupling of the acyl chlorides with primary amines gave the amides **8c−d** and **9c−e**.[34] The tetrazoles **8e** and **9f** were prepared from the nitriles **5b** and **6b** using sodium azide under microwave irradiation (Scheme 2).[35]

The biphenylic derivatives **13a−d** were prepared in two steps from the commercially available *p*-tolylboronic acid and substituted bromobenzenes. The 4′-(bromomethyl)biphenyl-2-carbonitrile is commercially available. The biphenylmethyl halides were coupled to the mercaptothiadiazoles **4A−C** to obtain the thioethers **14a−d**, **15a−b**, and **16a** (Scheme 3).[26] 3,4-Dihydroxybenzoic acid **17** was esterified to the methyl ester **18**, followed by cyclization with (±)-glycidyl tosylate or epibromohydrin to afford compound **19a**[36] as a mixture of enantiomers.[37−39] The hydrazide **21a** was prepared by methylation of **19a**, followed by the addition of hydrazine.[40] The reaction of the hydrazide **21a** with CS_2 gave the oxadiazole **22a**, which was coupled to 4′-(bromomethyl)biphenyl-2-carbonitrile to afford the thioether **23a**. The methyl ether in **23a** was cleaved by boron tribromide (BBr_3) to result in the alcohol **24a** (Scheme 4).[40] The compounds **23b−c** and **24a−b** were prepared under similar conditions; see Scheme 4. (*S*)-(+)-Glycidyl tosylate was used to obtain the *R*-enantiomer of compound **19b**.[37] The *S*-enantiomer of compound **19** was synthesized using (*R*)-(−)-glycidyl tosylate.[37] Mesylation of the alcohol **24b** and subsequent displacement of the mesylate by an amine afforded the acetal **26** (Scheme 4).[40]

Scheme 4[a]

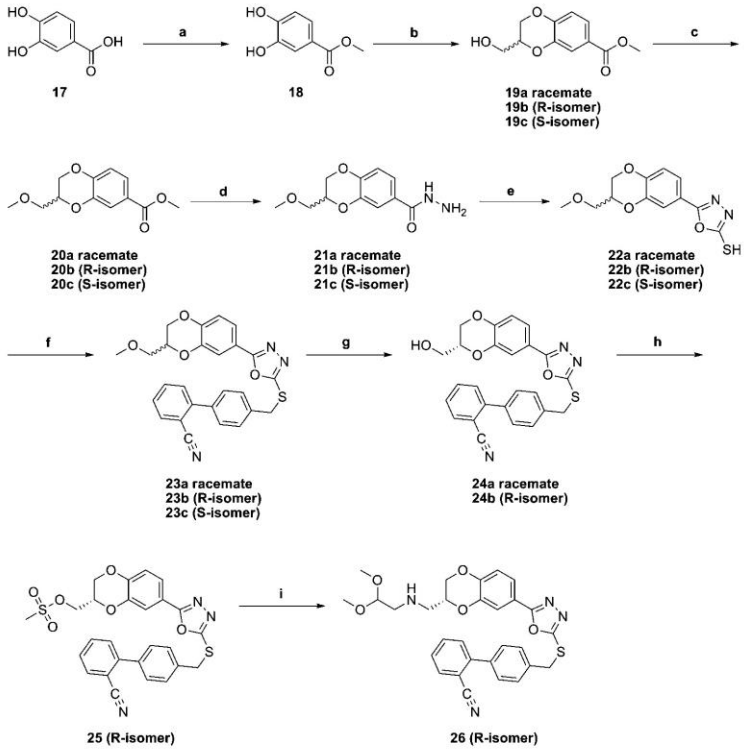

[a]Reagents and conditions: (a) $SOCl_2$, MeOH, 0−50 °C, 97%; (b) (*R*/*S*)-(±)-glycidyl tosylate or epibromohydrin, (*S*)-(+)-glycidyl tosylate or (*R*)-(−)-glycidyl tosylate, K_2CO_3, acetone or DMF, rt or 60 °C, 93−95%; (c) NaH, CH_3I, THF, 0 °C to rt, 68−71%; (d) $NH_2NH_2{\cdot}H_2O$, EtOH, reflux, 78−87%; (e) CS_2, Et_3N, EtOH, reflux, 81−91%; (f) biphenyl halide, 1N NaOH, DMF, rt, 84−88%; (g) BBr_3, DCM, −78 °C to rt; 73−79%; (h) CH_3SO_2Cl, Et_3N, DCM, 0 °C to rt, 98%; (i) amine, THF, Et_3N, 0 °C to reflux, 83%.

■ RESULTS AND DISCUSSION

Molecular Modeling. Compound **15a**, one of the most active inhibitors of the series, was docked, through Glide software, into the GSK-3β active site (PDB code: 3F88) with the aim to assess the ligand−protein interactions and to rationalize the SARs.[26] The docking experiments suggest that the oxadiazole ring positions itself in between the V70 and C199 side chains with one of the two nitrogens establishing an H-bond with the K85 side chain (Figure 2). The biphenyl branch forms a T-shaped interaction with P67 and hydrophobic contacts with the Q185 and Y140 carbons.[41] Furthermore, as shown in Figure 2, the CN substituent forms an H-bond with the T138 hydroxyl group. The latter interaction seems to improve the activity of our ligands, in fact, for example, **14c** is more active against GSK-3β than its analogue **14a**, which lacks the cyano group, and its analogue **14d**, equipped with the cyano group at the R2 site. As regards the **15a** binding mode, the dihydrobenzodioxine moiety establishes several hydrophobic interactions with L132, I62, A83, V110, and L188.

Moreover, one of the two oxygens of the dihydrodioxine ring forms an H-bond with the V135 NH in the hinge region, while

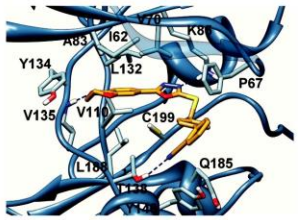

Figure 2. Molecular docking of compound **15a** into the X-ray structure of GSK-3β (PDB code: 3F88). This figure was prepared with Glide software.

the rest of the ring establishes hydrophobic contacts with the Y134. The latter interaction seems to be lost by **14c**, featuring the smaller benzodioxolane ring, while **16a**, a pyridine containing compound, forms a weaker H-bond with the same residue due to the position and the distance of the nitrogen atom of the pyridine ring from the NH of V135. The substitutions on the dihydrobenzodioxine moiety of **23** and **24**,

respectively, do not provide any further interaction with the enzyme, as the groups point out into the solvent. The same holds true for **26**, where the bulky substituent on the dihydrobenzodioxine ring may negatively affect the horseshoe shape (scorpion shape). The proposed binding mode also clarifies the undesirable effect of the substitution of the fluorine atom at the R2 site of the biphenyl branch in **15b**, which is 37-fold less potent for GSK-3β in comparison to **15a**. In fact, the electron-withdrawing atom weakens the H-bond between the cyano substituent and the T138 hydroxyl group; moreover, it comes in proximity of the negative ring density of Y140, providing repulsive edgewise interaction. The good selectivity toward GSK-3α versus GSK-3β which was observed for several compounds and especially for compound **15b**, is far to be trivial to explain. The superposition of the GSK-3β crystallographic structure (PDB code: 3F88) with a homology model built with Prime software (Schrodinger) shows that the differences between the two isoforms are all located out of the binding site and especially in the loop at C-terminus fragment (see the Supporting Information). Thus, it is conceivable that the selectivity of our compounds may be due to subtle enzyme differences, which may affect the ligand entrance/exit processes. This process may include an antechamber site, a step known to play a pivotal role in the inhibitor/enzyme recognition process.[42,43] By analyzing the enzyme surface and the residue mutations, the antechamber site in the GSK-3α or GSK-3β could be represented by the loop at C-terminus fragment as highlighted in Figure S1 in the Supporting Information. Obviously, the latter is a pure speculative hypothesis that has to be confirmed by more advanced theoretical work, mutational analysis, and additional experiments.

Biological Assays and Structure−Activity Relationship (SAR) Studies. The synthesized compounds were tested for their inhibitory activity against GSK-3β in an in house in vitro assay and further profiled in a commercial system based on the Z'-LYTE technology, available from Invitrogen Life Technologies (Carlsbad, CA, USA), using human recombinant GSK-3α or GSK-3β as the enzyme source. Most compounds displayed significant inhibitory activity against GSK-3β at 10 μM, and several compounds exerted more than 50% inhibitory activity against GSK-3β at the initial concentration (10 μM). The potent compounds were selected for IC_{50} determination. We observed differences in the IC_{50} determination between the in-house and the commercial assay and decided to use the results of the commercial system for comparison.

The structure−activity analysis suggested interactions with the GSK-3 backbone, Y134/D133, and the polar binding pocket, K85/E97/D200, to be essential for potent inhibition. These interactions require an acceptor−donor−acceptor motif on the inhibitor. We generated a simplified illustration in which we denoted acceptor (A) and donor (D) domains and drafted scaffold **I** as lead structure (Figure 1). We examined the effect of three heterocycles **5**−**7** as potential hinge binders and different substituents on the *S*-benzyl group (Scheme 1). The oxadiazole derivatives of the heterocycles **5** and **6** provided several GSK-3 inhibitors with an IC_{50} below 100 nM (Table 1) and confirmed previously reported activity.[26] The pyridines **7a**−**c** displayed decreased activity in comparison to the heterocycles **5** and **6**; this may be due to the position of the pyridine moiety in the ATP binding pocket. Thus, they were not pursued further. The compounds **5a** and **6a** indicated that an electron-withdrawing group is required at the 3-position. We introduced the cyano and ester group at the 4-position in order to reach out to R141 and the correlated acceptor/donor domain and thus to engage the ATP binding pocket in its entirety. Our data indicated that the electron-withdrawing group at the 3-position was also tolerated at the 4-position. The oxadiazoles **5b** and **6b−c** showed comparable activity to the 3-substituted derivatives and indicated space in the ATP binding pocket. On the basis of these results, we further examined the para-position of our lead structure. The carboxylic acids **8a** and **9a** resulted in a 4-fold less inhibitory activity against GSK-3β at 10 μM concentration compared to their esters **5c** and **6c** (Scheme 2). In the case of **5c**, the percentage of GSK-3β activity increased from 17% of up to 81% (Table 2). In addition, compound **8e**, bearing a hydrophilic tetrazole at the 4-position (IC_{50} value of 107 nM for GSK-3α and 172 nM for GSK-3β), showed decreased inhibitory activity compared to the ester **6c** (Scheme 2). Conversion of the carboxylic acids to the amides **8c−d** and **9c−e** resulted in an increased activity. Especially, compound **8c** showed good inhibitory property against GSK-3β with a remaining kinase activity of 9% at 10 μM (Table 2). These results and the molecular modeling suggested that compounds containing polar groups at the 4-position were less active than compounds containing hydrophobic groups. Hence, we tried to elongate our compounds with a phenyl ring at the 4-position. Compounds bearing a phenyl group in the para-position showed very good inhibitory activity. The docking analysis of the biphenylic derivatives suggested several hydrophobic contacts, which may be responsible for the enhanced potency. Especially, compound **15a** with an IC_{50} value of <5 nM for GSK-3α and GSK-3β was found to be a potent inhibitor of GSK-3 (Table 3). Slightly decreased activity was observed for compound **14a** with an IC_{50} value of 9 nM for GSK-3α and 176 nM for GSK-3β. We observed an IC_{50} of 2 nM for GSK-3α and 22 nM for GSK-3β for structure **14b**, whereas **14c**, which lacks the fluorine substituent, resulted in slightly decreased IC_{50} values in comparison to **14b**.

The selectivity for the GSK-3α isoform was higher when the substituents were absent in the series **14a−c**. The absence of selectivity for GSK-3α in **15a** in comparison with **14c** may be explained by the interaction with Y134 (see Molecular Modeling), which seems to be lost in **14c**. Remarkably, compound **14d** displayed up to 52-fold selectivity in the inhibition of GSK-3α versus GSK-3β. This selectivity was even enhanced with compound **15b,** which is characterized by an IC_{50} of 2 nM for GSK-3α and 185 nM for GSK-3β. Thus, only the interplay respectively of a combination of different substituents was adequate to gain selectivity against one GSK-3 isoform. This observation will be helpful if a discrimination of one GSK-3 isoform is needed. In addition, the physiological functions and pathological roles of GSK-3α can be addressed in vitro and eventually in vivo with these tools. The biphenyl derivative **16a** from the pyridine series showed remarkably increased activity in comparison to the used reference **7d**, 20-fold for GSK-3α, and 19-fold for GSK-3β (Table 1). The effect of the second phenyl suggested an interaction with the glycine-rich loop, such an interaction was reported to have significant effects on binding potency and selectivity recently.[41] Furthermore, the SAR and molecular modeling suggested that an electron-withdrawing group in the ortho position of the second phenyl ring, such as the cyano-group, contributes to the inhibitory activity by interaction with the amino acid T138. We examined different linker systems on the dihydrobenzodioxine moiety with the aim to enhance the interaction with the backbone. Unfortunately, they do not provide any further

Table 1. Inhibitory Activity against GSK-3α and GSK-3β, IC_{50} (μM)

Compound	GSK-3α	GSK-3β	Compound	GSK-3α	GSK-3β
5a	0.015	0.065	**7a**	3.206	3.162
5b	0.015	0.130	**7b**	7.379	10.0
6a	0.095	0.086	**7c**	2.244	1.318
6b	0.045	0.166	**7d**	0.390	0.790
6c	0.012	0.036	**8e**	0.107	0.172

interaction (see Molecular Modeling). The effect of the methoxy group on compound **23a** resulted in an IC_{50} value of 54 nM for GSK-3α and 233 nM for GSK-3β, respectively, 195 nM and 758 nM for compound **23b**. In the case of **23c**, good inhibitory activity was observed against both isoforms of GSK-3, especially for GSK-3α. These results suggest that the *R*-enantiomer **23b** is the distomer of this compound, whereas the *S*-enantiomer **23c** was found to be the eutomer. Despite our expectations that an amine may improve the activity, compound **26** showed markedly reduced potency.

The potent GSK-3 inhibitors **6c**, **14a–d**, **15a–b**, **16a**, and **23a–c** were selected for selectivity profiling and tested against four structurally related protein kinases (Cdk5/p35, CK1ε, AurKA, and PKCα).

Good selectivity was obtained for all compounds tested. Particularly, the biphenyl derivatives **14c**, **15a**, and **16a** showed more than 2000-fold selectivity against these kinases (Table 4). Compound **14d** was not just GSK-3α selective, it was even more selective over the other kinases than compound **15b**. The broader selectivity of compound **14d** was screened at a concentration of 1 μM against 50 human protein kinases (Figure 3); 48 out of the 50 kinases in this panel showed an activity higher than 80%, whereas GSK-3α displayed a residual activity of 5% only. The only kinase which was also significantly inhibited by this compound was GSK-3β with a remaining activity of 27.2%. Therefore, it can be concluded that, within the test panel, compound **14d** is a selective inhibitor of GSK-3α. A bioavailability profile of compound **14d** was evaluated,

Table 2. Inhibitory Activity against GSK-3β at 10 μM

Compound	GSK-3β activity in %	Compound	GSK-3β activity in %	Compound	GSK-3β activity in %
5c	17	**8c**	9	**9c**	37
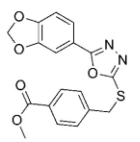		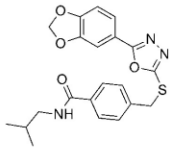		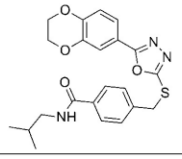	
6c	21	**8d**	31	**9d**	65
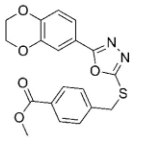		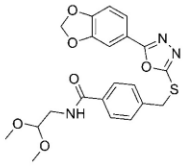		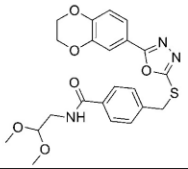	
8a	81	**9a**	102	**9e**	71
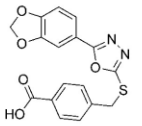		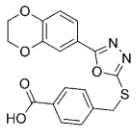		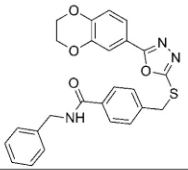	

and the results are shown in the Supporting Information. **14d** possesses a log *D* value of 3.58 and moderate metabolic stability. Nevertheless, the poor aqueous solubility and permeability are adverse properties which limit the potential use of the compound.

The biphenyl derivatives **14c−d**, **15a−b**, and **16a** were further tested for their in vivo activity on wild-type zebrafish embryos. We exposed the embryos to these compounds at early stages of development. The embryos were collected and maintained in E2 medium at ∼28 °C. The compounds were added 5 h post fertilization (hpf), and the phenotypes compared at 44−48 hpf. Compound **14c** causes the eyeless phenotype at 0.5 μM and a stunted and crooked tail at 1 μM. Similar phenotypes were obtained for compound **15a** at 2.5 μM and for compound **16a** at 20 μM (Figure 4). This correlates with the observation that Wnt signaling, and thus GSK-3β plays a crucial role in the development of metazoan and that known GSK-3 inhibitors like LiCl and the ruthenium complex (*R*)-7 perturb the zebrafish development.[44,45] The zebrafish embryo assay provides evidence of exposure and cell penetration of the biphenyl derivatives, especially for compound **14c**. Interestingly, compounds **14d** and **15b** showed no effect on wild-type zebrafish embryos, suggesting that GSK-3α plays a minor role in the zebrafish Wnt signaling pathway. The lack of response in the zebrafish assay by compounds **14d** and **15b** may be explained by poor cell permeability. However, the structurally analogues compounds **14c** and **15a**, which are characterized by comparable solubility, did result in a GSK-3β-phenotype. Thus, the comparison of these compounds **14c**/**15a** and **14d**/**15b** does not support poor exposure and cell penetration as the dominant factors on the in vivo assay of the α-selective inhibitors. The inhibition of GSK-3α was proposed to regulate β-adrenergic signaling in mice, thus we monitored the heart development of the zebrafish embryo after administration of compound **14d** until day 5 (see the Supporting Information).[15,46] However, no effect was observed until the fifth day of development. All compounds displayed no lethality in our concentration range (<30 μM).

SH-SY5Y neuroblastoma cells stably transfected with Tau.P301L were incubated with increasing concentrations of compounds **14c** and **15a** (0, 30, and 100 μM) for 6 and 24 h. Cells were analyzed for total protein tau by Western blotting with antibody Tau5, directed against nonphosphorylated protein tau. In addition, the same samples were probed with a selection of phospho-specific antibodies that recognize typical GSK-3 dependent epitopes on protein tau. Moreover, the electrophoretic mobility of protein tau is a reliable index of the degree of phosphorylation of protein Tau.P301L: the lesser mobile isoforms carry the most phosphate groups (Figure 5).

Both compounds dose- and time-dependently decreased the phosphorylation of protein tau, expressed relatively to total tau, as demonstrated by the decreased immunoreaction with antibodies pS199, pT231, pS396, and pS404 in Western blotting (Figure 5). Moreover, the marked increase in electrophoretic mobility of the various phospho-isoforms of protein tau induced by treatment of the stably transfected SH-SY5Y cells corroborates their effectiveness in preventing phosphorylation on typical GSK-3 dependent epitopes. The comparison of the biphenyl derivatives indicated that compound **14c** is more effective in preventing phosphorylation than compound **15a**.

Table 3. Inhibitory Activity of the Biphenyls against GSK-3α and GSK-3β, IC_{50} (μM)

Compound	GSK-3α	GSK-3β	Compound	GSK-3α	GSK-3β
14a	0.009	0.176	**15b**	0.002	0.185
14b	0.002	0.022	**16a**	0.019	0.041
14c	< 0.005	0.039	**23a**	0.054	0.233
14d	0.006	0.316	**23b**	0.195	0.758
15a	< 0.005	< 0.005	**23c**	0.015	0.129

This correlates with the observations made in the zebrafish embryo assay in which **14c** showed the best results.

■ CONCLUSION

On the basis of a simplified scheme of known and important interactions of GSK-3 inhibitors with the ATP binding pocket, we generated hypotheses for improved interaction of with this site. These hypotheses were challenged by three series of structurally closely related inhibitors which are all based on a central oxadiazole moiety. An appropriate decoration resulted in a more extended occupation of the ATP binding site. The most potent inhibitors displayed IC_{50} values in the low nanomolar range and good kinase selectivity versus four closely related kinases. Several inhibitors showed reported phenotypes in the zebrafish embryo assay without lethality at 30 μM. In addition, two inhibitors decreased the phosphorylation of tau protein in SH-SY5Y cells. The docking analysis of the potent inhibitors suggested an interaction with the glycine-rich loop, which was reported to have significant effects on the binding potency and selectivity by Li Feng et al.[41] To our knowledge, the selective inhibition of GSK-3α versus GSK-3β by the compounds **14d** and **15b** is the highest reported so far. In addition, compound **14d** did not show any strong inhibition for 48 out of 50 kinases. The contribution of GSK-3α and GSK-3β to the pathology of Alzheimer's disease is still subject of an ongoing debate.[47,48] Thus, these compounds may be useful tools and starting points for the synthesis of GSK-3α selective inhibitors with enhanced pharmacokinetic properties.

Table 4. Kinase Selectivity of Several Derivatives

	IC_{50} (μM)					
compd	GSK-3α	GSK-3β	Cdk5/p35	CK1ε	AurKA	PKCα
6c	0.012	0.036	>100	>100	>100	>100
14a	0.009	0.176	>100	>100	>100	>100
14b	0.003	0.022	>100	20	30	>100
14c	<0.005	0.039	>100	>100	>100	>100
14d	0.006	0.316	>100	60	30	>100
15a	<0.005	<0.005	>100	>100	>100	>100
15b	0.002	0.185	>100	>100	5	>100
16a	0.019	0.041	>100	>100	>100	>100
23a	0.054	0.233	>100	>100	30	>100
23b	0.195	0.758	>100	>100	>100	>100
23c	0.015	0.129	>100	>100	>100	>100

EXPERIMENTAL SECTION

General Information. All reactions using anhydrous conditions were carried out under argon atmosphere with dry solvents unless otherwise noted. All commercial chemicals were used without further purification. The ^{1}H NMR spectra were recorded on a Bruker AC 300 spectrometer at 300 MHz and Bruker AC 500 spectrometer at 500 MHz. The ^{13}C NMR spectra were recorded on a Bruker AC 300 spectrometer at 75 MHz and Bruker AC 500 spectrometer at 125 MHz. Chemical shifts are reported as ppm downfield from Me_4Si. Abbreviations used to explain the multiplicities: s = singlet, d = doublet, t = triplet, q = quartet, n = nonett, m = multiplet, br = broad. Coupling constants (J values) are given in hertz (Hz). Mass spectrometry was performed on a Bruker−Franzen Esquire LC mass spectrometer and a MAT 95 double focusing sector field MS. Microwave experiments were carried out using a Biotage Initiator microwave apparatus. All microwave experiments were carried out in sealed microwave process vials utilizing the standard absorbance level (300 W maximum power). High performance liquid chromatographies (HPLC) were carried out on an Agilent 1100 (column: reversed phase, Zorbax Eclipse XDB-C18, 4.6 mm × 150 mm; 254 nm). Solvent gradient = 90% A at 0 min, 30% A at 2 min, 10% A at 5 min; solvent A = 0.1% trifluoroacetic acid in water; solvent B = acetonitrile; flow rate 1.0 mL/min; temperature 35 °C. Flash column chromatography was carried out using Merck silica gel 60 (40−63 and 15−40 μm) and 60G (5−40 μm). Thin-layer chromatography (TLC) was carried out using aluminum sheets precoated with silica gel 60 F254 (0.2 mm; E. Merck). All compounds that were evaluated in biological assays had >95% purity using the HPLC method described above.

General Procedure A: Coupling of Aromatic Rings by a Suzuki Reaction (12a−d).[49] To a solution of the aryl bromide **11** (5 mmol) in 15 mL of toluene/EtOH (1/1) was added 0.17 g (0.14 mmol) of $Pd(PPh_3)_4$, and the mixture was stirred under argon atmosphere. Then 2 N aqueous Na_2CO_3 (7.5 mL) and 0.80 g (6 mmol) of 2-tolylboronic acid **10** were added. The mixture was refluxed at 80 °C for 1−2 days until reaction was completed (TLC). After cooling to room temperature, the product was diluted with water and extracted with EtOAc. The organic layers were dried with $MgSO_4$, filtered, and concentrated. Purification was performed by column chromatography using a mixture of cyclohexane/EtOAc.

General Procedure B: Bromination at the Benzylic Position (13a−d).[49] To a stirred solution of the appropriately substituted toluene in CCl_4 (10 mL per mmol) were added 0.95 equiv of NBS and AIBN (5 mg per mmol). The reaction mixture was refluxed at 80 °C for about 40 h and then cooled to room temperature. The product was diluted with water and extracted with EtOAc. The organic layers were dried with $MgSO_4$, filtered, and concentrated. Purification was performed by column chromatography using a mixture of cyclohexane/EtOAc.

Methyl Benzo[*d*][1,3]dioxole-5-carboxylate (2A). To a stirred solution of benzo[*d*][1,3]dioxole-5-carboxylic acid (1.66 g, 10 mmol) in MeOH (20 mL) was added $SOCl_2$ (1.45 mL, 20 mmol) dropwise over 1 h at 0 °C. The mixture solution was further stirred 12 h at 50 °C. The mixture was cooled to room temperature and diluted with water (25 mL). MeOH was evaporated and the pH adjusted to ~6 with aqueous $NaHCO_3$. The mixture was extracted three times

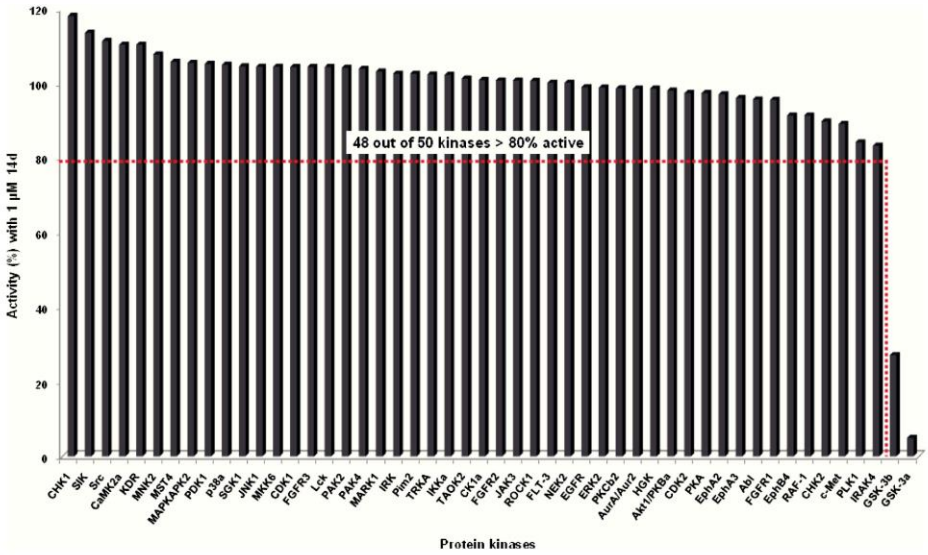

Figure 3. Screening of compound **14d** against a panel of human protein kinases. Each bar represents the activity of one individual protein kinase. Compound **14d** was tested at a concentration of 1 μM against 50 protein kinases. See Supporting Information for more details.

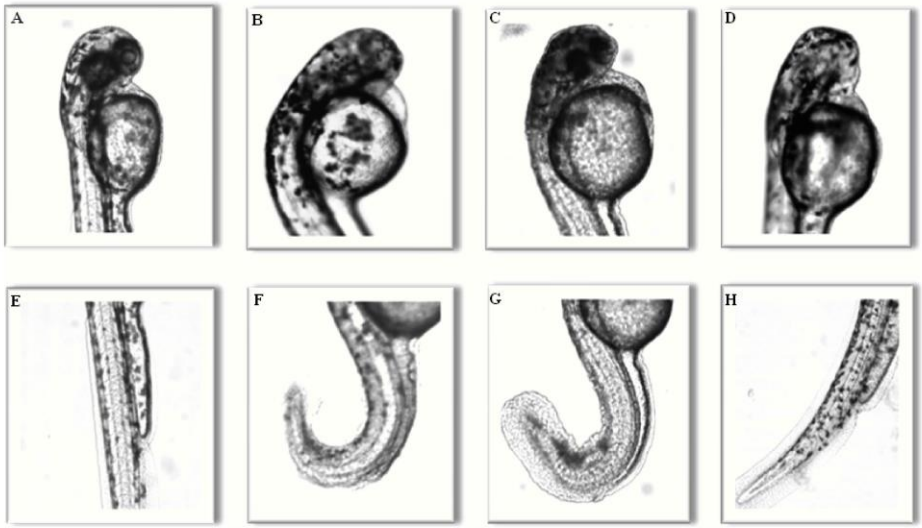

Figure 4. Effects on wild-type zebrafish embryos by compounds **14c**, **15a**, and **16a**. The embryos were collected and maintained in E2 medium at ~28 °C, compounds were added 5 hpf, and the phenotypes were compared at 44−48 hpf. (A,E) Head and tail of control embryos: DMSO (2%). (B,F) Head and tail of embryos treated with **14c**. This compound causes the eyeless phenotype at 0.5 μM and a stunted and crooked tail at 1.0 μM. (C,G) Head and tail of embryos treated with **15a**. A fluffy eye pigmentation and a stunted and crooked tail were observed at 2.5 μM. (D,H) Head and tail of embryos treated with **16a**. This compound causes the eyeless phenotype and a crooked tail at 20 μM.

with EtOAc and successively washed with brine. The organic layer was dried over $MgSO_4$ and concentrated under reduced pressure to give **2A** (1.6 g, 89%) as a colorless solid. ^{1}H NMR (DMSO-d_6, 500 MHz): δ [ppm] = 3.81 (3H, s), 6.14 (2H, s), 7.03 (1H, d, J = 8.1 Hz), 7.38 (1H, d, J = 1.7 Hz), 7.57 (1H, dd, J = 8.1 Hz, J = 1.7 Hz). ^{13}C NMR (DMSO-d_6, 125 MHz): δ [ppm] = 52.0, 102.1, 108.2, 108.5, 123.4, 125.0, 147.6, 151.4, 165.6. EI-MS: m/z = 180 (M^+).

The following compound **2B** was prepared in a similar manner to that described for **2A**.

Methyl 2,3-Dihydrobenzo[*b*][1,4]dioxine-6-carboxylate (2B). Yield 83%, colorless solid. ^{1}H NMR (DMSO-d_6, 500 MHz): δ [ppm] = 3.80 (3H, s), 4.19 (2H, m), 4.23 (2H, m), 6.80 (1H, m), 7.47 (2H, m). ^{13}C NMR (DMSO-d_6, 125 MHz): δ [ppm] = 50.5, 62.7, 63.2, 115.7, 117.6, 122.0, 141.7, 146.4, 165.2. EI-MS: m/z 194 (M^+).

Benzo[*d*][1,3]dioxole-5-carbohydrazide (3A). To a solution of **2A** (1.08 g, 6.0 mmol) in EtOH (30 mL) was added hydrazine hydrate (2.91 mL, 60 mmol), and the mixture was heated at reflux for 2 days. After cooling to room temperature, pure crystals are formed, collected by filtration, and washed several times with EtOH to give compound **3A** (0.72 g, 67%) as a colorless solid. ^{1}H NMR (DMSO-d_6, 500 MHz): δ [ppm] = 4.42 (2H, s), 6.07 (2H, s), 6.96 (1H, d, J = 8.1 Hz), 7.35 (1H, d, J = 1.7 Hz), 7.42 (1H, dd, J = 8.1 Hz, J = 1.7 Hz), 9.59 (1H, s). ^{13}C NMR (DMSO-d_6, 125 MHz): δ [ppm] = 101.5, 106.9, 107.8, 121.8, 127.2, 147.2, 149.5, 165.2. EI-MS: m/z = 180 (M^+).

Compound **3B** was prepared in a similar manner to that described for **3A**.

2,3-Dihydrobenzo[*b*][1,4]dioxine-6-carbohydrazide (3B). Yield 75%, light-yellow solid. ^{1}H NMR (methanol-d_4, 500 MHz): δ [ppm] = 4.28 (2H, m), 4.30 (2H, m), 6.89 (1H, d, J = 8.3 Hz), 7.30 (1H, dd, J = 8.3 Hz, J = 2.1 Hz), 7.33 (1H, d, J = 2.1 Hz), NH signals were not observed. ^{13}C NMR (methanol-d_4, 125 MHz): δ [ppm] = 65.9, 66.3, 117.9, 118.6, 121.9, 127.5, 145.2, 148.6, 169.6. EI-MS: m/z 194 (M^+).

5-(Benzo[*d*][1,3]dioxol-5-yl)-1,3,4-oxadiazole-2-thiol (4A). To a solution of **3A** (535 mg, 3.00 mmol) in EtOH (5 mL) were added carbon disulfide (397 μL, 6.60 mmol) and NEt_3 (469 μL, 3.30 mmol), and the mixture was heated at reflux overnight. The reaction mixture was diluted with EtOAc, and the organic layer was washed with 0.1 N HCl and brine and dried over Na_2SO_4. The solvent was evaporated under reduced pressure, and the obtained residue was recrystallized from cyclohexane/EtOAc to give **4A** (521 mg, 79%) as a pale-yellow solid. ^{1}H NMR (DMSO-d_6, 500 MHz): δ [ppm] = 6.14 (2H, s), 7.10 (1H, d, J = 8.1 Hz), 7.33 (1H, d, J = 1.6 Hz), 7.42 (1H, dd, J = 8.1 Hz, J = 1.6 Hz), SH signal was not observed. ^{13}C NMR (DMSO-d_6, 125 MHz): δ [ppm] = 102.1, 105.6, 109.1, 116.1, 121.5, 148.1, 150.6, 160.3, 177.2. EI-MS: m/z = 222 (M^+).

The compounds **4B−C** were prepared in a similar manner to that described for **4A**.

5-(2,3-Dihydrobenzo[*b*][1,4]dioxin-6-yl)-1,3,4-oxadiazole-2-thiol (4B). Yield 89%, light-brown solid. ^{1}H NMR (DMSO-d_6, 500 MHz): δ [ppm] = 4.32 (2H, m), 4.34 (2H, m), 7.05 (1H, d, J = 8.4 Hz), 7.30 (1H, d, J = 2.0 Hz), 7.36 (1H, dd, J = 8.4 Hz, J = 2.0 Hz), SH signal was not observed. ^{13}C NMR (DMSO-d_6, 125 MHz): δ [ppm] = 64.4, 64.8, 115.0, 115.7, 118.6, 120.0, 144.2, 147.3, 160.6, 177.6. EI-MS: m/z = 236 (M^+).

5-(Pyridin-4-yl)-1,3,4-oxadiazole-2-thiol (4C). Yield 83%, yellow solid. ^{1}H NMR (DMSO-d_6, 500 MHz): δ [ppm] = 7.81 (2H, dd, J = 4.4 Hz, J = 1.6 Hz), 8.81 (2H, dd, J = 4.4 Hz, J = 1.6 Hz), SH signal was not observed. ^{13}C NMR (DMSO-d_6, 125 MHz): δ [ppm] = 119.6, 129.7, 150.8, 158.7, 177.8. EI-MS: m/z = 179 (M^+).

3-((5-Benzo[*d*][1,3]dioxol-5-yl)-1,3,4-oxadiazol-2-ylthio)-methyl)benzonitrile (5a). To a solution of **4A** (55 mg, 0.25 mmol) and 1 N NaOH (0.25 mL, 0.25 mmol) in DMF (1 mL) was added 1-(bromomethyl)-3-methoxybenzene (75 mg, 0.38 mmol) at room temperature, and the mixture was stirred for 5 h. The precipitate formed was collected by filtration and washed once with less DMF (~1 mL) and thereafter several times with EtOH to give compound **5a** (55 mg, 64%) as a brown solid. ^{1}H NMR (DMSO-d_6, 500 MHz): δ [ppm] = 4.61 (2H, s), 6.16 (2H, s), 7.10 (1H, d, J = 8.1 Hz), 7.41 (1H, d, J = 1.4 Hz), 7.47 (1H, dd, J = 8.1 Hz, J = 1.5 Hz), 7.57 (1H, t,

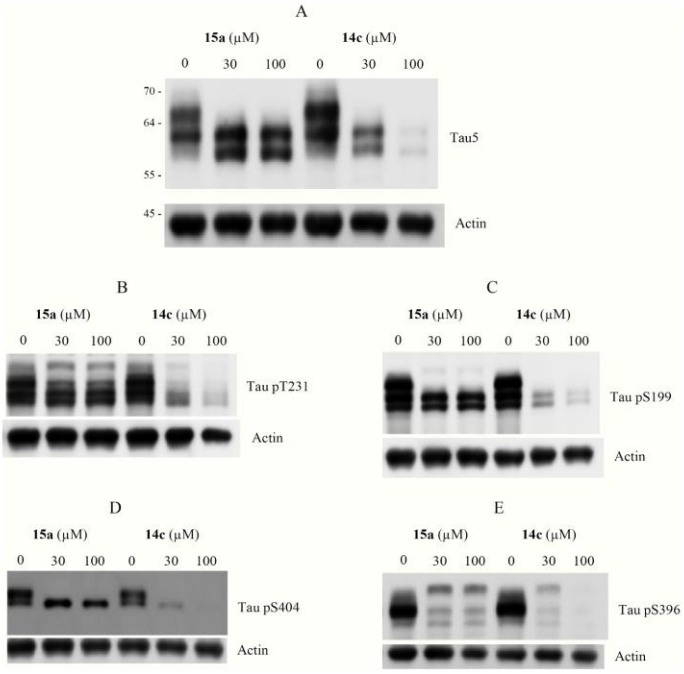

Figure 5. Western blotting for protein Tau.P301L expressed in stably transfected SH-SY5Y neuorblastoma cells, untreated (lanes marked 0) or treated for 6 h with compounds **14c** or **15a** (lanes marked 30 and 100 μM). Total protein tau was detected with antibody Tau5 (A). Phosphoepitopes on protein tau were detected with specific antibodies (B–E). Experiments were performed in triplicate, and representative blots are shown. Similar observations were obtained after 24 h of incubation. Note that compound **14c** specifically decreases the total concentration of protein tau, while levels of the internal marker (actin) remain unchanged.

J = 7.7 Hz), 7.76 (1H, d, J = 7.7 Hz), 7.84 (1H, d, J = 7.8 Hz), 7.96 (1H, s). ^{13}C NMR (DMSO-d_6, 125 MHz): δ [ppm] = 34.7, 102.1, 106.1, 109.1, 111.4, 116.6, 118.5, 121.7, 129.8, 131.4, 132.6, 133.9, 138.8, 148.1, 150.4, 162.2, 165.2. HPLC: 98%; t_R 7.21 min. EI-MS: m/z = 337 (M^+).

The compounds **5b–c**, **6a–c**, and **7a–c** were prepared in a similar manner to that described for **5a**. Note: Compounds which did not precipitate in solution were purified as follows. The reaction mixture was diluted with EtOAc and the organic layer was washed with water and brine, dried over $MgSO_4$, and concentrated in vacuo. The residue was purified by silica gel column chromatography (cyclohexane/EtOAc).

4-((5-Benzo[*d*][1,3]dioxol-5-yl)-1,3,4-oxadiazol-2-ylthio)-methyl)benzonitrile (5b). Yield 67%, brown solid. ^{1}H NMR (DMSO-d_6, 500 MHz): δ [ppm] = 4.64 (2H, s), 6.16 (2H, s), 7.11 (1H, d, J = 8.1 Hz), 7.42 (1H, d, J = 1.6 Hz), 7.48 (1H, dd, J = 8.1 Hz, J = 1.7 Hz) 7.68 (2H, d, J = 8.3 Hz), 7.82 (2H, d, J = 8.3 Hz). ^{13}C NMR (DMSO-d_6, 125 MHz): δ [ppm] = 35.2, 102.1, 106.1, 109.1, 110.4, 116.5, 118.6, 121.7, 130.0, 132.4, 142.8, 148.1, 150.5, 162.2, 165.2. HPLC: 95%; t_R 7.09 min. EI-MS: m/z = 337 (M^+).

Methyl 4-((5-(Benzo[*d*][1,3]dioxol-5-yl)-1,3,4-oxadiazol-2-ylthio)methyl Benzoate (5c). Yield 71%, pale-brown solid. ^{1}H NMR (DMSO-d_6, 500 MHz): δ [ppm] = 3.82 (3H, s), 4.63 (2H, s), 6.15 (2H, s), 7.10 (1H, d, J = 8.1 Hz), 7.41 (1H, d, J = 1.7 Hz), 7.48 (1H, dd, J = 8.1 Hz, J = 1.7 Hz), 7.62 (2H, d, J = 8.4 Hz), 7.92 (2H, d, J = 8.4 Hz). ^{13}C NMR (DMSO-d_6, 125 MHz): δ [ppm] = 35.4, 52.2, 102.2, 106.1, 109.2, 116.6, 121.7, 128.8, 129.4, 142.4, 148.1, 150.4, 162.3, 165.1, 165.9. HPLC: 96%; t_R 7.61 min. EI-MS: m/z = 370 (M^+).

3-((5-(2,3-Dihydrobenzo[*b*][1,4]dioxin-6-yl)-1,3,4-oxadiazol-2ylthio)methyl)benzonitrile (6a). Yield 73%, light-brown solid. ^{1}H NMR (DMSO-d_6, 500 MHz): δ [ppm] = 4.31 (2H, m), 4.34 (2H, m), 4.61 (2H, s), 7.05 (1H, d, J = 8.4 Hz), 7.39 (1H, d, J = 2.0 Hz), 7.42 (1H, dd, J = 8.4 Hz, J = 2.1 Hz), 7.57 (1H, t, J = 7.8 Hz), 7.77 (1H, dt, J = 7.8 Hz, J = 1.3 Hz), 7.84 (1H, dt, J = 7.8 Hz, J = 1.1 Hz), 7.96 (1H, t, J = 1.3 Hz). ^{13}C NMR (DMSO-d_6, 125 MHz): δ [ppm] = 35.2, 64.5, 64.7, 111.8, 115.5, 116.3, 118.5, 118.9, 120.4, 130.1, 131.8, 133.0, 134.4, 139.3, 144.2, 147.1, 162.7, 165.5. HPLC: 99%; t_R 7.53 min. EI-MS: m/z = 351 (M^+).

4-((5-(2,3-Dihydrobenzo[*b*][1,4]dioxin-6-yl)-1,3,4-oxadiazol-2-ylthio)methyl)benzonitrile (6b). Yield 56%, brown solid. ^{1}H NMR (DMSO-d_6, 500 MHz): δ [ppm] = 4.31 (2H, m), 4.34 (2H, m), 4.63 (2H, s), 7.05 (1H, d, J = 8.4 Hz), 7.37 (1H, d, J = 2.0 Hz), 7.41 (1H, dd, J = 8.4 Hz, J = 2.0 Hz), 7.67 (2H, d, J = 8.3 Hz), 7.81 (2H, d, J = 8.3 Hz). ^{13}C NMR (DMSO-d_6, 125 MHz): δ [ppm] = 35.3, 64.0, 64.4, 110.4, 115.0, 115.8, 118.2, 118.6, 119.9, 130.0, 132.4, 142.8, 143.8, 146.7, 162.2, 165.0. HPLC: 95%; t_R 7.49 min. EI-MS: m/z = 351 (M^+).

Methyl 4-((5-(2,3-Dihydrobenzo[*b*][1,4]dioxin-6-yl)-1,3,4-oxadiazol-2-ylthio)methyl) Benzoate (6c). Yield 49%, purple solid. ^{1}H NMR (DMSO-d_6, 500 MHz): δ [ppm] = 3.89 (3H, s), 4.36 (2H, m), 4.39 (2H, m), 4.67 (2H, s), 7.10 (1H, d, J = 8.4 Hz), 7.42 (1H, d, J = 2.0 Hz), 7.47 (1H, dd, J = 8.4 Hz, J = 2.0 Hz), 7.67 (2H, d, J = 8.3 Hz), 7.97 (2H, d, J = 8.3 Hz). ^{13}C NMR (DMSO-d_6, 125 MHz): δ [ppm] = 35.4, 52.1, 64.0, 64.4, 115.0, 115.8, 118.1, 120.0, 128.9, 129.4, 142.4, 143.8, 146.7, 162.3, 165.0, 165.8. HPLC: 99%; t_R 7.66 min.

EI-MS: m/z = 384 (M^+). HRMS (EI): m/z calcd for $C_{19}H_{16}N_2O_3S$ 384.0780, found 384.0809.

3-((5-(Pyridin-4-yl)-1,3,4-oxadiazol-2-ylthio)methyl)-benzonitrile (7a). Yield 41%, yellow solid. ^{1}H NMR (DMSO-d_6, 500 MHz): δ [ppm] = 4.66 (2H, s), 7.58 (1H, t, J = 7.8 Hz), 7.78 (1H, dt, J = 7.7 Hz, J = 1.3 Hz), 7.86 (1H, t, J = 1.2 Hz), 7.88 (2H, dd, J = 4.4 Hz, J = 1.6 Hz), 7.99 (1H, t, J = 1.4 Hz), 8.82 (2H, dd, J = 4.4 Hz, J = 1.6 Hz). ^{13}C NMR (DMSO-d_6, 125 MHz): δ [ppm] = 34.8, 111.4, 118.5, 120.0, 129.8, 130.0, 131.5, 132.7, 134.0, 138.6, 150.9, 163.8, 164.4. HPLC: 96%; t_R 4.51 min. EI-MS: m/z = 294 (M^+).

4-((5-(Pyridin-4-yl)-1,3,4-oxadiazol-2-ylthio)methyl)-benzonitrile (7b). Yield 77%, pale-yellow solid. ^{1}H NMR (DMSO-d_6, 500 MHz): δ [ppm] = 4.69 (2H, s), 7.71 (2H, d, J = 8.2 Hz), 7.83 (2H, d, J = 8.2 Hz), 7.88 (2H, dd, J = 4.4 Hz, J = 1.6 Hz), 8.82 (2H, dd, J = 4.5 Hz, J = 1.5 Hz). ^{13}C NMR (DMSO-d_6, 125 MHz): δ [ppm] = 35.2, 110.5, 118.6, 120.0, 130.0, 130.1, 132.4, 142.6, 150.8, 163.9, 164.4. HPLC: 95%; t_R 4.51 min. EI-MS: m/z = 294 (M^+).

2-(Benzylthio)-5-(pyridin-4-yl)-1,3,4-oxadiazole (7c). Yield 79%, light-yellow solid. ^{1}H NMR (DMSO-d_6, 500 MHz): δ [ppm] = 4.62 (2H, s), 7.30 (1H, m), 7.36 (2H, m), 7.50 (2H, m), 7.90 (2H, dd, J = 4.4 Hz, J = 1.6 Hz), 8.82 (2H, dd, J = 4.4 Hz, 1.6 Hz). ^{13}C NMR (DMSO-d_6, 125 MHz): δ [ppm] = 35.8, 120.0, 127.8, 128.6, 129.1, 130.0, 136.4, 150.8, 163.6, 164.7. HPLC: 100%; t_R 4.89 min. EI-MS: m/z = 269 (M^+).

2-(3-Iodobenzylthio)-5-(pyridin-4-yl)-1,3,4-oxadiazole (7d). **7d** was used as reference. It is commercially available from Calbiochem (361541 GSK-3β Inhibitor II; CAS number, 478482-75-6).

4-((5-(Benzo[*d*][1,3]dioxol-5-yl)-1,3,4-oxadiazol-2-ylthio)-methyl)benzoic Acid (8a). Methyl 4-((5-(benzo[d][1,3]dioxol-5-yl)-1,3,4-oxadiazol-2-ylthio)methyl benzoate **5c** (300 mg, 0.81 mmol) was added in 5 mL of a 2 N lithium hydroxide−tetrahydrofuran solution. The reaction mixture was stirred overnight at 60 °C under an argon atmosphere. The reaction mixture was diluted with water and neutralized with 1 N HCl. Afterward, EtOAc was added and the organic layer was washed with water and brine, dried over $MgSO_4$, and concentrated in vacuo to give **8a** (239 mg, 83%) as a rose solid. ^{1}H NMR (DMSO-d_6, 500 MHz): δ [ppm] = 4.56 (2H, s), 6.08 (2H, s), 7.04 (1H, d, J = 8.1 Hz), 7.35 (1H, d, J = 1.6 Hz), 7.43 (1H, dd, J = 8.1 Hz, J = 1.7 Hz), 7.53 (2H, d, J = 8.2 Hz), 7.84 (2H, d, J = 8.2 Hz), 12.8 (1H, s, br). ^{13}C NMR (DMSO-d_6, 125 MHz): δ [ppm] = 35.4, 102.1, 106.1, 109.1, 116.6, 121.7, 129.1, 129.5, 130.4, 141.7, 148.1, 150.4, 162.4, 165.1, 166.9. HPLC: 99%; t_R 6.15 min. EI-MS: m/z = 356 (M^+).

Compound **9a** was prepared in a similar manner to that described for **8a**.

Methyl 4-((5-(2,3-Dihydrobenzo[*b*][1,4]dioxin-6-yl)-1,3,4-oxadiazol-2-ylthio)methyl)benzoic Acid (9a). Yield 91%, colorless solid. ^{1}H NMR (DMSO-d_6, 500 MHz): δ [ppm] = 4.31 (2H, m), 4.34 (2H, m), 4.62 (2H, s), 7.05 (1H, d, J = 8.4 Hz), 7.38 (1H, d, J = 2.0 Hz), 7.43 (1H, dd, J = 8.4 Hz, J = 2.1 Hz), 7.59 (2H, d, J = 8.3 Hz), 7.91 (2H, d, J = 8.3 Hz), 12.95 (1H, s). ^{13}C NMR (DMSO-d_6, 125 MHz): δ [ppm] = 35.4, 64.1, 64.4, 115.1, 115.7, 118.2, 119.8, 129.3, 129.5, 130.1, 141.9, 143.8, 146.7, 162.4, 165.0, 166.8. HPLC: 96%; t_R 6.22 min. EI-MS: m/z = 370 (M^+).

4-((5-(Benzo[*d*][1,3]dioxol-5-yl)-1,3,4-oxadiazol-2-ylthio)-methyl)-*N*-isobutylbenzamide (8c). A mixture of 4-((5-(benzo-[d][1,3]dioxol-5-yl)-1,3,4-oxadiazol-2-ylthio)methyl)benzoic acid **8a** (100 mg, 0.28 mmol) and thionyl chloride (30.5 μL, 0.42 mmol) was refluxed in dry toluene (1 mL) for about 2 h. Excess thionyl chloride was removed by repeated evaporation in vacuo with fresh dry toluene (3 × 1 mL). 2-Methylpropan-1-amine (27.8 μL, 0.28 mmol) and K_2CO_3 (38 mg, 0.28 mmol) were added in dry acetone (1 mL) cooled to 0 °C and stirred for 30 min. The crude acyl chloride was dissolved in dry acetone (0.5 mL) and added dropwise to the solution. After the addition was complete, stirring continued for 2 h. The reaction mixture was then diluted with water, extracted three times with EtOAc, and successively washed with brine. The organic layer was dried over $MgSO_4$ and concentrated under reduced pressure. The obtained residue was recrystallized from EtOH to give **8c** (90 mg, 81%) as a beige solid. ^{1}H NMR (DMSO-d_6, 500 MHz): δ [ppm] = 0.86 (6H, d, J = 6.7 Hz), 1.81 (1H, n, J = 6.7 Hz), 3.05 (2H, t, J = 6.7 Hz), 4.60 (2H, s), 6.16 (2H, s), 7.10 (1H, d, J = 8.1 Hz), 7.43 (1H, d, J = 1.6 Hz), 7.50 (1H, dd, J = 8.1 Hz, J = 1.7 Hz), 7.54 (2H, d, J = 8.2 Hz), 7.78 (2H, d, J = 8.3 Hz), 8.42 (1H, t, J = 5.7 Hz). ^{13}C NMR (DMSO-d_6, 125 MHz): δ [ppm] = 20.2, 28.0, 35.4, 46.6, 102.1, 106.1, 109.2, 116.6, 121.8, 127.5, 128.8, 134.1, 139.8, 148.1, 150.5, 162.4, 165.1, 165.8. HPLC: 95%; t_R 7.11 min. EI-MS: m/z = 411 (M^+).

The following compounds **8d** and **9c−e** were prepared in a similar manner to that described for **8c**.

4-((5-(Benzo[*d*][1,3]dioxol-5-yl)-1,3,4-oxadiazol-2-ylthio)-methyl)-*N*-(2,2-dimethoxyethyl)benzamide (8d). Yield 79%, light-yellow solid. ^{1}H NMR (DMSO-d_6, 500 MHz): δ [ppm] = 3.27 (6H, s), 3.33 (2H, br), 4.48 (1H, t, J = 5.6 Hz), 4.61 (2H, s), 6.16 (2H, s), 7.11 (1H, d, J = 8.1 Hz), 7.44 (1H, d, J = 1.7 Hz), 7.50 (1H, dd, J = 8.1 Hz, J = 1.7 Hz), 7.55 (2H, d, J = 8.1 Hz), 7.80 (2H, d, J = 8.1 Hz), 8.52 (1H, t, J = 5.7 Hz). ^{13}C NMR (DMSO-d_6, 125 MHz): δ [ppm] = 35.4, 41.1, 53.2, 101.8, 102.2, 106.2, 109.2, 116.6, 121.7, 127.5, 128.9, 133.5, 140.1, 148.1, 150.4, 162.4, 165.1, 166.0. HPLC: 95%; t_R 6.07 min. EI-MS: m/z = 443 (M^+).

4-((5-(2,3-Dihydrobenzo[*b*][1,4]dioxin-6-yl)-1,3,4-oxadiazol-2-ylthio)methyl)-*N*-isobutyl Benzamide (9c). Yield 92%, light-brown solid. ^{1}H NMR (DMSO-d_6, 500 MHz): δ [ppm] = 0.93 (6H, d, J = 6.7 Hz), 1.88 (1H, n, J = 6.7 Hz), 3.12 (2H, t, J = 6.6 Hz), 4.37 (2H, m), 4.39 (2H, m), 4.66 (2H, s), 7.10 (1H, d, J = 8.4 Hz), 7.45 (1H, d, J = 2.0 Hz), 7.48 (1H, dd, J = 8.4 Hz, J = 2.0 Hz), 7.60 (2H, d, J = 8.2 Hz), 7.85 (2H, d, J = 8.2 Hz), 8.46 (1H, t, J = 5.7 Hz). ^{13}C NMR (DMSO-d_6, 125 MHz): δ [ppm] = 20.2, 28.1, 35.4, 46.6, 64.1, 64.4, 115.0, 115.8, 118.1, 119.9, 127.4, 128.8, 134.1, 139.7, 143.8, 146.7, 162.4, 164.9, 165.8. HPLC: 96%; t_R 7.16 min. EI-MS: m/z = 425 (M^+).

4-((5-(2,3-Dihydrobenzo[*b*][1,4]dioxin-6-yl)-1,3,4-oxadiazol-2-ylthio)methyl)-*N*-(2,2-dimethoxy ethyl)benzamide (9d). Yield 84%, beige solid. ^{1}H NMR (DMSO-d_6, 500 MHz): δ [ppm] = 3.28 (6H, s), 3.35 (2H, d, J = 5.7 Hz), 4.31 (2H, m), 4.34 (2H, m), 4.50 (1H, t, J = 5.6 Hz), 4.61 (2H, s), 7.05 (1H, d, J = 8.3 Hz), 7.40 (1H, d, J = 2.0 Hz), 7.43 (1H, dd, J = 8.3 Hz, J = 2.0 Hz), 7.55 (2H, d, J = 8.2 Hz), 7.81 (2H, d, J = 8.2 Hz), 8.52 (1H, t, J = 5.8 Hz). ^{13}C NMR (DMSO-d_6, 125 MHz): δ [ppm] = 35.4, 41.1, 53.2, 64.0, 64.4, 101.8, 115.0, 105.8, 108.2, 119.9, 127.4, 128.8, 133.5, 140.0, 143.8, 146.7, 162.4, 164.9, 165.9. HPLC: 95%; t_R 6.13 min. EI-MS: m/z = 457 (M^+).

***N*-Benzyl-4-((5-(2,3-dihydrobenzo[*b*][1,4]dioxin-6-yl)-1,3,4-oxadiazol-2-ylthio)methyl)benzamide (9e).** Yield 89%, beige solid. ^{1}H NMR (DMSO-d_6, 500 MHz): δ [ppm] = 4.31 (2H, m), 4.34 (2H, m), 4.47 (2H, d, J = 5.9 Hz), 4.62 (2H, s), 7.05 (1H, d, J = 8.4 Hz), 7.23 (1H, m), 7.32 (4H, m), 7.40 (1H, d, J = 2.0 Hz), 7.43 (1H, dd, J = 8.3 Hz, J = 2.0 Hz), 7.56 (2H, d, J = 8.2 Hz), 7.86 (2H, d, J = 8.2 Hz), 9.01 (1H, t, J = 5.9 Hz). ^{13}C NMR (DMSO-d_6, 125 MHz): δ [ppm] = 35.4, 42.6, 64.1, 64.4, 115.1, 115.8, 118.3, 119.8, 126.7, 127.3, 127.5, 128.4, 128.8, 133.7, 139.6, 140.1, 143.8, 146.7, 162.4, 165.0, 165.8. HPLC: 95%; t_R 7.66 min. EI-MS: m/z = 459 (M^+).

2-(4-(1*H*-Tetrazol-5-yl)benzylthio)-5-(benzo[*d*][1,3]dioxol-5-yl)-1,3,4-oxadiazole (8e). 4-((5-Benzo[d][1,3]dioxol-5-yl)-1,3,4-oxadiazol-2-ylthio)methyl)benzonitrile **5b** (34 mg, 0.10 mmol), NaN_3 (78 mg, 1.20 mmol), and NH_4Cl (64 mg, 1.20 mmol) were added to 1 mL of DMF and stirred for 5 h at 100 °C under microwave irradiation. After cooling to room temperature, the reaction solution was added to water (2−3 mL), acidified with 2 N HCl, and extracted three times with ethyl acetate. The combined organic layers were dried over Na_2SO_4, filtered, and the solvent evaporated off to provide **8e** (25 mg, 67%) as a beige solid. ^{1}H NMR (DMSO-d_6, 500 MHz): δ [ppm] = 4.65 (2H, s), 6.15 (2H, s), 7.11 (1H, d, J = 8.1 Hz), 7.43 (1H, d, J = 1.6 Hz), 7.50 (1H, dd, J = 8.1 Hz, J = 1.7 Hz), 7.71 (2H, d, J = 8.3 Hz), 8.00 (2H, d, J = 8.3 Hz), NH signal was not observed. ^{13}C NMR (DMSO-d_6, 125 MHz): δ [ppm] = 35.4, 102.1, 105.0, 106.2, 108.9, 109.1, 116.6, 119.7, 121.7, 127.1, 130.0, 148.1, 150.4, 162.4, 165.1. HPLC: 96%; t_R 5.92 min. EI-MS: m/z = 380 (M^+).

Compound **9f** was prepared in a similar manner to that described for **8e**.

2-(4-(1*H*-Tetrazol-5-yl)benzylthio)-5-(2,3-dihydrobenzo[*d*]-[1,4]dioxin-5-yl)-1,3,4-oxadiazole (9f). Yield 79%, puce solid. ^{1}H NMR (DMSO-d_6, 500 MHz): δ [ppm] = 4.35 (2H, m), 4.38 (2H, m), 4.70 (2H, s), 7.10 (1H, d, J = 8.4 Hz), 7.43 (1H, d, J = 2.0 Hz),

7.47 (1H, dd, J = 8.4 Hz, J = 2.1 Hz), 7.75 (2H, d, J = 8.3 Hz), 8.05 (2H, d, J = 8.3 Hz), NH signal was not observed. ^{13}C NMR (DMSO-d_6, 125 MHz): δ [ppm] = 35.5, 64.0, 64.4, 115.0, 115.8, 118.2, 119.9, 123.6, 127.1, 130.0, 140.1, 143.8, 146.7, 162.4, 165.1. HPLC: 95%; t_R 6.01 min. EI-MS: m/z = 394 (M^+).

The following compounds **14a−d**, **15a−b**, and **16a** were prepared in a similar manner to that described for **5a**.

2-(Benzo[*d*][1,3]dioxol-5-yl)-5-(biphenyl-4-ylmethylthio)-1,3,4-oxadiazole (14a). Yield 75%, beige solid. ^{1}H NMR (DMSO-d_6, 500 MHz): δ [ppm] = 4.55 (2H, s), 6.08 (2H, s), 7.04 (1H, d, J = 8.1 Hz), 7.28 (1H, m), 7.38 (3H, m), 7.45 (1H, dd, J = 8.1 Hz, J = 1.7 Hz), 7.48 (2H, d, J = 8.3 Hz), 7.58 (4H, m). ^{13}C NMR (DMSO-d_6, 125 MHz): δ [ppm] = 35.6, 102.1, 106.2, 109.1, 116.6, 121.7, 126.6, 126.8, 127.6, 128.9, 129.7, 135.8, 139.6, 148.1, 150.5, 162.6, 165.1. HPLC: 95%; t_R 9.12 min. EI-MS: m/z = 388 (M^+).

4′-((5-(Benzo[*d*][1,3]dioxol-5-yl)-1,3,4-oxadiazol-2-ylthio)-methyl)biphenyl-2-carbonitrile (14b). Yield 71%, brown solid. ^{1}H NMR (DMSO-d_6, 500 MHz): δ [ppm] = 4.66 (2H, s), 6.15 (2H, s), 7.11 (1H, d, J = 8.1 Hz), 7.45 (1H, d, J = 1.7 Hz), 7.51 (1H, dd, J = 8.1 Hz, J = 1.7 Hz), 7.57 (2H, d, J = 8.2 Hz), 7.65 (4H, m), 7.96 (1H, dd, J = 8.5 Hz, J = 2.3 Hz). ^{13}C NMR (DMSO-d_6, 125 MHz): δ [ppm] = 35.5, 102.1, 106.1, 109.1, 111.5, 111.6, 116.6, 117.3, 117.4, 120.3, 120.5, 121.0, 121.2, 121.7, 129.0, 129.4, 132.3, 132.4, 136.2, 137.5, 140.8, 140.9, 148.1, 150.4, 159.9, 161.9, 162.6, 165.1. HPLC: 95%; t_R 8.77 min. EI-MS: m/z = 431 (M^+). HRMS (EI): m/z calcd for $C_{23}H_{14}N_3O_3FS$ 431.0740, found 431.0728.

4-((5-(Benzo[*d*][1,3]dioxol-5-yl)-1,3,4-oxadiazol-2-ylthio)-methyl)-4-fluorobiphenyl-2-carbonitrile (14c). Yield 69%, gray solid. ^{1}H NMR (DMSO-d_6, 500 MHz): δ [ppm] = 4.66 (2H, s), 6.16 (2H, s), 7.11 (1H, d, J = 8.1 Hz), 7.45 (1H, d, J = 1.7 Hz), 7.51 (1H, dd, J = 8.1 Hz, J = 1.7 Hz), 7.56 (2H, d, J = 8.2 Hz), 7.65 (4H, m), 7.78 (1H, td, J = 7.7 Hz, J = 1.3 Hz), 7.95 (1H, dd, J = 7.7 Hz, J = 0.9 Hz). ^{13}C NMR (DMSO-d_6, 125 MHz): δ [ppm] = 35.5, 102.1, 106.1, 109.1, 110.1, 116.6, 118.5, 121.7, 128.3, 128.9, 129.4, 130.1, 133.5, 133.8, 137.2, 137.4, 140.0, 148.1, 150.4, 162.6, 165.1. HPLC: 96%; t_R 8.36 min. EI-MS: m/z = 413 (M^+). HRMS (EI): m/z calcd for $C_{23}H_{15}N_3O_3S$ 413.0835, found 413.0804.

4′-((5-(Benzo[*d*][1,3]dioxol-5-yl)-1,3,4-oxadiazol-2-ylthio)-methyl)biphenyl-4-carbonitrile (14d). Yield 51%, gray−brown solid. ^{1}H NMR (DMSO-d_6, 500 MHz): δ [ppm] = 4.63 (2H, s), 6.15 (2H, s), 7.10 (1H, d, J = 8.1 Hz), 7.43 (1H, d, J = 1.7 Hz), 7.51 (1H, dd, J = 8.1 Hz, J = 1.7 Hz), 7.61 (2H, d, J = 8.3 Hz), 7.73 (2H, d, J = 8.3 Hz), 7.87 (2H, d, J = 8.6 Hz), 7.91 (2H, d, J = 8.6 Hz). ^{13}C NMR (DMSO-d_6, 125 MHz): δ [ppm] = 35.9, 102.6, 106.6, 109.6, 110.6, 117.1, 119.3, 122.2, 127.7, 128.0, 130.3, 133.3, 138.0, 138.1, 144.5, 148.6, 150.9, 163.0, 165.5. HPLC: 97%; t_R 8.77 min. EI-MS: m/z = 413 (M^+). HRMS (EI): m/z calcd for $C_{23}H_{15}N_3O_3S$ 413.0835, found 413.0825.

4-((5-(2,3-Dihydrobenzo[*b*][1,4]dioxin-6-yl)-[1,3,4]oxadiazol-2-ylthio)methyl)biphenyl-2-carbonitrile (15a). Yield 74%, colorless solid. ^{1}H NMR (DMSO-d_6, 500 MHz): δ [ppm] = 4.31 (2H, m), 4.34 (2H, m), 4.65 (2H, s), 7.05 (1H, d, J = 8.4 Hz), 7.41 (1H, d, J = 2.0 Hz), 7.44 (1H, dd, J = 8.4 Hz, J = 2.0 Hz), 7.60 (6H, m), 7.79 (1H, td, J = 7.7 Hz, J = 1.2 Hz), 7.95 (1H, dd, J = 7.7 Hz, J = 0.9 Hz). ^{13}C NMR (DMSO-d_6, 125 MHz): δ [ppm] = 35.9, 64.4, 64.8, 110.5, 115.4, 116.3, 118.5, 118.8, 120.3, 128.6, 129.3, 129.7, 130.5, 133.8, 134.2, 137.5, 137.8, 144.1, 144.3, 147.1, 163.0, 165.3. HPLC: 100%; t_R 8.39 min. EI-MS: m/z 427 (M^+). HRMS (EI): m/z calcd for $C_{24}H_{17}N_3O_3S$ 427.0991, found 427.0962.

4′-((5-(2,3-Dihydrobenzo[*b*][1,4]dioxin-6-yl)-1,3,4-oxadiazol-2-ylthio)methyl)-4-fluorobiphenyl-2-carbonitrile (15b). Yield 29%, light-yellow solid. ^{1}H NMR (DMSO-d_6, 500 MHz): δ [ppm] = 4.32 (2H, m), 4.34 (2H, m) 4.65 (2H, s), 7.05 (1H, d, J = 8.4 Hz), 7.40 (1H, d, J = 2.1 Hz), 7.45 (1H, dd, J = 8.4 Hz, J = 2.1 Hz), 7.56 (2H, d, J = 8.2 Hz), 7.63 (2H, d, J = 8.2 Hz), 7.68 (2H, m), 7.97 (1H, dd, J = 9.0 Hz, J = 1.9 Hz). HPLC: 95%; t_R 8.76 min. EI-MS: m/z = 445 (M^+). HRMS (EI): m/z calcd for $C_{24}H_{16}N_3O_3FS$ 445.0897, found 445.0890.

4-((5-(Pyridine-4-yl)-1,3,4-oxadiazol-2-ylthio)methyl)-biphenyl-2-carbonitrile (16a). Yield 53%, colorless solid. ^{1}H NMR (DMSO-d_6, 500 MHz): δ [ppm] = 4.71 (2H, s), 7.58 (3H, m), 7.62 (1H, d, J = 7.7 Hz), 7.68 (2H, d, J = 8.1 Hz), 7.78 (1H, t, J = 7.7 Hz), 7.91 (2H, d, J = 4.1 Hz), 7.95 (1H, d, J = 7.7 Hz), 8.85 (2H, s, br). ^{13}C NMR (DMSO-d_6, 125 MHz): δ [ppm] = 35.4, 110.1, 118.5, 120.1, 128.2, 128.9, 129.4, 130.0, 130.1, 133.5, 133.7, 137.2, 137.3, 143.9, 150.8, 163.8, 164.8. HPLC: 99%; t_R 6.63 min. EI-MS: m/z = 370 (M^+). HRMS (EI): m/z calcd for $C_{21}H_{14}N_4OS$ 370.0889, found 370.0926.

Methyl 3,4-Dihydroxybenzoate (18). To a stirred solution of 3,4-dihydroxybenzoic acid (2.0 g, 13 mmol) in MeOH (25 mL) was added $SOCl_2$ (1.88 mL, 26 mmol) dropwise over 1 h at 0 °C. The solution was further stirred 12 h at 50 °C. The mixture was cooled to room temperature and diluted with water (30 mL). MeOH was evaporated and the pH adjusted to ∼6 with aqueous $NaHCO_3$. The mixture was extracted three times with EtOAc and successively washed with brine. The organic layer was dried over $MgSO_4$ and concentrated under reduced pressure to give **18** (2.1 g, 97%) as a colorless solid. ^{1}H NMR (DMSO-d_6, 500 MHz): δ [ppm] = 3.75 (3H, s), 6.80 (1H, d, J = 8.2 Hz), 7.31 (1H, dd, J = 8.2 Hz, J = 2.1 Hz), 7.35 (1H, d, J = 2.1 Hz), 9.35 (1H, s), 9.75 (1H, s). ^{13}C NMR (DMSO-d_6, 125 MHz): δ [ppm] = 51.5, 115.3, 116.2, 120.4, 121.7, 145.0, 150.4, 166.1. EI-MS: m/z = 168 (M^+).

Methyl 3-(Hydroxymethyl)-2,3-dihydrobenzo[*b*][1,4]-dioxine-6-carboxylate (19a). Methyl 3,4-dihydroxybenzoate **18** (0.8 g, 4.75 mmol) and K_2CO_3 (0.65 g, 4.75 mmol) were taken in dry acetone (10 mL) and stirred for 15 min at room temperature. Afterward, the solution was treated with epibromohydrin (0.40 mL, 4.75 mmol) and stirred overnight at 70 °C. The reaction mixture was diluted with water and extracted with EtOAc. The organic layer was washed with brine and dried over Na_2SO_4. The solvent was evaporated under reduced pressure and the crude product purified by silica gel column chromatography (DCM/EtOAc, 4:1) to give **19a** (1.01 g, 95%) as a colorless oil. ^{1}H NMR (DMSO-d_6, 500 MHz): δ [ppm] = 3.64 (2H, m), 3.80 (3H, s), 4.10 (1H, m), 4.20 (1H, m), 4.41 (1H, dd, J = 11.4 Hz, J = 2.3 Hz), 5.10 (1H, t, J = 5.7 Hz), 6.98 (1H, d, J = 8.4 Hz), 7.41 (1H, d, J = 2.0 Hz), 7.46 (1H, dd, J = 8.4 Hz, J = 2.0 Hz). ^{13}C NMR (DMSO-d_6, 125 MHz): δ [ppm] = 51.9, 59.7, 65.4, 73.6, 117.0, 117.9, 122.6, 122.7, 142.8, 147.4, 165.6. EI-MS: m/z = 224 (M^+).

Note: Alternatively (*R*/*S*)-(±)-glycidyl tosylate can be used to obtain compound **19a**. For more details see the synthesis of compound **19b−c**.

Methyl 3-(Methoxymethyl)-2,3-dihydrobenzo[*b*][1,4]-dioxine-6-carboxylate (20a). To a suspension of NaH (115 mg, 4.81 mmol) in 5 mL of anhydrous THF was added methyl 3-(hydroxymethyl)-2,3-dihydrobenzo[*b*][1,4]dioxine-6-carboxylate **19a** (900 mg, 4.01 mmol) at 0 °C. The mixture was stirred at room temperature for 30 min, followed by addition of methyl iodide (374 μL, 6.01 mmol). The reaction mixture was stirred at room temperature for 48 h, quenched with 10 mL of water, and extracted with ethyl acetate. The combined organic layer was dried over $MgSO_4$, the solvent was evaporated under reduced pressure, and the crude product purified by silica gel column chromatography (DCM/EtOAc, 20:1) to give **20a** (678 mg, 71%) as a colorless oil. ^{1}H NMR (DMSO-d_6, 500 MHz): δ [ppm] = 3.33 (3H, s), 3.60 (2H, m), 3.80 (3H, s), 4.09 (1H, m), 4.40 (2H, m), 6.99 (1H, m), 7.41 (1H, m), 7.47 (1H, m). ^{13}C NMR (DMSO-d_6, 125 MHz): δ [ppm] = 51.8, 58.7, 65.3, 70.3, 71.8, 117.0, 118.0, 122.7, 122.8, 142.6, 147.2, 165.5. EI-MS: m/z = 238 (M^+).

3-(Methoxymethyl)-2,3-dihydrobenzo[*b*][1,4]dioxine-6-carbohydrazide (21a). To a solution of **20a** (600 mg, 2.51 mmol) in EtOH (15 mL) was added hydrazine hydrate (731 μL, 15.06 mmol). and the mixture was heated at reflux for 2 days. After cooling to room temperature, the reaction mixture was diluted with water and extracted with EtOAc. The organic layer was washed with brine and dried over $MgSO_4$. The solvent was evaporated under reduced pressure and the crude product purified by silica gel column chromatography (MeOH/EtOAc, 1:10) to give **21a** (466 mg, 78%) as a colorless solid. ^{1}H NMR (DMSO-d_6, 500 MHz): δ [ppm] = 3.32 (3H, s), 3.59 (2H, m), 4.04 (1H, m), 4.36 (2H, m), 4.41 (2H, s), 6.92 (1H, d, J = 8.2 Hz), 7.35 (1H, dd, J = 8.2 Hz, J = 2.0 Hz), 7.37 (1H, d, J = 2.0 Hz), 9.52 (1H, s). ^{13}C NMR (DMSO-d_6, 125 MHz): δ [ppm] = 58.7, 65.1, 70.4, 71.8,

115.8, 116.6, 120.3, 126.5, 142.3, 145.3, 165.1. EI-MS: m/z = 238 (M^+).

Compound **22a** was prepared in a similar manner to that described for **4A**.

5-(3-(Methoxymethyl)-2,3-dihydrobenzo[*b*][1,4]dioxin-6-yl)-1,3,4-oxadiazole-2-thiol (22a). Yield 81%, orange solid. ^{1}H NMR (DMSO-d_6, 500 MHz): δ [ppm] = 3.32 (3H, s), 3.61 (2H, m), 4.10 (1H, m), 4.43 (2H, m), 7.07 (1H, m), 7.32 (1H, m), 7.37 (1H, m), 14.60 (1H, s). ^{13}C NMR (DMSO-d_6, 125 MHz): δ [ppm] = 58.7, 65.3, 70.3, 72.1, 114.6, 115.6, 118.0, 119.7, 143.4, 146.4, 160.1, 177.4. EI-MS: m/z = 280 (M^+).

Compound **23a** was prepared in a similar manner to that described for **5a**.

4′-((5-(3-(Methoxymethyl)-2,3-dihydrobenzo[*b*][1,4]dioxin-6-yl)-1,3,4-oxadiazol-2ylthio)methyl)biphenyl-2-carbonitrile (23a). Yield 88%, colorless solid. ^{1}H NMR (DMSO-d_6, 500 MHz): δ [ppm] = 3.33 (3H, s), 3.61 (2H, m), 4.10 (1H, m), 4.44 (2H, m), 4.66 (2H, s), 7.07 (1H, m), 7.45 (2H, m), 7.57 (3H, m), 7.63 (3H, m), 7.78 (1H, td, J = 7.6 Hz, J = 1.2 Hz), 7.95 (1H, dd, J = 7.7 Hz, J = 1.1 Hz). ^{13}C NMR (DMSO-d_6, 125 MHz): δ [ppm] = 35.4, 58.7, 65.2, 70.3, 72.0, 110.1, 115.1, 116.2, 118.0, 118.5, 119.9, 128.2, 128.8, 129.4, 130.1, 133.5, 133.8, 137.1, 137.4, 143.3, 143.9, 146.2, 162.6, 164.9. HPLC: 100%; t_R 8.59 min. EI-MS: m/z = 471 (M^+). HRMS (EI): m/z calcd for $C_{26}H_{21}N_3O_4S$ 471.1253, found 471.1264.

4′-((5-(3-(Hydroxymethyl)-2,3-dihydrobenzo[*b*][1,4]dioxin-6-yl)-1,3,4-oxadiazol-2-ylthio) methyl)biphenyl-2-carbonitrile (24a). To a solution of 4′-((5-(3-(methoxymethyl)-2,3-dihydrobenzo-[*b*][1,4]dioxin-6-yl)-1,3,4-oxadiazol-2ylthio)methyl)biphenyl-2-carbonitrile **23a** (400 mg, 0.85 mmol) in 10 mL of DCM was added 1 N solution of BBr_3 in hexane (850 μL, 0.85 mmol) under argon atmosphere at −78 °C. The reaction mixture was stirred at the same temperature for 1 h and allowed to warm to room temperature and further stirred for 24 h. After treatment with saturated $NaHCO_3$ solution, the reaction mixture was extracted with ethyl acetate. The combined organic layers were dried over $MgSO_4$ and concentrated under reduced pressure. The crude product was purified by silica gel column chromatography (cyclohexane/EtOAc, 1:2) to give compound **24a** (283 mg, 73%) as a light-yellow solid. ^{1}H NMR (DMSO-d_6, 500 MHz): δ [ppm] = 3.59 (1H, s, br), 3.64 (2H, m), 4.10 (1H, m), 4.24 (1H, m), 4.42 (1H, dd, J = 11.5 Hz, J = 2.2 Hz), 4.65 (2H, s) 7.06 (1H, d, J = 8.3 Hz), 7.43 (2H, m), 7.60 (6H, m), 7.78 (1H, td, J = 7.7 Hz, J = 1.2 Hz), 7.94 (1H, dd, J = 7.7 Hz, J = 1.0 Hz). ^{13}C NMR (DMSO-d_6, 125 MHz): δ [ppm] = 35.4, 59.6, 65.4, 73.7, 110.1, 115.1, 116.1, 117.9, 118.5, 119.8, 128.2, 128.8, 129.4, 130.1, 133.4, 133.8, 137.1, 137.4, 143.5, 144.0, 146.2, 162.6, 165.0. HPLC: 96%; t_R 7.39 min. EI-MS: m/z = 457(M^+).

(*R*)-Methyl 3-(Hydroxymethyl)-2,3-dihydrobenzo[*b*][1,4]-dioxine-6-carboxylate (19b). To a round-bottom flask equipped with magnetic stirring and a nitrogen inlet was added methyl-3,4-dihydroxybenzoate **18** (1.0 g, 6 mmol), (2*S*)-(+)-glycidyl tosylate (1.37 g, 6 mmol), K_2CO_3(0.99 g, 7.2 mmol), and DMF (15 mL). This mixture was heated to 60 °C for 5 h. The mixture was cooled to room temperature, diluted with water, and extracted with EtOAc. The organic layer was washed with brine and dried over Na_2SO_4. The solvent was evaporated under reduced pressure and the crude product purified by silica gel column chromatography (DCM/EtOAc, 4:1) to give **19b** (1.25 g, 93%) as a colorless oil. ^{1}H NMR (DMSO-d_6, 500 MHz): δ [ppm] = 3.64 (2H, m), 3.80 (3H, s), 4.10 (1H, m), 4.20 (1H, m), 4.41 (1H, dd, J = 11.4 Hz, J = 2.3 Hz), 5.08 (1H, t, J = 5.7 Hz), 6.98 (1H, d, J = 8.4 Hz), 7.41 (1H, d, J = 2.0 Hz), 7.46 (1H, dd, J = 8.4 Hz, J = 2.0 Hz). ^{13}C NMR (DMSO-d_6, 125 MHz): δ [ppm] = 51.9, 59.7, 65.5, 73.6, 117.0, 117.9, 122.6, 122.7, 142.8, 147.4, 165.6. HPLC: 96%; t_R 2.44 min. EI-MS: m/z = 224 (M^+).

Compound **19c** was prepared in a similar manner to that described for **19b**. (2*R*)-(−)-glycidyl tosylate was used instead of (2*S*)-(+)-glycidyl tosylate to obtain the *S*-isomer.

(*S*)-Methyl 3-(Hydroxymethyl)-2,3-dihydrobenzo[*b*][1,4]-dioxine-6-carboxylate (19c). Yield 89%, as a colorless oil. ^{1}H NMR (DMSO-d_6, 500 MHz): δ [ppm] = 3.64 (2H, m), 3.80 (3H, s), 4.10 (1H, m), 4.20 (1H, m), 4.41 (1H, dd, J = 11.4 Hz, J = 2.3 Hz), 5.10 (1H, s, br), 6.98 (1H, d, J = 8.4 Hz), 7.41 (1H, d, J = 2.0 Hz), 7.46 (1H, dd, J = 8.4 Hz, J = 2.0 Hz). ^{13}C NMR (DMSO-d_6, 125 MHz): δ [ppm] = 51.9, 59.7, 65.5, 73.6, 117.0, 117.9, 122.6, 122.7, 142.8, 147.4, 165.6. EI-MS: m/z = 224 (M^+).

Compounds **20b−c** were prepared in a similar manner to that described for **20a**.

(*R*)-Methyl 3-(Methoxymethyl)-2,3-dihydrobenzo[*b*][1,4]-dioxine-6-carboxylate (20b). Yield 68%, as a colorless oil. ^{1}H NMR (DMSO-d_6, 500 MHz): δ [ppm] = 3.33 (3H, s), 3.60 (2H, m), 3.81 (3H, s), 4.09 (1H, m), 4.40 (2H, m), 6.99 (1H, d, J = 8.4 Hz), 7.42 (1H, d, J = 2.0 Hz), 7.47 (1H, dd, J = 8.4 Hz, J = 2.0 Hz). ^{13}C NMR (DMSO-d_6, 125 MHz): δ [ppm] = 51.9, 58.7, 65.3, 70.3, 71.8, 117.1, 117.9, 122.8, 122.9, 142.6, 147.3, 165.6. EI-MS: m/z = 238 (M^+).

(*S*)-Methyl 3-(Methoxymethyl)-2,3-dihydrobenzo[*b*][1,4]-dioxine-6-carboxylate (20c). After extraction and evaporation of the solvent, compound **20c** was used without further purification.

Compounds **21b−c** were prepared in a similar manner to that described for **21a**.

(*R*)-3-(Methoxymethyl)-2,3-dihydrobenzo[*b*][1,4]dioxine-6-carbohydrazide (21b). Yield 87%, as a colorless solid. ^{1}H NMR (DMSO-d_6, 500 MHz): δ [ppm] = 3.32 (3H, s), 3.59 (2H, m), 4.04 (1H, m), 4.36 (2H, m), 4.41 (2H, s), 6.92 (1H, d, J = 8.3 Hz), 7.35 (1H, dd, J = 8.3 Hz, J = 2.0 Hz), 7.37 (1H, d, J = 2.0 Hz), 9.57 (1H, s). ^{13}C NMR (DMSO-d_6, 125 MHz): δ [ppm] = 58.7, 65.1, 70.4, 71.7, 115.8, 116.6, 120.4, 126.6, 142.3, 145.3, 165.1. EI-MS: m/z = 238 (M^+).

(*S*)-3-(Methoxymethyl)-2,3-dihydrobenzo[*b*][1,4]dioxine-6-carbohydrazide (21c). Yield 92%, as a colorless solid. ^{1}H NMR (DMSO-d_6, 500 MHz): δ [ppm] = 3.32 (3H, s), 3.59 (2H, m), 4.04 (1H, m), 4.36 (2H, m), 4.41 (2H, s), 6.92 (1H, d, J = 8.3 Hz), 7.36 (1H, dd, J = 8.3 Hz, J = 2.0 Hz), 7.37 (1H, d, J = 2.0 Hz), 9.57 (1H, s). ^{13}C NMR (DMSO-d_6, 125 MHz): δ [ppm] = 58.7, 65.1, 70.4, 71.8, 115.8, 116.6, 120.4, 126.6, 142.3, 145.3, 165.2. EI-MS: m/z = 238 (M^+).

Compounds **22b−c** were prepared in a similar manner to that described for **4A**.

(*R*)-5-(3-(Methoxymethyl)-2,3-dihydrobenzo[*b*][1,4]dioxin-6-yl)-1,3,4-oxadiazole-2-thiol (22b). Yield 91%, orange solid. ^{1}H NMR (DMSO-d_6, 500 MHz): δ [ppm] = 3.33 (3H, s), 3.61 (2H, m), 4.10 (1H, m), 4.42 (2H, m), 7.07 (1H, m), 7.31 (1H, m), 7.37 (1H, m), 14.62 (1H, s). ^{13}C NMR (DMSO-d_6, 125 MHz): δ [ppm] = 58.8, 65.3, 70.2, 72.1, 114.6, 115.6, 118.0, 119.7, 143.3, 146.4, 160.1, 177.2. EI-MS: m/z = 280 (M^+).

(*S*)-5-(3-(Methoxymethyl)-2,3-dihydrobenzo[*b*][1,4]dioxin-6-yl)-1,3,4-oxadiazole-2-thiol (22c). Yield 91%, orange solid. ^{1}H NMR (DMSO-d_6, 500 MHz): δ [ppm] = 3.33 (3H, s), 3.61 (2H, m), 4.09 (1H, m), 4.39 (2H, m), 7.02 (1H, m), 7.24 (1H, m), 7.30 (1H, m), SH signal was not observed. ^{13}C NMR (DMSO-d_6, 125 MHz): δ [ppm] = 58.6, 65.3, 70.0, 72.1, 114.6, 115.6, 117.7, 119.7, 143.3, 146.4, 160.1, 177.2. EI-MS: m/z = 280 (M^+).

Compounds **23b−c** were prepared in a similar manner to that described for **5a**.

(*R*)-4′-((5-(3-(Methoxymethyl)-2,3-dihydrobenzo[*b*][1,4]-dioxin-6-yl)-1,3,4-oxadiazol-2-ylthio) methyl)biphenyl-2-carbonitrile (23b). Yield 84%, colorless solid. ^{1}H NMR (DMSO-d_6, 500 MHz): δ [ppm] = 3.38 (3H, s), 3.66 (2H, m), 4.15 (1H, m), 4.47 (2H, m), 4.71 (2H, s), 7.13 (1H, m), 7.50 (2H, m), 7.65 (6H, m), 7.82 (1H, td, J = 7.7 Hz, J = 1.3 Hz), 8.00 (1H, dd, J = 7.7 Hz, J = 0.9 Hz). ^{13}C NMR (DMSO-d_6, 125 MHz): δ [ppm] = 35.4, 58.7, 65.2, 70.4, 72.0, 110.1, 115.1, 116.2, 118.0, 118.4, 119.9, 128.2, 128.8, 129.4, 130.1, 133.5, 133.8, 137.2, 137.4, 143.2, 143.9, 146.2, 162.6, 164.9. HPLC: 99%; t_R 8.70 min. EI-MS: m/z = 471 (M^+).

(*S*)-4′-((5-(3-(Methoxymethyl)-2,3-dihydrobenzo[*b*][1,4]-dioxin-6-yl)-1,3,4-oxadiazol-2-ylthio) methyl)biphenyl-2-carbonitrile (23c). Yield 84%, colorless solid. ^{1}H NMR (DMSO-d_6, 500 MHz): δ [ppm] = 3.33 (3H, s), 3.61 (2H, m), 4.10 (1H, m), 4.42 (2H, m), 4.66 (2H, s), 7.07 (1H, m), 7.44 (2H, m), 7.60 (6H, m), 7.78 (1H, td, J = 7.6 Hz, J = 1.3 Hz), 7.94 (1H, dd, J = 7.7 Hz, J = 0.9 Hz). ^{13}C NMR (DMSO-d_6, 125 MHz): δ [ppm] = 35.2, 58.7, 65.2, 70.1, 71.9, 110.1, 115.1, 116.2, 117.9, 118.4, 119.9, 128.2, 128.6, 129.4, 130.1, 133.5, 133.8, 137.2, 137.4, 143.2, 143.9, 146.2, 162.6, 164.9.

Table 5. Small Kinase Panel Values

kinase	enzyme conc (nM)	ATP conc (μM)	peptide used	peptide conc (μM)	buffer
GSK-3β	2	12.5	Ser/Thr 9 peptide	2	50 mM Hepes pH 7.5, 10 mM $MgCl_2$, 1 mM EGTA, 0.01% (w/v) Brij-35
GSK-3α	0.5	12.5	Ser/Thr 9 peptide	2	50 mM Hepes pH 7.5, 10 mM $MgCl_2$, 1 mM EGTA, 0.01% (w/v) Brij-35
CKIε	12	32	Ser/Thr 11 peptide	2	50 mM Hepes pH 7.5, 10 mM $MgCl_2$, 1 mM EGTA, 0.01% (w/v) Brij-35
Cdk5	10	12.5	Ser/Thr 12 peptide	2	50 mM Hepes pH 7.5, 10 mM $MgCl_2$, 1 mM EGTA, 0.01% (w/v) Brij-35
AurKA	20	10	Ser/Thr 1 peptide	2	50 mM Hepes pH 7.5, 10 mM $MgCl_2$, 1 mM EGTA, 0.01% (w/v) Brij-35
PKCα	0.15	10	Ser/Thr 7 peptide	2	50 mM Hepes pH 7.5, 10 mM $MgCl_2$, 1 mM EGTA, 0.01% (w/v) Brij-35

HPLC: 100%; t_R 8.65 min. EI-MS: m/z = 471 (M^+). HRMS (EI): m/z calcd for $C_{26}H_{21}N_3O_4S$ 471.1253, found 471.1269.

Compound **24b** was prepared in a similar manner to that described for **24a**.

(*R*)-4′-((5-(3-(Hydroxymethyl)-2,3-dihydrobenzo[*b*][1,4]-dioxin-6-yl)-1,3,4-oxadiazol-2-ylthio) methyl)biphenyl-2-carbonitrile (24b). Yield 79%, light-yellow solid. ^{1}H NMR (DMSO-d_6, 500 MHz): δ [ppm] = 3.40 (1H, s, br), 3.59 (2H, m), 4.04 (1H, m), 4.15 (1H, m), 4.34 (1H, dd, J = 11.5 Hz, J = 2.3 Hz), 4.57 (2H, s), 6.98 (1H, d, J = 8.3 Hz), 7.35 (2H, m), 7.53 (6H, m), 7.70 (1H, td, J = 7.7 Hz, J = 1.3 Hz), 7.85 (1H, dd, J = 7.7 Hz, J = 0.9 Hz). ^{13}C NMR (DMSO-d_6, 125 MHz): δ [ppm] = 35.4, 59.6, 65.4, 73.7, 110.1, 115.0, 116.1, 117.9, 118.5, 119.8, 128.2, 128.8, 129.3, 130.1, 133.4, 133.8, 137.1, 137.4, 143.5, 144.0, 146.2, 162.5, 164.9. HPLC: 95%; t_R 7.48 min. EI-MS: m/z = 457 (M^+).

(*S*)-((7-(5-(2′-Cyanobiphenyl-4-yl)methylthio)-1,3,4-oxadiazol-2-yl)-2,3-dihydrobenzo[*b*][1,4] dioxin-2-yl)-methylmethanesulfonate (25). To a solution of **24b** (238 mg, 0.52 mmol) in 10 mL of DCM was added Et_3N (0.72 mL, 5.2 mmol) followed by addition of methanesulfonyl chloride (402 μL, 5.2 mmol) at 0 °C. The reaction mixture was stirred at the same temperature for 1 h and further stirred at room temperature for 4 h. After treating with saturated $NaHCO_3$ solution, the reaction mixture was extracted with DCM. The combined organic layer was dried over $MgSO_4$, concentrated, and purified by column chromatography (EtOAc/cyclohexane, 1:1) to provide **25** (273 mg, 98%) yellow oil. ^{1}H NMR (DMSO-d_6, 500 MHz): δ [ppm] = 3.26 (3H, s), 4.17 (1H, m), 4.45 (1H, m), 4.50 (1H, dd, J = 11.6 Hz, J = 2.4 Hz), 4.55 (1H, dd, J = 11.6 Hz, J = 3.3 Hz), 4.62 (1H, m), 4.67 (2H, s), 7.11 (1H, d, J = 8.1 Hz), 7.48 (2H, m), 7.61 (6H, m), 7.77 (1H, td, J = 7.6 Hz, J = 1.3 Hz), 7.95 (1H, dd, J = 7.7 Hz, J = 0.8 Hz). ^{13}C NMR (DMSO-d_6, 125 MHz): δ [ppm] = 35.4, 36.8, 64.3, 67.8, 70.9, 110.1, 115.2, 116.4, 118.2, 118.5, 120.3, 128.2, 128.8, 129.4, 130.1, 133.5, 133.8, 137.1, 137.4, 142.7, 143.9, 145.9, 162.7, 164.9. HPLC: 96%; t_R 8.46 min. EI-MS: m/z = 535 (M^+).

(*R*)-4′-((5-(3-((2,2-Dimethoxyethylamino)methyl)-2,3-dihydrobenzo[*b*][1,4]dioxin-6-yl)-1,3,4-oxadiazol-2-ylthio)-methyl)biphenyl-2-carbonitrile (26). To a stirred solution of **25** (69 mg, 0.13 mmol) in 2 mL of THF was added 2,2-dimethoxyethylamine (140 μL, 1.3 mmol) and NEt_3 (180 μL, 1.3 mmol) at 0 °C, and the reaction mixture was stirred at room temperature for 5 days. The mixture was diluted with water and extracted with EtOAc. The organic layer was washed with brine and dried over $MgSO_4$. The solvent was evaporated under reduced pressure and the crude product purified by silica gel column chromatography (MeOH/EtOAc, 1:10) to give **26** (58 mg, 83%) as a dark-yellow oil. ^{1}H NMR (DMSO-d_6, 500 MHz): δ [ppm] = 1.91 (1H, m), 2.61 (2H, dd, J = 5.4 Hz, J = 0.7 Hz), 2.80 (2H, m), 3.18 (3H, s), 3.19 (3H, s), 4.00 (1H, m), 4.17 (1H, m), 4.30 (2H, m), 4.54 (2H, s), 6.87 (1H, m), 7.32 (2H, m), 7.44 (1H, dd, J = 7.6 Hz, J = 1.2 Hz), 7.46 (3H, m), 7.52 (2H, m), 7.64 (1H, td, J = 7.8 Hz, J = 1.3 Hz), 7.74 (1H, m). ^{13}C NMR (DMSO-d_6, 125 MHz): δ [ppm] = 36.7, 50.2, 52.1, 53.8, 53.9, 67.7, 74.1, 104.9, 111.8, 116.5, 117.8, 118.7, 119.1, 120.8, 129.0, 130.0, 130.4, 131.1, 134.1, 134.7, 138.4, 138.8, 144.7, 145.4, 147.6, 163.7, 166.3. HPLC: 95%; t_R 6.34 min. EI-MS: m/z = 544 (M^+).

GSK-3β in Vitro Assay. Purified GSK-3β (0.5 μg) was incubated in a reaction mixture of 50 mM Tris pH 7.3, 10 mM $MgAc_2$, 0.01% β-mercaptoethanol, ^{32}P[γ-ATP](100 μM, 0.5 μci/assay), and 100 μM of peptide substrate, pIRS-1 (RREGGMSRPAS(p)VDG (1). New molecules were added at various concentrations (1, 10, and 100 μM), and the reaction mixture was incubated for 15 min at 30 °C. The reactions were stopped, spotted on p81 paper (Whatman), washed with 10 mM phosphoric acid, and counted for radioactivity.[50] GSK-3β activity was calculated as the percentage of GSK-3β activity in the absence of inhibitor that was designated to 100%.

Small Kinase Panel. Compounds were serially diluted 1/3 in neat DMSO (10 serial dilutions), and these dilutions were further diluted 1/25 with reaction buffer. Then 2.5 μL of these solutions were added to the reaction mixture described below so that final compound concentration in the assay ranges from 100 μM to 5 nM in 1% (v/v) DMSO. When compounds showed high inhibition at 5 nM and therefore the data could not be fitted to the corresponding equation, they were re-evaluated in a new range from 400 nM to 20 pM (Table 5).

The enzymatic activity of the kinases was determined with a commercial system based on the Z′-LYTE technology, available from Invitrogen Life Technologies (Carlsbad, CA, USA), using human recombinant kinases as the enzyme source. This technology utilizes the fluorescence resonance energy transfer ("FRET") process between fluorescein and coumarin. The assay principle is based on the differential sensitivity of phosphorylated and nonphosphorylated peptide to proteolytic cleavage, which precludes the energy transfer process between the two fluorophores attached to both sides of the cleavage site. Hence, enzymatic phosphorylation will yield a phosphopeptide, which cannot be hydrolyzed by a suitable protease and energy transfer between the two fluorophores will occur. Opposingly, lack of phosphorylation will cause peptide hydrolysis hence lack of energy transfer as. The assay was performed in 96-well black plates, in a final volume of 10 μL, with components as detailed in Tables 1, 3, and 4.

In Vivo Activity on Zebrafish Embryos. The wt zebrafish was used in this study. The embryos were collected and placed into 24-well plates, 10 embryos per well, and maintained in E2 medium at ∼28 °C. Compounds were added 5 hpf (50% epiboly) and the embryos allowed to grow in chemical compound solution up to 2 days. The phenotypes were compared using the Axio Scope.A1 microscope system from Carl Zeiss at 44−48 hpf.[36,37,51]

Animal Husbandry. All animal experiment were conducted and documented according to the federal and local regulation. All embryo testing was stopped at day 5 of embryonic development.

SH-SY5Y Neuroblastoma Cells. SH-SY5Y neuroblastoma cells stably transfected with Tau.P301L in the pcDNA3 vector were grown to confluency in 6-well cluster plates (∼800000 cells/well) in DMEM-F12 medium supplemented with Glutamax and 15% fetal calf serum. The medium contained gentamycin (50 μg/mL) as general antibiotic and Geneticin (250 μg/mL) to maintain selection pressure on transfected cells. Cells were grown at 37 °C in a humidified incubator in an atmosphere of 5.0% CO_2 in air. Stock solutions of the

compounds in DMSO were added to serum-free culture medium to the specified concentrations, using DMSO in the same final concentrations as control. Cells were incubated with the compounds at 37 °C for the indicated periods of time. After incubation, spent medium was removed and cells washed once with PBS containing Ca^{2+} and Mg^{2+}. The cells were rapidly harvested by mechanical scraping after addition of hot 62.5 mM Tris pH 6.8 buffer, containing 1% SDS (180 μL per well). Protein extracts were collected by aspiration and reduced and denatured by addition of 1% β-mercaptoethanol and boiling for 10 min. After separation by SDS-PAGE on 10% Tris-glycine SDS-PAGE, proteins were analyzed by Western blotting using the ECL-system.[52] In brief, after SDS-PAGE, the separated proteins were transferred to nitrocellulose filter-sheets, which were treated against nonspecific binding by incubation in 5% nonfat milk in Tris buffered saline (TBS: 10 mM Tris.HCl, pH 7.2, 0.9% sodium chloride, 0.1% Tween). Blots were subsequently incubated with primary antibodies specifically directed against total protein tau or against its selected phosphorylated epitopes, as specified in Results and Discussion and in the figure legends. After incubation with suitably labeled secondary antibodies, the resulting immune reactions were recorded and analyzed digitally with dedicated apparatus and software (LAS4000, Image-QuantTL, GE Healthcare, Brussels, Belgium). Data for tau and phospho-tau were normalized against actin, revealed by Western blotting of the same samples on the same blots.

Docking Simulations. Molecular docking of **15a** into the X-ray structure of GSK-3β (PDB code: 3F88) was carried out using the Glide 5.5 program.[53] Maestro 9.0.211 was employed as the graphical user interface, and Figure 2 was rendered by the Chimera software package.[54,55]

Ligand and Protein Setup. The inhibitor structure was first generated through the Dundee PRODRG2 server.[56] Then geometry optimized ligand was prepared using Lig-Prep 2.3 as implemented in Maestro. The target protein was prepared through the Protein Preparation Wizard of the graphical user interface Maestro and the OPLS-2001 force field. Water molecules were removed. Hydrogen atoms were added, and minimization was performed until the rmsd of all heavy atoms was within 0.3 Å of the crystallographically determined positions. The binding pocket was identified by placing a 20 Å cube centered on the mass center of the cocrystallized inhibitor. Molecular docking calculations were performed with the aid of Glide 5.5 in extra-precision (XP) mode, using Glidescore for ligand ranking.[57,58] For multiple ligand docking experiments, an output maximum of 5000 ligand poses per docking run with a limit of 100 poses for each ligand was adopted.

Homology Modeling. The homology model was built using the crystal structure of GSK-3β (PDB code: 3F88). The sequence identity between GSK-3α and GSK-3β is 61%. The alignment was performed by Prime, which calculates alignments using a combination of sequence and secondary structure information. The sequence of the human GSK-3α was obtained from the Universal Protein Resource (http://www.uniprot.org/) (code: P49840) and aligned using Prime. The homology model was inspected to ensure that the side chains of the conserved residues were aligned to the template.

■ ASSOCIATED CONTENT

Supporting Information

Homology modeling, in vitro pharmacology, bioavailability profile of compound **14d** and NMR data of compounds **5b**, **5c**, **6b**, **6c**, **14b**, **14c**, **14d**, **15a**, **15b**, **16a**, **23a**, **23b**, and **23c**. This material is available free of charge via the Internet at http://pubs.acs.org.

■ AUTHOR INFORMATION

Corresponding Author

*Phone: +496151-164531. Fax: +496151-163278. E-mail: schmidt_boris@t-online.de (B.S.); Fabio.Lo-Monte@gmx.de (F.L.).

Notes

The authors declare no competing financial interest.

■ ACKNOWLEDGMENTS

This work was supported by a collaborative project financed by the 7th Framework Program of the European Union (neuro.GSK3).

■ ABBREVIATIONS USED

ATP, adenosine triphosphate; AD, Alzheimer's disease; BBB, blood−brain barrier; Cdk, cyclin-dependent kinase; GSK-3, glycogen synthase kinase-3; DMF, dimethylformamide; DMSO, dimethyl sulfoxide; EtOAc, ethyl acetate; EtOH, ethanol; hpf, hours post fertilization; HPLC, high performance liquid chromatography; MeOH, methanol; SAR, structure−activity relationship

■ REFERENCES

(1) Engel, T.; Goni-Oliver, P.; Gómez de Barreda, E.; Lucas, J. J; Hernandez, F.; Avila, J. Lithium, a Potential Protective Drug in Alzheimeŕs Disease. *Neurodegenerative Dis.* **2008**, *5*, 247−249.
(2) Citron, M. Alzheimer's disease: strategies for disease modification. *Nature Rev. Drug Discovery* **2010**, *9*, 387−397.
(3) Mazanetz, M. P.; Fischer, P. M. Untangling tau hyperphosphorylation in drug design for neurodegenerative diseases. *Nature Rev. Drug Discovery* **2007**, *6*, 464−479.
(4) Cohen, P.; Goedert, M. GSK3 Inhibitors: Development and Therapeutic Potential. *Nature Rev. Drug Discovery* **2004**, *3*, 479−487.
(5) Saitoh, M.; Kunitomo, J.; Kimura, E.; Iwashita, H.; Uno, Y.; Onishi, T.; Uchiyama, N.; Kawamoto, T.; Tanaka, T.; Mol, C. D.; Dougan, D. R.; Textor, G. P.; Snell, G. P.; Takizawa, M.; Itoh, F.; Kori, M. 2-[3-[4-(Alkylsulfinyl)phenyl]-1-benzofuran-5-yl]-5-methyl-1,3,4-oxadiazole Derivatives as Novel Inhibitors of Glycogen Synthase Kinase-3β with Good Brain Permeability. *J. Med. Chem.* **2009**, *52*, 6270−6286.
(6) Martinez, A. Preclinical Efficacy on GSK-3 Inhibitors: Towards a Future Generation of Powerful Drugs. *Med. Res. Rev.* **2008**, *28*, 773−796.
(7) Frame, S.; Cohen, P. GSK3 takes centre stage more than 20 years after its discovery. *Biochem. J.* **2001**, *359*, 1−16.
(8) Cohen, P.; Frame, S. The renaissance of GSK3. *Nature Rev. Mol. Cell Biol.* **2001**, *2*, 769−775.
(9) Martinez, A.; Castro, A.; Dorronsoro, I.; Alonso, M. Glycogen Synthase Kinase 3 (GSK-3)—Inhibitors as New Promising Drugs for Diabetes, Neurodegeneration, Cancer and Inflammation. *Med. Res. Rev.* **2002**, *22*, 373−384.
(10) Bhat, R. V.; Budd Haeberlein, S. L.; Avila, J. Glycogen synthase kinase 3: a drug target for CNS therapies. *J. Neurochem.* **2004**, *89*, 1313−1317.
(11) Zou, H.; Zhou, L.; Li, Y.; Cui, Y.; Zhong, H.; Pan, Z.; Yan, Z.; Quan, J. Benzo[*e*]isoindole-1,3-diones as potential Inhibitors of Glycogen Synthase Kinase-3 (GSK-3). Synthesis, Kinase Inhibitory Activity, Zebrafish Phenotype, and Modeling of Binding Mode. *J. Med. Chem.* **2010**, *53*, 994−1003.
(12) Kaidanovich-Beilin, O.; Lipina, T. V.; Takao, K.; van Eede, M.; Hattori, S.; Laliberté, C.; Khan, M.; Pkamoto, K.; Chambers, J. W.; Fletcher, P. J.; MacAulay, K.; Doble, B. W.; Henkelman, M.; Miyakawa, T.; Roder, J.; Woodgett, J. R. Abnormalities in brain structure and behavior in GSK-3alpha mutant mice. *Mol. Brain* **2009**, *2*, 1−23.
(13) Alon, L. T.; Pietrokovski, S.; Barkan, S.; Avrahami, L.; Kaidanovich-Beilin, O.; Woodgett, J. R.; Barnea, A.; Eldar-Finkelman, H. Selective loss of glycogen synthase kinase-3α in birds reveals distinct roles for GSK-3 isozymes in tau phosphorylation. *FEBS Lett.* **2011**, *585*, 1158−1162.

(14) Phiel, C. J.; Wislon, C. A.; Lee, V. M.-Y.; Klein, P. S. GSK-3α regulates production of Alzheimer's disease amyloid-β peptides. *Nature* **2003**, *423*, 435−439.
(15) Zhou, J.; Lal, H.; Chen, X.; Shang, X.; Song, J.; Li, Y.; Kerkela, R.; Doble, B. W.; MacAulay, K.; DeCaul, M.; Koch, W. J.; Farber, J.; Woodgett, J.; Gao, E.; Force, T. GSK-3α directly regulates β-adrenergic signaling and the response of the heart to hemodynamic stress in mice. *J. Clin. Invest.* **2010**, *120*, 2280−2291.
(16) Banerji, V.; Frumm, S. M.; Ross, K. N.; Li, L. S.; Schinzel, A. C.; Hahn, C. K.; Kakoza, R. M.; Chow, K. T.; Ross, L.; Alexe, G.; Tolliday, N.; Inguilizian, H.; Galinsky, I.; Stone, R. M.; DeAngelo, D. J.; Roti, G.; Aster, J. C.; Hahn, W. C.; Kung, A. L.; Stegmaier, K. The intersection of genetic and chemical genomic screens identifies GSK-3α as a target in human acute myeloid leukemia. *J. Clin. Invest.* **2012**, *122*, 935−947.
(17) Dajani, R.; Fraser, E.; Roe, S. M.; Young, N.; Good, V.; Dale, T. C.; Pearl, L. H. Crystal Structure of Glycogen Synthase Kinase 3β: Structural Basis for Phosphate-Primed Substrate Specificity and Autoinhibition. *Cell* **2001**, *105*, 721−732.
(18) Leclerc, S.; Garnier, M.; Hoessel, R.; Marko, D.; Bibb, J. A.; Snyder, G. L.; Greengard, P.; Biernat, J.; Wu, Y. Z.; Mandelkow, E. M.; Eisenbrand, G.; Meijer, L. Indirubins inhibit glycogen synthase kinase-3 beta and CDK5/p25, two protein kinases involved in abnormal tau phosphorylation in Alzheimer's disease. A property common to most cyclin-dependent kinase inhibitors? *J. Biol. Chem.* **2001**, *276*, 251−260.
(19) Leost, M.; Schultz, C.; Link, A.; Wu, Y. Z.; Biernat, J.; Mandelkow, E. M.; Bibb, J. A.; Snyder, G. L.; Greengard, P.; Zaharevitz, D. W.; Gussio, R.; Senderowicz, A. M.; Sausville, E. A.; Kunick, C.; Meijer, L. Paullones are potent inhibitors of glycogen synthase kinase-3beta and cyclin-dependent kinase 5/p25. *Eur. J. Biochem.* **2000**, *267*, 5983−5994.
(20) Martinez, A.; Alonso, M.; Castro, A.; Perez, C.; Moreno, F. J. First non-ATP competitive glycogen synthase kinase 3 beta (GSK-3beta) inhibitors: thiadiazolidinones (TDZD) as potential drugs for the treatment of Alzheimer's disease. *J. Med. Chem.* **2002**, *45*, 1292−1299.
(21) Smith, D. G.; Buffet, M.; Fenwick, A. E.; Haigh, D.; Ife, R. J.; Saunders, M.; Slingsby, B. P.; Stacey, R.; Ward, R. W. 3-Anilino-4-arylmaleimides: potent and selective inhibitors of glycogen synthase kinase-3 (GSK-3). *Bioorg. Med. Chem. Lett.* **2001**, *11*, 635−639.
(22) Lo Monte, F.; Kramer, T.; Boländer, A.; Plotkin, B.; Eldar-Finkelman, H.; Fuertes, A.; Dominguez, J. M.; Schmidt, B. Synthesis and biological evaluation of glycogen synthase kinase 3 (GSK-3) inhibitors: a fast and atom efficient access to 1-aryl-3-benzylureas. *Bioorg. Med. Chem. Lett.* **2011**, *21*, 5610−5615.
(23) Eldar-Finkelman, H.; Martinez, A. GSK-3 inhibitors: preclinical and clinical focus on CNS. *Front. Mol. Neurosci.* **2011**, *4*, 1−18.
(24) Kramer, T.; Schmidt, B.; Lo Monte, F. Small-molecule inhibitors of GSK-3—Structural insights and their application to Alzheimer's disease models. *Int. J. Alzheimer's Dis.* **2012**, in press.
(25) Naerum, L.; Norskov-Lauritsen, L.; Olesen, P. H. Scaffold hopping and optimization towards libraries of glycogen synthase kinase-3 inhibitors. *Bioorg. Med. Chem. Lett.* **2002**, *12*, 1525−1528.
(26) Saitoh, M.; Kunitomo, J.; Kimura, E.; Hayase, Y.; Kobayashi, H.; Uchiyama, N.; Kawamoto, T.; Tanaka, T.; Mol, C. D.; Dougan, D. R.; Textor, G. S.; Snell, G. P.; Itoh, F. Design, synthesis and structure−activity relationships of 1,3,4-oxadiazole derivatives as novel inhibitors of glycogen synthase kinase-3beta. *Bioorg. Med. Chem.* **2009**, *17*, 2017−2029.
(27) Oertby, E.; Pictet, A. Derivatives of Piperonylic Acid. *Ber. Dtsch. Chem. Ges.* **1910**, *43*, 1336−1340.
(28) Yu, T.; Hsu, L.; Wu, S. *Huaxue Xuebao* **1958**, *24*, 170−173.
(29) Mc Fayden, J. S.; Stevens, T. S. New method for the conversion of acids into aldehydes. *J. Chem. Soc.* **1936**, 584−587.
(30) Konig, H. B.; Seifken, W.; Offe, H. A. Sulfur-containing derivatives of pyridine carboxylic acids and compounds derived therefrom. *Chem. Ber.* **1954**, *87*, 825−834.
(31) Mazzone, G.; Bonina, F.; Arrigo-Reina, R. Synthesis and pharmacological activities of some 2-(alkylaminoalkyl)mercapto-5-aryl-(1,3,4-oxadiazoles). *Farmaco, Ed. Sci.* **1977**, *32*, 414−429.
(32) Omar, R. H.; El-Fattah, B. A. Synthesis of certain pyridyl 1,3,4-oxadiazoles of biological interest and study of the cleavage of certain substituted oxadiazole rings with primary amines. *Egypt. J. Pharm. Sci.* **1985**, *24*, 49−56.
(33) Akwabi-Ameyaw, A.; Bass, J. Y.; Caldwell, R. D.; Caravella, J. A.; Chen, L.; Creech, K. L.; Deaton, D. N.; Madauss, K. P.; Marr, H. B.; McFadyen, R. B.; Miller, A. B.; Navas, F., III; Parks, D. J.; Spearing, P. K.; Todd, D.; Williams, S. P.; Wisely, G. B. FXR agonist activity of conformationally constrained analogs of GW 4064. *Bioorg. Med. Chem.* **2009**, *19*, 4733−4739.
(34) Dolezal, M.; Palek, L.; Vinsova, J.; Buchta, V.; Jampilek, J.; Kralova, K. Substituted Pyrazinecarboxamides: Synthesis and Biological Evaluation. *Molecules* **2006**, *11*, 242−256.
(35) Schmidt, B.; Meid, D.; Kieser, D. Safe and fast tetrazole formation in ionic liquids. *Tetrahedron* **2007**, *63*, 492−496.
(36) Funke, A.; Paulsen, A.; Cibrario, N. Chloromethyl- and aminomethyl(acetyl)benzodioxan isomers and derivatives resulting from oxidation of the acetyl group. *Bull. Soc. Chim. Fr.* **1958**, 470−473.
(37) Hormann, R. E.; Tice, C. M.; Chortyk, O.; Smith, H.; Meteyer, T. Diacylhydrazine ligands for modulating the expression of exogenous genes in mammalian systems via an ecdysone receptor complex. PCT-WO 2004/072254 2004, pp 1−120.
(38) Alksnis, A. F.; Surna, J. A. Preparation of Benzodioxane Derivatives. GB Patent 1109275 1965, pp 1−2.
(39) Satoh, Y.; Powers, C.; Toledo, L. M.; Kowalski, T. J.; Peters, P. A.; Kimble, E. F. Derivatives of 2-[[*N*-(Aminocarbonyl)-*N*-hydroxyamino]methyl]-1,4-benzodioxan as Orally Active 5-Lipoxygenase Inhibitors. *J. Med. Chem.* **1995**, *38*, 68−75.
(40) Lee, J. Y.; Park, Y. K.; Seo, S. H.; Yang, B.; Park, H.; Lee, Y. S. 7-Substituted-[1,4]dioxano[2,3-*g*]quinazolines as Inhibitors of Epidermal Growth Factor Receptor Kinase. *Arch. Pharm. Pharm. Med. Chem.* **2002**, *10*, 487−494.
(41) Feng, L.; Geisselbrecht, Y.; Black, S.; Wilbuer, A.; Atilla-Gokcumen, G. E.; Filippakopoulos, P.; Kräling, K.; Celik, M. A.; Harms, K.; Maksimoska, J.; Marmorstein, R.; Frenking, G.; Knapp, S.; Essen, L.; Meggers, E. Structurally Sophisticated Octahedral Metal Complexes as Highly Selective Protein Kinase Inhibitors. *J. Am. Chem. Soc.* **2011**, *133*, 5976−5986.
(42) Limongelli, V.; Marinelli, L.; Cosconati, S.; La Motta, C.; Sartini, S.; Mugnaini, L.; Da Settimo, F.; Novellino, E.; Parrinello, M. Sampling protein motion and solvent effect during ligand binding. *Proc. Natl. Acad. Sci. U.S.A.* **2012**, *109*, 1467−1472.
(43) Limongelli, V.; Bonomi, M.; Marinelli, L.; Gervasio, F. L.; Cavalli, A.; Novellino, E.; Parrinello, M. Molecular basis of cyclooxygenase enzymes (COXs) selective inhibition. *Proc. Natl. Acad. Sci. U.S.A.* **2010**, *107*, 5411−5416.
(44) Atilla-Gokcumen, G. E.; Williams, D. S.; Bregman, H.; Pagano, N.; Meggers, E. Organometallic Compounds with Biological Activity: A Very Selective and Highly Potent Cellular Inhibitor for Glycogen Synthase Kinase 3. *ChemBioChem* **2006**, *7*, 1443−1450.
(45) Paquet, D.; Bhat, R.; Sydow, A.; Mandelkow, E.; Berg, S.; Hellberg, S.; Fälting, J.; Distel, M.; Köster, R. W.; Schmid, B.; Haass, C. A zebrafish model of tauopathy allows in vivo imaging of neuronal cell death and drug evaluation. *J. Clin. Invest.* **2009**, *119*, 1382−1395.
(46) Azoulay-Alfaguter, I.; Yaffe, Y.; Licht-Murava, A.; Urbanska, M.; Jaworski, J.; Pietrokovski, S.; Hirschberg, K.; Eldar-Finkelman, H. Distinct molecular regulation of glycogen synthase kinase-3alpha isozyme controlled by its N-terminal region: functional role in calcium/calpain signaling. *J. Biol. Chem.* **2011**, *286*, 13470−13480.
(47) Jaworski, T.; Dewachter, I.; Lechat, B.; Gees, M.; Kremer, A.; Demedts, D.; Borghgreaf, P.; Devijver, H.; Kügler, S.; Patel, S.; Woodgett, J. R.; Van Leuven, F. GSK-3α/β kinases and amyloid production in vivo. *Nature* **2011**, *480*, E4−E5.
(48) Phiel, C. J.; Wislon, C. A.; Lee, V. M.-Y.; Klein, P. S. Phiel et al. reply. *Nature* **2011**, *480*, E6.

(49) Tromp, R. A.; van Ameijde, S.; Pütz, C.; Sundermann, C.; Sundermann, B; von Frijtag Drabbe Künzel, J. K.; IJzerman, P. Inhibition of Nucleoside Transport by New Analogues of 4-Nitrobenzylthioinosine: Replacement of the Ribose Moiety by Substituted Benzyl Groups. *J. Med. Chem.* **2004**, *47*, 5441−5450.
(50) Liberman, Z.; Eldar-Finkelman, H. Serine 332 phosphorylation of insulin receptor substrate-1 by glycogen synthase kinase-3 attenuates insulin signaling. *J. Biol. Chem.* **2005**, *280*, 4422−4428.
(51) Kimmel, C. B.; Ballard, W. W.; Kimmel, S. R.; Ullmann, B.; Schilling, T. F. Stages of Embryonic Development of the Zebrafish. *Dev. Dyn.* **1995**, *203*, 253−310.
(52) Dutschmann, M.; Menuet, C.; Stettner, G. M.; Gertreau, C.; Borghgraef, P.; Devijver, H.; Gielis, L.; Hilaire, G.; Van Leuven, F. Upper airway dysfunction of Tau.P301L mice correlates with tauopathy in midbrain and ponto-medullary brainstem nuclei. *J. Neurosci.* **2010**, *30*, 1810−1821.
(53) *Glide*, version 5.5; Schrödinger, LLC: New York, 2009.
(54) *Maestro*, version 9.0.211; Schrödinger, LLC: New York, 2009.
(55) Pettersen, E. F.; Goddard, T. D.; Huang, C. C.; Couch, G. S.; Greenblatt, D. M.; Meng, E. C.; Ferrin, T. E. UCSF chimera—a visualization system for exploratory research and analysis. *J. Comput. Chem.* **2004**, *25*, 1605−1612.
(56) Schuttelkopf, A. W.; van Aalten, D. M. PRODRG: a tool for high-throughput crystallography of protein−ligand complexes. *Acta Crystallogr., Sect. D: Biol. Crystallogr.* **2004**, *60*, 1355−1363.
(57) Friesner, R. A.; Murphy, R. B.; Repasky, M. P.; Frye, L. L.; Greenwood, J. R.; Halgren, T. A.; Sanschagrin, P. C.; Mainz, D. T. Extra precision glide: docking and scoring incorporating a model of hydrophobic enclosure for protein-ligand complexes. *J. Med. Chem.* **2006**, *49*, 6177−6196.
(58) Friesner, R. A.; Banks, J. L.; Murphy, R. B.; Halgren, T. A.; Klicic, J. J.; Mainz, D. T.; Repasky, M. P.; Knoll, E. H.; Shelley, M.; Perry, J. K.; Shaw, D. E.; Francis, P.; Shenkin, P. S. Glide: a new approach for rapid, accurate docking and scoring. 1. Method and assesment of docking accuracy. *J. Med. Chem.* **2004**, *47*, 1739−1749.

SUPPORTING INFORMATION

Identification of Glycogen Synthase Kinase-3 Inhibitors with a Selective Sting for Glycogen Synthase Kinase-3α

Fabio Lo Monte,[a,] Thomas Kramer,[a] Jiamin Gu,[a] Upendra Rao Anumala,[a] Luciana Marinelli,[b] Valeria La Pietra,[b] Ettore Novellino,[b] Bénédicte Franco,[c] David Demedts,[c] Fred Van Leuven,[c] Ana Fuertes,[d] Juan Manuel Dominguez,[d] Batya Plotkin,[e] Hagit Eldar-Finkelman[e] and Boris Schmidt[a,]**

[a] Clemens Schöpf - Institute of Organic Chemistry and Biochemistry, Technische Universität Darmstadt, 64287 Darmstadt, Germany

[b] Dipartimento di Chimica Farmaceutica e Tossicologica, Università di Napoli "Federico II", 80131 Napoli, Italy

[c] Experimental Genetics Group, Department of Human Genetics, Katholieke Universiteit Leuven, 3000 Leuven, Belgium

[d] Noscira S.A., Drug Discovery, Tres Cantos 28760 - Madrid, Spain

[e] Department of Human Molecular Genetics and Biochemistry, Sackler School of Medicine, Tel Aviv University, 69978 Tel Aviv, Israel

* To whom correspondence should be addressed. Phone: +496151-164531.
Fax: +496151-163278.
E-Mail: schmidt_boris@t-online.de; Fabio.Lo-Monte@gmx.de

Table of contents

Homology Modeling

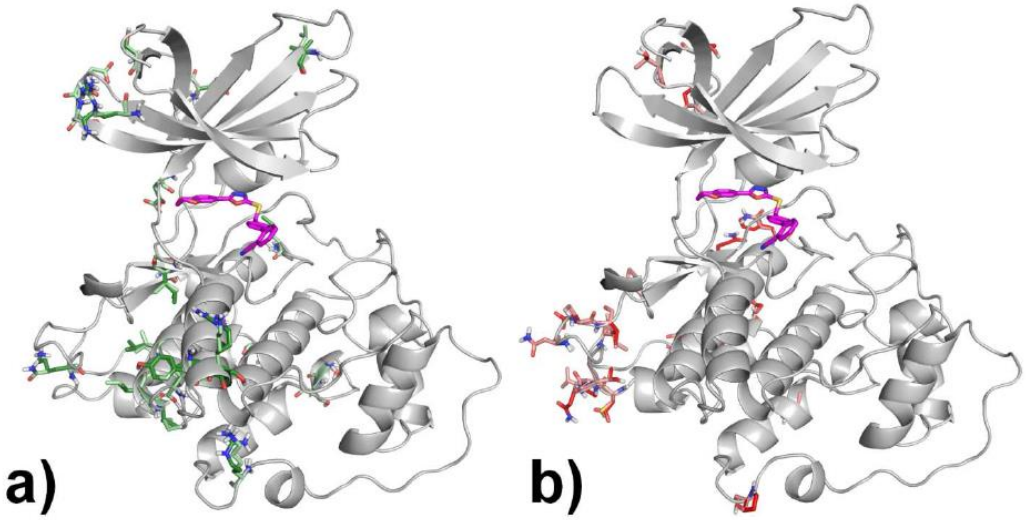

Figure S1. Superposition of 3D structure of GSK-3β (PDB code 3F88) and the homology-based 3D structure of GSK-3α. Both proteins are shown as white cartoons; conservative mutations are displayed as forest and light green stick, for GSK-3β and GSK-3α respectively (**a**), while non-conservative mutations are represented as red and pink sticks, for GSK-3β and GSK-3α respectively (**b**). It is evident that the majority of the mutations are located at the loop at the C-terminus fragment of the proteins (D345-T363 in GSK-3β and R407-A427 in GSK-3α).

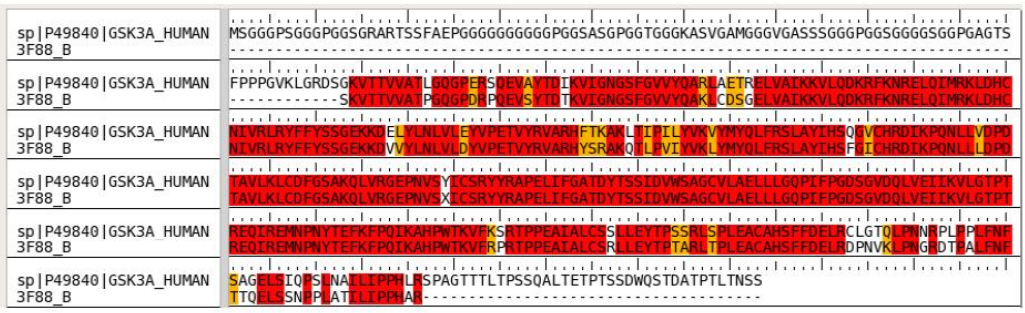

Figure S2. Alignment between GSK-3α (Swiss-Prot code: P49840) and GSK-3β sequences (PDB code: 3F88). Identical residues are colored in red, conservative residues in orange, while non-conservative residues are not painted. Gaps are represented as dashes.

***In Vitro* Pharmacology: Screening of compound 14d**

The ExpresS Diversity kinase profile is a fast turnaround profile conducted by Cerep. Percentage kinase activities with compound **14d** at one concentration (1 μM) in panels of human protein kinases determined by Cerep. Measurements were performed in duplicate and the average was taken.

CHK1	118,1		**FGFR2**	100,8
SIK	113,6		**JAK3**	100,8
Src	111,4		**ROCK1**	100,7
CaMK2α	110,4		**FLT-3**	100,2
KDR	110,4		**NEK2**	100,2
MNK2	107,8		**EGFR**	99
MST4	105,8		**ERK2**	98,9
MAPKAPK2	105,5		**PKCb2**	98,7
PDK1	105,2		**AurA/Aur2**	98,6
p38α	105		**HGK**	98,6
SGK1	104,6		**Akt1/PKBα**	98,1
JNK1	104,5		**CDK2**	97,4
MKK6	104,5		**PKA**	97,4
CDK1	104,4		**EphA2**	97,1
FGFR3	104,4		**EphA3**	96,1
Lck	104,4		**Abl**	95,7
PAK2	104,2		**FGFR1**	95,6
PAK4	103,9		**EphB4**	91,4
MARK1	103,2		**RAF-1**	91,4
IRK	102,6		**CHK2**	89,8
Pim2	102,6		**c-Met**	89,1
TRKA	102,4		**PLK1**	84,2
IKKα	102,3		**IRAK4**	83,3
TAOK2	101,3		**GSK-3β**	27,2
CK1α	100,9		**GSK-3α**	5

Assay Kinases	Source	Substrate/Stimulus/Tracer	Incubation	Measured Component
Abl kinase (h)	human recombinant (insect cells)	ATP + Ulight-TK peptide (100 nM)	60 min RT	phospho-Ulight-TK-peptide
Akt1/PKBα (h)	human recombinant (insect cells)	ATP + CREBtide (CKRREILSRRPSYRK) (25 nM)	60 min RT	phospho-CREBtide (CKRREILSRRPSYRK)
AurA/Aur2 kinase (h)	human recombinant (Sf21 cells)	ATP + Ulight-RRRSLLE (100 nM)	15 min RT	phospho-Ulight-RRRSLLE
CaMK2α *(h)*	human recombinant	ATP + Ulight-CGSGSGRPRTSSFAEG (50 nM)	30 min RT	phospho-Ulight-CGSGSGRPRTSSFAEG
CDC2/CDK 1 (h) (cycB)	human recombinant (insect cells)	ATP + Ulight-CFFKNIVTPRTPPPSQGK-amide (100 nM)	15 min RT	phospho-Ulight-CFFKNIVTPRTPPPSQGK-amide
CDK2 *(h)* (cycA)	human recombinant	ATP + Ulight-CFFKNIVTPRTPPPSQGK-amide (50 nM)	30 min RT	phospho-Ulight-CFFKNIVTPRTPPPSQGK-amide
CHK1 *(h)*	human recombinant (insect cells)	ATP + CREBtide (CKRREILSRRPSYRK) (25 nM)	30 min RT	phospho-CREBtide (CKRREILSRRPSYRK)
CHK2 *(h)*	human recombinant (insect cells)	ATP + CREBtide (CKRREILSRRPSYRK) (25 nM)	15 min RT	phospho-CREBtide (CKRREILSRRPSYRK)
CK1α *(h)*	human recombinant	ATP + Ulight-ARTKQTARKSTGGKAPRKQLAGCG (25 nM)	60 min RT	phospho-Ulight-ARTKQTARKSTGGKAPRKQLAGCG
c-Met kinase *(h)*	human recombinant (insect cells)	ATP + Ulight-CAGAGAIETDKEYYTVKD (25 nM)	60 min RT	phospho-Ulight-CAGAGAIETDKEYYTVKD
EGFR kinase *(h)*	human recombinant (insect cells)	ATP + Ulight-CAGAGAIETDKEYYTVKD (100 nM)	15 min RT	phospho-Ulight-CAGAGAIETDKEYYTVKD
EphA2 kinase *(h)*	human recombinant	ATP + Ulight-TK peptide (50 nM)	30 min RT	phospho-Ulight-TK-peptide
EphA3 kinase *(h)*	human recombinant	ATP + Ulight-TK peptide (50 nM)	60 min RT	phospho-Ulight-TK-peptide
EphB4 kinase *(h)*	human recombinant (insect cells)	ATP + Ulight-TK peptide (100 nM)	90 min RT	phospho-Ulight-TK-peptide

ERK2 *(h)* ($P42^{mapk}$)	human recombinant (*E. coli*)	ATP + Ulight-CFFKNIVTPRTPPPSQGK-amide (100 nM)	15 min RT	phospho-Ulight-CFFKNIVTPRTPPPSQGK-amide
FGFR1 kinase *(h)*	human recombinant (insect cells)	ATP + Ulight-CAGAGAIETDKEYYTVKD (100 nM)	60 min RT	phospho-Ulight-CAGAGAIETDKEYYTVKD
FGFR2 kinase *(h)*	human recombinant	ATP + Ulight-CAGAGAIETDKEYYTVKD (25 nM)	15 min RT	phospho-Ulight-CAGAGAIETDKEYYTVKD
FGFR3 kinase *(h)*	human recombinant	ATP + Ulight-CAGAGAIETDKEYYTVKD (100 nM)	90 min RT	phospho-Ulight-CAGAGAIETDKEYYTVKD
FLT-3 kinase *(h)*	human recombinant (insect cells)	ATP + Ulight-CAGAGAIETDKEYYTVKD (100 nM)	90 min RT	phospho-Ulight-CAGAGAIETDKEYYTVKD
GSK3α *(h)*	human recombinant	ATP + Ulight-CFFKNIVTPRTPPPSQGK-amide (100 nM)	60 min RT	phospho-Ulight-CFFKNIVTPRTPPPSQGK-amide
GSK3β *(h)*	human recombinant	ATP + Ulight-CFFKNIVTPRTPPPSQGK-amide (100 nM)	90 min RT	phospho-Ulight-CFFKNIVTPRTPPPSQGK-amide
HGK *(h)* (MAP4K4)	human recombinant	ATP + Ulight-FLGFTYVAP (50 nM)	90 min RT	phospho-Ulight-FLGFTYVAP
IKKα *(h)*	human recombinant (Sf21 cells)	ATP + Ulight-IkappaB-alpha (100 nM)	30 min RT	phospho-Ulight-IkappaB-alpha
IRAK4 *(h)*	human recombinant (insect cells)	ATP + Ulight-FLGFTYVAP (50 nM)	90 min RT	phospho-Ulight-FLGFTYVAP
IRK *(h)* (InsR)	human recombinant	ATP + Ulight-Poly GAT[EAY(1:1:1)]n (50 nM)	10 min RT	phospho-Ulight-Poly GAT[EAY(1:1:1)]n
JAK3 *(h)*	human recombinant	ATP + Ulight-CAGAGAIETDKEYYTVKD (100 nM)	60 min RT	phospho-Ulight-CAGAGAIETDKEYYTVKD
JNK1 *(h)*	human recombinant (*E. coli*)	ATP + Ulight-CFFKNIVTPRTPPPSQGK-amide (100 nM)	60 min RT	phospho-Ulight-CFFKNIVTPRTPPPSQGK-amide
KDR kinase *(h)* (VEGFR2)	human recombinant (Sf9 cells)	ATP + Ulight-CAGAGAIETDKEYYTVKD (100 nM)	60 min RT	phospho-Ulight-CAGAGAIETDKEYYTVKD
Lck kinase *(h)*	human recombinant (insect cells)	ATP + Ulight-Poly GAT[EAY(1:1:1)]n (25 nM)	30 min RT	phospho-Ulight-Poly GAT[EAY(1:1:1)]n
MAPKAPK 2 *(h)*	human recombinant (*E. coli*)	ATP + CREBtide (CKRREILSRRPSYRK) (25 nM)	15 min RT	phospho-CREBtide (CKRREILSRRPSYRK)
MARK1 *(h)*	human recombinant	ATP + Ulight-RRRSLLE (50 nM)	30 min RT	phospho-Ulight-RRRSLLE
MKK6 *(h)*	human recombinant	ATP + inactive p38a (50 nM)	10 min RT	phospho-p38a
MNK2 *(h)*	human recombinant (Sf21 cells)	ATP + CREBtide (CKRREILSRRPSYRK) (25 nM)	90 min RT	phospho-CREBtide (CKRREILSRRPSYRK)

MST4 kinase *(h)*	human recombinant	ATP + Ulight TM- PKC (50 nM)	30 min RT	Phospho-Ulight-TM-PKC
NEK2 *(h)*	human recombinant (insect cells)	ATP + Ulight-FLGFTYVAP (50 nM)	60 min RT	phospho-Ulight-FLGFTYVAP
p38α kinase *(h)*	human recombinant (*E. coli*)	ATP + Ulight-CFFKNIVTPRTPPPSQGK-amide (100 nM)	60 min RT	phospho-Ulight-CFFKNIVTPRTPPPSQG Kamide
PAK2 *(h)*	human recombinant (Sf9 cells)	ATP + Ulight-RRRSLLE (50 nM)	60 min RT	phospho-Ulight-RRRSLLE
PAK4 *(h)*	human recombinant (insect cells)	ATP + Ulight-RRRSLLE (50 nM)	30 min RT	phospho-Ulight-RRRSLLE
PDK1 *(h)*	human recombinant (insect cells)	ATP + Ulight-FLGFTYVAP (400 nM)	90 min RT	phospho-Ulight-FLGFTYVAP
Pim2 kinase *(h)*	human recombinant (insect cells)	ATP + CREBtide (CKRREILSRRPSYRK) (25 nM)	60 min RT	phospho-CREBtide (CKRREILSRRPSYRK)
PKA *(h)*	human recombinant (*E. coli*)	ATP + Ulight-RRRSLLE (50 nM)	10 min RT	phospho-Ulight-RRRSLLE
PKCβ2 *(h)*	human recombinant	ATP + CREBtide (CKRREILSRRPSYRK) (25 nM)	15 min RT	phospho-CREBtide (CKRREILSRRPSYRK)
PLK1 *(h)*	human recombinant	ATP + Ulight-FLGFTYVAP (40 nM)	60 min RT	phospho-Ulight-FLGFTYVAP
RAF-1 kinase *(h)*	human recombinant	ATP + Ulight-ARTKQTARKSTGGKAPRKQL AGCG (50 nM)	180 min RT	phospho-Ulight-ARTKQTARKSTGGKAP RKQ LAGCG
ROCK1 *(h)*	human recombinant	ATP + Ulight-RRRSLLE (50 nM)	30 min RT	phospho-Ulight-RRRSLLE
SGK1 *(h)*	human recombinant	ATP + Ulight-RRRSLLE (50 nM)	30 min RT	phospho-Ulight-RRRSLLE
SIK *(h)*	human recombinant (Sf21 cells)	ATP + CREBtide (CKRREILSRRPSYRK) (25 nM)	90 min RT	phospho-CREBtide (CKRREILSRRPSYRK)
Src kinase *(h)*	human recombinant (insect cells)	ATP + Ulight-Poly GAT[EAY(1:1:1)]n (5 nM)	10 min RT	phospho-Ulight-Poly GAT[EAY(1:1:1)]n
TAOK2 (TAO1) *(h)*	human recombinant	ATP + Ulight-FLGFTYVAP (40 nM)	60 min RT	phospho-Ulight-FLGFTYVAP
TRKA *(h)*	human recombinant (insect cells)	ATP + Ulight-Poly GAT[EAY(1:1:1)]n (5 nM)	10 min RT	phospho-Ulight-Poly GAT[EAY(1:1:1)]n

Bioavailability profile of compound 14d (conducted by Cerep)

Assay	Technique	Test concentration	Incubation	Detection mode
Aqueous solubility (PBS, pH 7.4)	shake-flask	200 µM	24hr/RT	HPLC-UV/VIS
Partition coefficient (log D, n-octanol /PBS, pH 7.4)	shake-flask	100 µM	60min/RT	HPLC-UV/VIS
Protein binding (plasma, human)	Equilibrium dialysis	10 µM	Overnight (18 ± 2hr) 37°C	HPLC-MS/MS

Assay	Source	Incubation	Detection mode
A-B permeability (Caco-2, pH 6.5/7.4)	Caco-2 cell line	0 and 60 min 37°C	HPLC-MS/MS

Assay	Source	Subtrate	Incubation	Measured Component	Detection mode
Metabolic stability (liver microsomes, human)	Human liver microsomes (0.3 mg/mL)	Test compound	0 and 60 min 37°C	Test compound	HPLC-MS/MS

Assay	Test Concentration (M)	Result
Partition coefficient (logD, n-octanol/PBS, pH 7.4)	1.0E-04	3.58
Protein binding (plasma, human)	1.0E-05	91% Protein Bound 121% Recovery
A-B permeability (Caco-2, pH 6.5/7.4)	1.0E-05	<0.1 Permeability 68% Recovery
Metabolic stability (liver microsomes, human)	1.0E-06	25% Parent Remaining
Aqueous solubility (PBS, pH 7.4)	2.0E-04	Below the limit of quantitation

Monitoring of the heart development on zebrafish embryos

The wt zebrafish was used in this study. The embryos were collected and placed into 24-well plates, ten embryos per well and maintained in E2 medium at ~28°C. Compounds were added 5 hpf (50% epiboly) and the embryos allowed to grow in chemical compound solution up to 5 days. The phenotypes were compared using the Axio Scope.A1 microscope system from Carl Zeiss at 48, 72 and 96 hpf. The heart beat was counted for one minute and compared to the control. - **Animal husbandry.** All animal experiments were conducted and documented according to the federal and local regulation. Due to the federal law and regulation all embryo testing was stopped at day 5 of embryonic development.

NMR Data of compounds 5b, **5c**, **6b**, **6c**, **14b**, **14c**, **14d**, **15a**, **15b**, **16a**, **23a**, **23b** and **23c**

The ^{1}H-NMR spectra were recorded on a Bruker AC 300 spectrometer at 300 MHz and Bruker AC 500 spectrometer at 500 MHz. The ^{13}C-NMR spectra were recorded on a Bruker AC 300 spectrometer at 75 MHz and Bruker AC 500 spectrometer at 125 MHz.

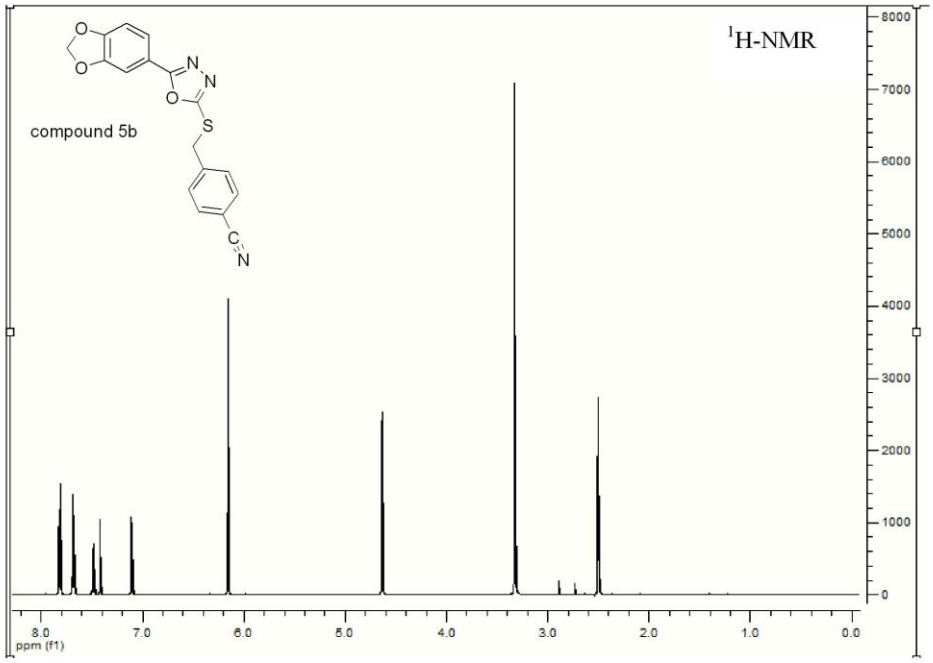
compound 5b
^{1}H-NMR
8000
7000
6000
5000
4000
3000
2000
1000
0
8.0
7.0
6.0
5.0
4.0
3.0
2.0
1.0
0.0
ppm (f1)

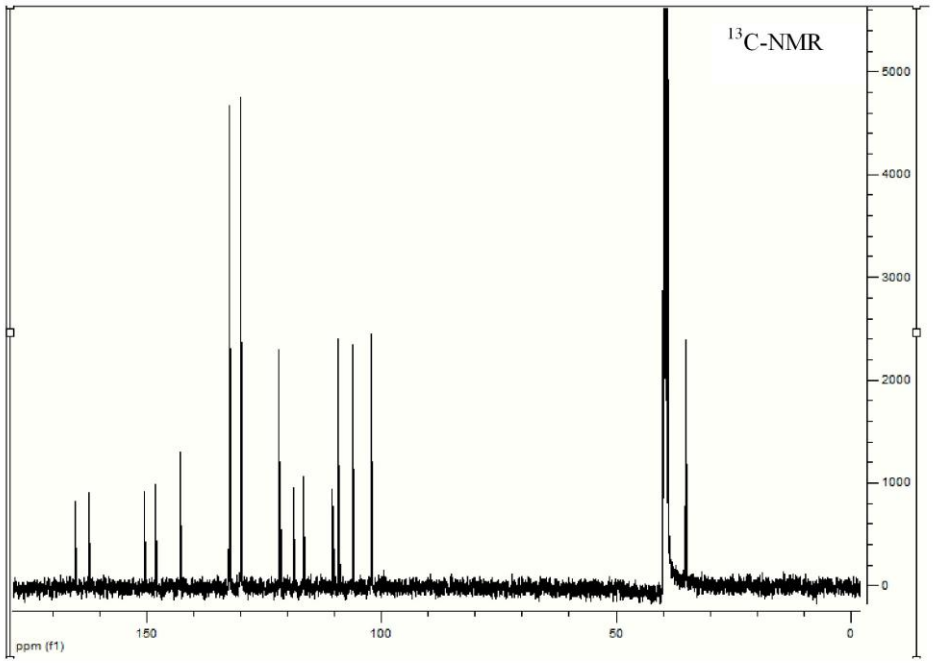
^{13}C-NMR
5000
4000
3000
2000
1000
0
150
100
50
0
ppm (f1)

S9

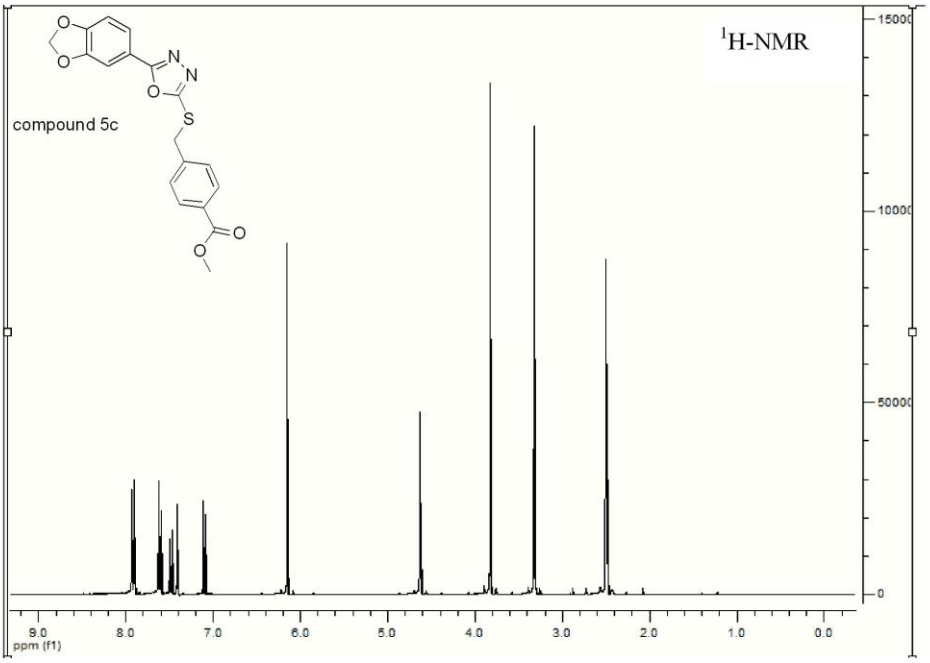
compound 5c
^{1}H-NMR
15000
10000
5000
0
9.0
8.0
7.0
6.0
5.0
4.0
3.0
2.0
1.0
0.0
ppm (f1)

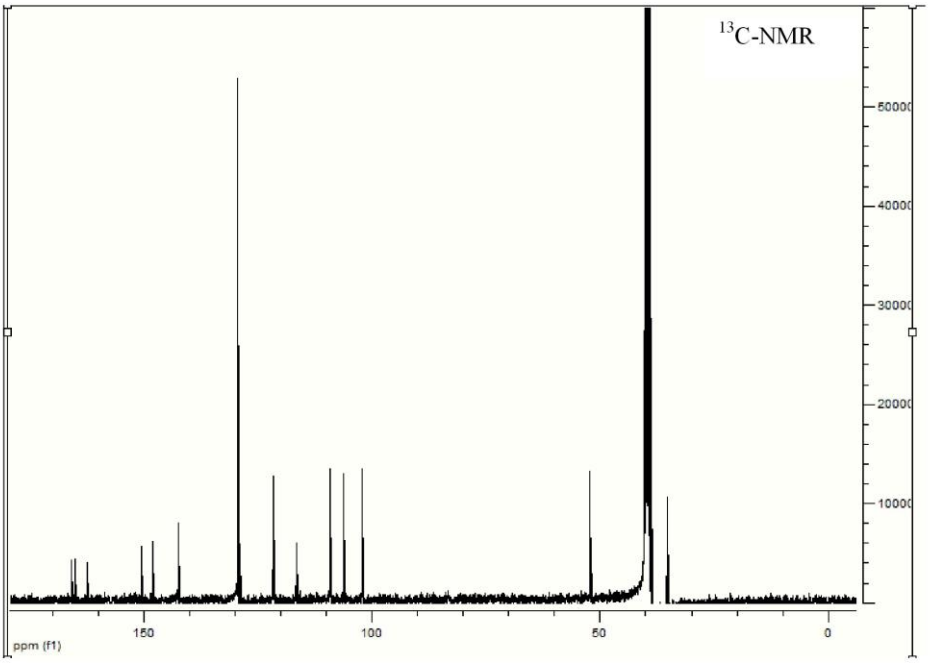
^{13}C-NMR
60000
40000
30000
20000
10000
150
100
50
0
ppm (f1)

S10

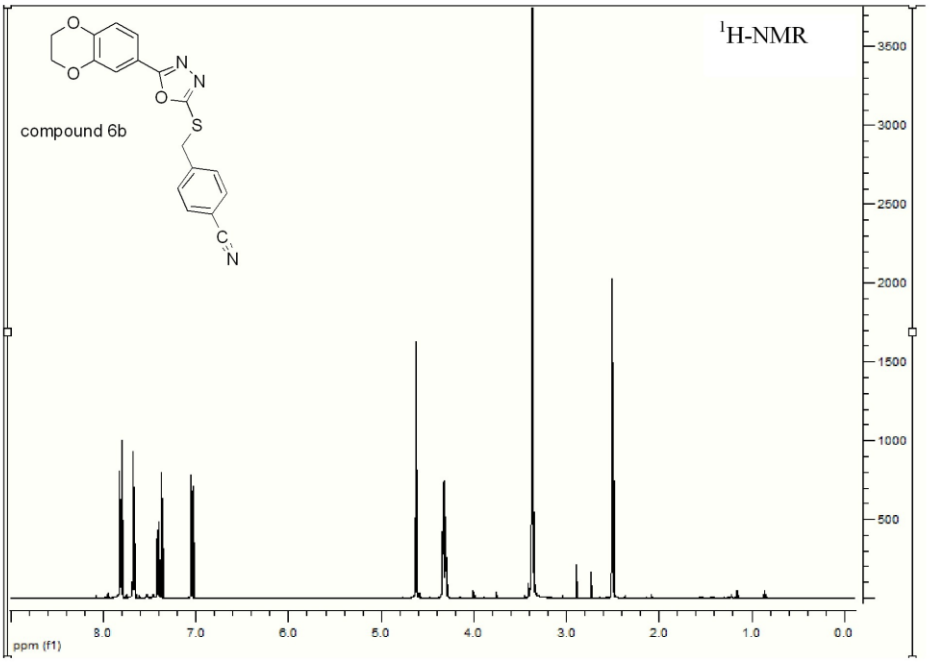

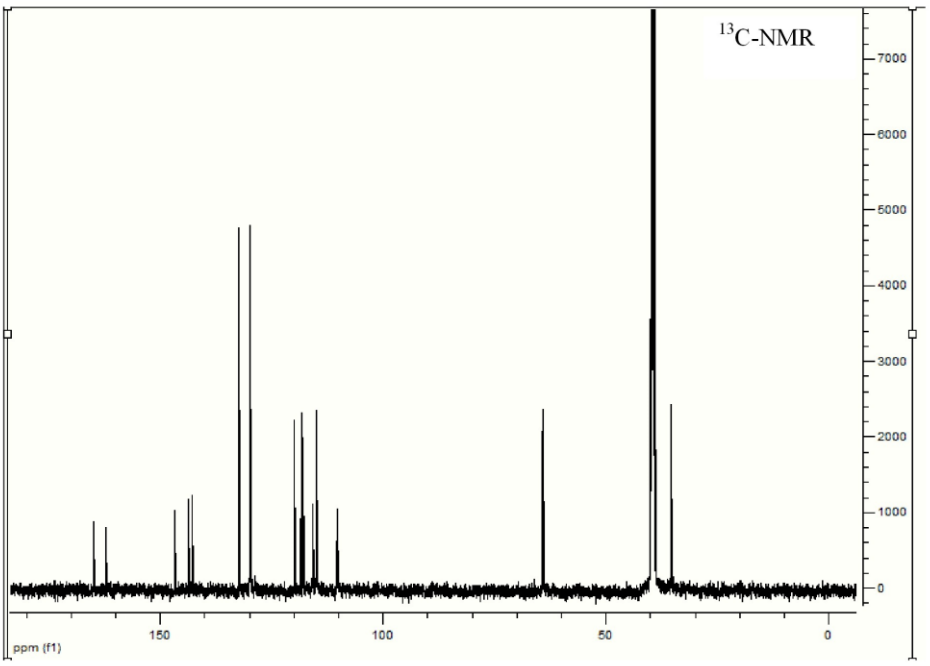

S11

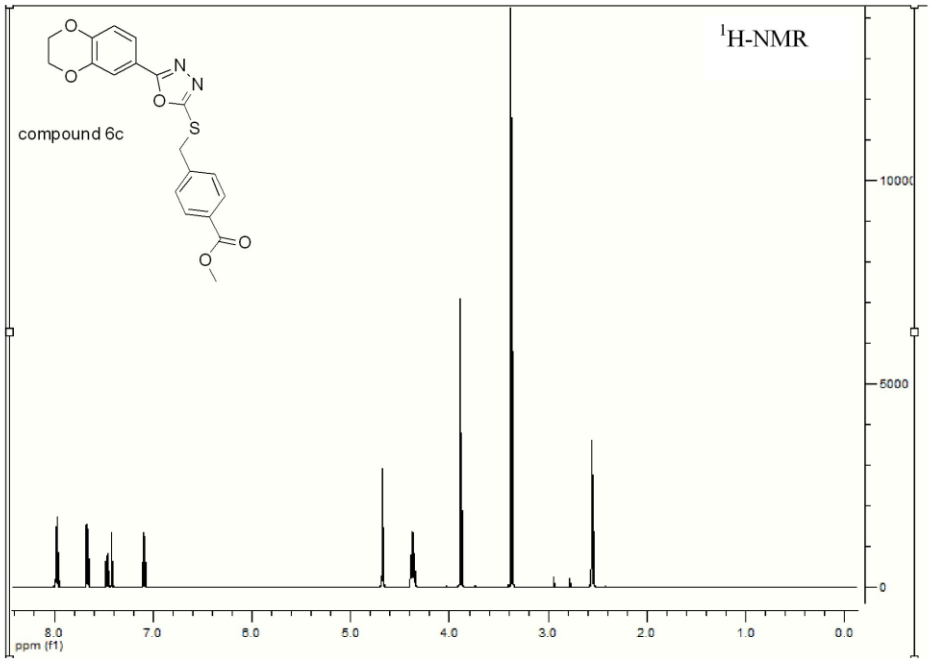
compound 6c
^{1}H-NMR
10000
5000
0
8.0
7.0
6.0
5.0
4.0
3.0
2.0
1.0
0.0
ppm (f1)

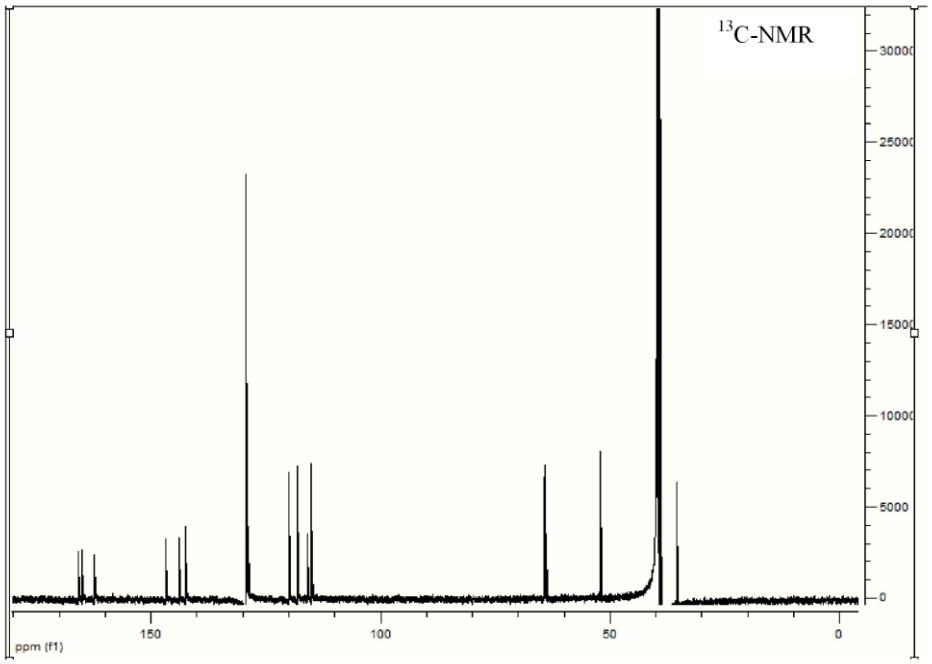
^{13}C-NMR
30000
25000
20000
15000
10000
5000
0
150
100
50
0
ppm (f1)

S12

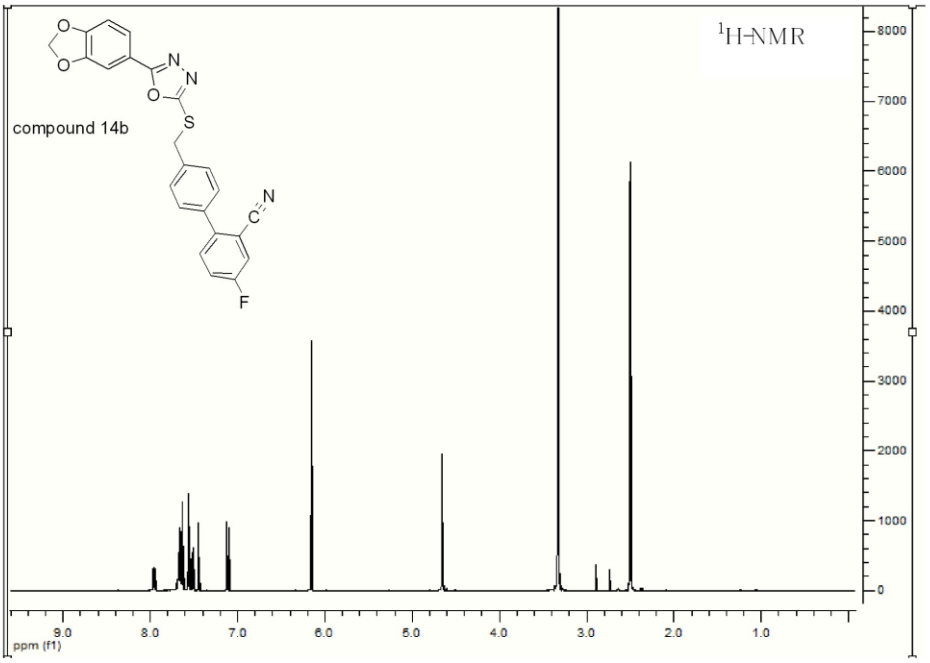

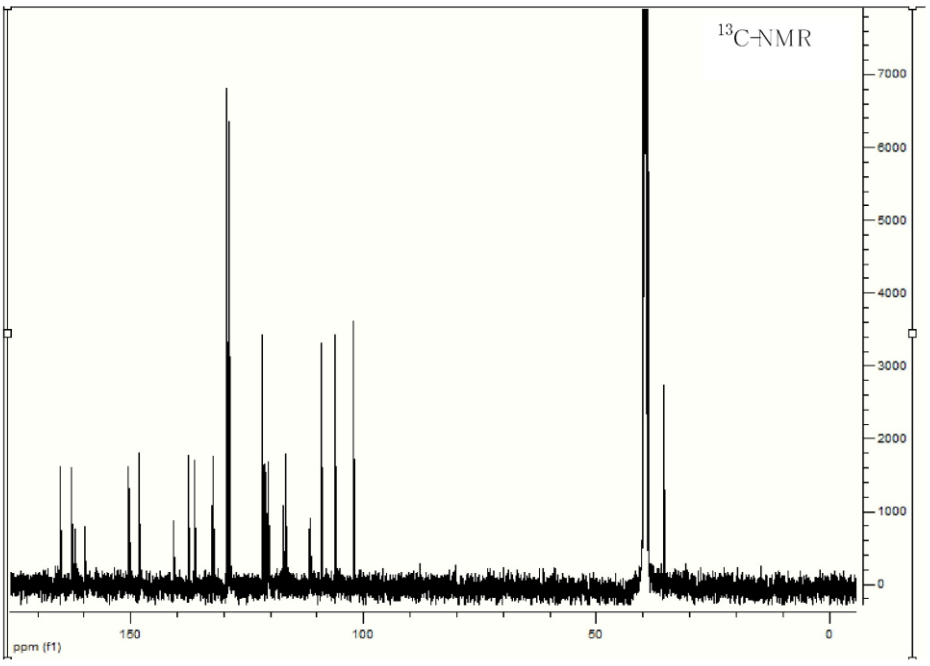

S13

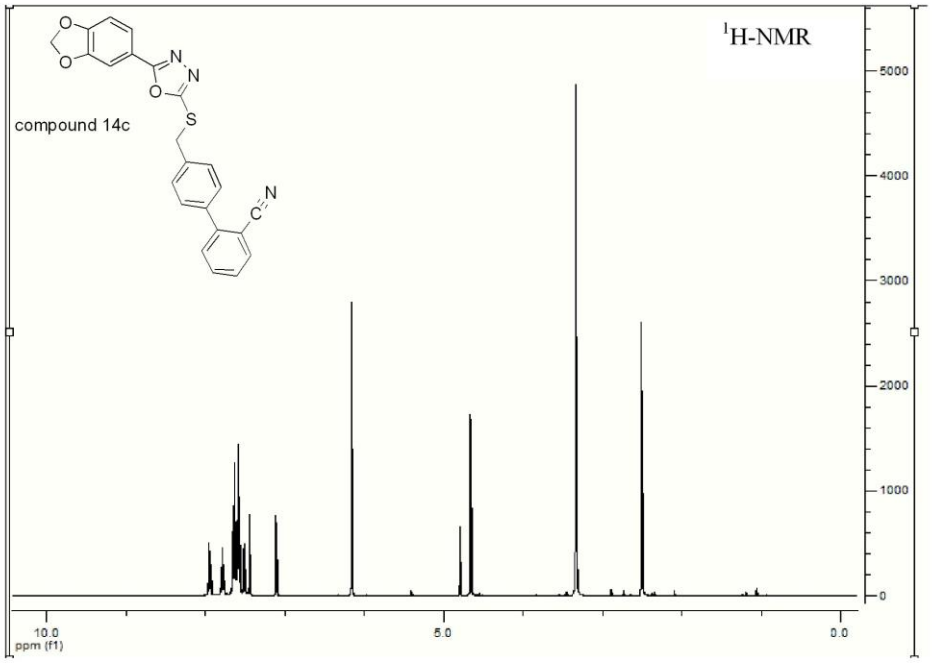
compound 14c
^{1}H-NMR
5000
4000
3000
2000
1000
0
10.0
ppm (f1)
5.0
0.0

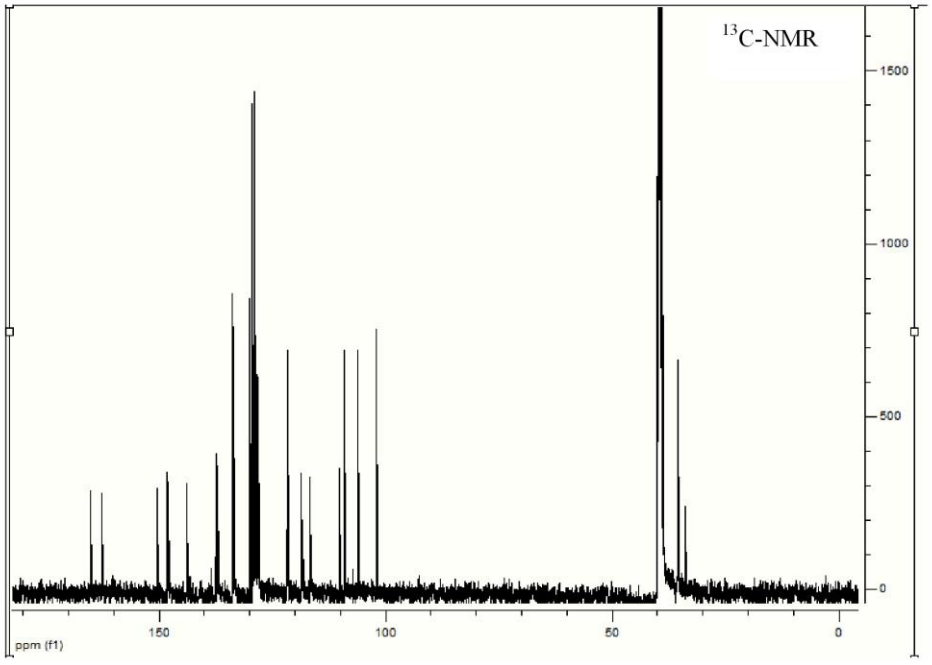
^{13}C-NMR
1500
1000
500
0
150
100
50
0
ppm (f1)

S14

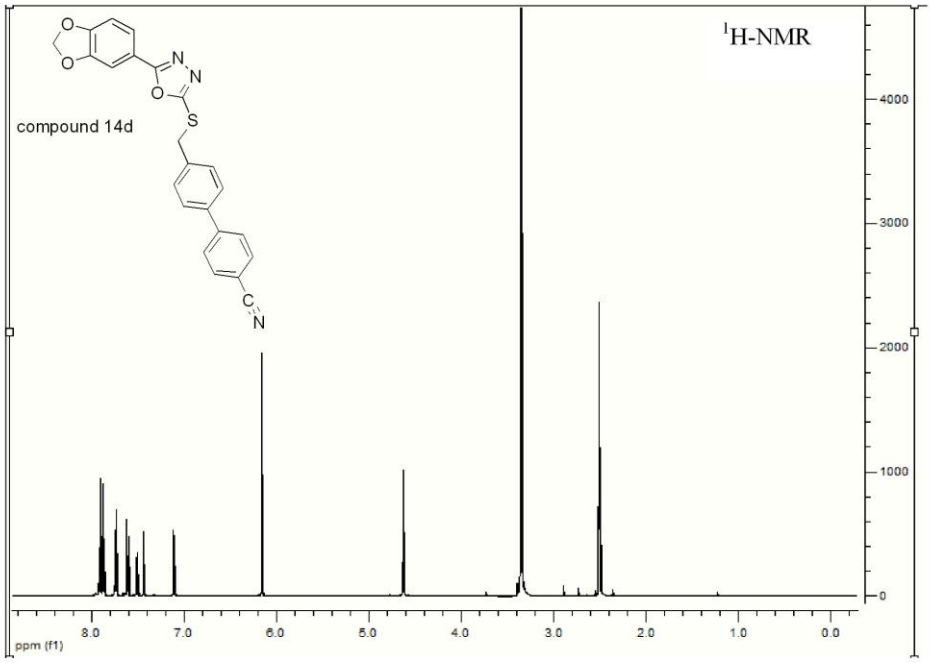
compound 14d
^{1}H-NMR
4000
3000
2000
1000
0
8.0
7.0
6.0
5.0
4.0
3.0
2.0
1.0
0.0
ppm (f1)

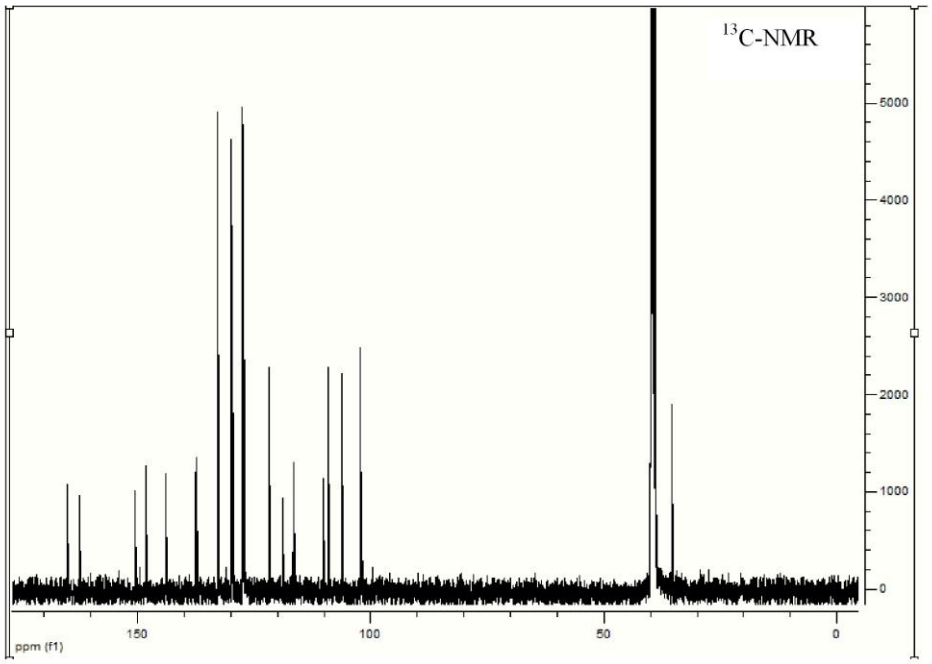
^{13}C-NMR
5000
4000
3000
2000
1000
0
150
100
50
0
ppm (f1)

S15

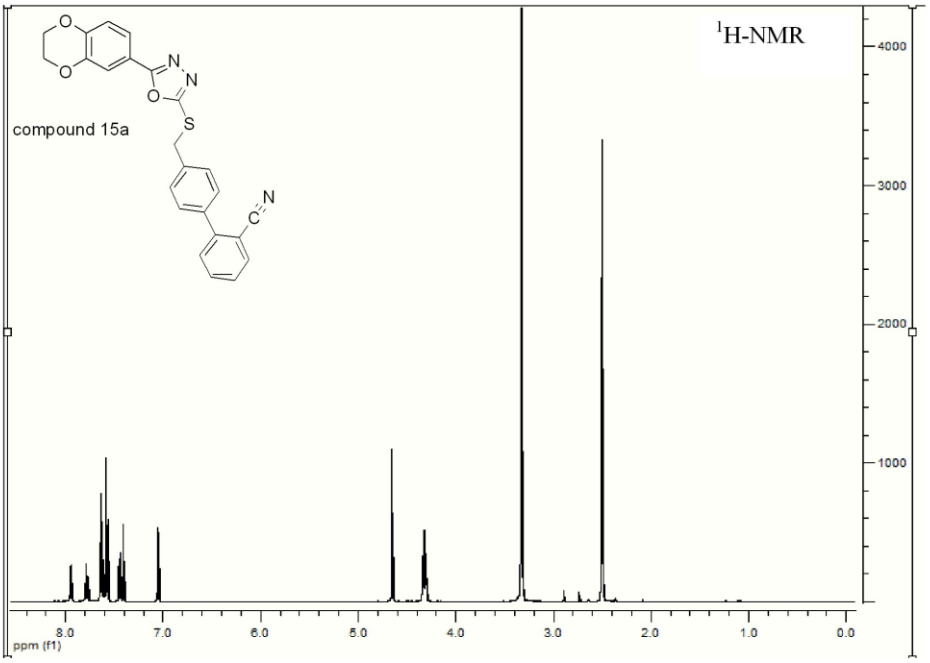
compound 15a
^{1}H-NMR
4000
3000
2000
1000
8.0
7.0
6.0
5.0
4.0
3.0
2.0
1.0
0.0
ppm (f1)

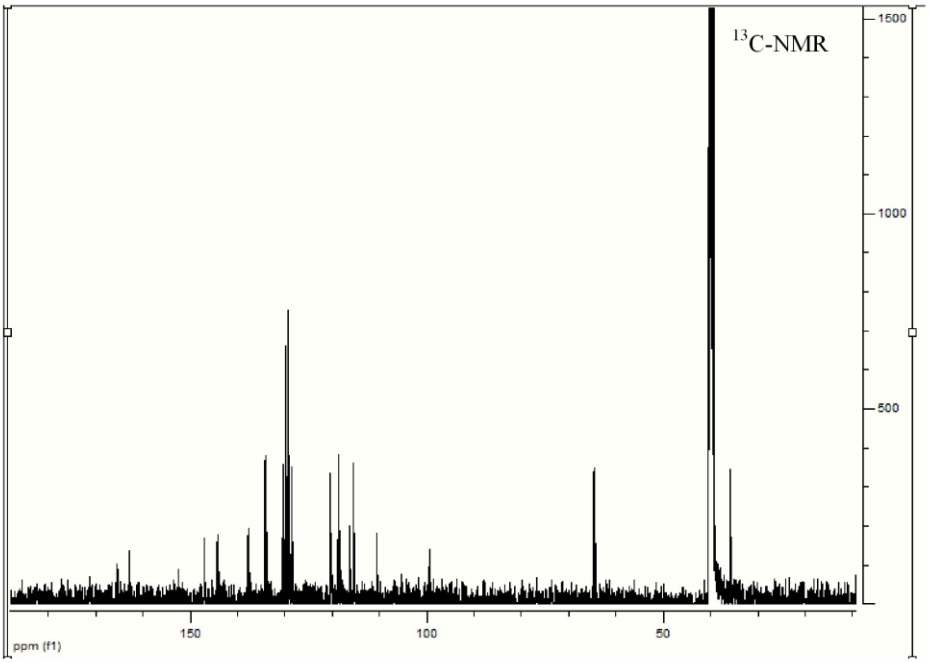
^{13}C-NMR
1500
1000
500
150
100
50
ppm (f1)

S16

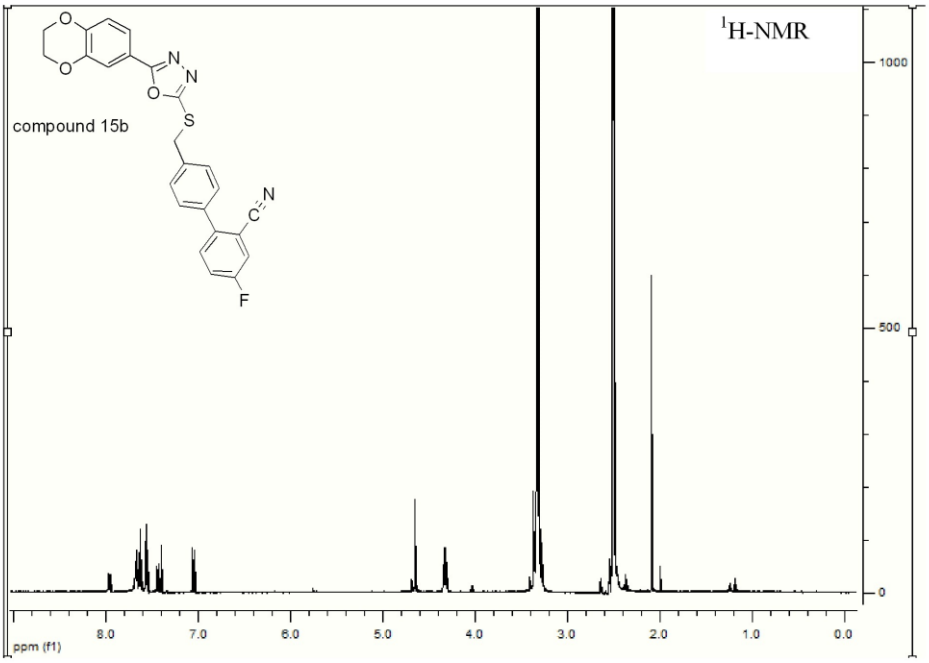

Due to solubility problems it was not possible to measure a ^{13}C-NMR. Compound **15b** was further verified via High Resolution Mass Spectrometry (HRMS).

S17

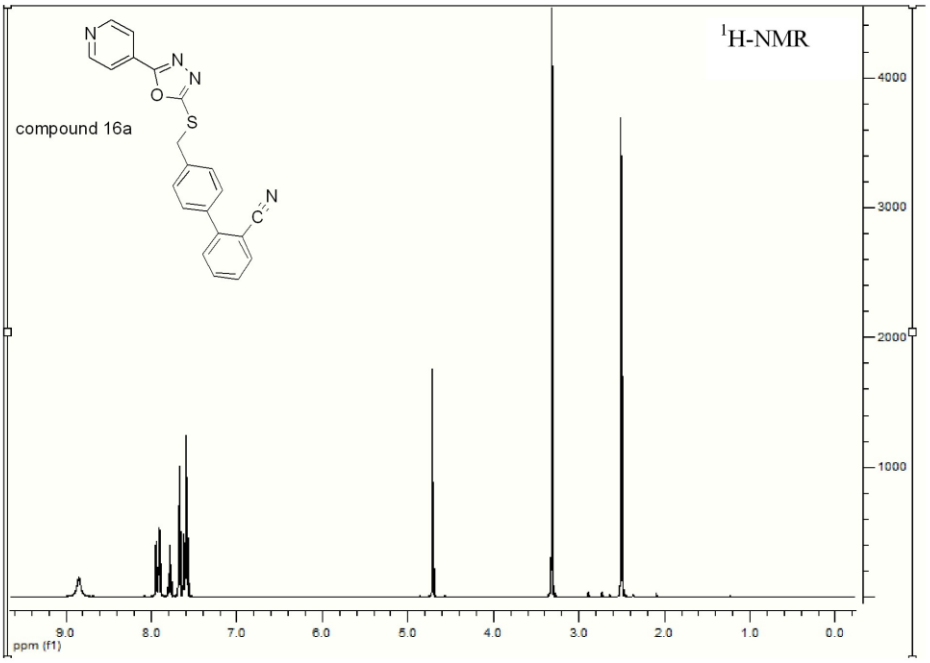
compound 16a
^{1}H-NMR
4000
3000
2000
1000
9.0
8.0
7.0
6.0
5.0
4.0
3.0
2.0
1.0
0.0
ppm (f1)

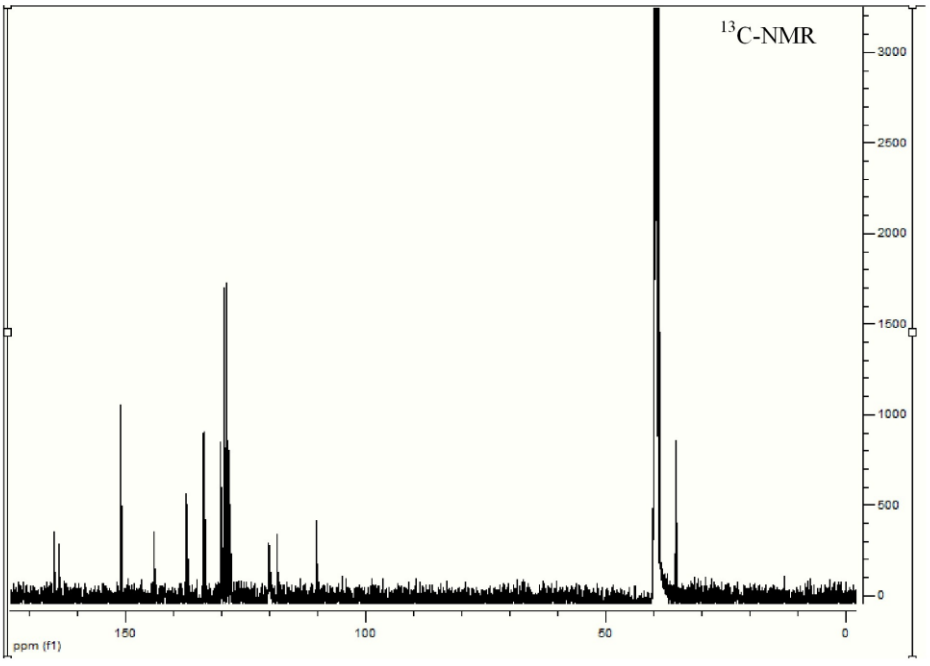
^{13}C-NMR
3000
2500
2000
1500
1000
500
0
150
100
50
0
ppm (f1)

S18

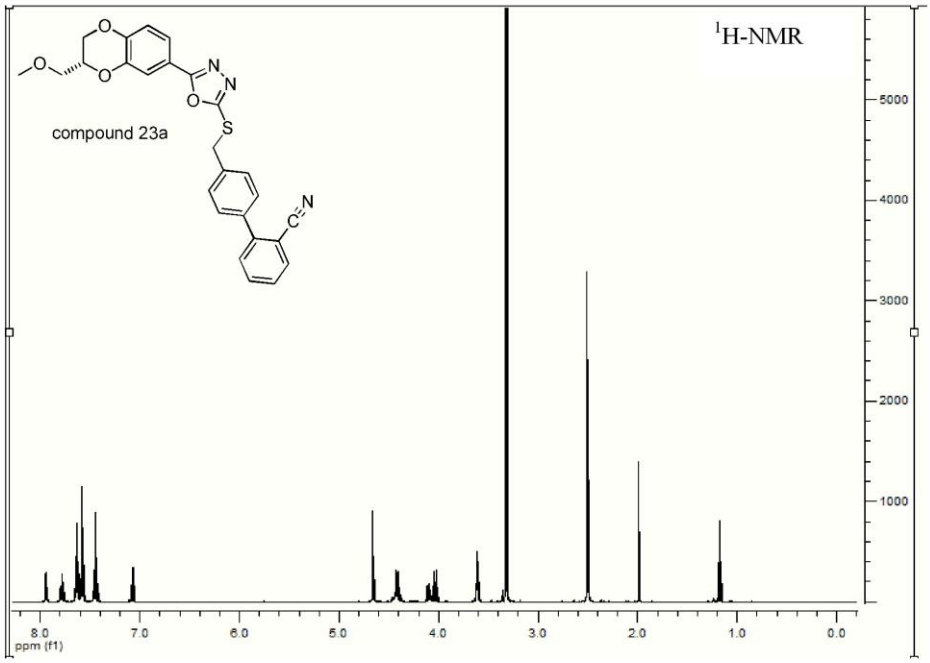
compound 23a
^{1}H-NMR
5000
4000
3000
2000
1000
8.0
7.0
6.0
5.0
4.0
3.0
2.0
1.0
0.0
ppm (f1)

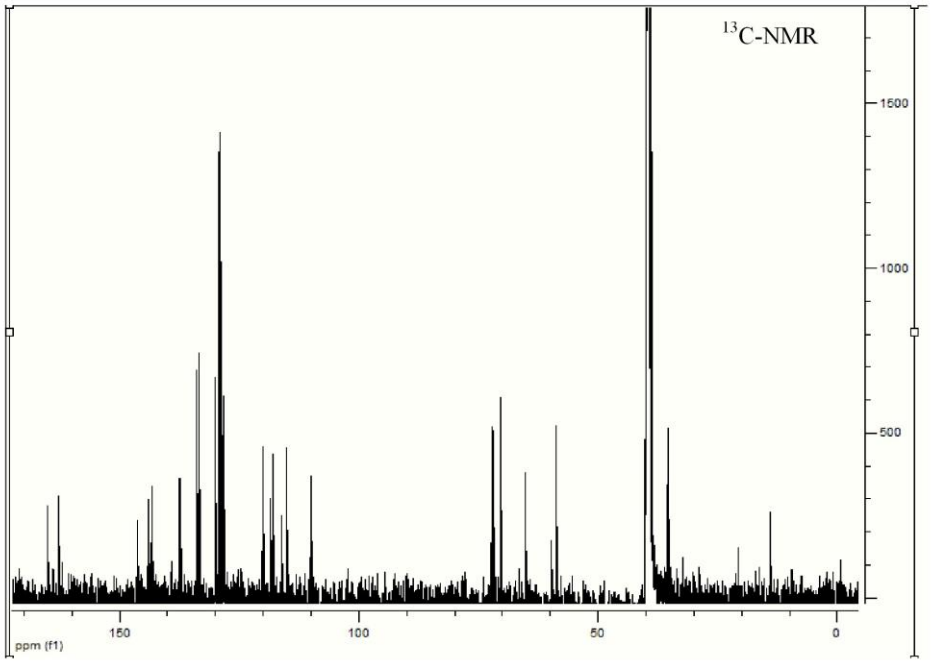
^{13}C-NMR
1500
1000
500
150
100
50
0
ppm (f1)

S19

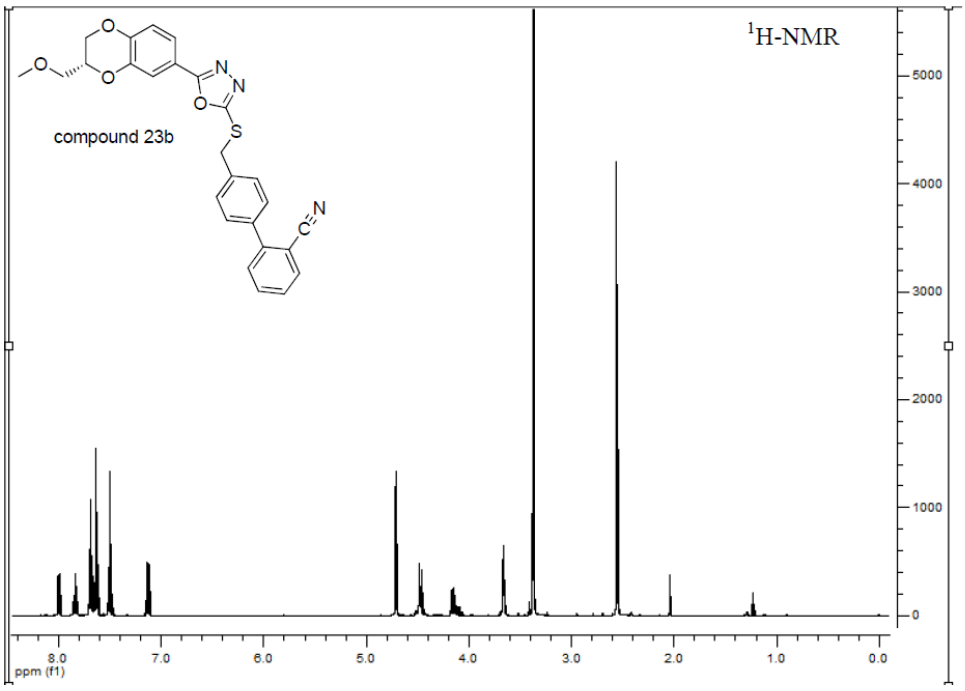
compound 23b
^{1}H-NMR
5000
4000
3000
2000
1000
0
8.0
7.0
6.0
5.0
4.0
3.0
2.0
1.0
0.0
ppm (f1)

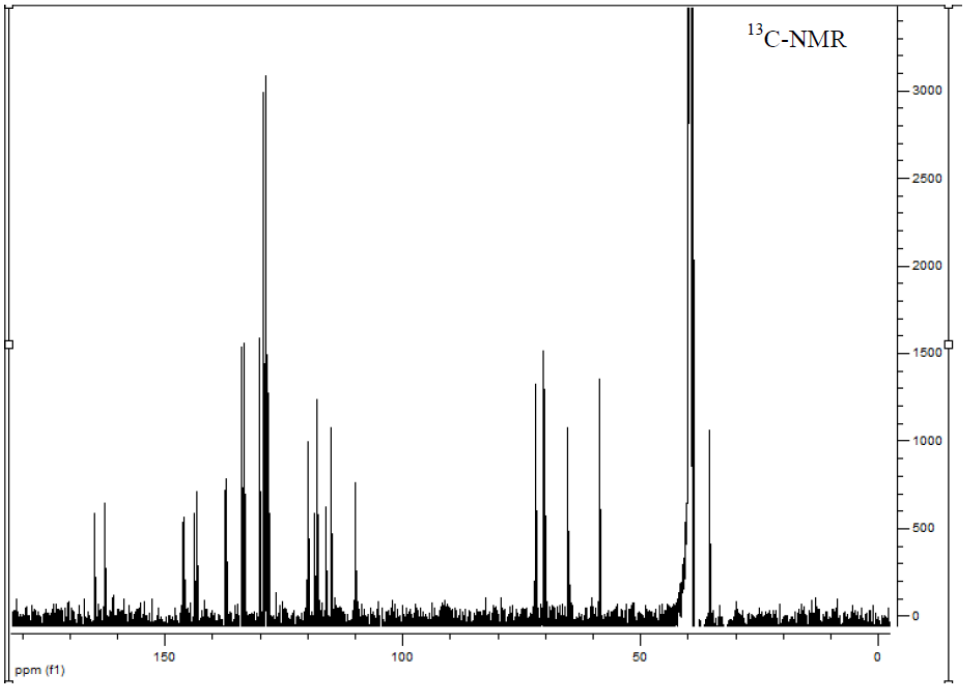
^{13}C-NMR
3000
2500
2000
1500
1000
500
0
150
100
50
0
ppm (f1)

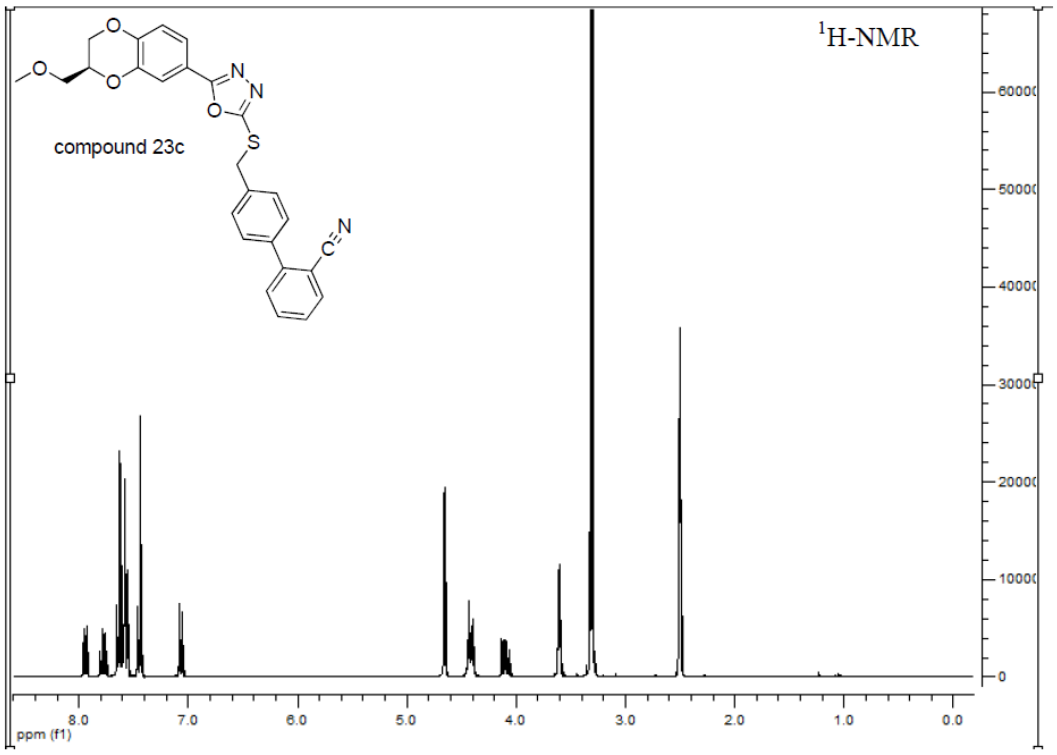

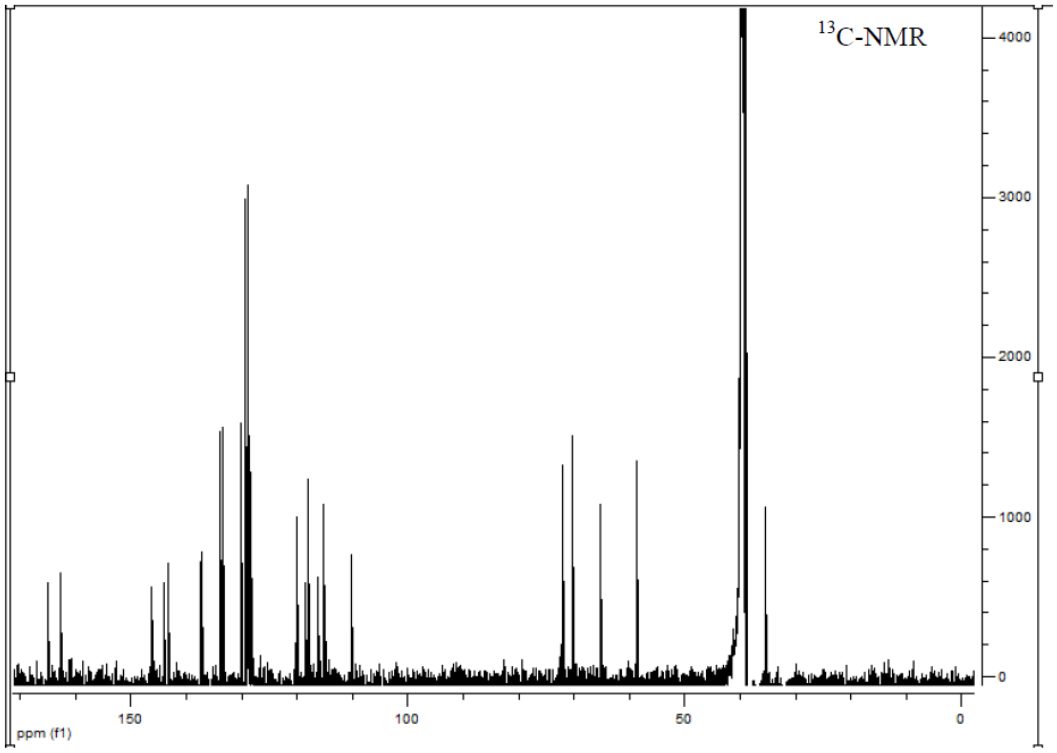

S21

3.1.6 Histology of compounds those are not part of the cumulative section.

In addition to RAs shown above (section 3.1.2), several other kinds of probes were also synthesized. These probes include 5*H*-imidazo[4,5-c]pyridines, 2-methoxy-1,4-bisstyryls, bis(arylvinyl) pyrimidines, bis(arylvinyl) pyrazines, quinoxalin-2-yl derivatives. All probes were then evaluated for their ability to display NFTs and SPs in post mortem AD brain tissues. The histology results of these probes are shown below.

3.1.6.1 *In vitro* histochemical staining of postmortem AD brain tissues with RA derivatives.

A group of RA derivatives was synthesized and evaluated for their ability to display NFTs and SPs in the post mortem human AD brain. These compounds displayed very good staining to NFTs over SPs. Histology data of these probes is shown below.

Table 3.1.6.1 Histology data of RA derivatives

BSc Code/Structure	Histology
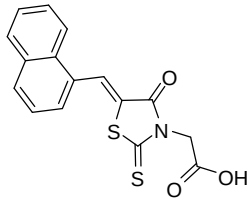 **BSc4757**	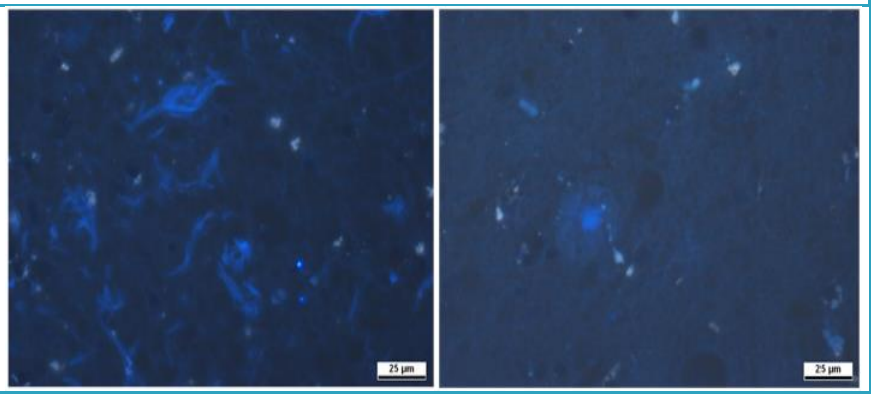 Neuropathological staining with BSc4757, displaying NFTs (left) and a SP (right). Imaged with fluorescence microscopy using DAPI filter. Staining effect (Aβ: + / NFT: ++).
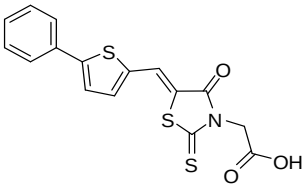 **BSc4820**	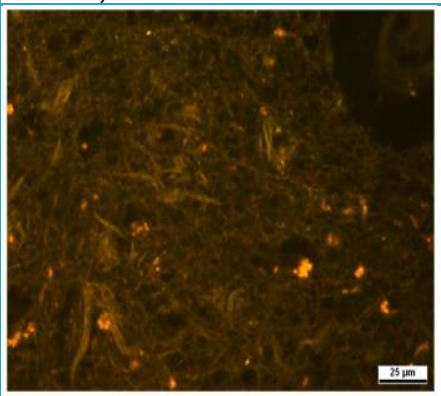 Neuropathological staining with BSc4820, displaying NFTs in high background tissue staining. Imaged with fluorescence microscopy using FITC filter. Staining effect (Aβ: - / NFT: ++).

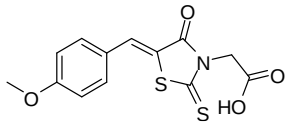

BSc4824

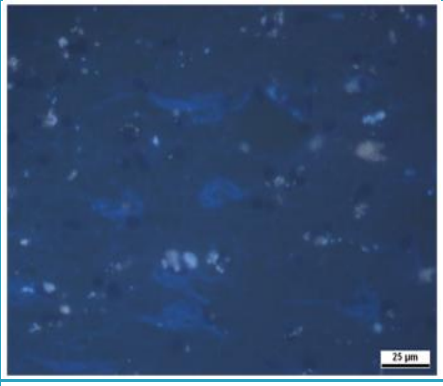

Neuropathological staining with BSc4824, displaying NFTs (left). Imaged with fluorescence microscopy using DAPI filter. Staining effect (Aβ: - / NFT: +).

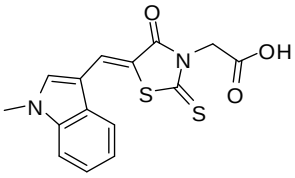

BSc4828

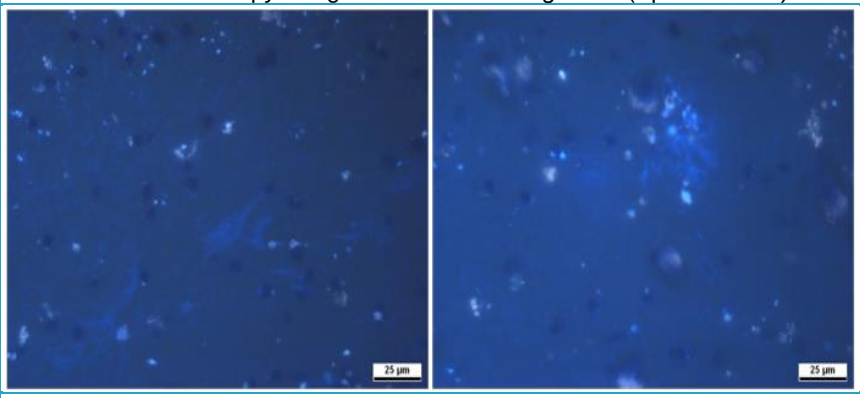

Neuropathological staining with BSc4828, displaying NFTs (left) and a SP (right). Imaged with fluorescence microscopy using DAPI filter. Staining effect (Aβ: + / NFT: +).

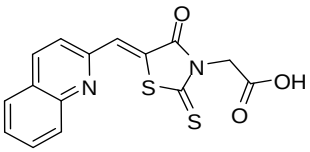

BSc4882

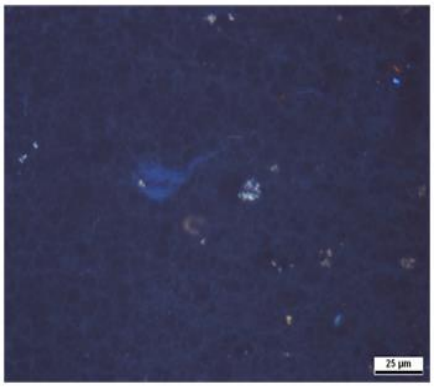

Neuropathological staining with BSc4882, displaying NFTs. Imaged with fluorescence microscopy using DAPI filter. Staining effect (Aβ: - / NFT: +).

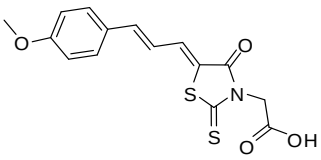

BSc4886

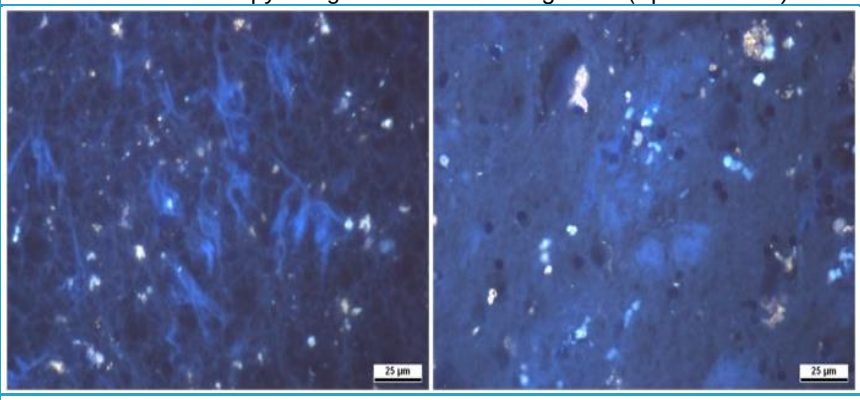

Neuropathological staining with BSc4886, displaying NFTs (left) and SPs

	(right). Imaged with fluorescence microscopy using DAPI filter. Staining effect (Aβ: + / NFT: ++).
Tissues: hippocampus; patient: female, 80 years old, CERAD Score: 3; NFTs-level: V. +++ stands for good staining, ++ stands for normal staining, + stands for weak staining, - stands for no stainng	

3.1.6.2 *In vitro* histochemical staining of postmortem AD brain tissues with 5H-imidazo[4,5-c]pyridines.

A group of 5H-imidazo[4,5-c]pyridine derivatives was synthesized and evaluated for the ability to display NFTs and SPs in post mortem human AD brain. These compounds displayed very good staining of NFTs versus SPs. However, these probes displayed poor affinities in the *Thiazine red R* displacement assay (data not shown). Histology data of these probes is shown below.

Table 3.1.6.2 Histology data of 5H-imidazo[4,5-c]pyridines

Compound Structure / Code	Histology
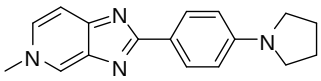 **BSc4883**	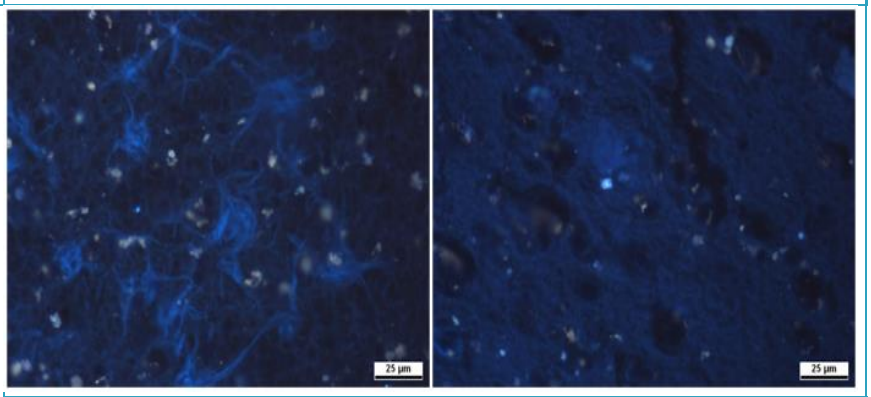 Neuropathological staining with BSc4883, displaying NFTs (left) and a SP (right-weak staining). Imaged with fluorescence microscopy using DAPI filter. Staining effect (Aβ: + / NFT: ++).
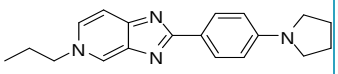 **BSc4888**	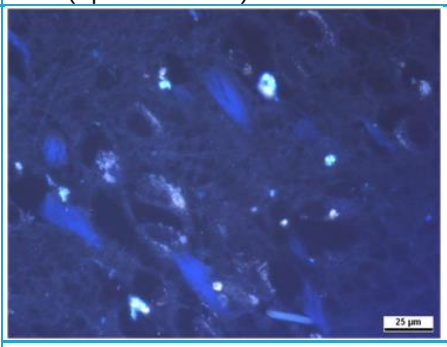 Neuropathological staining with BSc4888, displaying NFTs. Imaged with fluorescence microscopy using DAPI filter. SPs was not observed. Staining effect (Aβ: - / NFT: ++).

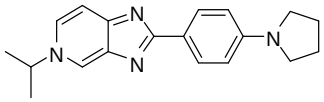	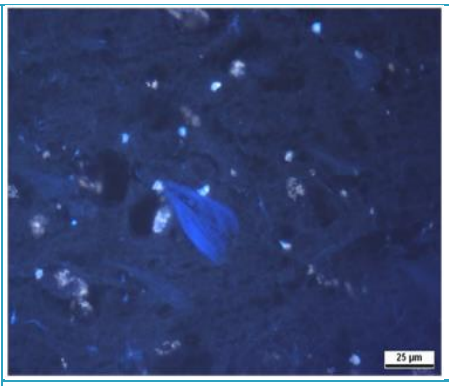
BSc4891	Neuropathological staining with BSc4891, displaying NFTs. Imaged with fluorescence microscopy using DAPI filter. SPs was not observed. Staining effect (Aβ: - / NFT: +++).
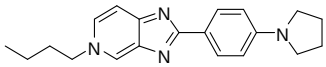	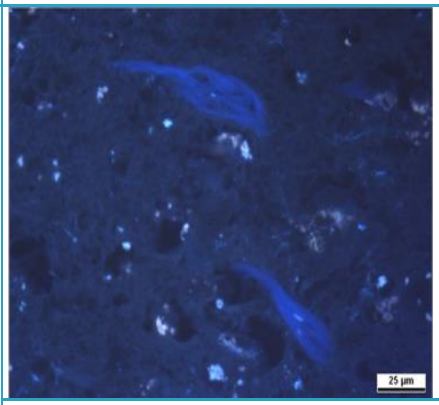
BSc4892	Neuropathological staining with BSc4892, displaying NFTs. Imaged with fluorescence microscopy using DAPI filter. SPs was not observed. Staining effect (Aβ: - / NFT: +++).
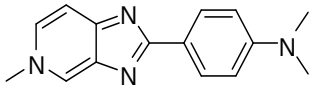	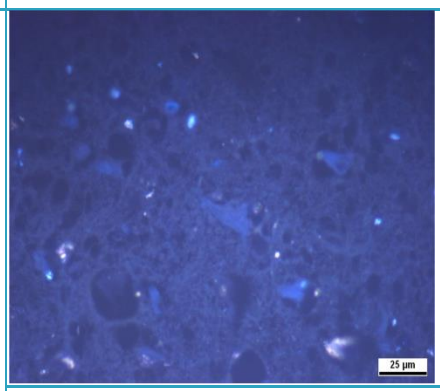
BSc4941	Neuropathological staining with BSc4941, displaying NFTs. Imaged with fluorescence microscopy using DAPI filter. SPs was not observed. Staining effect (Aβ: - / NFT: +).

<table>
<tr><td> 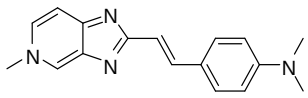
BSc4942</td><td> 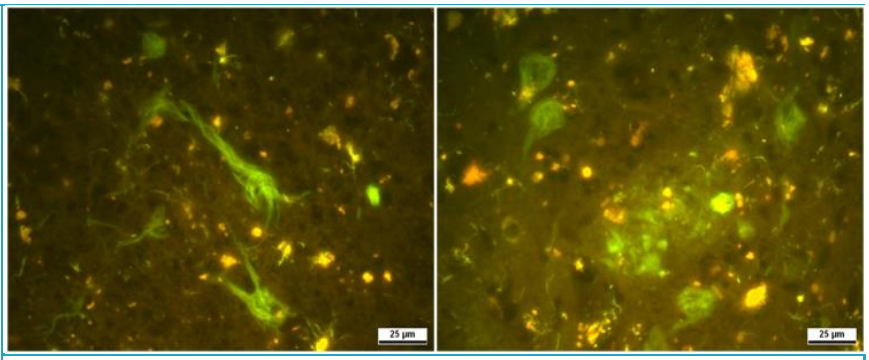
Neuropathological staining with BSc4942, displaying NFTs. Imaged with fluorescence microscopy using green filter. Tangles in plaques also can be observed. In addition to NFTs and SPs, astrocyte fibres are also stained. Staining effect (Aβ: + / NFT: +++).</td></tr>
<tr><td> 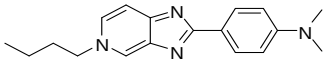
BSc4980</td><td> 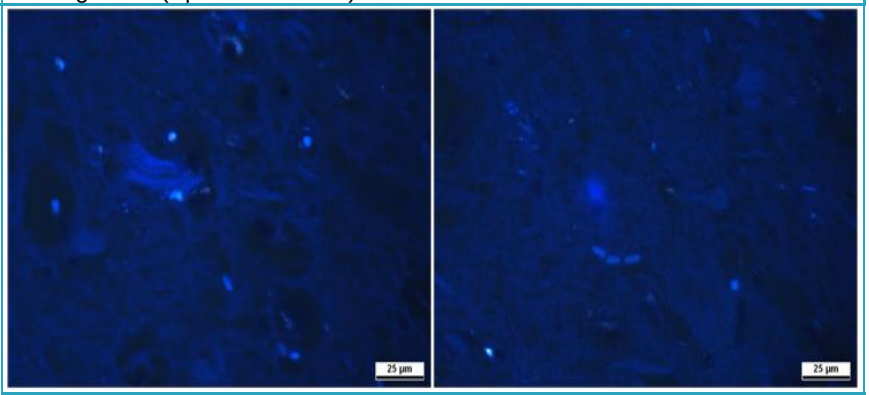
Neuropathological staining with BSc4980, displaying NFTs (left) and a SP (right)-weak staining). Imaged with fluorescence microscopy using DAPI filter. Staining effect (Aβ: + / NFT: +).</td></tr>
<tr><td colspan="2">Tissues: hippocampus; patient: female, 80 years old, CERAD-score: 3; NFTs level: V.
+++ stands for good staining, ++ stands for normal staining, + stands for weak staining, - stands for no stainng</td></tr>
</table>

3.1.6.3 *In vitro* histochemical staining of postmortem AD brain tissues with imidazopyridines.

A group of imidazopyridine derivatives was synthesized and evaluated for its ability to display NFTs and SPs in post mortem human AD brain. These compounds displayed very good staining to NFTs and SPs. However, no selectivity to either NFTs or SPs was observed with these probes. Histology data of these probes is shown below.

Table 3.1.6.3 Histology data of Imidazopyridines	
Compound Structure / Code	Histology
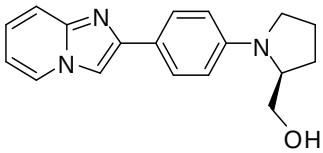 **BSc4546**	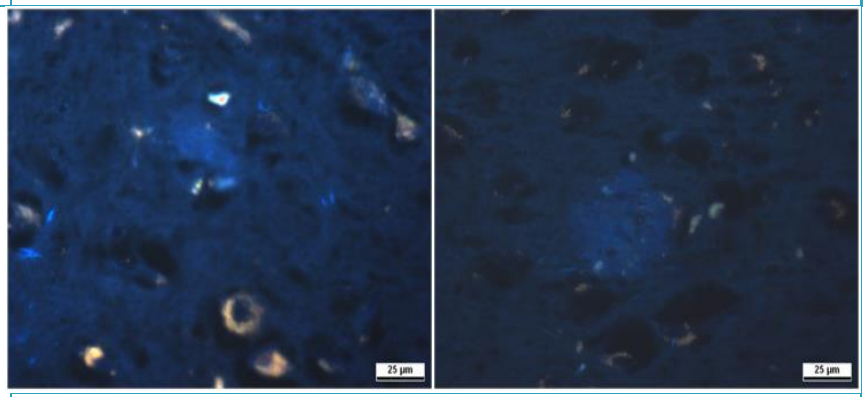 Neuropathological staining with BSc4546, displaying NFT (left) and a SP (right). Imaged with fluorescence microscopy using DAPI filter. Staining effect (Aβ: + / NFT: +).
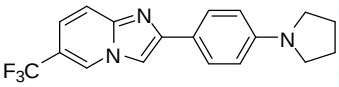 **BSc4698**	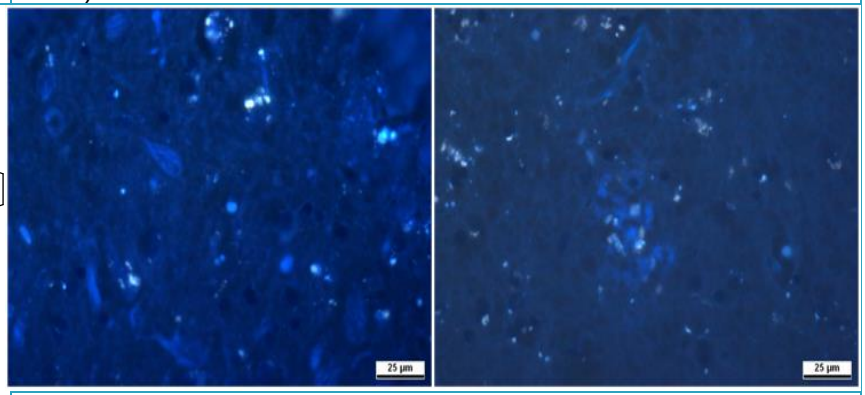 Neuropathological staining with BSc4698, displaying NFTs (left) and a SP (right). Imaged with fluorescence microscopy using DAPI filter. Staining effect (Aβ: + / NFT: +).
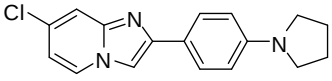 **BSc4699**	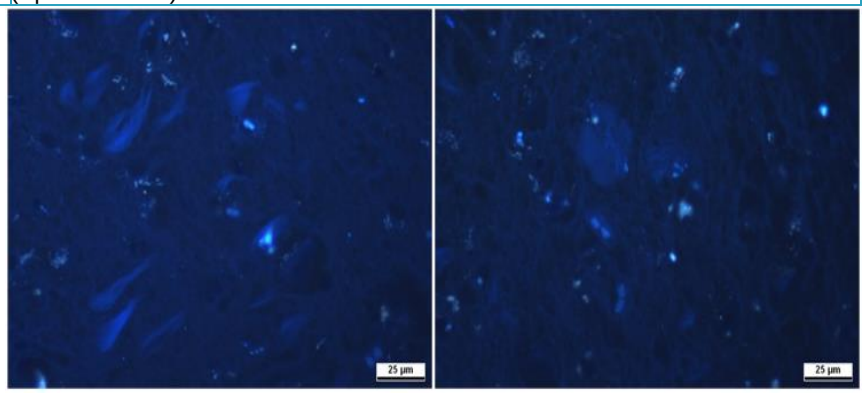 Neuropathological staining with BSc4699, displaying NFTs (left) and a SP (right). Imaged with fluorescence microscopy using DAPI filter. Staining effect (Aβ: + / NFT: +).

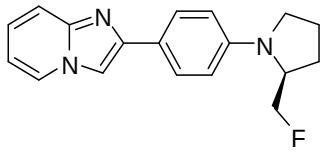

BSc4762

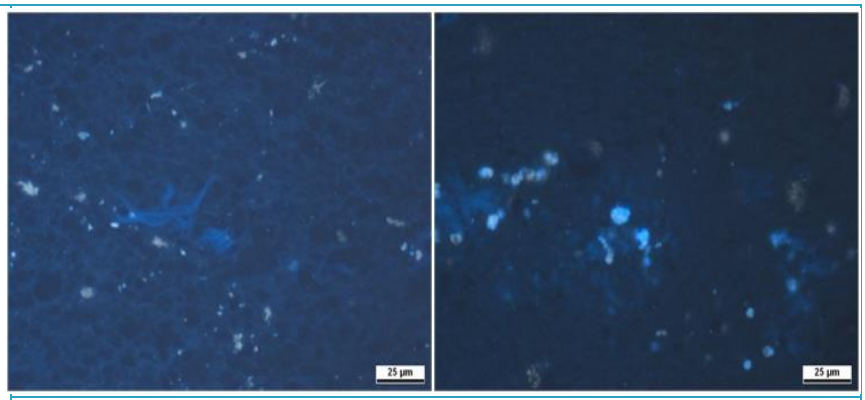

Neuropathological staining with BSc4762, showing displaying NFTs (left) and a SP (right). Imaged with fluorescence microscopy using DAPI filter. Staining effect (Aβ: + / NFT: +).

Tissues: hippocampus; patient: male, 71 years old, CERAD-score: 3; NFTslevel: V.
+++ stands for good staining, ++ stands for normal staining, + stands for weak staining, - stands for no stainng

3.1.6.4 *In vitro* histochemical staining of postmortem AD brain tissues with 2-methoxy-1, 4-bisstyryls.

A group of 2-methoxy-1,4-bisstyryl derivatives was synthesized and evaluated for its ability to display NFTs and SPs in post mortem human AD brain. These compounds displayed very good staining SPs over NFTs. Histology data of these probes is shown below.

Table 3.1.6.4 Histology data of 2-methoxy-1,4-bisstyryl derivatives

Compound Structure / Code	Histology
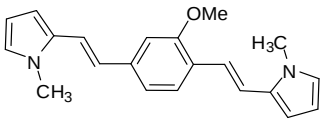 **BSc4344**	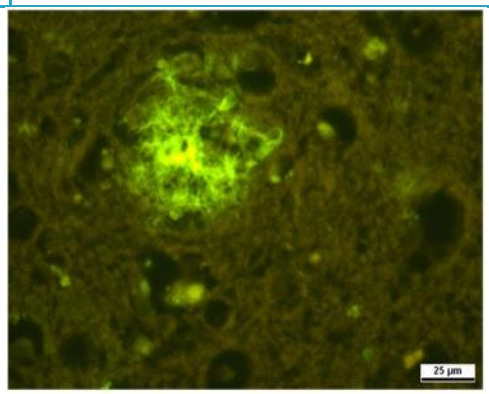 Neuropathological staining with BSc4344, displaying a SP. Imaged with fluorescence microscopy using FITC filter. Staining effect (Aβ: ++ / NFT: -).

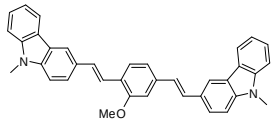

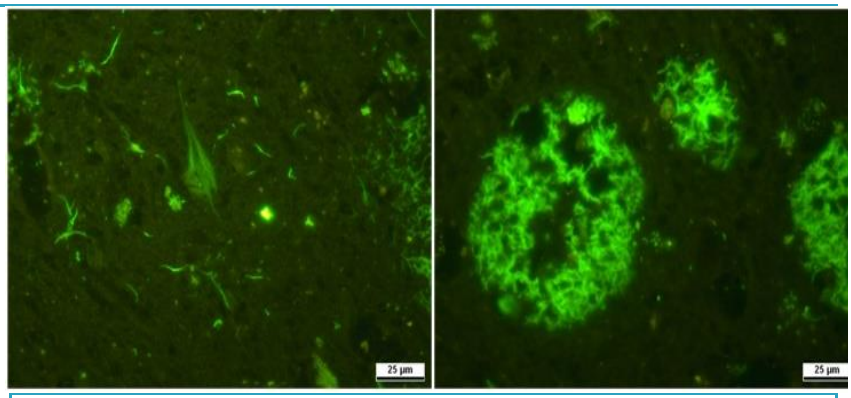

BSc4346

Neuropathological staining with BSc4346, displaying NFTs (left) a SP (right). Imaged with fluorescence microscopy using FITC filter. Staining effect (Aβ: +++ / NFT: +++).

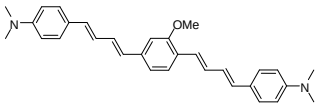

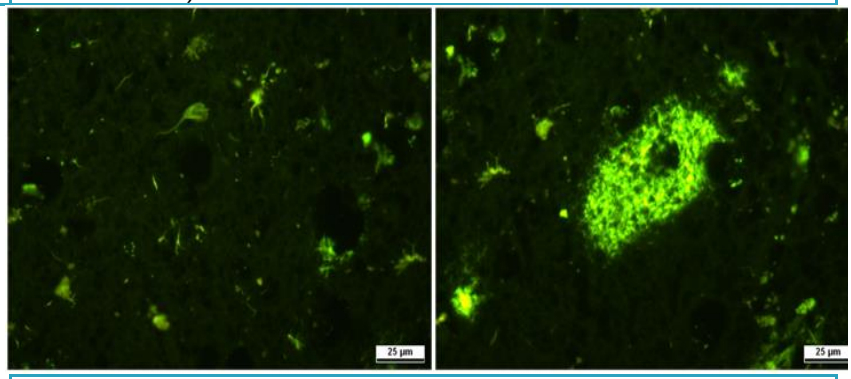

BSc4351

Neuropathological staining with BSc4351, displaying NFTs (left) and a SP (right). Imaged with fluorescence microscopy using FITC filter. Staining effect (Aβ: +++ / NFT: +++).

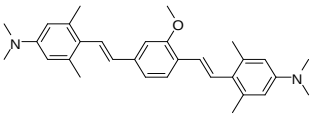

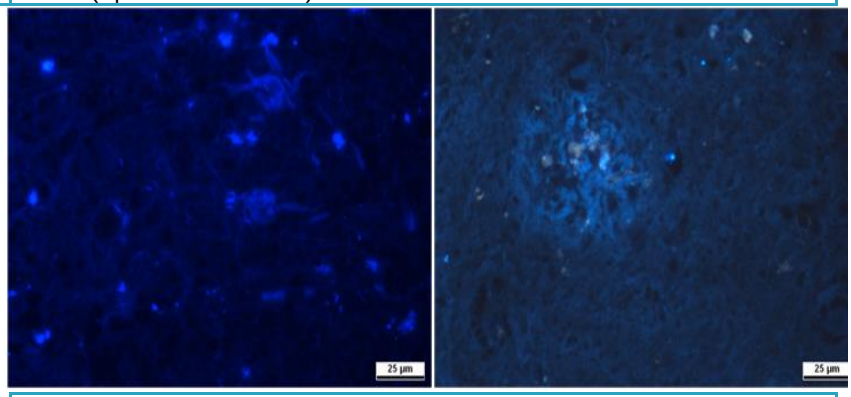

BSc4887

Neuropathological staining with BSc4887, displaying NFTs and a SP. Imaged with fluorescence microscopy using DAPI filter. Staining effect (Aβ: ++ / NFT: ++).

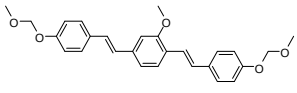

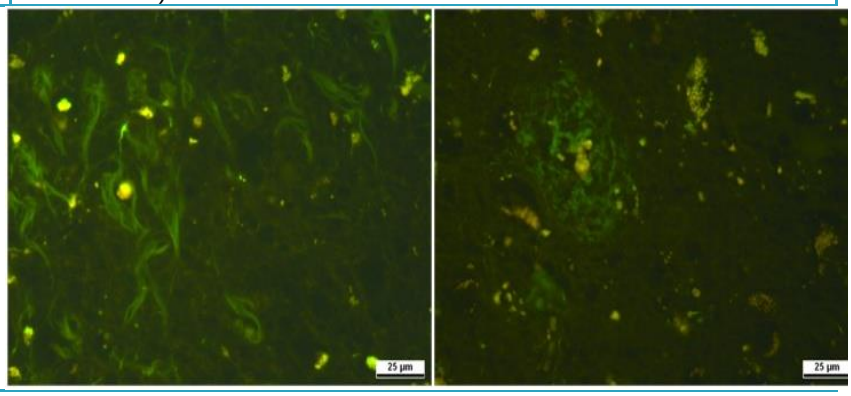

BSc4990	Neuropathological staining with BSc4990, displaying NFTs and a SP. Imaged with fluorescence microscopy using FITC filter. Staining effect (Aβ: ++ / NFT: ++).
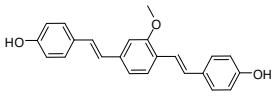 **BSc3924**	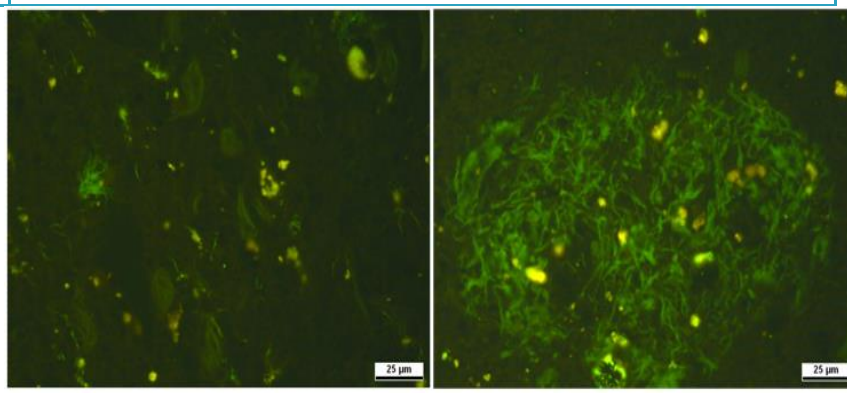 Neuropathological staining with BSc3924, displaying NFTs and a SP. Imaged with fluorescence microscopy using FITC filter. Staining effect (Aβ: ++ / NFT: ++).
Tissues: hippocampus; patient: male, 90 years old, CERAD-score: 3; NFTs level: V. +++ stands for good staining, ++ stands for normal staining, + stands for weak staining, - stands for no stainng	

3.1.6.5 *In vitro* histochemical staining of postmortem AD brain tissues with bis(arylvinyl) pyrimidines.

A group of bis(arylvinyl) pyrimidine derivatives was synthesized and evaluated for its ability to display NFTs and SPs in post mortem human AD brain. These compounds displayed very good staining of SPs and NFTs. However, probes with either ortho substitution to the dimethylamino group or dimethylamino pyridines (BSc4938, BSc4939, BSc4984 and BSc4988) resulted in poor histology. Histology data of these probes is shown below.

Table 3.1.6.5 Histology data of bis(arylvinyl) pyrimidines

Compound Structure / Code	Histology
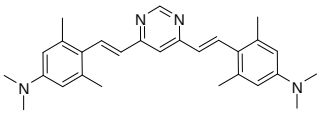 **BSc4890**	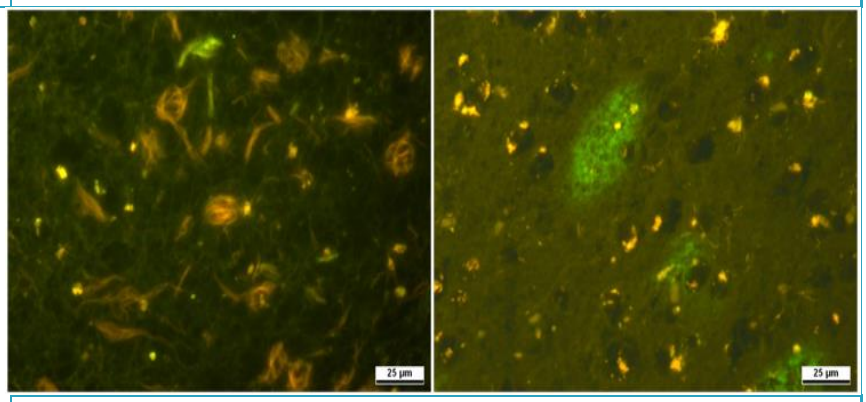 Neuropathological staining with BSc4890, displaying NFTs (left) and a SP (right). Imaged with fluorescence microscopy using FITC filter. Staining effect (Aβ: +++ / NFT: +++).

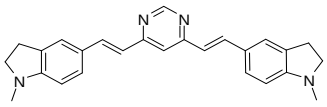

BSc4935

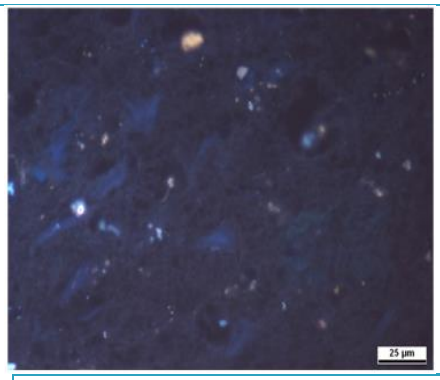

Neuropathological staining with BSc4935, displaying NFTs. Imaged with fluorescence microscopy using DAPI filter. Staining effect (Aβ: - / NFT: +).

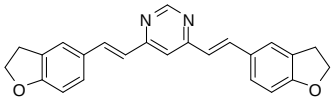

BSc4936

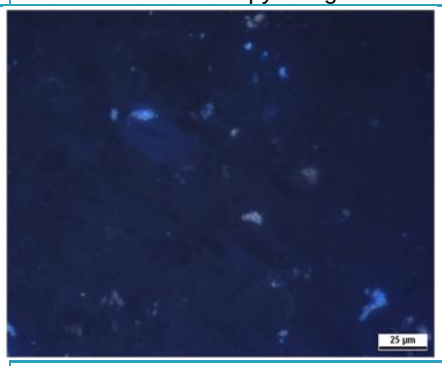

Neuropathological staining with BSc4936, displaying NFTs. Imaged with fluorescence microscopy using DAPI filter. Staining effect (Aβ: - / NFT: +).

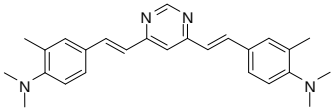

BSc4938

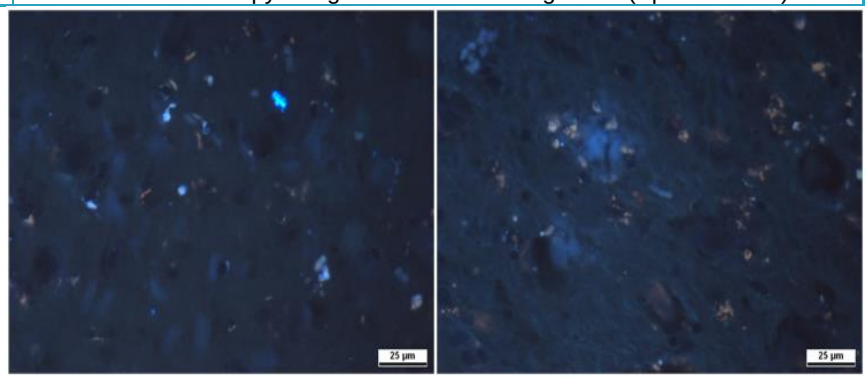

Neuropathological staining with BSc4938, displaying NFTs (left) and a SP (right). Imaged with fluorescence microscopy using DAPI filter. Staining effect (Aβ: + / NFT: +).

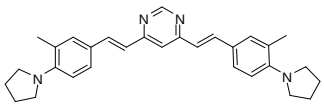

BSc4939

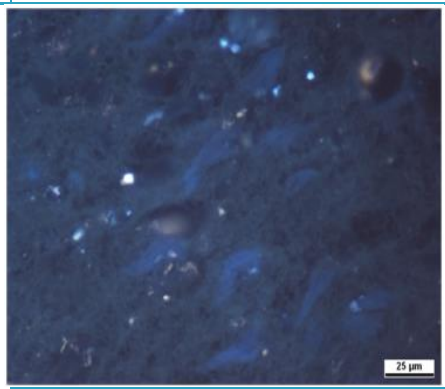

Neuropathological staining with BSc4939, displaying NFTs. Imaged with fluorescence microscopy using DAPI filter. Staining effect (Aβ: - / NFT: -).

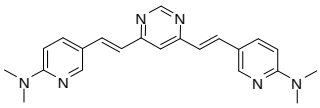

BSc4984

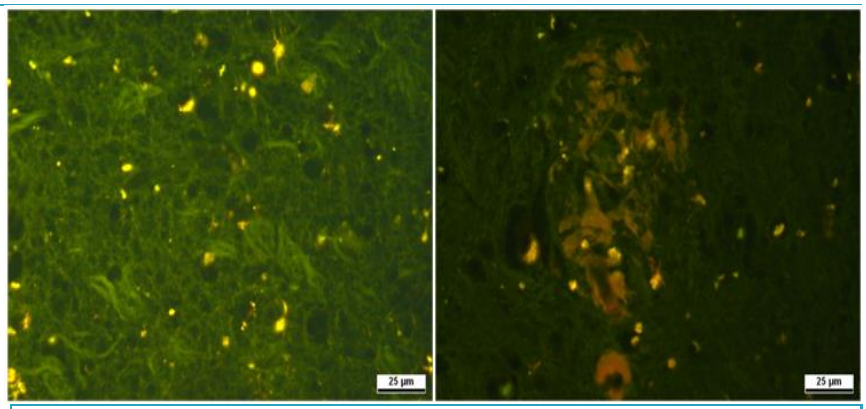

Neuropathological staining with BSc4984, displaying NFTs (left) and a SP (right) under FITC filter. Staining effect (Aβ: +++ / NFT: +).

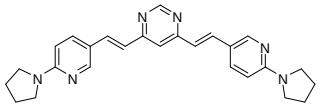

BSc4988

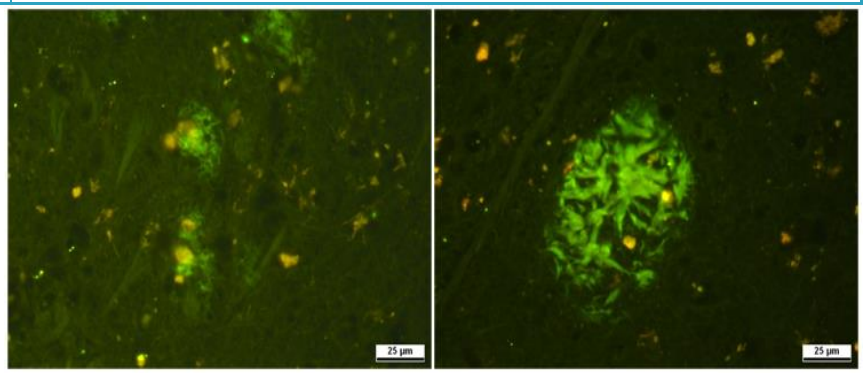

Neuropathological staining with BSc4988, displaying NFTs (left) and a SP (right). Imaged with fluorescence microscopy using FITC filter. Staining effect (Aβ: +++ / NFT: +).

Tissues: hippocampus; patient: male, 72 years old, CERAD Score: 3; NFTs-level: V.
+++ stands for good staining, ++ stands for normal staining, + stands for weak staining, - stands for no stainng

3.1.6.6 *In vitro* histochemical staining of postmortem AD brain tissues with bis(arylvinyl) pyrazines.

A group of bis(arylvinyl) pyrazine derivatives was synthesized and evaluated for their ability to display NFTs and SPs in the post mortem human AD brain. These compounds displayed very good staining of SPs and NFTs. However, affinities of these probes *in vitro* resulted in no activitiy against *Thiazine red R* displacement (data not shown). Histology data of these probes is shown below.

Table 3.1.6.6 Histology of bis(arylvinyl) pyrazines	
Compound Structure / Code	**Histology**
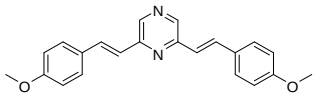 **BSc4758**	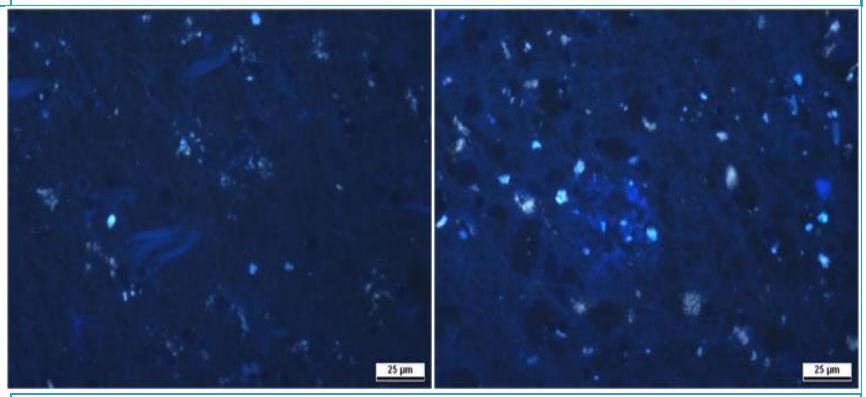 Neuropathological staining with BSc4758, displaying NFTs (left) and a SP (right). Imaged with fluorescence microscopy using DAPI filter. Staining effect (Aβ: + / NFT: -).
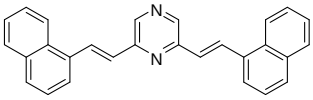 **BSc4760**	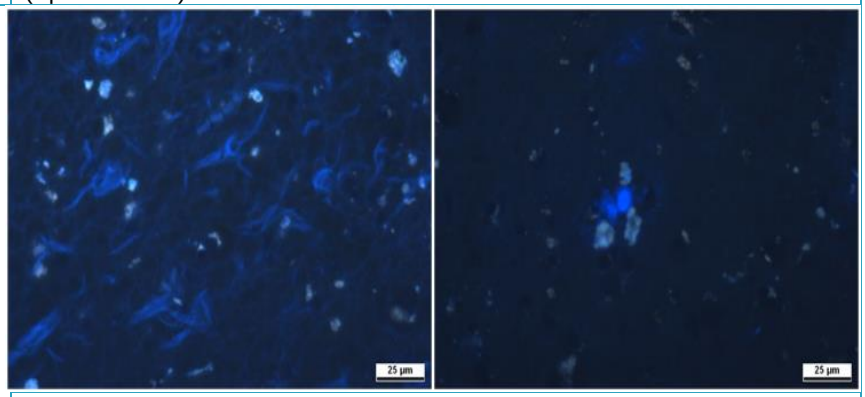 Neuropathological staining with BSc4760, displaying NFTs (left) and a SP (right). Imaged with fluorescence microscopy using DAPI filter. Staining effect (Aβ: + / NFT: ++).
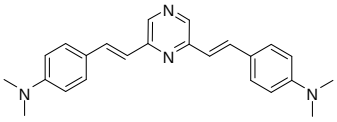 **BSc4761**	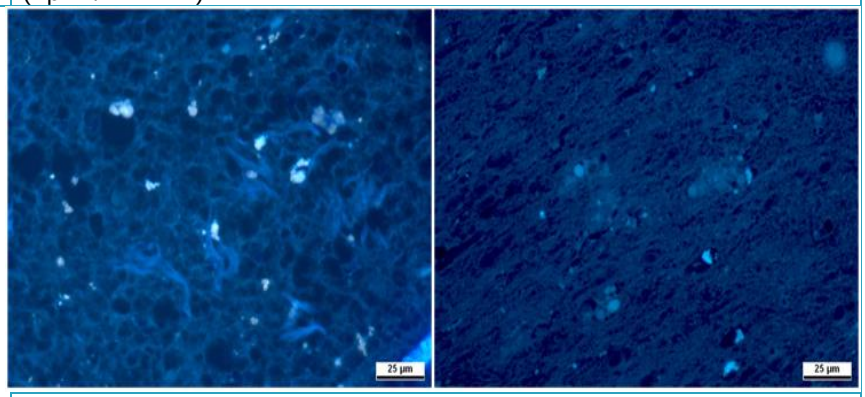 Neuropathological staining with BSc4761, displaying NFTs (left) and a SP (right). Imaged with fluorescence microscopy using DAPI filter. Staining effect (Aβ: + / NFT: +).

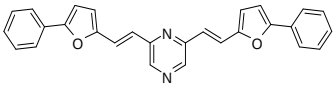

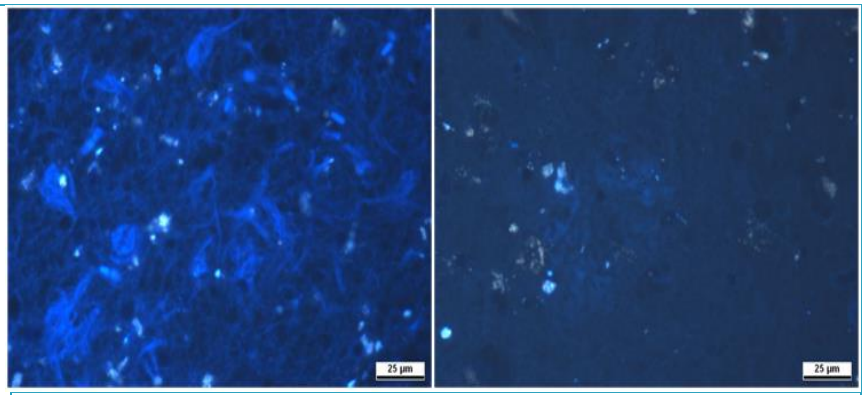

BSc4767

Neuropathological staining with BSc4767, displaying NFTs (left) and a weakly stained SP (right). Imaged with fluorescence microscopy using DAPI filter. Staining effect (Aβ: + / NFT: ++).

Tissues: hippocampus; patient: female, 80 years old, CERAD Score: 3; NFTs-level: V.
+++ stands for good staining, ++ stands for normal staining, + stands for weak staining, - stands for no stainng

3.1.6.7 *In vitro* histochemical staining of postmortem AD brain tissues with quinoxalin-2-yl derivatives.

A set of three quinoxalin-2-yl derivatives was synthesized and evaluated for its ability to display NFTs and SPs in post mortem human AD brain. These compounds displayed very good staining of SPs over NFTs. Histology data of these probes is shown below.

Table 3.1.6.7 Histology data of quinoxalin-2-yl derivatives

Compound Structure / Code	Histology
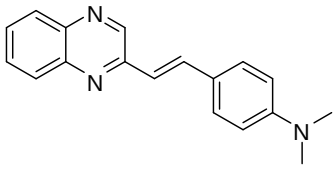 **BSc4991**	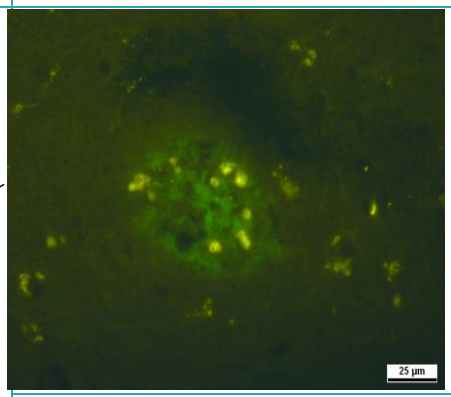 Neuropathological staining with BSc4991, displaying a SP. Imaged with fluorescence microscopy using FITC filter. Staining effect (Aβ: ++ / NFT: -).

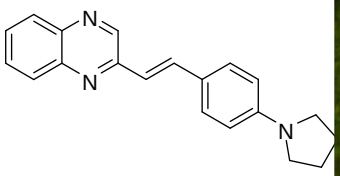

BSc4992

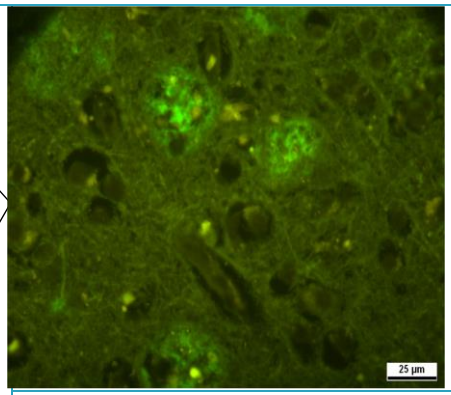

Neuropathological staining with BSc4992, displaying SPs. Imaged with fluorescence microscopy using FITC filter. Staining effect (Aβ: ++ / NFT: -).

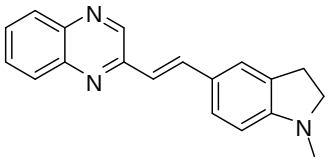

BSc4993

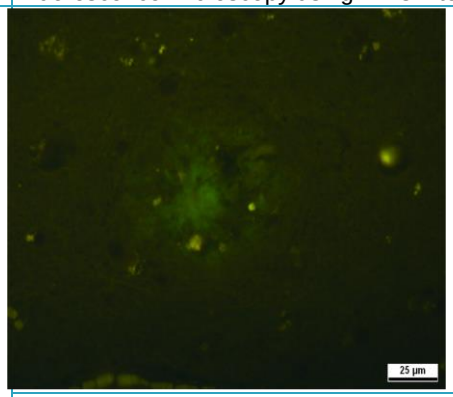

Neuropathological staining with BSc4993, displaying weakly stained SP. Imaged with fluorescence microscopy using FITC filter. Staining effect (Aβ: + / NFT: -).

Tissues: hippocampus; patient: female, 80 years old, CERAD Score: 3; NFTs-level: V.
+++ stands for good staining, ++ stands for normal staining, + stands for weak staining, - stands for no stainng

4.0 SUMMARY AND OUTLOOK

By structural modification of known amyloid imaging agents and tau aggregation inhibitors, several classes of compounds were synthesized with different absorption and emission properties for the imaging of NFTs and SPs in AD brain. The compound classes include rhodanine-3-acetic acids (RAs), bis(arylvinyl)pyrazines, quinoxalins, cyanobiphenyls, dicyano styryls, phenylene vinylenes, 2-methoxy-1,4-bisstyryls, bis(arylvinyl)pyrimidines, imidazo[4,5-c] pyridines, carbazoles, imidazo[1,2-a]pyridines, and squaramides. All of these compounds were synthesized by different synthetic methods and their absorption properties were measured. Histological examination was conducted with these compounds on AD patient brain tissues obtained at autopsy.

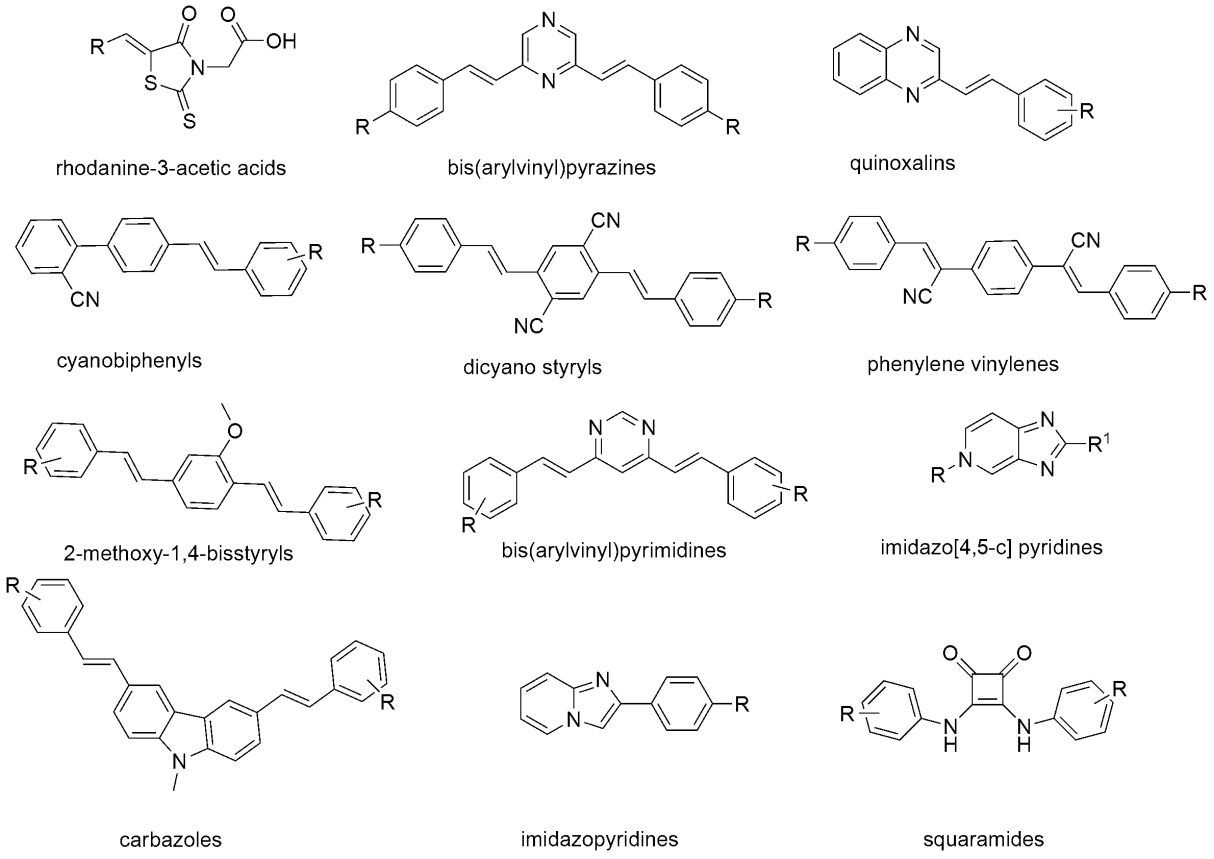

Figure 4.1: General Structures of the synthesized probes.

Firstly, RAs have been discussed and these compounds have shown very good to excellent staining by fluorescence microscopy to flame shaped NFTs over SPs in brain sections of an AD patient obtained at autopsy **(**probes 1-7 in **chapter 3.1.2)**.

RAs were then evaluated for cytotoxicity in zebrafish embryos and HepG2 cells. It was observed that these compounds have no or negligible cytotoxicity in both assays. The cytotoxicity results indicate that these compounds can further proceed to *in vivo* mice experiments. RAs were evaluated in P301S mice that express tau aggregates in the retina. Observations with these compounds resulted in no staining to tau aggregates in the retina **(chapter 3.1.2)**. It was assumed that different tau isoforms are responsible for the formation of different types of aggregates. Furthermore, it may also be possible that RA derivatives bind to fibrillary tau aggregates of post mortem AD brain and not to the non-fibrillary tau aggregates of the retina.

Secondly, a group of 2-styrylindolium based probes was evaluated for their ability to display NFTs in postmortem human AD brain sections **(chapter 3.1.3)**. 2-styrylindolium based probes, clearly visualized NFTs in postmortem human AD brain sections. However, affinity data to amyloid aggregates was not quantified for compound 9 (**in chapter 3.1.3**) due to interference of autofluorescence of the probe with *Thiazine red R*.

Thirdly, a set of water soluble trimethine cyanine dyes was evaluated as fluorescent imaging agents for tau aggregates in the postmortem human AD brain sections and tau aggregates in the Bowman glands of olfactory epithelium tissues **(chapter 3.1.4)**. These probes visualized tau aggregates of human AD brain and olfactory epithelium tissues by fluorescence microscopy. Further *in vivo* evaluation of these probes may result in fluorescence imaging agents for AD diagnosis.

Fourthly, a set of oxadiazole derivatives was identified as GSK3 inhibitors and the most effective inhibitors displayed IC_{50} values in the low nano molar range and good kinase selectivity against four closely related kinases **(chapter 3.1.5)**. The zebrafish cytotoxicity evaluation resulted in no mortality at concentration <30 μM.

Fifthly, several other probes were designed and synthesized for fluorescence imaging of NFTs. Of them, 5H-imidazo[4,5-c]pyridines visualized NFTs in postmortem AD brain tissues **(Table 3.1.6.2)**. **BSc4942** in this class also visualized astrocyte fibers along with NFTs. These compounds displayed good staining of NFTs. However, *in vitro* affinity data (data not shown) with *Thiazine red R* showed that these compounds have poor affinities to *in vitro* tau aggregates. It is known that the chemically induced tau aggregates are not reliable replacement for NFTs as they vary in size and morphology. Another reason may be that these probes bind to a different binding region than the binding region of *Thiazine red R* of

tau aggregates and may not able to replace *Thiazine red R*, which in turn, resulted in poor affinities of modified IMPy derivatives.

Further to histology of postmortem brain sections for NFTs, histology of these compounds was also performed with postmortem olfactory epithelium tissues to image tau aggregates. These compounds displayed good staining of tau aggregates in Bowman glands of olfactory epithelium tissues and these tau deposits can be clearly visualized by fluorescence microscopy **(Figure 4.2)**.

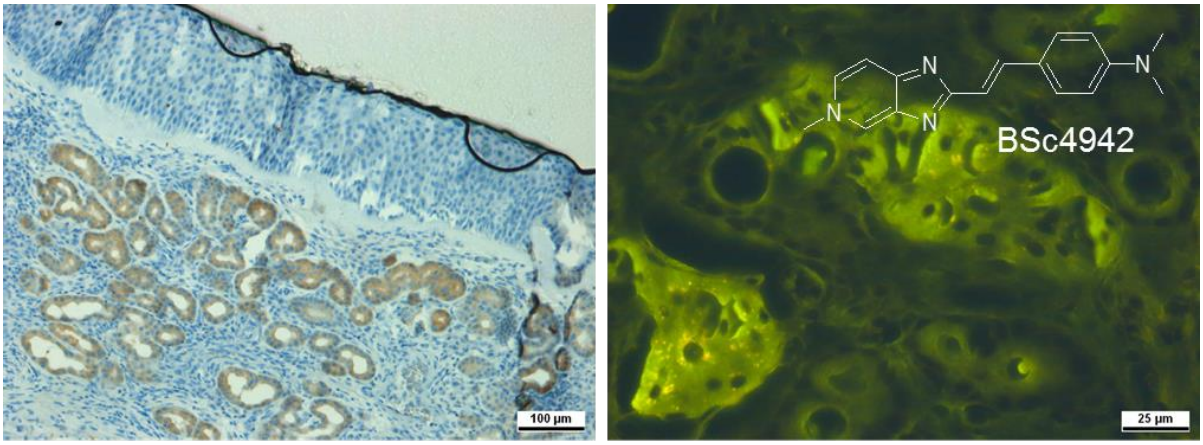

Figure 4.2: Immunohistology and *in vitro* histochemical staining of post mortem AD olfactory epithelium tissues. BSc4942 display tau aggregates in Bowman glands of olfactory epithelium tissues. (Tissues: olfactory epithelium; patient: male, 78 years old, CERAD-score: 3; NFTs level: V)

Sixthly, probes with two photon imaging properties were designed and synthesized for the fluorescence imaging of NFTs. MeX04 is a fluorescent ligand which is known to bind to NFTs and SPs **(Table 3.1.6.4)**. Modification of this structure resulted in probes that stain SPs. In addition to this, cyano groups on the central benzene ring were introduced to improve the two photon absorption properties. Due to the bulky size of the cyano group this compound was unable to stain SPs. Also methoxy derivatives stained NFTs and SPs in post mortem AD patient brain tissue, but these compounds have very poor solubilities and may not be suitable for *in vivo* imaging.

Seventhly, to improve the solubility of fluorescent probes, a pyrimidine ring was introduced in place of a methoxy benzene moiety. The resulting pyrimidine compounds were evaluated for their staining ability of NFTs and SPs **(Table 3.1.6.5)**. Surprisingly, the new pyrimidine derivatives showed excellent fluorescent properties and stained both NFTs and plaques, especially the pyrimidine compounds showed improved solubility. We explored the structure activity relationship of these compounds. The introduction of groups such as fluoro or methyl or nitrogen ortho to the *N, N*-dimethyl groups on the aryl rings resulted in compounds with

dramatic reduction of their ability to stain to NFTs or SPs. Pyrazine probes also displayed poor absorption properties and weak staining **(Table 3.1.6.6)**.

Finally, few other probes such as quinoxaline derivatives, squaric acid derivative and squaramide derivatives were synthesized for fluorescence imaging of NFTs. Quinoxaline derivatives showed staining to SPs over NFTs **(Table 3.1.6.7),** whereas squaric acids displayed poor staining. Squaramides had visualized NFTs by fluorescence microscopy with post mortem AD brain tissues, but due to high back ground tissue staining, NFTs were visualized at low constrast.

In summary, top 5 tau selective probes and their histology data are listed below **(Table 4.3)**.

Table 4.3: Histology of Top 5 NFT selective probes

Entry	BSc No.	*c*Log*P*	MW	Histology
1	4823	2.19	348.4	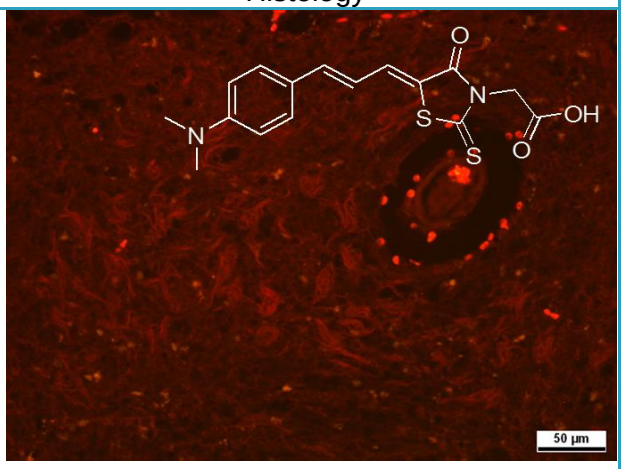
2	4825	3.03	367.4	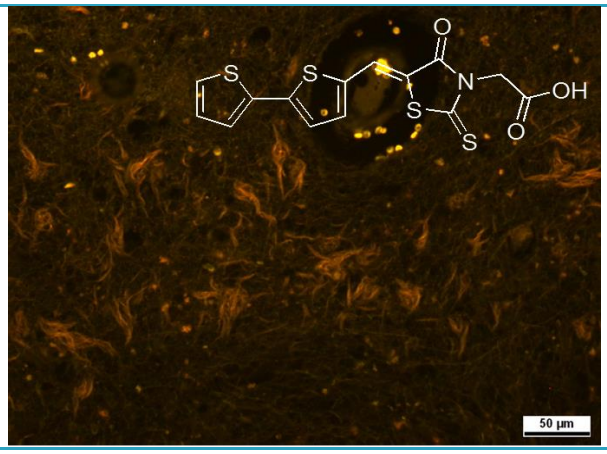

3	4826	3.11	391.4	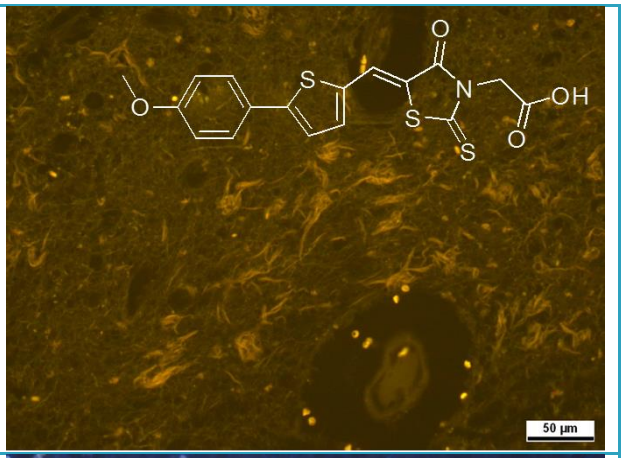
4	4892	4.67	320.4	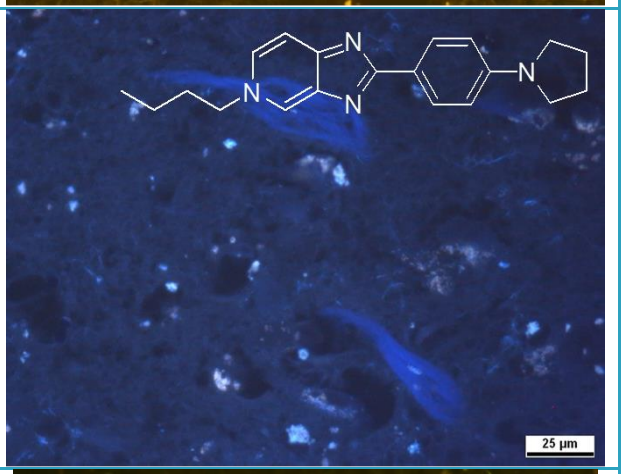
5	4942	3.42	278.3	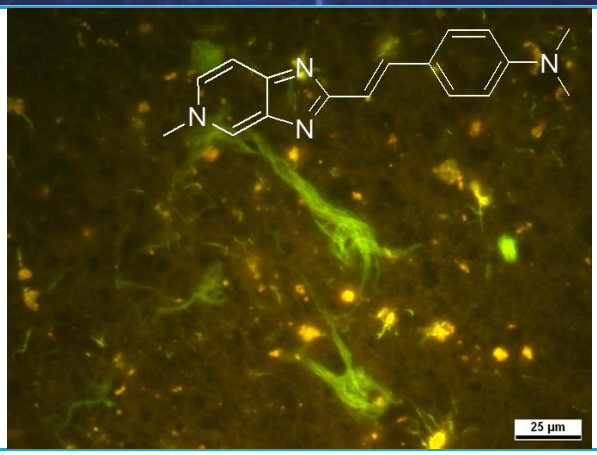

Further modifications may be needed to improve the solubility of these compounds, which can be achieved by the introduction of PEGylating groups and fluoro PEGylating groups for *in vivo* applications. The BBB permeation of RAs may be further improved by introducing groups such as fluoro PEG.

Amyvid® contains three polyethylene glycol units and a fluorine atom. These units are known to improve the BBB permeation and the core is known to bind to SPs in patients with cognitive failure. Similar strategies may be applied to improve the BBB penetration of RA by introducing PEG units as shown below.

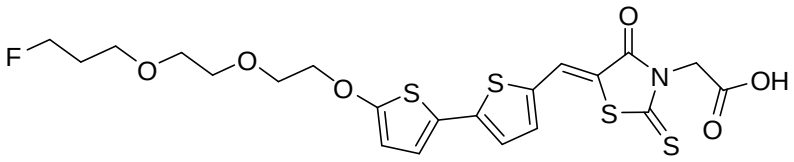

The same strategy can be also applied to IMPy derivatives. Addition of Fluoro PEG unit to this compound may result in better BBB permeation.

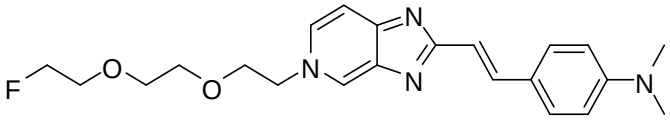

We observed that tertiary amine groups maintain selectivity to tangles over plaques. Hence, introduction of tertiary amine groups keeps selectivity for tangles constant and also improves solubility for *in vivo* applications. For example, compound below may result in improved solubility in comparison with other pyrimidine probes.

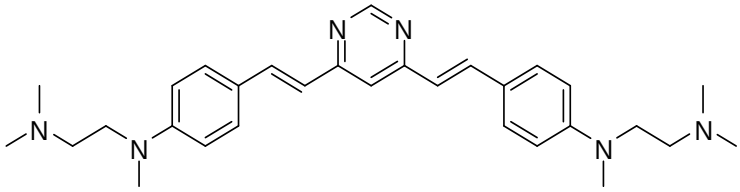

5.0 METHODS

All methods were performed according the methods reported in **chapter 3.1.2 & 3.1.5**.

6.0 SUPPORTING INFORMATION

6.1 Instrumentation and General Experimental Conditions

All commercial chemicals, reagents, solvents were purchased from Sigma-Aldrich, Acros Organic, Alfa Aesar, TCI Europe, VWR, and Apollo Scientific and were used without any further purification. All reactions were performed under N_2 atmosphere using dry solvents unless otherwise specified. ^{1}H-NMR spectra were recorded on a Bruker AC300, ARX300 and DRX 500 spectrometer at 300 MHz and 500 MHz respectively. The ^{13}C-NMR spectra were recorded on a Bruker AC300, ARX300 and DRX 500 spectrometer at 75 MHz and 125 MHz respectively. Chemical shifts values are reported as parts per million (ppm) downfield from Me_4Si. Absorption and emission data of the probes were obtained on Shimadzu UV-2401PC and TECAN infinite M 1000 pro. Mass spectrometry was performed on a MAT 95 double focusing sector field MS. Flash column chromatography was carried out with Merck silica gel 60 (15-40 mm) and a TELEDYNE ISCO Combiflash Rf 4x system (Flow rate: 5-200 ml/min, Maximum pressure: 200 psi, column size: 4 gm to 40 gm: UV range: 254 to 360 nm). Thin-layer chromatography (TLC) was carried out with aluminum sheets precoated with silica gel 60 F254 (0.2 mm, Merck). Chromatographic spots were visualized by UV light. HPLC was carried out using an Agilent 1100 (Column: reverse phase, Zorbax Eclipse XDB-C8, 4.6 x 150 mm, Wavelength: 254 nm, Solvent System: Acetonitrile/Water (gradient), Method: 12 min run time. 70% water: 30% ACN for first one minute and it reaches to 90% ACN by 12 min controlled by Chemstation software. Brain sections were obtained from Klinikum Darmstadt. Compounds with poor solubility were confirmed by ^{1}H-NMR only.

6.2 Synthesis of rhodanine-3-acetic acid derivatives

Synthetic scheme

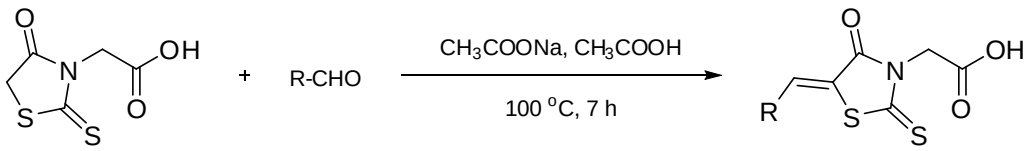

40 **41a-h** **42a-h**

Compound	R
42a	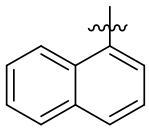
42b	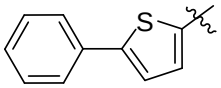
42c	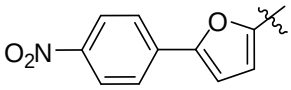
42d	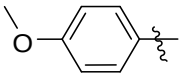
42e	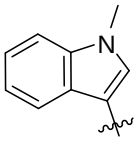
42f	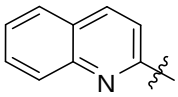
42g	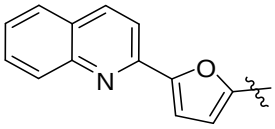
42h	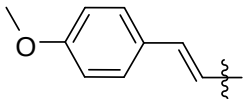

6.2.1 General procedure for the synthesis of rhodanine-3-acetic acids

Sodium acetate (3 eq.) was added to a solution of aldehyde (**41a-h)** (1 eq.) and rhodanine-3-acetic acid (**40)** (1 eq.) in glacial acetic acid (5 ml) and the reaction mixture was stirred for 7 hours at 100 ^{o}C, forming a precipitate after cooling to room temperature. The resultant crude product was recovered by filtration and recrystallized from acetone/water mixture to give compound **42a-h**.

(*Z*)-2-(5-(Naphthalen-1-ylmethylene)-4-oxo-2-thioxothiazolidin-3-yl)acetic acid 42a (BSc4757)

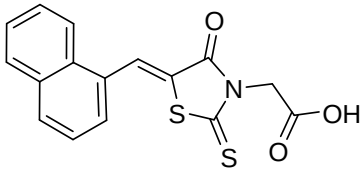

The title compound was synthesized by following the general procedure mentioned in **6.2.1.**

Reactants: 1-naphthaldehyde **(41a)** (156 mg, 1.0 mmol), rhodanine-3-acetic acid **(40)** (191 mg, 1.0 mmol), sodium acetate (246 mg, 3.0 mmol), glacial acetic acid (5 mL).

Yield: 263 mg, 80%.

A bright yellow solid. **HPLC**: R_t = 8.05 min. **^{1}H-NMR** (300 MHz, DMSO-d_6): δ [ppm] = 8.54 (s, 1H), 8.20 (d, *J* = 7.9 Hz, 1H), 8.13 (d, *J* = 8.0 Hz, 1H), 8.09 – 8.03 (m, 1H), 7.79 – 7.61 (m, 4H), 4.78 (s, 2H) acid proton not visible. **^{13}C-NMR** (75 MHz, DMSO-d_6): δ [ppm] = 194.26, 167.73, 166.24, 133.79, 132.11, 131.49, 131.16, 130.44, 129.42, 128.22, 127.74, 127.47, 126.26, 125.72, 123.92, 45.54. **MS** (EI, 70 eV): *m/z* = 329 [M^+]. **UV/Vis** (Ethanol): λ_{max} = 390 nm.

(*Z*)-2-(4-Oxo-5-((5-phenylthiophen-2-yl)methylene)-2-thioxothiazolidin-3-yl)acetic acid 42b (BSc4820)

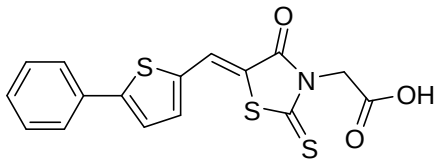

The title compound was synthesized by following the general procedure mentioned in **6.2.1.**

Reactants: 5-phenylthiophene-2-carbaldehyde **(41b)** (188 mg, 1.0 mmol), rhodanine-3-acetic acid **(40)** (191 mg, 1.0 mmol), sodium acetate (246 mg, 3.0 mmol), glacial acetic acid (5 mL).

Yield: 288 mg, 80%.

A yellowish orange solid. **HPLC**: R_t = 8.22 min. **^{1}H-NMR** (500 MHz, DMSO-d_6): δ [ppm] = 13.42 (b, 1H), 8.18 (s, 1H), 7.83 (ddd, *J* = 8.8, 6.3, 4.0 Hz, 3H), 7.79 (d, *J* = 4.0 Hz, 1H), 7.52 – 7.47 (m, 2H), 7.46 – 7.41 (m, 1H), 4.74 (s, 2H). **^{13}C-NMR** (125 MHz, DMSO-d_6): δ [ppm] = 192.41, 167.72, 166.48, 152.52, 142.86, 138.50, 136.83, 132.87, 129.88, 127.32, 126.39, 119.26, 114.67, 45.64. **MS** (EI, 70 eV): *m/z* = 361 [M^+]. **UV/Vis** (Ethanol): λ_{max} = 436 nm.

(*Z*)-2-(5-((5-(4-Nitrophenyl)furan-2-yl)methylene)-4-oxo-2-thioxothiazolidin-3-yl)acetic acid 42c (BSc4821)

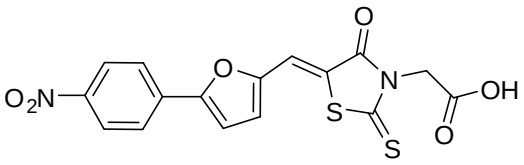

The title compound was synthesized by following the general procedure mentioned in **6.2.1.**

Reactants: 5-(4-nitrophenyl)furan-2-carbaldehyde **(41c)** (217 mg, 1.0 mmol), rhodanine-3-acetic acid **(40)** (191 mg, 1.0 mmol), sodium acetate (246 mg, 3.0 mmol), glacial acetic acid (5 mL).

Yield: 292 mg, 75%.

An orange solid. **HPLC**: R_t = 7.68 min. **^{1}H-NMR** (500 MHz, DMSO-d_6): δ [ppm] = 8.42 – 8.37 (m, 2H), 8.09 – 8.03 (m, 2H), 7.72 (s, 1H), 7.62 (d, *J* = 3.8 Hz, 1H), 7.42 (d, *J* = 3.8 Hz, 1H), 4.54 (s, 2H). **^{13}C-NMR** (125 MHz, DMSO-d_6): δ [ppm] = 194.02, 167.18, 166.72, 155.82, 151.37, 147.31, 134.70, 125.60, 125.24, 123.21, 121.01, 118.35, 114.29, 47.16. **MS** (EI, 70 eV): *m/z* = 390 [M^+]. **UV/Vis** (Ethanol): λ_{max} = 440 nm.

(Z)-2-(5-(4-Methoxybenzylidene)-4-oxo-2-thioxothiazolidin-3-yl)acetic acid 42d (BSc4824)

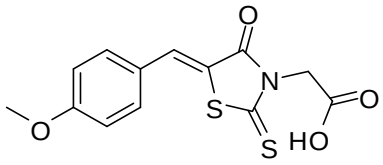

The title compound was synthesized by following the general procedure mentioned in **6.2.1.**

Reactants: 4-methoxybenzaldehyde **(41d)** (136 mg, 1.0 mmol), rhodanine-3-acetic acid **(40)** (191 mg, 1.0 mmol), sodium acetate (246 mg, 3.0 mmol), glacial acetic acid (5 mL).

Yield: 197 mg, 64%.

A greenish yellow solid. **HPLC**: R_t = 6.86 min. **^{1}H-NMR** (500 MHz, DMSO-d_6): δ [ppm] = 13.28 (s, 1H), 7.86 (s, 1H), 7.66 (d, *J* = 8.8 Hz, 2H), 7.17 – 7.11 (d, *J* = 8.8 Hz, 2H), 4.74 (s, 2H), 3.86 (s, 3H). **^{13}C-NMR** (125 MHz, DMSO-d_6): δ [ppm] = 193.56, 167.76, 166.88,

162.23, 134.62, 133.57, 125.85, 118.94, 115.70, 56.10, 45.46. **MS** (EI, 70 eV): *m/z* = 309 [M^+]. **UV/Vis** (Ethanol): λ_{max} = 390 nm.

(*Z*)-2-(5-((1-Methyl-1H-indol-3-yl)methylene)-4-oxo-2-thioxothiazolidin-3-yl)acetic acid 42e (BSc4828)

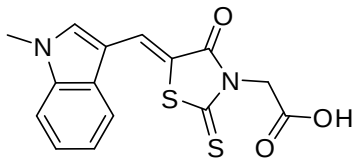

The title compound was synthesized by following the general procedure mentioned in **6.2.1.**

Reactants: 1-methyl-1H-indole-3-carbaldehyde **(41e)** (159 mg, 1.0 mmol), rhodanine-3-acetic acid **(40)** (191 mg, 1.0 mmol), sodium acetate (246 mg, 3.0 mmol), glacial acetic acid (5 mL).

Yield: 222 mg, 67%.

An orange solid. **HPLC**: R_t = 7.12 min. **^{1}H-NMR** (500 MHz, DMSO-d_6): δ [ppm] = 13.38 (s, 1H), 8.14 (s, 1H), 8.04 (s, 1H), 8.02 (d, *J* = 7.9 Hz, 1H), 7.61 (d, *J* = 8.1 Hz, 1H), 7.39 – 7.33 (td, *J* = 7.9, 0.9 Hz, 1H), 7.32 – 7.27 (td, *J* = 8.1, 1.0 Hz, 1H), 4.74 (s, 2H), 3.97 (s, 3H). **^{13}C-NMR** (125 MHz, DMSO-d_6): δ [ppm] = 192.69, 167.93, 166.50, 137.53, 134.76, 127.76, 126.84, 124.00, 122.45, 119.22, 114.17, 111.54, 110.53, 45.46, 33.97. **MS** (EI, 70 eV): *m/z* = 332 [M^+]. **UV/Vis** (Ethanol): λ_{max} = 441 nm.

(*Z*)-2-(4-Oxo-5-(quinolin-2-ylmethylene)-2-thioxothiazolidin-3-yl)acetic acid 42f (BSc4882)

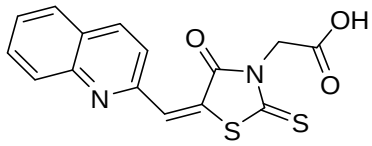

The title compound was synthesized by following the general procedure mentioned in **6.2.1.**

Reactants: Quinoline-2-carbaldehyde **(41f)** (157 mg, 1.0 mmol), rhodanine-3-acetic acid **(40)** (191 mg, 1.0 mmol), sodium acetate (246 mg, 3.0 mmol), glacial acetic acid (5 mL).

Yield: 132 mg, 40%.

A yellowish green solid. **^{1}H-NMR** (500 MHz, Acetone-d_6): δ [ppm] = 8.52 (d, *J* = 8.4 Hz, 1H), 8.29 (d, *J* = 8.5 Hz, 1H), 8.05 (d, *J* = 8.2 Hz, 1H), 8.00 (d, *J* = 8.4 Hz, 1H), 7.96 (s, 1H), 7.91 (ddd, *J* = 8.4, 6.9, 1.4 Hz, 1H), 7.72 (ddd, *J* = 8.1, 6.9, 1.1 Hz, 1H), 4.90 (s, 2H). **^{13}C-NMR** (125 MHz, DMSO-d_6): δ [ppm] = 200.50, 167.84, 166.89, 151.93, 147.50, 138.09, 131.44, 129.29, 128.88, 128.68, 128.59, 128.49, 127.56, 125.24, 45.11. **MS** (EI, 70 eV): *m/z* = 330 [M^+]. **UV/Vis** (Ethanol): λ_{max} = 404 nm.

(*Z*)-2-(4-Oxo-5-((5-(quinolin-2-yl)furan-2-yl)methylene)-2-thioxothiazolidin-3-yl)acetic acid 42g (BSc4884)

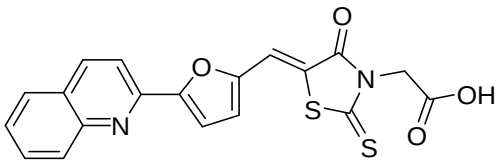

The title compound was synthesized by following the general procedure mentioned in **6.2.1.**

Reactants: 5-(quinolin-2-yl)furan-2-carbaldehyde **(41g)** (35 mg, 0.156 mmol), rhodanine-3-acetic acid **(40)** (29.8 mg, 0.156 mmol), sodium acetate (38.5 mg,0.47 mmol), glacial acetic acid (2 mL).

Yield: 25 mg, 40%.

A solid. **HPLC**: R_t = 7.45 min. **^{1}H-NMR** (500 MHz, DMSO-d_6): δ [ppm] = 8.60 (d, *J* = 8.6 Hz, 1H), 8.07 (s, 1H), 8.05 (s, 1H), 8.03 (d, *J* = 7.9 Hz, 1H), 7.85 (s, 1H), 7.83 (d, *J* = 8.3 Hz, 1H), 7.66 (d, *J* = 7.1 Hz, 1H), 7.63 (d, *J* = 3.7 Hz, 1H), 7.49 (d, *J* = 3.7 Hz, 1H), 4.77 (s, 2H). **MS** (EI, 70 eV): *m/z* = 396 [M^+]. **UV/Vis** (Ethanol): λ_{max} = 447 nm.

2-((*Z*)-5-((*E*)-3-(4-Methoxyphenyl)allylidene)-4-oxo-2-thioxothiazolidin-3-yl)acetic acid 42h (BSc4886)

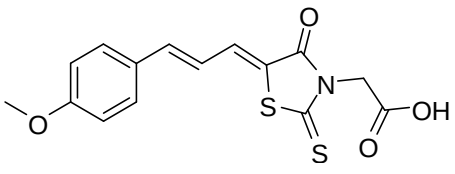

The title compound was synthesized by following the general procedure mentioned in **6.2.1.**

Reactants: (*E*)-3-(4-methoxyphenyl)acrylaldehyde **(41h)** (162 mg, 1.0 mmol), rhodanine-3-acetic acid **(40)** (191 mg, 1.0 mmol), sodium acetate (246 mg,0.47 mmol), glacial acetic acid (5 mL).

Yield: 241 mg, 72%.

An orange solid. **^{1}H-NMR** (500 MHz, DMSO-d_6): δ [ppm] = 7.68 (d, *J* = 8.82 Hz, 2H), 7.54 (dd, *J* = 0.87, 11.63 Hz, 1H), 7.37 (d, *J* = 15.02 Hz, 1H), 7.02 – 6.92 (m, 3H), 4.55 (s, 2H), 3.81 (s, 3H). **^{13}C-NMR** (125 MHz, DMSO-d_6): δ [ppm] = 193.20, 167.67, 166.36, 161.54, 146.17, 134.80, 130.55, 128.77, 122.31, 121.79, 115.00, 55.86, 46.59. **UV/Vis** (Ethanol): λ_{max} = 421 nm.

6.3 Synthesis of thiohydantoin derivative

Synthetic scheme

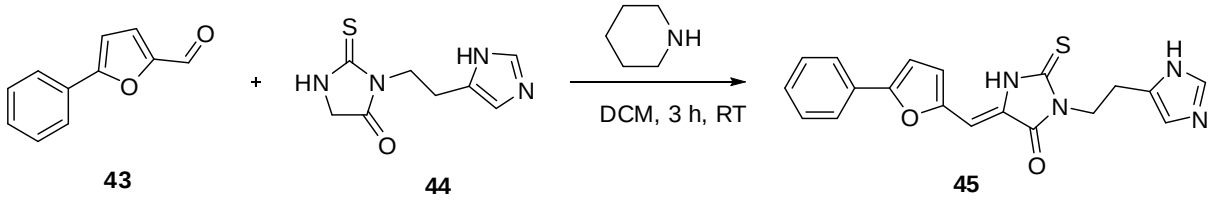

3-(2-(1*H*-Imidazol-5-yl)ethyl)-5-((5-phenylfuran-2-yl)methylene)-2-thioxoimidazolidin-4-one 45 (BSc4768)

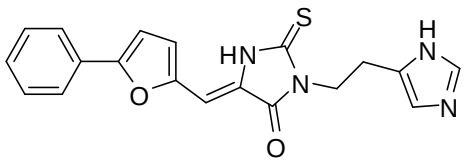

A mixture of 3-(2-(1*H*-Imidazol-4-yl)ethyl)-2-thioxoimidazolidin-4-one **(44)** (80 mg, 0.38 mmol) and 5-phenyl-2-furfaraldehyde **(43)** (65mg, 0.38 mmol), piperdine (60 µl) in dichloromethane were stirred for 3 hours at room temperature. The solvent was removed and the crude solid was filtered by column chromatography on silica gel using dichloromethane and methanol mixture (9:1) as eluent.

Yield: 118 mg, 70%.

An orange solid. **HPLC:** R_t = 4.89 min. **^{1}H-NMR** (500 MHz, DMSO-d_6): δ [ppm] = 12.06 (s, 2H), 7.95 (d, *J* = 7.1 Hz, 2H), 7.57 (s, 1H), 7.49 (dd, *J* = 8.4, 7.1 Hz, 2H), 7.38 (d, *J* = 3.9 Hz, 2H), 7.22 (d, *J* = 3.7 Hz, 1H), 6.85 (s, 1H), 6.55 (s, 1H), 4.07 – 3.94 (m, 2H), 2.88 (dd, *J* = 8.7, 6.7 Hz, 2H). **^{13}C-NMR** (125 MHz, DMSO-d_6): δ [ppm] = 177.80, 164.07, 156.62, 149.24, 135.29, 134.51, 129.69, 129.28, 129.00, 127.79, 125.10, 123.81, 119.47, 110.17, 100.50, 41.04, 25.50. **MS** (EI, 70 eV): *m/z* = 364 [M^+]. **UV/Vis** (Ethanol): λ_{max} = 437 nm.

6.4. Synthesis of 5*H*-imidazo[4,5-c]pyridine derivatives.

Synthetic scheme

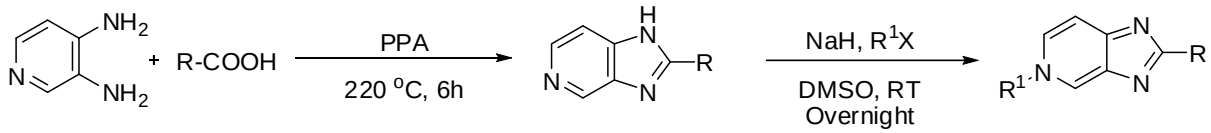

46 **47a-c** **48a-c** **49a-h**

Compound	R	R^1
47a, 48a, 49a	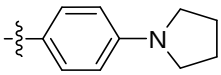	CH_3
49b	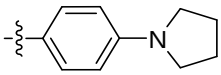	*n*-Pr
49c	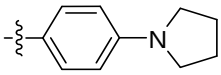	*i*-Pr
49d	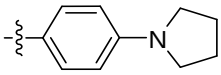	*n*-Bu
49e	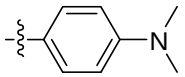	CH_3
47b, 48b, 49f	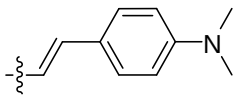	CH_3
47c, 48c, 49g	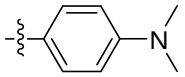	*n*-Bu
49h	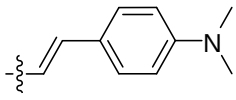	*n*-Bu

2-(4-(Pyrrolidin-1-yl)phenyl)-1*H*-imidazo[4,5-c]pyridine (48a)

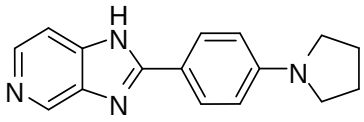

A mixture of pyridine-3,4-diamine **(46)** (1.0 gm, 0.009 mol), 4-(pyrrolidin-1-yl)benzoic acid **(47a)** (1.75 gm, 0.009 mol) and polyphosphoric acid (PPA) (35 gm) were heated at 220 ^{o}C for 6 hours with vigorous stirring. The reaction mixture was allowed to cool to room temperature and poured into ice/water and the mixture is neutralized by the addition of ammonium hydroxide. The crude product was collected by filtration and washed with water, dried with Na_2SO_4 and then purified by column chromatography on silica gel using dichloromethane and methanol mixture (9:1) as eluent.

Yield: 1.52 gm, 63%.

A solid. **HPLC**: R_t = 2.83 min. **^{1}H-NMR** (500 MHz, DMSO-d_6): δ [ppm] = 13.00 (s, 1H), 8.92 (s, 1H), 8.36 (d, *J* = 5.6 Hz, 1H), 8.06 (d, *J* = 8.8 Hz, 2H), 7.50 (d, *J* = 5.4 Hz, 1H), 6.62 (d, *J* = 8.9 Hz, 2H), 3.36 (t, *J* = 6.6 Hz, 4H), 2.05 (t, *J* = 6.5 Hz, 4H). **MS** (EI, 70 eV): *m/z* = 264 [M^+].

(*E*)-4-(2-(1H-Imidazo[4,5-c]pyridin-2-yl)vinyl)-*N*,*N*-dimethylaniline (48b)

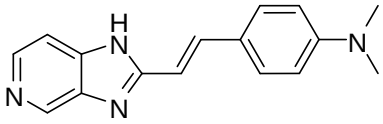

This compound was obtained by the same synthetic procedure as described for **(48a),** using **(46)** (327 mg, 3.0 mmol), **(47b)** (579 mg, 3.03 mmol) and an excess of PPA (12 gm).

Yield: 520 mg, 65%.

A solid. **^{1}H-NMR** (300 MHz, DMSO-d_6): δ [ppm] = 8.80 (d, *J* = 0.8 Hz, 1H), 8.24 (d, *J* = 5.5 Hz, 1H), 7.65 (d, *J* = 16.4 Hz, 1H), 7.50 (d, *J* = 8.8 Hz, 2H), 7.46 (dd, *J* = 5.5, 0.9 Hz, 1H), 6.94 (d, *J* = 16.4 Hz, 1H), 6.76 (d, *J* = 8.9 Hz, 2H), 5.70 (s, 1H), 2.97 (s, 6H).

6.4.1 General procedure for the alkylation of 5*H*-imidazo[4,5-c]pyridines

To a solution of amine (**48a-c)** (1 eq.) at 0 ^{o}C was added sodium hydride (1.1 eq.) in dimethylsulfoxide and stirred for 5 min. To this solution, was added alkyl halide (1.5 eq.) and

the reaction mixture was stirred overnight at room temperature. Excess sodium hydride was quenched with ice and the product extracted with ethyl acetate. The combined organic phases were washed with brine, dried over sodium sulfate, filtered and concentrated *in vacuo*. The crude product was purified by column chromatography on silica gel using dichloromethane and methanol mixture (9:1) as eluent.

5-Methyl-2-(4-(pyrrolidin-1-yl)phenyl)-5*H*-imidazo[4,5-c]pyridine 49a (BSc4883)

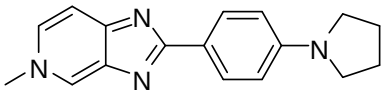

The title compound was synthesized by following the general procedure mentioned in **6.4.1.**

Reactants: 2-(4-(pyrrolidin-1-yl)phenyl)-1*H*-imidazo[4,5-c]pyridine **(48a)** (132 mg, 0.5 mmol), sodium hydride **(40)** (42 mg, 1.05 mmol), methyl iodide (78 mg,0.55 mmol), dimethylsulfoxide (2 mL).

Yield: 100 mg, 72%.

A pale yellow solid. **HPLC**: R_t = 3.18 min. **^{1}H-NMR** (500 MHz, Chloroform-d): δ [ppm] = 8.40 (d, *J* = 8.9 Hz, 2H), 8.27 (s, 1H), 7.64 (d, *J* = 6.7 Hz, 1H), 7.50 (dd, *J* = 6.7, 1.5 Hz, 1H), 6.67 (d, *J* = 8.9 Hz, 2H), 4.14 (s, 3H), 3.43 – 3.37 (m, 4H), 2.07 – 2.03 (m, 4H). **^{13}C-NMR** (125 MHz, Chloroform-d): δ [ppm] = 174.09, 156.64, 149.26, 146.31, 130.15, 129.84, 128.30, 121.03, 111.48, 111.44, 47.55, 46.18, 25.50. **MS** (EI, 70 eV): *m/z* = 278 [M^+]. **UV/Vis** (Ethanol): λ_{max} = 403 nm.

5-Propyl-2-(4-(pyrrolidin-1-yl)phenyl)-5H-imidazo[4,5-c]pyridine 49b (BSc4888)

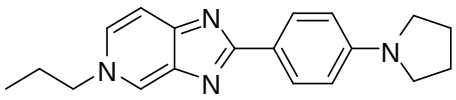

The title compound was synthesized by following the general procedure mentioned in **6.4.1.**

Reactants: 2-(4-(pyrrolidin-1-yl)phenyl)-1*H*-imidazo[4,5-c]pyridine **(48a)** (132 mg, 0.5 mmol), sodium hydride **(40)** (42 mg, 1.05 mmol), *n*-propyl bromide (50 µL, 0.55 mmol), dimethylsulfoxide (2 mL).

Yield: 102 mg, 67%.

A deep yellow solid. **HPLC**: R_t = 4.38 min. **^{1}H-NMR** (500 MHz, Chloroform-d): δ [ppm] = 8.40 (d, 2H), 8.34 (s, 1H), 7.66 (d, 1H), 7.52 (dd, *J* = 6.7, 1.4 Hz, 1H), 6.67 (d, 2H), 4.22 (t, *J* = 7.1 Hz, 2H), 3.46 – 3.34 (m, 4H), 2.06 – 2.02 (m, 4H), 2.02 – 1.96 (m, 2H), 0.99 (t, *J* = 7.4 Hz, 3H). **^{13}C-NMR** (125 MHz, Chloroform-d): δ [ppm] = 174.00, 156.84, 149.21, 146.11, 130.36, 129.82, 129.42, 127.65, 121.11, 111.42, 61.32, 47.54, 25.50, 24.93, 10.79. **MS** (EI, 70 eV): *m/z* = 306 [M^+]. **UV/Vis** (Ethanol): λ_{max} = 413 nm.

5-Isopropyl-2-(4-(pyrrolidin-1-yl)phenyl)-5*H*-imidazo[4,5-c]pyridine 49c (BSc4891)

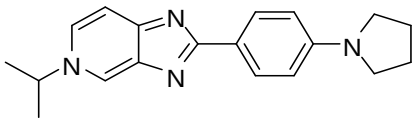

The title compound was synthesized by following the general procedure mentioned in **6.4.1.**

Reactants: 2-(4-(pyrrolidin-1-yl)phenyl)-1*H*-imidazo[4,5-c]pyridine **(48a)** (132 mg, 0.5 mmol), sodium hydride **(40)** (42 mg, 1.05 mmol), *i*-propyl iodide (55 μL, 0.55 mmol), dimethylsulfoxide (2 mL).

Yield: 110 mg, 72%.

A yellowish green solid. **HPLC**: R_t = 4.37 min. **^{1}H-NMR** (500 MHz, Chloroform-d): δ [ppm] = 8.44 (d, *J* = 1.5 Hz, 1H), 8.41 (d, *J* = 8.8 Hz, 2H), 7.66 (d, *J* = 6.8 Hz, 1H), 7.63 (dd, *J* = 6.8, 1.6 Hz, 1H), 6.68 (d, *J* = 8.8 Hz, 2H), 4.62 – 4.51 (m, 1H), 3.45 – 3.36 (m, 4H), 2.07 – 2.03 (m, 4H), 1.67 (d, *J* = 6.2 Hz, 6H). **^{13}C-NMR** (125 MHz, Chloroform-d): δ [ppm] = 170.53, 157.07, 149.22, 146.17, 129.81, 127.51, 125.23, 121.07, 111.59, 111.43, 61.23, 47.55, 25.50, 23.61. **MS** (EI, 70 eV): *m/z* = 306 [M^+]. **UV/Vis** (Ethanol): λ_{max} = 397 nm.

5-Butyl-2-(4-(pyrrolidin-1-yl)phenyl)-5*H*-imidazo[4,5-c]pyridine 49d (BSc4892)

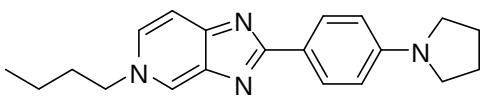

The title compound was synthesized by following the general procedure mentioned in **6.4.1.**

Reactants: 2-(4-(pyrrolidin-1-yl)phenyl)-1*H*-imidazo[4,5-c]pyridine **(48a)** (264 mg, 1.0 mmol), sodium hydride **(40)** (84 mg, 2.1 mmol), *n*-butyl iodide (125 μL, 1.1 mmol), dimethylsulfoxide (4 mL).

Yield: 240 mg, 75%.

A yellowish green solid. **HPLC**: R_t = 5.20 min. **^{1}H-NMR** (500 MHz, Chloroform-d): δ [ppm] = 8.39 (d, *J* = 5.7 Hz, 2H), 8.30 (d, *J* = 1.5 Hz, 1H), 7.64 (d, *J* = 6.7 Hz, 1H), 7.52 (dd, *J* = 6.7, 1.6 Hz, 1H), 6.67 (d, *J* = 5.7 Hz, 2H), 4.25 (t, *J* = 7.2 Hz, 2H), 3.42 – 3.37 (m, 4H), 2.07 – 2.02 (m, 4H), 1.98 – 1.89 (m, 2H), 1.43 – 1.33 (m, 2H), 0.98 (t, *J* = 7.4 Hz, 3H). **^{13}C-NMR** (125 MHz, Chloroform-d): δ [ppm] = 181.75, 174.07, 156.84, 149.19, 146.27, 129.79, 129.37, 127.56, 121.20, 111.42, 59.51, 47.54, 33.56, 25.50, 19.47, 13.45. **MS** (EI, 70 eV): *m/z* = 320 [M^+]. **UV/Vis** (Ethanol): λ_{max} = 406 nm.

***N,N*-Dimethyl-4-(5-methyl-5*H*-imidazo[4,5-c]pyridin-2-yl)aniline 49e (BSc4941)**

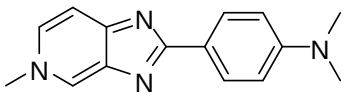

The title compound was synthesized by following the general procedure mentioned in **6.4.1.**

Reactants: 4-(1*H*-imidazo[4,5-c]pyridin-2-yl)-*N*,*N*-dimethylaniline **(48c)** (238 mg, 1.0 mmol), sodium hydride **(40)** (84 mg, 2.1 mmol), methyl iodide (68 µL, 1.1 mmol), dimethylsulfoxide (4 mL).

Yield: 181 mg, 72%.

A greenish-yellow solid. **HPLC**: R_t = 1.62 min. **^{1}H-NMR** (500 MHz, DMSO-d_6): δ [ppm] = 8.67 (s, 1H), 8.19 (d, *J* = 9.0 Hz, 2H), 7.92 (dd, *J* = 6.7, 1.6 Hz, 1H), 7.56 (d, *J* = 6.7 Hz, 1H), 6.78 (d, *J* = 9.0 Hz, 2H), 4.17 (s, 3H), 2.98 (s, 6H). **^{13}C-NMR** (125 MHz, DMSO-d_6): δ [ppm] = 172.36, 156.10, 151.52, 146.18, 131.63, 130.64, 129.27, 123.39, 112.08, 111.15, 45.88, 40.92. **UV/Vis** (Ethanol): λ_{max} = 392 nm.

(*E*)-N,N-Dimethyl-4-(2-(5-methyl-5*H*-imidazo[4,5-c]pyridin-2-yl)vinyl)aniline 49f (BSc4942)

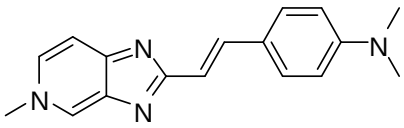

The title compound was synthesized by following the general procedure mentioned in **6.4.1.**

Reactants: (*E*)-4-(2-(1H-imidazo[4,5-c]pyridin-2-yl)vinyl)-*N*,*N*-dimethylaniline **(48b)** (264 mg, 1.0 mmol), sodium hydride **(40)** (84 mg, 2.1 mmol), methyl iodide (68 µL, 1.1 mmol), dimethylsulfoxide (4 mL).

Yield: 148 mg, 53%.

A yellowish orange solid. **^{1}H-NMR** (500 MHz, Methanol-d_4): δ [ppm] = 8.66 (d, *J* = 1.2 Hz, 1H), 8.04 (dd, *J* = 6.7, 1.5 Hz, 1H), 7.77 (d, *J* = 16.2 Hz, 1H), 7.66 (d, *J* = 6.7 Hz, 1H), 7.49 (d, *J* = 5.7 Hz, 2H), 7.02 (d, *J* = 16.2 Hz, 1H), 6.77 (d, *J* = 6.7 Hz, 2H), 4.27 (s, 3H), 3.02 (s, 6H). **^{13}C-NMR** (125 MHz, Methanol-d_4): δ [ppm] = 169.82, 153.41, 151.43, 143.34, 138.40, 133.31, 130.89, 128.40, 124.01, 114.12, 111.94, 110.72, 45.52, 39.04. **UV/Vis** (Ethanol): λ_{max} = 395 nm.

4-(5-Butyl-5H-imidazo[4,5-c]pyridin-2-yl)-N,N-dimethylaniline 49g (BSc4980)

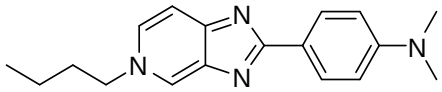

The title compound was synthesized by following the general procedure mentioned in **6.4.1.**

Reactants: 4-(1*H*-imidazo[4,5-c]pyridin-2-yl)-*N,N*-dimethylaniline **(48c)** (476 mg, 2.0 mmol), sodium hydride **(40)** (168 mg, 4.2 mmol), *n*-butyl iodide (250 μL, 2.2 mmol), dimethylsulfoxide (5 mL).

Yield: 299 mg, 51%.

A mustard yellow color solid. **^{1}H-NMR** (300 MHz, Chloroform-d): δ [ppm] = 8.40 (s, 1H), 8.35 (d, *J* = 8.92 Hz, 2H), 7.65 (d, *J* = 6.70 Hz, 1H), 7.56 (d, *J* = 6.73 Hz, 1H), 6.78 (d, *J* = 8.92 Hz, 2H), 4.24 (t, *J* = 7.19 Hz, 2H), 3.03 (s, 6H), 1.98 – 1.83 (m, 2H), 1.34 (q, *J* = 7.51 Hz, 2H), 0.94 (t, *J* = 7.35 Hz, 3H). **^{13}C-NMR** (75 MHz, Chloroform-d): δ [ppm] = 172.28, 155.92, 151.90, 144.95, 130.13, 129.74, 128.13, 120.88, 111.80, 111.74, 59.73, 33.55, 26.90, 19.45, 13.43. **UV/Vis** (Ethanol): λ_{max} = 416 nm.

(*E*)-4-(2-(5-Butyl-5*H*-imidazo[4,5-c]pyridin-2-yl)vinyl)-*N*,*N*-dimethylaniline 49h (BSc4981)

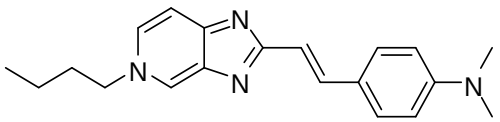

The title compound was synthesized by following the general procedure mentioned in **6.4.1.**

Reactants: (*E*)-4-(2-(1H-imidazo[4,5-c]pyridin-2-yl)vinyl)-*N,N*-dimethylaniline **(48b)** (50 mg, 0.19 mmol), sodium hydride **(40)** (16 mg, 0.4 mmol), *n*-butyl iodide (23 μL, 0.2 mmol), dimethylsulfoxide (1 mL).

Yield: 32 mg, 53%.

A brick red solid. **^{1}H-NMR** (300 MHz, Methanol-d_4): δ [ppm] = 8.75 (d, *J* = 1.41 Hz, 1H), 8.14 (dd, *J* = 6.79, 1.52 Hz, 1H), 7.78 (d, *J* = 16.18 Hz, 1H), 7.69 (d, *J* = 6.73 Hz, 1H), 7.50 (d, *J* = 8.85 Hz, 2H), 7.01 (d, *J* = 16.15 Hz, 1H), 6.76 (d, *J* = 8.87 Hz, 2H), 4.47 (t, *J* = 7.40 Hz, 2H), 3.01 (s, 6H), 2.09 – 1.87 (m, 2H), 1.45 – 1.35 (m, 2H), 1.00 (t, *J* = 7.36 Hz, 3H). **^{13}C NMR** (75 MHz, Methanol-d_4): δ [ppm] = 170.29, 154.24, 152.95, 144.26, 140.38, 134.36, 131.67, 129.96, 125.18, 114.72, 113.32, 112.19, 60.94, 40.43, 34.79, 20.52, 13.85. **UV/Vis** (Ethanol): λ_{max} = 397 nm.

6.5 Synthesis of imidazo[1,2-a]pyridine derivatives

Synthetic Scheme

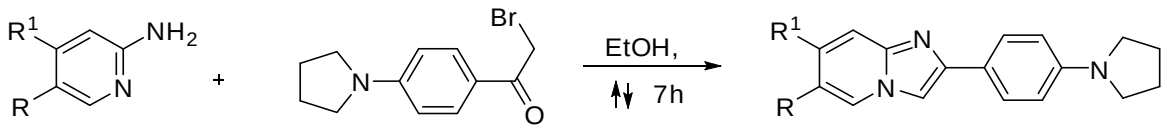

49a-b **50** **51a-b**

Compound	R	R^1
49a, 51a	CF_3	H
49b, 51b	H	Cl

6.5.1 General procedure for the synthesis of imidazo[1,2-a]pyridine derivatives

A mixture of aminopyridine (**49a-b)** (1.0 eq.) and 2-bromo-1-(4-(pyrrolidin-1-yl)phenyl) ethanone **(50)** (1.0 eq.) in ethanol were heated to reflux for 7 hours. The reaction mixture was then cooled to room temperature, neutralized with $NaHCO_3$, forming a precipitate. The solid was filtered off and washed with cold ethanol. The crude product is further purified by column chromatography on silica gel using cyclohexane and ethyl acetate mixture (8:2) as an eluent.

2-(4-(Pyrrolidin-1-yl)phenyl)-6-(trifluoromethyl)imidazo[1,2-a]pyridine 51a (BSc4698)

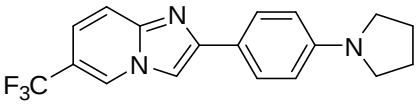

The title compound was synthesized by following the general procedure mentioned in **6.5.1.**

Reactants: 5-(trifluoromethyl)pyridin-2-amine **(49a)** (255 mg, 1.57 mmol), 2-bromo-1-(4-(pyrrolidin-1-yl)phenyl)ethanone **(50)** (421 mg, 1.57 mmol), Ethanol (10 mL)

Yield: 309 mg, 59%.

A yellowish white solid. **HPLC**: R_t = 5.72 min. **^{1}H-NMR** (500 MHz, DMSO-d_6): δ [ppm] = 9.13 (s, 1H), 8.29 (s, 1H), 7.80 (d, *J* = 8.9 Hz, 2H), 7.70 (d, *J* = 10.0 Hz, 1H), 7.42 (dd, *J* = 9.4, 1.9 Hz, 1H), 6.62 (d, *J* = 8.8 Hz, 2H), 3.31 – 3.27 (m, 4H), 2.01 – 1.95 (m, 4H). **MS** (EI, 70 eV): *m/z* = 331 [M^+]. **UV/Vis** (Ethanol): λ_{max} = 382 nm.

7-Chloro-2-(4-(pyrrolidin-1-yl)phenyl)imidazo[1,2-a]pyridine 51b (BSc4699)

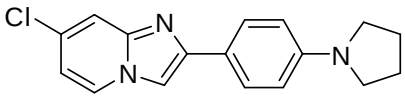

The title compound was synthesized by following the general procedure mentioned in **6.5.1.**

Reactants: 4-chloropyridin-2-amine **(49b)** (257 mg, 2.0 mmol), 2-bromo-1-(4-(pyrrolidin-1-yl)phenyl)ethanone **(50)** (536 mg, 2.0 mmol), Ethanol (10 mL)

Yield: 422 mg, 71%.

A gray solid. **HPLC:** R_t = 5.16 min. **^{1}H-NMR** (500 MHz, DMSO-d_6): δ [ppm] = 8.50 (dd, *J* = 7.2, 0.7 Hz, 1H), 8.20 (s, 1H), 7.78 – 7.74 (d, *J* = 8.8 Hz, 2H), 7.66 (d, *J* = 2.1 Hz, 1H), 6.92 (dd, *J* = 7.2, 2.1 Hz, 1H), 6.60 (d, *J* = 8.8 Hz, 2H), 3.30 – 3.24 (m, 4H), 2.01 – 1.93 (m, 4H). **MS** (EI, 70 eV): *m/z* = 297 [M^+]. **UV/Vis** (Ethanol): λ_{max} = 379 nm.

(*S*)-2-(4-(2-(Fluoromethyl)pyrrolidin-1-yl)phenyl)imidazo[1,2-a]pyridine 55 (BSc4762)

Synthetic Scheme:

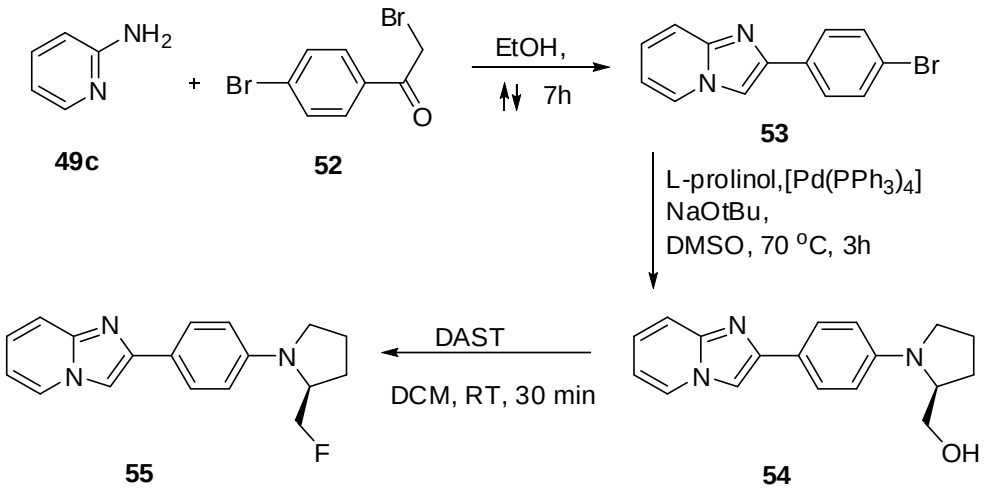

2-(4-Bromophenyl)imidazo[1,2-a]pyridine 53

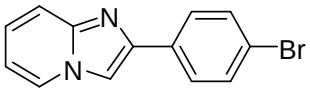

Pyridin-2-amine **(49c)** (1.0 gm, 0.01 mmol) and 2-bromo-1-(4-bromophenyl)ethanone **(52)** (2.95 gm, 0.01 mol) were added to ethanol (30 mL) and heated to reflux for overnight. The reaction mixture was cooled down, neutralized with $NaHCO_3$ solution and the precipitates were filtered off. The crude product is further purified by recrystallization from ethanol.

Yield: 2.61 gm, 90%.

A colorless solid. **HPLC:** R_t = 2.97 min. **^{1}H-NMR** (500 MHz, DMSO-d_6): δ [ppm] = 8.10 (dt, *J* = 6.8, 1.2 Hz, 1H), 7.86 – 7.82 (m, 2H), 7.81 (s, 1H), 7.62 (dt, *J* = 6.1, 3.1 Hz, 1H), 7.59 – 7.56 (m, 1H), 7.55 – 7.53 (m, 1H), 7.18 (ddd, *J* = 9.1, 6.8, 1.3 Hz, 1H), 6.79 (td, *J* = 6.8, 1.1 Hz, 1H). **^{13}C-NMR** (75 MHz, DMSO-d_6): δ [ppm] = 145.76, 144.74, 132.80, 131.84, 127.57, 125.62, 124.92, 121.88, 117.61, 112.62, 108.21. **MS** (EI, 70 eV): *m/z* = 273 [M^+].

(*S*)-(1-(4-(Imidazo[1,2-a]pyridin-2-yl)phenyl)pyrrolidin-2-yl)methanol 54 (BSc4546)

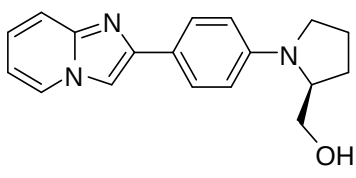

A mixture of 2-(4-bromophenyl)imidazo[1,2-a]pyridine **(53)** (400 mg, 1.46 mmol), (*S*)-pyrrolidin-2-ylmethanol (428 µL, 4.39 mmol), sodium *tert*-butoxide (422 mg, 4.392 mmol), 2,2'-bis(diphenylphosphino)-1,1'-binaphthyl (BINAP) (108 mg, 0.174 mmol) and $Pd_2(dba)_3$ (67 mg, 0.05 mmol) in DMSO (6 mL) was heated under argon at 70 °C for 3 hours. After cooling to room temperature, water was added to the reaction mixture and extracted into ethyl acetate. Ethyl acetate layers were washed with water and brine, the organic fraction was dried with sodium sulfate, and concentrated using rotary evaporator. The crude material was purified by flash chromatography on silica gel using hexane and ethyl acetate mixture (7:3) as eluent.

Yield: 107 mg, 25%.

A colorless solid. **HPLC**: R_t = 2.21 min. **^{1}H-NMR** (300 MHz, DMSO-d_6): δ [ppm] = 8.44 (dd, *J* = 4.4, 3.4 Hz, 1H), 8.15 (s, 1H), 7.73 (d, *J* = 8.8 Hz, 2H), 7.49 (d, *J* = 9.0 Hz, 1H), 7.17 (ddd, *J* = 9.0, 6.7, 1.2 Hz, 1H), 6.82 (td, *J* = 6.7, 1.1 Hz, 1H), 6.66 (d, *J* = 8.8 Hz, 2H), 4.77 (dd, *J* = 6.2, 5.2 Hz, 1H), 3.72 (t, *J* = 6.2 Hz, 1H), 3.58 – 3.46 (m, 1H), 3.28 – 3.14 (m, 2H), 3.08 (dd, *J* = 16.7, 8.0 Hz, 1H), 2.14 – 1.79 (m, 4H). **^{13}C-NMR** (125 MHz, DMSO-d_6): δ [ppm] = 147.57, 145.94, 145.09, 127.08, 126.85, 124.58, 121.59, 116.50, 112.23, 112.16, 107.28, 61.60, 60.64, 48.63, 28.42, 23.18. **MS** (EI, 70 eV): *m/z* = 293 [M^+]. **UV/Vis** (Ethanol): λ_{max} = 360 nm.

(*S*)-2-(4-(2-(Fluoromethyl)pyrrolidin-1-yl)phenyl)imidazo[1,2-a]pyridine 55 (BSc4762)

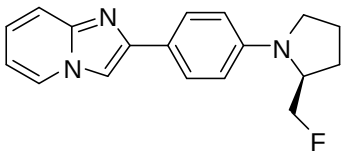

To a solution of the hydroxyl compound **(54)** (100 mg, 0.34 mmol) in dry dichloromethane was slowly added a solution of dimethylaminosulfur trifluoride (DAST) (82.4 mg, 0.51 mmol) in dry dichloromethane (10 mL) at -78 °C. The solution was slowly brought to room temperature and stirred for 30 min. The reaction mixture was poured into a beaker containing ice to decompose any unreacted DAST and extracted with dichloromethane. The organic phases were dried and evaporated and the residue was chromatographed on silica gel using hexane and ethylacetate mixture (9:1) as eluent.

Yield: 20 mg, 20%.

A light pink solid. **HPLC**: R_t = 4.82 min. **^{1}H-NMR** (300 MHz, Chloroform-d): δ [ppm] = 8.12 (d, *J* = 6.7 Hz, 1H), 7.87 (d, *J* = 8.8 Hz, 2H), 7.76 (s, 1H), 7.68 (s, 1H), 7.19 (t, *J* = 7.8 Hz, 1H), 6.80 (t, *J* = 6.3 Hz, 1H), 6.74 (d, *J* = 8.8 Hz, 2H), 4.53 (ddd, *J* = 46.8, 9.2, 3.8 Hz, 1H), 4.32 (ddd, *J* = 47.6, 9.2, 7.6 Hz, 1H), 4.14 – 4.05 (m, 1H), 3.59 – 3.51 (m, 1H), 3.25 (dd, *J* = 15.0, 8.0 Hz, 1H), 2.10 (qd, *J* = 14.0, 8.3 Hz, 4H). **^{13}C-NMR** (125 MHz, Acetone-d_6): δ [ppm] = 147.34, 146.28, 145.29, 126.92, 126.12, 123.75, 122.69, 116.50, 112.07, 111.54, 106.63, 82.84 (*J* = 172.64 Hz), 57.91, 57.73, 48.51, 27.78 (*J* = 2 Hz), 23.09. **MS** (EI, 70 eV): *m/z* = 295 [M^+]. **UV/Vis** (Ethanol): λ_{max} = 345 nm.

6.6. Synthesis of 9-methyl-3,6-distyryl-9*H*-carbazole derivatives

Synthetic scheme

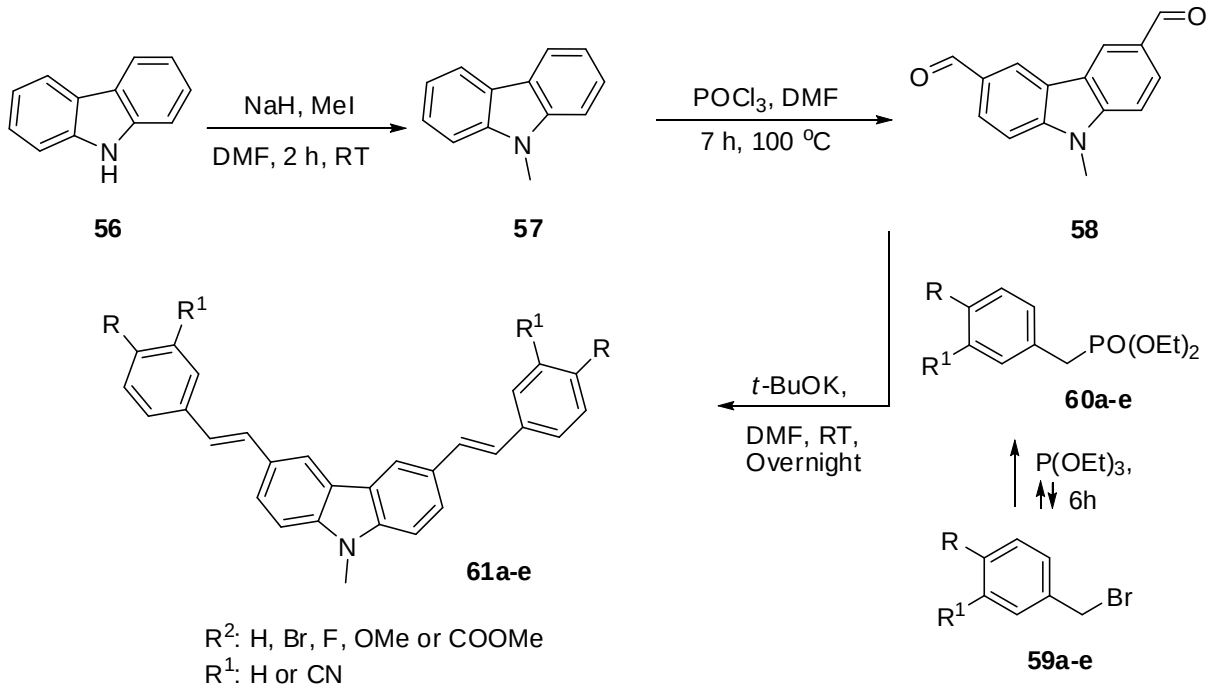

Compound	R	R^1
59a, 60a, 61a	H	CN
59b, 60b, 61b	OCH_3	H
59c, 60c, 61c	Br	H
59d, 60d, 61d	$COOCH_3$	H
59e, 60e, 61e	F	H

9-Methyl-9*H*-carbazole 57

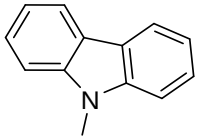

To a suspension of sodium hydride (2.39 gm, 0.059 mmol) in dry DMF (20 mL) was added carbazole **(56)** (10 gm, 0.059 mmol) and after stirring at room temperature for 10 min, a mixture of methyl iodide (3.75 mL, 0.060 mmol) in DMF (5 mL) was added drop wise. After 1 hour additional stirring, the mixture was diluted with ice water and extracted three times with ethylacetate. The extracts were combined; dried and the solvents evoparated to afford the product which was purified by recrystallization from ethanol.

Yield: 8.56 gm, 79%

A colorless solid. **HPLC**: R_t = 7.96 min. **^{1}H-NMR** (300 MHz, DMSO-d_6): δ [ppm] = 8.18 – 8.11 (d, 2H), 7.58 (dd, *J* = 8.2, 0.7 Hz, 2H), 7.46 (ddd, *J* = 8.3, 5.9, 1.2 Hz, 2H), 7.20 (ddd, *J* = 8.0, 7.1, 1.0 Hz, 2H), 3.86 (s, 3H). **^{13}C NMR** (75 MHz, DMSO-d_6): δ [ppm] = 141.03, 126.12, 122.39, 120.63, 119.13, 109.53, 29.38.

9-Methyl-9*H*-carbazole-3,6-dicarbaldehyde 58

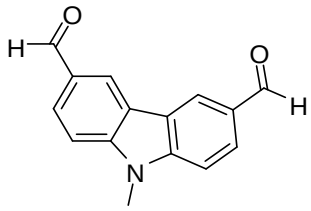

Phosphorous oxy chloride (30 mL, 0.331 mmol) was added to a solution of dry DMF (32 mL, 0.44 mmol) at 0-5 ^oC and stirred for 30 min under an argon atmosphere. To this mixture, a solution of 9-methyl-9H-carbazole **(57)** (2.0 gm, 0.011 mmol) in DMF (10 mL, 0.11 mmol) added drop wise and the reaction slowly heated up to 80 ^oC and stirred for 8 hours. The mixture was poured into crushed ice, stirred for 5 min, neutralized with $NaHCO_3$ solution, extracted with ethyl acetate washed with water, dried and solvent removed *in vacuo*. Further purification of the crude product was performed by column chromatography on silica gel using cyclohexane and ethylacetate mixture (7:3) as eluent.

Yield: 1.2 gm, 46%.

A pale yellow solid. **HPLC**: R_t = 6.16 min. **^{1}H-NMR** (300 MHz, Chloroform-d): δ [ppm] = 10.13 (s, 2H), 8.64 (d, 2H), 8.09 (dd, *J* = 8.5, 1.6 Hz, 2H), 7.54 (d, *J* = 8.5 Hz, 2H), 3.95 (s, 3H). **^{13}C-NMR** (75 MHz, Chloroform-d): δ [ppm] = 191.44, 145.23, 129.74, 127.96, 124.04, 123.08, 109.54, 29.78.

6.6.1 General procedure for the synthesis phosphonate esters.

A mixture of triethyl phosphite (3.0 eq.) and corresponding alkyl bromide **(59a-e)** (1.0 eq.) was refluxed at 160 ^oC for 6 hours. The reaction mixture was distilled under reduced pressure to remove unreacted triethyl phosphite, which results the desired products.

Diethyl 3-cyanobenzylphosphonate 60a

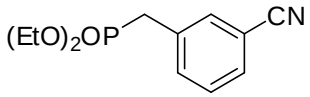

The title compound was synthesized by following the general procedure mentioned in **6.6.1.**

Reactants: 3-(bromomethyl)benzonitrile **(59a)** (1.0 gm, 0.0051 mmol), Triethyl phosphite (2.6 mL, 0.0153 mmol)

Yield: 1.2 gm, 98%.

A colorless liquid. **^{1}H-NMR** (300 MHz, DMSO-d_6): δ [ppm] = 7.76 – 7.68 (m, 2H), 7.62 (dd, *J* = 5.8, 4.2 Hz, 1H), 7.54 (dd, *J* = 11.7, 4.3 Hz, 1H), 3.96 (dq, *J* = 8.3, 7.0 Hz, 4H), 3.41 (d, *J* = 18.8 Hz, 2H), 1.16 (t, *J* = 7.1 Hz, 6H). **^{31}P-NMR** (121 MHz, Chloroform-d): 24.58 min. **MS** (EI, 70 eV): *m/z* = 253 [M^+].

Diethyl 4-methoxybenzylphosphonate 60b

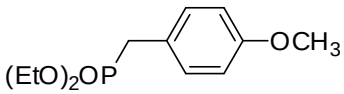

The title compound was synthesized by following the general procedure mentioned in **6.6.1.**

Reactants: 1-(bromomethyl)-4-methoxybenzene **(59b)** (0.7 mL, 0.005 mmol), Triethyl phosphite (2.6 mL, 0.015 mmol)

Yield: 1.25 mg, 98%.

A colorless liquid. **^{1}H-NMR** (300 MHz, Chloroform-d): δ [ppm] =7.21 (dt, *J* = 8.1, 5.6 Hz, 1H), 6.91 – 6.82 (m, 2H), 6.81 – 6.74 (m, 1H), 4.15 – 3.89 (m, 4H), 3.78 (s, 3H), 3.11 (d, *J* = 21.7 Hz, 2H), 1.37 – 1.11 (m, 6H).

Diethyl 4-bromobenzylphosphonate 60c

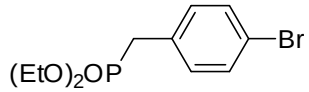

The title compound was synthesized by following the general procedure mentioned in **6.6.1.**

Reactants: 1-bromo-4-(bromomethyl)benzene **(59c)** (1.0 gm, 0.004 mmol), Triethyl phosphite (2.05 mL, 0.012 mmol)

Yield: 1.2 gm, 98%.

A colorless liquid. **^{1}H-NMR** (300 MHz, Chloroform-d): δ [ppm] = 7.33 (dd, *J* = 8.5, 1.0 Hz, 2H), 7.09 (dd, *J* = 8.6, 2.5 Hz, 2H), 4.00 – 3.87 (m, 4H), 3.00 (d, *J* = 21.7 Hz, 2H), 1.16 (td, *J* = 7.1, 0.3 Hz, 6H).

Methyl 4-((diethoxyphosphoryl)methyl)benzoate 60d

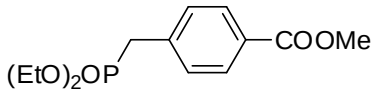

The title compound was synthesized by following the general procedure mentioned in **6.6.1.**

Reactants: Methyl 4-(bromomethyl)benzoate **(59d)** (500 mg, 2.18 mmol), Triethyl phosphite (1.12 mL, 6.54 mol)

Yield: 580 mg, 93%.

A colorless liquid. **^{1}H-NMR** (300 MHz, Chloroform-d): δ [ppm] = 7.95 (d, *J* = 7.8 Hz, 2H), 7.34 (dd, *J* = 8.4, 2.4 Hz, 2H), 4.04 – 3.92 (m, 4H), 3.87 (s, 3H), 3.17 (d, *J* = 22.1 Hz, 2H), 1.21 (t, *J* = 7.1 Hz, 6H).

Diethyl 4-fluorobenzylphosphonate 60e

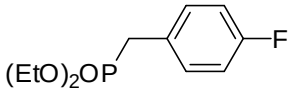

The title compound was synthesized by following the general procedure mentioned in **6.6.1.**

Reactants: methyl 1-(bromomethyl)-4-fluorobenzene **(59d)** (500 mg, 2.64 mmol), Triethyl phosphite (1.36 mL, 7.92 mmol)

Yield: 617 mg, 95%.

A colorless liquid. **^{1}H-NMR** (300 MHz, Chloroform-d): δ [ppm] = 7.23 (ddq, *J* = 11.1, 5.6, 2.8 Hz, 2H), 7.01 – 6.92 (m, 2H), 4.08 – 3.88 (m, 4H), 3.08 (d, *J* = 21.4 Hz, 2H), 1.27 – 1.16 (m, 6H).

6.6.2 General procedure for the synthesis of 9-methyl-3,6-distyryl-9H-carbazole derivatives.

To a solution of potassium *tert*-butoxide (4.0 eq.) in DMF (5 mL) was added the corresponding phosphonate salt (2.0 eq.) at 0 ^{o}C and stirred for 30 min. A solution of aldehyde (1.0 eq.) in DMF was added to the reaction mixture slowly and stirred for overnight at room temperature. Water was added to the reaction and the formed precipitate was filtered, dried, the residue was purified by washing with methanol (10 mL). Further purification (for **61a, 61b**) was performed by column chromatography on silica gel using cyclohexane and dichloromethane mixture (1:1) as eluent.

3,3'-(1*E*,1'*E*)-2,2'-(9-Methyl-9*H*-carbazole-3,6-diyl)bis(ethene-2,1-diyl)dibenzo nitrile 61a (BSc4494)

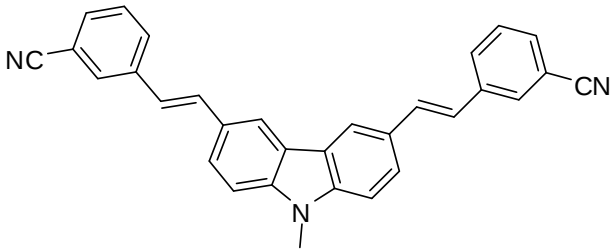

The title compound was synthesized by following the general procedure mentioned in **6.6.2.**

Reactants: 9-methyl-9*H*-carbazole-3,6-dicarbaldehyde **(58)** (200 mg, 0.84 mmol), diethyl 3-cyanobenzylphosphonate **(60a)** (426 mg, 1.68 mmol), potassium *tert*-butoxide (377.2 mg, 3.36 mmol)

Yield: 238 mg, 65%.

The titled compound synthesized using starting materials (**53a)** and (**52)**. Pale yellow solid. **HPLC**: R_t = 10.20 min. **^{1}H-NMR** (500 MHz, DMSO-d_6): δ [ppm] = 8.44 (s, 2H), 8.11 (s, 2H), 7.96 (d, *J* = 7.9 Hz, 2H), 7.81 (dd, *J* = 8.6, 1.5 Hz, 2H), 7.70 (d, *J* = 7.7 Hz, 2H), 7.68 – 7.59 (m, 6H), 7.34 (d, *J* = 16.4 Hz, 2H), 3.93 (s, 3H). **^{13}C-NMR** (125 MHz, DMSO-d_6): δ [ppm] = 141.64, 139.54, 132.48, 131.16, 130.66, 130.41, 129.79, 128.48, 125.69, 124.08, 122.87, 119.37, 112.36, 110.30, 99.99, 29.77. **MS** (EI, 70 eV): *m/z* = 435 [M^+]. **UV/Vis** (Ethanol): λ_{max} = 319 nm.

3,6-Bis(4-methoxystyryl)-9-methyl-9*H*-carbazole 61b (BSc4495)

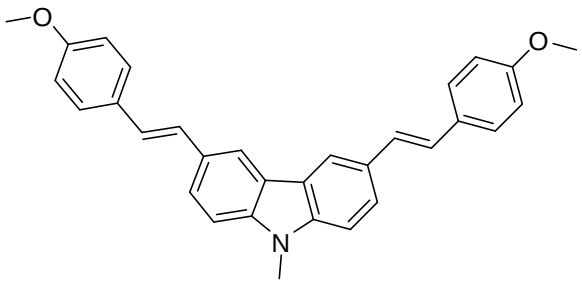

The title compound was synthesized by following the general procedure mentioned in **6.6.2.**

Reactants: 9-methyl-9*H*-carbazole-3,6-dicarbaldehyde **(58)** (100 mg, 0.42 mmol), diethyl 4-methoxybenzylphosphonate **(60b)** (217 mg, 0.84 mmol), potassium *tert*-butoxide (188 mg, 1.68 mmol)

Yield: 131 mg, 70%.

A white solid. **HPLC**: R_t = 10.76 min. **^{1}H-NMR** (500 MHz, DMSO-d_6): δ [ppm] = 8.45 (s, 2H), 7.77 (dd, *J* = 8.5, 1.5 Hz, 2H), 7.61 (d, *J* = 8.5 Hz, 2H), 7.45 (d, *J* = 16.4 Hz, 2H), 7.31 (t, *J* = 7.8 Hz, 2H), 7.27 (d, *J* = 16.4 Hz, 2H), 7.21 (d, *J* = 7.7 Hz, 4H), 6.84 (dd, *J* = 8.1, 1.7 Hz, 2H), 3.91 (s, 3H), 3.83 (s, 6H). **MS** (EI, 70 eV): *m/z* = 445 [M^+]. **UV/Vis** (Ethanol): λ_{max} = 350 nm.

3,6-Bis(4-bromostyryl)-9-methyl-9*H*-carbazole 61c (BSc4497)

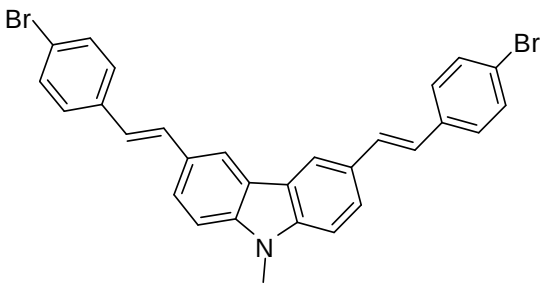

The title compound was synthesized by following the general procedure mentioned in **6.6.2.**

Reactants: 9-methyl-9*H*-carbazole-3,6-dicarbaldehyde **(58)** (100 mg, 0.42 mmol), diethyl 4-bromobenzylphosphonate **(60c)** (307 mg, 0.84 mmol), potassium *tert*-butoxide (188 mg, 1.68 mmol)

Yield: 206 mg, 90%.

A colorless solid. **HPLC**: R_t = 11.40 min. **^{1}H-NMR** (500 MHz, Chloroform-d): δ [ppm] = 8.27 (s, 2H), 7.71 (dd, *J* = 8.5, 1.6 Hz, 2H), 7.52 (d, 8.5 Hz, 4H), 7.45 (d, 8.5 Hz, 4H), 7.41 (d, *J* = 8.5 Hz, 2H), 7.33 (d, *J* = 16.3 Hz, 2H), 7.12 (d, *J* = 16.3 Hz, 2H), 3.90 (s, 3H). **MS** (EI, 70 eV): *m/z* = 543 [M^+]. **UV/Vis** (Ethanol): λ_{max} = 357 nm.

3,6-Bis(4-fluorostyryl)-9-methyl-9*H*-carbazole 61d (BSc4498)

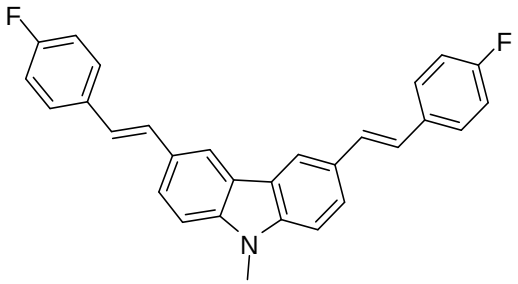

The title compound was synthesized by following the general procedure mentioned in **6.6.2.**

Reactants: 9-methyl-9*H*-carbazole-3,6-dicarbaldehyde **(58)** (150 mg, 0.63 mmol), diethyl 4-fluorobenzylphosphonate **(60d)** (310 mg, 1.26 mmol), potassium *tert*-butoxide (283 mg, 2.52 mmol)

Yield: 213 mg, 80%.

A colorless solid. **HPLC**: R_t = 10.90 min. **^{1}H-NMR** (500 MHz, Chloroform-d): δ [ppm] = 8.27 (d, *J* = 1.6 Hz, 1H), 7.70 (dd, *J* = 8.5, 1.7 Hz, 1H), 7.58 – 7.52 (m, 2H), 7.41 (d, *J* = 8.5 Hz, 1H), 7.26 (d, *J* = 16.4 Hz, 1H), 7.15 (d, *J* = 16.3 Hz, 1H), 7.12 – 7.08 (m, 2H), 3.90 (s, 1H). **MS** (EI, 70 eV): *m/z* = 421 [M^+]. **UV/Vis** (DMSO): λ_{max} = 385 nm.

Dimethyl 4,4'-(1*E*,1'*E*)-2,2'-(9-methyl-9*H*-carbazole-3,6-diyl)bis(ethene-2,1 diyl) dibenzoate 61e (BSc4499)

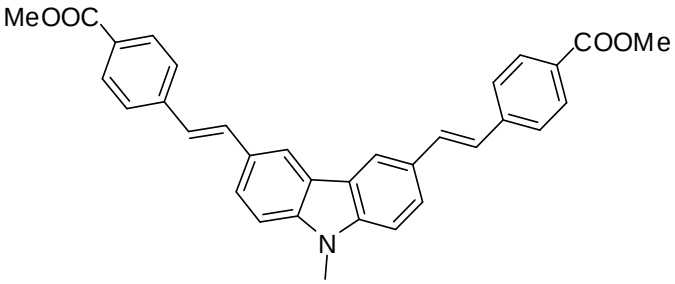

The title compound was synthesized by following the general procedure mentioned in **6.6.2.**

Reactants: 9-methyl-9*H*-carbazole-3,6-dicarbaldehyde **(58)** (75 mg, 0.32 mmol), methyl 4-((diethoxyphosphoryl)methyl)benzoate **(60e)** (181 mg, 0.63 mmol), potassium *tert*-butoxide (143 mg, 1.26 mmol)

Yield: 120 mg, 76%.

A colorless solid. **^{1}H-NMR** (300 MHz, DMSO-d_6): δ [ppm] = 8.30 (d, *J* = 1.5 Hz, 1H), 8.07 (d, 2H), 7.73 (dd, *J* = 8.6, 1.6 Hz, 1H), 7.63 (d, *J* = 8.3 Hz, 2H), 7.46 (d, *J* = 14.8 Hz, 1H), 7.42 (d, *J* = 7.1 Hz, 1H), 7.21 (d, *J* = 16.3 Hz, 1H), 3.95 (s, 3H), 3.90 (s, 2H). **MS** (EI, 70 eV): *m/z* = 501 [M^+].

6.7 Synthesis of 2-cyano biphenyl derivatives

Synthetic scheme

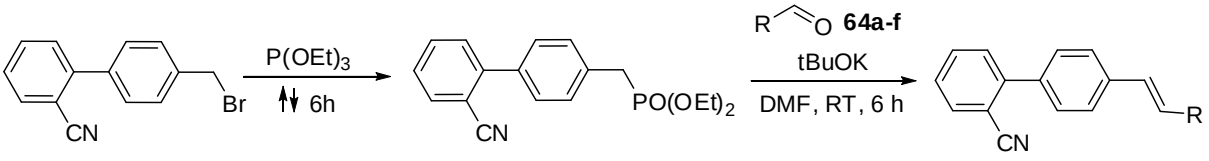

62 **63** **65a-f**

Compound	R
64a, 65a	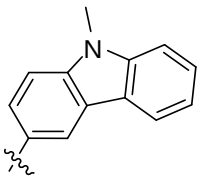

64b, 65b 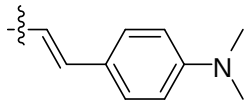

64c, 65c 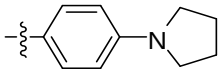

64d, 65d 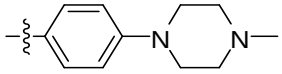

64e, 65e 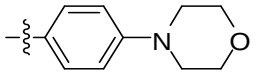

64f, 65f 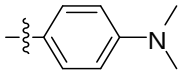

6.7.1. General procedure for the synthesis of 2-cyano biphenyl compounds

To a solution of potassium *tert*-butoxide (3.0 eq.) in DMF was added diethyl (2'-cyanobiphenyl-4-yl)methylphosphonate **63** (1.0 eq.) at 0 ^{o}C and stirred for 30 min. A solution of corresponding aldehyde in DMF was added to the reaction mixture slowly and stirred reaction for overnight at room temperature. Dilute HCl and water was added to the reaction and the reaction mixture is extracted into ethyl acetate, the ethyl acetate layers were combined and washed with water, dried, evaporated and the residue was purified by column chromatography on silica gel (eluents: cyclohexane and dichloromethane mixture (1:1) for **65a**, **65b**, **65c, 65f**; dichloromethane and methanol (9:1) for **65d**, **65e**).

(*E*)-4'-(2-(9-Methyl-9*H*-carbazol-3-yl)vinyl)biphenyl-2-carbonitrile 65a (BSc4490)

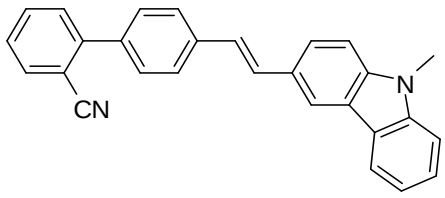

The title compound was synthesized by following the general procedure mentioned in **6.7.1.**

Reactants: Diethyl (2'-cyanobiphenyl-4-yl)methylphosphonate **(63)** (800 mg, 2.42 mmol), 9-methyl-9*H*-carbazole-3-carbaldehyde **(64a)** (508 mg, 2.42 mmol), *t*-BuOK (814 mg, 7.26 mmol), DMF (6 mL).

Yield: 644 mg, 69%.

A greenish white solid. **HPLC**: R_t = 10.01 min. **^{1}H-NMR** (300 MHz, Chloroform-d): δ [ppm] = 8.26 (s, 1H), 8.16 (d, *J* = 7.7 Hz, 1H), 7.79 (d, *J* = 7.7 Hz, 1H), 7.71 (dd, *J* = 14.5, 4.9 Hz, 4H), 7.61 (dd, *J* = 11.7, 3.4 Hz, 3H), 7.56 – 7.46 (m, 2H), 7.45 – 7.37 (m, 4H), 7.20 (d, *J* = 16.3 Hz, 1H), 3.86 (s, 3H). **MS** (EI, 70 eV): *m/z* = 384 [M^+]. **UV/Vis** (Ethanol): λ_{max} = 346 nm.

4'-((1*E*,3*E*)-4-(4-(Dimethylamino)phenyl)buta-1,3-dienyl)biphenyl-2-carbonitrile 65b (BSc4491)

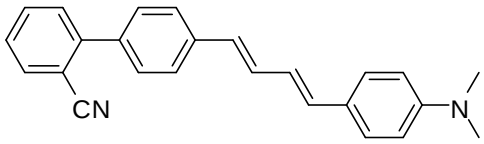

The title compound was synthesized by following the general procedure mentioned in **6.7.1.**

Reactants: Diethyl (2'-cyanobiphenyl-4-yl)methylphosphonate **(63)** (300 mg, 0.91 mmol), (*E*)-3-(4-(dimethylamino)phenyl)acrylaldehyde **(64b)** (159 mg, 0.91 mmol), potassium *tert*-butoxide (306 mg, 2.73 mmol), DMF (6 mL).

Yield: 191 mg, 60%.

A greenish yellow solid. **HPLC**: R_t = 6.66 min. **^{1}H-NMR** (300 MHz, Chloroform-d): δ [ppm] = 7.77 (dd, *J* = 7.7, 0.9 Hz, 1H), 7.69 – 7.61 (m, 1H), 7.56 – 7.51 (m, 5H), 7.47 – 7.35 (m, 3H), 7.03 (dd, *J* = 15.4, 10.3 Hz, 1H), 6.83 (dd, *J* = 15.2, 10.4 Hz, 1H), 6.74 – 6.59 (m, 4H), 3.00 (s, 6H). **MS** (EI, 70 eV): *m/z* = 350 [M^+]. **UV/Vis** (Ethanol): λ_{max} = 388 nm.

(*E*)-4'-(4-(Pyrrolidin-1-yl)styryl)biphenyl-2-carbonitrile 65c (BSc4542)

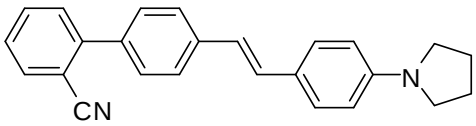

The title compound was synthesized by following the general procedure mentioned in **6.7.1.**

Reactants: Diethyl (2'-cyanobiphenyl-4-yl)methylphosphonate **(63)** (329 mg, 1.0 mmol), 4-(pyrrolidin-1-yl)benzaldehyde **(64c)** (175 mg, 1.0 mmol), potassium *tert*-butoxide (336 mg, 3.0 mmol), DMF (4 mL).

Yield: 245 mg, 70%.

A yellow solid. **HPLC**: R_t = 8.96 min. **^{1}H-NMR** (300 MHz, Chloroform-d): δ [ppm] = 7.77 (dd, *J* = 7.7, 1.0 Hz, 1H), 7.68 – 7.52 (m, 6H), 7.48 – 7.39 (m, 3H), 7.14 (d, *J* = 16.2 Hz, 1H), 6.94 (d, *J* = 16.3 Hz, 1H), 6.59 (d, *J* = 8.6 Hz, 2H), 3.35 (t, *J* = 6.6 Hz, 4H), 2.11 – 1.95 (m, 4H). **MS** (EI, 70 eV): *m/z* = 350 [M^+]. **UV/Vis** (Ethanol): λ_{max} = 379 nm.

(*E*)-4'-(4-(4-Methylpiperazin-1-yl)styryl)biphenyl-2-carbonitrile 65d (BSc4543)

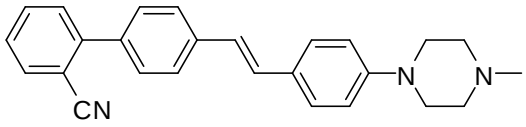

The title compound was synthesized by following the general procedure mentioned in **6.7.1.**

Reactants: Diethyl (2'-cyanobiphenyl-4-yl)methylphosphonate **(63)** (329 mg, 1.0 mmol), 4-(4-methylpiperazin-1-yl)benzaldehyde **(64d)** (204 mg, 1.0 mmol), potassium *tert*-butoxide (336 mg, 3.0 mmol), DMF (4 mL).

Yield: 265 mg, 70%.

A pale yellow solid. **^{1}H-NMR** (300 MHz, Chloroform-d): δ [ppm] = 7.78 (ddd, *J* = 7.7, 1.3, 0.5 Hz, 1H), 7.70 – 7.61 (m, 2H), 7.60 (d, *J* = 2.2 Hz, 1H), 7.58 – 7.53 (m, 3H), 7.47 (d, *J* = 4.4 Hz, 1H), 7.46 – 7.40 (m, 2H), 7.14 (d, *J* = 16.3 Hz, 1H), 7.01 (d, *J* = 16.3 Hz, 1H), 6.94 (t, *J* = 5.8 Hz, 2H), 3.32 – 3.24 (m, 4H), 2.64 – 2.57 (m, 4H), 2.38 (s, 3H). **MS** (EI, 70 eV): *m/z* = 379 [M^+]. **UV/Vis** (Ethanol): λ_{max} = 357 nm.

(*E*)-4'-(4-Morpholinostyryl)biphenyl-2-carbonitrile 65e (BSc4544)

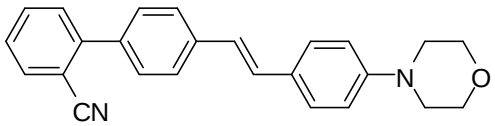

The title compound was synthesized by following the general procedure mentioned in **6.7.1.**

Reactants: Diethyl (2'-cyanobiphenyl-4-yl)methylphosphonate **(63)** (329 mg, 1.0 mmol), 4-morpholinobenzaldehyde **(64e)** (191 mg, 1.0 mmol), potassium *tert*-butoxide (336 mg, 3.0 mmol), DMF (4 mL).

Yield: 264 mg, 72%.

A greenish white solid. **HPLC**: R_t = 8.15 min. **^{1}H-NMR** (300 MHz, Chloroform-d): δ [ppm] = 7.84 – 7.74 (m, 1H), 7.71 – 7.39 (m, 9H), 7.14 (d, *J* = 16.3 Hz, 1H), 7.02 (d,

J = 16.3 Hz, 1H), 6.93 (d, *J* = 8.6 Hz, 2H), 3.96 – 3.82 (m, 4H), 3.33 – 3.12 (m, 4H). **MS** (EI, 70 eV): *m/z* = 366 [M^+]. **UV/Vis** (Ethanol): λ_{max} = 353 nm.

(*E*)-4'-(4-(Dimethylamino)styryl)biphenyl-2-carbonitrile 65f (BSc4690)

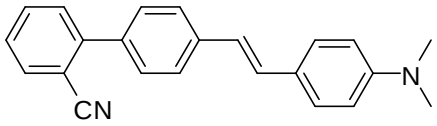

The title compound was synthesized by following the general procedure mentioned in **6.7.1.**

Reactants: Diethyl (2'-cyanobiphenyl-4-yl)methylphosphonate **(63)** (329 mg, 1.0 mmol), 4-(dimethylamino)benzaldehyde **(64f)** (149 mg, 1.0 mmol), potassium *tert*-butoxide (336 mg, 3.0 mmol), DMF (4 mL).

Yield: 230 mg, 71%.

A greenish yellow solid. **^{1}H-NMR** (300 MHz, Chloroform-d): δ [ppm] = 7.81 – 7.73 (m, 1H), 7.69 – 7.52 (m, 6H), 7.49 – 7.38 (m, 3H), 7.14 (d, *J* = 16.25 Hz, 1H), 6.97 (d, *J* = 16.25 Hz, 1H), 6.74 (d, *J* = 8.82 Hz, 2H), 3.01 (s, 6H). **^{13}C-NMR** (75 MHz, Chloroform-d): δ [ppm] = 150.28, 145.26, 138.75, 136.11, 133.84, 132.78, 129.92, 129.89, 128.99, 127.76, 127.30, 126.26, 125.47, 123.40, 118.89, 112.39, 111.01, 40.45. **UV/Vis** (Ethanol): λ_{max} = 372 nm.

6.8 Synthesis of bis styryl derivatives

6.8.1 Phenylene vinylene compounds

Synthetic scheme

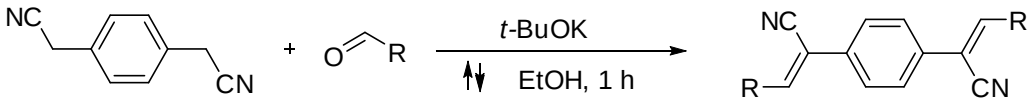

66 **67a, 64d, 64f** **68a-c**

Compound	R
64f, 68a	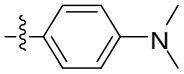
67a, 68b	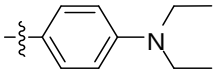
64d, 68c	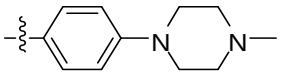

6.8.1.1 General procedure for the synthesis phenylene vinylene compounds.

Potassium *tert*-butoxide (3.0 eq.) was added to a solution of 1,4-phenylenediacetonitrile **(66)** (1.0 eq.) and corresponding aldehyde (2.0 eq.) in ethanol. The resulting solution was refluxed for 8 hours under argon atmosphere. A precipitate formed upon cooling to room temperature. It was filtered and purified by column chromatography on silica gel (eluents: cyclohexane and ethyl acetate mixture (9:1) for **68a** and **68b**; dichloromethane and methanol (9:1) for **68c**).

(2*Z*,2'*Z*)-2,2'-(1,4-Phenylene)bis(3-(4-(dimethylamino)phenyl)acrylonitrile) 68a (BSc4691)

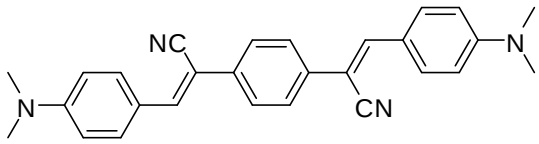

The title compound was synthesized by following the general procedure mentioned in **6.8.1.1.**

Reactants: 2,2'-(1,4-phenylene)diacetonitrile **(66)** (156 mg, 1.0 mmol), 4-(dimethylamino) benzaldehyde **(64f)** (298 mg, 2.0 mmol), potassium *tert*-butoxide (336 mg, 3.0 mmol), Ethanol (10 mL).

Yield: 138 mg, 33%.

An orange solid. **HPLC**: R_t = 9.90 min. **^{1}H-NMR** (300 MHz, Chloroform-d): δ [ppm] = 7.90 (d, *J* = 8.9 Hz, 4H), 7.68 (s, 4H), 7.46 (s, 2H), 6.77 (d, *J* = 8.9 Hz, 4H), 3.09 (s, 12H). **MS** (EI, 70 eV): *m/z* = 418 [M^+]. **UV/Vis** (Ethanol): λ_{max} = 423 nm.

(2*Z*,2'*Z*)-2,2'-(1,4-Phenylene)bis(3-(4-(diethylamino)phenyl)acrylonitrile) 68b (BSc4692)

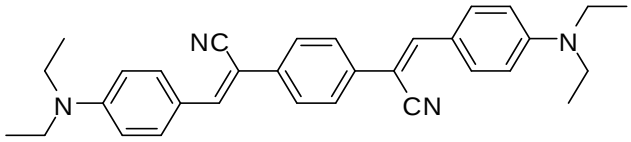

The title compound was synthesized by following the general procedure mentioned in **6.8.1.1.**

Reactants: 2,2'-(1,4-phenylene)diacetonitrile **(66)** (156 mg, 1.0 mmol), 4-(diethylamino) benzaldehyde **(67a)** (354 mg, 2.0 mmol), potassium *tert*-butoxide (336 mg, 3.0 mmol), Ethanol (10 mL).

Yield: 176 mg, 37%.

A red solid. **^{1}H-NMR** (300 MHz, DMSO-d_6): δ [ppm] = 7.87 (d, *J* = 8.9 Hz, 4H), 7.65 (s, 4H), 7.43 (s, 2H), 6.71 (d, *J* = 9.0 Hz, 4H), 3.45 (q, *J* = 7.0 Hz, 8H), 1.30 – 1.18 (t, *J* = 7.3 Hz, 12H). **MS** (EI, 70 eV): *m/z* = 474 [M^+]. **UV/Vis** (Ethanol): λ_{max} = 440 nm.

(2*Z*,2'*Z*)-2,2'-(1,4-Phenylene)bis(3-(4-(4-methylpiperazin-1-yl)phenyl)acrylonitrile) 68c (BSc4693)

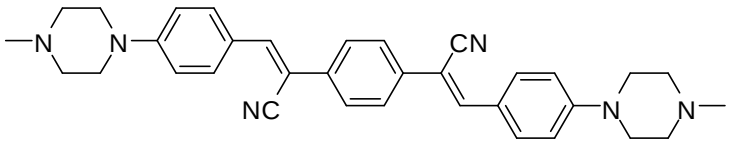

The title compound was synthesized by following the general procedure mentioned in **6.8.1.1.**

Reactants: 2,2'-(1,4-phenylene)diacetonitrile **(66)** (156 mg, 1.0 mmol), 4-(4-methylpiperazin-1-yl)benzaldehyde **(64d)** (204 mg, 2.0 mmol), potassium *tert*-butoxide (336 mg, 3.0 mmol), Ethanol (10 mL).

Yield: 180 mg, 34%.

An orange solid. **HPLC**: R_t = 4.19 min. **^{1}H-NMR** (300 MHz, Chloroform-d): δ [ppm] = 7.89 (d, *J* = 9.0 Hz, 4H), 7.69 (s, 4H), 7.47 (s, 2H), 6.95 (d, *J* = 9.1 Hz, 4H), 3.43 – 3.35 (m, 8H), 2.63 – 2.56 (m, 8H), 2.38 (s, 6H). **MS** (EI, 70 eV): *m/z* = 528 [M^+]. **UV/Vis** (Ethanol): λ_{max} = 408 nm.

6.8.2 2-methoxy-1,4-bisstyryl derivatives

Synthetic Scheme

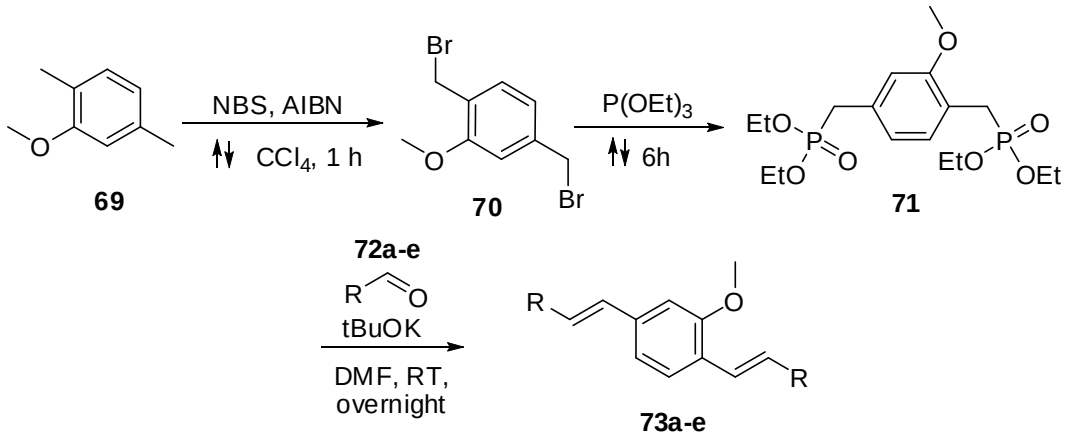

Compound	R
72a, 73a	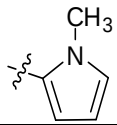
64a, 73b	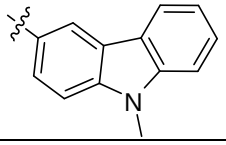
72c, 73c	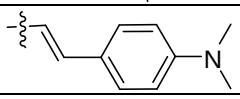
72d, 73d	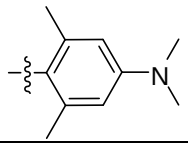
72e, 73e	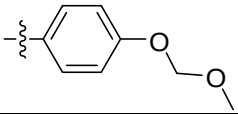

Tetraethyl (2-methoxy-1,4-phenylene)bis(methylene)diphosphonate 71

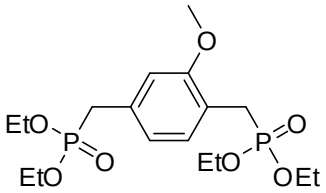

To a stirred solution of 2-methoxy-1,4-dimethyl benzene **69** (1.36 g, 10.0 mmol) in CCl_4 (30 mL) was added NBS (6.23 g, 35.0 mmol) and AIBN (0.23 g, 1.4 mmol) at room temperature. The reaction mixture was refluxed for 1 h. The cooled reaction mixture was then washed with H_2O and dried over $MgSO_4$. After removal of the solvent in vacuo, the residue was crystalized from cyclohexane to afford the 1,4-bis(bromomethyl)-2-methoxybenzene **(70)**, which was used in the next reaction without further purification.

A mixture of triethyl phosphite (2.49 g, 15.0 mmol) and 1,4-bis(bromomethyl)-2-methoxybenzene **(70)** (1.47 g, 5.0 mmol) was heated to 160 ^oC for 6h. The residue was purified by column chromatography on silica gel using cyclohexane and ethylacetate mixture (9:1) as an eluent to afford the title compound in quantitative yield.

A colorless solid. **^{1}H-NMR** (500 MHz, DMSO-d_6): δ [ppm] = 7.16 (dd, *J* = 7.5, 2.0 Hz, 1H), 6.92 (s, 1H), 6.82 (d, *J* = 7.5 Hz, 1H), 4.00-3.87 (m, 8H), 3.77 (s, 3H), 3.24-3.09 (m, 4H), 1.20-1.12 (m, 12H). **^{13}C-NMR** (125 MHz, DMSO-d_6): δ [ppm] = 156.5, 132.1, 130.5, 121.5, 118.2, 112.3, 61.2 (d, *J* = 16.5 Hz), 55.3, 32.2 (d, *J* = 137.0 Hz), 16.1 (t, *J* = 3.3 Hz).

6.8.2.1 General procedure for the synthesis of 2-methoxy-1,4-bisstyryl derivatives.

To a solution of potassium *tert*-butoxide (4.0 eq.) in DMF (5 ml) was added tetraethyl (2-methoxy-1,4-phenylene)bis(methylene)diphosphonate **71** (1.0 eq.) at 0 ^oC and stirred for 30 min. A solution of corresponding aldehyde **(72a-e)** (1.6 – 2.0 eq.) in DMF (1 mL) was added to the reaction mixture slowly and stirred reaction for overnight at room temperature. Dilute HCl and water was added to the reaction and the reaction mixture is extracted into ethyl acetate, the ethyl acetate layers were combined and washed with water, dried, evaporated and the residue was purified by column chromatography on silica gel using cyclohexane and dichloromethane (1:1; for **73a**, **73b** and **73c**) or cyclohexane and ethyl acetate mixture (10:1 for **73d**, **73e**) as eluent.

2,2'-(1*E*,1'*E*)-2,2'-(2-Methoxy-1,4-phenylene)bis(ethene-2,1-diyl)bis(1-methyl-1*H*-pyrrole) 73a (BSc4344)

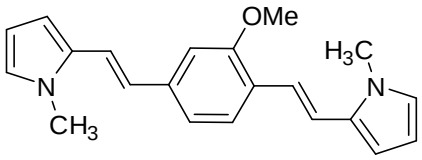

The title compound was synthesized by following the general procedure mentioned in **6.8.2.1.**

Reactants: Tetraethyl (2-methoxy-1,4-phenylene)bis(methylene)diphosphonate **(71)** (100 mg, 0.25 mmol), 1-methyl-1H-pyrrole-2-carbaldehyde **(72a)** (42 µL, 0.4 mmol), potassium *tert*-butoxide (107 mg, 4.0 mmol).

Yield: 23 mg, 30%.

A dark brown solid. **HPLC**: R_t = 9.19 min. **^{1}H-NMR** (500 MHz, DMSO-d_6): δ [ppm] = 7.60 (d, *J* = 8.0 Hz, 1H), 7.21 – 7.11 (m, 4H), 7.08 – 7.02 (m, 1H), 6.86 (dd, *J* = 15.9, 7.9 Hz, 1H), 6.81 – 6.75 (m, 2H), 6.48 (dd, *J* = 3.7, 1.6 Hz, 1H), 6.41 (dd, *J* = 3.7, 1.6 Hz, 1H), 6.06 – 6.01 (m, 2H), 3.90 (s, 3H), 3.72 (s, 3H), 3.68 (s, 3H). **^{13}C-NMR** (125 MHz, DMSO-d_6): δ [ppm] = 157.14, 138.50, 132.88, 132.32, 126.66, 125.70, 125.48, 124.89, 124.60, 119.95, 119.53, 118.17, 118.12, 109.31, 108.87, 108.79, 107.46, 106.85, 56.44, 34.62, 34.49. **MS** (EI, 70 eV): *m/z* = 318 [M^+]. **UV/Vis** (Ethanol): λ_{max} = 385 nm.

3,3'-(1*E*,1'*E*)-2,2'-(2-Methoxy-1,4-phenylene)bis(ethene-2,1-diyl)bis(9-methyl-9*H*-carbazole) 73b (BSc4346)

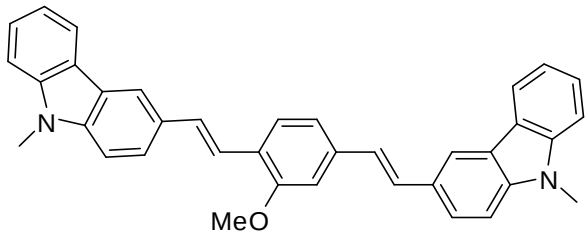

The title compound was synthesized by following the general procedure mentioned in **6.8.2.1.**

Reactants: Tetraethyl (2-methoxy-1,4-phenylene)bis(methylene)diphosphonate **(71)** (200 mg, 0.5 mmol), 9-methyl-9*H*-carbazole-3-carbaldehyde **(64a)** (164 mg, 0.78 mmol), potassium *tert*-butoxide (219 mg, 1.96 mmol).

Yield: 76 mg, 30%.

A yellow solid. **HPLC**: R_t = 11.29 min. **^{1}H-NMR** (300 MHz, DMSO-d_6): δ [ppm] = 8.17 (d, *J* = 1.6 Hz, 2H), 8.07 (d, *J* = 2.3 Hz, 1H), 8.04 (d, *J* = 2.3 Hz, 1H), 7.63 (ddd, *J* = 8.3, 6.6, 1.5 Hz, 2H), 7.56 (dd, *J* = 13.4, 6.7 Hz, 1H), 7.49 (s, 1H), 7.43 (t, *J* = 3.4 Hz, 1H), 7.41 (dd, *J* = 3.1, 1.1 Hz, 1H), 7.39 (dd, *J* = 3.1, 1.1 Hz, 1H), 7.33 (d, *J* = 2.5 Hz, 1H), 7.29 (t, *J* = 3.7 Hz, 3H), 7.27 (d, *J* = 4.3 Hz, 1H), 7.24 (d, *J* = 3.2 Hz, 1H), 7.20 (dd, *J* = 3.2, 0.9 Hz, 1H), 7.15 (dd, *J* = 3.2, 1.0 Hz, 1H), 7.04 (d, *J* = 7.0 Hz, 2H), 3.98 – 3.90 (m, 3H), 3.76 (d, *J* = 0.9 Hz, 6H). **MS** (EI, 70 eV): *m/z* = 518 [M^+]. **UV/Vis** (DMSO): λ_{max} = 404 nm.

4,4'-(1*E*,1'*E*,3*E*,3'*E*)-4,4'-(2-Methoxy-1,4-phenylene)bis(buta-1,3-diene-4,1-diyl)bis(*N*,*N*-dimethylaniline) 73c (BSc4351)

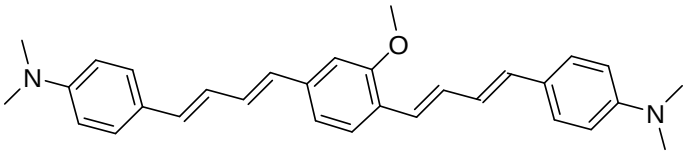

The title compound was synthesized by following the general procedure mentioned in **6.8.2.1.**

Reactants: Tetraethyl (2-methoxy-1,4-phenylene)bis(methylene)diphosphonate **(71)** (200 mg, 0.5 mmol), (*E*)-3-(4-(dimethylamino)phenyl)acrylaldehyde **(72c)** (137 mg, 0.78 mmol), potassium *tert*-butoxide (219 mg, 1.96 mmol).

Yield: 77 mg, 35%.

A orange solid. **HPLC**: R_t = 5.69 min. **^{1}H-NMR** (300 MHz, DMSO-d_6): δ [ppm] = 7.48 (s, 1H), 7.34 (d, *J* = 8.6 Hz, 1H), 7.06 (d, *J* = 12.9 Hz, 1H), 6.82 (d, *J* = 15.4 Hz, 1H), 6.70 (dd, *J* = 9.1, 2.9 Hz, 2H), 6.62 (dd, 1H), 3.88 (s, 3H), 2.93 (d, *J* = 1.6 Hz, 12H). **MS** (EI, 70 eV): *m/z* = 450.26 [M^+]. **UV/Vis** (Ethanol): λ_{max} = 427 nm.

4,4‘-(1*E*,1‘*E*)-2,2‘-(2-Methoxy-1,4-phenylene)bis(ethene-2,1-diyl)bis(*N*,*N*,3,5-tetramethylaniline) 73d (BSc4887)

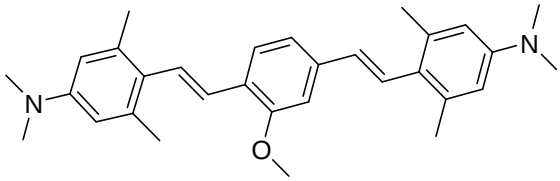

The title compound was synthesized by following the general procedure mentioned in **6.8.2.1.**

Reactants: Tetraethyl (2-methoxy-1,4-phenylene)bis(methylene)diphosphonate **(71)** (204 mg, 0.5 mmol), 4-(dimethylamino)-2,6-dimethylbenzaldehyde **(72d)** (177 mg, 1.0 mmol), potassium *tert*-butoxide (224 mg, 2.00 mmol).

Yield: 138 mg, 61%.

A yellow solid. **HPLC**: R_t = 4.68 min. **^{1}H-NMR** (500 MHz, DMSO-d_6): δ [ppm] = 7.59 (d, *J* = 8.3 Hz, 1H), 7.21 (d, *J* = 16.6 Hz, 1H), 7.17 – 7.15 (m, 2H), 7.13 (d, *J* = 16.8 Hz, 1H), 6.79 (d, *J* = 16.8 Hz, 1H), 6.58 (d, *J* = 16.6 Hz, 1H), 6.47 (d, *J* = 2.8 Hz, 4H), 3.87 (s, 3H), 2.89 (d, *J* = 3.1 Hz, 12H), 2.33 (d, *J* = 11.5 Hz, 12H). **^{13}C-NMR** (125 MHz, Chloroform-d): δ [ppm] = 156.88, 149.24, 149.12, 138.32, 137.30, 137.26, 132.04, 127.08, 126.81, 126.76, 126.62, 126.07, 125.48, 118.70, 112.60, 112.51, 108.63, 55.72, 40.67, 40.59, 21.93, 21.90. **MS** (EI, 70 eV): *m/z* = 454 [M^+]. **UV/Vis** (Ethanol): λ_{max} = 371 nm.

4,4'-(1*E*,1'*E*)-2,2'-(2-Methoxy-1,4-phenylene)bis(ethene-2,1diyl)bis((methoxy methoxy)benzene) 73e (BSc4990)

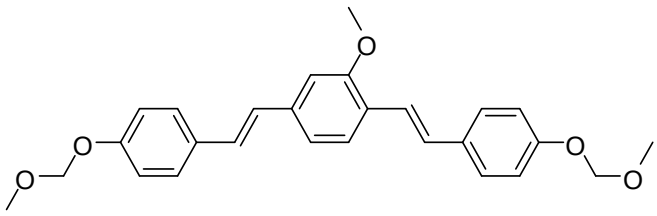

The title compound was synthesized by following the general procedure mentioned in **6.8.2.1.**

Reactants: Tetraethyl (2-methoxy-1,4-phenylene)bis(methylene)diphosphonate **(71)** (204 mg, 0.5 mmol), 4-(methoxymethoxy)benzaldehyde **(72e)** (177 mg, 1.0 mmol), potassium *tert*-butoxide (224 mg, 2.00 mmol).

Yield: 186 mg, 82%.

A light green solid. **HPLC**: R_t = 9.80 min. **^{1}H-NMR** (500 MHz, Chloroform-d): δ [ppm] = 7.48 (d, *J* = 8.00 Hz, 1H), 7.39 (dd, *J* = 8.74, 6.86 Hz, 4H), 7.27 (d, *J* = 16.46 Hz, 1H), 7.05 – 7.01 (m, 2H), 7.00 (d, *J* = 7.37 Hz, 1H), 6.98 – 6.93 (m, 6H), 6.90 (d, *J* = 16.24 Hz, 1H), 5.12 (d, *J* = 3.41 Hz, 4H), 3.87 (s, 3H), 3.42 (d, *J* = 2.05 Hz, 6H). **^{13}C-NMR** (125 MHz, Chloroform-d): δ [ppm] = 156.97, 156.94, 156.71, 137.83, 132.07, 131.28, 128.26, 127.94, 127.70, 127.01, 126.31, 125.98, 121.61, 119.21, 116.49, 116.40, 108.56, 94.47, 94.45, 56.05, 56.02, 55.58.

4,4'-(1*E*,1'*E*)-2,2'-(2-Methoxy-1,4-phenylene)bis(ethene-2,1-diyl)diphenol 74 (BSc3924)

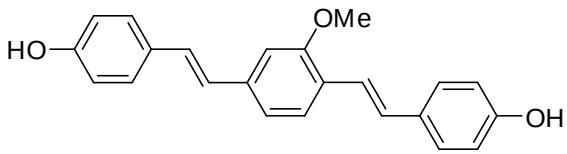

74

A solution of 4,4'-(1*E*,1'*E*)-2,2'-(2-methoxy-1,4-phenylene)bis(ethene-2,1-diyl)bis((methoxy methoxy)benzene) **(73e)** (180 mg, 0.41 mmol) in glacial acetic acid and water (4:1) is heated at 90-95 °C for 1 hour. Reaction mixture extracted with dichloromethane and washed the organic layers with water, dried, evaporated under vacuum. The crude compound was purified by column chromatography on silica gel using cyclohexane and ethylacetate mixture (2:1) as eluent.

Yield: 104 mg, 73%.

A yellow green solid. **^{1}H-NMR** (500 MHz, DMSO-d_6): δ [ppm] = 9.57 (s, 2H), 7.59 (d, *J* = 8.02 Hz, 1H), 7.44 (d, *J* = 8.63 Hz, 2H), 7.39 (d, *J* = 8.63 Hz, 2H), 7.23 – 7.17 (m, 3H), 7.16 – 7.10 (m, 2H), 7.02 (d, *J* = 16.36 Hz, 1H), 6.78 (dd, *J* = 8.52, 5.51 Hz, 4H), 3.91 (s, 3H). **^{13}C-NMR** (125 MHz, DMSO-d_6): δ [ppm] 157.29, 157.12, 156.39, 137.69, 128.64, 128.29, 128.13, 127.81, 127.63, 125.86, 125.07, 124.85, 119.36, 118.87, 115.56, 108.56, 55.50. **UV/Vis** (Ethanol): λ_{max} = 397 nm.

6.9 Bis Styryl terephthalonitrile derivative

2,5-Bis(4-(dimethylamino)styryl)terephthalonitrile 78 (BSc4545)

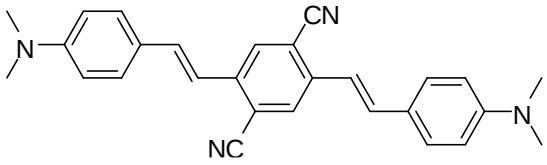

Synthesis

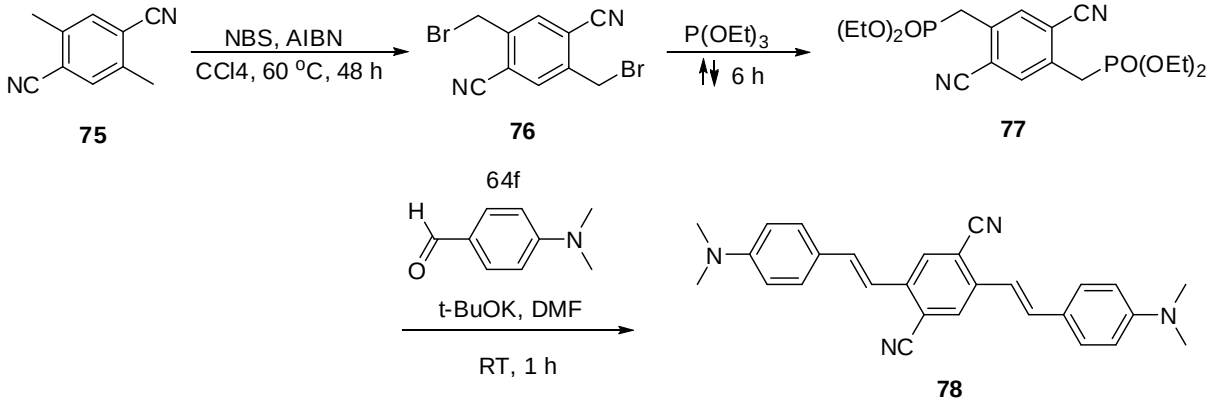

2,5-Bis(bromomethyl)terephthalonitrile 76

To a stirred solution of 2,5-dimethylterephthalonitrile (156 mg, 1.0 mmol) in CCl_4 (20 mL) was added NBS (711 mg, 4.0 mmol) and AIBN (5 mg, 0.03 mmol) at room temperature. The reaction mixture was refluxed for 48 h. The cooled reaction mixture was then washed with H_2O and dried over $MgSO_4$. After removal of the solvent in vacuo, the residue was purified by column chromatography on silica gel using cyclohexane and ethylacetate mixture (10:1) as eluent.

Yield: 63 mg, 20%

^{1}H-NMR (300 MHz, Chloroform-d): δ [ppm] = 7.87 (s, 2H), 4.62 (s, 4H).

Tetraethyl (2,5-dicyano-1,4-phenylene)bis(methylene)diphosphonate 77

A mixture of triethyl phosphite (49 µL, 0.28 mmol) and 2,5-bis(bromomethyl)terephthalonitrile **(76)** (30 mg, 0.09 mmol) was heated to 160 °C for 6h. Excess triethyl phopshite was removed by distillation resulted in light yellow oil, which slowly crystalized in to a solid.

Yield: 41 mg, 99%.

^{1}H-NMR (300 MHz, Chloroform-d): δ [ppm] = 7.81 (d, *J* = 1.9 Hz, 2H), 4.25 – 4.01 (m, 8H), 3.39 (d, *J* = 21 Hz, 4H), 1.31 (t, *J* = 7.1 Hz, 12H).

2,5-bis(4-(dimethylamino)styryl)terephthalonitrile 78 (**BSc4545**)

To a solution of *t*-BuOK (39 mg, 0.35 mmol) in DMF (3 mL) was added tetraethyl (2,5-dicyano-1,4-phenylene)bis(methylene)diphosphonate **(77)** (50 mg, 0.12 mmol) at 0 ^{o}C and stirred for 30 min. A solution of aldehyde **(64f)** (27 mg, 0.19 mmol) in DMF (1 mL) was added to the reaction mixture slowly and stirred the reaction for overnight at room temperature. Water was added to the reaction and the reaction mixture is extracted into ethyl acetate, ethyl acetate layers were combined and washed with water, dried, evaporated and the residue was purified by column chromatography using on silica gel using hexane and dichloromethane mixture (1:4) as eluent.

Yield: 28 mg, 57%.

A brick red powder. **HPLC**: R_t = 7.23 min. **^{1}H-NMR** (300 MHz, Chloroform-d): δ [ppm] = 7.97 (s, 1H), 7.49 (d, *J* = 8.9 Hz, 1H), 7.21 (s, 1H), 7.15 (d, *J* = 16.1 Hz, 1H), 6.74 (d, *J* = 8.8 Hz, 1H), 3.04 (s, 1H). **MS** (EI, 70 eV): *m/z* = 418 [M^+]. **UV/Vis** (DMSO): λ_{max} = 480 nm.

6.10 Synthesis of bis(arylvinyl) pyrimidine derivatives

Synthetic scheme

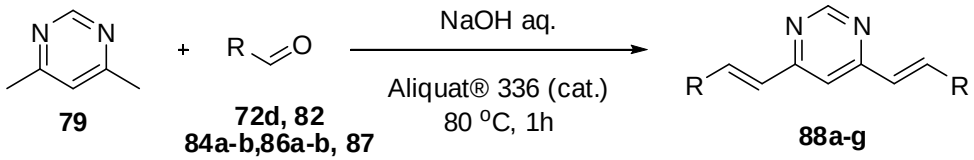

79 + **72d, 82 84a-b,86a-b, 87** → **88a-g**

Compound	R
72d, 88a	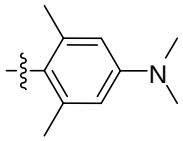
82, 88b	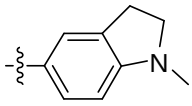
87, 88c	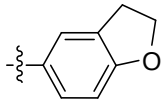

84a, 88d 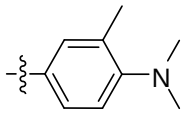

84b, 88e 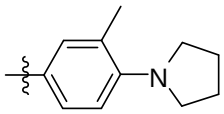

86a, 88f 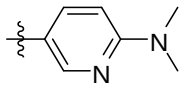

86b, 88g 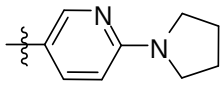

6.10.1 General procedure for the synthesis of 88a-g

A stirred mixture of 4,6-dimethylpyrimidine **(79)** (1 eq.) and the corresponding aldehyde (2.0 eq.) in aqueous sodium hydroxide (5M, 5 mL) containing Aliquat® 336 (0.15 eq.) was heated at 80 ^{o}C for 1 hour. The mixture was allowed to cool, and the precipitate was filtered off, washed with water, and purified by washing with cold methanol. Further purification was performed (for **88a**) by column chromatography using dichloromethane and methanol mixture (9.5:0.5) as eluent.

4,4'-(1*E*,1'*E*)-2,2'-(Pyrimidine-4,6-diyl)bis(ethene-2,1-diyl)bis(*N*,*N*,3,5-tetramethylaniline) 88a (BSc4890)

Synthetic scheme

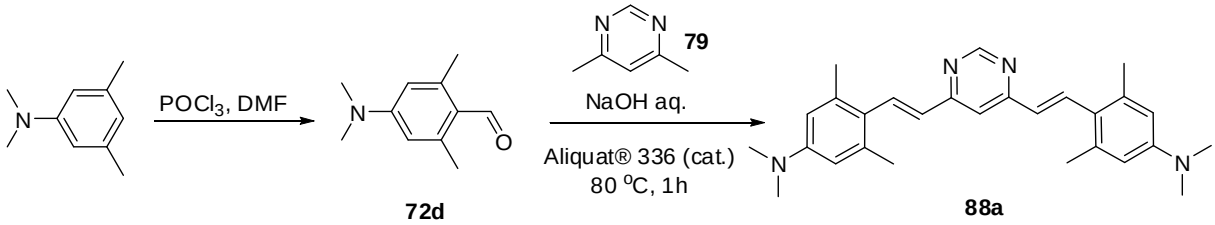

4-(Dimethylamino)-3,5-dimethylbenzaldehyde 72d

Phosphorous oxychloride (372 μL, 4.0 mmol) was added to a solution of dry DMF (1238 μL, 16.0 mmol) at 0-5 ^{o}C and stirred for 30 min under nitrogen atmosphere. To this mixture, a solution of arene (1960 μL, 12.0 mmol) in DMF added drop wise and reaction slowly heated up to 80 ^{o}C and stirred for 8 hours. The mixture was poured into crushed ice, neutralized with $NaHCO_3$ solution, stirred for 5 min, extracted with ethyl acetate washed with water, dried and

solvent removed *in vacuo*. Further purification of the crude product was performed by column chromatography on silica gel using cyclohexane and ethylacetae mixture (5:1) as eluent.

Yield: 915 mg, 43%.

A solid. **^{1}H-NMR** (300 MHz, Chloroform-d): δ [ppm] = 10.37 (s, 1H), 6.33 (s, 2H), 3.06 (s, 6H), 2.61 (s, 6H). **^{13}C-NMR** (75 MHz, Chloroform-d): δ [ppm] = 190.52, 152.87, 144.16, 121.64, 112.03, 39.86, 21.58.

4,4'-(1*E*,1'*E*)-2,2'-(pyrimidine-4,6-diyl)bis(ethene-2,1-diyl)bis(*N*,*N*,3,5-tetramethylaniline) 88a (BSc4890)

The title compound was synthesized by following the general procedure mentioned in **6.10.1.**

Reactants: 4,6-dimethylpyrimidine **(79)** (20 mg, 0.184 mmol), 4-(dimethylamino)-2,6-dimethylbenzaldehyde **(72d)** (65 mg, 0.369 mmol), Aliquat® 336 (11 mg, 0.03 mmol).

Yield: 63 mg, 80%.

A yellowish green solid. **HPLC**: R_t = 4.08 min. **^{1}H-NMR** (500 MHz, Chloroform-d): δ [ppm] = 8.96 (s, 1H), 7.98 (d, *J* = 15.3 Hz, 2H), 7.07 (s, 1H), 6.53 (d, *J* = 16.1 Hz, 2H), 6.39 (s, 4H), 2.90 (s, 12H), 2.38 (s, 12H). **^{13}C-NMR** (125 MHz, Chloroform-d): δ [ppm] = 163.27, 158.65, 149.85, 138.54, 135.23, 128.22, 123.38, 115.33, 112.38, 40.27, 22.33. **MS** (EI, 70 eV): *m/z* = 426 [M^+]. **UV/Vis** (Ethanol): λ_{max} = 427 nm.

4,6-Bis((*E*)-2-(1-methylindolin-5-yl)vinyl)pyrimidine 88b (BSc4935)

Synthetic Scheme

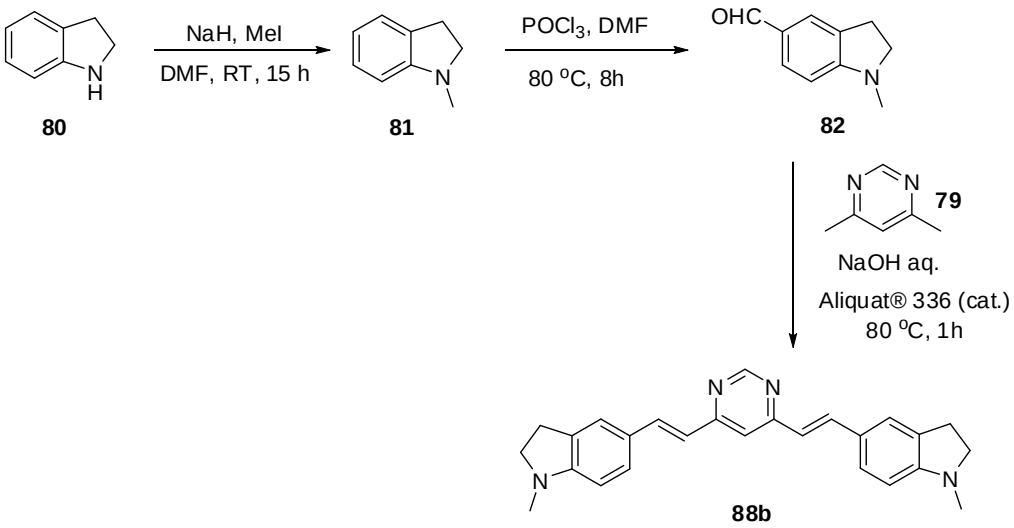

1-Methylindoline 81

Sodium hydride (240 mg, 6.0 mmol) was added in several batches to a chilled solution of indoline (477 mg, 4.0 mmol) in THF (4 mL). Methyl iodide (323 μL, 5.2 mmol) was then added drop wise with stirring, while maintaining the temperature of 0 ^{o}C. The resulting solution was maintained at room temperature for 15 h, and then diluted with ethanol (10 mL). The mixture was concentrated and then the product was extracted with dichloromethane. The organic layers were combined, dried, filtered and concentrated to provide 1-methylindoline.

Yield: 325 mg, 61%.

A brown liquid. **^{1}H-NMR** (300 MHz, Chloroform-d): δ [ppm] = 7.15 – 7.07 (m, 2H), 6.70 (td, *J* = 7.4, 0.9 Hz, 1H), 6.57 – 6.49 (m, 1H), 3.33 (t, *J* = 7.5 Hz, 2H), 2.98 (t, *J* = 7.4 Hz, 2H), 2.78 (s, 3H).

1-Methylindoline-5-carbaldehyde 82

Phosphorous oxychloride (174 μL, 1.87 mmol) was added to a solution of dry DMF (871 μL, 11.26 mmol) at 0-5 ^{o}C and stirred for 30 min under nitrogen atmosphere. To this mixture, a solution of 1-methyl indoline **(81)** (500 mg, 3.75 mmol) in 1,2-dichloroethane (3 mL) added drop wise and the reaction slowly heated up to 80 ^{o}C and stirred for 8 hours. The mixture was poured into crushed ice, neutralized with $NaHCO_3$ solution, stirred for 5 min, extracted with ethyl acetate washed with water, dried and solvent removed *in vacuo*. Further purification of the crude product was performed by column chromatography on silica gel using hexane and ethyl acetate mixture (8:2) as eluent.

Yield: 254 mg, 42%

A solid. **^{1}H-NMR** (500 MHz, Chloroform-d): δ [ppm] = 9.70 (s, 1H), 7.60 (d, *J* = 1.5 Hz, 1H), 7.59 – 7.57 (m, 1H), 6.42 (d, *J* = 8.1 Hz, 1H), 3.58 (t, *J* = 8.5 Hz, 2H), 3.06 (t, *J* = 8.4 Hz, 2H), 2.91 (s, 3H). **^{13}C-NMR** (125 MHz Chloroform-d): δ [ppm] = 189.96, 157.85, 134.24, 130.47, 126.91, 124.40, 104.59, 54.88, 34.07, 27.40.

4,6-Bis((*E*)-2-(1-methylindolin-5-yl)vinyl)pyrimidine 88b (BSc4935)

The title compound was synthesized by following the general procedure mentioned in **6.10.1.**

Reactants: 4,6-dimethylpyrimidine **(79)** (54 mg, 0.5 mmol), 1-methylindoline-5-carbaldehyde **(82)** (161 mg, 1.0 mmol), Aliquat® 336 (30 mg, 0.075 mmol).

Yield: 183 mg, 93%.

A yellow solid. **HPLC**: R_t = 7.29 min. **^{1}H-NMR** (500 MHz, Chloroform-d): δ [ppm] = 8.99 (s, 1H), 7.83 (d, *J* = 15.8 Hz, 2H), 7.40 (s, 2H), 7.34 (dd, *J* = 8.1, 1.3 Hz, 2H), 7.14 (s, 1H), 6.84 (d, *J* = 15.8 Hz, 2H), 6.45 (d, *J* = 8.1 Hz, 2H), 3.45 (t, *J* = 8.3 Hz, 4H), 3.03 (t, *J* = 8.2 Hz, 4H), 2.84 (s, 6H). **^{13}C-NMR** (125 MHz, Chloroform-d): δ [ppm] = 163.02, 158.14, 154.60, 137.64, 130.86, 129.44, 125.38, 122.99, 120.52, 115.05, 106.17, 55.55, 35.19, 28.21. **UV/Vis** (Ethanol): λ_{max} = 440 nm.

4,6-Bis((*E*)-2-(2,3-dihydrobenzofuran-5-yl)vinyl)pyrimidine 88c (BSc4936)

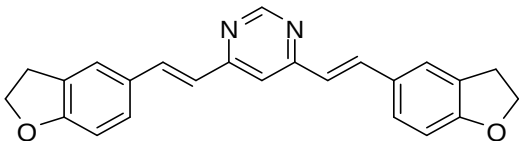

The title compound was synthesized by following the general procedure mentioned in **6.10.1.**

Reactants: 4,6-dimethylpyrimidine **(79)** (108 mg, 1.0 mmol), 2,3-dihydrobenzofuran-5-carbaldehyde **(87)** (296 mg, 2.0 mmol), Aliquat® 336 (60 mg, 0.15 mmol).

Yield: 339 mg, 92%.

A yellowish white solid. **HPLC**: R_t = 7.31 min. **^{1}H-NMR** (500 MHz, Chloroform-d): δ [ppm] = 9.06 (s, 1H), 7.88 (t, *J* = 12.7 Hz, 2H), 7.50 (s, 2H), 7.40 (dt, *J* = 8.9, 4.4 Hz, 2H), 7.20 (s, 1H), 6.92 (d, *J* = 15.9 Hz, 2H), 6.83 (d, *J* = 8.3 Hz, 2H), 4.65 (t, *J* = 8.7 Hz, 4H), 3.27 (t, *J* = 8.7 Hz, 4H). **^{13}C-NMR** (125 MHz, Chloroform-d): δ [ppm] = 162.91, 161.59, 158.34, 137.13, 128.90, 128.63, 128.01, 124.03, 122.80, 115.71, 109.70, 71.76, 29.43. **UV/Vis** (Ethanol): λ_{max} = 379 nm.

4,4'-(1*E*,1'*E*)-2,2'-(pyrimidine-4,6-diyl)bis(ethene-2,1-diyl)bis(*N*,*N*,2 trimethylaniline) 88d (BSc4938)

Synthetic scheme

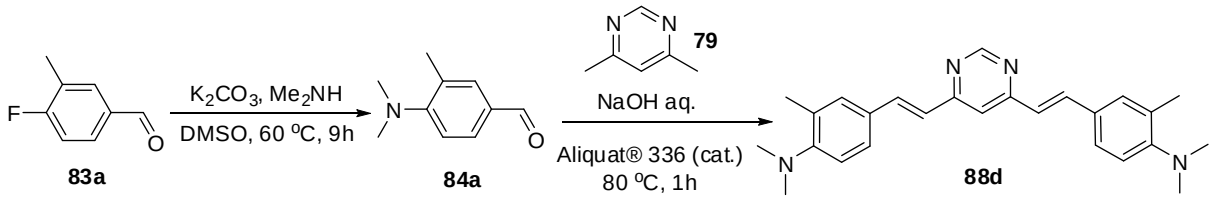

4-(dimethylamino)-3-methylbenzaldehyde 84a

To a solution of 4-fluoro-2-methylbenzaldehyde **(83a)** (138 mg, 1.0 mmol) in DMSO (3 mL) was added dimethylamine (135 μL, 1.2 mmol) and potassium carbonate (414 mg, 3.0 mmol) and heated at 60 °C for 9 hours. The reaction mixture then cooled to room temperature, water was added and partitioned between ethyl acetate and water layers. The ethyl acetate is removed *in vacuo* to give a crude solid which is further purified by column chromatography on silica gel using cyclohexane and ethyl acetate mixture (4:1) as eluent.

Yield: 98 mg, 60%.

A solid. **^{1}H-NMR** (300 MHz, Chloroform-d): δ [ppm] = 9.83 (s, 1H), 7.63 (dd, *J* = 8.3, 1.3 Hz, 2H), 7.01 (d, 1H), 2.83 (s, 6H), 2.36 (s, 3H).

4,4'-(1*E*,1'*E*)-2,2'-(pyrimidine-4,6-diyl)bis(ethene-2,1-diyl)bis(*N*,*N*,2 trimethylaniline) 88d (BSc4938)

The title compound was synthesized by following the general procedure mentioned in **6.10.1.**

Reactants: 4,6-dimethylpyrimidine (**79)** (80 mg, 0.74 mmol), 4-(dimethylamino)-3-methylbenzaldehyde **(84a)** (241 mg, 1.5 mmol), Aliquat® 336 (44 mg, 0.11 mmol).

Yield: 262 mg, 89%.

A brown solid. **^{1}H-NMR** (500 MHz, Chloroform-d): δ [ppm] = 9.08 (d, *J* = 1.1 Hz, 1H), 7.85 (d, *J* = 15.9 Hz, 2H), 7.46 – 7.39 (m, 5H), 7.23 (d, *J* = 1.2 Hz, 1H), 7.04 – 7.01 (m, 2H), 6.98 (s, 1H), 6.95 (s, 1H), 2.77 (s, 13H), 2.38 (s, 7H). **^{13}C-NMR** (125 MHz, Chloroform-d): δ [ppm] = 162.95, 158.59, 154.10, 136.81, 131.69, 130.60, 129.53, 126.35, 123.64, 118.29, 115.72, 43.83, 18.92.

4,6-Bis(3-methyl-4-(pyrrolidin-1-yl)styryl)pyrimidine 88e (BSc4939)

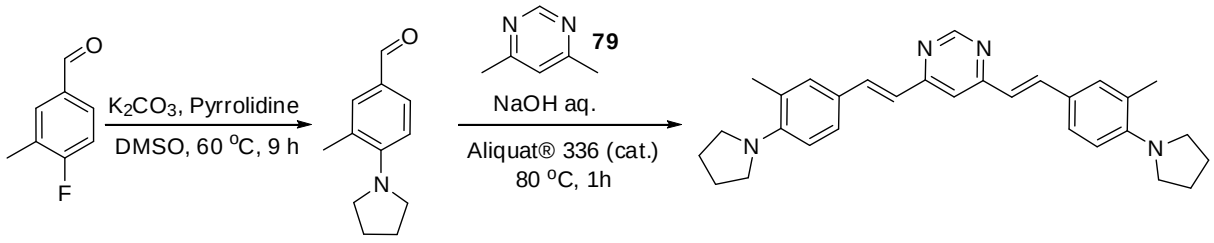

83a **84b** **88e**

3-methyl-4-(pyrrolidin-1-yl)benzaldehyde 84b

To a solution of 4-fluoro-2-methylbenzaldehyde **(83a)** (488 μL, 1.0 mmol) in DMSO (10 mL) was added pyrrolidine (385 μL, 4.8 mmol) and potassium carbonate (1658 mg, 12.0 mmol) and heated at 60 °C for 9 hours. The reaction mixture was then cooled to room temperature; water was added and partitioned between ethyl acetate and water layers. The ethyl acetate is removed *in vacuo* to give a residue which is further purified by column chromatography on silica gel using cyclohexane and ethyl acetate mixture (4:1) as eluent.

Yield: 430 mg, 57%.

A liquid. **^{1}H-NMR** (500 MHz, Chloroform-d): δ [ppm] = 9.78 (s, 1H), 7.61 (d, *J* = 6.5 Hz, 2H), 6.80 (d, *J* = 8.6 Hz, 1H), 3.50 (t, *J* = 6.5 Hz, 4H), 2.47 (s, 3H), 2.05 – 1.98 (m, 4H).

4,6-Bis(3-methyl-4-(pyrrolidin-1-yl)styryl)pyrimidine 88e (BSc4939)

The title compound was synthesized by following the general procedure mentioned in **6.10.1.** **Reactants:** 4,6-dimethylpyrimidine **(79)** (54 mg, 0.5 mmol), 3-methyl-4-(pyrrolidin-1-yl)benzaldehyde **(84b)** (189 mg, 1.0 mmol), Aliquat® 336 (30 mg, 0.15 mmol).

Yield: 209 mg, 93%.

A bright yellow solid. **^{1}H-NMR** (500 MHz, Chloroform-d): δ [ppm] = 9.03 (d, *J* = 1.0 Hz, 1H), 7.82 (d, *J* = 15.9 Hz, 2H), 7.43 – 7.34 (m, 4H), 7.22 (d, *J* = 1.1 Hz, 1H), 6.91 (d, *J* = 15.9 Hz, 2H), 6.83 (d, *J* = 8.2 Hz, 2H), 3.40 – 3.29 (m, 8H), 2.41 (s, 6H), 2.03 – 1.93 (m, 8H). **^{13}C-NMR** (125 MHz, Chloroform-d): δ [ppm] = 163.07, 158.54, 150.73, 136.90, 131.48, 127.03, 126.77, 126.53, 122.07, 115.28, 115.16, 50.98, 25.36, 21.44. **MS** (EI, 70 eV): *m/z* = 450 [M^{+}]. **UV/Vis** (Ethanol): λ_{max} = 434 nm.

5,5'-(1*E*,1'*E*)-2,2'-(Pyrimidine-4,6-diyl)bis(ethene-2,1-diyl)bis(*N*,*N*-dimethylpyridin-2-amine) 88f (BSc4984)

Synthetic scheme

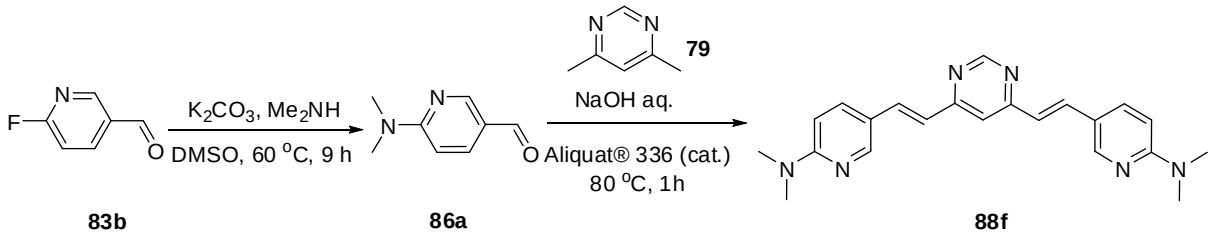

83b **86a** **88f**

6-(Dimethylamino)nicotinaldehyde 86a

To a solution of 6-fluoronicotinaldehyde **(83b)** (500 mg, 4.0 mmol) in DMSO (8 mL) was added dimethylamine (460 μL, 4.8 mmol) and potassium carbonate (1658 mg, 12.0 mmol) and heated at 60 °C for 9 hours. The reaction mixture was then cooled to room temperature; water was added and partitioned between ethyl acetate and water layers. The ethyl acetate is removed *in vacuo* to give a crude solid which is further purified by column chromatography on silica gel using cyclohexane and ethyl acetate mixture (4:2) as eluent.

Yield: 360 mg, 60%.

A solid. **HPLC**: R_t = 0.77 min. **^{1}H-NMR** (300 MHz, Chloroform-d): δ [ppm] = 9.74 (d, *J* = 0.66 Hz, 1H), 8.53 (dd, *J* = 2.33, 0.74 Hz, 1H), 7.88 (dd, *J* = 9.05, 2.34 Hz, 1H), 6.53 (dt, *J* = 9.06, 0.75 Hz, 1H), 3.18 (s, 6H). **^{13}C-NMR** (75 MHz, Chloroform-d): δ [ppm] = 189.07, 161.29, 154.46, 136.01, 121.66, 105.66, 38.15.

5,5'-(1*E*,1'*E*)-2,2'-(Pyrimidine-4,6-diyl)bis(ethene-2,1-diyl)bis(*N*,*N*-dimethylpyridin-2-amine) 88f (BSc4984)

The title compound was synthesized by following the general procedure mentioned in **6.10.1.**

Reactants: 4,6-dimethylpyrimidine (**79)** (108 mg, 1.0 mmol), 6-(dimethylamino) nicotinaldehyde (**86a)** (300 mg, 2.0 mmol), Aliquat® 336 (60 mg, 0.15 mmol).

Yield: 339 mg, 91%.

A yellow solid. **HPLC**: R_t = 0.83 min. **^{1}H-NMR** (500 MHz, Chloroform-d): δ [ppm] = 8.93 (d, *J* = 1.17 Hz, 1H), 8.27 (d, *J* = 2.41 Hz, 2H), 7.71 (d, *J* = 15.96 Hz, 2H), 7.67 (dd, *J* = 9.01, 2.47 Hz, 2H), 7.08 (d, *J* = 1.24 Hz, 1H), 6.75 (d, *J* = 15.83 Hz, 2H), 6.48 (d, *J* = 8.98 Hz, 2H),

3.07 (s, 12H). **^{13}C-NMR** (125 MHz, Chloroform-d): δ [ppm] = 162.86, 159.23, 158.50, 149.37, 134.71, 134.16, 121.61, 119.68, 115.30, 106.00, 38.15. **UV/Vis** (Ethanol): λ_{max} = 378 nm.

4,6-Bis((*E*)-2-(6-(pyrrolidin-1-yl)pyridin-3-yl)vinyl)pyrimidine 88g (BSc4988)

Synthetic scheme

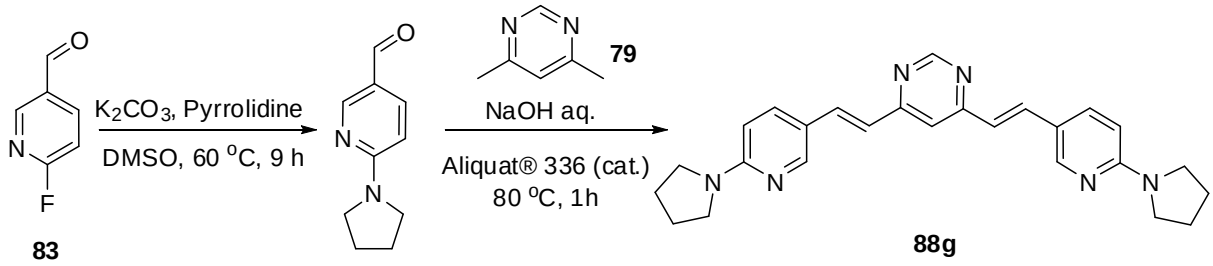

6-(pyrrolidin-1-yl)nicotinaldehyde 86b

To a solution of 6-fluoronicotinaldehyde (250 mg, 2.0 mmol) in DMSO (5 mL) was added pyrrolidine (197 µL, 2.4 mmol) and potassium carbonate (829 mg, 6.0 mmol) and heated at 60 °C for 9 hours. The reaction mixture was then cooled to room temperature; water was added and partitioned between ethyl acetate and water layers. The ethyl acetate is removed *in vacuo* to give a crude solid which is further purified by column chromatography on silica gel using cyclohexane and ethyl acetate mixture (4:2) as eluent.

Yield: 218 mg, 62%.

A solid. **HPLC**: R_t = 0.85 min. **^{1}H-NMR** (300 MHz, Chloroform-d): δ [ppm] = 9.76 (s, 1H), 8.55 (d, *J* = 2.34 Hz, 1H), 7.27 (s, 1H), 6.41 (d, *J* = 8.93 Hz, 1H), 3.57 (s, 4H), 2.18 – 1.82 (m, 4H). **^{13}C-NMR** (75 MHz, Chloroform-d): δ [ppm] = 189.14, 159.27, 155.14, 135.72, 121.73, 106.86, 47.14, 25.36.

4,6-bis((*E*)-2-(6-(pyrrolidin-1-yl)pyridin-3-yl)vinyl)pyrimidine 88g (BSc4988)

The title compound was synthesized by following the general procedure mentioned in **6.10.1.**

Reactants: 4,6-dimethylpyrimidine **(79)** (15 mg, 0.14 mmol), 6-(pyrrolidin-1-yl) nicotinaldehyde (**86b)** (50 mg, 0.28 mmol), Aliquat® 336 (8 mg, 0.04 mmol).

Yield: 55 mg, 93%.

A yellow solid. **HPLC**: R_t = 1.91 min. **^{1}H-NMR** (500 MHz, Chloroform-d): δ [ppm] = 8.93 (d, *J* = 1.15 Hz, 1H), 8.27 (d, *J* = 2.32 Hz, 2H), 7.73 (s, 1H), 7.69 (d, *J* = 2.83 Hz, 2H), 7.67 (d, *J* = 2.42 Hz, 1H), 7.09 (d, *J* = 1.25 Hz, 1H), 6.75 (d, *J* = 15.90 Hz, 2H), 6.35 (d, *J* = 8.91 Hz, 2H), 3.46 (t, *J* = 4.86 Hz, 8H), 2.05 – 1.89 (m, 8H). **^{13}C-NMR** (125 MHz, Chloroform-d): δ [ppm] = 162.84, 158.49, 156.83, 149.28, 134.75, 134.18, 121.48, 119.57, 115.26, 107.17, 47.03, 25.49. **UV/Vis** (Ethanol): λ_{max} = 412 nm.

6.11 Synthesis of bis(arylvinyl) pyrazines

Synthetic Scheme

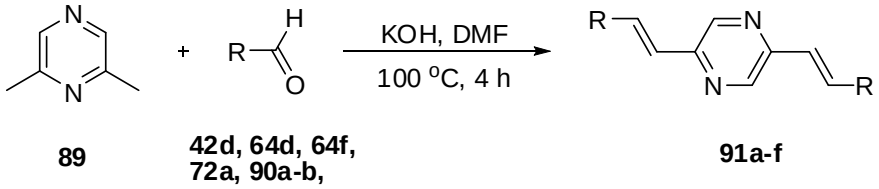

89 **42d, 64d, 64f, 72a, 90a-b,** **91a-f**

Compound	R
42d, 91a	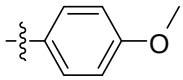
90a, 91b	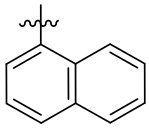
64f, 91c	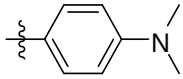
64d, 91d	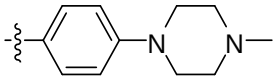
90b, 91e	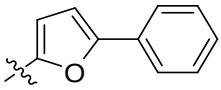
72a, 91f	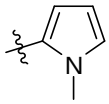

6.11.1 General procedure for the synthesis:

A sample vial was charged with 2, 5-dimethylpyrazine **(89)** (1 eq.) and corresponding aldehyde (2 eq.) in DMF. After 5 min of stirring at room temperature, KOH (3.0 eq.) was added and the reaction mixture was heated to 100 °C and stirred at this temperature for 4 hours. After cooling to room temperature, the mixture was portioned between water and ethyl acetate. The ethyl acetate layers were extracted and solvent was removed *in vacuo* to obtain a crude solid. Further purification was performed by column chromatography on silica gel

using dichloromethane (for **91b**, **91e** and **91f**), dichloromethane and ethyl acetate mixture (9.5:0.5) (for **91a** and **91c**), dichloromethane and methanol mixture (9.5:0.5) (for **91d**) as eluent.

2,6-Bis(4-methoxystyryl)pyrazine 91a (BSc4758)

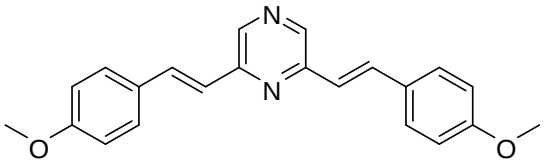

The title compound was synthesized by following the general procedure mentioned in **6.11.1.**

Reactants: 2,6-dimethylpyrazine **(89)** (216 mg, 2.0 mmol), 4-methoxybenzaldehyde **(42d)** (545 mg, 4.0 mmol), KOH (449 mg, 8.0 mmol), DMF (5 mL).

Yield: 193 mg, 28%.

A pale yellow solid. **^{1}H-NMR** (300 MHz, DMSO-d_6): δ [ppm] = 8.56 (s, 2H), 7.82 (d, *J* = 16.2 Hz, 2H), 7.67 (d, *J* = 9.3, 2.4 Hz, 4H), 7.23 (d, *J* = 16.2 Hz, 2H), 7.00 (d, *J* = 9.3, 2.4 Hz, 4H), 3.81 (s, 6H). **^{13}C-NMR** (75 MHz, DMSO-d_6): δ [ppm] = 160.40, 150.54, 141.67, 134.51, 129.29, 129.15, 122.77, 114.83, 55.72. **MS** (EI, 70 eV): *m/z* = 344 [M^+]. **UV/Vis** (Ethanol): λ_{max} = 376 nm.

2,6-Bis((*E*)-2-(naphthalen-1-yl)vinyl)pyrazine 91b (BSc4760)

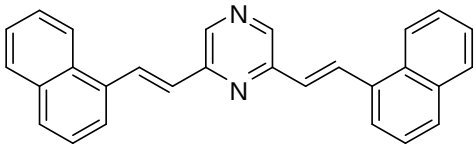

The title compound was synthesized by following the general procedure mentioned in **6.11.1.**

Reactants: 2,6-dimethylpyrazine **(89)** (432 mg, 4.0 mmol), 1-naphthaldehyde **90a** (1086 μL, 8.0 mmol), KOH (897 mg, 16.0 mmol), DMF (10 mL).

Yield: 307 mg, 20%.

A yellow solid. **^{1}H-NMR** (300 MHz, DMSO-d_6): δ [ppm] = 8.91 (s, 2H), 8.73 (d, *J* = 16.0 Hz, 2H), 8.45 (d, *J* = 8.5 Hz, 2H), 8.08 – 7.96 (m, 6H), 7.69 – 7.56 (m, 6H), 7.51 (d, *J* = 15.9 Hz, 2H). **MS** (EI, 70 eV): *m/z* = 384 [M^+]. **UV/Vis** (Ethanol): λ_{max} = 375 nm.

4,4'-(1*E*,1'*E*)-2,2'-(Pyrazine-2,6-diyl)bis(ethene-2,1-diyl)bis(*N*,*N*-dimethylaniline) 91c (BSc4761)

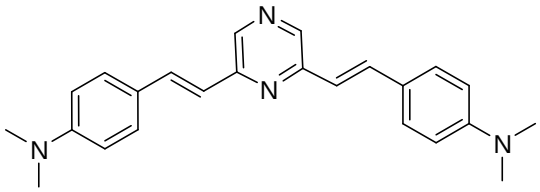

The title compound was synthesized by following the general procedure mentioned in **6.11.1.**

Reactants: 2, 6-dimethylpyrazine **(89)** (432 mg, 4.0 mmol), 4-(dimethylamino)benzaldehyde **(64f)** (1193 mg, 8.0 mmol), KOH (673 mg, 16.0 mmol), DMF (5 mL).

Yield: 310 mg, 21%.

A yellow solid. HPLC: R_t = 5.03 min. **^{1}H-NMR** (300 MHz, DMSO-d_6): δ [ppm] = 8.45 (s, 2H), 7.74 (d, *J* = 16.1 Hz, 2H), 7.55 (d, *J* = 8.8 Hz, 4H), 7.07 (d, *J* = 16.1 Hz, 2H), 6.76 (d, *J* = 8.9 Hz, 4H), 2.97 (s, 12H). **^{13}C-NMR** (75 MHz, DMSO-d_6): δ [ppm] = 151.19, 150.96, 140.74, 135.07, 129.04, 124.24, 119.98, 112.55, 40.14. **MS** (EI, 70 eV): *m/z* = 370 [M^+]. **UV/Vis** (Ethanol): λ_{max} = 418 nm.

2,6-Bis(4-(4-methylpiperazin-1-yl)styryl)pyrazine 91d (BSc4763)

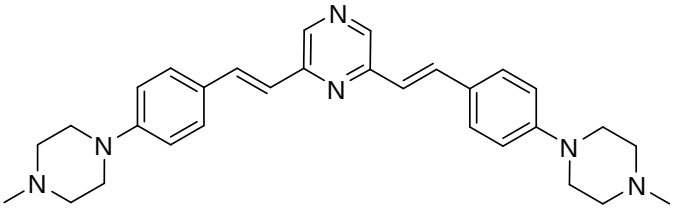

The title compound was synthesized by following the general procedure mentioned in **6.11.1.**

Reactants: 2,6-dimethylpyrazine **(89)** (500 mg, 4.62 mmol), 4-(4-methylpiperazin-1-yl)benzaldehyde **(64d)** (1.89 gm, 9.24 mmol), KOH (1.037 gm, 18.49 mmol), DMF (12 mL).

Yield: 445 mg, 20%.

A solid. **^{1}H-NMR** (500 MHz, Acetone-d_6): δ [ppm] = 8.47 (s, 2H), 7.86 (d, *J* = 16.0 Hz, 2H), 7.60 (d, *J* = 8.9 Hz, 4H), 7.16 (d, *J* = 16.0 Hz, 2H), 7.02 (d, *J* = 8.9 Hz, 4H), 3.30 (t, 8H), 2.53 (t, 8H), 2.29 (s, 6H). **^{13}C-NMR** (125 MHz, DMSO-d_6): δ [ppm] = 150.67, 141.17, 134.78, 128.92, 126.80, 121.33, 115.37, 114.29, 54.61, 47.44, 46.16. **MS** (EI, 70 eV): *m/z* = 480 [M^+].

UV/Vis (Ethanol): λ_{max} = 399 nm.

2,6-Bis((*E*)-2-(5-phenylfuran-2-yl)vinyl)pyrazine 91e (BSc4767)

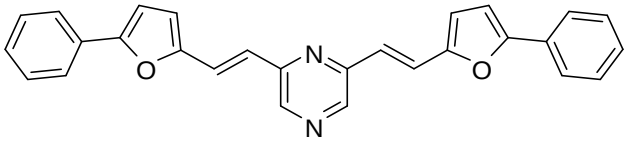

The title compound was synthesized by following the general procedure mentioned in **6.11.1.**

Reactants: 2,6-dimethylpyrazine **(89)** (108 mg, 1.0 mmol), 5-phenylfuran-2-carbaldehyde **(90b)** (344 mg,2.0 mmol), KOH (224 mg, 4.0 mmol), DMF (2 mL).

Yield: 125 mg, 30%.

A solid. **^{1}H-NMR** (500 MHz, DMSO-d_6): δ [ppm] = 8.63 (s, 2H), 7.86 (dd, *J* = 8.3, 1.1 Hz, 4H), 7.76 (d, *J* = 15.8 Hz, 2H), 7.49 (dd, *J* = 10.7, 4.9 Hz, 4H), 7.40 – 7.33 (m, 2H), 7.28 (d, *J* = 15.8 Hz, 2H), 7.14 (d, *J* = 3.5 Hz, 2H), 6.93 (d, *J* = 3.5 Hz, 2H). **^{13}C-NMR** (125 MHz, DMSO-d_6): δ [ppm] = 154.37, 152.25, 149.96, 142.49, 130.16, 129.46, 128.59, 124.31, 122.62, 122.00, 115.45, 109.15. **MS** (EI, 70 eV): *m/z* = 416 [M^+]. **UV/Vis** (Ethanol): λ_{max} = 361 nm.

2,6-Bis((*E*)-2-(1-methyl-1H-pyrrol-2-yl)vinyl)pyrazine 91f (BSc4827)

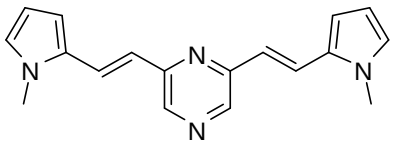

The title compound was synthesized by following the general procedure mentioned in **6.11.1.**

Reactants: 2,6-dimethylpyrazine **(89)** (250 mg, 2.3 mmol), 1-methyl-1*H*-pyrrole-2-carbaldehyde **(72a)** (468 μL, 4.6 mmol), KOH (518 mg, 9.2 mmol), DMF (5 mL).

Yield: 269 mg, 40%.

A solid. **^{1}H-NMR** (500 MHz, DMSO-d_6): δ [ppm] = 8.50 (s, 2H), 7.76 (d, *J* = 15.9 Hz, 2H), 6.96 (d, *J* = 15.9 Hz, 2H), 6.92 – 6.89 (m, 2H), 6.67 (dd, *J* = 3.8, 1.5 Hz, 2H), 6.12 – 6.09 (m, 2H), 3.77 (s, 6H). **^{13}C-NMR** (125 MHz, DMSO-d_6): δ [ppm] = 150.83, 140.65, 131.04, 126.16, 123.35, 120.38, 109.49, 108.96, 34.32. **MS** (EI, 70 eV): *m/z* = 290 [M^+]. **UV/Vis** (Ethanol): λ_{max} = 391 nm.

6.12 Synthesis of quinoxalin-2-yl derivatives

Synthetic Scheme

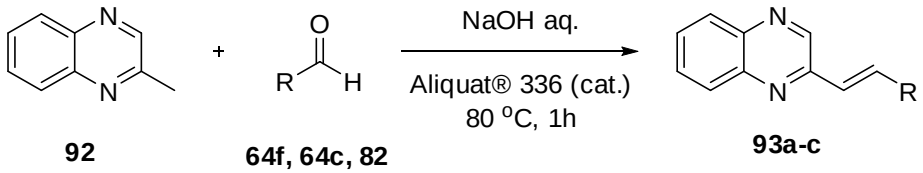

92 **64f, 64c, 82** **93a-c**

Compound	R
64f, 93a	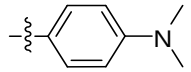
64c, 93b	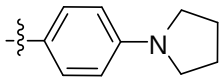
82, 93c	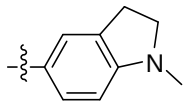

6.12.1 General procedure for the synthesis of quinoxalin-2-yl derivatives

A stirred mixture of 2-methylquinoxaline (1 eq.) and the corresponding aldehyde (1.0 eq.) in aqueous sodium hydroxide (5M, 5 mL) containing Aliquat 336 (0.1 eq.) was heated at 80 °C for 1 hour. The mixture was allowed to cool, and the precipitate was filtered off, washed with water, cold methanol and dried.

(*E*)-*N,N*-Dimethyl-4-(2-(quinoxalin-2-yl)vinyl)aniline 93a (BSc4991)

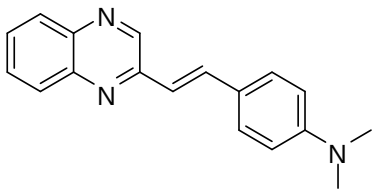

The title compound was synthesized by following the general procedure mentioned in **6.12.1.**

Reactants: 2-methylquinoxaline **(92)** (144 mg, 1.0 mmol), 4-(dimethylamino)benzaldehyde **(64f)** (149 mg, 1.0 mmol), Aliquat 336 (80 mg)

Yield: 220 mg, 80%.

A yellow solid. **HPLC**: R_t = 4.58 min. **^{1}H-NMR** (500 MHz, DMSO-d_6): δ [ppm] = 9.18 (s, 1H), 8.02 (dd, *J* = 8.32, 1.46 Hz, 1H), 8.00 (dd, *J* = 8.33, 1.42 Hz, 1H), 7.92 (d, *J* = 16.21 Hz, 1H),

7.80 (ddd, *J* = 8.36, 6.90, 1.52 Hz, 1H), 7.73 (ddd, *J* = 8.25, 6.91, 1.43 Hz, 1H), 7.61 (d, *J* = 8.83 Hz, 2H), 7.28 (d, *J* = 16.24 Hz, 1H), 6.78 (d, *J* = 8.86 Hz, 2H), 2.99 (s, 6H). **^{13}C-NMR** (125 MHz, Chloroform-d): δ [ppm] = 151.55, 151.11, 144.54, 142.47, 141.12, 136.97, 130.11, 129.07, 128.99, 128.78, 128.50, 124.15, 120.48, 112.18, 40.28. **UV/Vis** (Ethanol): λ_{max} = 428 nm.

(*E*)-2-(4-(Pyrrolidin-1-yl)styryl)quinoxaline 93b (BSc4992)

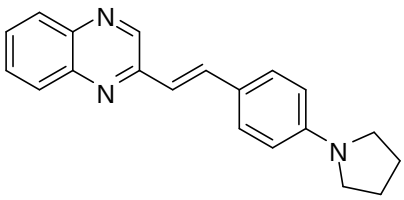

The title compound was synthesized by following the general procedure mentioned in **6.12.1.**

Reactants: 2-methylquinoxaline **(92)** (144 mg, 1.0 mmol), 4-(pyrrolidin-1-yl)benzaldehyde **(64c)** (175 mg, 1.0 mmol), Aliquat 336 (80 mg)

Yield: 234 mg, 78%.

A orange-yellow solid. HPLC: R_t = 7.77 min. **^{1}H-NMR** (500 MHz, Chloroform-d): δ [ppm] = 8.93 (s, 1H), 7.99 – 7.93 (m, 2H), 7.75 (d, *J* = 16.20 Hz, 1H), 7.64 (ddd, *J* = 8.41, 6.91, 1.51 Hz, 1H), 7.56 (ddd, *J* = 8.33, 6.91,1.45 Hz, 1H), 7.48 (d, *J* = 8.71 Hz, 2H), 7.09 (d, *J* = 16.12 Hz, 1H), 6.51 (d, *J* = 8.77 Hz, 2H), 3.40 – 3.00 (m, 4H), 2.06 – 1.81 (m, 4H). **^{13}C-NMR** (125 MHz, Chloroform-d): δ [ppm] = 151.47, 148.78, 144.62, 141.02, 137.70, 130.19, 129.31, 129.05, 128.41, 123.32, 119.36, 111.85, 47.61, 25.48. **UV/Vis** (Ethanol): λ_{max} = 440 nm.

(*E*)-2-(2-(1-Methylindolin-5-yl)vinyl)quinoxaline 93c (BSc4993)

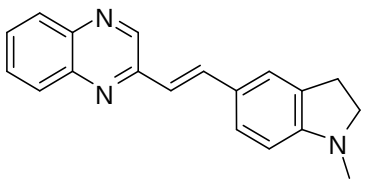

The title compound was synthesized by following the general procedure mentioned in **6.12.1.**

Reactants: 2-methylquinoxaline **(92)** (144 mg, 1.0 mmol), 1-methylindoline-5-carbaldehyde **(82)** (175 mg, 1.0 mmol), Aliquat 336 (80 mg)

Yield: 230 mg, 80%.

A greenish orange solid. HPLC: R_t = 6.14 min. **^{1}H-NMR** (500 MHz, DMSO-d_6): δ [ppm] = 9.15 (s, 1H), 8.03 – 8.00 (m, 1H), 7.99 (ddd, *J* = 8.37, 1.50, 0.59 Hz, 1H), 7.89 (d, *J* = 16.22 Hz, 1H), 7.80 (ddd, *J* = 8.37, 6.89, 1.50 Hz, 1H), 7.72 (ddd, *J* = 8.31, 6.92, 1.45 Hz, 1H), 7.51 (s, 1H), 7.44 – 7.37 (m, 1H), 7.25 (d, *J* = 16.21 Hz, 1H), 6.53 (d, *J* = 8.08 Hz, 1H), 3.40 (t, *J* = 8.32 Hz, 2H), 3.03 – 2.93 (m, 2H), 2.79 (s, 3H). **^{13}C-NMR** (125 MHz, DMSO-d_6): δ [ppm] = 151.58, 148.42, 145.14, 141.90, 140.40, 137.06, 130.22, 129.11, 128.72, 128.49, 128.39, 122.81, 119.30, 111.79, 47.23, 24.94. **UV/Vis** (Ethanol): λ_{max} = 432 nm.

6.13 Synthesis of squarine derivative

Synthetic Scheme

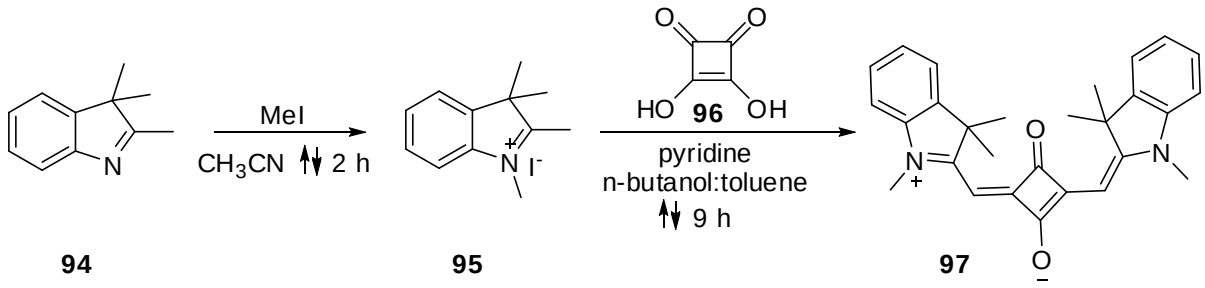

1,2,3,3-Tetramethyl-3H-indolium iodide 95

To a solution of 2,3,3-trimethyl-3H-indole **(94)** (3.7 gm, 23.2 mmol) in 15 mL dry acetonitrile was added methyl iodide (1.6 mL, 25.6 mmol) at room temperature. The solution was refluxed for 2 h and then cooled with an icebath. The pink precipitate was filtered off and washed with acetonitrile.

Yield: 5.94 gm, 85%.

A pink solid. **^{1}H-NMR** (500 MHz, DMSO-d_6): δ [ppm] = 7.93 - 7.89 (m, 1H), 7.84 - 7.81 (m, 1H), 7.65 - 7.59 (m, 2H), 3.97 (s, 3H), 2.77 (s, 3H), 1.53 (s, 6H). **^{13}C-NMR** (125 MHz, DMSO-d_6): δ [ppm] = 195.9, 142.0, 141.5, 129.2, 128.7, 123.1, 115.0, 53.8, 34.6, 21.6, 14.0.

3-Oxo-4-((1,3,3-trimethyl-3H-indolium-2-yl)methylene)-2-((*E*)-(1,3,3-trimethyl indolin-2-ylidene)methyl)cyclobut-1-enolate 97 (BSc4766)

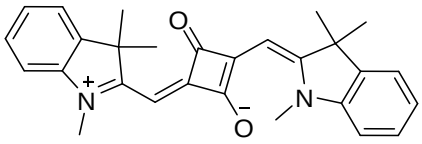

Squaric acid **(96)** (114 mg, 1.0 mmol) was heated under reflux in a mixture of toluene (10 mL) and n-butanol (10 mL). Upon dissolution of squaric acid, a pyridine (2.5 mL) solution of intermediate **(95)** (301 mg, 1 mmol) was added. After refluxing for 0.5 h, a further pyridine solution (2.5 mL) of intermediate **(95)** (301 mg, 1 mmol) was added. After refluxing for 9 hours, the reaction mixture was cooled to room temperature and the solvent removed by rotatory evaporation. The residue was treated with diethylether and the resulting precipitate was filtered. Further purification was achieved by column chromatography on silica gel using dichloromethane and methanol mixture as eluent.

Yield: 255 mg, 60%

A deep blue solid. **HPLC:** R_t = 8.30 min. **^{1}H-NMR** (500 MHz, Chloroform-d): δ [ppm] = 7.37 (d, *J* = 7.3 Hz, 2H), 7.34 (td, *J* = 7.7, 1.1 Hz, 2H), 7.17 (td, *J* = 7.5, 0.8 Hz, 2H), 7.02 (d, *J* = 7.9 Hz, 2H), 5.94 (s, 2H), 3.55 (d, *J* = 34.6 Hz, 6H), 1.80 (s, 12H). **^{13}C-NMR** (125 MHz, Chloroform-d) δ [ppm] = 186.20, 182.47, 180.18, 170.82, 143.03, 141.93, 127.81, 123.78, 122.25, 109.16, 86.81, 49.24, 30.59, 27.08. **MS** (EI, 70 eV): *m/z* = 424 [M^+]. **UV/Vis** (Ethanol): λ_{max} = 626 nm.

6.14 Synthesis of squaramides

Synthetic scheme

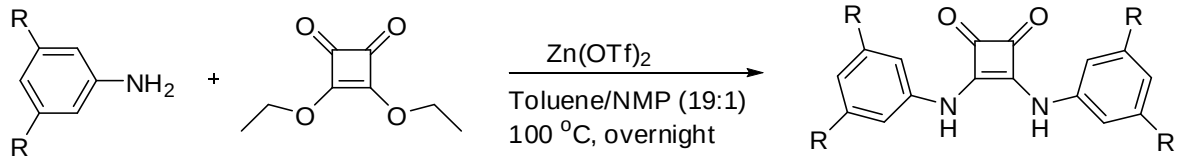

98a-b **99** **100a-b**

Compound	R
100a	-CF_3
100b	-H

6.14.1 General procedure for the synthesis of squaramides

To a toluene, *N*-methyl pyrrolidine (19:1) mixture (20 mL) was added amine (2.1 eq.), diethyl squarate (1.0 eq.) and zinc triflate (0.2 eq.). The reaction mixture was then heated to 100 ^{o}C for overnight. The resulted solid cooled down to room temperature, filtered, washed with toluene. Solid was suspended in isopropanol and refluxed overnight to remove all NMP.

3,4-bis(3,5-bis(trifluoromethyl)phenylamino)cyclobut-3-ene-1,2-dione 100a (BSc4986)

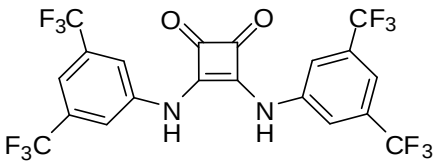

The title compound was synthesized by following the general procedure mentioned in **6.14.1.**

Reactants: 3,5-bis(trifluoromethyl)aniline **(98a)** (655 μL, 4.2 mmol), 3,4-diethoxycyclobut-3-ene-1,2-dione **(99)** (295 μL, 2.0 mmol), Zinc triflate (145 mg, 0.4 mmol)

Yield: 643 mg, 60%.

A colorless solid. **HPLC:** R_t = 8.74 min. **^{1}H-NMR** (500 MHz, Acetone-d_6): δ [ppm] =7.99 (s, 4H), 7.57 (s, 2H), 2.82 (s, 2H). **^{13}C-NMR** (125 MHz, Acetone-d_6): δ [ppm] = 184.20, 166.83, 141.59, 133.04 (q, *J* = 33 Hz), 125.27, 123.11 (q, *J* = 271 Hz), 120.05, 117.12. **MS** (EI, 70 eV): *m/z* = 536 [M^+]. **UV/Vis** (Ethanol): λ_{max} = 339 nm.

3,4-Bis(phenylamino)cyclobut-3-ene-1,2-dione 100b (BSc4987)

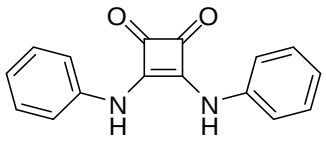

The title compound was synthesized by following the general procedure mentioned in **6.14.1.**

Reactants: Aniline **(98b)** (182 μL, 1.0 mmol), 3,4-diethoxycyclobut-3-ene-1,2-dione **(99)** (148 μL, 1.0 mmol), Zinc triflate (72 mg, 0.2 mmol)

Yield: 137 mg, 52%.

A white solid. **HPLC:** R_t = 5.66 min. **^{1}H-NMR** (300 MHz, DMSO-d_6): δ [ppm] = 9.86 (s, 2H), 7.54 – 7.46 (m, 4H), 7.44 – 7.31 (m, 4H), 7.16 – 7.01 (m, 2H). **^{13}C-NMR** (75 MHz, DMSO-d_6): δ [ppm] = 181.55, 165.60, 138.49, 129.35, 123.25, 118.43.

REFERENCES

[1] A. Alzheimer's, *Alzheimers Dement.* **2012**, *8*, 131-168.
[2] A. Wimo, B. Winblad, H. Aguero-Torres, E. von Strauss, *Alzheimer Dis. Assoc. Disord.* **2003**, *17*, 63-67.
[3] A. Burns, S. Iliffe, *BMJ* **2009**, *338*, b158-b158.
[4] S. Gauthier, B. Reisberg, M. Zaudig, R. C. Petersen, K. Ritchie, K. Broich, S. Belleville, H. Brodaty, D. Bennett, H. Chertkow, J. L. Cummings, M. de Leon, H. Feldman, M. Ganguli, H. Hampel, P. Scheltens, M. C. Tierney, P. Whitehouse, B. Winblad, *Lancet* **2006**, *367*, 1262-1270.
[5] D. Neary, J. Snowden, D. Mann, *Lancet Neurol.* **2005**, *4*, 771-780.
[6] G. C. Roman, T. K. Tatemichi, T. Erkinjuntti, J. L. Cummings, J. C. Masdeu, J. H. Garcia, L. Amaducci, J. M. Orgogozo, A. Brun, A. Hofman, et al., *Neurol.* **1993**, *43*, 250-260.
[7] K. M. Langa, N. L. Foster, E. B. Larson, *JAMA* **2004**, *292*, 2901-2908.
[8] L. S. Forno, *J. Neuropathol. Exp. Neurol.* **1996**, *55*, 259-272.
[9] R. D. Adams, C. M. Fisher, S. Hakim, R. G. Ojemann, W. H. Sweet, *N. Engl. J. Med.* **1965**, *273*, 117-126.
[10] M. G. Spillantini, M. Goedert, *Ann. N.Y. Acad. Sci.* **2000**, *920*, 16-27.
[11] R. Jakob-Roetne, H. Jacobsen, *Angew. Chem. Int. Ed.* **2009**, *48*, 3030-3059.
[12] F. Chiti, C. M. Dobson, in *Annu. Rev. Biochem., Vol. 75*, Annual Reviews, Palo Alto, **2006**, pp. 333-366.
[13] J. R. Knickman, E. K. Snell, *Health Serv. Res.* **2002**, *37*, 849-884.
[14] J. P. Seab, W. J. Jagust, S. T. Wong, M. S. Roos, B. R. Reed, T. F. Budinger, *Magn. Reson. Med.* **1988**, *8*, 200-208.
[15] D. J. Selkoe, *Physiol. Rev.* **2001**, *81*, 741-766.
[16] T. Miyakawa, S. Katsuragi, K. Araki, T. Hashimura, T. Kimura, R. Kuramoto, *Virchows. Arch. B* **1989**, *57*, 267-273.
[17] D. J. Selkoe, C. R. Abraham, in *Methods Enzymol., Vol. Volume 134* (Ed.: B. V. Richard), Academic Press, **1986**, pp. 388-404.
[18] H. Braak, E. Braak, *Neurobiol. Aging* **1997**, *18*, 351-357.
[19] D. R. Thal, U. Rub, M. Orantes, H. Braak, *Neurology* **2002**, *58*, 1791-1800.
[20] J. R. Burke, A. D. Roses, *Int. J. Neurol.* **1991**, *25-26*, 41-51.
[21] A. Goate, M. C. Chartier-Harlin, M. Mullan, J. Brown, F. Crawford, L. Fidani, L. Giuffra, A. Haynes, N. Irving, L. James, et al., *Nature* **1991**, *349*, 704-706.
[22] G. G. Glenner, C. W. Wong, *Biochem. Biophys. Res. Commun.* **1984**, *122*, 1131-1135.
[23] W. Annaert, P. Cupers, P. Saftig, B. De Strooper, *Ann. N. Y. Acad. Sci.* **2000**, *920*, 158-164.
[24] D. C. Bird TD. Pagon RA, et al., . *Vol. 1999 Sep 24*, GeneReviews™ [Internet]. Seattle (WA): University of Washington, Seattle; 1993- ed., p. [Updated 2012 Aug 2012].
[25] A. M. Saunders, W. J. Strittmatter, D. Schmechel, P. H. George-Hyslop, M. A. Pericak-Vance, S. H. Joo, B. L. Rosi, J. F. Gusella, D. R. Crapper-MacLachlan, M. J. Alberts, et al., *Neurology* **1993**, *43*, 1467-1472.
[26] W. J. Strittmatter, A. M. Saunders, D. Schmechel, M. Pericak-Vance, J. Enghild, G. S. Salvesen, A. D. Roses, *PNAS* **1993**, *90*, 1977-1981.
[27] aW. J. Strittmatter, K. H. Weisgraber, D. Y. Huang, L. M. Dong, G. S. Salvesen, M. Pericak-Vance, D. Schmechel, A. M. Saunders, D. Goldgaber, A. D. Roses, *PNAS* **1993**, *90*, 8098-8102; bD. J. Selkoe, *J. Biol. Chem.* **1996**, *271*, 18295-18298.
[28] aG. William Rebeck, J. S. Reiter, D. K. Strickland, B. T. Hyman, *Neuron* **1993**, *11*, 575-580; bT. Polvikoski, R. Sulkava, M. Haltia, K. Kainulainen, A. Vuorio, A. Verkkoniemi,

L. Niinisto, P. Halonen, K. Kontula, *N. Engl. J. Med.* **1995**, *333*, 1242-1247; cB. T. Hyman, H. L. West, G. W. Rebeck, S. V. Buldyrev, R. N. Mantegna, M. Ukleja, S. Havlin, H. E. Stanley, *PNAS* **1995**, *92*, 3586-3590.
[29] D. E. Schmechel, A. M. Saunders, W. J. Strittmatter, B. J. Crain, C. M. Hulette, S. H. Joo, M. A. Pericak-Vance, D. Goldgaber, A. D. Roses, *PNAS* **1993**, *90*, 9649-9653.
[30] L. A. Shobab, G. Y. Hsiung, H. H. Feldman, *Lancet Neurol.* **2005**, *4*, 841-852.
[31] aM. C. Morris, D. A. Evans, J. L. Bienias, C. C. Tangney, D. A. Bennett, R. S. Wilson, N. Aggarwal, J. Schneider, *Arch. Neurol.* **2003**, *60*, 940-946; bJ. A. Luchsinger, R. Mayeux, *Lancet neurology* **2004**, *3*, 579-587; cS. Kalmijn, L. J. Launer, A. Ott, J. C. M. Witteman, A. Hofman, M. M. B. Breteler, *Ann. Neurol.* **1997**, *42*, 776-782.
[32] O. Philipson, A. Lord, A. Gumucio, P. O'Callaghan, L. Lannfelt, L. N. Nilsson, *Febs J.* **2010**, *277*, 1389-1409.
[33] G. G. Glenner, C. W. Wong, *Biochem. Biophys. Res. Commun.* **1984**, *120*, 885-890.
[34] D. J. Selkoe, *Trends Cell. Biol.* **1998**, *8*, 447-453.
[35] J. T. Jarrett, E. P. Berger, P. T. Lansbury, *Biochemistry* **1993**, *32*, 4693-4697.
[36] H. V. Vinters, *Stroke* **1987**, *18*, 311-324.
[37] J. Hardy, D. Allsop, *Trends Pharmacol. Sci.*, T - ppublish.
[38] R. E. Tanzi, L. Bertram, *Cell* **2005**, *120*, 545-555.
[39] J. Hardy, D. Allsop, *Trends Pharmacol. Sci.* **1991**, *12*, 383-388.
[40] J. W. Lustbader, M. Cirilli, C. Lin, H. W. Xu, K. Takuma, N. Wang, C. Caspersen, X. Chen, S. Pollak, M. Chaney, F. Trinchese, S. Liu, F. Gunn-Moore, L. F. Lue, D. G. Walker, P. Kuppusamy, Z. L. Zewier, O. Arancio, D. Stern, S. S. Yan, H. Wu, *Science* **2004**, *304*, 448-452.
[41] B. L. Kagan, Y. Hirakura, R. Azimov, R. Azimova, M. C. Lin, *Peptides* **2002**, *23*, 1311-1315.
[42] M. E. Bamberger, G. E. Landreth, *Microsc. Res. Tech.* **2001**, *54*, 59-70.
[43] H. Kanemitsu, T. Tomiyama, H. Mori, *Neurosci. Lett.* **2003**, *350*, 113-116.
[44] W. Q. Qiu, M. F. Folstein, *Neurobiol. Aging* **2006**, *27*, 190-198.
[45] D. Lauer, A. Reichenbach, G. Birkenmeier, *Exp. Neurol.* **2001**, *167*, 385-392.
[46] B. J. Cummings, C. J. Pike, R. Shankle, C. W. Cotman, *Neurobiol. Aging* **1996**, *17*, 921-933.
[47] D. W. Dickson, H. A. Crystal, C. Bevona, W. Honer, I. Vincent, P. Davies, *Neurobiol. Aging* **1995**, *16*, 285-298.
[48] P. V. Arriagada, J. H. Growdon, E. T. Hedley-Whyte, B. T. Hyman, *Neurology* **1992**, *42*, 631-631.
[49] B. Schonheit, R. Zarski, T. G. Ohm, *Neurobiol. Aging* **2004**, *25*, 697-711.
[50] aK. Broersen, F. Rousseau, J. Schymkowitz, *Alzheimers Res Ther* **2010**, *2*, 12; bP. Seubert, C. Vigo-Pelfrey, F. Esch, M. Lee, H. Dovey, D. Davis, S. Sinha, M. Schlossmacher, J. Whaley, C. Swindlehurst, et al., *Nature* **1992**, *359*, 325-327; cJ. Hardy, D. J. Selkoe, *Science* **2002**, *297*, 353-356.
[51] C. Vigo-Pelfrey, D. Lee, P. Keim, I. Lieberburg, D. B. Schenk, *J. Neurochem.* **1993**, *61*, 1965-1968.
[52] D. G. Georganopoulou, L. Chang, J.-M. Nam, C. S. Thaxton, E. J. Mufson, W. L. Klein, C. A. Mirkin, *PNAS* **2005**, *102*, 2273-2276.
[53] L. Mucke, E. Masliah, G.-Q. Yu, M. Mallory, E. M. Rockenstein, G. Tatsuno, K. Hu, D. Kholodenko, K. Johnson-Wood, L. McConlogue, *J. Neurosci.* **2000**, *20*, 4050-4058.
[54] D. Patterson, K. Gardiner, F. T. Kao, R. Tanzi, P. Watkins, J. F. Gusella, *PNAS* **1988**, *85*, 8266-8270.
[55] W. P. Esler, M. S. Wolfe, *Science* **2001**, *293*, 1449-1454.
[56] R. Sandbrink, C. L. Masters, K. Beyreuther, *Ann. N.Y. Acad. Sci.* **1996**, *777*, 281-287.

[57] A. M. Wertkin, R. S. Turner, S. J. Pleasure, T. E. Golde, S. G. Younkin, J. Q. Trojanowski, V. M. Lee, *PNAS* **1993**, *90*, 9513-9517.
[58] F. S. Esch, P. S. Keim, E. C. Beattie, R. W. Blacher, A. R. Culwell, T. Oltersdorf, D. McClure, P. J. Ward, *Science* **1990**, *248*, 1122-1124.
[59] F. Checler, *J. Neurochem.* **1995**, *65*, 1431-1444.
[60] H. W. Querfurth, F. M. LaFerla, *N. Engl. J. Med.* **2010**, *362*, 329-344.
[61] N. Benseny-Cases, M. Cocera, J. Cladera, *Biochem. Biophys. Res. Commun.* **2007**, *361*, 916-921.
[62] T. Shirahama, A. S. Cohen, *Jour. Cell. Biol.* **1967**, *33*, 679-708.
[63] J. D. Sipe, *Annu. Rev. Biochem.* **1992**, *61*, 947-975.
[64] C. J. Barrow, M. G. Zagorski, *Science* **1991**, *253*, 179-182.
[65] C. J. Barrow, A. Yasuda, P. T. Kenny, M. G. Zagorski, *J. Mol. Biol.* **1992**, *225*, 1075-1093.
[66] E. F. Pettersen, T. D. Goddard, C. C. Huang, G. S. Couch, D. M. Greenblatt, E. C. Meng, T. E. Ferrin, *J. Comput. Chem.* **2004**, *25*, 1605-1612.
[67] T. Luhrs, C. Ritter, M. Adrian, D. Riek-Loher, B. Bohrmann, H. Dobeli, D. Schubert, R. Riek, *PNAS* **2005**, *102*, 17342-17347.
[68] A. T. Petkova, Y. Ishii, J. J. Balbach, O. N. Antzutkin, R. D. Leapman, F. Delaglio, R. Tycko, *PNAS* **2002**, *99*, 16742-16747.
[69] T. Lührs, C. Ritter, M. Adrian, D. Riek-Loher, B. Bohrmann, H. Döbeli, D. Schubert, R. Riek, *PNAS* **2005**, *102*, 17342-17347.
[70] A. T. Petkova, W.-M. Yau, R. Tycko, *Biochemistry* **2005**, *45*, 498-512.
[71] J. P. Colletier, A. Laganowsky, M. Landau, M. Zhao, A. B. Soriaga, L. Goldschmidt, D. Flot, D. Cascio, M. R. Sawaya, D. Eisenberg, *PNAS* **2011**, *108*, 16938-16943.
[72] M. D. Weingarten, A. H. Lockwood, S. Y. Hwo, M. W. Kirschner, *PNAS* **1975**, *72*, 1858-1862.
[73] B. Wolozin, P. Davies, *Ann. Neurol.* **1987**, *22*, 521-526.
[74] M. Goedert, *Ann. N. Y. Acad. Sci.* **1996**, *777*, 121-131.
[75] M. Goedert, M. G. Spillantini, R. Jakes, D. Rutherford, R. A. Crowther, *Neuron* **1989**, *3*, 519-526.
[76] L. Buee, T. Bussiere, V. Buee-Scherrer, A. Delacourte, P. R. Hof, *Brain Res. Rev.* **2000**, *33*, 95-130.
[77] R. Shin, K. Ogomori, T. Kitamoto, J. Tateishi, *Am. J. Pathol.* **1989**, *134*, 1365-1436.
[78] D. Panda, J. C. Samuel, M. Massie, S. C. Feinstein, L. Wilson, *PNAS* **2003**, *100*, 9548-9553.
[79] J. M. Bunker, L. Wilson, M. A. Jordan, S. C. Feinstein, *Mol. Biol. Cell* **2004**, *15*, 2720-2728.
[80] M. Hutton, C. L. Lendon, P. Rizzu, M. Baker, S. Froelich, H. Houlden, S. Pickering-Brown, S. Chakraverty, A. Isaacs, A. Grover, J. Hackett, J. Adamson, S. Lincoln, D. Dickson, P. Davies, R. C. Petersen, M. Stevens, E. de Graaff, E. Wauters, J. van Baren, M. Hillebrand, M. Joosse, J. M. Kwon, P. Nowotny, L. K. Che, J. Norton, J. C. Morris, L. A. Reed, J. Trojanowski, H. Basun, L. Lannfelt, M. Neystat, S. Fahn, F. Dark, T. Tannenberg, P. R. Dodd, N. Hayward, J. B. J. Kwok, P. R. Schofield, A. Andreadis, J. Snowden, D. Craufurd, D. Neary, F. Owen, B. A. Oostra, J. Hardy, A. Goate, J. van Swieten, D. Mann, T. Lynch, P. Heutink, *Nature* **1998**, *393*, 702-705.
[81] D. Munoz-Garcia, S. K. Ludwin, *Ann. Neurol.* **1984**, *16*, 467-480.
[82] Q. Bai, E. A. Burton, *Biochim. Biophys. Acta* **2011**, *1812*, 353-363.
[83] C. X. Gong, F. Liu, I. Grundke-Iqbal, K. Iqbal, *J. Neural. Transm.* **2005**, *112*, 813-838.
[84] E. Kopke, Y. C. Tung, S. Shaikh, A. C. Alonso, K. Iqbal, I. Grundke-Iqbal, *J. Biol. Chem.* **1993**, *268*, 24374-24384.

[85] aE. M. Mandelkow, G. Drewes, J. Biernat, N. Gustke, J. Van Lint, J. R. Vandenheede, E. Mandelkow, *FEBS Lett.* **1992**, *314*, 315-321; bS.-D. Yang, J.-S. Song, J.-S. Yu, S.-G. Shiah, *J. Neurochem.* **1993**, *61*, 1742-1747.
[86] S. Takahashi, T. Saito, S. Hisanaga, H. C. Pant, A. B. Kulkarni, *J. Biol. Chem.* **2003**, *278*, 10506-10515.
[87] G. Drewes, B. Trinczek, S. Illenberger, J. Biernat, G. Schmitt-Ulms, H. E. Meyer, E. M. Mandelkow, E. Mandelkow, *J. Biol. Chem.* **1995**, *270*, 7679-7688.
[88] G. Li, H. Yin, J. Kuret, *J. Biol. Chem.* **2004**, *279*, 15938-15945.
[89] D. P. Hanger, B. H. Anderton, W. Noble, *Trends Mol. Med.* **2009**, *15*, 112-119.
[90] aT. Li, C. Hawkes, H. Y. Qureshi, S. Kar, H. K. Paudel, *Biochemistry* **2006**, *45*, 3134-3145; bA. Sengupta, Q. Wu, I. Grundke-Iqbal, K. Iqbal, T. J. Singh, *Mol. Cell Biochem.* **1997**, *167*, 99-105.
[91] C. Bancher, C. Brunner, H. Lassmann, H. Budka, K. Jellinger, G. Wiche, F. Seitelberger, I. Grundke-Iqbal, K. Iqbal, H. M. Wisniewski, *Brain Res.* **1989**, *477*, 90-99.
[92] M. Galván, J. P. David, A. Delacourte, J. Luna, R. Mena, *J. Alzheimers Dis.* **2001**, *3*, 417-425.
[93] P. Friedhoff, M. von Bergen, E.-M. Mandelkow, E. Mandelkow, *Biochim. Biophys. Acta, Mol. Basis Dis.* **2000**, *1502*, 122-132.
[94] aP. Friedhoff, A. Schneider, E.-M. Mandelkow, E. Mandelkow, *Biochemistry* **1998**, *37*, 10223-10230; bH. Wille, G. Drewes, J. Biernat, E. M. Mandelkow, E. Mandelkow, *J. Cell. Biol.* **1992**, *118*, 573-584; cM. E. King, T. C. Gamblin, J. Kuret, L. I. Binder, *J. Neurochem.* **2000**, *74*, 1749-1757; dS. Hiraoka, T. M. Yao, K. Minoura, K. Tomoo, M. Sumida, T. Taniguchi, T. Ishida, *Biochem. Biophys. Res. Commun.* **2004**, *315*, 659-663.
[95] P. Friedhoff, M. von Bergen, E.-M. Mandelkow, P. Davies, E. Mandelkow, *PNAS* **1998**, *95*, 15712-15717.
[96] S. Barghorn, E. Mandelkow, *Biochemistry* **2002**, *41*, 14885-14896.
[97] C. M. Wischik, R. A. Crowther, M. Stewart, M. Roth, *J. Cell. Biol.* **1985**, *100*, 1905-1912.
[98] aB. Bulic, M. Pickhardt, E. Mandelkow, *J. Med. Chem.* **2013**; bB. Bulic, M. Pickhardt, E. M. Mandelkow, E. Mandelkow, *Neuropharmacol.* **2010**, *59*, 276-289.
[99] J. Busciglio, A. Lorenzo, J. Yeh, B. A. Yankner, *Neuron* **1995**, *14*, 879-888.
[100] aA. Alvarez, R. Toro, A. Caceres, R. B. Maccioni, *FEBS Lett.* **1999**, *459*, 421-426; bA. Takashima, K. Noguchi, K. Sato, T. Hoshino, K. Imahori, *PNAS* **1993**, *90*, 7789-7793.
[101] J. C. Blanks, D. R. Hinton, A. A. Sadun, C. A. Miller, *Brain Res.* **1989**, *501*, 364-372.
[102] I. Greeve, D. Kretzschmar, J. A. Tschape, A. Beyn, C. Brellinger, M. Schweizer, R. M. Nitsch, R. Reifegerste, *J. Neurosci.* **2004**, *24*, 3899-3906.
[103] M. Koronyo-Hamaoui, Y. Koronyo, A. V. Ljubimov, C. A. Miller, M. K. Ko, K. L. Black, M. Schwartz, D. L. Farkas, *NeuroImage* **2011**, *54, Supplement 1*, S204-S217.
[104] N. Gupta, J. Fong, L. C. Ang, Y. H. Yücel, *Can. J. Ophthalmol.* **2008**, *43*, 53-60.
[105] C. Schon, N. A. Hoffmann, S. M. Ochs, S. Burgold, S. Filser, S. Steinbach, M. W. Seeliger, T. Arzberger, M. Goedert, H. A. Kretzschmar, B. Schmidt, J. Herms, *PLoS ONE* **2012**, *7*, e53547.
[106] W. Ying, *Future Neurology* **2008**, *3*, 1-4.
[107] aS. E. Arnold, E. B. Lee, P. J. Moberg, L. Stutzbach, H. Kazi, L. Y. Han, V. M. Lee, J. Q. Trojanowski, *Ann. Neurol.* **2010**, *67*, 462-469; bD. Kieser, *Technische Universität Darmstadt* **2011**; cA. Bolander, D. Kieser, C. Voss, S. Bauer, C. Schon, S. Burgold, T. Bittner, J. Holzer, R. Heyny-von Haussen, G. Mall, V. Goetschy, C. Czech, H. Knust, R. Berger, J. Herms, I. Hilger, B. Schmidt, *J. Med. Chem.* **2012**, *55*, 9170-9180.
[108] J. A. Besson, J. R. Crawford, N. T. Evans, H. G. Gemmell, D. Roeda, *J. R. Soc. Med.* **1992**, *85*, 231-234.
[109] J. M. Ollinger, J. A. Fessler, *IEEE Signal Processing Magazine* **1997**, *14*, 43-55.

[110] M. Raichle, in *Brain Metastasis, Vol. 2* (Eds.: L. Weiss, H. Gilbert, J. Posner), Springer Netherlands, **1980**, pp. 246-253.
[111] T. T. Wager, R. Y. Chandrasekaran, X. Hou, M. D. Troutman, P. R. Verhoest, A. Villalobos, Y. Will, *ACS Chem. Neurosci.* **2010**, *1*, 420-434.
[112] A. K. Schutz, A. Soragni, S. Hornemann, A. Aguzzi, M. Ernst, A. Bockmann, B. H. Meier, *Angew. Chem. Int. Ed.* **2011**, *50*, 5956-5960.
[113] W. E. Klunk, J. W. Pettegrew, D. J. Abraham, *J. Histochem. Cytochem.* **1989**, *37*, 1273-1281.
[114] P. Frid, S. V. Anisimov, N. Popovic, *Brain Res. Rev.* **2007**, *53*, 135-160.
[115] W. E. Klunk, M. L. Debnath, J. W. Pettegrew, *Neurobiol. Aging* **1995**, *16*, 541-548.
[116] Mathis CA, Mahmood K, Debnath ML, et. al., *J. Label Comp. Radiopharm.* **1997**, *40*, 94–95.
[117] aK. Sato, M. Higuchi, N. Iwata, T. C. Saido, K. Sasamoto, *Eur. J. Med. Chem.* **2004**, *39*, 573-578; bD. M. Skovronsky, B. Zhang, M.-P. Kung, H. F. Kung, J. Q. Trojanowski, V. M.-Y. Lee, *PNAS* **2000**, *97*, 7609-7614; cW. E. Klunk, B. J. Bacskai, C. A. Mathis, S. T. Kajdasz, M. E. McLellan, M. P. Frosch, M. L. Debnath, D. P. Holt, Y. M. Wang, B. T. Hyman, *J. Neuropathol. Exp. Neurol.* **2002**, *61*, 797-805.
[118] Z. P. Zhuang, M. P. Kung, C. Hou, D. M. Skovronsky, T. L. Gur, K. Plossl, J. Q. Trojanowski, V. M. Y. Lee, H. F. Kung, *J. Med. Chem.* **2001**, *44*, 1905-1914.
[119] aA. S. Crystal, B. I. Giasson, A. Crowe, M. P. Kung, Z. P. Zhuang, J. Q. Trojanowski, V. M. Y. Lee, *J. Neurochem.* **2003**, *86*, 1359-1368; bW. E. Klunk, B. J. Bacskai, C. A. Mathis, S. T. Kajdasz, M. E. McLellan, M. P. Frosch, M. L. Debnath, D. P. Holt, Y. Wang, B. T. Hyman, *J. Neuropathol. Exp. Neurol.* **2002**, *61*, 797-805.
[120] D. P. Flaherty, S. M. Walsh, T. Kiyota, Y. Dong, T. Ikezu, J. L. Vennerstrom, *J. Med. Chem.* **2007**, *50*, 4986-4992.
[121] Z. Zha, S. R. Choi, K. Ploessl, B. P. Lieberman, W. Qu, F. Hefti, M. Mintun, D. Skovronsky, H. F. Kung, *J. Med. Chem.* **2011**, *54*, 8085-8098.
[122] aH. Naiki, K. Higuchi, M. Hosokawa, T. Takeda, *Anal. Biochem.* **1989**, *177*, 244-249; bH. LeVine, 3rd, *Protein Sci.* **1993**, *2*, 404-410.
[123] aM. Biancalana, S. Koide, *Biochim. Biophys. Acta* **2010**, *1804*, 1405-1412; bW. Dzwolak, M. Pecul, *FEBS Lett.* **2005**, *579*, 6601-6603.
[124] W. E. Klunk, Y. Wang, G. F. Huang, M. L. Debnath, D. P. Holt, C. A. Mathis, *Life Sci.* **2001**, *69*, 1471-1484.
[125] J. Wei, C. Wu, D. Lankin, A. Gulrati, T. Valyi-Nagy, E. Cochran, V. Pike, A. Kozikowski, Y. Wang, *Curr. Alzheimer Res.* **2005**, *2*, 109-114.
[126] Z.-P. Zhuang, M.-P. Kung, C. Hou, K. Plössl, D. Skovronsky, T. L. Gur, J. Q. Trojanowski, V. M. Y. Lee, H. F. Kung, *Nucl. Med. Biol.* **2001**, *28*, 887-894.
[127] M. P. Kung, C. Hou, Z. P. Zhuang, B. Zhang, D. Skovronsky, J. Q. Trojanowski, V. M. Lee, H. F. Kung, *Brain Res.* **2002**, *956*, 202-210.
[128] L. Cai, J. S. Liow, S. S. Zoghbi, J. Cuevas, C. Baetas, J. Hong, H. U. Shetty, N. M. Seneca, A. K. Brown, R. Gladding, S. S. Temme, M. M. Herman, R. B. Innis, V. W. Pike, *J. Med. Chem.* **2008**, *51*, 148-158.
[129] M. Koole, D. M. Lewis, C. Buckley, N. Nelissen, M. Vandenbulcke, D. J. Brooks, R. Vandenberghe, K. Van Laere, *J. Nucl. Med.* **2009**, *50*, 818-822.
[130] C. A. Mathis, Y. Wang, D. P. Holt, G. F. Huang, M. L. Debnath, W. E. Klunk, *J. Med. Chem.* **2003**, *46*, 2740-2754.
[131] W. E. Klunk, H. Engler, A. Nordberg, Y. Wang, G. Blomqvist, D. P. Holt, M. Bergström, I. Savitcheva, G.-F. Huang, S. Estrada, B. Ausén, M. L. Debnath, J. Barletta, J. C. Price, J. Sandell, B. J. Lopresti, A. Wall, P. Koivisto, G. Antoni, C. A. Mathis, B. Långström, *Ann. Neurol.* **2004**, *55*, 306-319.

[132] W. E. Klunk, B. J. Lopresti, M. D. Ikonomovic, I. M. Lefterov, R. P. Koldamova, E. E. Abrahamson, M. L. Debnath, D. P. Holt, G. F. Huang, L. Shao, S. T. DeKosky, J. C. Price, C. A. Mathis, *J. Neurosci.* **2005**, *25*, 10598-10606.
[133] A. E. Johnson, F. Jeppsson, J. Sandell, D. Wensbo, J. A. Neelissen, A. Jureus, P. Strom, H. Norman, L. Farde, S. P. Svensson, *J. Neurochem.* **2009**, *108*, 1177-1186.
[134] N. P. Verhoeff, A. A. Wilson, S. Takeshita, L. Trop, D. Hussey, K. Singh, H. F. Kung, M. P. Kung, S. Houle, *The American journal of geriatric psychiatry* **2004**, *12*, 584-595.
[135] C. C. Rowe, U. Ackerman, W. Browne, R. Mulligan, K. L. Pike, G. O'Keefe, H. Tochon-Danguy, G. Chan, S. U. Berlangieri, G. Jones, K. L. Dickinson-Rowe, H. P. Kung, W. Zhang, M. P. Kung, D. Skovronsky, T. Dyrks, G. Holl, S. Krause, M. Friebe, L. Lehman, S. Lindemann, L. M. Dinkelborg, C. L. Masters, V. L. Villemagne, *Lancet neurol.* **2008**, *7*, 129-135.
[136] Y. Kudo, N. Okamura, S. Furumoto, M. Tashiro, K. Furukawa, M. Maruyama, M. Itoh, R. Iwata, K. Yanai, H. Arai, *J. Nucl. Med.* **2007**, *48*, 553-561.
[137] K. Furukawa, S. Ikeda, N. Okamura, M. Tashiro, N. Tomita, S. Furumoto, R. Iwata, K. Yanai, Y. Kudo, H. Arai, *Circulation* **2012**, *125*, 556-557.
[138] E. Teng, V. Kepe, S. A. Frautschy, J. Liu, N. Satyamurthy, F. Yang, P. P. Chen, G. B. Cole, M. R. Jones, S. C. Huang, D. G. Flood, S. P. Trusko, G. W. Small, G. M. Cole, J. R. Barrio, *Neurobiol. Dis.* **2011**, *43*, 565-575.
[139] R. E. Majocha, J. M. Reno, R. P. Friedland, C. VanHaight, L. R. Lyle, C. A. Marotta, *J. Nucl. Med.* **1992**, *33*, 2184-2189.
[140] L. B. Lovat, A. A. O'Brien, S. F. Armstrong, S. Madhoo, C. J. Bulpitt, M. N. Rossor, M. B. Pepys, P. N. Hawkins, *Alzheimer Dis. Assoc. Disord.* **1998**, *12*, 208-210.
[141] Y. Saito, J. Buciak, J. Yang, W. M. Pardridge, *PNAS* **1995**, *92*, 10227-10231.
[142] N. Okamura, T. Suemoto, S. Furumoto, M. Suzuki, H. Shimadzu, H. Akatsu, T. Yamamoto, H. Fujiwara, M. Nemoto, M. Maruyama, H. Arai, K. Yanai, T. Sawada, Y. Kudo, *J. Neurosci.* **2005**, *25*, 10857-10862.
[143] M. T. Fodero-Tavoletti, N. Okamura, S. Furumoto, R. S. Mulligan, A. R. Connor, C. A. McLean, D. Cao, A. Rigopoulos, G. A. Cartwright, G. O'Keefe, S. Gong, P. A. Adlard, K. J. Barnham, C. C. Rowe, C. L. Masters, Y. Kudo, R. Cappai, K. Yanai, V. L. Villemagne, *Brain* **2011**, *134*, 1089-1100.
[144] K. Matsumura, M. Ono, S. Hayashi, H. Kimura, Y. Okamoto, M. Ihara, R. Takahashi, H. Mori, H. Saji, *MedChemComm* **2011**, *2*, 596-600.
[145] K. Matsumura, M. Ono, H. Kimura, M. Ueda, Y. Nakamoto, K. Togashi, Y. Okamoto, M. Ihara, R. Takahashi, H. Saji, *ACS Med. Chem. Lett.* **2012**, *3*, 58-62.
[146] M. Ono, S. Hayashi, K. Matsumura, H. Kimura, Y. Okamoto, M. Ihara, R. Takahashi, H. Mori, H. Saji, *ACS Chem. Neurosci.* **2011**, *2*, 269-275.
[147] H. Watanabe, M. Ono, H. Kimura, K. Matsumura, M. Yoshimura, Y. Okamoto, M. Ihara, R. Takahashi, H. Saji, *Bioorg. Med. Chem. Lett.* **2012**, *22*, 5700-5703.
[148] W. Zhang, J. Arteaga, D. K. Cashion, G. Chen, U. Gangadharmath, L. F. Gomez, D. Kasi, C. Lam, Q. Liang, C. Liu, V. P. Mocharla, F. Mu, A. Sinha, A. K. Szardenings, E. Wang, J. C. Walsh, C. Xia, C. Yu, T. Zhao, H. C. Kolb, *J. Alzheimers Dis.* **2012**, *31*, 601-612.
[149] X. Shao, G. M. Carpenter, T. J. Desmond, P. Sherman, C. A. Quesada, M. Fawaz, A. F. Brooks, M. R. Kilbourn, R. L. Albin, K. A. Frey, P. J. H. Scott, *ACS Med. Chem. Lett.* **2012**, *3*, 936-941.
[150] P. T. So, C. Y. Dong, B. R. Masters, K. M. Berland, *Annu. Rev. Biomed. Eng.* **2000**, *2*, 399-429.
[151] B. P. Espósito, S. Epsztejn, W. Breuer, Z. I. Cabantchik, *Anal. Biochem.* **2002**, *304*, 1-18.
[152] E. Betzig, G. H. Patterson, R. Sougrat, O. W. Lindwasser, S. Olenych, J. S. Bonifacino, M. W. Davidson, J. Lippincott-Schwartz, H. F. Hess, *Science* **2006**, *313*, 1642-1645.

[153] M. J. Rust, M. Bates, X. Zhuang, *Nat. Methods* **2006**, *3*, 793-795.
[154] R. Weissleder, U. Mahmood, *Radiology* **2001**, *219*, 316-333.
[155] aM. R. Longmire, M. Ogawa, Y. Hama, N. Kosaka, C. A. Regino, P. L. Choyke, H. Kobayashi, *Bioconjug. Chem.* **2008**, *19*, 1735-1742; bY. Hama, Y. Urano, Y. Koyama, M. Bernardo, P. L. Choyke, H. Kobayashi, *Bioconjug. Chem.* **2006**, *17*, 1426-1431.
[156] H. Kobayashi, M. Ogawa, R. Alford, P. L. Choyke, Y. Urano, *Chem. Rev.* **2010**, *110*, 2620-2640.
[157] E. E. Nesterov, J. Skoch, B. T. Hyman, W. E. Klunk, B. J. Bacskai, T. M. Swager, *Angew. Chem. Int. Ed.* **2005**, *44*, 5452-5456.
[158] M. Ono, M. Ishikawa, H. Kimura, S. Hayashi, K. Matsumura, H. Watanabe, Y. Shimizu, Y. Cheng, M. Cui, H. Kawashima, H. Saji, *Bioorg. Med. Chem. Lett.* **2010**, *20*, 3885-3888.
[159] Q. A. Li, J. S. Lee, C. Ha, C. B. Park, G. Yang, W. B. Gan, Y. T. Chang, *Angew. Chem. Int. Ed.* **2004**, *43*, 6331-6335.
[160] Q. Li, J. Min, Y.-H. Ahn, J. Namm, E. M. Kim, R. Lui, H. Y. Kim, Y. Ji, H. Wu, T. Wisniewski, Y.-T. Chang, *ChemBioChem* **2007**, *8*, 1679-1687.
[161] C. Ran, X. Xu, S. B. Raymond, B. J. Ferrara, K. Neal, B. J. Bacskai, Z. Medarova, A. Moore, *J. Am. Chem. Soc.* **2009**, *131*, 15257-15261.
[162] M. Hintersteiner, A. Enz, P. Frey, A. L. Jaton, W. Kinzy, R. Kneuer, U. Neumann, M. Rudin, M. Staufenbiel, M. Stoeckli, K. H. Wiederhold, H. U. Gremlich, *Nature biotechnology* **2005**, *23*, 577-583.
[163] M. Ono, H. Watanabe, H. Kimura, H. Saji, *ACS Chem. Neurosci.* **2012**, *3*, 319-324.
[164] Y. Koronyo, B. C. Salumbides, K. L. Black, M. Koronyo-Hamaoui, *Neurodegener. Dis.* **2012**, *10*, 285-293.
[165] R. A. Prentis, Y. Lis, S. R. Walker, *Br. J. Clin. Pharmacol.* **1988**, *25*, 387-396.
[166] G. J. Lieschke, P. D. Currie, *Nat. Rev. Genet.* **2007**, *8*, 353-367.
[167] aE. McGowan, F. Pickford, J. Kim, L. Onstead, J. Eriksen, C. Yu, L. Skipper, M. P. Murphy, J. Beard, P. Das, K. Jansen, M. Delucia, W. L. Lin, G. Dolios, R. Wang, C. B. Eckman, D. W. Dickson, M. Hutton, J. Hardy, T. Golde, *Neuron* **2005**, *47*, 191-199; bM. Knobloch, U. Konietzko, D. C. Krebs, R. M. Nitsch, *Neurobiol. Aging* **2007**, *28*, 1297-1306; cA. Ronnback, S. Zhu, K. Dillner, M. Aoki, L. Lilius, J. Naslund, B. Winblad, C. Graff, *Neurobiol. Aging* **2011**, *32*, 280-292; dA. Lord, H. Kalimo, C. Eckman, X.-Q. Zhang, L. Lannfelt, L. N. G. Nilsson, *Neurobiol. Aging* **2006**, *27*, 67-77; eM. C. Herzig, D. T. Winkler, P. Burgermeister, M. Pfeifer, E. Kohler, S. D. Schmidt, S. Danner, D. Abramowski, C. Sturchler-Pierrat, K. Burki, S. G. van Duinen, M. L. C. Maat-Schieman, M. Staufenbiel, P. M. Mathews, M. Jucker, *Nat. Neurosci.* **2004**, *7*, 954-960; fR. Radde, T. Bolmont, S. A. Kaeser, J. Coomaraswamy, D. Lindau, L. Stoltze, M. E. Calhoun, F. Jaggi, H. Wolburg, S. Gengler, C. Haass, B. Ghetti, C. Czech, C. Holscher, P. M. Mathews, M. Jucker, *EMBO Rep* **2006**, *7*, 940-946; gC. Sturchler-Pierrat, D. Abramowski, M. Duke, K.-H. Wiederhold, C. Mistl, S. Rothacher, B. Ledermann, K. Bürki, P. Frey, P. A. Paganetti, C. Waridel, M. E. Calhoun, M. Jucker, A. Probst, M. Staufenbiel, B. Sommer, *PNAS* **1997**, *94*, 13287-13292; hE. B. Lee, B. Zhang, K. Liu, E. A. Greenbaum, R. W. Doms, J. Q. Trojanowski, V. M.-Y. Lee, *J. Cell. Biol.* **2005**, *168*, 291-302; iL. Cao, B. R. Schrank, S. Rodriguez, E. G. Benz, T. W. Moulia, G. T. Rickenbacher, A. C. Gomez, Y. Levites, S. R. Edwards, T. E. Golde, B. T. Hyman, G. Barnea, M. W. Albers, *Nat. Commun.* **2012**, *3*, 1009.
[168] aL. M. Ittner, Y. D. Ke, F. Delerue, M. Bi, A. Gladbach, J. van Eersel, H. Wolfing, B. C. Chieng, M. J. Christie, I. A. Napier, A. Eckert, M. Staufenbiel, E. Hardeman, J. Gotz, *Cell* **2010**, *142*, 387-397; bL. M. Ittner, T. Fath, Y. D. Ke, M. Bi, J. van Eersel, K. M. Li, P. Gunning, J. Götz, *PNAS* **2008**, *105*, 15997-16002; cS. Sato, J. Xu, S. Okuyama, L. B. Martinez, S. M. Walsh, M. T. Jacobsen, R. J. Swan, J. D. Schlautman, P. Ciborowski, T.

Ikezu, *J. Neurosci.* **2008**, *28*, 14511-14521; dK. Schindowski, A. Bretteville, K. Leroy, S. Begard, J. P. Brion, M. Hamdane, L. Buee, *Am. J. Pathol.* **2006**, *169*, 599-616; eD. Terwel, R. Lasrado, J. Snauwaert, E. Vandeweert, C. Van Haesendonck, P. Borghgraef, F. Van Leuven, *J. Biol. Chem.* **2005**, *280*, 3963-3973; fB. Zhang, M. Higuchi, Y. Yoshiyama, T. Ishihara, M. S. Forman, D. Martinez, S. Joyce, J. Q. Trojanowski, V. M. Lee, *J. Neurosci.* **2004**, *24*, 4657-4667; gM. Higuchi, T. Ishihara, B. Zhang, M. Hong, A. Andreadis, J. Trojanowski, V. M. Lee, *Neuron* **2002**, *35*, 433-446.

[169] aT. Arendt, J. Stieler, A. M. Strijkstra, R. A. Hut, J. Rüdiger, E. A. Van der Zee, T. Harkany, M. Holzer, W. Härtig, *J. Neurosci.* **2003**, *23*, 6972-6981; bW. Hartig, J. Stieler, A. S. Boerema, J. Wolf, U. Schmidt, J. Weissfuss, T. Bullmann, A. M. Strijkstra, T. Arendt, *Eur. J. Neurosci.* **2007**, *25*, 69-80.

[170] L. Gasparini, R. Anthony Crowther, K. R. Martin, N. Berg, M. Coleman, M. Goedert, M. G. Spillantini, *Neurobiol. Aging* **2011**, *32*, 419-433.

[171] H. L. Stickney, M. J. Barresi, S. H. Devoto, *Dev. Dynam.* **2000**, *219*, 287-303.

[172] J. T. Shin, M. C. Fishman, *Annu. Rev. Genomics Hum. Genet.* **2002**, *3*, 311-340.

[173] aH. Feitsma, E. Cuppen, *Molecular cancer research : MCR* **2008**, *6*, 685-694; bJ. D. Clifton, E. Lucumi, M. C. Myers, A. Napper, K. Hama, S. A. Farber, A. B. Smith, III, D. M. Huryn, S. L. Diamond, M. Pack, *PLoS ONE* **2010**, *5*, e12386; cT. J. Chico, P. W. Ingham, D. C. Crossman, *Trends Cardiovasc. Med.* **2008**, *18*, 150-155; dM. Newman, G. Verdile, R. N. Martins, M. Lardelli, *Biochim. Biophys. Acta* **2011**, *1812*, 346-352.

[174] R. Ulrich, S. H. Friend, *Nature Rev.* **2002**, *1*, 84-88.

Upendra Rao Anumala
Max-Planck-Straße 4
64807 Dieburg

Darmstadt, 25.07.2013

Erklärung

Ich erkläre hiermit, dass ich meine Dissertation selbständig und nur mit den angegebenen Hilfsmitteln angefertigt habe.

Upendra Rao Anumala

Upendra Rao Anumala
Max-Planck-Straße 4
64807 Dieburg

Darmstadt, 25.07.2013

Erklärung

Ich erkläre hiermit, noch keinen Promotionsversuch unternommen zu haben.

Upendra Rao Anumala

Curriculum Vitae

Personal Data

Name:	Upendra Rao Anumala
Date of Birth:	11th Aug 1981
Place of Birth:	Nelakondpally, Andhra Pradesh, India
Nationality:	Indian
Marital Status:	Single

Educational Background

4/2001 – 4/2004	Bachelor of Science Institution: Kakatiya University, Warangal, India
5/2004 – 5/2006	Master of Science Institution: Osmania University, Hyderabad, India
2/2010 - Present	Doctoral thesis under the supervision of Prof. Dr. Boris Schmidt at Technische Universitat Darmstadt, Darmstadt, Germany

Work Experience

5/2006 – 12/2007	Dr. Reddy's Laboratories Ltd, Hyderabad, India
12/2007 – 8/2008	Inogent Laboratories Private Limited, Hyderabad, India
12/2008 – 8/2009	GlaxoSmithKline, Cork, Ireland